frontiers | Research Topics

Remote sensing for ecosystem studies

Edited by
Pavan Kumar, Manoj Kumar, Ram Kumar Singh,
Meenu Rani and Yonghao Xu

Coordinated by
Manmohan Dobriyal

Published in
Frontiers in Environmental Science
Frontiers in Remote Sensing
Frontiers in Ecology and Evolution
Frontiers in Earth Science

ISSN 1664-8714
ISBN 978-2-8325-4027-5
DOI 10.3389/978-2-8325-4027-5

About Frontiers

Frontiers is more than just an open access publisher of scholarly articles: it is a pioneering approach to the world of academia, radically improving the way scholarly research is managed. The grand vision of Frontiers is a world where all people have an equal opportunity to seek, share and generate knowledge. Frontiers provides immediate and permanent online open access to all its publications, but this alone is not enough to realize our grand goals.

Frontiers journal series

The Frontiers journal series is a multi-tier and interdisciplinary set of open-access, online journals, promising a paradigm shift from the current review, selection and dissemination processes in academic publishing. All Frontiers journals are driven by researchers for researchers; therefore, they constitute a service to the scholarly community. At the same time, the *Frontiers journal series* operates on a revolutionary invention, the tiered publishing system, initially addressing specific communities of scholars, and gradually climbing up to broader public understanding, thus serving the interests of the lay society, too.

Dedication to quality

Each Frontiers article is a landmark of the highest quality, thanks to genuinely collaborative interactions between authors and review editors, who include some of the world's best academicians. Research must be certified by peers before entering a stream of knowledge that may eventually reach the public - and shape society; therefore, Frontiers only applies the most rigorous and unbiased reviews. Frontiers revolutionizes research publishing by freely delivering the most outstanding research, evaluated with no bias from both the academic and social point of view. By applying the most advanced information technologies, Frontiers is catapulting scholarly publishing into a new generation.

What are Frontiers Research Topics?

Frontiers Research Topics are very popular trademarks of the *Frontiers journals series*: they are collections of at least ten articles, all centered on a particular subject. With their unique mix of varied contributions from Original Research to Review Articles, Frontiers Research Topics unify the most influential researchers, the latest key findings and historical advances in a hot research area.

Find out more on how to host your own Frontiers Research Topic or contribute to one as an author by contacting the Frontiers editorial office: frontiersin.org/about/contact

Remote sensing for ecosystem studies

Topic editors

Pavan Kumar — Rani Lakshmi Bai Central Agricultural University, India
Manoj Kumar — Forest Research Institute (FRI), India
Ram Kumar Singh — TERI School of Advanced Studies (TERI SAS), India
Meenu Rani — Kumaun University, India
Yonghao Xu — Linköping University, Sweden

Topic Coordinator

Manmohan Dobriyal — Rani Lakshmi Bai Central Agricultural University, India

Citation

Kumar, P., Kumar, M., Singh, R. K., Rani, M., Xu, Y., Dobriyal, M., eds. (2023). *Remote sensing for ecosystem studies*. Lausanne: Frontiers Media SA.
doi: 10.3389/978-2-8325-4027-5

Table of contents

frontiers | Frontiers in Environmental Science

TYPE Original Research
PUBLISHED 04 January 2023
DOI 10.3389/fenvs.2022.1071631

OPEN ACCESS

EDITED BY
Yonghao Xu,
Institute of Advanced Research in Artificial Intelligence (IARAI), Austria

REVIEWED BY
Xianhua Guo,
Chongqing Three Gorges University, China
Zhang Shengwei,
Inner Mongolia Agricultural University, China
Honghai Kuang,
Southwest University, China

*CORRESPONDENCE
Xueli Chang,
xlchang@126.com

SPECIALTY SECTION
This article was submitted to Environmental Informatics and Remote Sensing, a section of the journal Frontiers in Environmental Science

RECEIVED 16 October 2022
ACCEPTED 02 December 2022
PUBLISHED 04 January 2023

CITATION
Dong C, Qiao R, Yang Z, Luo L and Chang X (2023), Eco-environmental quality assessment of the artificial oasis of Ningxia section of the Yellow River with the MRSEI approach.
Front. Environ. Sci. 10:1071631.
doi: 10.3389/fenvs.2022.1071631

Eco-environmental quality assessment of the artificial oasis of Ningxia section of the Yellow River with the MRSEI approach

Chunyuan Dong[1], Rongrong Qiao[2], Zhicheng Yang[1,3], Lihui Luo[3] and Xueli Chang[1]*

[1]School of Resources and Environmental Engineering, Ludong University, Yantai, China, [2]School of Life Sciences, Nanjing University, Nanjing, China, [3]Northwest Institute of Eco-Environment and Resources, Chinese Academy of Sciences, Lanzhou, China

Remote sensing ecological index (RSEI) has the advantages of rapid, repeatable and relatively accurate in regional eco-environment quality assessment. Due to the lack of consideration of the interaction of adjacent analysis units in RSEI calculation, there is a few uncertainties in the assessment results. Based on RSEI, the landscape diversity index (LDI) was introduced, which considered the heterogeneity caused by the difference between the assessment unit and the adjacent one, and rebuilt modified remote sensing ecological index (MRSEI) to evaluate the eco-environment quality in the artificial oasis of Ningxia section of Yellow River. The results showed that the area of Fair and Poor grades in the low MRSEI year (2000) was greater than that of other grades, and the area of Moderate and Fair grades was greater than that of other grades in the high MRSEI year (2020). The conversion characteristics of different grades were Poor and Fair grades to adjacent high grades. During the study period, the eco-environment quality of the study area was improved, and the composition and pattern of land use types had a significant impact on MRSEI. Introduction of LDI-improved MRSEI can not only include the heterogeneous effect between the analysis unit and the adjacent one, but also consider the spatial scale effect of LDI to make the evaluation results more credible. However, some evaluation factors of RSEI and MRSEI (e.g., LDI, NDVI, and NDBSI) represent the accumulation of surface status over long-time scales, while others (e.g., Wet and LST) reflects only short-time scale features of the land surface. Therefore, how to eliminate the uncertainty caused by temporal scale mismatch is a challenge for RSEI and MRSEI applications.

KEYWORDS

eco-environmental quality, oasis, land use/cover, Yellow River, MRSEI

1 Introduction

Regional eco-environmental quality is directly affected by local natural resources and human exploitation system, and the amplification effect of human activity intensity on eco-environmental quality is very significant. Especially in developing countries with the largest land area in the world and rapid industrialization and urbanization, the rate of

change of land use/cover has greatly influenced regional or global climate and environmental change (Yang et al., 2020; Mukesh et al., 2021). In recent decades, using satellite remote sensing data and geographic information systems to extract and analyze land surface information is a very common and effective method to rapidly assess regional eco-environmental quality (Ellis, et al., 2006; Willis, 2015). Thus, these data are used to identify basic ecosystem properties and to judge their different components, such as leaf area index, aboveground biomass, and land cover type (Reza and Abdullah, 2011; de Araujo Barbosa et al., 2015), and these techniques have also been widely used in ecological and environmental surveys in China and other parts of the world (Tilt et al., 2007; Chen, et al., 2014; Kennedy et al., 2014; Willis, 2015; White et al., 2016). Various remote sensing ecological indicators play an important role in quantifying and mapping the characteristics and functions of ecosystems. In these findings, methodologies typically focus on only one aspect of the eco-environment and then produce a single ecological factor for evaluation (Nichol, 2009). For example, normalized differential vegetation index (NDVI), leaf area index (LAI), normalized differential water index (NDWI), and light index (LI) have been used to describe spatiotemporal changes in vegetation, biodiversity, water bodies, bare land, and cities (Choudhary et al., 2019; Kappas and Propastin 2012; Fu et al., 2013). Especially in the pattern analysis of land surface temperature (LST), it was found that the heat island effect in Leipzig (Germany), was more reliable in densely urbanized areas than in areas with low population density (Schwarz et al., 2012). The sandy vegetation pattern in Horqin (China) was negatively correlated with land surface temperature, and the more complex the vegetation structure, the closer the correlation (Qiao et al., 2021). These studies are of great significance for carrying out more targeted ecological restoration work, and are also the current hotspots for quantitatively describing and estimating the spatio-temporal dynamics of eco-environmental quality and promoting sustainable development in different regions.

After the improvement of a single remote sensing index for the evaluation of a certain land surface attribute state, combined with pressure-state-response (PSR) model and analytic hierarchy process (AHP), a method of comprehensively using multiple remote sensing indicators to determine regional eco-environmental quality has been formed (Fulton Elizabeth, 2010; Yu and Hong, 2022; Tom´ as et al., 2004; Patrício et al., 2016). In this method, structure construction and factor weight distribution are the key. Because the factor weight system must contain subjective weight, and expert knowledge and experience such as AHP must be integrated into the analysis process (Zhao et al., 2016), which is not conducive to the rapid evaluation of the eco-environmental quality of a certain region. The multi-dimensional and multi-feature technology developed in the past decade has shown great advantages in regional eco-environmental quality assessment (Boori et al., 2018; Xu et al., 2018; Wu et al., 2020). In particular, Xu (2013) proposed the Remote Sensing Ecological Index (RSEI), which integrates four calculated indicators based on remote sensing bands to represent four major ecological elements (NDVI; Wet; NDBSI; LST), and principal component analysis (PCA) based on covariance was used to determine the comprehensive contribution of the four factors to eco-environmental quality. The effectiveness of the proposed method was evaluated in different landscape types, such as urban landscape, alpine grassland landscape, Loess Plateau landscape and agricultural and forestry mixed with water landscape. (Hu and Xu, 2018; Liu et al., 2019; Sun et al., 2020; Yuan, et al., 2021). However, two problems in RSEI have attracted the attention of researchers (Yuan, et al., 2021). One is that RSEI calculated based on grid data cannot express the differences caused by homogeneity (or heterogeneity) of adjacent grids. Secondly, the evaluation factors used by RSEI usually have a high correlation with each other, and NDVI has the highest eigenvalue on PC1, which leads to some contradictions in comparing RSEI results in ecological interpretation of different multi-ecosystems landscapes. That is, the area with the dominant agricultural land ecosystem may obtain a higher RSEI value. So how do you avoid these problems in your RSEI evaluation? The introduction of landscape diversity index (LDI) may be an appropriate method to correct the above deficiency, because the calculation of LDI takes into account the differences of basic unit attributes within a certain scale. At the same time, there are a large number of shared and paid resources to choose from land cover interpretation products based on Landsat data, and there are also some landscape analysis software to calculate LDI, such as PCA.

If LDI is added to modify RSEI (MRSEI), the first problem to be solved is to determine the appropriate scale, that is, to obtain the scale-dependent characteristics of LDI (Li et al., 2018; Liang and Li, 2018; Yang, et al., 2021). Previous studies have shown that there are differences in scale dependence between similar or different landscape areas. Therefore, identifying the scale dependence of LDI in the study area is the basis of landscape analysis.

In terms of the practical significance of eco-environmental quality assessment, there is no doubt that AHP, RSEI or MRSEI, are not only meaningful in theory for judging the status and change trend of eco-environmental quality in the study area, but also an important means for regional sustainable development planning, management and evaluation in practice. For example, the RSEI study for different geographical units and types such as watersheds (Gao and Zhang, 2021; Luo et al., 2022) and National Nature Reserve (Liu et al., 2019) show great practical significance. The Yellow River Oasis Area in Ningxia Hui Autonomous Region is densely covered with lakes and wetlands, and is the core area of the National Yellow River Economic Zone, as well as the key area of ecological function zoning. How the regional

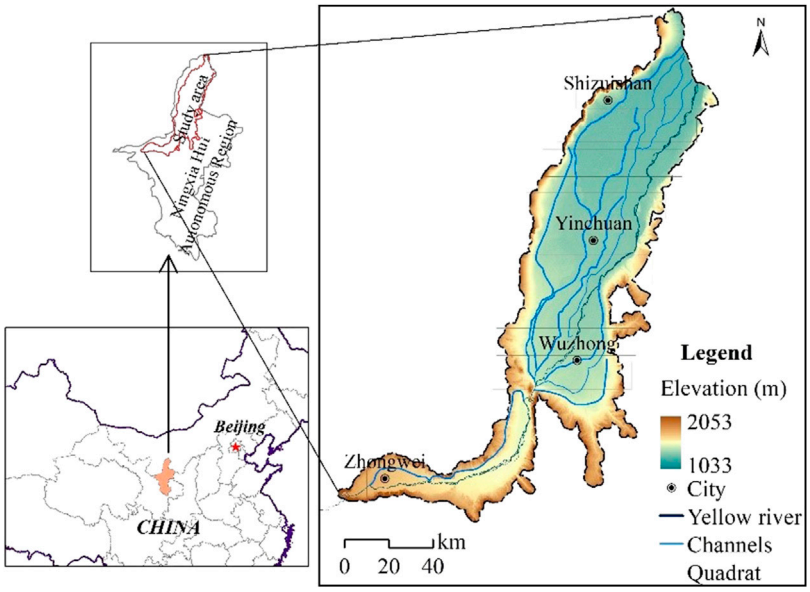

FIGURE 1
Location of the study area.

environment changes have attracted much attention from the state and local governments, and how to implement the rapid and effective environmental quality assessment of artificial oasis is a challenge for the academic community.

Here, we used MRSEI method to evaluate the changes of the oasis of Ningxia section of the Yellow River in recent decades by increasing the LDI factor, to identify the main driving factors, and to evaluate the value of MRSEI in the analysis of eco-environmental quality.

2 Materials and methods

2.1 Study area

The oasis in Ningxia section of the Yellow River is located in the northern part of Ningxia Hui Autonomous Region, which ranges from 37°20′ ~ 39°20′ N, 105°0′ ~ 107°0′E, and an area of about 10,831.3 km^2. The core area of Ningxia section of the Yellow River is an artificial oasis composed of the Weining and the Yinchuan irrigation district connected by the Yellow River, with oases areas accounting for more than 60% (Figure 1). Farmland, lakes and wetlands are densely distributed in the study area. The main irrigation channels are longitudinally distributed east trunk Canal, west trunk canal, Han Yan Canal, Tang Lai Canal and so on. The soil is mainly alluvial soil and meadow soil. The natural vegetation is mainly date forest scattered shrub woddland, composed of *Elaeagnus angustifolia*, *Lycium chinense*, *Tamarix chinensis* and *Phragmites communis* and so on. This area is the core area of the national Yellow Economic Zone, and also the key area of China's national ecological function zoning.

2.2 Satellite data and pre-processing

Conventional Landsat imagery has been widely used for large-scale and periodic ecological monitoring (e.g., NDVI and LU). Using a shared dataset supported by the U.S. Geological Survey (USGS), including the Landsat data Collection, 2 Tier 1 and Top of atmospheric (TOA) Reflectance (https://earthengine.google.com/), the spatial resolution of the data of 30 m. Data were preprocessed with atmospheric and geometric corrections. To ensure the similarity of vegetation growth conditions and the comparability of ecological results, the data were collected from July 5 to 22 August 2000 and August 19 to 28 August 2020, respectively. Since the study area involved three images (129,033, 129,034 and 130,034), the data of Landsat 5 TM and Landsat 8 OLI were selected to be concatenated into one image, respectively.

Land use (LU) data were obtained from the Data Center for Resources and Environmental Sciences, Chinese Academy of Sciences (Chen, et al., 2014; Zhang. 2020). The study area involved eight types of land surfaces, including cultivated land, woodland, shrub, grassland, wetland, water body, urban and built-up areas, and wasteland, with the overall interpretation

accuracy (Kappa coefficient) ranging from .78 to .82 (https://www.resdc.cn/).

2.3 Identification of LDI threshold

LDI is an indicator to measure the number of landscape composition types and the proportion of its area information in landscape ecology research, and is also the main level of biodiversity research. A higher LDI means a higher diversity of ecosystem types in the study area. Therefore, LDI is credible as an assessment factor for eco-environmental quality. Here, the LDI is represented by Shannon-Weiner index and calculated in the neighborhood analysis method of ArcGIS. It can be computed using the following equation:

$$\boldsymbol{LDI} = -\sum_{i=1}^{m} \boldsymbol{P_i} \times \boldsymbol{LnP_i} \tag{1}$$

where P_i is the proportion of a certain land use type to the area of the analysis unit. A quadrat gradient as 90 m × 90 m, 300 m × 300 m, 600 m × 600 m, 900 m × 900 m, 1200 m × 1200 m, 1500 m × 1500 m, 3000 m × 3,000 m, 4500 m × 4500 m and 6000 m × 6000 m was used to calculate the scale-dependent characteristics and thresholds of LDI in 2000 and 2020, respectively.

2.4 Assessment factor normalization and MRSEI calculations

The calculation methods of NDVI, WET, NDBSI, and LST in this study are consistent with the literature (Yuan et al., 2021). Since the MRSEI assessment takes grid as the basic unit, it does not consider the influence of the diversity of adjacent units, and ignores the girds are not only affected by the influence factor of the same spatial domain, but also have a significant effect between adjacent units, that is, the edge effects phenomenon in ecology. To compensate for this shortcoming in MRSEI, we added the LDI factor to RSEI and renamed it as MRSEI. Due to the differences in unit and quantity sizes of the input factors, normalization is required to unify the index values between 0 and 1. In this paper, the forward normalization (Eq. 2) method is used for standardization.

$$\boldsymbol{F_i} = (\boldsymbol{X_i} - \boldsymbol{X_{imin}}) / (\boldsymbol{X_{imax}} - \boldsymbol{X_{imin}}) \tag{2}$$

In Eq. 2, F represents the input factor, and i represents LDI, NDVI, WET, NDBSI, and LST, respectively; X represents the input factor cell value. After the evaluative factors were normalized, MRSEI was calculated using Eq. 3:

$$\boldsymbol{MRSEI} = \sum_{i}^{n} \boldsymbol{PC_n}(\boldsymbol{ESV}, \boldsymbol{NDVI}, \boldsymbol{WET}, \boldsymbol{NDBSI}, \boldsymbol{LST}) \times \boldsymbol{EV_i} \times \boldsymbol{ET_i} \tag{3}$$

where MRSEI is a modified remote sensing ecological index, and the larger the MRSEI value, the better the eco-environment; Vice versa. N represents the number of components whose principal component eigenvalues accumulate to more than 90%. In MRSEI analysis, the input factor is 5, therefore, $1 \le i \le 5$ (i is an integer). EV_i and ET_i are ith eigenvalues and accumulative eigenvalues of eigenvectors, respectively. In order to make the MRSEI values of different years comparable, the calculated MESEI was normalized again with a positive difference of the range to unify them between 0 and 1. The spatial heterogeneity analysis of MRSEI was based on the classification and treated by the equivalent interval method, which was defined as: poor (0–.2), fair (.2–.4), moderate (.4–.6), good (.6–.8), and excellent (.8–1.0).

The entire MRSEI of study area can be calculated by Eq. 4:

$$\boldsymbol{MRSEI_{Total}} = \sum_{i}^{n} \boldsymbol{M_i} \times \boldsymbol{PA_i} \tag{4}$$

where M_i is the average $\mathrm{MRSEI_{Total}}$ of Class i grades in the assessment area, and PA_i is the relative area of $\mathrm{MRSEI_{Total}}$ Class i grades in the assessment area. Statistical analysis was done with SPSS and Excel. The correlation coefficients of different evaluation factors were examined for R significance. The thresholds were $R_{4,\ .05} = .811$ and $R_{4,\ .01} = .917$, respectively.

2.5 Relationship between MRSEI and land use type

The MRSEI was obtained by calculating landscape diversity index (LDI), greenness (NDVI), humidity (WET), dryness (NDBSI) and heat (LST). The impact of these five factors on MRSEI was direct. In regional MRSEI determination, land use type will indirectly affect all factors involved in MRSEI, especially in MRSEI analysis on time series. Therefore, unary multiple linear regression was used to calculate the impact of LU on MRSEI after completing MRSEI analysis. The regression analysis took MRSEI as the dependent variable, and the area of the eight land use types mentioned above as the dependent variable. Stepwise linear regression was used for optimization selection, and the model with the highest significance was selected. Due to the large area of various land use types, range normalization was carried out before modeling so that all dependent variables fell into (0–1).

In order to test the accuracy of the regression model constructed by LU, standard error (SE) and mean error coefficient (MEC) were selected to test the model. A total of 10 test samples were distributed in parallel throughout the study area (Figure 1).

The calculation formula is as follows:

$$\boldsymbol{SE} = \sqrt{\sum_{i=1}^{n} \frac{(\boldsymbol{y} - \boldsymbol{y'})^2}{\boldsymbol{n} - 1}} \tag{5}$$

$$\boldsymbol{MEC} = \frac{\sum_{i=1}^{n} |(\boldsymbol{y} - \boldsymbol{y'})/\boldsymbol{y}|}{\boldsymbol{n} - 1} \tag{6}$$

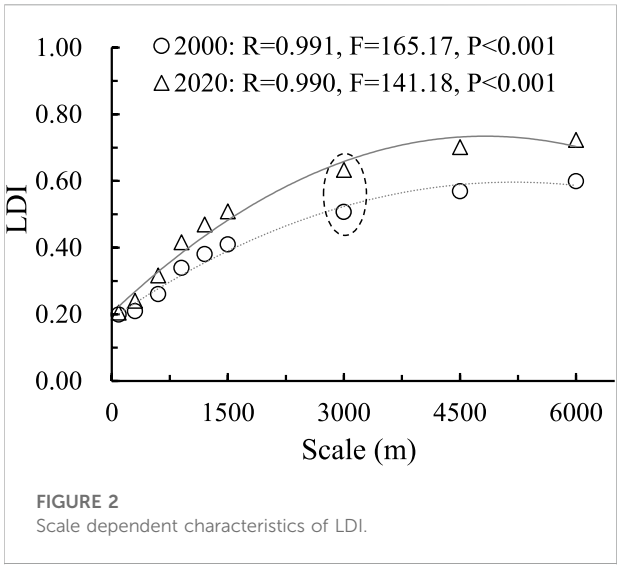

FIGURE 2
Scale dependent characteristics of LDI.

TABLE 1 Pearson correlation semi-matrix of evaluative indicators in 2000 and 2020 (* and **: Two tails check is significant at the level of .05 and .01 levels respectively).

Year	Indicators	LDI	NDVI	WET	NDBSI	LST
2000	LDI	1.000				
	NDVI	-.165	1.000			
	WET	-.164	.778	1.000		
	NDBSI	.158	-.831*	-.958**	1.000	
	LST	.163	-.761	-.842*	.845*	1.000
2020	LDI	1.000				
	NDVI	-.298	1.000			
	WET	-.270	.867*	1.000		
	NDBSI	.269	-.869*	-.979**	1.000	
	LST	.254	-.684	-.824*	.838*	1.000

where y is the MRSEI calculated value based on the PCA method, y' is estimated using the obtained optimized regression model and LU data, and n is the number of validated samples.

3 Results

3.1 The scale dependent threshold for the LDI

The LU in the two periods were analyzed, and the average value of LDI was calculated to determine the scale dependence. It was found that there was a significant trend described by quadratic equation ($p < .001$ $R > .990$). The inflection point of LDI change could be captured within the range of 6,000 m (at 3,000 m, in the ellipse in Figure 2). When the analytical scale was smaller than the inflection point scale, the LDI showed a steep increase trend. When the analysis scale was larger than the inflection point scale, LDI showed a gentle increasing trend. Therefore, the basic unit of 3,000 m × 3,000 m was used to calculate the LDI in this paper. After the calculation, the LDI was resampled to 30 m × 30 m in order to be consistent with the other three indexes in resolution.

3.2 Relationship between evaluation factors for PCA

After the introduction of LDI, the original relationship and degree of association of MRSEI evaluation factors did not change (Table 1), and NDVI and WET were also kept in the same group, and the load vector in PC1 component was positive, which was the driving factor for the improvement of eco-environmental quality (Table 2). NDBSI and LST belong to the same group, and

TABLE 2 The results of principal component analysis of five evaluation factors in 2000 and 2020.

Indicators	2000		2020	
	PC1	PC2	PC1	PC2
LDI	.251	.968	-.377	.926
NDVI	-.654	.171	.786	.320
WET	-.363	.092	.172	.074
NDBSI	.397	-.108	-.178	-.077
LST	.469	-.117	-.422	-.168
Eigenvalues	.026	.013	.031	.013
Percent of eigenvalues	61.2	29.9	64.7	26.7
Accumulative of eigenvalues	61.2	91.0	64.7	91.4
MRSEI	.435		.448	

the load vector was negative in PC1 component, which was the driving factor of eco-environmental quality deterioration. The between-group positive association and between-group negative association were also unchanged. Except for the correlation between NDVI and LST in 2000, all the other combinations had high significance. It should be emphasized that the correlation between LDI and other factors was low, and the maximum correlation coefficient (absolute value) of the 2 years did not exceed .298. LDI increased the dimensions of eco-environmental quality assessment and made the results more inclusive.

The PCA results in 2000 and 2020 showed (Table 2) that the cumulative contribution rate of PC1 and PC2 exceeded 90% after dimensionality reduction analysis of the five evaluation factors.

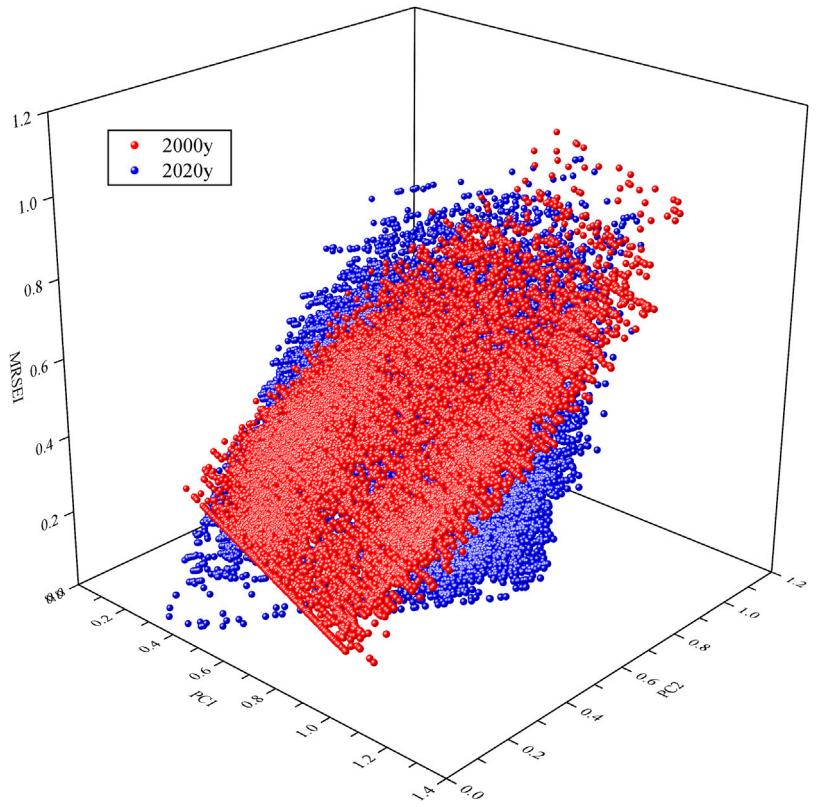

FIGURE 3
A 3D-scatter plot showing the relationship among MRSEI, PC1 and PC2 (red balls, 2000; blue balls, 2020).

Among them, the maximum load vectors of PC2 axis were LDI, which were .968 and .926 respectively, far exceeding other evaluation factors, indicating that LDI maintains multi-dimensional representation.

From the relationship between MRSEI and PC1 and PC2 (Figure 3), when the cumulative contribution rate exceeded 90% and the number of components was 2, the change of MRSEI showed complexity. At the overall level, the NDVI of MRSEI in PC1 component was .285 (±.216), and the LDI of MRSEI in PC2 component was .386 (±.141). The lowest region of MRSEI changes formed by the two components appeared in the high value region of PC1 component and the low-quality region of PC2 component (lower right corner of Figure 3), while the high value region appeared in the low value region of PC1 component and the high-quality region of PC2 component (upper left corner of Figure 3). In 2020, the dominant NDVI in PC1 component was .451 (±.281), and the dominant LDI in PC2 component was .468 (±.181). The lowest MRSEI change region formed by the two components appeared in the low-quality region of PC1 and PC2 components (lower left corner of Figure 3). However, the high value area appeared in the intersection area of high value of PC1 and PC2 components (upper right corner of Figure 3). The obvious trend was that when the MRSEI changed from the low MRSEI in 2000 to the high MRSEI in 2020 (Figure 4), MRSEI showed a change trend of rotation to the right with its value center as the axis. The ecological interpretation was as follows: the resultant force of evaluation factor in the state of regional average had a relatively stable median MRSEI value; When the regional eco-environment changed for the better (from 2000 to 2020), the distribution of the low value of MRSEI was restricted by the high value of the component controlled by NDVI and the low value of the component controlled by LDI, and transformed to the low value of the component controlled by them. On the contrary, the MRSEI high value distribution was restricted by the low value of the component controlled by NDVI and the high value of the component controlled by LDI, and converted to the high value of the component controlled by them.

According to above mention, it could be inferred that in the process of improving eco-environmental quality in the multi-ecosystems region, under the certain condition of PC2 (dominated by LDI), the effect of PC1 (dominated by NDVI) on MRSEI changed from a decreasing to an increasing trend with the increase of PC1. The distribution range of MRSEI high value changed from .4–.6 of PC1 in 2000 to .6–.8 in 2020. However, the effect of PC2 on MRSEI was obviously different, and its effect was increasing during this period. The high value region of MRSEI

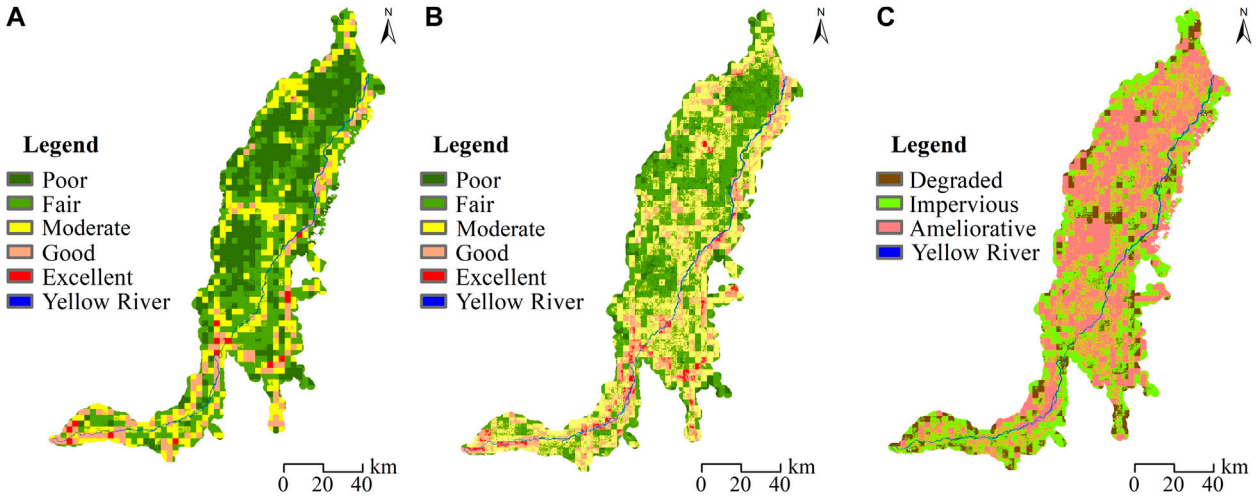

FIGURE 4
Spatial distribution of different MRSEI grades along the Yellow River Oasis in Ningxia [**(A)**, MRSEI of 2000; **(B)**, MRSEI of 2020; **(C)**, change from 2000 to 2020].

TABLE 3 The status of different MRSEI grades in 2000 and 2020.

Year	Type	Area (km^2)	Ratio (%)	Patch number	Mean area (km^2)
2000	Poor	3,138.3	29.2	2,556	1.22
	Fair	3,911.1	36.4	4,292	.91
	Moderate	2,539.7	23.6	2,549	.99
	Good	1,109.4	10.3	989	1.11
	Excellent	132.2	1.2	145	.91
2020	Poor	631.9	5.8	10,943	.06
	Fair	4,233.1	39.1	17,137	.25
	Moderate	4,236.4	39.1	21,145	.2
	Good	1,544.2	14.3	12,463	.12
	Excellent	185.1	1.7	3,578	.05

was consistent with that of PC2. This is very obvious during the improvement of MRSEI in the study area, the influence of NDVI on MRSEI varied greatly, while the influence of LDI on MRSEI was relatively stable.

3.3 Ecological quality status and hierarchical pattern

According to the spatial distribution analysis of MRSEI classification pattern, in the 2 years of the study, the areas with high eco-environmental quality were mainly distributed near the boundary of the study area and the two banks of the Yellow River (Figures 4A,B), indicating that the artificial oasis area in the semi-arid region had obvious boundary effect on a large scale. In time (Table 3), in 2000, the Fair and Poor areas with low eco-environmental quality were relatively large, which were 3,911.1 km^2 and 3,138.3 km^2, accounting for 65.1% of the total area. On the contrary, the areas of Good and Excellent grades with high eco-environmental quality were relatively small, which were 1,109.4 km^2 and 132.2 km^2 respectively, accounting for only 11.5% of the total area. In 2020, the area of Fair level increased to 4,233.1 km^2, but the area of Poor level decreased greatly, only 631.9 km^2 remained, and the area of low-level

TABLE 4 Change results of different MRSEI grades from 2000 to 2020.

Changed status	Total area (km^2)	Ratio (%)	Patch number	Mean area (km^2)
Degraded	1,049.6	9.7	9,752	.108
Impervious	4,357.7	4.2	29,836	.146
Ameliorative	5,423.5	5.1	19,802	.274

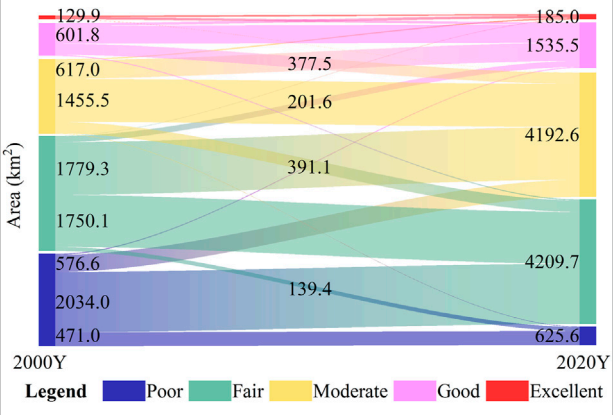

FIGURE 5
The details of transferred area of different MRSEI grades during 2000–2020 in the oasis of Ningxia section of the Yellow River.

ecological quality accounted for 44.9% of the total area. On the contrary, the areas of Good and Excellent, which had high eco-environmental quality, increased to 1,544.2 km^2 and 185.1 km^2, respectively, accounting for 16.0% of the total area. The Moderate level increased by 15.7 percent from 2,539.7 km^2 in 2000 to 4,236.4 km^2 in 202.

From 2000 to 2020, the number and average patch area of different grades showed an obvious increasing trend. Factor analysis in the above section showed that the overall levels of NDVI and LDI in 2000 were lower than those in 2020, indicating that the classification pattern of MRSEI tended to be fragmented during the study period (Table 3). For details of the excellent level, its area was distributed over a total area of 132.2 km^2 in 2000 to 185.1 km^2 in 2020, but the average patch area decreased from .91 km^2 to .05. km^2. This phenomenon indicates that the excellent area in the study area had changed from concentrated continuous distribution to scattered distribution, which can be seen from Figures 4A, B, and most of the intact excellent areas (grids) in 2000 are fragmented in 2020.

From 2000 to 2020, the eco-environmental quality changed towards good. The improved type was the main body in the middle and upper part of the study area, and the impervious type was the main body in the lower part of the study area (Figure 4C). The improved and impervious area were 5,423.5 km^2 and 4,357.7 km^2 respectively, accounting for 9.3% of the total area, while the area of the degraded area was only 1,049.6 km^2, accounting for less than 10% (Table 4). For the details of the changes (Figure 5), the Poor grade was mainly characterized by the transformation to Fair and Moderate grades, which were 2034.0 km^2 and 576.6 km^2, respectively. The general grade was characterized by transformation to Moderate grade and good grade, which were 1779.3 km^2 and 201.6 km^2, respectively. The moderate grade was mainly transformed to moderate grade and good grade, which were 391.6 km^2 and 617.0 km^2, respectively. The good grade was mainly transformed to moderate grade, which were 377.5 km^2. The excellent grade increased from 129.9 km^2 in 2000 to 185.0 km^2 in 2020, mainly from the "moderate" and "good" grades. The quality of eco-environment has been improved not only at the whole area scale, but also at the patch scale.

From the perspective of driving forces of the transformation mechanism during 2000–2020, LU change under the guidance of policies such as urbanization process, eco-environmental protection measures and adjustment of agricultural planting structure pattern is the main driving force of MRSEI transformation.

3.4 Effect of LU composition on MRSEI

The composition and pattern of LU types are affected by evaluation factors such as NDVI and LDI, which in turn affect MRSEI. Therefore, LU types affect MRSEI. Forward stepwise linear regression analysis showed that the relationship between oasis MRSEI and LU types in the oasis of Ningxia section of the Yellow River was different in different years (Table 5). In the year with low MRSEI levels (2000), there was a significant multivariate linear relationship between MRSEI and the variables (LU type) such as grassland, shrubland, artificial surface and barren land area. The regression equation was $MRSEI_{2000}$ = .348–.245 grassland +2.943 shrubs +.678 urban land and built-up land +2.368 wasteland (R^2 = .925, F = 7.460, p = .025), among which wasteland and artificial surface area were more important. Accounted for .491 and .401, respectively. In the year with high MRSEI (2020), there was also a significant multivariate linear relationship between MRSEI and shrub, wetland, water and artificial surface area. The regression equation was $MRSEI_{2020}$ =

TABLE 5 Results of forward stepwise linear regression of the eco-environmental quality (MRSEI value, predictive variable) and the land use/cover type areas (explanatory variables) in the Oasis of Ningxia section of the Yellow River.

Predictive variable	Constant	Explanatory variables	Coefficient	Importance	*P*
2000 MRSEI	.348	grassland	-.245	.075	.166
		shrubbery	2.943	.034	.325
		urban and built lands	.678	.401	.013
		barren	2.368	.491	.009
2020 MRSEI	.445	shrubbery	-7.733	.359	.006
		wetland	17.525	.759	.001
		Water body	-1.571	.192	.020
		urban and built lands	.248	.482	.003

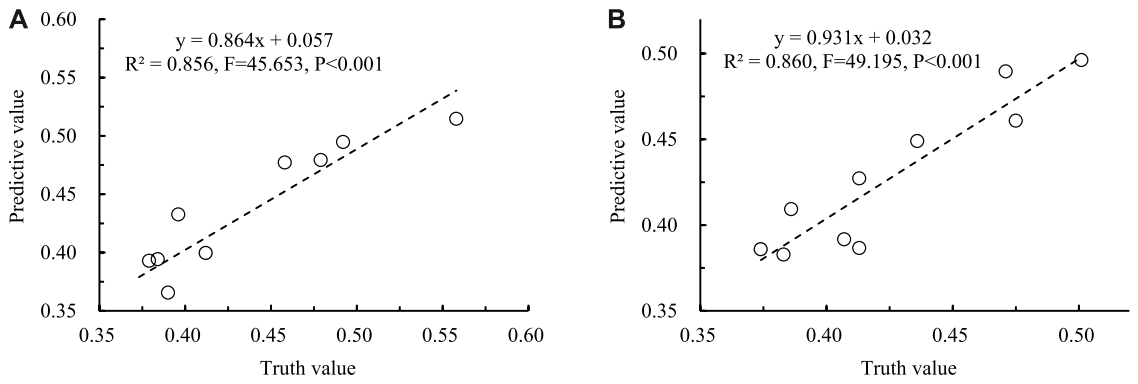

FIGURE 6
Relationship between truth values and predictive values of MRSEI [**(A)**, 2000; **(B)**, 2020].

.455–7.733 shrubs +17.525 wetland -1.571 Water +.248 urban and built-up land (R^2 = .914, F = 13.330, p = .007), and the wetland area was the most important (.759).

The accuracy test of the above regression model showed that SE and MEC were 2.41% and 4.87% in 2000 and 1.68% and 3.75% in 2020, respectively. This indicates that the higher the overall level of MRSEI, the higher the accuracy of the corresponding model (the lower the error rate), and the relationship between MRSEI and its predicted value varies with year (p < .001) (Figure 6).

In terms of the statistical analysis of the prediction results (Table 6), the MRSEI predicted mean was .002 more than the true value and the standard deviation and coefficient of variation were almost identical in 2000. In 2020, the MRSEI predicted mean was .002 less than the true value, and the standard deviation and coefficient of variation of the true value were .004 and .008 more than the predicted value, respectively. It is explained that the multiple regression model constructed based on LU type and forward stepwise linear regression method would basically express (predict) the influence mechanism of LU on MRSEI changes.

4 Discussion

This study shows that the introduction of LDI can modify the regional eco-environment assessment method based on MRSEI model, which not only considers the element composition around the MRSEI analysis unit, but also considers the spatial scale effect of LDI, which can make the assessment results more credible.

The LDI spatial threshold of different landscape types was different, but it did not change much in specific regions (Li, et al., 2018; Liang and li, 2018; Yang et al., 2021). Our study shows that the LDI spatial threshold of the oasis of the Ningxia section of the Yellow River is 3,000 m (Figure 2 ellipse).

After the introduction of LDI, the relationship between the existing factors was not affected by LDI, as the maximum

TABLE 6 Statistical analysis comparison of MRSEI prediction value and truth value.

	2000		2020	
	Truth value	Predictive value	Truth value	Predictive value
Mean	.426	.428	.432	.430
Standard deviation	.043	.044	.062	.058
Coefficient variable	.102	.102	.143	.135

correlation coefficient did not exceed .3 within 2 years (Table 1), which verified that MRSEI was complementary to RSEI. At the same time, PCA results after the introduction of LDI significantly reduced the phenomenon that more than 75% of the eigenvalues were concentrated on PC1 (Xu et al., 2019; Yuan et al., 2021). The improvement of the method makes up for the lack of attention to heterogeneity in the evaluation of regional environmental quality. By introducing LDI, MRSEI reduces the dimensionality of multiple factors and disperses them into multiple dimensions (the cumulative eigenvalue is greater than 90%), which highlights the complexity and multiplicity of MRSEI. Determining the scale dependence of LDI (Figure 2) can not only ensure the expression of heterogeneity between adjacent elements, but also avoid the uncertainty of MRSEI results caused by the scale effect of LDI (O'neill et al., 1996; Gallé, et al., 2020). The method of this study improves the deficiency that RSEI does not express the eco-environmental quality of water body in regional eco-environment assessment.

To recognize whether the MRSEI results have organized for the oasis, the multiple regression approach with MRSEI, PC1 and PC2 are subsequently applied to the Ningxia section of Yellow River. The regression could be expresses as MRSEI = .041E-5+.156PC1+.768PC2 (R = .999, F = 1.246E9, p < .001) when the overall level of MRSEI is lower (2000). And it also could be expressed as MRSEI = .012–.034PC1+.796PC2 (R = .999, F = 1.094E9, p < .001) when the overall level of MRSEI was higher (2020). Compared the MRSEI findings with the RSEI in different regions, MRSEI values (.43) in Ningxia section of the Yellow River was more than RSEI value (.24) in the desert area (Jiang et al., 2019; Li et al., 2019), less than RSEI value (.63) in forested/vegetation-dense areas (Wang et al., 2016), and close to RSEI value (.43–.54) in tableland of loess plateau region (Sun et al., 2020). This indicated that the LDI introduction does not conflict with the original RSEI assessment results from the overall characteristics, and the change is only the spatial pattern of the eco-environment quality. Simultaneously, it was evident from Figure 4A and Figure 4B where MRSEI calculations do not require water body exclusion and form distinct MRSEI high-value zones in the land-water body transition zone (along the Yellow River) and the oasis edge zone. In terms of the MRSEI change characteristics from lower level (2000) to higher level (2020), the MRSEI degraded area was almost distributed in the edge area of the oasis and the water body or land transition zone along the Yellow River besides of the less scattered distribution in the urban areas such as Yinchuan in the middle of the study area (Figure 4C), and this phenomenon once again confirmed the occurrence of edge effects and vulnerability among different ecosystems from a dynamic perspective (Hofmeister et al., 2013; Estoque et al., 2017; Mansoury et al., 2021). Due to the grade level change details (Figure 5), transferred areas occurred mostly in adjacent levels and less cross-level. Among of them, Poor and Fair had the largest upward conversion, with 2034.0 km^2 and 1779.3 km^2, respectively. The overall conversion characteristics were mainly Poor class area decreased significantly and Moderate class area increased significantly, increasing by −3,019.0 km^2 and 1,61.6 km^2, respectively. The phenomena indicated that the improvement of the eco-environment in the semi-arid artificial oasis area generally occurred below Moderate level, and the change scope above good level was not large.

LU type is the basis for calculating LDI in the assessment of the eco-environment quality, its composition and pattern not only directly affect LDI, but also have an indirect effect on RSEI or MRSEI through influencing the distribution of all evaluative factors (Liu et al., 2007; Xu et al., 2018; Yuan et al., 2021). Based on the spatial sampling (Figure 1) and the LU classification, multiple stepwise regression analysis that selected MRSEI as predictive variable and LU types as explanatory variables showed that had inconsistent explanatory variable combinations in different yearly MRSEI levels. In the low MRSEI levels (2000), grasslands, shrublands, urban and built-up lands and barren land lands areas had a good predictive result on MRSEI, with an accuracy of more than 95%. In the higher MRSEI levels (2020), shrubland, wetland, water body and urban and built-up lands had a good predictive result on MRSEI, the accuracy also reached more than 95%. Importance values indicated that urban and built-up lands and barren land area with low ecological quality in 2000 shown to have a greater impact on MRSEI, while water body and wetland with higher ecological quality in 2020 had a greater impact on MRSEI, this result is basically consistent with that of RSEI change research in Dongting Lake and can be mutually verified (Yuan et al., 2021).

However, a common defect of RSEI and MRSEI is that the participating evaluation factors LDI, NDVI, and NDBSI reflect the long-term accumulated surface reflection characteristics, while Wet and LST only reflect the short-term surface reflection characteristics (Bindlish and Barros, 2001; Sobrino et al., 2008; Qiao et al., 2021). The removal of this uncertainty due to time scale mismatch is a challenge for RSEI and MRSEI applications. In addition, from the application prospect of MRSEI, as long as the study area is a multi-ecosystem, LDI introduction has both theoretical basis and practical significance, because LDI can express the complexity of evaluation units and adjacent units.

5 Conclusion

In regional eco-environment assessment, MRSEI can make up for the defects that RSEI cannot evaluate water areas. The introduction of LDI with defined threshold values fully expresses the heterogeneity (diversity) of adjacent units of analysis.

From 2000 to 2020, the $MRSEI_{Total}$ in the study area changed from .435 to .448, both of which were at a moderate grade, but the area of good and excellent increased, and the transformation from poor and moderate level to adjacent high level was the main direction.

LU types have indirect effects on MRSEI through the composition and pattern of impact assessment factors. When the MRSEI level was high, shrub, wetland, water and urban built-up area were the main influencing factors. When the MRSEI level is low, grassland, shrub, urban built-up area and barren area are the main influencing factors.

Data availability statement

The original contributions presented in the study are included in the article/Supplementary Material, further inquiries can be directed to the corresponding author.

Author contributions

CD: Contributed ideas and designed the study, collected the remote sensing data with support from, conducted the data analysis and wrote the manuscript with the help of all the other authors. RQ: Did the field surveys and collected survey data, collected the remote sensing data with support from, conducted the data analysis. ZY: Collected the remote sensing data with support from. LL: Contributed ideas and designed the study, conducted the data analysis and wrote the manuscript with the help of all the other authors. XC: Contributed ideas and designed the study, collected the remote sensing data with support from, identified the study area boundary, conducted the data analysis and wrote the manuscript with the help of all the other authors, did the field surveys and collected survey data, supported. All authors gave final approval for publication, did the field surveys and collected survey data.

Funding

This research was funded by the Key Research and Development Program of Ningxia Hui Autonomous Region (2021BGE02010), National Natural Science Foundation of China (41271193).

Acknowledgments

The authors sincerely thank for the data support from "Data Center of Resources and Environmental Sciences of the Chinese Academy of Sciences (https://www.resdc.cn/)", and thank the editors and reviewers for their kindly view and constructive suggestions.

Conflict of interest

The authors declare that the research was conducted in the absence of any commercial or financial relationships that could be construed as a potential conflict of interest.

Publisher's note

Supplementary material

The Supplementary Material for this article can be found online at: https://www.frontiersin.org/articles/10.3389/fenvs.2022.1071631/full#supplementary-material

References

Bindlish, R., and Barros, A. P. (2001). Parameterization of vegetation backscatter in radar-based, soil moisture estimation. *Remote Sens. Environ.* 76 (1), 130–137. doi:10.1016/s0034-4257(00)00200-5

Boori, M. S., Paringer, R., Choudhary, K., and Kupriyanov, A. (2018). Comparison of hyperspectral and multi-spectral imagery to building a spectral library and land cover classification performance. *Comput. Opt.* 42 (6), 1035–1045. doi:10.18287/2412-6179-2018-42-6-1035-1045

Chen, J., Ban, Y., and Li, S. (2014). China: Open access to Earth land-cover map. *Nature* 514 (7523), 434. doi:10.1038/514434c

Choudhary, K., Shi, W., Boori, M. S., and Corgne, S. (2019). Agriculture phenology monitoring using NDVI time series based on remote sensing satellites: A case study of guangdong, China. *Opt. Mem. Neural Netw.* 28 (3), 204–214. doi:10.3103/s1060992x19030093

de Araujo Barbosa, C. C., Atkinson, P. M., and Dearing, J. A. (2015). Remote sensing of ecosystem services: A systematic review. *Ecol. Indic.* 52, 430–443. doi:10.1016/j.ecolind.2015.01.007

Ellis, E. C., Wang, H. Q., Xiao, H. S., Peng, K., Liu, X. P., Lie, S. C., et al. (2006). Measuring long-term ecological changes in densely populated landscapes using current and historical high-resolution imagery. *Remote Sens. Environ.* 100 (457-4), 457–473. doi:10.1016/j.rse.2005.11.002

Estoque, R. C., Murayama, Y., and Myint, S. W. (2017). Effects of landscape composition and pattern on land surface temperature: An urban heat island study in the megacities of southeast asia. *Sci. Total Environ.* 577, 349–359. doi:10.1016/j.scitotenv.2016.10.195

Fu, Y., Lu, X., Zhao, Y., Zeng, X., and Xia, L. (2013). Assessment impacts of weather and land use/land cover (lulc) change on urban vegetation net primary productivity (NPP): A case study in guangzhou, China. *Remote Sens. (Basel).* 2013 (5), 4125–4144. doi:10.3390/rs5084125

Fulton Elizabeth, A. (2010). Approaches to end-to-end ecosystem models. *J. Mar. Syst.* 81 (1-2), 171–183. doi:10.1016/j.jmarsys.2009.12.012

Gallé, R., Geppert, C., Földesi, R., Tscharntke, T., and Batáry, P. (2020). Arthropod functional traits shaped by landscape-scale field size, local agri-environment schemes and edge effects. *Basic Appl. Ecol.* 48, 102–111. doi:10.1016/j.baae.202.09.006

Gao, W. L., Zhang, S. W., Rao, X., Lin, X., and Li, R. (2021). Landsat TM/OLI-Based ecological and environmental quality survey of Yellow River basin, inner Mongolia section. *Remote Sens.* 13 (21), 4477. doi:10.3390/rs13214477

Hofmeister, J, Jan, H, Brabec, M, Hédl, R, and Modrý, M (2013). Strong influence of long-distance edge effect on herb-layer vegetation in forest fragments in an agricultural landscape. *Perspect. Plant Ecol. Evol. Syst.* 15 (6), 293–303. doi:10.1016/j.ppees.2013.08.004

Hu, X., and Xu, H. (2018). A new remote sensing index for assessing the spatial heterogeneity in urban ecological quality: A case from fuzhou city, China. *Ecol. Indic.* 89, 11–21. doi:10.1016/j.ecolind.2018.02.006

Jiang, C. L., Wu, L., Liu, D., and Wang, S. M. (2019). Dynamic monitoring of eco-environmental quality in arid desert area by remote sensing: Taking the gurbantunggut desert China as an example. *J. Appl. Ecol.* 30, 877–883. doi:10.13287/j.1001-9332.201903.008

Kappas, M. W., and Propastin, P. A. (2012). Review of available products of leaf area index and their suitability over the formerly soviet central Asia. *J. Sens.* 11, 582159. doi:10.1155/2012/582159

Kennedy, R. E., Andréfouët, S., Cohen, W. B., Gómez, C., Griffiths, P., Hais, M., et al. (2014). Bringing an ecological view of change to Landsat-based remote sensing. *Front. Ecol. Environ.* 12, 339–346. doi:10.1890/130066

Li, Q., Yang, Y., Wang, Z., Cui, J., Yang, G., and Lian, G. (2019). Dynamic change analysis of remote sensing ecological index in Aksu based on TM data analysis. *Southwest China J. Agric. Sci.* 32, 1646–1651. doi:10.16213/j.cnki.scjas.2019.7.030

Li, Y. Y., You, L. L., Chen, Y. S., and Huang, J. X. (2018). Spatial-temporal characteristics of multi-pond landscape change and their driving factors in the Chaohu Basin, China. *Acta Ecol. Sin.* 38 (17), 6280–6291. doi:10.5846/stxb201708281551

Liang, J. X., and Li, X. J. (2018). Characteristics of temporal-spatial differentiation in landscape pattern vulnerability in Nansihu Lake wetland, China. *Chin. J. Appl. Ecol.* 29 (2), 626–634. doi:10.13287/j.1001-9332.201802.018

Liu, M., Liu, C., and Wang, K. (2007). Eco-security in Dongting Lake watershed: Its changes and relevant driving forces. *Chin. J. Ecol.* 26, 1271–1276. doi:10.13292/j.1000-4890.2007.0220

Liu, Q., Yang, Z., Han, F., Shi, H., Wang, Z., and Chen, X. (2019). Ecological environment assessment in world natural heritage site based on remote-sensing data. A case study from the bayinbuluke. *Sustainability* 11, 6385. doi:10.3390/su11226385

Luo, M., Zhang, S. W., Huang, L., Liu, Z. Q., Yang, L., Li, R. S., et al. (2022). Temporal and spatial changes of ecological environment quality based on RSEI: A case study in ulan mulun river basin, China. *Sustainability* 14, 13232. doi:10.3390/su142013232

Mansoury, M, Hamed, M, Karmustaji, R, Hannan, F A, and Safrany, S T. (2021). The edge effect: A global problem. The trouble with culturing cells in 96-well plates. *Biochem. Biophysics Rep.* 26, 100987. doi:10.1016/j.bbrep.2021.100987

Mukesh, S. B., Komal, C., Rustam, P., and Alexander, K. (2021). Eco-environmental quality assessment based on pressure-state-response framework by remote sensing and GIS. *Remote Sens. Appl. Soc. Environ.* 23 (2021), 10053. doi:10.1016/j.rsase.2021.100530

Nichol, J. (2009). An emissivity modulation method for spatial enhancement of thermal satellite images in urban heat island analysis. *Photogramm. Eng. remote Sens.* 75, 547–556. doi:10.14358/pers.75.5.547

O'neill, R., Hunsaker, C., Timmins, S. P., Jackson, B. L., Jones, K. B., Riitters, K. H., et al. (1996). Scale problems in reporting landscape pattern at the regional scale. *Landsc. Ecol.* 11 (3), 169–180. doi:10.1007/bf02447515

Patrício, J., Elliott, M., Mazik, K., Papadopoulou, K.-N., and Smith, C. J. (2016). DPSIR—Two decades of trying to develop a unifying framework for marine environmental management? *Front. Mar. Sci.* 3, 177. doi:10.3389/fmars.2016.00177

Qiao, R. R., Dong, C. Y., Ji, S. X., and Chang, X. L. (2021). Spatial scale effects of the relationship between fractional vegetation coverage and land surface temperature in Horqin sandy land, north China. *Sensors* 21 (20), 6914. doi:10.3390/s21206914

Reza, M. I. H., and Abdullah, S. A. (2011). Regional index of ecological integrity: A need for sustainable management of natural resources. *Ecol. Indic.* 11, 220–229. doi:10.1016/j.ecolind.2010.08.010

Schwarz, N., Schlink, U., Franck, U., and Großmann, K. (2012). Relationship of land surface and air temperatures and its implications for quantifying urban heat island indicators: An application for the city of Leipzig (Germany). *Ecol. Indic.* 18, 693–704. doi:10.1016/j.ecolind.2012.01.001

Sobrino, J. A., Jimenez-Muoz, J. C., Soria, G., Romaguera, M., Guanter, L., Moreno, J., et al. (2008). Land surface emissivity retrieval from different VNIR and TIR sensors. *IEEE Trans. Geosci. Remote Sens.* 46, 316–327. doi:10.1109/tgrs.2007.904834

Sun, C., Li, X., Zhang, W., and Li, X. (2020). Evolution of ecological security in the tableland region of the Chinese loess plateau using a remote-sensing-based index. *Sustainability* 12, 3489. doi:10.3390/su12083489

Tilt, J. H., Unfried, T. M., and Roca, B. (2007). Using objective and subjective measures of neighborhood greenness and accessible destinations for understanding walking trips and BMI in Seattle, Washington. *Am. J. Health Promot.* 21, 371–379. doi:10.4278/0890-1171-21.4s.371

Tom as, B., Ramos, S., Caeiro, J., and de Melo, J. (2004). Environmental indicator frameworks to design and assess environmental monitoring programs. *Impact Assess. Proj. Apprais.* 22 (1), 47–62. doi:10.3152/147154604781766111

Wang, S., Zhang, X., Zhu, T., Yang, W., and Zhao, J. (2016). Assessment of ecological environment quality in the Changbai Mountain Nature Reserve based on remote sensing technology. *Prog. Geogr.* 35, 1269–1278. doi:10.18306/dlkxjz.2016.10.010

White, D. C., Lewis, M. M., Green, G., and Gotch, T. B. (2016). A generalizable NDVI-based wetland delineation indicator for remote monitoring of groundwater flows in the Australian Great Artesian Basin. *Ecol. Indic.* 60, 1309–1320. doi:10.1016/j.ecolind.2015.01.032

Willis, K. S. (2015). Remote sensing change detection for ecological monitoring in United States protected areas. *Biol. Conserv.* 182, 233–242. doi:10.1016/j.biocon.2014.12.006

Wu, T. X., Sang, S., Wang, S. D., Yang, Y. Y., and Li, M. Y. (2020). Remote sensing assessment and spatiotemporal variations analysis of ecological carrying capacity in the Aral Sea Basin. *Sci. Total Environ.* 735 (2020), 139562. doi:10.1016/j.scitotenv.2020.139562

Xu, H. (2013). A remote sensing index for assessment of regional ecological changes. *China Environ. Sci.* 33 (5), 889–897. doi:10.3969/j.issn.1000-6923.2013.05.019

Xu, H., Wang, M., Shi, T., Guan, H., Fang, C., and Lin, Z. (2018). Prediction of ecological effects of potential population and impervious surface increases using a remote sensing based ecological index (RSEI). *Ecol. Indic.* 93, 730–740. doi:10.1016/j.ecolind.2018.05.055

Xu, H., Wang, Y., Guan, H., Shi, T., and Hu, X. (2019). Detecting ecological changes with a remote sensing based ecological index (RSEI) produced time series and change vector analysis. *Remote Sens. (Basel).* 11, 2345. doi:10.3390/rs11202345

Yang, G., Zhang, Z. J., Cao, Y. G., Zhuang, Y. N., Yang, K., and Bai, Z. K. (2021). Spatial-temporal heterogeneity of landscape ecological risk of large-scale open-pit mining area in north Shanxi. *Chin. J. Ecol.* 40 (1), 187–198. doi:10.13292/j.1000-4890.202101.003

Yang, Y., Bao, W., Li, Y., Wang, Y., and Chen, Z. (2020). Land use transition and its eco-environmental effects in the beijing–tianjin–hebei urban agglomeration: A production–living–ecological perspective. *Land* 9, 285. doi:10.3390/land9090285

Yu, D. J., and Hong, X. Y. (2022). A theme evolution and knowledge trajectory study in AHP using science mapping and main path analysis. *Expert Syst. Appl.* 205, 117675. doi:10.1016/j.eswa.2022.117675

Yuan, B. D., Fu, L. N., Zou, Y. A., Zhang, S. Q., Chen, X. S., Li, F., et al. (2021). Spatiotemporal change detection of ecological quality and the associated affecting factors in Dongting Lake Basin, based on RSEI. *J. Clean. Prod.* 302 (2021), 126995. doi:10.1016/j.jclepro.2021.126995

Zhang, X. (2020). *Global land-cover classification and mapping at 30 m using quantitative remote sensing technique*. Beijing: University of Chinese Academy of Sciences, p133. doi:10.44231/d.cnki.gktxc.2020.000011

Zhao, J., Jin, J., Zhu, J., Xu, J., Hang, Q., Chen, Y., et al. (2016). Water resources risk assessment model based on the subjective and objective combination weighting methods. *Water Resour. manage.* 30 (2016), 3027–3042. doi:10.1007/s11269-016-1328-4

frontiers | Frontiers in Environmental Science

TYPE Original Research
PUBLISHED 12 January 2023
DOI 10.3389/fenvs.2022.1074376

OPEN ACCESS

EDITED BY
Yonghao Xu,
Institute of Advanced Research in Artificial Intelligence (IARAI), Austria

REVIEWED BY
Shizhen Chang,
Institute of Advanced Research in Artificial Intelligence (IARAI), Austria
Iman Rousta,
Yazd University, Iran

*CORRESPONDENCE
Guoxin Lan,
feman7122@163.com

SPECIALTY SECTION
This article was submitted to Environmental Informatics and Remote Sensing, a section of the journal Frontiers in Environmental Science

RECEIVED 19 October 2022
ACCEPTED 28 December 2022
PUBLISHED 12 January 2023

CITATION
Jiang X, Guo X, Wu Y, Xu D, Liu Y, Yang Y and Lan G (2023), Ecological vulnerability assessment based on remote sensing ecological index (RSEI): A case of Zhongxian County, Chongqing. *Front. Environ. Sci.* 10:1074376. doi: 10.3389/fenvs.2022.1074376

Ecological vulnerability assessment based on remote sensing ecological index (RSEI): A case of Zhongxian County, Chongqing

Xiaolan Jiang[1,2], Xianhua Guo[1,2], Yan Wu[2], Denghui Xu[1,2], Yixuan Liu[1,2], Yuzheng Yang[1,2] and Guoxin Lan[1,2]*

[1]Research Institute of Three Gorges, Chongqing Three Gorges University, Chongqing, China, [2]Key Laboratory of Water Environment Evolution and Pollution Control in Three Gorges Reservoir, Chongqing Three Gorges University, Chongqing, China

The ecological vulnerability evaluation index was established through Normalized Difference Vegetation Index (NDVI), Wetness (WET), Normalized Difference Build-up and Soil Index (NDBSI) and Land Surface Temperature (LST) indicators, comprehensively evaluate the ecological vulnerability of Zhongxian County of Chongqing in 2002, 2009, and 2016 by Principal Components Analysis (PCA), and analyze its spatio-temporal evolution. The vulnerability areas of five levels were calculated respectively, and the overall index of ecological vulnerability was also calculated. The index of remote sensing ecological index (RSEI) and Normalized Difference Vegetation Index decreased first and then increased; the Wetness index showed an upward trend; the Normalized Difference Build-up and Soil Index index increased first and then decreased; and the Land Surface Temperature index decreased. The ecological vulnerability body index (EVBI) shows a downward trend, and the incremental changes are mainly concentrated in the negligible vulnerability areas and light vulnerability area, while the medium vulnerability, strong vulnerability and extreme vulnerability area generally show a downward trend. Furthermore, the new increment of ecological vulnerability grade area concentrates on negligible vulnerability area and light vulnerability area from 2002 to 2016. In general, the ecological vulnerability gradually shifts to low vulnerability, and the ecological environment tends to develop healthily.

KEYWORDS

ecological vulnerability, RSEI, PCA, spatiotemporal evolution, ecological environment

1 Introduction

The social economy is developing rapidly, with intensifying contradiction between human and ecological environment. The irrational utilization of resources leads to the destruction of the surrounding ecological balance to a certain extent (Yan and Zhao, 2009), and affects the sustainable development of the ecosystem. The ecological fragility problem is more serious, which is the focus of sustainable development research and has attracted the attention of many scholars worldwide (Jackson et al., 2004; Ma et al., 2015; Gao and Zhang, 2018; Tian et al., 2021; Wang et al., 2021). The deepening scientific research diversifies ecological vulnerability assessment methods. For example, Zhang et al. (2021a) used fuzzy comprehensive method and analytic hierarchy process to study the ecological fragility of Yongding River. Teng et al. (2022) constructed an exposure-sensitivity-adaptive vulnerability assessment framework, established an ecological and social index system, determined the index weight by entropy

weight method, and evaluated the change rules of ecological vulnerability (EV) and social vulnerability (SV). Zhang et al. (2021b) calculated the vulnerability of landscape types to determine the ecological vulnerability of coastal zone. Based on remote sensing (RS) and geographic information system (ArcGIS) technology, Wang and Su (2018) constructed the "Pressure-State-Response" framework and used PCA to evaluate the ecological vulnerability. Besides, Liu et al. (2020) built an ecological sensitivity-ecological resilience-ecological pressure model to calculate the weight using the PCA method, and systematically evaluate the ecological vulnerability. The ecological vulnerability assessment helps us to understand the current the *status quo* of regional ecological vulnerability, which has a positive effect on the implementation of ecological environment governance plan. The data sources of evaluation indicators mainly include remote sensing, meteorological and other data. In addition, some studies combine RS and ArcGIS technology for ecological vulnerability evaluation. However, there are few studies that make full use of remote sensing indicators and remote sensing models for in-depth analysis of ecological vulnerability evaluation. Wu (2005) constructed the ecological environment vulnerability equation and evaluation system based on RS technology, and used ASTER and TM data fusion technology to conduct quantitative remote sensing research on ecological environment vulnerability vegetation; Bai et al. (2009) extracted eight ecological factors including vegetation index, soil brightness and soil moisture index, elevation and slope, temperature and precipitation, and land use through RS and ArcGIS technology as evaluation indicators, and used the analytical hierarchy process (AHP) to evaluate the vulnerability of ecological environment; Zhu (2020) created 10 small indicators and 4 large indicators through the analysis of long time series multi-source remote sensing data (NDVI data, reflectance data, land use data, DEM data, lighting data, soil moisture data, precipitation data) and non-remote sensing data (protected areas), forming a set of assessment system to analyze the ecological vulnerability of the study area. Since the index system is subject to subjective influence, all the selected indicators are included in the evaluation model and the independence of the indicators is ignored, resulting in increased calculation and inaccurate results (Yao et al., 2016). Based on previous research results, multi index comprehensive evaluation model built by the evaluation method of the combination of ArcGIS and RS technology can effectively solve the problem of large-scale ecological vulnerability evaluation. It can not only reflect the current situation and distribution characteristics of ecological vulnerability, but also have objectivity and high reliability.

Zhongxian County is in the middle of Chongqing and in the hinterland of the sensitive and vulnerable area of ecological environment-the Three Gorges Reservoir area. Ecological vulnerability assessment is of great significance to master its ecological vulnerability characteristics and identify ecological and environmental problems (Wang et al., 2010). Therefore, this study employed remote sensing and geographic information system technology, and established an index system with NDVI, WET, NDBSI and LST based on RSEI (Xu, 2013) to comprehensively evaluate the ecological vulnerability of Zhongxian County from 2002 to 2016 using PCA, and reveal the spatio-temporal evolution of ecological vulnerability. This study aims to provide theoretical support and scientific basis for government decision-making for the ecological vulnerability protection of Zhongxian County.

2 Materials and methods

2.1 Study area

Zhongxian County (107° 3′E-108° 14′E, 30° 03′N-30° 35′N) is adjacent to Wanzhou District in the northeast, Dianjiang County in the west, Shizhu Tujia Autonomous County in the southeast, Fengdu County in the southwest and Liangping District in the north, with an area of about 2,178 km^2 (Figure 1). The territory of Zhongxian County is characterized by rolling hills, crisscross streams and rivers, and mainly hilly landform. It has the subtropical southeast monsoon mountain climate with the characteristics of warm and cold, sufficient sunshine and so on, which is significantly affected by the hilly terrain. Zhongxian County is a subtropical evergreen broad-leaved forest belt with various vegetation types, which is suitable for the growth of many plants.

2.2 Data source and processing

Zhongxian County of Chongqing was chosen as the research area, and the remote sensing data set is provided by Geospatial Data Cloud site, Computer Network Information Center, Chinese Academy of Sciences (http://www.gscloud.cn) Landsat 5 TM image in 2002 and 2009, and Landsat 8 OLI image in 2016. Landsat 5 TM is a thematic mapper improved on the basis of MSS. It consists of seven bands, with a spatial resolution of 30 m for bands 1–5 and 7, and 120 m for band 6 (thermal infrared band). Landsat 8 carries an OLI land imager and a TIRS thermal infrared sensor. The OLI land imager consists of 9 bands with a spatial resolution of 30 m, including a 15 m panchromatic band. The TIRS thermal infrared sensor consists of 2 separate thermal infrared bands with a resolution of 100 m.The remote sensing images in 2002, 2009, and 2016 were radiometric calibrated by the environment for visualizing images (ENVI5.3) software, and the pixel value of the original image was converted into the reflectivity of the sensor. FLAASH (Fast line-of-sight atmospheric analysis of spectral hypercubes) absolute atmospheric correction images were adopted to reduce the differences in atmosphere and terrain of remote sensing images in different periods, and the impact on RSEI comparison between different images. The images of the study area were cropped, and the images of different phases were registered according to the quadratic polynomial and the nearest pixel method. The root mean square error of registration is less than .5 pixels. The data must be preprocessed, which is especially important for RSEI comparison between different categories and different temporal phases (Landsat 5 TM and Landsat 8 OLI_TIRS). When calculating the humidity index of the tasseled cap transformation, the correct formula should be selected, and the humidity of OLI cannot be calculated by the formula of TM, and the data based on reflectance cannot be calculated by the formula based on DN value. The DEM image of Zhongxian County is derived from the SRTMDEM 90M resolution raw elevation data provided by Geospatial Data Cloud site, Computer Network Information Center, Chinese Academy of Sciences (http://www.gscloud.cn). The world map is derived from the Natural Earth website (http://naturalearthdata.com), the administrative division

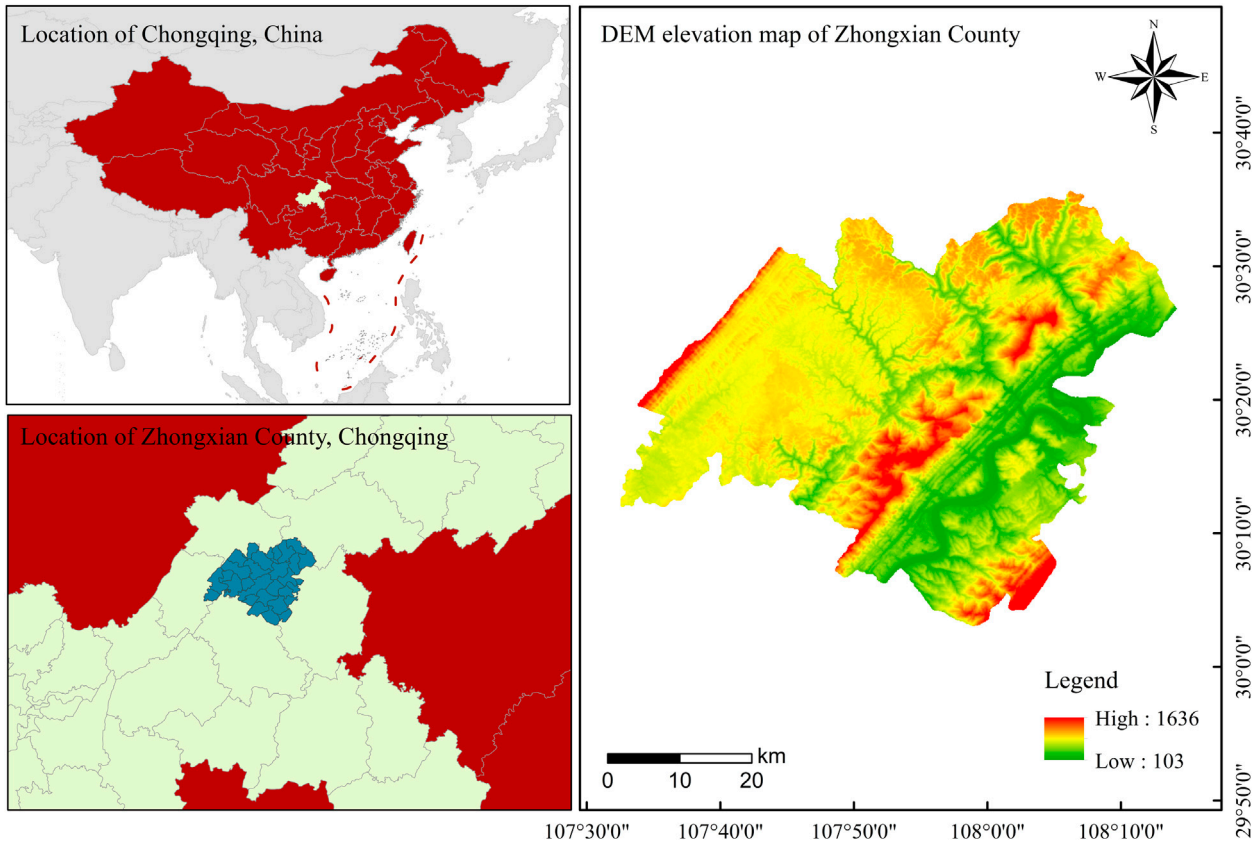

FIGURE 1
Location of Zhongxian County, China.

map of China is derived from the website (https://github.com/GaryBikini/ChinaAdminDivisonSHP), and the administrative division map of Chongqing City and Zhongxian County is derived from 91 Weitu Assistant.

2.3 Research methods

2.3.1 Construction of evaluation index

Normalized Difference Vegetation Index (NDVI). Normalized Difference Vegetation Index (NDVI) is closely related to plant biomass, leaf area index and vegetation coverage (Goward et al., 2002), which was chosen in this paper to replace the greenness index, and the formula is as follows:

$$NDVI = (p_{NIR} - p_R)/(p_{NIR} + p_R) \quad (1)$$

where p_{NIR} and p_R is the reflectance of near infrared band and red band of Landsat 5 TM and Landsat 8 OLI_TIRS, respectively.

Wetness (WET): The brightness, greenness and humidity components of tassel hat transformation are related to surface physical parameters (Huang et al., 2002; Wang and Dong, 2013). Here, the Wetness index (WET) is expressed by humidity component. The expressions of reflectance image data of Landsat 5 TM and Landsat 8 OLI_TIRS are as follows (Crist, 1985; Baig et al., 2014):

$$Wet_{TM} = 0.0315p_B + 0.2021p_G + 0.3102p_R + 0.1594p_{NIR} - 0.6806p_{SWIR1} - 0.6109p_{SWIR2} \quad (2)$$

$$Wet_{OLI} = 0.1511p_B + 0.1972p_G + 0.3283p_R + 0.3407p_{NIR} - 0.7117p_{SWIR1} - 0.4559p_{SWIR2} \quad (3)$$

where p_B, p_G, p_R, p_{NIR}, p_{SWIR1}, and p_{SWIR2} represent the reflectance of the blue, green, red, near infrared, shortwave infrared 1 and shortwave infrared 2 bands of Landsat 5 TM and Landsat 8 OLI_TIRS, respectively.

Normalized Difference Build-up and Soil Index (NDBSI). Urban land leads to the "drying" of the surface. In this paper, index-based built-up index (IBI) is used to replace the building index in the NDBSI. At the same time, the exposed land on the surface will also cause surface drying. NDBSI (Xu, 2013) can be calculated by the combination of index-based built-up index (IBI) and soil index (SI) (NASA, 2012):

$$NDBSI = (IBI + SI)/2 \quad (4)$$

among,

$$IBI = \frac{\{2p_{SWIR1}/(p_{SWIR1} + p_{NIR}) - [p_{NIR}/(p_{NIR} + p_R) + p_G/(p_G + p_{SWIR1})]\}}{\{2p_{SWIR1}/(p_{SWIR1} + p_{NIR}) + [p_{NIR}/(p_{NIR} + p_R) + p_G/(p_G + p_{SWIR1})]\}} \quad (5)$$

$$SI = [(p_{SWIR1} + p_R) - (p_B + p_{NIR})/(p_{SWIR1} + p_R) + (p_B + p_{NIR})] \quad (6)$$

where p_G, p_B, p_R, p_{NIR}, and p_{SWIR1} are the reflectance of green, blue, red, near infrared and short wave infrared 1 bands of Landsat 5 TM and Landsat 8 OLI_TIRS remote sensing images, respectively.

TABLE 1 Principal component analysis of each index.

	Principal component coefficient							
	Principal component	NDVI	WET	NDBSI	LST	characteristic value(λ)	Contribution rate (%)	Cumulative contribution rate (%)
2002	PC1	.30823	.69286	-.53954	-.36582	.01602	58.1833	58.1833
	PC2	.86611	-.46149	-.16475	.09870	.00878	31.8663	90.0496
	PC3	.02784	.32123	-.19904	.92543	.00247	8.9739	99.0235
	PC4	.39252	.45142	.80133	.00385	.00027	.9765	100.0000
2009	PC1	.37592	.57527	-.59417	-.41799	.01602	69.1266	69.1266
	PC2	.83399	-.35970	-.10546	.40492	.00878	16.2134	85.3400
	PC3	-.22024	.47777	-.24884	.81321	.00247	13.5068	98.8468
	PC4	.33859	.55805	.75757	-.00434	.00027	1.1532	100.0000
2016	PC1	.53986	.39012	-.67250	-.32265	.01894	77.3425	77.3425
	PC2	.39995	-.07374	-.15377	.90053	.00346	14.1453	91.4878
	PC3	.65342	-.63227	.29747	-.29118	.00193	7.8938	99.3816
	PC4	.34875	.66529	.66001	.01228	.00015	.6184	100.0000

Land Surface Temperature (LST): The LST index is represented by land surface temperature (Xu, 2013), and the temperature value T at the sensor was calculated by using the model (NASA, 2018) in Landsat user manual. The real land surface temperature can be obtained only through specific emissivity correction:

$$L = gain \times DN + bias \tag{7}$$

$$T = K_2/\ln(K_1/L + 1) \tag{8}$$

$$LST = T/[1 + (\lambda T/p)\ln\varepsilon] \tag{9}$$

where L is the radiance value of Landsat 5 TM thermal infrared 6 band and Landsat 8 OLI_TIRS thermal infrared 10 band, and DN is the pixel value of the band. Gain and bias are the gain value and offset value of thermal infrared band respectively. T is the temperature value at the sensor, and K_1 and K_2 is the calibration parameter. Landsat 5 TM image, K_1 = 607.76 W/(m^2·sr·μm), K_2 = 1,260.56 K, in Landsat 8 OLI_TIRS image K_1 = 774.89 W/(m^2·sr·μm), K_2 = 1,321.08 K, λ is the wavelength of thermal infrared band, p = 1.438 × 10^{-2} m K, and ε is the surface specific emissivity.

2.3.2 Index standardization

Different dimensions will cause the weight of each indicator to be unbalanced. Therefore, it is necessary to standardize the indicators and unify their dimensions between [0, 1] before PCA calculation (Xu, 2013). The normalization formula of each indicator is as follows:

$$SI_n = \frac{I_n - I_{min}}{I_{max} - I_{min}} \tag{10}$$

where SI_n is the standardized value of the *n*th index, and its value is between [0, 1]. I_n, I_{max} and I_{min} represent the value, maximum value and minimum values of the *n*th index in pixel n, respectively.

2.3.3 Evaluation method

The ecological vulnerability index (EVI) can be calculated to understand the status and characteristics of ecological vulnerability. The construction of the eco-index should accommodate both the appearance of a single indicator and the combination of information from the above four indicators. Therefore, how to represent multiple variables above with a single variable, that is key to this study. A frequently used method is to simply add up the individual indicators (Kearney et al., 1995), or to group the indicators to find the mean value and then add them up (Wang et al., 2007), or to multiply them by their respective weights and then add them up (Williams et al., 2009). However, both the correlation between indicators and the artificial determination of weights and other relevant factors can affect the results. Multidimensional statistical method of principal component analysis is a multidimensional data compression technique that selects a few important variables by linear transformation of multiple variables, and it takes the method of sequentially rotating the coordinate axes vertically to concentrate the multidimensional information into a few characteristic components, which often represent certain characteristic information (Xu, 2013). Therefore, this study was conducted by using the principal component transformation to construct the remote sensing ecological index, and the main information was concentrated on the first 1–2 principal components by removing the correlation among the indicators through the rotation of the spatial axes of the feature spectra. One of the other advantages of using principal component analysis is that the weights of each indicator are not artificially determined, but are determined automatically and objectively based on the contribution of each indicator to each principal component quantity. What this leads to is that bias in the results caused by weight settings that vary from individual to individual and from method to method can be avoided in the calculation. However, there is correlation among the evaluation indicators, and the information of each indicator will overlap during calculation, so the principal component analysis method is used. Principal component analysis can transform multiple indicators into a few uncorrelated

TABLE 2 Classification standard of ecological vulnerability in Zhongxian County, Chongqing (Fan et al., 2009; Ifeanyi et al., 2010; Ma et al., 2015; He et al., 2018).

Vulnerability	Grade	Standardized value of ecological vulnerability index	Ecological characteristics
Negligible vulnerability	I	<2.0	The structure and functions of the ecosystem are reasonably improved, and the ecosystem is stable with low pressure, strong ability to resist external disturbance and self-recovery, no ecological abnormality and low ecological vulnerability
Light vulnerability	II	2.0–4.0	The structure and function of the ecosystem are relatively complete, and the ecosystem bears less pressure. The ecosystem is relatively stable, and has strong ability to resist external disturbance and self-recovery. There are potential ecological anomalies and low ecological vulnerability
Medium vulnerability	III	4.0–6.0	The structure and function of the ecosystem can still be maintained, and the pressure is large. The system is relatively unstable, and the external interference is more sensitive, the self-recovery ability is weak, and there is a small number of ecological abnormalities, and the ecological fragility is higher
Strong vulnerability	IV	6.0–8.0	Defects in the ecosystem structure and function, high pressure, unstable ecosystem, strong sensitivity to external interference, great difficulty in recovery after damage, many ecological abnormalities and high ecological vulnerability
Extreme vulnerability	V	≥8.0	The structure and function of the ecosystem are severely degraded and under great pressure. The ecosystem is extremely unstable and sensitive to external disturbance. It is extremely difficult or even irreversible to recover after damage, even irreversible, ecological abnormalities appear in a large area, and the ecological vulnerability is very high

TABLE 3 Four indicators and RSEI statistics in 2002 and 2016.

	2002		2009		2016	
Index	Mean value	Standard deviation	Mean value	Standard deviation	Mean value	Standard deviation
NDVI	.6716	.1233	.3834	.3741	.4931	.3817
WET	.6675	.1983	.7232	.1948	.7644	.0686
NDBSI	.6248	.2549	.7572	.2446	.5668	.2656
LST	.5721	.1042	.2234	.2310	.2731	.2635
RSEI	.5405	.0720	.5122	.0967	.7098	.0755

comprehensive indicators, and reflect the information expressed by more variables using fewer comprehensive indicators. Based on GIS 10.7 system calculation, this paper made principal component analysis on standardized indexes of NDVI, WET, NDBSI and LST. When the cumulative contribution rate of principal component reaches more than 85%, it can represent the information reflected by most variables (Table 1), and further calculate EVI (Yao et al., 2016; Wang and Su, 2018):

$$EVI = r_1\gamma_1 + r_2\gamma_2 + \cdots + r_n\gamma_n \quad (11)$$

where EVI is the ecological vulnerability index. r_n and γ_n represent the contribution rate of the *n*th principal component and the *n*th principal component respectively.

Table 1 shows that the cumulative contribution rates of the PC1, PC2 and PC3 among the four indicators in Zhongxian County in 2002, 2009, and 2016 were 99.0235%, 98.8468%, and 99.3816% respectively, all greater than 85%, suggesting that they have concentrated the main information of the four indicators. In PC1, both NDVI and WET are positive, suggesting that both are good for the environment development, and both NDBSI and LST are negative.

Based on the PCA, the inversion model of ecological vulnerability assessment was calculated through Eq. 11 and Table 1 as follows:

$$EVI_{2002} = 0.5818 \times PC1 + 0.3187 \times PC2 + 0.0897 \times PC3 \quad (12)$$

$$EVI_{2009} = 0.6913 \times PC1 + 0.1621 \times PC2 + 0.1351 \times PC3 \quad (13)$$

$$EVI_{2016} = 0.7734 \times PC1 + 0.1415 \times PC2 + 0.0789 \times PC3 \quad (14)$$

where EVI_{2002}, EVI_{2009}, and EVI_{2016} represent the ecological vulnerability index in 2002, 2009 and 2016 respectively, and PC1-PC3 is the first three principal component factors of principal component analysis. Their cumulative contribution rate in the 3 years reached 99%, but most of the information of the PC4 is noise. So, the PC4 is ignored.

2.3.4 Classification of ecological vulnerability and overall index of ecological vulnerability

In order to better measure the ecological vulnerability, vulnerability index need to be standardized, and the formula is as follows:

$$SI_{EVI} = \frac{EVI_n - EVI_{min}}{EVI_{max} - EVI_{min}} \times 10 \quad (15)$$

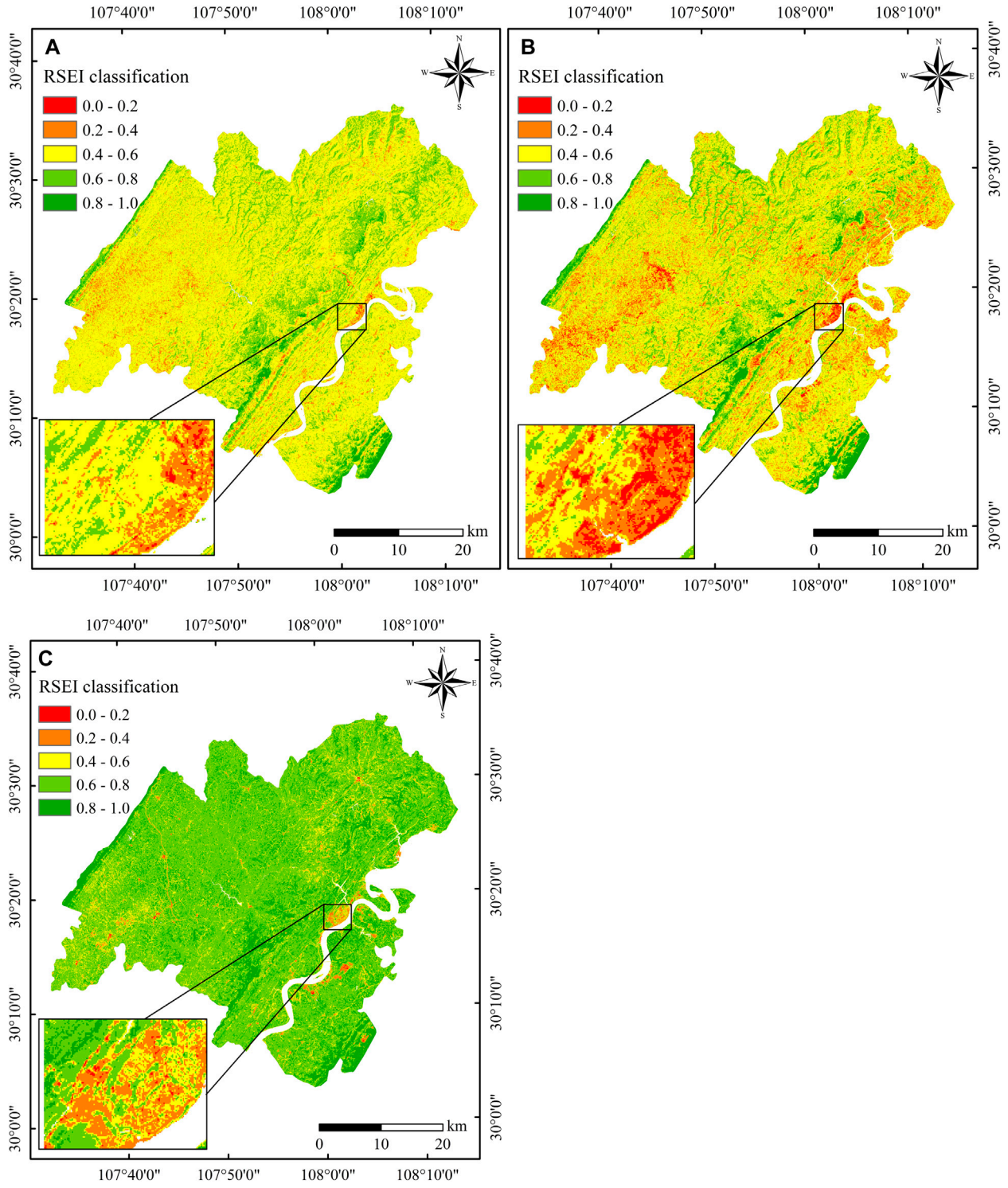

FIGURE 2
2002 **(A)**, 2009 **(B)** and 2016 **(C)** RSEI of Zhongxian County (water body mask treatment, the picture at the lower left corner shows the location of Zhongxian County administrative center).

where SI_{EVI} represents the standardized value, and it is between 0 and 10. EVI_n, EVI_{min}, and EVI_{max} represent the actual value, minimum value and maximum value of ecological vulnerability index, respectively. The standardized EVI was divided into five vulnerability levels (Fan et al., 2009; Ifeanyi et al., 2010; Ma et al., 2015; He et al., 2018) according to the relevant ecological vulnerability classification standards (Table 2), which are negligible vulnerability, light vulnerability, medium vulnerability, strong vulnerability and extreme vulnerability.

The ecological vulnerability body index (EVBI) calculated by multiplier model can analyze the overall difference of ecological

TABLE 4 Area and EVBI distribution of ecological vulnerability in different years in Zhongxian County, Chongqing.

	2002		2009		2016	
Grade	Area (km^2)	EVBI	Area (km^2)	EVBI	Area (km^2)	EVBI
I	27.0414	.012365	64.7010	.030532	653.9742	.299028
II	348.4044	.318614	556.4673	.525184	1,254.4140	1.14755
III	1,360.5140	1.866274	1,324.6460	1.875266	181.7620	.249331
IV	390.5784	.714364	169.4421	.319833	30.5271	.055834
V	7.4772	.017095	3.8763	.009146	2.3895	.005463
Total	2,134.0152	2.928711	2,119.1328	2.759961	2,123.0667	1.75681

vulnerability in Zhongxian County, and the algorithm is as follows (Yao et al., 2016):

$$EVBI = \sum_{i=1}^{n} P_i \times A_i / S \quad (16)$$

where EVBI indicates the overall index of ecological vulnerability. P_i Indicates the class i vulnerability level value. A_i indicates the area of class i vulnerability. S represents the total area of the area. n Indicates the total number of vulnerability levels.

2.3.5 Extracting the spatio-temporal evolution pattern of ecological fragility

Based on ArcGIS 10.7 system, this paper spatially superimposed the ecological vulnerability level map in 2002–2009, 2009–2016 and 2002–2016 to extract the dynamic map of ecological vulnerability change. The algorithm is as follows (Deng et al., 2016; Guo et al., 2019):

$$Code_{Classification_{2002\_2009}} = 10 \times Code_{Classification_{\_2002}} + Code_{Classification_{\_2009}} \quad (17)$$

$$Code_{Classification_{2009\_2016}} = 10 \times Code_{Classification_{\_2009}} + Code_{Classification_{\_2016}} \quad (18)$$

$$Code_{Classification_{2002\_2016}} = 100 \times Code_{Classification_{\_2002}} + 10 \times Code_{Classification_{\_2009}} + Code_{Classification_{\_2016}} \quad (19)$$

where $Code_{Classification_{\_2002}}$, $Code_{Classification_{\_2009}}$ and $Code_{Classification_{\_2016}}$ represent five vulnerability level type codes, respectively. I-V represent negligible, light, medium, strong and extreme vulnerability respectively. $Code_{Classification_{2002\_2009}}$ is the change type code of ecological vulnerability level, which represents the transformation from ecological vulnerability level type in 2002 to ecological vulnerability level type in 2009. For example, I-V indicates the transformation from negligible vulnerability in 2002 to extreme vulnerability in 2009.

3 Results

3.1 Change characteristics of ecological vulnerability index

Table 3 demonstrates the statistical values of four indicators and the RSEI in 2002, 2009, and 2016. Due to the great diurnal temperature variation, the Land surface temperature index (LST) can only be compared through normalization (Carlson and Arthur, 2000; Xu et al., 2009). Therefore, the four indexes were normalized and the null value was removed to obtain the statistical values of each index. Table 3 shows the analysis results, the mean value of NDVI index beneficial to the ecological environment decreased from .6716 in 2002 to .3834 in 2009, with a decreased of 42.91%, and then increased to .4931 in 2016, indicating that the decrease of vegetation coverage in Zhongxian County gradually increased after a significant decline. In the other hand, the mean value of WET index increased from .6675 in 2002 to .7644 in 2016, an increase of 14.52%, suggesting that the water conservation capacity of Zhongxian County has improved. The mean values of NDBSI and LST indicators that having adverse effects on the ecological environment have decreased. The mean values of NDBSI increased from .6248 in 2002 to .7572 in 2009, and decreased to .5668 in 2016, and LST decreased significantly from .5721 in 2002 to .2234 in 2009 and increased to .2731 in 2016, indicating that the surface exposure of Zhongxian County has been reduced, the difference between hydrothermal balance has been reduced, and the adverse impact on the future ecological environment has been weakened. Based on the changes of the above four indicators, it roughly shows that the ecological environment of Zhongxian County is on the rise as a whole, and the environmental change is gradually developing in a good direction. The mean value of the RSEI decreased from .5405 in 2002 to .5122 in 2009 and increased to .7098 in 2016, indicating that the ecological environment quality in the study area fluctuated from 2002 to 2016, but the overall development trend showed a benign development trend, which was basically consistent with the comprehensive results of the indicators. The RSEI of Zhongxian County in 2002, 2009, and 2016 were shown in Figure 2. In order to further highlight the representativeness of the RSEI, the ecological index was divided into five grades, representing five grades including poor (I: .0–.2), poor (II: .2–.4), medium (III: .4–.6), good (IV: .6–.8) and excellent (V: .8–1.0). In 2002, the RSEI was dominated by medium (III) grade, accounting for 69.83%, and the percentages of good (IV) and excellent (V) grades were 22.47% and 1.39%, respectively, which were mainly distributed in areas with high terrain and little impact of human activities, while poor (I) and poor (II) areas accounted for .09% and 6.22%, which were mainly distributed in areas with frequent human activities. In 2009, the RSEI was dominated by medium (III) grade, accounting for 59.11%, poor (I) and poor (II) grades accounted for 1.06% and 17.17% respectively, and good (IV) and excellent (V) grades accounted for 19.94% and 2.72%

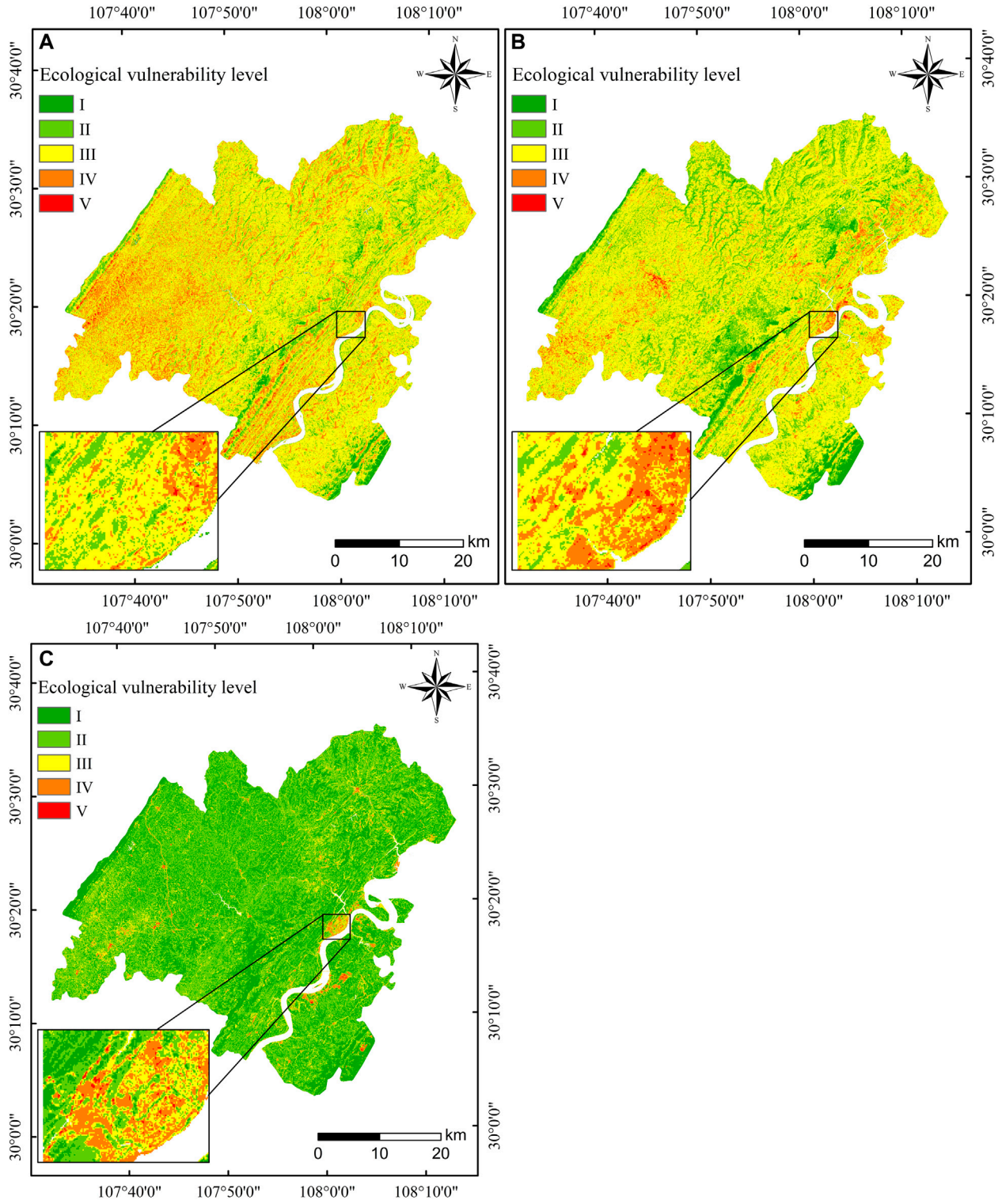

FIGURE 3
Spatial distribution of ecological vulnerability level in Zhongxian County in 2002 **(A)**, 2009 **(B)** and 2016 **(C)** (water body mask treatment, the picture at the lower left corner shows the location of Zhongxian administrative center).

respectively. In 2016, the RSEI was dominated by good (IV) grade, accounting for 72.17%, and medium (III) and excellent (V) grades accounted for 11.21% and 14.89% respectively and the area of poor (I) and poor (II) areas was the least, accounting for .12% and 1.62%. Among them, the areas with poor ecological environment quality were mainly concentrated in urban areas. On the whole, the quality of the ecological environment of Zhongxian County from 2002 to 2016 has improved.

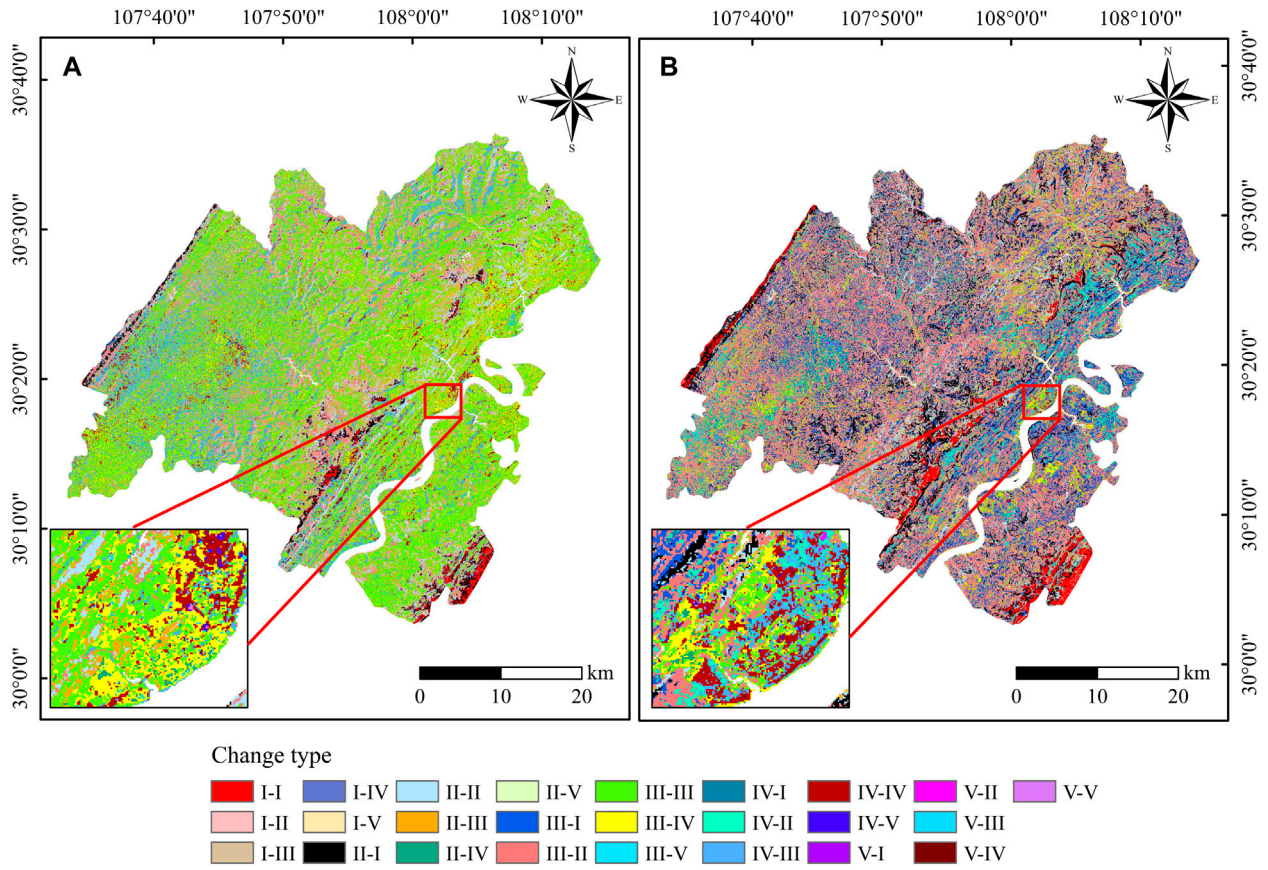

FIGURE 4
2002–2009 **(A)**, 2009–2016 **(B)** temporal and spatial evolution pattern of ecological vulnerability in Zhongxian County (water mask treatment, the picture at the lower left corner shows the location of Zhongxian County administrative center).

TABLE 5 Area transfer matrix of different ecological vulnerability levels in Zhongxian County from 2002 to 2009 (km²).

Vulnerability level		2009					Total of 2000	Reduction of 2000
		Negligible vulnerability	Light vulnerability	Medium vulnerability	Strong vulnerability	Extreme vulnerability		
2000	Negligible vulnerability	18.8271	5.3928	.9135	.1035	.0054	25.2423	6.4152
	Light vulnerability	44.2962	211.7187	79.0515	8.8353	.2988	344.2005	132.4818
	Medium vulnerability	1.3545	326.7990	927.8190	93.8583	2.1222	1,351.9530	424.1340
	Strong vulnerability	.1602	11.6982	313.0740	62.7012	1.2276	388.8612	326.1600
	Extreme vulnerability	.0000	.0486	3.3075	3.8475	.2196	7.4232	7.2036
	Total of 2009	64.6380	555.6573	1,324.1655	169.3458	3.8736	2,117.6802	—
	Increment of 2009	45.8109	343.9386	396.3465	106.6446	3.6540	—	896.3946

TABLE 6 Area transfer matrix of different ecological vulnerability levels in Zhongxian County from 2009 to 2016 (km²).

Vulnerability level		2016					Total of 2009	Reduction of 2009
		Negligible vulnerability	Light vulnerability	Medium vulnerability	Strong vulnerability	Extreme vulnerability		
2009	Negligible vulnerability	55.7811	7.4718	.8676	.3627	.0918	64.5750	8.7939
	Light vulnerability	274.3758	263.1519	15.4710	2.1735	.1647	555.3369	292.1850
	Medium vulnerability	288.3375	885.0816	132.8013	16.7679	.9918	1,323.9801	1,191.1788
	Strong vulnerability	34.2963	97.3287	27.9585	8.8038	.9036	169.2909	160.4871
	Extreme vulnerability	1.1709	1.0755	.5949	.7884	.2340	3.8637	3.6297
	Total of 2016	653.9616	1,254.1095	177.6933	28.8963	2.3859	2,117.0466	—
	Increment of 2016	598.1805	990.9576	44.8920	20.0925	2.1519	—	1,656.2745

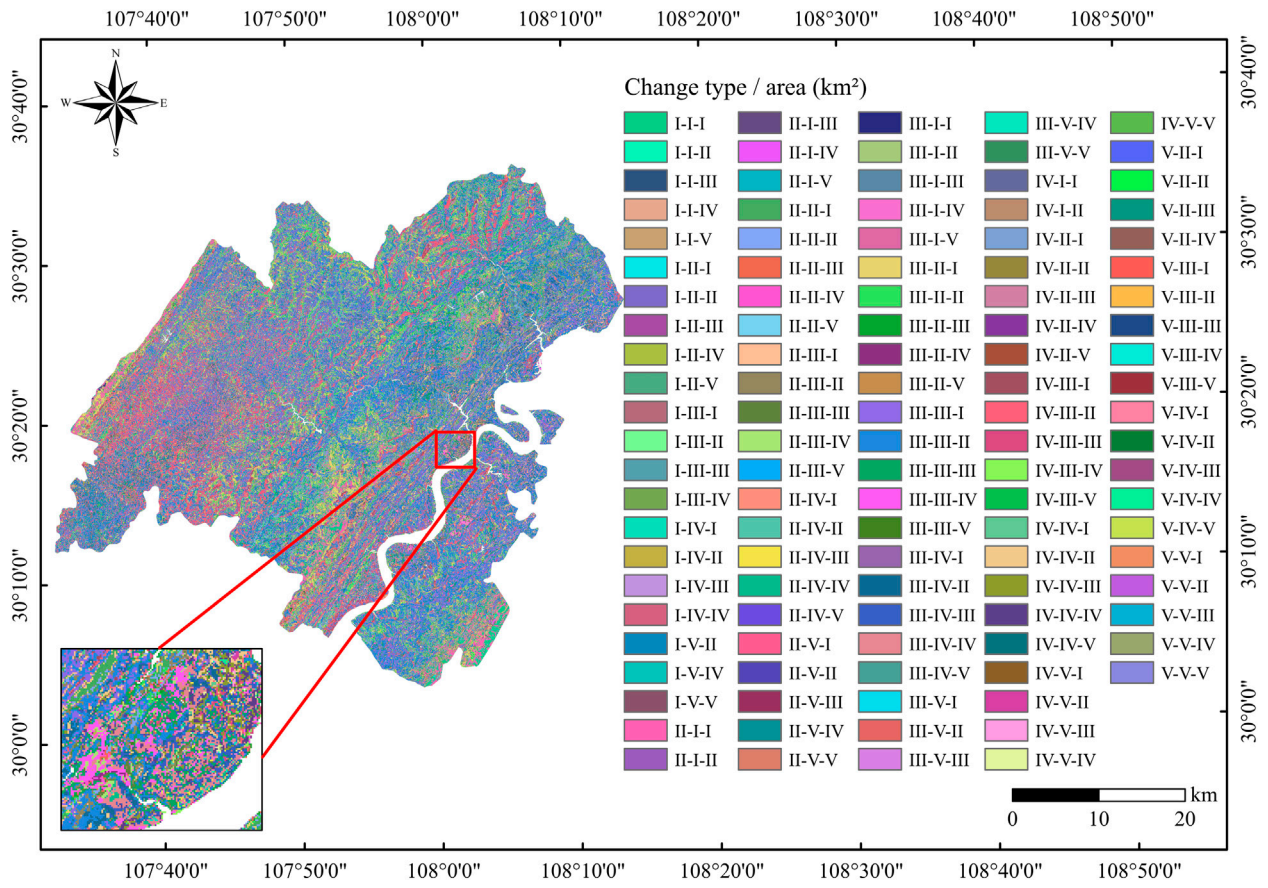

FIGURE 5
Temporal and spatial evolution pattern of ecological vulnerability in Zhongxian County from 2002 to 2016 (water mask treatment, the picture at the lower left corner shows the location of Zhongxian administrative center).

TABLE 7 Dynamic change of area of different ecological vulnerability levels from 2002 to 2016 (km²).

Vulnerability	Vulnerability level	Unchanged area	Reduction area	Increment area
Negligible vulnerability	I	16.2585	8.3835	637.6878
Light vulnerability	II	85.8339	258.2001	1,168.0578
Medium vulnerability	III	80.9667	1,270.6686	96.4980
Strong vulnerability	IV	3.5865	385.2261	25.2738
Extreme vulnerability	V	.0207	7.4025	2.3634

3.2 Overall characteristics of ecological vulnerability

By calculating the ecological vulnerability body index (EVBI) of the four indicators, the ecological vulnerability grade area and EVBI distribution in 2002, 2009, and 2016 were inversed (Table 4), and the overall distribution pattern of ecological vulnerability in Zhongxian County was analyzed. The total ecological vulnerability area of the five grades of Zhongxian County decreased from 2,134.0152/km^2 in 2002–2,119.1328/km^2 in 2009, and increased to 2,123.0626/km^2 in 2016. The total value of ecological vulnerability body index (EVBI) decreased from 2.9986 in 2002 to 2.759961 in 2009, and fell to 1.75681 in 2016, with a large decline. According to the classification standard of ecological fragility in Zhongxian County, the ecological vulnerability was mainly medium vulnerability and strong vulnerability in 2002, the medium vulnerability grade accounted for 62.21% of the total area, while the strong vulnerability grade was 17.86%. In 2009, it was mainly medium vulnerability and light vulnerability, accounting for 62.51% and 26.26% of the total area respectively. In 2016, it was mainly light vulnerability and negligible vulnerability, accounting for 57.36% and 29.90% of the total area respectively. The areas of medium vulnerability, strong vulnerability and extreme vulnerability areas in 2009 decreased by 35.8680/km^2, 221.1363/km^2 and 3.6009/km^2 respectively compared with 2002, and the areas of strong vulnerability areas decreased significantly. In 2016, the area of medium vulnerability, strong vulnerability and extreme vulnerability areas decreased by 1,142.8840/km^2, 138.915/km^2 and 1.4868/km^2 respectively compared with 2009, and the area of medium vulnerability areas decreased significantly. From 2002 to 2016, the area of negligible vulnerability and light vulnerability areas continued to grow, with an increase of 626.9328/km^2 and 906.0096/km^2 respectively, indicating significant changes in vulnerability.

As shown in Figure 3, the ecological vulnerability grade of Zhongxian County was dominated by medium vulnerability and strong vulnerability in 2002, which were distributed in bands and flakes, and the negligible, light and extreme vulnerability areas were roughly distributed in dots and blocks. Among them, the spatial distribution of medium vulnerability and strong vulnerability areas in the southwest was dense, which was mainly due to the densely populated distribution and the great impact of human activities. In 2009, Zhongxian County was mainly distributed in light and medium vulnerability areas, and negligible vulnerability areas, strong vulnerability areas and extreme vulnerability areas were generally distributed in bands and dots. The areas with high vulnerability were significantly affected by human activities, while areas with low vulnerability were mainly affected by terrain, with less human activities, less pressure, and strong ability to resist external interference and self-recovery. In 2016, Zhongxian County was mainly distributed in negligible vulnerability areas and light vulnerability areas, and the medium vulnerability, strong vulnerability and extreme vulnerability areas were roughly scattered in dots. The areas with high vulnerability were mostly areas with high economic level, large urbanization construction land, small green space and frequent human economic activities. The areas with low vulnerability were mainly limited by their geographical conditions, small population density and low impact of human economic activities. The good surface vegetation coverage can promote the reduction of its ecological vulnerability. Through the analysis of the overall situation of ecological vulnerability, the overall ecological vulnerability of Zhongxian County in Chongqing was found to be mainly increased to the negligible vulnerability and light vulnerability area from 2002 to 2016, and the medium vulnerability, strong vulnerability and extreme vulnerability areas showed a downward trend. The overall index of ecological vulnerability decreased. The ecological vulnerability weakened with the implementation of ecological restoration and protection measures, and the ecosystem was restored and improved.

3.3 Spatio-temporal evolution characteristics of ecological vulnerability

The spatial variation of ecological vulnerability level in Zhongxian County during the past 15 years was further analyzed, the study was divided into two periods (2002–2009 and 2009–2016) for longitudinal comparative analysis. The spatial-temporal evolution characteristics of ecological vulnerability was calculated by Eqs 17, 18 (Figure 4), and the area transfer matrix of different levels of ecological vulnerability was calculated during 2002–2009 and 2009–2016 (Tables 5, 6). From 2002 to 2009, the area transfers of various ecological vulnerability levels totaled 896.3946/km^2 (Table 5). From 2002 to 2009, the level of ecological vulnerability mainly transferred from medium vulnerability and strong vulnerability to light vulnerability and medium vulnerability. In 2002, the transfer amount of medium vulnerability and strong vulnerability was 424.1340/km^2 and 326.1600/km^2 respectively, accounting for 47.31% and 36.39% of the total amount of ecological vulnerability; the transfer amount of negligible, light and extreme vulnerability was 6.4152/km^2, 132.4818/km^2 and 7.2036/km^2, respectively, accounting for .72%, 14.78% and .80% of the total transfer volume. In 2009, the new increment of light vulnerability and medium vulnerability was 343.9386/km^2 and 396.3465/km^2 respectively, accounting for 38.37% and 44.22% of the total new increment; the new increment of negligible vulnerability, strong vulnerability and extreme vulnerability was 45.8109/km^2, 106.6446/km^2

and 3.6540/km^2, accounting for 5.11%, 11.90% and .41% of the total increment. From 2009 to 2016, the area transfers of various ecological vulnerability levels totaled 1,656.2745/km^2 (Table 6). From 2002 to 2009, the level of ecological vulnerability mainly transferred from light vulnerability and medium vulnerability to negligible vulnerability and light vulnerability. In 2009, the transfer amount of light vulnerability and medium vulnerability was 292.1850/km^2 and 1,191.1788/km^2 respectively, accounting for 17.64% and 71.92% of the total amount of ecological vulnerability; the transfer volume of negligible, strong and extreme vulnerability was 8.7939/km^2, 160.4871/km^2, and 3.6297/km^2, accounting for .53%, 9.69% and .22% of the total transfer volume. In 2016, the new increment of negligible vulnerability and light vulnerability was 598.1805/km^2 and 990.9576/km^2 respectively, accounting for 36.12% and 59.83% of the total new increment; the new increment of medium vulnerability, strong vulnerability and extreme vulnerability was 44.892/km^2, 20.0925/km^2, and 2.1519/km^2 respectively, accounting for 2.71%, 1.21%, and .13% of the total increment.

With the support of ArcGIS 10.7 software, the spatial variation of ecological vulnerability levels during 2002–2016 was calculated by Eq. 19 (Figure 5), and the area dynamic change of different ecological vulnerability levels in Zhongxian County during 2002–2016 was obtained (Table 7). Overall, the new increase in the area of ecological vulnerability level from 2002 to 2016 is mainly in the area of negligible vulnerability areas, light vulnerability areas and medium vulnerability areas, while the transfer amount is mainly light vulnerability areas, medium vulnerability areas and strong vulnerability areas. Affected by natural and geographical conditions, areas with large topographic fluctuations and less human activities have low ecological vulnerability, flat terrain and areas along the river basin have high ecological vulnerability (Figure 5). On the whole, the distribution pattern of ecological vulnerability is higher in the eastern and southwestern regions, and lower in the central and southeastern regions. With the promulgation of national policies and the implementation of ecological and environmental protection measures, ecological vulnerability has been gradually shifted to low vulnerability. Although the accelerated urbanization process has led to the growth of strong vulnerability areas and extreme vulnerability areas, the growth rate is still small, and shows a downward trend. Generally speaking, the ecological environment of Zhongxian County is gradually developing in a good direction.

4 Discussion

The purpose of this study is to make a comprehensive quantitative assessment of ecological vulnerability in Zhongxian County, and to analyze the spatio-temporal evolution characteristics of ecological vulnerability. In order to evaluate the ecological vulnerability in more detail, the RSEI in 2002, 2009 and 2016 was calculated, and the ecological vulnerability assessment index system was constructed by using the indicators of NDVI, WET, NDBSI, and LST, and the ecological vulnerability of Zhongxian County was analyzed by the principal component analysis method. From 2002 to 2016, the RSEI showed a trend of first decreasing and then increasing, in which the WET index showed an increasing trend, the LST index showed a decreasing trend, the NDVI index showed a decreasing trend and then increasing trend, and the NDBSI index showed a rising trend and then decreasing trend. In general, the ecological environment quality was developing towards a good trend. The degree of ecological vulnerability is related to vegetation index, wetness, bare land surface, urban land and land surface temperature, which is consistent with the results of other studies (Tang et al., 2022; Zhang et al., 2022). In addition to investigating the change characteristics of ecological vulnerability indicators, another aspect of this study is to analyze the spatial and temporal evolution pattern of ecological vulnerability. From 2002 to 2016, the overall index of ecological vulnerability showed a downward trend. By 2016, the level of ecological vulnerability was mainly negligible vulnerability and light vulnerability, and most areas shifted to negligible vulnerability and light vulnerability, and the ecological vulnerability gradually changed to low vulnerability. In terms of spatial distribution, the distribution of ecological vulnerability from high to low basically showed a trend of gradual transition from plain to mountainous region, which was consistent with other reports (Li, 2010; Jin and Xu, 2022; Singh et al., 2022).

Due to the characteristics of multi-band and strong correlation of multispectral images, the internal information of multispectral images is highly redundant (Sun et al., 2016). The index calculated based on remote sensing image may have information redundancy. In order to avoid the influence of human factors and subjective conditions when constructing the ecological vulnerability assessment index system, the index system of RSEI was selected (Xu, 2013). There was no obvious correlation between the index systems. In addition, it can reflect the vegetation cover, soil moisture, surface exposure and land surface temperature (Wang et al., 2016), while the spatial principal component analysis can remove certain correlations among indicators and reduce data redundancy (Xu, 2013; Pan and Xiao, 2015). To sum up, this paper selects the indicators of NDVI, WET, NDBSI, and LST to construct an ecological vulnerability assessment index system, and principal component analysis is a desirable evaluation method. In this study, the ecological vulnerability of Zhongxian County was objectively evaluated through remote sensing and evaluation model to reveal the evolution drivers of its ecological vulnerability. In view of the obvious spatial differentiation characteristics of each index impact factor in different geographical units, the local government should coordinate the effective balance between economic development and ecological vulnerability management. Appropriate measures should be taken to prevent ecological fragility from becoming more fragile.

5 Results

Combined with remote sensing and ArcGIS technology, this paper calculates the RSEI through remote sensing model and constructs the ecological vulnerability evaluation index system, comprehensively and quantitatively evaluates the ecological vulnerability of Zhongxian County in 2002, 2009, and 2016 by PCA method, and analyzes the spatio-temporal evolution characteristics of ecological vulnerability. The key points of my conclusion are as follows.

(1) Based on the distribution characteristics, the RSEI showed a trend of first decreasing and then increasing, from .5405 in 2002 to .5122 in 2009, and then rising to .7098 in 2016. Among them, the average value of NDVI that are conducive to the ecological environment quality has a trend of first decreasing and then increasing, the WET has an upward trend, while the average value of NDBSI that are not conducive to the ecological environment quality has a trend of first

increasing and then decreasing, and the LST has a downward trend, indicating that the vegetation coverage in Zhongxian County has decreased and then increased, the degree of surface exposure has decreased, and the difference between water and heat balance has decreased. On the whole, the impact on future ecological vulnerability is weakened.

(2) The EVBI of Zhongxian County shows a downward trend. From 2002 to 2016, the EVBI changed from medium vulnerability and strong vulnerability to negligible vulnerability and light vulnerability, and the medium vulnerability, strong vulnerability and extreme vulnerability showed a general downward trend. The ecological vulnerability gradually weakens with the implementation of ecological restoration and protection measures, that is, the improvement of ecological environment is gradual.

(3) The increment of ecological vulnerability level in 2002–2009 is mainly the increase in the area of light and medium vulnerability area, while the transfer amount is mainly the transfer of medium vulnerability and strong vulnerability. The increment of ecological vulnerability level in 2009–2016 is mainly the increase in the area of negligible vulnerability and light vulnerability area, while the transfer amount is mainly the transfer of light vulnerability and medium vulnerability. In general, the ecological vulnerability gradually changes to low vulnerability, and the ecological environment of Zhongxian County tends to benign development.

Data availability statement

The original contributions presented in the study are included in the article/supplementary material, further inquiries can be directed to the corresponding author.

Author contributions

First Author XJ: conceptualization; development or design of methodology; validation; formal analysis; writing—original draft preparation; visualization; data curation. Author YW: supervision; writing—review and editing. Author XG: supervision; funding acquisition; writing—review and editing. Author GL: supervision; project administration; funding acquisition; writing—review and editing. Author XD: writing—review; data curation. Author LY: data curation. Author YY: data curation. All authors have read and agreed to the published version of the manuscript.

Funding

This research was funded by XG, grant number (National Social Science Fund I: 21BMZ141, Supported by the Open Fund of the Research Center for Sustainable Development of the Three Gorges Reservoir Area: 2021sxxyjd01, Humanities and Social Sciences Research Planning Project of Chongqing Municipal Education Commission: 21SKGH432) and GL, grant number (Chongqing Wanzhou District Science and Technology Committee Project: 201503050, Open Fund for Chongqing Key Laboratory of Water Environment Evolution and Pollution Control in the Three Gorges Reservoir Area: WEPKL2012MS-03).

Conflict of interest

The authors declare that the research was conducted in the absence of any commercial or financial relationships that could be construed as a potential conflict of interest.

Publisher's note

References

Bai, Y., Ma, H., Zhang, B., Liang, j., Li, Z., Li, H., et al. (2009). Eco-environmental vulnerability analysis around Qinghai lake based on RS and GIS technology[J]. *Remote Sens. Technol. Appl.* 24 (05), 635–641. doi:10.11873/j.issn.1004-0323.2009.5.635

Baig, M. H. A., Zhang, L. F., Shuai, T., and Tong, Q. (2014). Derivation of a tasselled cap transformation based on Landsat 8 at-satellite reflectance. *Remote Sens. Environ.* 5 (5), 423–431. doi:10.1080/2150704x.2014.915434

Carlson, T. N., and Arthur, S. T. (2000). The impact of land use — Land cover changes due to urbanization on surface microclimate and hydrology: A satellite perspective. *Glob. Planet. Change* 25 (1/2), 49–65. doi:10.1016/s0921-8181(00)00021-7

Crist, E. P. (1985). A TM Tasseled Cap equivalent transformation for reflectance factor data. *Remote Sens. Environ.* 17 (3), 301–306. doi:10.1016/0034-4257(85)90102-6

Deng, H., Shao, J., Wang, J., Gao, M., and Wei, C. (2016). Land use driving forces and its future scenario simulation in the Three Gorges Reservoir Area using CLUE-S model[J]. *Acta Geogr. Sin.* 71 (11), 1979–1997. doi:10.11821/dlxb201611009

Fan, Z., Liu, M., Shen, W., and Lin, L. (2009). GIS-Based assessment on eco-vulnerability of jiangxi province. *J. Geo-information Sci.* 11 (02), 202–208. doi:10.3724/sp.j.1047.2009.00202

Gao, Y., and Zhang, H. (2018). The study of ecological environment fragility based on remote sensing and GIS. *J. Indian Soc. Remote Sens.* 46 (5), 793–799. doi:10.1007/s12524-018-0759-1

Goward, S. N., Xue, Y. K., and Czajkowski, K. P. (2002). Evaluating land surface moisture conditions from the remotely sensed temperature/vegetation index measurements: An exploration with the simplified simple biosphere model [J]. *Remote Sens. Environ.* 79 (2/3), 225–242. doi:10.1016/s0034-4257(01)00275-9

Guo, Z., Wei, W., Pang, S., Li, Z., Zhou, J., and Xie, B. (2019). Spatio-temporal evolution and motivation analysis of ecological vulnerability in arid inland river basin based on spca and remote sensing index: A case study on the shiyang river basin[J]. *Acta Ecol. Sin.* 39 (07), 2558–2572. doi:10.5846/stxb201805211114

He, L., Shen, J., and Zhang, Y. (2018). Ecological vulnerability assessment for ecological conservation and environmental management. *J. Environ. Manag.* 206, 1115–1125. doi:10.1016/j.jenvman.2017.11.059

Huang, C., Wylie, B., Yang, L., Homer, C., and Zylstra, G. (2002). Derivation of a tasselled cap transformation based on Landsat 7 at-satellite reflectance. *Int. J. Remote Sens.* 23 (8), 1741–1748. doi:10.1080/01431160110106113

Ifeanyi, C. E., Adoh, E. N., and Alabi, M. O. (2010). Evaluation of eco-environmental vulnerability in Efon-Alaye using remote sensing and GIS techniques [J]. *J. Geogr. Regional Plan.* 3 (1), 8–16. doi:10.5897/JGRP.9000051

Jackson, L. E., Bird, S. L., Matheny, R. W., O'Neill, R. V., White, D., Boesch, K. C., et al. (2004). A regional approach to projecting land-use change and resulting ecological vulnerability. *Environ. Monit. Assess.* 94 (1-3), 231–248. doi:10.1023/b:emas.0000016891.24052.bf

Jin, L., and Xu, Q. (2022). Ecological vulnerability assessment of Sichuan Province based on SRP model[J]. *Ecol. Sci.* 41 (02), 156–165. doi:10.14108/j.cnki.1008-8873.2022.02.019

Kearney, M. S., Rogers, A. S., and Townshend, J. R. G. (1995). *Developing a model for determining coastal marsh "health"//third thematic conference on remote sensing for marine and coastal environments* [J]. Seattle, Washington, 527–537.

Li, Wei (2010). *Study on the ecological vulnerability in shiyang river basin based on RS and GIS approach[D]*. Lanzhou: Northwest Normal University.

Liu, J., Zhao, J., Shen, S., and Zhao, Y. (2020). Ecological vulnerability assessment of Qilian Mountains region based on SRP conceptual model[J]. *Arid. Land Geogr.* 43 (06), 1573–1582. doi:10.12118/j.issn.1000-6060.2020.06.19

Ma, J., Li, C., Hong, W., Peng, M., Yujing, Y., Qingshui, R., et al. (2015). Dynamic evaluation of ecological vulnerability in the three Gorges Reservoir region in chongqing municipality, China [J]. *Acta Ecol. Sin.* 35 (21), 7117–7129. doi:10.5846/STXB201309252364

NASA (2012). *Landsat 7 science data users handbook. [M]* Available at:.

NASA (2018). *Landsat 8 date users handbook [M]*.

Pan, J., and Xiao, L. (2015). Assessment of landscape ecological security and optimization of landscape pattern based on spatial principal component analysis and resistance model in arid inland area: A case study of ganzhou District, zhangye city. *Northwest China[J]* 26 (10), 3126–3136. doi:10.13287/j.1001-9332.20150921.027

Singh, B M., Komal, C., Rustam, P., and Alexander, K. (2022). Using RS/GIS for spatiotemporal ecological vulnerability analysis based on DPSIR framework in the Republic of Tatarstan, Russia[J]. *Ecol. Inf.* 67. 101490. doi:10.1016/j.ecoinf.2021.101490

Sun, W., Zhang, L., Zhang, L., and Lai, Y. M. (2016). A dissimilarity-weighted sparse self-representation method for band selection in hyperspectral imagery classification. *IEEE J. Sel. Top. Appl. Earth Observations Remote Sens.* 9 (9), 4374–4388. doi:10.1109/jstars.2016.2539981

Tang, H., Fang, J., Xie, R., Ji, X., Li, D., and Yuan, J. (2022). Impact of land cover change on a typical mining region and its ecological environment quality evaluation using remote sensing based ecological index (RSEI). *Sustainability* 14 (19), 12694. doi:10.3390/su141912694

Teng, Y., Zhan, J., Liu, S., Agyemanga, F. B., Li, Z., Wang, C., et al. (2022). Integrating ecological and social vulnerability assessment in Qinghai Province, China. *Phys. Chem. Earth* 126 (2), 103115. doi:10.1016/j.pce.2022.103115

Tian, J., Guo, C., and Wang, J. (2021). Quantitative Assessment of the Ecological Vulnerabiliyt of Baiyangdian Wetlands in the north China Plain[J]. *J. Resour. Ecol.* 12 (06), 814–821. doi:10.5814/J.ISSN.1674-764X.2021.06.009

Wang, L., Xi, C., Fu, Q., and Su, Y. (2010). Landscape Pattern-Based Eco-Environment Vulnerability Assessment of Three Gorges Reservoir Area[J]. *Res. Environ. Sci.* 23 (10), 1268–1273. doi:10.13198/j.res.2010.10.56.wanglj.008

Wang, P., Zhao, W., and Ke, X. (2021). Evaluation and Spatiotemporal Evolution of Ecological Vulnerability of Qianjiang Based on SRP Model[J]. *Res. Soil Water Conservation* 28 (05), 347–354. doi:10.13869/j.cnki.rswc.2021.05.040

Wang, S., Zhang, X., Zhu, T., Yang, W., and Zhao, J. (2016). Assessment of ecological environment quality in the Changbai Mountain Nature Reserve based on remote sensing technology[J]. *Prog. Geogr.* 35 (10), 1269–1278. doi:10.18306/dlkxjz.2016.10.010

Wang, Y., and Dong, Z. (2013). Extraction of Remote Sensing Image Vegetation Information Based on the Tasseled Cap Transformation Image Fusion[J]. *Geospatial Inf.* (04), 85–86+9. doi:10.11709/j.issn.1672-4623.2013.04.031

Wang, Z. H., Ma, H. Z., Zhou, D. J., and Sha, Z. (2007). Integrated evaluation of eco-environment based on RS/GIS: a case study of the South-to-north Water Transfer Project in Yalongjiang River [J]. *J. Salt Lake Res.* 15 (1), 1–4. doi:10.3969/j.issn.1008-858X.2007.01.001

Wang, Z., and Su, Y. (2018). Analysis of Eco-environment vulnerability characteristics of Hanzhong City, near the water source midway along the route of the south-to-north water transfer project, China[J]. *Acta Ecol. Sin.* 38 (02), 432–442. doi:10.5846/stxb201609261944

Williams, M., Longstaff, B., Buchanan, C., Llanso, R., and Dennison, W. (2009). Development and evaluation of a spatially-explicit index of Chesapeake Bay health. *Mar. Pollut. Bull.* 59 (1/3), 14–25. doi:10.1016/j.marpolbul.2008.11.018

Wu, H. (2005). *The ration RS research of eco-environment frangibility based on multi-source data[D]*. Fuzhou: Fujian Normal University.

Xu, H. Q., Ding, F., and Wen, X. L. (2009). Urban Expansion and Heat Island Dynamics in the Quanzhou Region, China. *IEEE J. Sel. Top. Appl. Earth Observations Remote Sens.* 2 (2), 74–79. doi:10.1109/jstars.2009.2023088

Xu, H. (2013). A remote sensing urban ecological index and its application[J]. *Acta Ecol. Sin.* 33 (24), 7853–7862. doi:10.5846/stxb201208301223

Yan, M., and Zhao, G. (2009). Ecological environment condition evaluation of estuarine area based on quantitative remote sensing——a case study in Kenli County[J]. *China Environ. Sci.* 29 (02), 163–167. doi:10.3321/j.issn:1000-6923.2009.02.010

Yao, X., Yu, K., Liu, J., Yang, S. P., He, P., Deng, Y. B., et al. (2016). Spatial and temporal changes of the ecological vulnerability in a serious soil erosion area, Southern China. *Chin. J. Appl. Ecol.* 27 (03), 735–745. doi:10.13287/j.1001-9332.201603.022

Zhang, J., Gao, P., Dong, X., Teng, L., Xu, J., and Dun, X. (2021). Ecological Vulnerability Assessment of Qingdao Coastal Zone Based on Landscape Pattern Analysis[J]. *J. Ecol. Rural Environ.* 37 (08), 1022–1030. doi:10.19741/j.issn.1673-4831.2020.0860

Zhang, X., Hantong, Q., and Yang, W. (2021). Assessment of ecological vulnerability of water source in Yongding River based on fuzzy comprehensive evaluation method[J]. *Environ. Prot. Sci.* 47 (03), 159–163. doi:10.16803/j.cnki.issn.1004-6216.2021.03.027

Zhang, X., Liu, K., Li, X., Wang, S., and Wang, J. (2022). Vulnerability assessment and its driving forces in terms of NDVI and GPP over the Loess Plateau, China. *Phys. Chem. Earth* 125, 103106. doi:10.1016/j.pce.2022.103106

Zhu, Y. (2020). *Analysis of ecological vulnerability in Northeast China International based on remote sensing technology[D]*. Beijing): China University of Geosciences.

frontiers | Frontiers in Earth Science

TYPE Original Research
PUBLISHED 25 January 2023
DOI 10.3389/feart.2022.1077885

OPEN ACCESS

EDITED BY
Yonghao Xu,
Institute of Advanced Research in Artificial Intelligence (IARAI), Austria

REVIEWED BY
Laxmikant Sharma,
Central University of Rajasthan, India
Qiang Yu,
Beijing Forestry University, China

*CORRESPONDENCE
Zongyao Sha,
zongyaosha@163.com

†These authors have contributed equally to this work and share first authorship

SPECIALTY SECTION
This article was submitted to Environmental Informatics and Remote Sensing, a section of the journal Frontiers in Earth Science

RECEIVED 23 October 2022
ACCEPTED 02 December 2022
PUBLISHED 25 January 2023

CITATION
Li X, Li R and Sha Z (2023), Modeling carbon uptake by vegetation of grassland ecosystems and its associated factors in China based on remote sensing.
Front. Earth Sci. 10:1077885.
doi: 10.3389/feart.2022.1077885

Modeling carbon uptake by vegetation of grassland ecosystems and its associated factors in China based on remote sensing

Xuejie Li[1†], Ruren Li[1†] and Zongyao Sha[2*]

[1]School of Transportation and Geomatics Engineering, Shenyang Jianzhu University, Shenyang, China, [2]School of Remote Sensing Engineering, Wuhan University, Wuhan, China

In order to reveal the spatial variation characteristics and influencing factors of grassland net primary productivity (NPP) in China, this paper uses remote sensing data, land use data and meteorological data to simulate and estimate China's grassland net primary productivity from 2001 to 2019 using the Carnegie-Ames-Stanford Approach (CASA). The trend analysis and complex correlation analysis were used to analyze the relationship with the temporal and spatial changes of grassland NPP from the perspectives of climate factors, topography, longitude and latitude. The results show that: 1) In the past 19 years, the China's grassland NPP has generally shown a fluctuating upward trend, the spatial distribution of NPP variation shows a characteristic of low in the west and high in the east, with the increased area accounting for 70.39% of the total grassland area, and the low NPP values are mainly distributed in the northwestern part of Tibet and Qinghai and the central part of Inner Mongolia, the average annual NPP is 257.13 g $C{\cdot}m^{-2}{\cdot}a^{-1}$. 2) The change of mean NPP value of grassland in China is more dependent on precipitation (*p*) than air temperature (T). 3) Grassland NPP showed a decreasing trend with the increase of altitude, and the NPP on the gradient with DEM between 200 m and 500 m was the highest (483.86 $g{\cdot}C{\cdot}m^{-2}{\cdot}a^{-1}$); The maximum annual mean value (448.42 g $C{\cdot}m^{-2}{\cdot}a^{-1}$) is fallen over the sharp slope of 35°–45°; the NPP of grassland increases with the slope (from shade to sunny), and the NPP of grassland on the semi-sunny slope increases. The annual average NPP is the highest (270.87 g $C{\cdot}m^{-2}{\cdot}a^{-1}$). 4) The mean value of grassland NPP was negatively correlated with the change of latitude, and showed a "wave-like" downward trend from south to north; the mean value of grassland NPP was positively related to the change of longitude. The correlation relationship shows a "stepped" upward trend from west to east.

KEYWORDS

carnegie-ames-stanford approach, remote sensing, grassland ecosystem, carbon sequestration, China

1 Introduction

In the context of global climate change, studying the carbon sequestration potential of terrestrial ecosystems is not only an important indicator for estimating the Earth's supporting capacity, but also helps to understand the global carbon balance and evaluate the sustainable development of terrestrial ecosystems (Christopher et al., 1998; Carraro and Massetti, 2011; Shen et al., 2016; Chen et al., 2017; Li et al., 2020).Grassland ecosystem is one of the most important and widely distributed ecosystem types in terrestrial ecosystems, and it is also one of the most important carbon stocks and carbon sources/sinks on land. China's grasslands cover almost 41.17% of national territorial area, it accounts for 6%–8% of the total grassland area in the world, and plays a pivotal role in the global carbon cycle and climate regulation, and plays an important role in developing animal husbandry, maintaining biodiversity, conserving soil and water, and maintaining ecosystem balance (Xie et al., 2001; Yang et al., 2012; Li et al., 2014; Tang et al., 2014; Xu et al., 2020). Therefore, estimating the carbon sequestration potential of the net primary productivity of grassland ecosystems correctly in China is of great significance for studying the carbon cycle of terrestrial ecosystems and regulating global climate change (Piao et al., 2004). However, current research on carbon storage and sequestration in grassland ecosystems is relatively one-sided in terms of its influencing factors, while studies on topography, latitude and longitude are still relatively weak. Therefore, it is quite essential to carry out in-depth research on the carbon sequestration potential of grassland ecosystems, so as to enhance the scientific understanding of the carbon sequestration potential of grasslands in global climate change and ecosystem management.

NPP is the amount of organic matter accumulated by green plants in unit area and unit time through photosynthesis (Fang et al., 2001; Xu et al., 2020), That is, the NPP of grassland is the most direct indicator to reflect the growth characteristics and health status of grassland ecosystems, and it is also an important ecological indicator for the sustainable development of ecosystems (Zhao et al., 2014; Du et al., 2021). Accurate estimation of NPP and analysis of its spatial distribution and influencing factors are helpful to understand the response state of ecosystems in the context of global climate change (Chen et al., 2022), It is of great significance to further clarify the carbon sequestration potential of grassland ecosystems in China, and also to provide a scientific reference for the carbon cycle characteristics of terrestrial ecosystems in the context of global climate change. Mastering the interannual variation rule of grassland NPP, analyzing and researching the relationship between index NPP, water and heat factors, and geographical elements has important theoretical and practical value for evaluating the environmental quality of terrestrial ecosystems, regulating ecological processes, and estimating terrestrial carbon sinks (Niu, 2000; Hou et al., 2007; Wang et al., 2016; Liu et al., 2019).

This paper depends on the grassland distribution data in China, combined with the remote sensing data and meteorological data of the same period, and calculates various grassland NPPs based on the CASA model, and uses trend analysis, correlation analysis and other methods to explore the change trend of grassland NPP in China from 2001 to 2019. Its spatial distribution characteristics and influencing factors aim to provide a scientific reference for the research on dynamic changes of grassland ecosystem functions, ecological environmental protection, soil and water conservation, and climate regulation in China.

2 Materials and methods

2.1 Study area

The study area covers only 22 provinces, 5 autonomous regions and four municipalities directly under the Central Government in China. Which are: Beijing (BJ), tianjin (TJ), hebei (HB) , shanxi (SX), Inner Mongolia (IML), liaoning (LN), jilin (JL), heilongjiang (HLJ), Shanghai (SH), jiangsu (JS), zhejiang (ZJ), anhui (AH), fujian (FJ), jiangxi (JX), shandong (SD), henan (HN), hubei (HB), hunan (HN), guangdong (GD), guangxi (GX), hainan (HN), sichuan (SC), guizhou (GZ), yunnan (YN), chongqing (CQ) , Tibet (TB), shaanxi (SAX), gansu (GS), qinghai (QH), ningxia (NX), xinjiang (XJ) (Figure 1A). China is located in the east of Asia and on the west coast of the Pacific Ocean (Wang et al., 2022) Most parts temperate, a few tropical, no cold zone. The terrain of China is high in the west and low in the east, with a stepped distribution. The terrain is diverse, mainly dominated by plateaus and mountains, crisscrossed by mountains.There are the Qinghai-Tibet Plateau with an average altitude of more than 4 km, basins and plateau regions with an average altitude of 1-2 km, and hills with an altitude of less than 500 m. Due to China's vast territory, wide latitude, quite different distance from the sea, various terrain types and mountain trends, the combination of temperature and precipitation is diverse, forming a complex and diverse climate. There are all kinds of monsoon climate, temperate continental climate, alpine climate. Winter is cold and dry, summer is warm and rainy. Grassland resources in China are of large area, wide distribution, various types and miscellaneous, and of low quality. Grassland resources are distributed in all provinces, regions and cities, and the concentrated contiguous grassland is mainly distributed in the Qinghai-Tibet Plateau, the arid and semi-arid areas in the north and the grassy hills and slopes in the south. It is precisely under such complex and changeable natural resource conditions that China's vegetation is rich in species, its distribution is intricate,

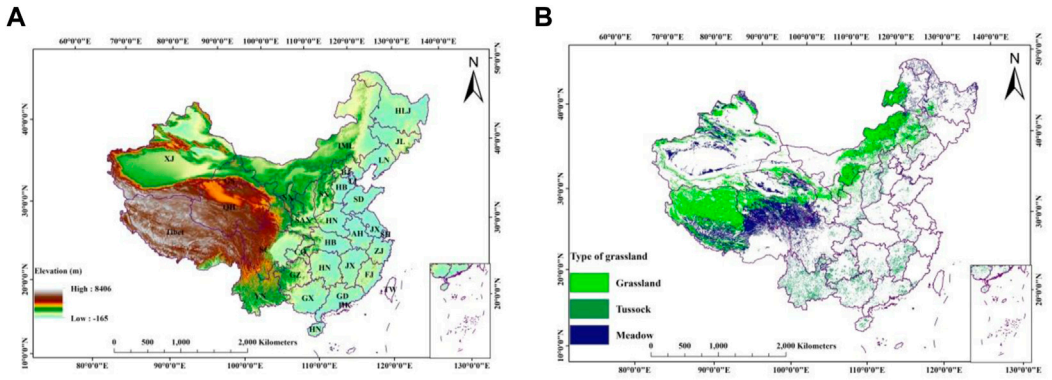

FIGURE 1
(A) Elevation chart of China (excluding Hong Kong, Macao and Taiwan). **(B)** Spatial distribution characteristics of grassland types in China.

TABLE 1 Data source statistical table.

Name	NDVI(MOD13A2)	NPP(MOD17A3HFG)	DEM
Source	http://edcimswww.cr.usgs.gov/pub/imswelcome/	http://edcimswww.cr.usgs.gov/pub/imswelcome/	http://www.gscloud.cn/
Resolution	The spatial resolution is 1,000 m	The spatial resolution is 500 m	The spatial resolution is 30 m

and the stability of the ecological environment is affected by many factors.

2.2 Data source

The remote sensing data comes from the MODIS data of the National Aeronautics and Space Administration (NASA) (Li et al., 2021). The time series is from 2001 to 2019, and the remote sensing data used include MOD13A2 data (NDVI), MOD17A3HFG data (NPP), and elevation data (DEM) from the Geospatial Data Cloud (Table 1). The meteorological data (contains latitude and longitude) of total solar radiation, monthly average temperature, and monthly precipitation are derived from the monthly data set of China's surface climate data provided by the China Meteorological Science Data Sharing Service Network (http://cdc.cma.gov.cn). The vegetation type data comes from the 1:1,000,000 Chinese Vegetation Type Atlas by the Data Center of Resource and Environmental Sciences (https://www.resdc.cn/), Chinese Academy of Sciences. The vegetation classification atlas contains 11 vegetation type groups, the distribution status of 796 vegetation units in 54 vegetation types, and the horizontal regional and vertical regional distribution rules. According to this vegetation atlas, grassland includes three vegetation types: meadow, tussock and grassland (Figure 1B). These three vegetation types account for 30. 82% of the vegetation area in China.

The 2001–2012 the field measurement data of a small part of grassland were obtained from A Global Database of Soil Respiration Data, Version 5.0 (https://daac.ornl.gov/cgi-bin/dsviewer.pl?ds_id=1827). These data will be uniformly processed into raster data with a resolution of 1,000 m through ArcGIS 10.2.

2.3 NPP simulation and results validation

In this study, the improved CASA model of Zhu Wenquan et al. was used to simulate the grassland NPP in China (Zhu et al., 2007). The NPP in this model is mainly determined by the photosynthetically active radiation (APAR) absorbed by the vegetation and the actual light energy utilization rate (ε). The specific calculation formula is as follows:

$$\mathrm{NPP}(x,t) = \mathrm{APAR}(x,t) \times \varepsilon(x,t) \quad (1)$$

where NPP(x, t) is the net primary productivity of pixel x in month t; APAR(x, t) is the photosynthetically active radiation absorbed by pixel x in month t; ε(x, t) is pixel x Actual light energy utilization in month t (Xu et al., 2020; Li et al., 2021).

$$\mathrm{APAR}(x,t) = \mathrm{SOL}(x,t) \times \mathrm{FPAR}(x,t) \times 0.5 \quad (2)$$

Where: SOL (x, t) is the total solar radiation of pixel x in month t ($MJ \cdot m^{-2}$); 0.5 is the proportion of solar effective radiation that

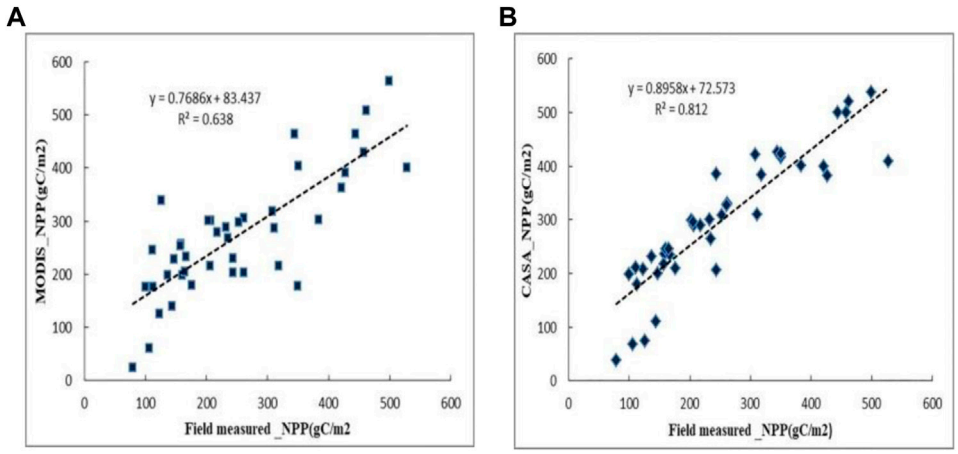

FIGURE 2
Simulation verification results of MODIS-Measured **(A)**, CASA-Measured **(B)**.

can be used by vegetation to the total solar radiation; FPAR(x, t) represents the absorption ratio of the incident photosynthetically active radiation (PAR) by the vegetation layer.

Light utilization efficiency (ε) refers to the efficiency with which vegetation converts its absorbed photosynthetically active radiation (PAR) into organic carbon, which is mainly affected by temperature and moisture, and is calculated as follows:

$$\varepsilon(x,t) = T_1(x,t) \times T_2(x,t) \times W(x,t) \times \varepsilon_{max} \quad (3)$$

Where: T_1 (x, t) and T_2 (x, t) represent the effect of temperature on the utilization of light energy. For the detail calculation method, see the literature (Zhu et al., 2005; Wang et al., 2022); W (x, t) represents the effect of moisture on the utilization of light energy. ε_{max} represents the maximum light energy utilization rate of vegetation under ideal conditions, and its value is different due to different vegetation types. In this study, 0.542 g C·MJ^{-1} was used to keep consistent with previous studies (Zhou et al., 2017).

Since the actual measurement of NPP is difficult to achieve, this paper uses the MOD17A3HFG data (NPP) and field measured data obtained by other research scholars to compare and verify the NPP estimation results. The statistical results are as follows: MODIS-Measured has a strong correlation with an adjusted R^2 of 0.638 (Figure 2A); CASA-Measured has a strong correlation with an adjusted R^2 of 0.812 (Figure 2B). The above verification results show that the CASA model is suitable for the estimation and simulation of grassland NPP in China.

2.4 Trend analysis of NPP

In this paper, the univariate linear regression method is used to analyze the trend changes of the annual average NPP, annual precipitation and annual average temperature of each pixel of grassland in China from 2001 to 2019. The calculation principles are as follows (Li et al., 2011; Jin et al., 2020):

$$\theta_{slope} = \frac{n\sum_{i=1}^{n}(i \times NPP_i) - \sum_{i=1}^{n} i \sum_{i=1}^{n} NPP_i}{n\sum_{i=1}^{n} i^2 - \left(\sum_{i}^{n} i\right)^2} \quad (4)$$

Where θ_{slope} is the inter-annual rate of NPP change; n is 19 for years from 2001 to 2019; and NPP_i is the value of annual NPP at year i. If $\theta_{slope} > 0$, it means that NPP shows an increasing trend, otherwise, it is a decreasing trend. F test was used to test its significance, and the calculation formula was:

$$F = U \times \frac{n-2}{Q} \quad (5)$$

Where $U = \sum_{i=1}^{n}(\hat{y}_i - \bar{y})^2$ is the sum of regression squares, $Q = \sum_{i=1}^{n}(y_i - \hat{y}_i)^2$ is the sum of residual squares, y_i is the value of NPP in year i, $\hat{y}_i$ is the regression value of NPP in year i, and $\bar{y}$ is the average value of 19a NPP. According to the test results, it can be divided into the following grades: very significantly reduced ($\theta_{slope} < 0, P < 0.01$), significantly reduced ($\theta_{slope} < 0, 0.01 < P < 0.05$), no significant reduced ($\theta_{slope} < 0, P > 0.05$); very significantly increase ($\theta_{slope} > 0, P < 0.01$), significantly increase ($\theta_{slope} > 0, 0.01 < P < 0.05$), no significantly increase ($\theta_{slope} > 0, P > 0.05$).

2.5 Correlation analysis

Correlation analysis is used to reflect the direction and degree of correlation between elements. In this paper, the Pearson correlation coefficient, partial correlation coefficient, and complex correlation coefficient method are used to analyze the correlation and significance level of annual vegetation

NPP with temperature and precipitation. The calculation principles are as follows (Murakami et al., 2004; Dowding and Haufe, 2018; Li et al., 2019; Xie et al., 2020):

$$R_{xy} = \frac{\sum_{i=1}^{n}\left[\left(X_i - \bar{X}\right)\left(Y_i - \bar{Y}\right)\right]}{\sqrt{\sum_{i=1}^{n}\left(X_i - \bar{X}\right)^2 \sum_{i=1}^{n}\left(Y_i - \bar{Y}\right)^2}} \quad (6)$$

where: R_{xy} is the relationship between variables x and y; n is the number of years; X_i is the vegetation NPP in the i year; Y_i is the annual average meteorological factor (temperature and precipitation) in the i year; $\bar{X}$ and $\bar{Y}$ are respectively n-year mean of variables x and y.

Partial correlation coefficient calculation formula:

$$R_{xy.z} = \frac{R_{xy} - R_{yz}R_{xz}}{\sqrt{\left(1 - R_{yz}^2\right)\left(1 - R_{xz}^2\right)}} \quad (7)$$

Where $R_{xy.z}$ is the partial correlation coefficient between the dependent variable z (representing air temperature in this study) and the independent variable y after fixing the independent variable x (representing precipitation in this study). The significance test is generally performed using the *t* test:

$$t = \frac{R_{xy.z}}{\sqrt{1 - R_{xy.z}^2}}\sqrt{n - m - 1} \quad (8)$$

where $R_{xy.z}$ is the Partial correlation coefficient, m is the number of independent variables.

The formula for calculating the complex correlation coefficient:

$$R_{y.xz} = \sqrt{1 - \left(1 - R_{xy}^2\right)\left(1 - R_{yz.x}^2\right)} \quad (9)$$

where $R_{y.xz}$ is the complex correlation coefficient between the dependent variable y and the independent variables x, z. Its significance test uses the F test:

$$F = \frac{R_{y.xz}^2}{1 - R_{y.xz}^2}\frac{n - k - 1}{k} \quad (10)$$

2.6 Quantitative evaluation of the contribution of precipitation and temperature to NPP

Traditionally, an increase in NPP has been used as an indicator of vegetation restoration, whereas a decrease in NPP represents vegetation degradation (Yan et al., 2019). Based on Eq. 4, a positive θ_{slope} in NPP represents grassland restoration, whereas a negative S denotes grassland degradation. If precipitation and temperature are determined to cause NPP changes, the relative role of climate change and human activities in NPP changes can be quantitatively evaluated. With reference to Yan Yuchao et al. scenario setting scheme on NPP changes, the influence of climate change and human activities on NPP in the Shule River Basin is measured, as shown in Table 2.

In this study, when the contribution proportion of PC to grassland restoration or degradation was larger than that of TC, it was defined as "climate-dominated restoration or degradation". Similarly, when the contribution proportion of TC to grassland restoration or degradation was greater than that of PC, it was defined as "human-dominated restoration or degradation".

3 Results and analysis

3.1 Spatial and temporal distribution characteristics of grassland NPP in China

3.1.1 Time-varying characteristics

The average NPP value of grassland in China from 2001 to 2019 was 257.13 g·C·m^{-2}·a^{-1}. Based on the literature, the results of this study are similar to those obtained by many scholars, but there are also some differences, which may be caused by different grassland classification standards, data sources and research periods. Overall, the interannual change of grassland NPP showed a fluctuating upward trend, and the linear growth trend reached a significant level ($p < 0.01$), with an average change rate of 2.69. g·C·m^{-2}·a^{-1} (Figure 3).

Statistics on the NPP values of grassland types (meadow, tussock and grassland) in China (excluding Hong Kong, Macao and Taiwan regions) in the past 20 years show that the results (Figure 4) show that the interannual variation trends of average NPP of different grassland types are also quite different: In the 19 years , the NPP values of grassland and tussock all showed an increasing trend, and the change rates were 2.32 and 10.35 g·C·m^{-2}·a^{-1} respectively , accounting for 52.45% and 10.89% of the total grassland area respectively. THowever, the overall increase trend of meadow from 2001 to 2019 was not obvious, with a change rate of 0.999 g·C·m^{-2}·a^{-1}, accounting for 36.66% of the total grassland area. The causes of this phenomenon may be closely related to overgrazing, precipitation, total solar radiation, temperature and human activities.

3.1.2 Spatial distribution characteristics

From 2001 to 2019, the distribution of grassland NPP in China had obvious spatial heterogeneity, and the overall trend showed a downward trend from the southeast to the northwest (Figure 5). Among them, the areas with NPP greater than 600 g·C·m^{-2}·a^{-1} are concentrated in the border areas of QH and SC as well as YN and GX. The grassland types of the region are mainly tussock and meadow, accounting for 11% of the total grassland area. The areas with NPP concentrations of 400–600 g·C·m^{-2}·a^{-1} are mainly distributed in the east of QH Province, the northeastern of IML and HLJ and southern region. In some areas, meadows are widely distributed, accounting for

TABLE 2 Six scenarios for quantifying the contribution proportions of *p* and T to grassland restoration and degradation.

	Scenario	P_{-con}	T_{-con}	Contribution proportion of PC(%)	Contribution proportion of TC (%)
$\theta_{slope} > 0$	1	>0	>0	$\frac{100 \times \lvert P\_con \rvert}{\lvert P\_con \rvert + \lvert T\_con \rvert}$	$\frac{100 \times \lvert T\_con \rvert}{\lvert P\_con \rvert + \lvert T\_con \rvert}$
	2	>0	<0	100	0
	3	<0	>0	0	100
$\theta_{slope} < 0$	1	<0	<0	$\frac{100 \times \lvert P\_con \rvert}{\lvert P\_con \rvert + \lvert T\_con \rvert}$	$\frac{100 \times \lvert T\_con \rvert}{\lvert P\_con \rvert + \lvert T\_con \rvert}$
	2	<0	>0	100	0
	3	>0	<0	0	100

P_{-con} and T_{-con} represent the contributions of precipitation and temperature to the inter-annual NPP, changes, respectively; PC and TC, represent the change of precipitation and temperature, respectively.

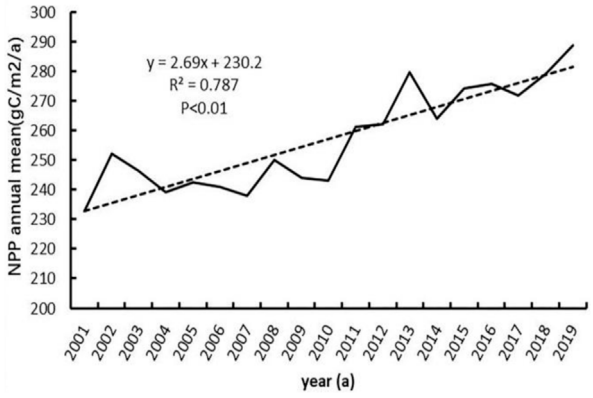

FIGURE 3
Interannual variation of grassland NPP in China (excluding Hong Kong, Macao and Taiwan) from 2001 to 2019.

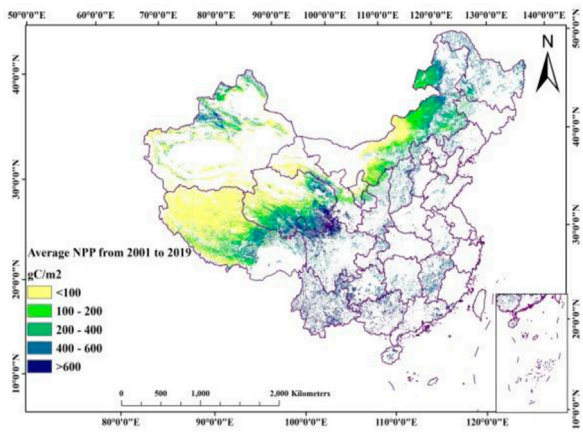

FIGURE 5
Spatial distribution characteristics of mean NPP of grassland in China (excluding Hong Kong, Macao and Taiwan) from 2001 to 2019.

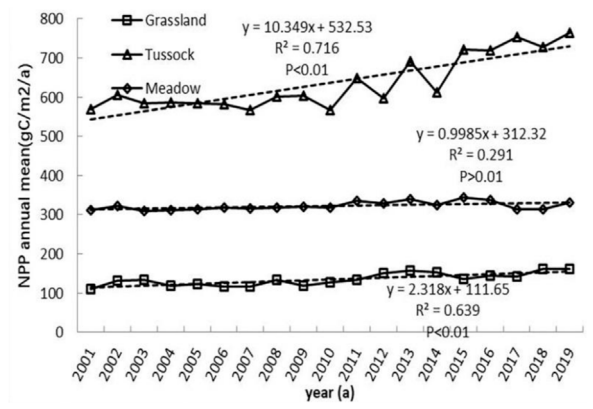

FIGURE 4
Interannual variation trend of NPP of different grassland types from 2001 to 2019.

18.51% of the total grassland area, and the average NPP value is relatively high. The areas with NPP concentrations of 400–600 g·C·m^{-2}·a^{-1} are mainly distributed in the IML, NX, QH and the southeastern of Tibet, and a small part is also distributed in the northern part of SAX and SX accounts for 19.05% of the total grassland area. The grassland NPP values below 100 g·C·m^{-2}·a^{-1} are mainly concentrated in the northern part of Tibet, the northwestern GS Province, central IML. In the region, the grassland vegetation type is mainly grassland, accounting for 36.23% of the total grassland area, and the vegetation NPP value is relatively low. The NPP values of other grasslands were mainly distributed in 100–200 g·C·m^{-2}·a^{-1}, the distribution is scattered and mainly distributed in the northwest of China , accounting for 15.21% of the total grassland area. All in all, the average NPP values of tussock and meadow were higher, up to 636.02 and 322.3 g·C·m^{-2}·a^{-1} respectively, and the area proportions were

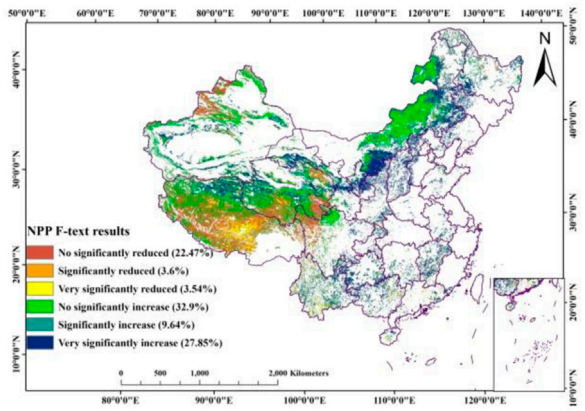

FIGURE 6
Variation trend and significance test of grassland NPP in China.

10.89% and 36.66% respectively. The lowest average NPP value of grassland was only 134.83 g·C·m^{-2}·a^{-1}, accounting for 52.45% of the area.

In order to study the variation trend of grassland NPP in China quantitatively, the spatial variation of grassland NPP from 2001 to 2019 was divided into six levels (Figure 6). On the whole, the spatial variation characteristics show a low west-east distribution, with the increased area accounting for 70.39% of the total grassland area, the grassland NPP in most areas is increasing, and the change value of the increase area is about 0~50 g·C·m^{-2}·a^{-1}, and the change value of the decrease area is 0~49 g·C·m^{-2}·a^{-1} or so. It can be seen from statistical calculations that the areas with extremely significant increase and significant increase account for 27.85% and 9.64% of the total grassland area respectively, and they are mainly distributed in Inner Mongolia, Ningxia, Gansu, Shaanxi, Shanxi, northern Hebei and central Qinghai in China. The significantly reduced and non-significantly reduced areas accounted for 7.14% and 22.47% of the total grassland area, mainly in Tibet, Qinghai, Sichuan and Xinjiang.

3.2 The relationship between the spatiotemporal distribution of NPP and climate parameters

On the whole, the precipitation and air temperature in the grassland area in China from 2001 to 2019 showed an increasing trend, and the trend change rates were 2.7 and 0.02 g·C·m^{-2}·a^{-1} respectively (Figure 7). According to the relationship between the annual average temperature and annual precipitation and NPP in the corresponding period of statistics, the inter-annual fluctuation of grassland NPP in China from 2001 to 2019 was mainly affected by precipitation, and the change of NPP was roughly consistent with the trend of precipitation. It is 5,694.74 mm, and the corresponding NPP value is reaching 275.677 g·C·m^{-2}, which is related to the extremely abnormal precipitation in 2016, compared with other in 2016 and 2014, the precipitation was significantly higher, and the increase in precipitation accumulation led to an increase in NPP, on a relative basis, the NPP was high, second only to 2019, which made the NPP value in 2016 and 2014 increase compared with other years. The variation trend of NPP is opposite to that of temperature, but the influence of temperature on NPP is smaller than that of annual precipitation, and the regularity of the relationship between temperature and NPP is obviously weaker than that of precipitation and NPP.

It can be seen from Figures 8A–D that the correlation coefficient between NPP and the average annual precipitation is between −0.891 and 0.964, and the average correlation coefficient is 0.073. Among them, the negatively correlated areas accounted for 18.04% of the total grassland area, mainly distributed in southern QH Province, northwestern SC Province and YN. The reason may be that the area belongs to the cold and wet environment, which inhibits the growth of vegetation. The positively correlated areas were mainly distributed in the northern part of Northeast China, the southern part of Qinghai-Tibet region and the northern part of Xinjiang, and the positively correlated areas accounted for 81.96% of the total grassland area. Overall, grassland NPP was positively correlated with annual precipitation, that is, precipitation would promote the increase of grassland NPP to a certain extent. There was a positive correlation between NPP and annual mean temperature as a whole. The correlation coefficient was between −0.864 and 0.894, and the average correlation coefficient was 0.03. The areas with no significant correlation between the two accounted for 32.13% of the total grassland area. The 0.83% of the regional NPP was significantly positively correlated with temperature, the distribution is wide, not concentrated, and the spatial heterogeneity is obvious.

It can be seen from Figures 8E–H that the mean partial correlation coefficients between NPP and precipitation and temperature are 0.086 and 0.008 respectively, and the positive correlation areas passing the significance test are 35.78% and 8.83% respectively. It shows that when only considering the influence of temperature on NPP, compared with the correlation between temperature and NPP under the influence of precipitation, the change of NPP has a weaker correlation with temperature. There is still a strong correlation between NPP and precipitation. The main reason is that the increase in precipitation improves soil water supply conditions, enhances the photosynthetic rate, and thus improves productivity. At the same time, the lower temperature in the plateau and mountainous areas can reduce evapotranspiration, thereby reducing the possibility of evapotranspiration.

The use of water loss is conducive to vegetation growth. It can be seen from Figures 8I,J that the composite correlation coefficient between grassland NPP and temperature-

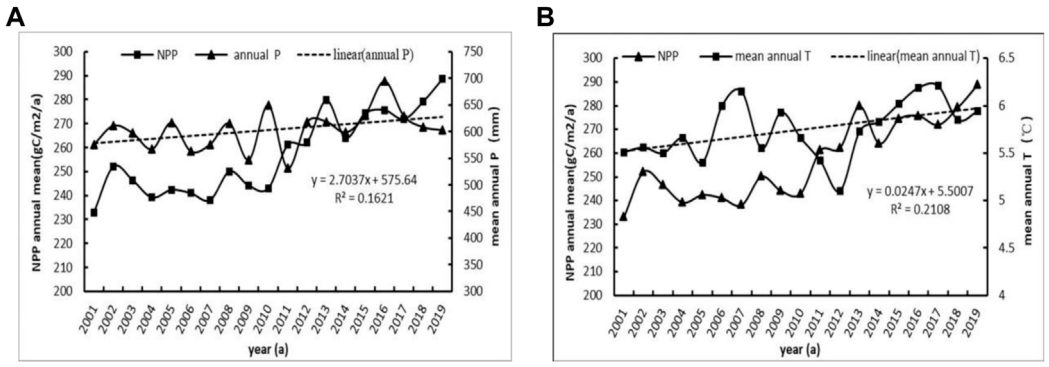

FIGURE 7
The relationship between NPP and annual precipitation **(A)**, annual mean temperature **(B)** of grassland in China from 2001 to 2019.

precipitation in China is between 0.001 and 0.972, showing a spatial pattern of higher in the north and lower in the middle. The areas with multiple correlation coefficients higher than 0.5 are distributed mainly in the northeastern and central northern Inner Mongolia, central and northern Ningxia, and northwestern Tibet in China. The regional distribution of the multiple correlation coefficients between 0.45 and 0.5 is mainly in the northeastern Inner Mongolia, the northwestern and central Qinghai-Tibet regions, and the northwestern Xinjiang. The multiple correlation coefficients of the remaining areas are relatively small, probably because these areas have lower relative altitudes, more abundant water content, and higher temperatures, so they are less affected by the comprehensive regulation of temperature and precipitation.The partial correlation coefficient can describe the degree of correlation between grassland NPP and climatic factors, whereas the contributions of climatic factors to grassland NPP changes cannot be quantified. Therefore, to quantitatively evaluate the contributions of climatic factors to NPP changes, the results of Tem_con, Pre_con, and Rad_con are shown in Figures 8K,L. It is clear from the contribution distribution map that precipitation has a greater impact than temperature, so it can be concluded that precipitation has a more obvious interaction on grassland productivity. This paper only considers precipitation and temperature, and there are many other factors that need to be explored more comprehensively.

3.3 The relationship between the spatiotemporal distribution of NPP and terrain

According to statistics, the annual average NPP value of grassland in China from 2001 to 2019 showed different characteristics with the increase of altitude (Figure 9A): the overall trend showed a downward trend, and the grassland was mainly distributed in the plateau area. Among them, the maximum annual mean value of grassland NPP (483.86 g·C·m^{-2}·a^{-1}) was concentrated in the hilly area with an altitude of 200–500 m, accounting for 5.12% of the total grassland area. With the increase of altitude, the average NPP value of grassland is in a trend of first increasing and then decreasing. In the plain area below 200 m, the annual average NPP value of grassland has a gentle downward trend, and its value is 464 g·C·m^{-2}· a^{-1}, when the altitude is in the range of 500–2000 m, the annual mean value of grassland NPP (316.49 g·C·m^{-2}·a^{-1}) has an obvious downward trend. When the altitude downward again to the plateau area above 2000 m, the change is that the average annual NPP value of grassland was 204.29 g·C·m^{-2}·a^{-1}. The hills and plains with an altitude of less than 500 m accounted for the least proportion of grassland, but with the increase of altitude, the proportion to the total grassland increased gradually. Therefore, it can be concluded that different levels of elevation also have a certain impact on the carbon sequestration potential of grassland in China. The annual average NPP value of grassland in China shows the characteristics with different slope aspects (Figure 9B): from shady to sunny, the overall trend is increasing, and the annual average value of grassland NPP on the semi-sunny slope is the highest at 270.87 g·C·m^{-2}·a^{-1}, followed by semi-shady slopes (265.68 g·C·m^{-2}·a^{-1}), sunny slopes (245.36 g·C·m^{-2}·a^{-1}), shady slopes (244.63 g·C·m^{-2}·a^{-1}), the lowest is the flat area with no slope aspect (223.38 g·C·m^{-2}·a^{-1}), while the semi-shady slope covers the largest area, accounting for 38.09% of the total grassland area, and The region of flat area without slope aspect has the smallest proportion (0.44%). Shady slopes have a larger proportion than sunny slopes, but the NPP values are opposite, indicating that grasslands prefer to grow on the sunny side. Therefore, different slope aspects also have an impact on the carbon sequestration potential of grassland. The research conclusion shows that the NPP of the grassland on the flat areas is the last but one, its area is the largest, accounting

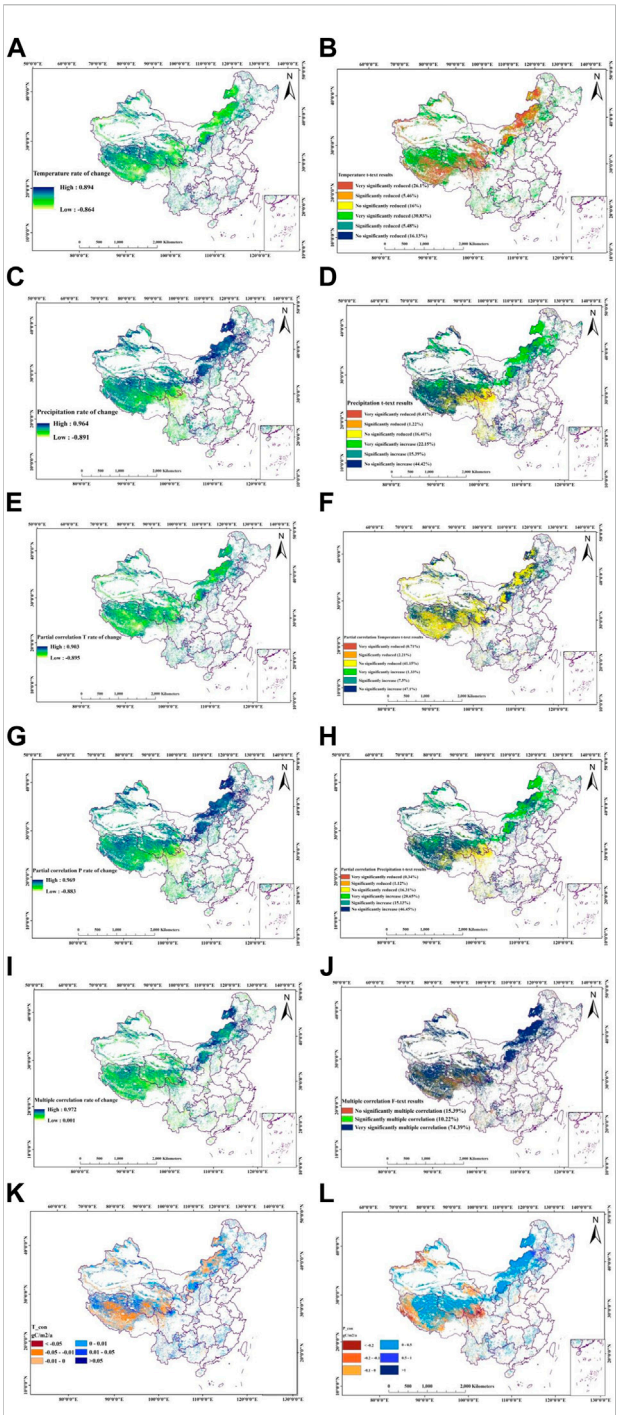

FIGURE 8
Spatial changes of annual temperature **(A)**, average annual precipitation **(C)**, partial annual temperature **(E)**, partial annual precipitation **(G)**, and multiple correlation **(I)** and Spatial variation trends in annual temperature **(B)**, annual mean precipitation **(D)**, partial annual temperature **(F)**, partial annual precipitation **(H)**, multiple correlation **(J)** of grasslands in China during 2001–2019. Spatial distributions of the contributions of **(K)** temperature (T_con) and **(L)** precipitation (P_con) to grassland NPP changes.

for 75.6868% of the total area of grassland, tens of thousands of times of the area of steep slope, but the NPP value is only about half of the steep slope, its carbon sequestration effect is not good enough, there is still a lot of room for improvement, need to strengthen the protection.The annual mean NPP value of grassland in China shows the characteristics with the increase of slope (Figure 9C): the overall trend is decreasing, mainly distributed in flat and gentle slopes, and a small part in slopes, steep slopes, sharp slopes and dangerous slopes. Among them, the maximum value of grassland NPP (448.42 g·C·m^{-2}·a^{-1}) is in the sharp slope of 35°–45°, the second is the steep slope (417.33 g·C·m-2·A-1). From the flat to the slope, the NPP value is in a state of continuous increase, with good carbon sequestration effect, but there is a lot of room for improvement, and the minimum value (87.65 g·C·m^{-2}·a^{-1}) is greater than 45° on the dangerous slope. With the increase of the slope, the change of NPP is in the trend of increase first and then decrease, and the slope below 45° has been in the trend of gradual increase, and then with the increase of the slope, the NPP begins to decrease obviously. These changes are due to different soil and water conservation at different slopes, resulting in different soil fertility and drainage performance, so there are certain differences in the carbon sequestration capacity of grasslands at different slopes.

3.4 The relationship between NPP spatiotemporal distribution in latitude and longitude

From the perspective of zonal variation (Figure 10A), the average NPP value of grassland in China from 2001 to 2019 was 374.58 g·C·m^{-2}·a^{-1}. In general, the average NPP value of grassland in China within 19 years was negatively correlated with the latitude change. The distribution of the average NPP value in China showed obvious latitude zonality, and it showed a "wave-like" downward trend from south to north, and the change rate was 11.14 g·C/(m2·a·10°), and through the $p > 0.05$ significance level test, the downward trend is obvious. Among them, the maximum average NPP value is 1,057.79 g·C·m^{-2}·a^{-1}, which is distributed in the southern region with a latitude of 16° or so, which may be due to the abundant precipitation, suitable climate, and relatively good soil water and soil conservation in this region, which is more conducive to the growth of vegetation, thereby enhancing the carbon sequestration capacity of grassland. The lowest NPP is 5.69 g·C·m^{-2}·a^{-1}, which is distributed in the central area between 31–32° latitude. The NPP value in this area is generally low, which may be due to the relatively aridity in this area, which affects vegetation growth, further leading to grassland carbon sequestration potential.

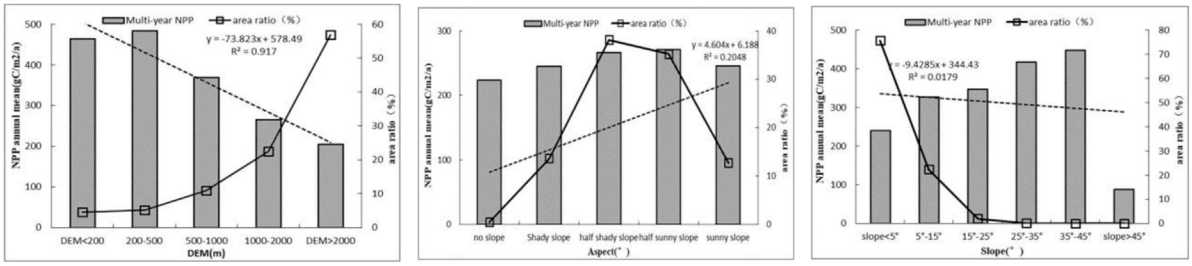

FIGURE 9
Relationship between topographic factors and grassland NPP. **(A)** Changes in the relationship between annual NPP and DEM. **(B)** Changes in the relationship between annual NPP and Aspect. **(C)** Changes in the relationship between annual NPP and Slope.

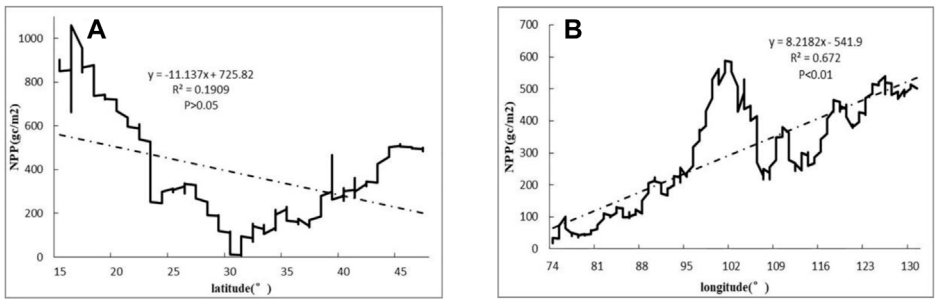

FIGURE 10
(A) Changes in the relationship between annual NPP and lattitude. **(B)** Changes in the relationship between annual NPP and longtitude.

From the perspective of the meridional variation rule (Figure 10B), the average NPP value of grassland in China from 2001 to 2019 was 296.56 g·C·m^{-2}·a^{-1}. In 2019, the mean NPP value of grassland in China was positively correlated with the change of longitude. The distribution of mean NPP value showed obvious longitude zonality, rising in a "stepped" manner from west to east, and the change rate was 8.22 g·C/(m2·a·10°), and through the $p < 0.01$ significance level test, the upward trend is obvious. Among them, the maximum average NPP value is 588.09 g·C·m^{-2}·a^{-1}, which is mainly distributed in the central region with longitude of 101–102°. It may be due to the abundant precipitation and suitable climate in this region, which is more conducive to the growth of vegetation, thus enhancing the carbon sequestration capacity of grassland. The lowest NPP is 17.02 g·C·m^{-2}·a^{-1}, which is distributed in the western desert area with a longitude of about 74°. The NPP value in this area is generally low, which may be due to the relatively low precipitation and high temperature in this area. It is difficult for vegetation to grow in arid and high temperature areas, which reduces the carbon sequestration potential of grassland. These changes are caused by the differences in the geographical environment and soil and water conservation at different latitudes and longitudes. Different environments will cause different growth conditions of vegetation, and different soil and water conservation will lead to different soil fertility and drainage performance. Therefore, there are also certain differences in the carbon sequestration capacity of grassland with different latitudes and longitudes.

4 Discussion

In this study, the NPP of grassland in China was simulated and estimated based on the CASA model, and the spatial and temporal distribution characteristics and influencing factors of grassland NPP in China were comprehensively analyzed using trend analysis and complex correlation analysis, and the impact of climate change and influencing factors on vegetation NPP was discussed. The results show that from 2001 to 2019, China's grassland NPP showed a decreasing trend from southeast to northwest. The vegetation coverage is also different, and the ecological structure stability of each region is also different. The results in this paper are similar to those obtained by Shen et al. (2016) based on the literature data that the NPP of natural grassland in China is 89–320 g·C·m^{-2}·a^{-1}. Zhou Wei et al., Zhu

Wenquan, Gao et al. (2012) used the CASA model to estimate the annual average of grassland NPP per unit area in China to be 282.0, 231, and 217.90 $g{\cdot}C{\cdot}m^{-2}{\cdot}a^{-1}$ respectively. The estimated results are similar, indicating that the results of this study have reference value.

From the impact of climate change on grassland NPP, this study shows that precipitation and temperature in the past 19 years have played an important role in promoting grassland NPP, but there are certain differences in the dominant factors in different sub-regions. Among them, grassland NPP is more dependent on precipitation than air temperature. This study reveals that precipitation plays an important role in promoting vegetation growth, which is consistent with the findings of most researchers (Liu et al., 2019). In addition, while precipitation and air temperature promote vegetation growth, they also increase the dark respiration rate of vegetation, resulting in a decrease in NPP. Therefore, precipitation and air temperature can promote grassland NPP at a certain threshold, but may have opposite effects when exceeding a certain limit (He, 2008).

From the impact of terrain factors on grassland NPP, altitude, slope and slope aspect have obvious differentiation effects on temperature and precipitation, which will lead to large differences in regional illumination, soil moisture and nutrients, thus affecting regional vegetation spatial pattern. In addition, the flow and conversion of surface materials and energy at different altitude gradients, slopes and slopes are also the main influencing factors that limit the spatial distribution of vegetation (Pan et al., 2009; You et al., 2011). This study found that grassland NPP generally decreased with the increase of altitude, and there were great differences in the fluctuation trend of grassland NPP in each altitude gradient. In terms of slope, the NPP of the grass on the steep slope is the highest, while that on the dangerous slope is the lowest. The reason for the analysis is that the steep slope has better soil and water conservation, resulting in fertile soil and good drainage, which are beneficial to the growth of plants; on the contrary, the steep slope is opposite and the vegetation coverage is low, resulting in a low carbon sequestration potential. In terms of slope aspect, there is no obvious regularity in the response characteristics of grassland NPP changes to temperature and precipitation on different slope aspect gradients. The solar radiation received by the surface and the potential evapotranspiration are different (Soltani et al., 2016). The sunny slope is full of sunlight, but the high temperature will lead to accelerated soil water evapotranspiration, which will inhibit the growth of vegetation; the shady slope is full of moisture, but the temperature and light are relatively weak, which will also inhibit the photosynthesis of vegetation, so the growth of vegetation on different slopes tends to be different from that of vegetation. The biological uniqueness of each vegetation type has a great relationship (Wang et al., 2016).

From the perspective of the influence of latitude and longitude on grassland NPP, latitude/longitude not only reflects water/heat differentiation across the globe but also indicates lots of other influential factors. It argues that many other factors, including Sun shine hours, atmospheric circulation, soil nutrition are closely related to latitude/longitude belts. Although this study cannot cover all the influnce factors but analyzed the changes of NPP along latitude/longitude belts. And the changes in different latitude and longitude will also lead to the changes in environmental temperature, humidity, topography, soil and many other environmental factors, which will affect the growth of vegetation, and then affect the carbon sequestration potential of vegetation. This study found that, in terms of latitude, grassland NPP showed a “wave-like” decline trend from south to north. The grassland NPP is higher in the southern regions of low latitudes. It is due to sufficient precipitation, suitable climate, relatively good soil water and soil conservation, which is more conducive to the growth of vegetation, thus enhancing the carbon sequestration capacity of grassland. In terms of longitude, grassland NPP showed a “step-like” upward trend from west to east (Wang et al., 2022). Grasslands in the central region have higher NPP. The reason analysis shows that the area has excellent water and heat conditions, flat terrain, sufficient sunlight, high vegetation coverage, good soil and water conservation, which promotes vegetation growth and enhances the ability of vegetation to sequester carbon.

China’s grassland covers nearly 40% of its total area, which is larger than the forest area, but its productivity is lower than the global average. Research on temporal and spatial changes and influencing factors can better understand the occurrence and development trend of vegetation productivity, which is helpful for the assessment of future climate change and national two-carbon strategy. In terms of grassland management, it can be seen from the conclusions of this paper that grassland productivity increases or decreases rapidly in some areas. Therefore, it can be started from this perspective to protect the basic area of grassland industry and improve the grassland quality and growth environment. In areas where there has been a decrease or no significant increase, it is important to strengthen conservation efforts and promote a grassland culture to further contribute to grassland carbon sequestration potential. By studying the influence of potential factors, it is possible, on the one hand, to gain a more comprehensive understanding of the measures that are conducive to adjusting the growth and development of vegetation and enhancing its carbon sequestration capacity. On the other hand, it can also help to improve the intensity of overgrazing and the implementation of policies such as the return of cropland to grass, adding to the improvement of urban sprawl and the enhancement of carbon sequestration potential. In addition, it is an important guide for the development of policies and management of grassland resources by grassland management departments.

Although this study provided a comprehensive analysis of NPP changes and climate effects in grasslands of China, there may still be some limitations. First, owing to the uncertainty of satellite remote sensing data, NPP data could contain some inaccuracies which may affect the results of this study. Second, the interpolation method of meteorological data in this study may lead to some inaccuracy in meteorological results, which could have an impact on the analysis of the results of this study. In addition, many factors influence vegetation growth in China's grassland.This study only considered three influence factors, geographic location, terrain and climate, and the relationships of grassland NPP with other environmental factors need to be further explored. Finally, changes in NPP are affected by multiple factors, such as terrain, climate change and human activities. Although this study extracted unchanged grassland, the influences of human activities on grassland vegetation could not be completely excluded. In addition, the results of this study are not verified by field measured data (Ma et al., 2022). In terms of grassland management, corresponding suggestions can be put forward according to the rate of increase or decrease of grassland productivity in some areas. For example, in areas with rapid increase of NPP, the management and protection efforts should be improved. In areas with low slope or no significant increase of NPP, the protection efforts should be strengthened to improve grassland quality and growth environment, protect the basic area of grassland industry and promote grassland culture. This further contributes to grassland carbon sequestration potential. Therefore, in future studies, the effects of human activities on grasslands and the inaccuracies caused by the measurement of satellite remote sensing data should be further studied.

5 Conclusion

In the past 19 years, China's grassland NPP has generally shown a fluctuating upward trend, and its spatial distribution has gradually decreased from southeast to northwest. The relationship between the spatiotemporal distribution of grassland NPP and climate change in China from 2001 to 2019: The spatial distribution of the first-order partial correlation and general correlation between grassland NPP and precipitation and temperature are: the area ratio of partial correlation with precipitation is greater than the area proportion with partial correlation with temperature. The relationship between temporal and spatial distribution of grassland NPP and terrain in China from 2001 to 2019: With the increase of altitude, there is a general downward trend, and grassland is distributed mainly in the plateau area. The variation of NPP at different altitudes (DEM) presents: hill>plain>mountain>basin>plateau. The variation of NPP with different slope aspects is as follows: semi-sunny slope>semi-shady slope>sunny slope>shady slope>no slope aspect. With the increase of the slope, the overall trend is decreasing, the variation of NPP with different slopes showed: sharp slope>steep slope>slope> gentle slope>flat>dangerous slope. The relationship between temporal and spatial distribution of grassland NPP in China from 2001 to 2019 and latitude and longitude: From the perspective of zonal variation, the mean value of NPP showed a "wave-like" downward trend from south to north. From the perspective of the meridional variation rule, the mean NPP shows a "step-like" rising trend from west to east.

Data availability statement

The original contributions presented in the study are included in the article/supplementary material, further inquiries can be directed to the corresponding author.

Author contributions

ZS conceptualized this study. XL and RL carried out the data analysis and composed the manuscript. All authors have read and agreed to the published version of this manuscript.

Funding

This work was supported in part by the National Natural Science Foundation of China (Nos. 41871296 and 42171447) and the Key Laboratory of Natural Resources Monitoring in Tropical and Subtropical Area of South China, Ministry of Natural Resources (No. 2022NRM006).

Acknowledgments

We acknowledge the support of all co-authors for their constructive and helpful comments and the organization of this study.

Conflict of interest

The authors declare that the research was conducted in the absence of any commercial or financial relationships that could be construed as a potential conflict of interest.

Publisher's note

References

Carraro, C., and Massetti, E. (2012). Energy and climate change in China. *Environment and Development Economics* 17 (6), 689–713. doi:10.22004/ag.econ.101294

Chen, X. J., Zhang, C. C., Zhang, J. T., and Wang, J., (2022). Analysis of the spatiotemporal evolution patterns of vegetation net primary productivity and its influencing factors based on CASA model. *Res. Soil Water Conservation* (03), 253–261. doi:10.13869/j.cnki.rswc.2022.03.033

Chen, Y. Z., Ju, W. M., Groisman, P., Li, J., Propastin, P., and Xu, X., (2017). Quantitative assessment of carbon sequestration reduction induced by disturbances in temperate Eurasian steppe. *Environ. Res. Lett* 11, 115005. doi:10.1088/1748-9326/aa849b

Christopher, B., Field, Michael, J., BehrenfeldJames, T., and Falkowski, P. (1998). Primary production of the biosphere: Integrating terrestrial and oceanic components. *Science* 5374, 237–240. doi:10.1126/science.281.5374.237

Dowding, I., and Haufe, S. (2018). Powerful statistical inference for nested data using sufficient summary statistics. *Front. Hum. Neurosci.* 12, 103. doi:10.3389/fnhum.2018.00103

Du, B. B., Alateng, T. Y., Bao, G., Wang, N., and Ling, K. J., (2021). Simulation of net primary productivity of xilingol grassland based on CASA model. *Res. Soil Water Conservation* (05), 293–300. doi:10.13869/j.cnki.rswc.2021.05.034

Fang, J. Y., Ke, J. H., Tang, Z. Y., and Chen, A. P., (2001). Implications and estimations of four terrestrial productivity parameters. *Acta Phytoecol. Sin* (04), 414–419.

Gao, Y. N., Yu, G. R., Zhang, L., Liu, M., Huang, M., and Wang, Q. F., (2012). The changes of net primary productivity in Chinese terrestrial ecosystem: Based on process and parameter model. *Prog. Geogr.* (01), 109–117. doi:10.11820/dlkxjz.2012.01.014

He, H. Y. (2008). Modeling forest NPP patterns on the Tibetan Plateau and its responses to climate change. *China Acad. For. Sci.* doi:10.7666/d.D602776

Hou, Y. Y., Liu, Q. H., Yan, H., and Tian, G. L. (2007). Variation trends of China terrestrial vegetation net primary productivity and its responses to climate factors in 1982-2000. *Chin. Acad. Agric. Sci* 18 (07), 1546–1553. doi:10.13287/j.1001-9332.2007.0259

Jin, K., Wang, F., Han, J. Q., Shi, S. Y., and Ding, W. B., (2020). Contribution of climatic change and hunan activities to vegetation NDVI change over China during 1982-2015. *Acta Geogr. Sin* (05), 961–974. doi:10.11821/dlxb202005006

Li, H. X., Liu, G. H., and Fu, B. J. (2011). Response of vegetation to climate change and human activity based on NDVI in the Three-River Headwaters region. *Acta Ecol. Sin* 31 (19), 5495–5504.

Li, J. K., Yang, Y. T., Zhang, H. R., Huang, L., and Gao, Y. M., (2019). Spatio-temporal variations of net primary productivity and its natural and human factors analysis in Qinling-Daba Mountains in the past 15 years. *Acta Ecologica Sinica*. 39 (22), 8504–8515. doi:10.5846/stxb201807231575

Li, M., Wu, J., Feng, Y., Niu, B., He, Y., and Zhang, X. (2021). Climate variability rather than livestock grazing dominates changes in alpine grassland productivity across Tibet. *Front. Ecol. Evol* 9, 631024. doi:10.3389/fevo.2021.631024

Li, M. D., Cui, Y. P., Fu, Y. M., Li, N., Tang, X. Y., and Liu, X. Y., (2020). Simulating the potential sequestration of three major greenhouse gases in China's natural ecosystems. *Forests* 11 (2), 128 doi:10.3390/f11020128

Li, X. B., Fan, R. X., and Liu, X. D. (2014). Advance in studies on carbon storage and carbon process in grassland ecosystem of China. *Ecol. Environ. Sci* 23 (11), 1845–1851. doi:10.16258/j.cnki.1674-5906.2014.11.023

Liu, X. J., Dong, L., Zhao, J., Du, Z. Q., and Zhang, H., (2019). Dynamic state of desert vegetation productivity and its relationship with water-heat factors in China. *Arid Zone Res* 36 (2), 459–466. doi:10.13866/j.azr.2019.02.23

Liu, Y. Y., Yue, Y. Q., Wang, Q., Du, X., Li, J., and Gang, C., (2019). Evaluating the responses of net primary productivity and carbon use efficiency of global grassland to climate variability along an aridity gradient. *Sci. Total Environ* 652, 671–682. doi:10.1016/j.scitotenv.2018.10.295

Ma, R., Xia, C., Liu, Y., Wang, Y., Zhang, J., and Shen, X., (2022). Spatiotemporal change of net primary productivity and its response to climate change in temperate grasslands of China. *Front. Plant Sci* 13, 899800. doi:10.3389/fpls.2022.899800

Murakami, K., Kojima, T., and Sakaki, Y. (2004). Assessment of clusters of transcription factor binding sites in relationship to human promoter, CpG islands and gene expression. *BMC Genomics* 5, 16. doi:10.1186/1471-2164-5-16

Niu, J. M. (2000). Relationship between main vegetation types and climatic factors in inner Mongolia Chinese Academy of agricultural Sciences, 47–52. doi:10.13287/j.1001-9332.2000.0013

Pan, H. L., Li, M. H., Cai, X. H., Wu, J., Du, Z., and Liu, X. L., (2009). Responses of growth and ecophsiology of plants to altitude. *Ecol. Environ. Sci* (02), 722–730. doi:10.16258/j.cnki.1674-5906.2009.02.036

Piao, S. L., Fang, J. Y., He, J. S., and Yu, X. (2004). Spatial distribution of grassland biomass in China. *Chin. J. Plant Ecol* 28 (04), 491–498. doi:10.17521/cjpe.2004.0067

Shen, H. H., Zhu, Y. K., Zhao, X., and Gao, S. (2016). Analysis of current grassland resources in China(in Chinese). *Chin. Sci. Bull* 61, 139–154. doi:10.1360/N972015-00732

Soltani, M., Laux, P., Kunstmann, H., Stan, K., Sohrabi, M. M., and Molanejad, M., (2016). Assessment of climate variations in temperature and precipitation extreme events over Iran. *Theor. Appl. Climatol* 126, 775–795. doi:10.1007/s00704-015-1609-5

Tang, C. J., Fu, X. Y., Jiang, D., Zhang, X., and Zhou, S. (2014). Simulating spatiotemporal dynamics of sichuan grassland net primary productivity using the CASA model and *in situ* observations. *Sci. World J* 2014, 1–2. doi:10.1155/2014/956963

Wang, H., Liu, G. H., Li, Z. S., Ye, X., Wang, M., and Gong, L. (2016). Impacts of climate change on net primary productivity in arid and semiarid regions of China. *Chin. Geogr. Sci* 26 (1), 35–47. doi:10.1007/s11769-015-0762-1

Wang, J., and Feng, Q. (2016). Extreme temperatures indexes in northern shaanxi during 1960-2013. *J. Desert Res* (04), 1097–1105. doi:10.7522/j.issn.1000-694X.2016.00080

Wang, S., Ping, C., Wang, N., Wen, J., Zhang, K., and Yuan, K., (2022). Quantitatively determine the dominant driving factors of the spatial-temporal changes of vegetation-impacts of global change and human activity. *Open Geosci* 14 (1), 568–589. doi:10.1515/geo-2022-0374

Xie, G. D., Zhang, Y. L., Lu, C. X., Zheng, D., and Cheng, S. K., (2001). Study on valuation of rangeland ecosystem services of China. *J. Nat. Resour* (01), 47–53. doi:10.3321/j.issn:1000-3037.2001.01.009

Xie, S. J., Liu, Y. H., and Yao, F. X. (2020). Spatio-temporal characterisitics of NDVI and its relationship with climate change in Beijing from 1998 to 2015. *Res. Soil Water Conservation* (03), 190–196+202+2. doi:10.13869/j.cnki.rswc.2020.03.028

Xu, Y., Hu, X., Liu, Z., and Zhang, H. (2020). Research advances in net primary productivity of terrestrial ecosystem. *J. Geoscience Environ. Prot* 8, 48–54. doi:10.4236/gep.2020.88005

Yan, Y. C., Liu, X. P., Wen, Y. Y., and Ou, J. (2019). Quantitative analysis of the contributions of climatic and human factors to grassland productivity in northern China. *Ecol. Indic* 103, 542–553. doi:10.1016/j.ecolind.2019.04.020

Yang, T. T., Wu, X. H., Wang, J, T., Li, P., and Shi, H. X., (2012). Estimation of carbon storage in grassland ecosystem in China. *J. Arid Land Resour. Environ* (03), 127–130. doi:10.13448/j.cnki.jalre.2012.03.015

You, Q. L., Kang, S. C., Aguilar, E., Pepin, N., Flugel, W. A., and Yan, Y., (2011). Changes in daily climate extremes in China and their connection to the large scale atmospheric circulation during 1961–2003. *Clim. Dyn* 36, 2399–2417. doi:10.1007/s00382-009-0735-0

Zhao, F., Xu, B., Yang, X. C., Jin, Y., Li, J., and Xia, L., (2014). Remote sensing estimates of grassland aboveground biomass based on MODIS net primary productivity (NPP)A case study in the xilingol grassland of northern China. *Remote Sens* 6 (6), 5368–5386. doi:10.3390/rs6065368

Zhou, W., Mu, F. Y., Gang, C. C., Guan, D. J., He, J. F., and Li, J. L., (2017). Spatio-temporal dynamics of grassland net primary productivity and their relationship with climatic factors from 1982 to 2010 in. *ChinaActa Ecol. Sin* 37 (13), 4335–4345doi. doi:10.5846/stxb201408291724

Zhu, W. Q. (2005). *Estimation of net primary productivity of Chinese terrestrial vegetation based on remote sensing and its relationship with global climate change.* Doctoral dissertation. China: Beijing Normal University.

Zhu, W. Q., Pan, Y. Z., Long, Z. H., Chen, Y. Z., Li, J., and Hu, H. B., (2005). Estimating net primary productivity of terrestrial vegetation based on GIS and RS:A Case study in Inner Mongolia, China. *J. Remote Sens* (03), 300–307.

Zhu, W. Q., Pan, Y. Z., and Zhang, J. S. (2007). Estimation of net primary productivity of Chinese terrestrial vegetation based on remote sensing. *J. Plant Ecol* 31 (03), 413–424. doi:10.17521/cjpe.2007.0050

frontiers | Frontiers in Earth Science

TYPE Original Research
PUBLISHED 24 February 2023
DOI 10.3389/feart.2023.1084399

OPEN ACCESS

EDITED BY
Manoj Kumar,
Forest Research Institute (FRI), India

REVIEWED BY
Xuguang Tang,
Southwest University, China
Xiangjin Shen,
Northeast Institute of Geography and Agroecology (CAS), China
Dehua Mao,
Northeast Institute of Geography and Agroecology (CAS), China
Keshav Tyagi,
Forest Research Institute (FRI), India
Agnish Kumar Das,
Forest Research Institute (FRI), India

*CORRESPONDENCE
Jiangping Chen,
chen_jp@whu.edu.cn
Zhanpeng Chen,
chyczp1441@163.com

SPECIALTY SECTION
This article was submitted to Environmental Informatics and Remote Sensing,
a section of the journal
Frontiers in Earth Science

RECEIVED 30 October 2022
ACCEPTED 14 February 2023
PUBLISHED 24 February 2023

CITATION
Li Z, Chen J, Chen Z, Sha Z, Yin J and Chen Z (2023), Quantifying the contributions of climate factors and human activities to variations of net primary productivity in China from 2000 to 2020.
Front. Earth Sci. 11:1084399.
doi: 10.3389/feart.2023.1084399

Quantifying the contributions of climate factors and human activities to variations of net primary productivity in China from 2000 to 2020

Zijian Li[1], Jiangping Chen[1,2]*, Zhanpeng Chen[3]*, Zongyao Sha[1,4], Jianhua Yin[1] and Zhaotong Chen[1]

[1]School of Remote Sensing and Information Engineering, Wuhan University, Wuhan, China, [2]Key Laboratory of National Geographical Census and Monitoring, Ministry of Natural Resources, Wuhan, China, [3]Institute of Land Resources Surveying and Mapping of Guangdong Province, Guangzhou, China, [4]Key Laboratory of Natural Resources Monitoring in Tropical and Subtropical Area of South China, Ministry of Natural Resources, Guangzhou, China

Net primary productivity (NPP) plays a vital role in the globe carbon cycle. Quantitative assessment of the effects of climate changes and human activities on net primary productivity dynamics is vital for understanding the driving mechanisms of vegetation change and sustainable development of ecosystems. This study investigates the contributions of climatic factors and human activities to vegetation productivity changes in China from 2000 to 2020 based on the residual trend analysis (RESTREND) method. The results showed that the annual average net primary productivity in China was 325.11 g C/m^2/year from 2000 to 2020 and net primary productivity showed a significantly increasing trend (p<0.05) at a rate of 2.32 g C/m^2/year. Net primary productivity increased significantly (p<0.05) across 40.90% of China over the study period, while only 1.79% showed a significantly declining trend (p<0.05). The contributions of climatic factors and human activities to net primary productivity increase were 1.169 g C/m^2/year and 1.142 g C/m^2/year, respectively. Climate factors contributed positively mainly in Sichuan Basin, the Loess Plateau, the Mongolian Plateau, and Northeast China Plain. Positive contributions of human activities to net primary productivity mainly occurred in the Loess Plateau, Central China, and the Greater Khingan Mountains. The effects of climatic factors and human activities on net primary productivity changes varied among sub-regions. In Tropical Monsoon Climate Region and Subtropical Monsoon Climate Region, human activities had greater impacts on net primary productivity increase than climate factors, while climate factors were the dominant factor for net primary productivity recovery in other sub-regions. In addition, during 2000–2020, net primary productivity was dominated by both climate factors and human activities in 49.84% of China, while areas dominated solely by climate factors and human activities accounted for 13.67% and 10.92%, respectively. Compared to changed land cover types, the total net primary productivity as well as the increase of total net primary productivity in China was mostly contributed by unchanged land cover types, which contributed more than 90%.

KEYWORDS

net primary productivity (NPP), climate factors, human activities, residual trend analysis, China

1 Introduction

Net primary productivity (NPP) is the remainder of the total amount of organic matter produced by green plants per unit area per unit time, excluding that consumed by their own respiration (Roxburgh et al., 2005). NPP is an important indicator of regional ecosystem function, ecosystem stability and self-healing capacity (Melillo et al., 1993; Running et al., 2004). It is not only an important component of the global carbon cycle (Cramer et al., 1999; Crabtree et al., 2009), but also reflects the combined effects of climate changes and human activities on terrestrial vegetation (Gower et al., 1999; Nemani et al., 2003). Therefore, the analysis of the spatiotemporal evolution patterns and driving factors of vegetation NPP can provide a scientific basis for evaluating the quality of regional terrestrial ecosystems, effective management of natural resources, and sustainable socioeconomic development in the context of global climate change (Qi et al., 2019).

The driving factors of NPP changes can be divided into climate changes and human activities (Chen et al., 2014; Sun et al., 2015). It is believed that increased CO_2 fertilization effects in climate enhance vegetation NPP (Piao et al., 2011; Wang et al., 2020), which contributes a negative feedback effect on global warming. Regional temperature, precipitation and solar radiation are the most important climate factors driving NPP changes (Churkina and Running, 1998; Nemani et al., 2003; Running et al., 2004). Temperature, in high latitudes and altitudes, e.g., northeastern China (Li H. et al., 2021) and the Qinghai-Tibet Plateau (Xu et al., 2016; Wang S. et al., 2017), exerts the key climatic driver for NPP increases. The increase in temperature at cold regions can enhance activities of photosynthetic enzymes, reduce speed of chlorophyll degradation, and prolong the vegetation growth season, thus promote vegetation productivity (Liu et al., 2016; Dusenge et al., 2019). In arid and semi-arid areas, precipitation plays a decisive role in the NPP dynamics among the climatic factors, and the increase of precipitation enhances vegetation photosynthesis by affecting soil water content (Wang et al., 2001; Jiang Y. et al., 2020; Li C. et al., 2021). Solar radiation can influence soil temperature, and its increase reduces soil moisture and hinders root growth, thus decreasing productivity especially in low-land grassland ecosystems (Zhou et al., 2012; Wu G. et al., 2021). However, previous studies have also found that excessive solar radiation exerted a negative effect on vegetation productivity in the Qinghai-Tibet Plateau (Luo et al., 2018; Yan et al., 2019).

In addition, anthropogenic factors are also important drivers of vegetation dynamic. In order to improve the environment, the Chinese government has launched a variety of initiatives, including Three-North Shelter Forest Program, Grain to Green Program (GTGP), and Grazing Withdrawal Program (GWP) (Wang B. et al., 2017; Li et al., 2021a). The Loess Plateau, one of the world's most eroded regions, is a prioritized pilot region of the ongoing GTGP program and has shifted from a net carbon source to a net carbon sink by converting cultivated land on steep slopes to perennial vegetation (Feng et al., 2013; Gang et al., 2018). Decreased grazing pressure and conversion from grazing lands to grasslands resulting from these programs have made a significant contribution to vegetation restoration, and have greatly improved the carbon storage in the Qinghai-Tibet Plateau, and Inner Mongolia Grassland (Chi et al., 2018; Li et al., 2021b). In order to prevent and control rocky desertification issues in southwestern China, a series of key national ecological restoration projects such as the Natural Forest Protection Project and the Karst Rocky Desertification Comprehensive Control and Restoration Project have been launched and the world's leading level of vegetation productivity restoration have been achieved (Gang et al., 2019; Tang et al., 2022). China's climate is complex and diverse with an abundant number of ecosystems, spanning from south to north across tropical zone to cold temperate zone, and from the humid zone in the southeast to the arid zone in the northwest (Yang et al., 2017; Lai et al., 2018). However, effects of climate factors and human activities vary across climate zones and ecosystem types due to the interaction of complex geographic topography and climate change (Zhao et al., 2018; Chen Y. et al., 2019). Relatively few studies have been concerned with such differences due to climatic zones. Therefore, it is necessary to assess the relative roles of climate changes and human activities in vegetation dynamics quantitatively under different climatic zones, for an in-depth understanding of the mechanisms driving vegetation change.

Recently, several methods have been adopted to determine the interaction of climate factors and human activities on vegetation dynamics, such as the regression model method, redundancy analysis, and the Miami memorial model (Li D. et al., 2018; Wu N. et al., 2021; Xiong et al., 2021). The regression model method is the simplest, but it is hard to describe the complex interactions between vegetation and climatic factors, between that and human activities (Turner and Carpenter, 2017; Liu et al., 2020), and independent variable factors are difficult to quantify spatially, lead to uncertainties in the results (Wu N. et al., 2021). The biophysical model-based method can separate the relative contributions of climate change and human activities on vegetation dynamics by simulating potential NPP (PNPP) and actual NPP (ANPP) (Li et al., 2016; Li C. et al., 2021), but it needs lots of physiological and ecological parameters, which may cause the uncertainties of the model (Zhou et al., 2015). The residual trend analysis method (RESTREND) (Evans and Geerken, 2004) is a simple calculation that can separate spatially the impact of human activities on vegetation from the impact of climate changes using the residue of multiple regression between climate factors and vegetation indicators to quantify the extent of human activities (Wu et al., 2022; Yin et al., 2022). The disadvantage of method is that model calibration in the year assuming without human interference would introduce errors into the model itself (Jiang H. et al., 2020). Understanding the influence mechanisms of NPP is essential to providing targeted guidance for constructing ecological restoration programs.

Previous studies focus on a specific or local region, and there are fewer studies on the entire China, as a decisive region in the global carbon cycle. Accordingly, the objectives of this study were to 1) analyze the spatial distribution and temporal dynamic

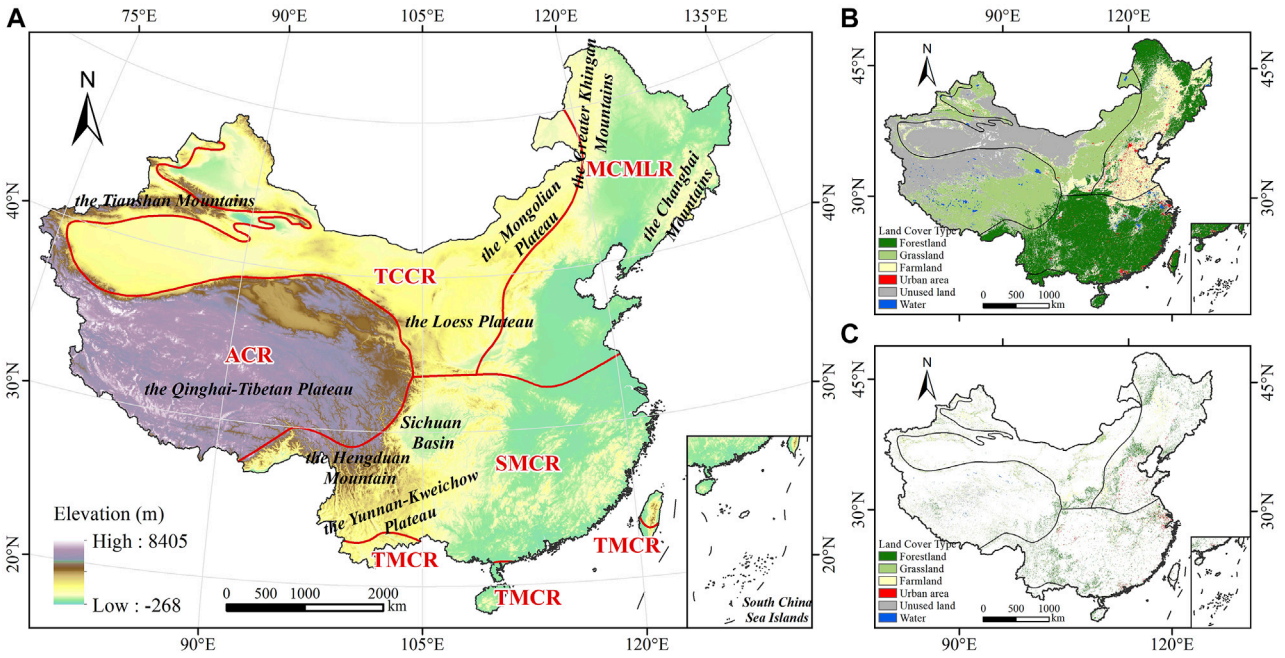

FIGURE 1
(A) The spatial pattern of elevation, the location of five sub-regions, and the distribution of **(B)** unchanged and **(C)** changed land cover types from 2001 to 2020. The legend of **(B)** means that the land cover type in 2020 was the same as that in 2001. The legend of **(C)** means the land cover type after conversion.

characteristics of NPP in China from 2000 to 2020; 2) quantify the contributions of climate factors and human activities to NPP dynamics in China; 3) explore the major driving factors of NPP changes under different climate types; 4) analyze the NPP dynamics for different land cover types.

2 Materials and methods

2.1 Study area and data

China, the third largest country in the world, was chosen as the study region, which had a complex topography, diverse climate, and rich variety of vegetation with an intricate distribution. China spanned a wide range of latitudes, with large differences in distance from the sea, as well as different terrain, resulting in diverse combinations of temperature and precipitation, forming a wide variety of climates. The local vegetation growth was significantly impacted by various climate types, thus we divided China into five regions (Figure 1) based on climate type for a more specific analysis (Song et al., 2011): 1) Tropical Monsoon Climate Region (TMCR); 2) Subtropical Monsoon Climate Region (SMCR); 3) Monsoon Climate Region of Medium Latitudes (MCMLR); 4) Temperate Continental Climate Region (TCCR); 5) Alpine Climate Region (ACR). During the growing season (from April to October), the average temperature differences across the country were not significant (except for ACR) with 24.4, 21.2, 16.2, 17.3, and 4.3°C. The cumulative precipitation rose from the northwest (170 mm) to the southeast (1,465 mm). On the contrary, the cumulative solar radiation increased from the southeast (3,702 MJ/m^2) to the northwest (5,161 MJ/m^2).

NPP data were derived from the Moderate Resolution Imaging Spectroradiometer (MODIS) Net Primary Production Gap-Filled Yearly L4 Global 500 m SIN Grid (MOD17A3HGF v006) from the National Aeronautics and Space Administration (NASA) (https://lpdaac.usgs.gov/) with a temporal resolution of 1 year and a spatial resolution of 500 m. The data were calculated by using an NPP estimation model established based on the Biome Biogeochemical model and the light use efficiency model. The downloaded NPP data from 2000 to 2020 were mosaiced, uniformly projected in WGS_1984_UTM_Zone_48N, converted to real values, and resampled to 1,000 m.

Monthly meteorological data of the growing season (from April to October) from 2000 to 2020 consisted of temperature, precipitation, and solar radiation. Temperature and precipitation data were obtained from the National Tibetan Plateau Data Center (https://data.tpdc.ac.cn/zh-hans/) with a spatial resolution of 1,000 m, which were generated by using Delta downscaling method based on the global climate dataset published by CRU and WorldClim. Solar radiation data were obtained from the National Centers for Environmental Prediction (NCEP) Climate Forecast System (CFS) (https://cfs.ncep.noaa.gov/) with a spatial resolution of 0.2°, and NCEP upgraded CFS to version 2 (CFSv2) on 30 March 2011. Data were resampled to 1,000 m. In this study, we defined the growing season as from April to October in order to be consistent across the whole country (Piao et al., 2010; Peng et al., 2011). The average temperature, the cumulative precipitation, and the cumulative solar radiation during the growing season from 2000 to 2020 were calculated.

Land cover data were downloaded from MODIS Land Cover Type Yearly L3 Global 500 m SIN Grid (MCD12Q1 v006) (https://

lpdaac.usgs.gov/) for the uniformity of data sources, and were resampled to 1,000 m. MODIS land cover types have been provided since 2001, thus data for 2001 and 2020 were used. Annual Plant Functional Types classification of MCD12Q1 was used for this study. In this study, we first analyzed NPP variations of the entire China and then areas of unchanged land cover types, as the area of changed land cover types accounted for only 7.29% of China, and the distribution was scattered (Figure 1).

Socio-economic data including gross domestic product (GDP) and population were obtained from the China Statistical Yearbooks (various issues) of the National Bureau of Statistics of China (http://www.stats.gov.cn/). Climate type distribution data were obtained from the Resources and Environment Science and Data Center, Chinese Academy of Sciences (http://www.resdc.cn/).

2.2 Methods

2.2.1 Trend analysis

The Theil-Sen trend analysis method was used to estimate the NPP change trend (Xu et al., 2020). The formula is as follows:

$$S_{NPP} = median\left[\frac{NPP_j - NPP_i}{j - i}\right], \forall i < j \tag{1}$$

Where S_{NPP} is the Theil-Sen trend of NPP and NPP_i and NPP_j are the values of NPP in year i and j, respectively. $S_{NPP} > 0$ indicates an increasing trend, and the converse denotes a decreasing trend.

The Mann-Kendall (MK) test was used to indicate the significance of the NPP trend (Dameneh et al., 2021). The formula is as follows:

$$S = \sum_{i=1}^{n-1}\sum_{j=i+1}^{n} sgn\left(NPP_j - NPP_i\right) \tag{2}$$

$$sgn\left(NPP_j - NPP_i\right) = \begin{cases} +1, NPP_j - NPP_i > 0 \\ 0, NPP_j - NPP_i = 0 \\ -1, NPP_j - NPP_i < 0 \end{cases} \tag{3}$$

$$Z = \begin{cases} \frac{S-1}{\sqrt{Var(S)}}, S > 0 \\ 0, S = 0 \\ \frac{S+1}{\sqrt{Var(S)}}, S < 0 \end{cases} \tag{4}$$

$$Var(S) = \frac{n(n-1)(2n+5)}{18} \tag{5}$$

Where n is the duration, in years, of the study period (n =21). When $|Z| > Z_{1-\alpha/2}$, the NPP trend is considered statistically significant. The 5% significant level which refers to $Z_{1-\alpha/2}$ =1.96 was used for the MK test in this study.

2.2.2 Contributions of climate factors and human activities to NPP

The main drivers of NPP changes are climate changes and human activities. The residual trend analysis (RESTREND) was used to calculate the contributions of climate factors (temperature, precipitation, and solar radiation) and human activities to NPP (Evans and Geerken, 2004). The formula is as follows:

$$\begin{aligned} S_{NPP} &= C(C) + UF = C(T) + C(P) + C(R) + UF \\ &\approx \left(\frac{\partial NPP}{\partial T}\right) \times \left(\frac{\partial T}{\partial n}\right) + \left(\frac{\partial NPP}{\partial P}\right) \times \left(\frac{\partial P}{\partial n}\right) + \left(\frac{\partial NPP}{\partial R}\right) \times \left(\frac{\partial R}{\partial n}\right) + C(H) \end{aligned} \tag{7}$$

Where S_{NPP} is the Theil-Sen trend of NPP. $C(C), C(T), C(P), C(R)$ are the contributions of climate, temperature, precipitation, and solar radiation to NPP, respectively. $C(C)$ is the sum of $C(T)$, $C(P)$, and $C(R)$. n is the number of study years. $C(T)$ is the product of $\partial NPP/\partial T$ (the slope of the linear regression line between NPP and temperature) and $\partial T/\partial n$ (the slope of the linear regression line between temperature; n). $C(P)$ and $C(R)$ are calculated similarly. In this study, the average temperature, the cumulative precipitation, and the cumulative solar radiation during the growing season (from April to October) were calculated. UF is residual value between S_{NPP}; $C(C)$. In this study; UF is interpreted as the change rate of the contribution of human activities to NPP, namely; $C(H)$ (Chen et al., 2021a; Ge et al., 2021).

2.2.3 Scenario design and quantitative evaluation methods

By combining the NPP trend with the contributions of the driving factors, six scenarios were produced according to the different permutations of value ranges of S_{NPP}, $C(C)$, and $C(H)$ (Table 1). Increased NPP is considered as an indicator of vegetation recovery, whereas a negative S_{NPP} stands for vegetation degradation (Zhou et al., 2015; Chen et al., 2021b). Positive $C(C)$ and $C(H)$ represent that climate factors and human activities facilitated an increase in NPP, whereas the negative $C(C)$ and $C(H)$ represent that climate factors and human activities caused a decline in NPP.

3 Results

3.1 Spatial and temporal variation of NPP

Figure 2A shows the spatial distribution of NPP from 2000 to 2020. In China, the annual average NPP ranged from 0 g C/m^2/year to 1943.59 g C/m^2/year and the average NPP in the region was 325.11 g C/m^2/year. The distribution pattern of NPP in China was higher in southeast and lower in northwest. TMCR had the highest NPP among the five sub-regions, with the average NPP of 1,110.11 g C/m^2/year. The average NPP in SMCR, MCMLR, and TCCR were 700.64 g C/m^2/year, 385.21 g C/m^2/year, and 105.41 g C/m^2/year, respectively. ACR had the lowest average NPP of 102.88 g C/m^2/year. As shown in Figure 2B, NPP increased in most of China in 2020 compared to 2000. NPP increased most significantly in the northeastern mountainous areas, the southern Loess Plateau, and Sichuan basin, with an increase of NPP of more than 200 g C/m^2/year. It can be seen that the NPP values in the southern Qinghai-Tibetan Plateau, the southern Yunnan-Kweichow Plateau, and the northern Greater Khingan Mountains were obviously reduced, with a decrease of NPP of more than 100 g C/m^2/year.

The annual NPP variations from 2000 to 2020 in China and five sub-regions were shown in Figure 2C. The annual average NPP in China showed a significantly increasing trend (p<0.05) at a rate of

TABLE 1 Six scenarios of NPP changes influenced by climate factors and human activities.

S_{NPP}	$C(C)$	$C(H)$	Contribution		Scenario
			Climate (%)	Human (%)	
>0	>0	>0	$\frac{\lvert C(C)\rvert}{\lvert C(C)\rvert+\lvert C(H)\rvert}\times 100$	$\frac{\lvert C(H)\rvert}{\lvert C(C)\rvert+\lvert C(H)\rvert}\times 100$	Recovery for both factors
	>0	<0	100	0	Recovery for climate factors
	<0	>0	0	100	Recovery for human activities
<0	<0	<0	$\frac{\lvert C(C)\rvert}{\lvert C(C)\rvert+\lvert C(H)\rvert}\times 100$	$\frac{\lvert C(H)\rvert}{\lvert C(C)\rvert+\lvert C(H)\rvert}\times 100$	Degradation for both factors
	<0	>0	100	0	Degradation for climate factors
	>0	<0	0	100	Degradation for human activities

TABLE 2 The contribution ratios of climate factors and human activities to NPP trend across China and five sub-regions.

Contribution ratio (%)	NPP variation		NPP recovery		NPP degradation	
	Climate	Human	Climate	Human	Climate	Human
China	50.58	49.42	50.25	49.75	47.58	52.42
TMCR	34.30	65.70	73.29	26.71	45.29	54.71
SMCR	40.79	59.21	42.58	57.42	48.85	51.15
MCMLR	53.84	46.16	53.31	46.69	24.70	75.30
TCCR	50.80	49.20	50.80	49.20	50.48	49.52
ACR	72.28	27.72	71.11	28.89	57.17	42.83

2.32 g C/m^2/year. In TMCR, NPP declined insignificantly (p>0.05) at a rate of −0.61 g C/m^2/year. However, NPP in the other four sub-regions showed a significant increasing trend (p<0.05). The increasing rate in MCMLR was highest, which was 4.44 g C/m^2/year, while NPP in ACR showed the lowest increasing rate of 0.62 g C/m^2/year. The increasing rate of SMCR and TCCR was 2.92 g C/m^2/year and 2.11 g C/m^2/year, respectively.

The spatial variations of NPP were observed, as shown in Figure 3. The classification in the legend of Figure 3A was determined by the distribution of NPP trend values, which between −5 and 10 accounted for 95% of the pixels. The NPP change trend in China ranged from −81.71 g C/m^2/year to 81.71 g C/m^2/year. NPP increased in 64.54% of China and 40.90% of the area increased significantly (p<0.05). The areas with rapid NPP increase were mainly distributed in Sichuan Basin, the Loess Plateau, and the Greater Khingan Mountains. In contrast, the decreasing trend of NPP accounted for 9.90% and 1.79% of the area declined significantly. The areas with NPP decrease mainly appeared in the southern Qinghai-Tibetan Plateau, the southern Yunnan-Kweichow Plateau, and southeastern China. Figure 3C shows the percentage changes of NPP for different regions. Areas of significant increases of NPP in TMCR, SMCR, MCMLR, TCCR, and ACR accounted for 23.55%, 43.77%, 67.20%, 37.17%, and 24.20%, respectively. NPP showed a significant decreasing trend across 19.33% of TMCR, 4.96% of SMCR, 0.61% of MCMLR, 0.15% of TCCR, and 0.45% of ACR, respectively.

3.2 Contributions of climate factors and human activities to NPP

The contributions of climate factors and human activities to NPP changes were calculated based on RESTREND (Figure 4). In China, the average contributions due to temperature, precipitation, and solar radiation to NPP were 0.205 g C/m^2/year, 0.467 g C/m^2/year, and 0.496 g C/m^2/year, respectively (Figure 4F). Besides, the contributions of climate and human activities were 1.169 g C/m^2/year and 1.142 g C/m^2/year. $C(C)$ of TMCR, SMCR, MCMLR, TCCR, and ACR were 0.482 g C/m^2/year, 1.225 g C/m^2/year, 2.312 g C/m^2/year, 1.066 g C/m^2/year, and 0.452 g C/m^2/year, respectively. However, human activities negatively contributed to NPP changes in TMCR, with the contribution of −0.924 g C/m^2/year. In contrast, $C(H)$ of SMCR, MCMLR, TCCR, and ACR were 1.778 g C/m^2/year, 1.982 g C/m^2/year, 1.033 g C/m^2/year, and 0.173 g C/m^2/year, respectively, having positive contributions to increases of NPP. Specific to each region, human activities played a primary role in NPP dynamics in TMCR and SMCR, whereas climate change was the dominant factor in the remaining regions, namely, MCMLR, TCCR, and ACR.

As shown in Figure 4A, temperature contributed positively in 46.27% of the area of China mainly including the Qinghai-Tibetan Plateau, the Loess Plateau, the Yunnan-Kweichow Plateau, and northeastern China, while temperature contributed negatively in 28.21% of China mainly including the Mongolian Plateau, eastern and southern China. Areas with positive contributions of

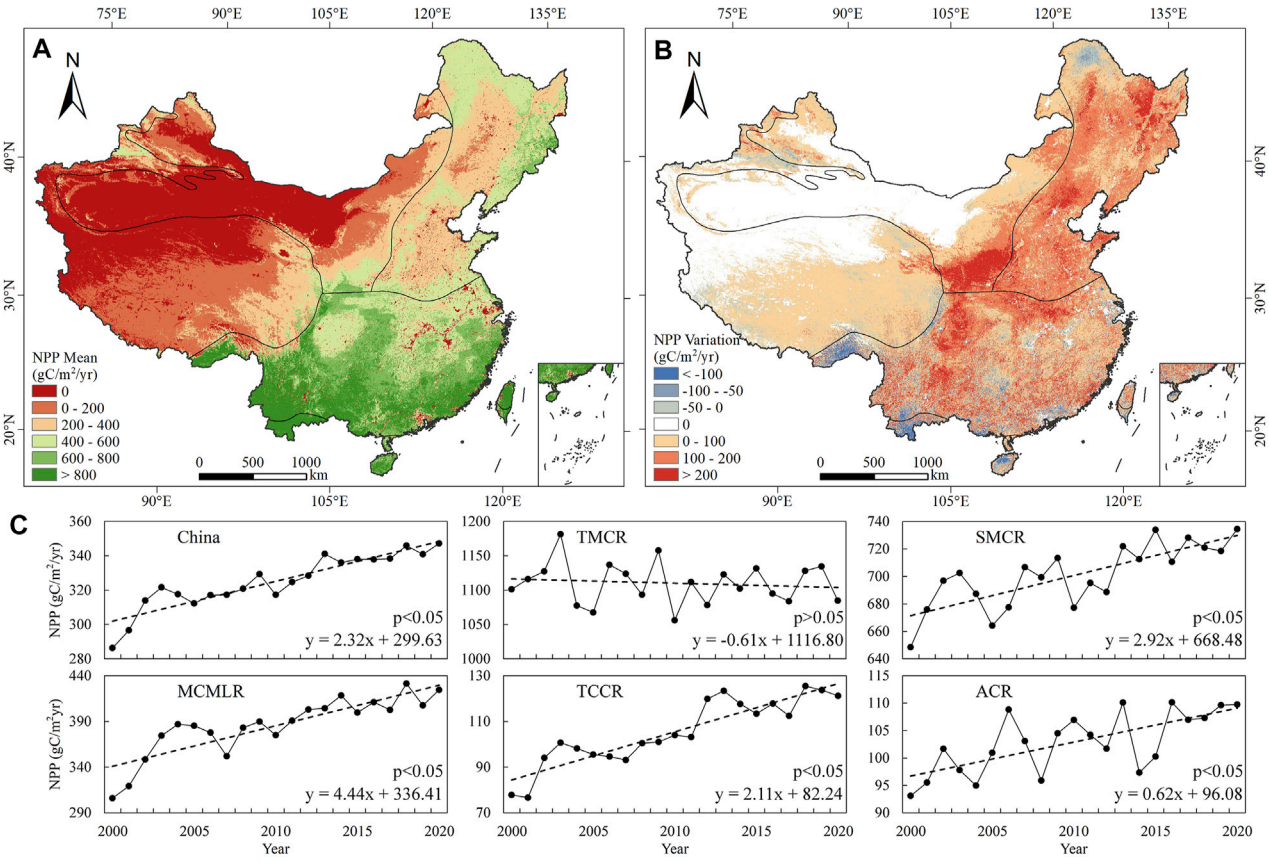

FIGURE 2
Spatial distribution of **(A)** annual average NPP, **(B)** NPP variations, and **(C)** NPP inter-annual variations in China and five sub-regions from 2000 to 2020.

precipitation accounted for 54.06% of China (Figure 4B), mainly including Sichuan Basin, the Loess Plateau, and the Mongolian Plateau, whereas areas with negative contributions of precipitation accounted for 20.41% and were mainly distributed in the Qinghai-Tibetan Plateau, central and southeastern China. Solar radiation made positive contributions in 53.25% of China and negative contributions in 21.24% of China (Figure 4C). Moreover, areas of contributions of solar radiation were similar to that of precipitation. Additionally, positive contributions of human activities were scattered in most areas of China (55.67%) (Figure 4E). However, negative contributions of human activities were mainly distributed in the Qinghai-Tibetan Plateau, the southern Yunnan-Kweichow Plateau, and southeastern China.

3.3 The relative impacts of climate factors and human activities on NPP

Figure 5 shows the spatial distribution of the contribution ratio of climate factors and human activities to NPP change trend from 2000 to 2020. Excluding stable area which accounted for 25.56% of China, areas with the contribution ratio of climate factors greater than 70% were mainly scattered in the Qinghai-Tibetan Plateau, Sichuan Basin, northwestern, and northeastern China, accounted for 24.86% of China (Figure 5A). The area percentage of the contribution ratio of climate factors from 30% to 70% was 21.41%. And the area percentage where the contribution ratio of climate factors less than 30% was 28.17%. Moreover, in 27.57% of China, mainly including central and southeastern China, the contribution ratio of human activities exceeded 70% (Figure 5B). The contribution ratio of human activities of 21.55% of China ranged from 30% to 70%, and 25.32% of China had a contribution ratio less than 30% of human activities.

As shown in Table 2, the contribution ratio of climate factors and human activities to NPP trend was discussed outside of stable area, which was calculated from the average contributions of climate factors and human activities in each sub-region. Overall, climate factors contributed 50.58% to NPP changes. Human activities were the main drivers of NPP changes in TMCR (65.70%) and SMCR (59.21%), while climate factors were the key factors in MCMLR (53.84%), TCCR (50.80%), and ACR (72.28%). In areas with NPP recovery, climate factors dominated in all sub-regions except for SMCR. In areas with NPP degradation, climate factors played a major role in TCCR and ACR, while the contribution ratios of human activities were higher in TMCR, SMCR and MCMLR.

Figure 6 shows the area affected by both climate factors and human activities accounted for 49.84% of China. NPP changes were dominated by climate factors in 13.67% of China, while NPP

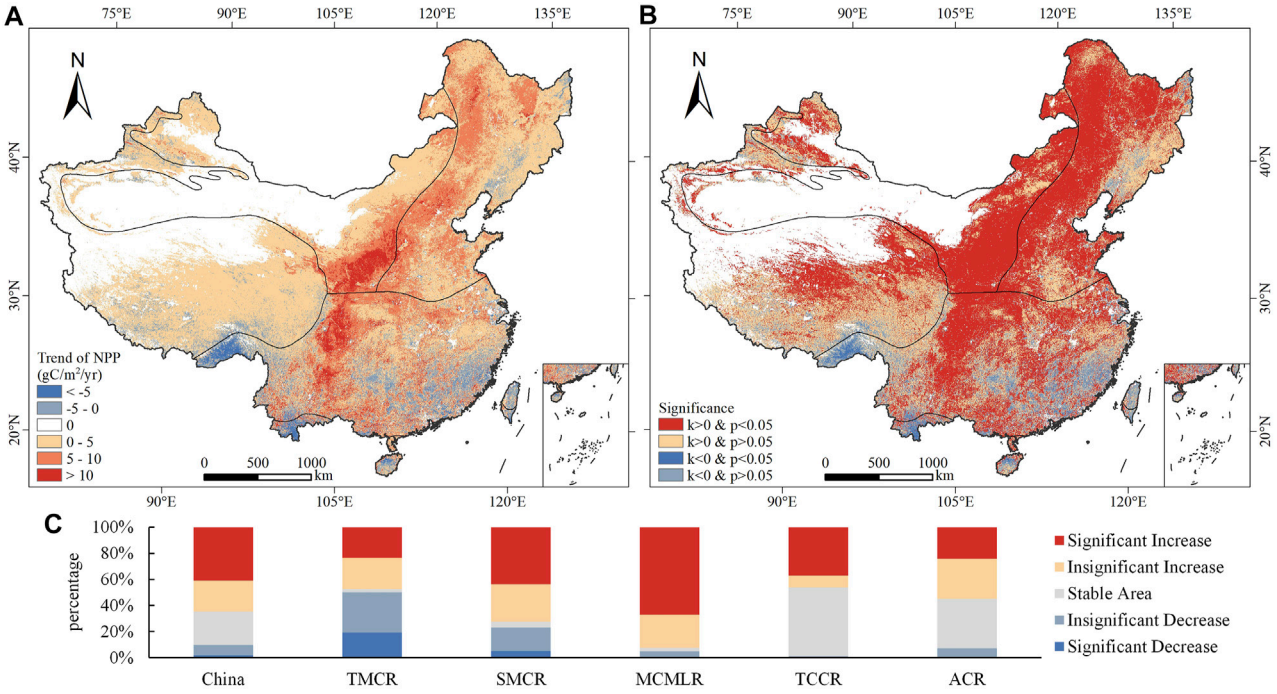

FIGURE 3
(A) Annual change trend of NPP and **(B)** the corresponding significance. **(C)** Statistical results of the percentage changes of NPP for different regions. The legend of **(C)** is the same as that of **(B)**, and stable area means that trend of NPP is 0 or no vegetation.

changes in 10.92% of China were human-dominated. Driving factors of NPP recovery and degradation showed spatial differences in China. On the spatial distribution (Figure 6A), the RC was mainly scattered in the eastern Qinghai-Tibetan Plateau, Sichuan basin, the Mongolian Plateau, and northeastern China. The RH was mainly distributed in central China. And the RB occurred in most areas of China. In contrast, the DC was mainly distributed in the southern flank of the East Himalayas and Taiwan Island. The DH mainly appeared in the southern Yunnan-Kweichow Plateau and southeastern China. And the DB mainly occurred in the southern Qinghai-Tibetan Plateau, the southern Yunnan-Kweichow Plateau, and southeastern China.

Figure 6B shows the area percentage of NPP changes caused by climate factors and human activities. Areas of increases of NPP in which the driving factors were both factors accounted for 45.23%, while areas in which increases of NPP were caused by climate factors and human activities accounted for 11.29% and 8.02%, respectively. However, both factors caused decreases of NPP in 4.61% of China, whereas areas affected by climate factors and human activities in 2.39% and 2.90% of China with such decreases. Both climate factors and human activities were the most important factors for increases of NPP in five sub-regions. The second most important factors for increases of NPP in TMCR, MCMLR, TCCR, and ACR were climate factors, and in SMCR were human activities. In addition, the major driving factors of NPP decreases in TMCR, SMCR, MCMLR, and TCCR were both climate factors and human activities, and in ACR were human activities. The secondary driving factors of NPP decreases in TMCR, SMCR, MCMLR, and TCCR were human activities, and in ACR were both factors.

3.4 Variations of NPP under different types of land cover

We first divided land cover types in China into unchanged and changed land cover types from 2001 to 2020. As shown in Table 3, from 2001 to 2020, the area percentage of unchanged and changed land cover types in China were 92.71% and 7.29%, respectively. The mean NPP of unchanged land cover types increased by 16.48%, while the mean NPP of changed land cover types increased by 24.46%. The statistic total NPP showed that the total NPP percentage of unchanged land cover types in both years was approximately 93% of the overall. In terms of change, the total NPP for the entire China rose by 495.70 Tg C/year, with the increase of total NPP of unchanged land cover types accounting for 90.04% of the overall increase. Therefore, we focused on the analysis of unchanged land cover types due to their contribution to NPP and its growth.

As shown in Figure 7A, forestland (28.08%) and grassland (27.41%) were the most extensive land cover types. Most forestland was located in the southern and northeastern regions of China, and grassland was mainly distributed in the northern and northwestern regions. Farmland was concentrated on the central and northeastern China. Unused land was mainly located in northwestern China. Among the unchanged land cover types, the highest mean NPP was found in forestland, followed by farmland and grassland, and the lowest in water (Figure 7B). The mean NPP

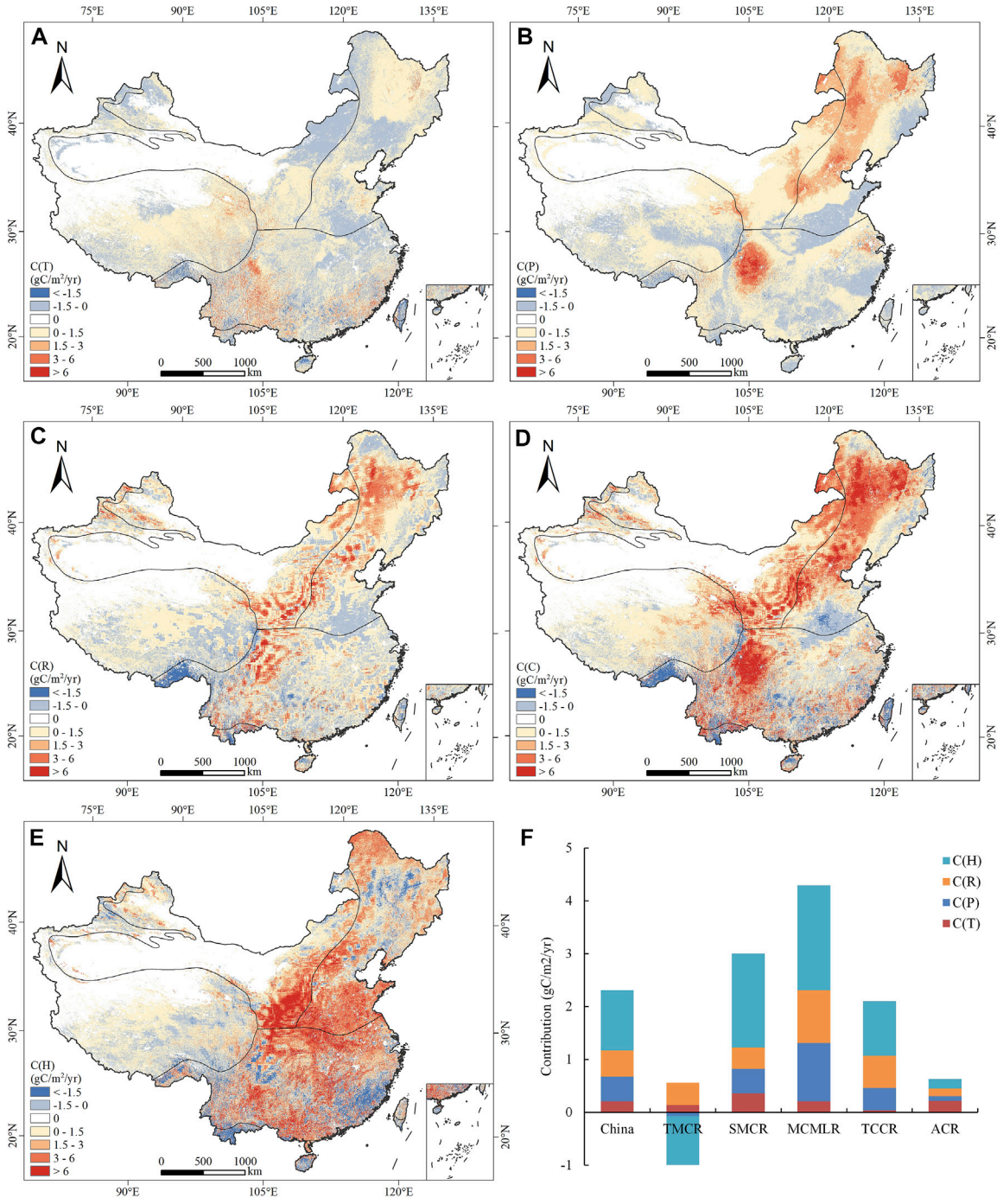

FIGURE 4
The contributions of climate factors [**(A)** temperature, **(B)** precipitation, **(C)** solar radiation, **(D)** climate] and **(E)** human activities to NPP trend from 2000 to 2020. **(F)** The average contributions of climate factors and human activities in China and five sub-regions.

for each of the six land cover types increased from 2001 to 2020. The highest increase in mean NPP was observed in farmland with 110.34 g C/m^2/year, and mean NPP of forestland and grassland increased by 63.46 g C/m^2/year and 55.77 g C/m^2/year, respectively. The total NPP showed a similar trend as the mean NPP. Forestland had the highest total NPP increase with 174.12 Tg C/year, while grassland and farmland were followed with 149.36 Tg C/year and 120.69 Tg C/year of total NPP increase, respectively.

4 Discussion

4.1 Evaluation of the NPP results

In previous studies, Ji et al. (2008) estimated the averaged total NPP of China over 1981-2000 with 2.94 Pg C. During the same period, Peng et al. (2021) determined the NPP by CABLE2.1 and TRENDY ensemble in China varied between 2.7 and 4.0 Pg C. Wang

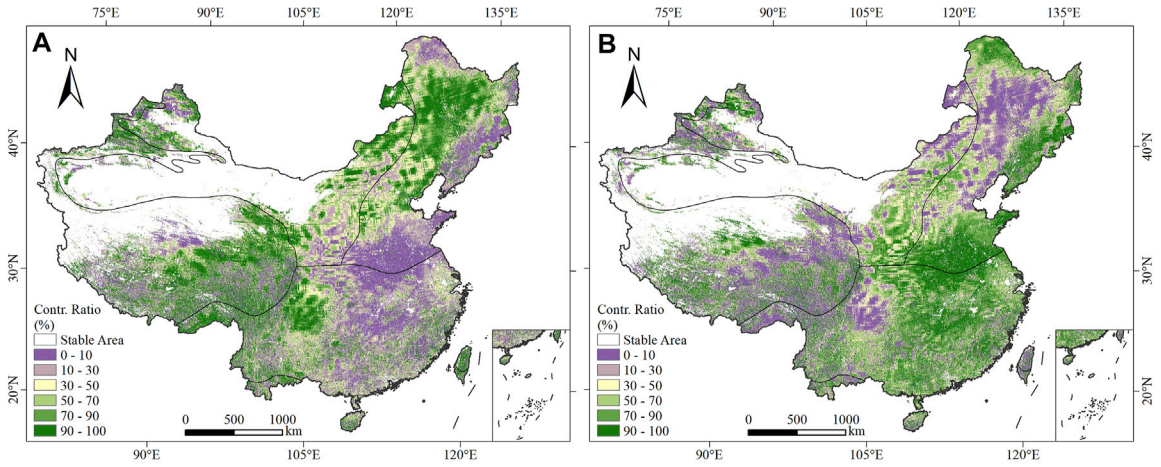

FIGURE 5
Spatial distribution of the contribution ratio of **(A)** climate factors and **(B)** human activities.

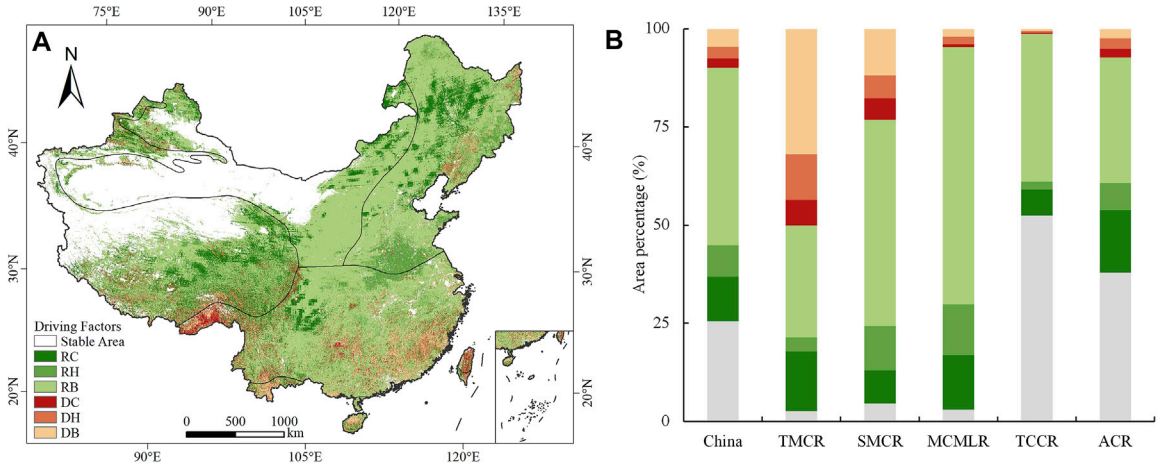

FIGURE 6
(A) Spatial distribution of driving factors to NPP. **(B)** Area percentage of NPP dynamics affected by climate factors and human activities for China and five sub-regions. RC, Recovery for climate factors; RH, Recovery for human activities; RB, Recovery for both factors; DC: Degradation for climate factors; DH, Degradation for human activities; DB, Degradation for both factors. The legend of **(B)** is the same as that of **(A)**.

TABLE 3 Mean and total NPP changes of land cover types from 2001 to 2020.

Land cover type	Area (km^2)	Mean NPP (g C/m^2/year)			Total NPP (Tg C/year)		
		2001	2020	Difference	2001	2020	Difference
Unchanged types	9057669	298.91	348.19	+49.27	2707.45	3153.76	+446.31
Changed types	712195	283.56	352.90	+69.35	201.95	251.34	+49.39
Total area	9769864	297.79	348.53	+50.74	2909.40	3405.10	+495.70

J. et al. (2017) calculated the average total NPP from 37 existing NPP data sets in China from 2000 to 2012 with 2.92 ± 0.12 Pg C. Liu et al. (2022) estimated the annual total NPP of vegetation in China's terrestrial ecosystems varied between 2.72 and 3.29 Pg C from 2000 to 2019, with a multiyear average of 3.09 Pg C. In this study, the total NPP from 2000 to 2020 in China estimated

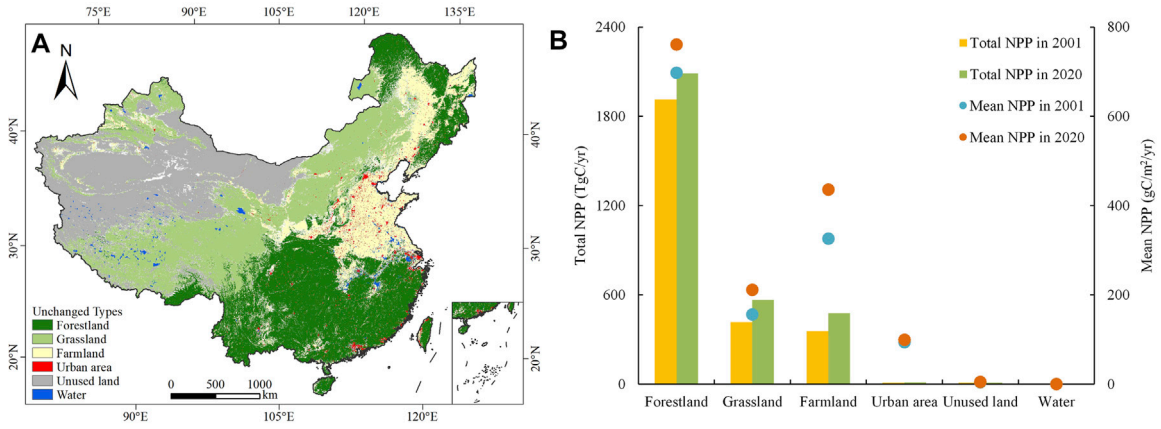

FIGURE 7
(A) Spatial distribution and **(B)** statistics of mean and total NPP variations of the unchanged land cover types from 2001 to 2020.

ranged from 2.81 to 3.41 Pg C, with results consistent with these values. Overall, the trend of total NPP was 0.023 Pg C/year, similar to previous findings (Lai et al., 2018; Liu et al., 2022), who found rates of 0.025 and 0.022 Pg C/year, respectively. For the spatial dimension, pixels with a positive trend in NPP accounted for most of the total pixels, consistent with previous studies (Yang et al., 2017; Ge et al., 2021). The significant decline of NPP mainly occurred in the southern Qinghai-Tibetan Plateau and the southern Yunnan-Kweichow Plateau, which was also found by Luo et al. (2018) and Wang J. et al. (2017), with NPP also showing a decreasing trend in southeastern China (Wen et al., 2019).

4.2 Impacts of climate factors on NPP changes

Climate change was identified as the main drivers affecting NPP distribution and dynamics (Song and Ma, 2011; Liu et al., 2015). Changes in temperature, precipitation and solar radiation affected NPP by altering soil moisture and soil microorganisms, affecting vegetation respiration and photosynthesis (Horion et al., 2013; He et al., 2015). Overall, climate factors contributed positively in 59.45% of China and negatively in 15.05%, which had spatial heterogeneities in the impact of NPP (Figures 4, 8).

For most of the forestland in southern China, due to sufficient precipitation and high temperature in the growing season, vegetation cover represented by NDVI increased, and there was a correlation between NPP and NDVI (Sun et al., 2002), which led to the increase in NPP. Adequate precipitation also enhanced the carbon sequestration capacity of forestland in the Sichuan Basin to increase NPP (Chen et al., 2021a; Wang et al., 2021a). The NPP of forestland in the Greater Khingan Mountains and the Changbai Mountains in northeastern China was positively correlated with temperature and solar radiation, with temperature being the main limiting factor for vegetation growth in the cold temperate region, while increased solar radiation would also enhance vegetation photosynthetic capacity (Yan et al., 2021). The southern Qinghai-Tibetan Plateau showed a decreasing trend of NPP, mainly distributed in subtropical broad-leaved forest with good water and heat conditions. Therefore, the effects of temperature and precipitation on the growth of vegetation in the region was considered to have reached equilibrium or saturation. In the event of significant climate change, the growth of vegetation will be inhibited (Deng et al., 2022). In the southern Yunnan-Kweichow Plateau, precipitation was the most important factor of NPP dynamics in the region's tropical seasonal rainforests (Linger et al., 2020), and there was a warm-dry trend in climate here that enhanced the effect of drought on NPP decline (Zhou et al., 2022). The increase in vapor pressure deficit and temperature greatly increased the demand for atmospheric evaporation, further causing vegetation stomata to close, resulting in lower leaf intercellular CO_2 concentrations and limiting photosynthesis (Li et al., 2010).

Temperature and solar radiation were the dominant climatic factors affecting grassland growth in the Qinghai-Tibetan Plateau (Xu et al., 2016). In the central and eastern Qinghai-Tibetan Plateau, warmer temperature contributed positively to the increase of NPP of alpine grassland because of a lengthened growing season and a more rapid rate of photosynthesis (Gu et al., 2017), and there was also a significant positive correlation between solar radiation and NPP of grassland, where plant chlorophyll content was increased and photosynthesis was enhanced (Meng et al., 2020). Conversely, temperature and solar radiation were negatively correlated with NPP at higher elevations in the western Qinghai-Tibetan Plateau, possibly because increases in temperature led to melting of snow and permafrost, which disrupted the structure of vegetative root systems and hindered grassland growth (Xiong et al., 2016). In addition, excessive solar radiation increased evaporation of surface soil and limited water availability, which may prevent the growth of herbaceous plants with shallow root systems (Yang et al., 2017). Precipitation had a suppressive effect on grassland growth in southeastern plateau (Gao et al., 2013; Xiong et al., 2021), and its increase may reduce solar radiation, which inhibits photosynthesis (Yang et al., 2015). Alternatively, precipitation could contribute to soil erosion, which decreased soil organic matter content, and reduced alpine grassland NPP (Xu et al., 2016). In arid and semi-arid areas, e.g., the Mongolian Plateau and the Loess Plateau,

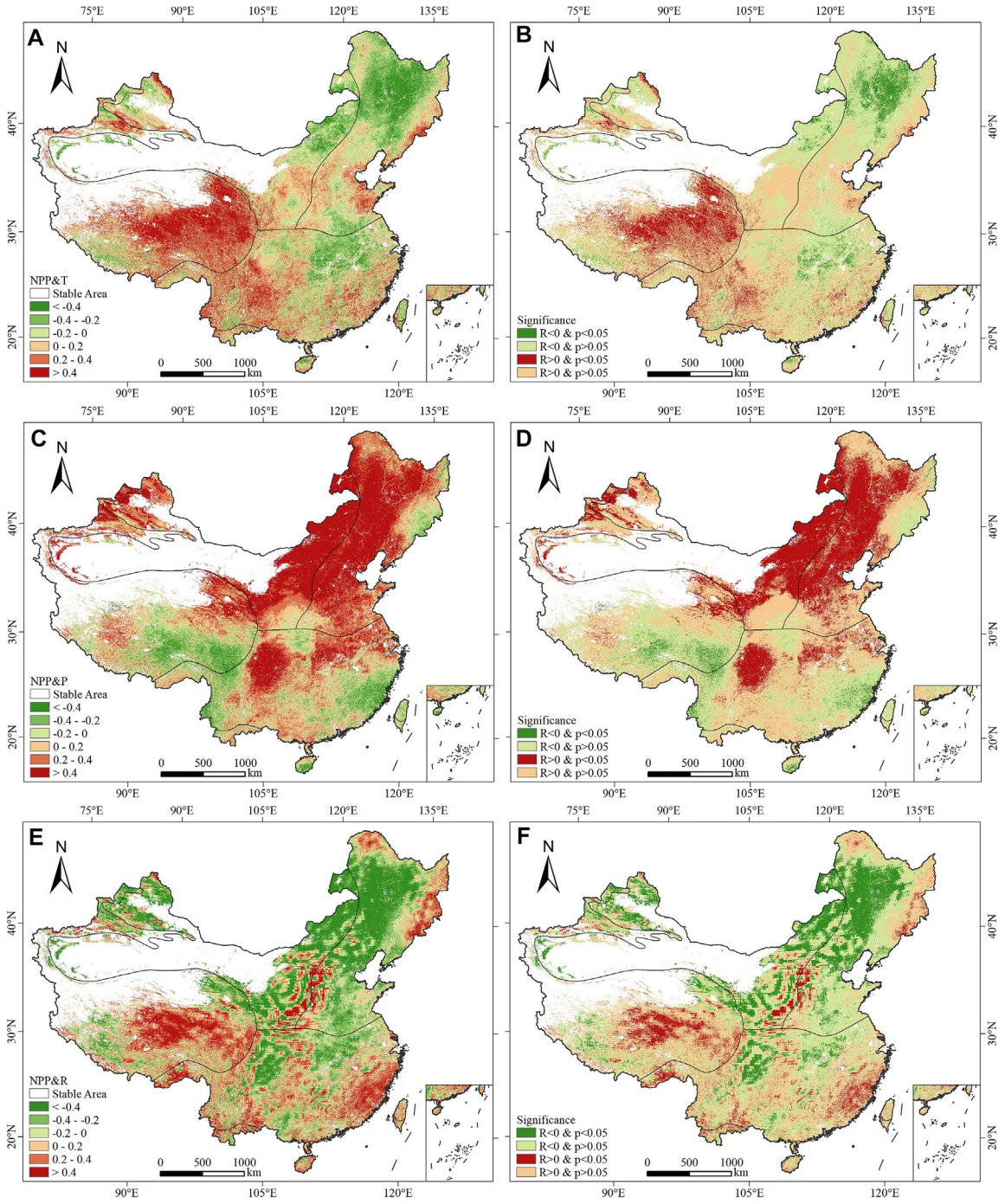

FIGURE 8
Spatial distribution of the correlation coefficients between NPP and **(A)** temperature, **(C)** precipitation, **(E)** solar radiation and **(B,D,F)** their corresponding significance.

precipitation was an important controlling driver of grassland growth which was confirmed in the previous studies (Zhao et al., 2019; Jiang H. et al., 2020; Wu N. et al., 2021). NPP was negatively correlated with temperature in the arid land of the Mongolian Plateau, mainly due to the fact that warming exacerbated the negative effects of drought on grassland growth (Zeng and Yang, 2008).

In the northeast agricultural region of China, the average temperature of growing season met the requirements of the first few stages of crop growth, but at maturity, it exceeded the optimum temperature for crop growth, while the average precipitation of growing season did not exceed the optimum humidity (Piao et al., 2010). Therefore, NPP showed a positive correlation with precipitation and a negative correlation with temperature. In

addition, in central China, due to excessive warmth and decrease in precipitation, the photosynthesis of plants was weakened, resulting in a negative contribution to farmland NPP (Chen et al., 2021b).

In addition, droughts are a comprehensive and frequently occurred natural disaster affected by multiple climate factors, and will greatly influence vegetation growth and reduce the net primary production (Zhao and Running, 2010; van der Molen et al., 2011). During drought, soil water content decreased and vegetation stomata closed, thus limiting plant growth (van der Molen et al., 2011; Chen et al., 2013; Su et al., 2018). Drought also indirectly affected ecosystem productivity by increasing pest and disease infestation and causing forest fires (Xiao and Zhuang, 2007; Anderegg et al., 2013). Previous studies have shown that five typical drought events occurred in China from 1982 to 2015, resulting in a decline in NPP in more than 23% of the area (Lai et al., 2018), and the effects of drought on NPP were mainly located in farming-pastoral ecotones of arid and semi-arid ecosystems (Li et al., 2020). Although with strong carbon sequestration capacity, vegetation growth in southwestern China was highly vulnerable to drought suppression, and the effects of drought on ecosystem water-use efficiency were seasonal, which affected ecosystem productivity (Wang et al., 2021b). In this area, in a region with complicated and fragmentized topography, drought may not evidently decrease the NPP, but may enormously impact NPP in a region with overall flat topography (Guan et al., 2018).

For some regional studies in neighboring China, in the Western Himalaya, the land cover type in India was mainly forestland, while in China it was dominated by unused land and grassland. Due to the difference in vegetation types as well as hydrothermal conditions between the two regions, NPP variation in the Indian Western Himalayan region was negatively correlated with temperature (Kumar et al., 2019), while it was positively in the Chinese Western Himalayan region (Figure 8). However, precipitation and solar radiation exhibited a consistent trend with NPP change in both regions (Sharma et al., 2022). Central Asia and northwest China were both arid and semi-arid zones with temperate continental climate, and precipitation was the main climatic driver controlling the NPP variations in most areas of both regions (Jiang et al., 2017; Chen T. et al., 2019). The Lancang-Mekong River was known as the Lancang River in China and the Mekong River in Southeast Asia. In the Lancang River basin, where hydrothermal conditions were poor, the correlation between NPP and temperature was positive. In contrast, NPP was negatively correlated with temperature in the Mekong River Basin where good hydrothermal conditions existed, and the correlation between NPP and precipitation in space was not obvious (Li W. et al., 2018).

4.3 Impacts of human activities on NPP changes

Human activities were also significant factors affecting the recovery or degradation of vegetation (Cai et al., 2015; Naeem et al., 2020). In arid and semi-arid regions of northwestern China, human activities were the dominant driving factors in desertification development (Zhang et al., 2011; Zhou et al., 2015). Human activities including overgrazing, overuse of water

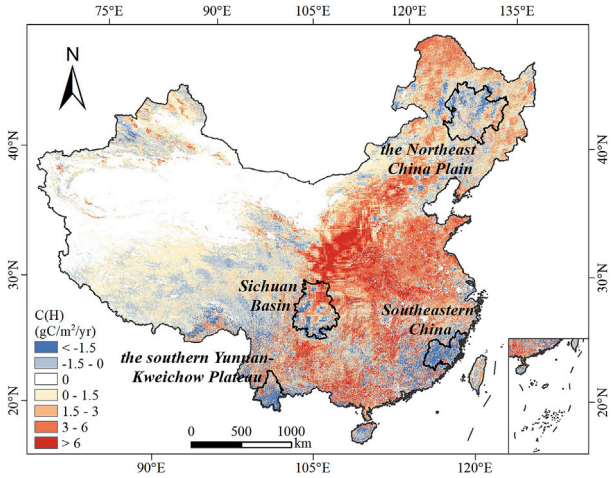

FIGURE 9
The contribution map of human activities to NPP trend from 2000 to 2020 and four typical regions with high negative contributions in Sichuan Basin, the southern Yunnan-Kweichow Plateau, southeastern China, and the Northeast China Plain.

resources and deforestation have caused damage to natural vegetation, leading to desertification expansion (Li et al., 2016; Li C. et al., 2021). Grazing affected biomass through feeding, affected the physical structure of the soil through trampling, making bare topsoil vulnerable to erosion by strong wind (Jiang H. et al., 2020). In recent decades, with the implementation of a series of ecological restoration projects like the Grain to Green Program (GTGP) and Grazing Withdrawal Program (GWP), the vegetation in the northwestern China has been well protected and restored (Liu et al., 2019a). The GTGP was launched in 1999 to replace cropland and grazing land with grassland and woodland in fragile regions (Mu et al., 2013) and the GWP was initiated in 2003 to reduce the grazing pressure on natural grassland by forbidding grazing and employing cultivated pastures (Xu et al., 2016), which contributed positively to the Qinghai-Tibet Plateau, the Loess Plateau, the Mongolian Plateau, and Xinjiang Uygur Autonomous Region on vegetation restoration (Yang et al., 2014; Cai et al., 2015; Gang et al., 2018; Shi et al., 2022).

In the North China Plain and the Middle and Lower Yangtze River Plain, human cultivation activities contributed to NPP increases (Ge et al., 2021), and were mainly manifested in the improvement of agricultural machinery level, technology and investment, which improved the efficiency and mechanization of farm irrigation and promoted the development of cultivated land quality. The Natural Forest Protection Program aimed to prohibit logging in the southwest China and significantly reduce deforestation in the northeast China and other natural forest areas (Xu et al., 2006), which has reduced soil erosion and improved vegetation conditions in the Hengduan Mountain and the Greater Khingan Mountains (Yin et al., 2020).

With socio-economic development, land cover and use have changed dramatically at the same time, which will affect the ecological environment (Yang et al., 2021). We selected four typical regions with high negative contribution of human

TABLE 4 Land cover changes in four typical regions from 2001 to 2020 (unit: km²).

Area	Land cover	Translates to						
		Forestland	Grassland	Farmland	Urban area	Unused land	Water	Total
Sichuan Basin	Forestland	20276	1,230	21	11	0	0	21538
	Grassland	8852	58650	19592	782	16	284	88176
	Farmland	15	8373	47275	1,590	1	2	57256
	Urban area	0	0	0	2869	0	0	2869
	Unused land	0	49	0	8	74	17	148
	Water	5	169	18	19	4	177	392
	Total	29148	68471	66906	5279	95	480	170379
Southern Yunnan-Kweichow Plateau	Forestland	60337	169	195	7	1	3	60712
	Grassland	420	62	53	0	0	9	544
	Farmland	578	58	703	1	0	6	1,346
	Urban area	0	0	0	140	0	0	140
	Unused land	0	0	0	0	0	0	0
	Water	0	0	0	0	0	0	0
	Total	61335	289	951	148	1	18	62742
South-eastern China	Forestland	76294	619	115	503	0	4	77535
	Grassland	333	381	13	48	9	0	784
	Farmland	321	89	555	208	0	0	1,173
	Urban area	0	0	0	3307	0	0	3307
	Unused land	0	3	0	2	17	0	22
	Water	0	1	0	0	0	276	277
	Total	76948	1,093	683	4068	26	280	83098
Northeast China Plain	Forestland	31077	369	475	2	0	2	31925
	Grassland	532	39179	19427	79	168	377	59762
	Farmland	1856	2736	130690	409	10	236	135937

(Continued on following page)

10.3389/feart.2023.1084399

10.3389/feart.2023.1084399

TABLE 4 (*Continued*) Land cover changes in four typical regions from 2001 to 2020 (unit: km^2).

Area	Land cover	Translates to						
		Forestland	Grassland	Farmland	Urban area	Unused land	Water	Total
	Urban area	0	0	0	3183	0	0	3183
	Unused land	0	302	2	1	177	156	638
	Water	0	57	3	0	13	1,286	1,359
	Total	33465	42643	150597	3674	368	2057	232804

activities for analysis, including Sichuan Basin, the southern Yunnan-Kweichow Plateau, southeastern China, and the Northeast China Plain (Figure 9). During the study period, land cover changed significantly in these regions (Table 4). In Sichuan Basin, 22.22% of grassland and 5.71% of forestland translated to farmland, and urban area increased by 84.00%. Similarly, urban area in the Northeast China Plain increased by 15.43%, and 32.51% of grassland translated to farmland, which meant human agricultural activities with the conversion of large amounts of grassland to farmland may lead to a decrease in NPP (Tian et al., 2020; Li H. et al., 2021). In southeastern China, which was one of the more economically developed regions in China, urban area increased by 23.01%, and 17.73% of farmland translated to urban area. Several studies have shown that the process of urbanization has caused a certain degree of damage to the ecological environment (Wu et al., 2014; Liu X. et al., 2019).

Moreover, continuous urban expansion, rapid economic development, and sustained population growth were also considered to be factors affecting NPP (Ma et al., 2012; Li et al., 2022). Generally, these four typical regions experienced rapid economic development from 2000 to 2020, and the average annual rates of GDP growth in Sichuan Basin, the southern Yunnan-Kweichow Plateau, southeastern China, and the Northeast China Plain were 13.95%, 14.81%, 13.12%, and 8.67%, respectively. Regional population size was often cited as the main reason for the decline in ecosystem services, and GDP density growth inevitably limits NPP increase (Cincotta et al., 2000; Qiu et al., 2018). In addition, ecological damage in the southern Yunnan-Kweichow Plateau was mainly caused by high-intensity development activities such as tourism (Tang et al., 2015).

4.4 Limitations of this study

It should be noted that some uncertainties existed in this study. First, MODIS NPP data may contain some uncertainties owing to the lack of site-level measured data, which had some impacts on the results of study. Nevertheless, the dataset has been proven to be reliable in previous studies (Peng et al., 2016; Liu et al., 2019b), and has been widely used in research on global and regional NPP (Zhao et al., 2005; Zhang et al., 2014; Sha et al., 2020). Second, MODIS NPP data and land cover data were both resampled to 1,000 m, which sacrifices accuracy to some extent, resulting in each pixel potentially not reflecting the actual land cover types (Shen et al., 2020; Shen et al., 2022). Third, in MODIS NPP data, the NPP value of water, barren land, urban/built-up was 0. However, the classification of the land cover data used in this study may not correspond exactly to the classification used in the MODIS NPP data, resulting in non-zero values of mean NPP for water, unused land, and urban area counted in this study. Fourth, in this study, only three climate factors, temperature, precipitation, and solar radiation, were considered, while other factors such as CO_2 concentration, Nitrogen deposition, and soil moisture were ignored, which also affected vegetation NPP dynamics (Mu et al., 2008; Du et al., 2014; He et al., 2017). Finally, the method (RESTREND) used in this study ignores the complex interactions between climate change and human activities, and only considers the linear relationship between NPP and impact factors. Although the method has some shortcomings, its ability to quantify

the relative contributions of vegetation dynamics drivers is significant for understanding the driving mechanisms.

5 Conclusion

In this study, we investigated spatiotemporal characteristics of NPP in China from 2000 to 2020. The influences of climate factors and human activities on NPP were also analyzed quantitatively. The main conclusions are summarized as follows:

(1) The annual average NPP of the entire China increased from 2000 (286.31 g C/m^2/year) to 2020 (348.53 g C/m^2/year) at a rate of 2.32 g C/m^2/year, and a total NPP increase of 596.73 Tg C/year was found. Areas of significant increase in NPP accounted for 40.90% of China, with only 1.79% showing a significant declining trend.
(2) Climate factors contributed more to NPP variations in China from 2000 to 2020 than human activities, and the contributions of climate factors and human activities were 1.169 g C/m^2/year and 1.142 g C/m^2/year. In terms of NPP recovery, NPP was dominated by both climate factors and human activities in 45.23% of China. Regarding NPP degradation, areas dominated by both factors, climate factors, and human activities accounted for 4.61%, 2.39%, and 2.90%, respectively.
(3) The proportion of area with unchanged land cover types was 92.71% of the entire China. The total NPP increase of unchanged land cover types accounted for 90.04% of the total increase, and was mainly contributed by forestland, grassland and farmland.

Overall, both climate factors and human activities have contributed to NPP variation in China. The results improve the understanding of how ecosystems in China have been affected by climate factors and human activities in the last two decades, and also provide guidance for formulating ecosystem management and governance strategies to protect the environment and achieve sustainable development.

Data availability statement

The original contributions presented in the study are included in the article/supplementary material, further inquiries can be directed to the corresponding authors.

Author contributions

Conceptualization, JC and ZPC; Methodology, JC and ZS; Software, JY and ZTC; data collection, ZL and ZTC; Funding acquisition, ZPC and ZS; Supervision, JC and ZPC; Writing—original draft preparation, ZL; Writing—review and editing, ZL, JC, and JY. All authors read and approved the submitted version.

Funding

This work was supported by the Key Laboratory of Natural Resources Monitoring in Tropical and Subtropical Area of South China, Ministry of Natural Resources (No. 2022NRM006) and the Open Fund of Key Laboratory of National Geographical Census and Monitoring, Ministry of Natural Resources (No. 2022NGCM02).

Conflict of interest

The authors declare that the research was conducted in the absence of any commercial or financial relationships that could be construed as a potential conflict of interest.

Publisher's note

References

Anderegg, W. R. L., Kane, J. M., and Anderegg, L. D. L. (2013). Consequences of widespread tree Mortality triggered by drought and temperature stress. *Nat. Clim. Change* 3 (1), 30–36. doi:10.1038/nclimate1635

Cai, H., Yang, X., and Xu, X. (2015). Human-induced grassland degradation/restoration in the central Tibetan Plateau: The effects of ecological protection and restoration projects. *Ecol. Eng.* 83, 112–119. doi:10.1016/j.ecoleng.2015.06.031

Chen, B., Zhang, X., Tao, J., Wu, J., Wang, J., Shi, P., et al. (2014). The impact of climate change and anthropogenic activities on alpine grassland over the Qinghai-Tibet Plateau. *Agric. For. Meteorol.* 189, 11–18. doi:10.1016/j.agrformet.2014.01.002

Chen, S., Wen, Z., Ma, M., and Wu, S. (2021a). Disentangling climatic factors and human activities in governing the old and new forest productivity. *Remote Sens.* 13 (18), 3746. doi:10.3390/rs13183746

Chen, S., Zhang, Y., Wu, Q., Liu, S., Song, C., Xiao, J., et al. (2021b). Vegetation structural change and CO2 fertilization more than offset gross primary production decline caused by reduced solar radiation in China. *Agric. For. Meteorol.* 296, 108207. doi:10.1016/j.agrformet.2020.108207

Chen, T., Bao, A., Jiapaer, G., Guo, H., Zheng, G., Jiang, L., et al. (2019). Disentangling the relative impacts of climate change and human activities on arid and semiarid grasslands in Central Asia during 1982-2015. *Sci. Total Environ.* 653, 1311–1325. doi:10.1016/j.scitotenv.2018.11.058

Chen, T., Werf, G. R. V. D., Jeu, R. A. M. D., Wang, G., and Dolman, A. J. (2013). A global analysis of the impact of drought on net primary productivity. *Hydrol. Earth Syst. Sci.* 17 (10), 3885–3894. doi:10.5194/hess-17-3885-2013

Chen, Y., Gu, H., Wang, M., Gu, Q., Ding, Z., Ma, M., et al. (2019). Contrasting performance of the remotely-derived GPP products over different climate zones across China. *Remote Sens.* 11 (16), 1855. doi:10.3390/rs11161855

Chi, D., Wang, H., Li, X., Liu, H., and Li, X. (2018). Assessing the effects of grazing on variations of vegetation NPP in the Xilingol Grassland, China, using a grazing pressure index. *Ecol. Indic.* 88, 372–383. doi:10.1016/j.ecolind.2018.01.051

Churkina, G., and Running, S. W. (1998). Contrasting climatic controls on the estimated productivity of global terrestrial biomes. *Ecosystems* 1 (2), 206–215. doi:10.1007/s100219900016

Cincotta, R. P., Wisnewski, J., and Engelman, R. (2000). Human population in the biodiversity hotspots. *Nature* 404 (6781), 990–992. doi:10.1038/35010105

Crabtree, R., Potter, C., Mullen, R., Sheldon, J., Huang, S. L., Harmsen, J., et al. (2009). A modeling and spatio-temporal analysis framework for monitoring environmental

change using NPP as an ecosystem indicator. *Remote Sens. Environ.* 113 (7), 1486–1496. doi:10.1016/j.rse.2008.12.014

Cramer, W., Kicklighter, D. W., Bondeau, A., Moore, B., Churkina, G., Nemry, B., et al. (1999). Comparing global models of terrestrial net primary productivity (NPP): Overview and key results. *Glob. Change Biol.* 5, 1–15. doi:10.1046/j.1365-2486.1999.00009.x

Dameneh, H. E., Gholami, H., Telfer, M. W., Comino, J. R., Collins, A. L., and Jansen, J. D. (2021). Desertification of Iran in the early twenty-first century: Assessment using climate and vegetation indices. *Sci. Rep.* 11 (1), 20548. doi:10.1038/s41598-021-99636-8

Deng, X., Wu, L., He, C., and Shao, H. (2022). Study on spatiotemporal variation pattern of vegetation coverage on Qinghai-Tibet Plateau and the analysis of its climate driving factors. *Int. J. Environ. Res. Public Health* 19 (14), 8836. doi:10.3390/ijerph19148836

Du, Z., Wang, W., Zeng, W., and Zeng, H. (2014). Nitrogen deposition enhances carbon sequestration by plantations in northern China. *PLoS One* 9 (2), e87975. doi:10.1371/journal.pone.0087975

Dusenge, M. E., Duarte, A. G., and Way, D. A. (2019). Plant carbon metabolism and climate change: Elevated CO2 and temperature impacts on photosynthesis, photorespiration and respiration. *New Phytol.* 221 (1), 32–49. doi:10.1111/nph.15283

Evans, J., and Geerken, R. (2004). Discrimination between climate and human-induced dryland degradation. *J. Arid. Environ.* 57 (4), 535–554. doi:10.1016/S0140-1963(03)00121-6

Feng, X., Fu, B., Lu, N., Zeng, Y., and Wu, B. (2013). How ecological restoration alters ecosystem services: An analysis of carbon sequestration in China's Loess Plateau. *Sci. Rep.* 3, 2846. doi:10.1038/srep02846

Gang, C., Gao, X., Peng, S., Chen, M., Guo, L., and Jin, J. (2019). Satellite observations of the recovery of forests and grasslands in western China. *J. Geophys. Res. Biogeo.* 124 (7), 1905–1922. doi:10.1029/2019JG005198

Gang, C., Zhao, W., Zhao, T., Zhang, Y., Gao, X., and Wen, Z. (2018). The impacts of land conversion and management measures on the grassland net primary productivity over the Loess Plateau, Northern China. *Sci. Total Environ.* 645, 827–836. doi:10.1016/j.scitotenv.2018.07.161

Gao, Y., Zhou, X., Wang, Q., Wang, C., Zhan, Z., Chen, L., et al. (2013). Vegetation net primary productivity and its response to climate change during 2001-2008 in the Tibetan Plateau. *Sci. Total Environ.* 444, 356–362. doi:10.1016/j.scitotenv.2012.12.014

Ge, W., Deng, L., Wang, F., and Han, J. (2021). Quantifying the contributions of human activities and climate change to vegetation net primary productivity dynamics in China from 2001 to 2016. *Sci. Total Environ.* 773, 145648. doi:10.1016/j.scitotenv.2021.145648

Gower, S. T., Kucharik, C. J., and Norman, J. M. (1999). Direct and indirect estimation of leaf area index, f(APAR), and net primary production of terrestrial ecosystems. *Remote Sens. Environ.* 70 (1), 29–51. doi:10.1016/S0034-4257(99)00056-5

Gu, F., Zhang, Y., Huang, M., Tao, B., Guo, R., and Yan, C. (2017). Effects of climate warming on net primary productivity in China during 1961-2010. *Ecol. Evol.* 7 (17), 6736–6746. doi:10.1002/ece3.3029

Guan, X., Shen, H., Li, X., Gan, W., and Zhang, L. (2018). Climate control on net primary productivity in the complicated mountainous area: A case study of yunnan, China. *IEEE J. Sel. Top. Appl. Earth Obs. Remote Sens.* 11 (12), 4637–4648. doi:10.1109/JSTARS.2018.2863957

He, C., Tian, J., Gao, B., and Zhao, Y. (2015). Differentiating climate- and human-induced drivers of grassland degradation in the Liao River Basin, China. *Environ. Monit. Assess.* 187 (1), 4199. doi:10.1007/s10661-014-4199-2

He, L., Chen, J., Liu, J., Belair, S., and Luo, X. (2017). Assessment of SMAP soil moisture for global simulation of gross primary production. *J. Geophys. Res. Biogeo.* 122 (7), 1549–1563. doi:10.1002/2016JG003603

Horion, S., Cornet, Y., Erpicum, M., and Tychon, B. (2013). Studying interactions between climate variability and vegetation dynamic using a phenology based approach. *Int. J. Appl. Earth Obs. Geoinf.* 20, 20–32. doi:10.1016/j.jag.2011.12.010

Ji, J., Huang, M., and Li, K. (2008). Prediction of carbon exchanges between China terrestrial ecosystem and atmosphere in 21st century. *Sci. China Ser. D-Earth. Sci.* 51 (6), 885–898. doi:10.1007/s11430-008-0039-y

Jiang, H., Xu, X., Guan, M., Wang, L., Huang, Y., and Jiang, Y. (2020). Determining the contributions of climate change and human activities to vegetation dynamics in agro-pastural transitional zone of northern China from 2000 to 2015. *Sci. Total Environ.* 718, 134871. doi:10.1016/j.scitotenv.2019.134871

Jiang, L., Jiapaer, G., Bao, A., Guo, H., and Ndayisaba, F. (2017). Vegetation dynamics and responses to climate change and human activities in Central Asia. *Sci. Total Environ.* 599, 967–980. doi:10.1016/j.scitotenv.2017.05.012

Jiang, Y., Guo, J., Peng, Q., Guan, Y., Zhang, Y., and Zhang, R. (2020). The effects of climate factors and human activities on net primary productivity in Xinjiang. *Int. J. Biometeorol.* 64 (5), 765–777. doi:10.1007/s00484-020-01866-4

Kumar, M., SavitaSingh, H., Pandey, R., Singh, M. P., Ravindranath, N. H., Kalra, N., et al. (2019). Assessing vulnerability of forest ecosystem in the Indian Western Himalayan region using trends of net primary productivity. *Biodivers. Conserv.* 28 (8-9), 2163–2182. doi:10.1007/s10531-018-1663-2

Lai, C., Li, J., Wang, Z., Wu, X., Zeng, Z., Chen, X., et al. (2018). Drought-Induced reduction in net primary productivity across mainland China from 1982 to 2015. *Remote Sens.* 10 (9), 1433. doi:10.3390/rs10091433

Li, C., Wang, Y., Wu, X., Cao, H., Li, W., and Wu, T. (2021). Reducing human activity promotes environmental restoration in arid and semi-arid regions: A case study in northwest China. *Sci. Total Environ.* 768, 144525. doi:10.1016/j.scitotenv.2020.144525

Li, D., Xu, D., Wang, Z., You, X., Zhang, X., and Song, A. (2018). The dynamics of sand-Stabilization services in Inner Mongolia, China from 1981 to 2010 and its relationship with climate change and human activities. *Ecol. Indic.* 88, 351–360. doi:10.1016/j.ecolind.2018.01.018

Li, H., Zhang, H., Li, Q., Zhao, J., Guo, X., Ying, H., et al. (2021). Vegetation productivity dynamics in response to climate change and human activities under different topography and land cover in northeast China. *Remote Sens.* 13 (5), 975. doi:10.3390/rs13050975

Li, J., Wang, Y., and Liu, L. (2020). Responses of the terrestrial ecosystem productivity to droughts in China. *Front. Earth Sci.* 8. doi:10.3389/feart.2020.00059

Li, M., Yu, H., Meng, B., Sun, Y., Zhang, J., Zhang, H., et al. (2021a). Drought reduces the effectiveness of ecological projects: Perspectives from the inter-annual variability of vegetation index. *Ecol. Indic.* 130, 108158. doi:10.1016/j.ecolind.2021.108158

Li, M., Zhang, X., Wu, J., Ding, Q., Niu, B., and He, Y. (2021b). Declining human activity intensity on alpine grasslands of the Tibetan Plateau. *J. Environ. Manage.* 296, 113198. doi:10.1016/j.jenvman.2021.113198

Li, Q., Zhang, C., Shen, Y., Jia, W., and Li, J. (2016). Quantitative assessment of the relative roles of climate change and human activities in desertification processes on the Qinghai-Tibet Plateau based on net primary productivity. *Catena* 147, 789–796. doi:10.1016/j.catena.2016.09.005

Li, W., Li, C., Liu, X., He, D., Bao, A., Yi, Q., et al. (2018). Analysis of spatial-temporal variation in NPP based on hydrothermal conditions in the Lancang-Mekong River Basin from 2000 to 2014. *Environ. Monit. Assess.* 190 (6), 321. doi:10.1007/s10661-018-6690-7

Li, X., Luo, Y., and Wu, J. (2022). Decoupling relationship between urbanization and carbon sequestration in the Pearl River Delta from 2000 to 2020. *Remote Sens.* 14 (3), 526. doi:10.3390/rs14030526

Li, Z., Zhang, Y., Wang, S., Yuan, G., Yang, Y., and Cao, M. (2010). Evapotranspiration of a tropical rain forest in Xishuangbanna, southwest China. *Hydrol. Process.* 24 (17), 2405–2416. doi:10.1002/hyp.7643

Linger, E., Hogan, J. A., Cao, M., Zhang, W., Yang, X., and Hu, Y. (2020). Precipitation influences on the net primary productivity of a tropical seasonal rainforest in southwest China: A 9-year case study. *For. Ecol. Manage.* 467, 118153. doi:10.1016/j.foreco.2020.118153

Liu, C., Dong, X., and Liu, Y. (2015). Changes of NPP and their relationship to climate factors based on the transformation of different scales in Gansu, China. *Catena* 125, 190–199. doi:10.1016/j.catena.2014.10.027

Liu, G., Shao, Q., Fan, J., Ning, J., Rong, K., Huang, H., et al. (2022). Change trend and restoration potential of vegetation net primary productivity in China over the past 20 years. *Remote Sens.* 14 (7), 1634. doi:10.3390/rs14071634

Liu, H., Jiao, F., Yin, J., Li, T., Gong, H., Wang, Z., et al. (2020). Nonlinear relationship of vegetation greening with nature and human factors and its forecast - a case study of Southwest China. *Ecol. Indic.* 111, 106009. doi:10.1016/j.ecolind.2019.106009

Liu, Q., Fu, Y., Zhu, Z., Liu, Y., Liu, Z., Huang, M., et al. (2016). Delayed autumn phenology in the Northern Hemisphere is related to change in both climate and spring phenology. *Glob. Change Biol.* 22 (11), 3702–3711. doi:10.1111/gcb.13311

Liu, X., Pei, F., Wen, Y., Li, X., Wang, S., Wu, C., et al. (2019). Global urban expansion offsets climate-driven increases in terrestrial net primary productivity. *Nat. Commun.* 10 (1), 5558. doi:10.1038/s41467-019-13462-1

Liu, Y., Wang, Q., Zhang, Z., Tong, L., Wang, Z., and Li, J. (2019a). Grassland dynamics in responses to climate variation and human activities in China from 2000 to 2013. *Sci. Total Environ.* 690, 27–39. doi:10.1016/j.scitotenv.2019.06.503

Liu, Y., Zhang, Z., Tong, L., Khalifa, M., Wang, Q., Gang, C., et al. (2019b). Assessing the effects of climate variation and human activities on grassland degradation and restoration across the globe. *Ecol. Indic.* 106, 105504. doi:10.1016/j.ecolind.2019.105504

Luo, Z., Wu, W., Yu, X., Song, Q., Yang, J., Wu, J., et al. (2018). Variation of net primary production and its correlation with climate change and anthropogenic activities over the Tibetan plateau. *Remote Sens.* 10 (9), 1352. doi:10.3390/rs10091352

Ma, T., Zhou, C., and Pei, T. (2012). Simulating and estimating tempo-spatial patterns in global human appropriation of net primary production (hanpp): A consumption-based approach. *Ecol. Indic.* 23, 660–667. doi:10.1016/j.ecolind.2012.05.026

Melillo, J. M., Mcguire, A. D., Kicklighter, D. W., Moore, B., Vorosmarty, C. J., and Schloss, A. L. (1993). Global climate-change and terrestrial net primary production. *Nature* 363 (6426), 234–240. doi:10.1038/363234a0

Meng, Z., Liu, M., Gao, C., Zhang, Y., She, Q., Long, L., et al. (2020). Greening and browning of the coastal areas in mainland China: Spatial heterogeneity, seasonal variation and its influential factors. *Ecol. Indic.* 110, 105888. doi:10.1016/j.ecolind.2019.105888

Mu, Q., Zhao, M., Running, S. W., Liu, M., and Tian, H. (2008). Contribution of increasing CO2 and climate change to the carbon cycle in China's ecosystems. *J. Geophys. Res. Biogeo.* 113 (G1). doi:10.1029/2006JG000316

Mu, S., Zhou, S., Chen, Y., Li, J., Ju, W., and Odeh, I. O. A. (2013). Assessing the impact of restoration-induced land conversion and management alternatives on net primary productivity in Inner Mongolian grassland, China. *Glob. Planet. Change* 108, 29–41. doi:10.1016/j.gloplacha.2013.06.007

Naeem, S., Zhang, Y., Tian, J., Qamer, F. M., Latif, A., and Paul, P. K. (2020). Quantifying the impacts of anthropogenic activities and climate variations on vegetation productivity changes in China from 1985 to 2015. *Remote Sens.* 12 (7), 1113. doi:10.3390/rs12071113

Nemani, R. R., Keeling, C. D., Hashimoto, H., Jolly, W. M., Piper, S. C., Tucker, C. J., et al. (2003). Climate-driven increases in global terrestrial net primary production from 1982 to 1999. *Science* 300 (5625), 1560–1563. doi:10.1126/science.1082750

Peng, D., Wu, C., Zhang, B., Huete, A., Zhang, X., Sun, R., et al. (2016). The influences of drought and land-cover conversion on inter-annual variation of NPP in the Three-North shelterbelt program zone of China based on MODIS data. *PLoS One* 11 (6), e0158173. doi:10.1371/journal.pone.0158173

Peng, J., Dan, L., Ying, K., Yang, S., Tang, X., and Yang, F. (2021). China's interannual variability of net primary production is dominated by the central China region. *J. Geophys. Res. Atmos.* 126 (4), e2020JD033362. doi:10.1029/2020JD033362

Peng, S., Chen, A., Xu, L., Cao, C., Fang, J., Myneni, R. B., et al. (2011). Recent change of vegetation growth trend in China. *Environ. Res. Lett.* 6 (4), 044027. doi:10.1088/1748-9326/6/4/044027

Piao, S., Ciais, P., Huang, Y., Shen, Z., Peng, S., Li, J., et al. (2010). The impacts of climate change on water resources and agriculture in China. *Nature* 467 (7311), 43–51. doi:10.1038/nature09364

Piao, S., Ciais, P., Lomas, M., Beer, C., Liu, H., Fang, J., et al. (2011). Contribution of climate change and rising CO2 to terrestrial carbon balance in East asia: A multi-model analysis. *Glob. Planet. Change* 75 (3-4), 133–142. doi:10.1016/j.gloplacha.2010.10.014

Qi, X., Jia, J., Liu, H., and Lin, Z. (2019). Relative importance of climate change and human activities for vegetation changes on China's silk road economic belt over multiple timescales. *Catena* 180, 224–237. doi:10.1016/j.catena.2019.04.027

Qiu, C., Hu, J., Yang, F., Liu, F., and Li, X. (2018). Human pressures on natural reserves in yunnan province and management implications. *Sci. Rep.* 8 (1), 3260. doi:10.1038/s41598-018-21654-w

Roxburgh, S. H., Berry, S. L., Buckley, T. N., Barnes, B., and Roderick, M. L. (2005). What is NPP? Inconsistent accounting of respiratory fluxes in the definition of net primary production. *Funct. Ecol.* 19 (3), 378–382. doi:10.1111/j.1365-2435.2005.00983.x

Running, S. W., Nemani, R. R., Heinsch, F. A., Zhao, M., Reeves, M., and Hashimoto, H. (2004). A continuous satellite-derived measure of global terrestrial primary production. *Bioscience* 54 (6), 547–560. doi:10.1641/0006-3568(2004)054[0547:Acsmog]2.0.Co;2

Sha, Z., Bai, Y., Lan, H., Liu, X., Li, R., and Xie, Y. (2020). Can more carbon be captured by grasslands? A case study of inner Mongolia, China. *Sci. Total Environ.* 723, 138085. doi:10.1016/j.scitotenv.2020.138085

Sharma, S., Joshi, P. K., and Furst, C. (2022). Unravelling net primary productivity dynamics under urbanization and climate change in the Western Himalaya. *Ecol. Indic.* 144, 109508. doi:10.1016/j.ecolind.2022.109508

Shen, X., Liu, B., Jiang, M., and Lu, X. (2020). Marshland loss warms local land surface temperature in China. *Geophys. Res. Lett.* 47 (6), e2020GL087648. doi:10.1029/2020GL087648

Shen, X., Liu, Y., Zhang, J., Wang, Y., Ma, R., Liu, B., et al. (2022). Asymmetric impacts of diurnal warming on vegetation carbon sequestration of marshes in the Qinghai Tibet Plateau. *Glob. Biogeochem. Cycles* 36 (7), e2022GB007396. doi:10.1029/2022GB007396

Shi, X., Shi, M., Zhang, N., Wu, M., Ding, H., Li, Y., et al. (2022). Effects of climate change and human activities on gross primary productivity in the Heihe River Basin, China. *Environ. Sci. Pollut. Res.* 30, 4230–4244. doi:10.1007/s11356-022-22505-y

Song, Y., Achberger, C., and Linderholm, H. W. (2011). Rain-season trends in precipitation and their effect in different climate regions of China during 1961-2008. *Environ. Res. Lett.* 6 (3), 034025–034346. doi:10.1088/1748-9326/6/3/034025

Song, Y., and Ma, M. (2011). A statistical analysis of the relationship between climatic factors and the Normalized Difference Vegetation Index in China. *Int. J. Remote Sens.* 32 (14), 3947–3965. doi:10.1080/01431161003801336

Su, B., Huang, J., Fischer, T., Wang, Y., Kundzewicz, Z. W., Zhai, J., et al. (2018). Drought losses in China might double between the 1.5 °C and 2.0 °C warming. *Proc. Natl. Acad. Sci. U. S. A.* 115 (42), 10600–10605. doi:10.1073/pnas.1802129115

Sun, R., Liu, C., and Zhu, Q. (2002). Dynamic change of net primary productivity and fractional vegetation cover in the Yellow River Basin using multi-temporal AVHRR NDVI Data. *J. Geog. Sci.* 12 (1), 29–34. doi:10.1007/bf02837424

Sun, Y., Yang, Y., Zhang, L., and Wang, Z. (2015). The relative roles of climate variations and human activities in vegetation change in North China. *Phys. Chem. Earth* 87-88, 67–78. doi:10.1016/j.pce.2015.09.017

Tang, L., Gao, L., and Shi, L. (2015). Sustainable management and protection of ecosystems in shangri-La county, yunnan province, China: Introduction. *Int. J. Sustain. Dev. World Ecol.* 22 (2), 99–102. doi:10.1080/13504509.2014.943331

Tang, X., Xiao, J., Ma, M., Yang, H., Li, X., Ding, Z., et al. (2022). Satellite evidence for China's leading role in restoring vegetation productivity over global karst ecosystems. *For. Ecol. Manage.* 507, 120000. doi:10.1016/j.foreco.2021.120000

Tian, J., Wang, B., Zhang, C., Li, W., and Wang, S. (2020). Mechanism of regional land use transition in underdeveloped areas of China: A case study of northeast China. *Land Use Policy* 94, 104538. doi:10.1016/j.landusepol.2020.104538

Turner, M. G., and Carpenter, S. R. (2017). Ecosystem modeling for the 21st century. *Ecosystems* 20 (2), 211–214. doi:10.1007/s10021-016-0076-x

van der Molen, M. K., Dolman, A. J., Ciais, P., Eglin, T., Gobron, N., Law, B. E., et al. (2011). Drought and ecosystem carbon cycling. *Agric. For. Meteorol.* 151 (7), 765–773. doi:10.1016/j.agrformet.2011.01.018

Wang, B., Gao, P., Niu, X., and Sun, J. (2017). Policy-driven China's Grain to green program: Implications for ecosystem services. *Ecosyst. Serv.* 27, 38–47. doi:10.1016/j.ecoser.2017.07.014

Wang, J., Dong, J., Yi, Y., Lu, G., Oyler, J., Smith, W. K., et al. (2017). Decreasing net primary production due to drought and slight decreases in solar radiation in China from 2000 to 2012. *J. Geophys. Res. Biogeo.* 122 (1), 261–278. doi:10.1002/2016JG003417

Wang, J., Price, K. P., and Rich, P. M. (2001). Spatial patterns of NDVI in response to precipitation and temperature in the central Great Plains. *Int. J. Remote Sens.* 22 (18), 3827–3844. doi:10.1080/01431160010007033

Wang, M., Ding, Z., Wu, C., Song, L., Ma, M., Yu, P., et al. (2021a). Divergent responses of ecosystem water-use efficiency to extreme seasonal droughts in Southwest China. *Sci. Total Environ.* 760, 143427. doi:10.1016/j.scitotenv.2020.143427

Wang, M., Wang, S., Zhao, J., Ju, W., and Hao, Z. (2021b). Global positive gross primary productivity extremes and climate contributions during 1982-2016. *Sci. Total Environ.* 774, 145703. doi:10.1016/j.scitotenv.2021.145703

Wang, S., Zhang, B., Yang, Q., Chen, G., Yang, B., Lu, L., et al. (2017). Responses of net primary productivity to phenological dynamics in the Tibetan Plateau, China. *Agric. For. Meteorol.* 232, 235–246. doi:10.1016/j.agrformet.2016.08.020

Wang, S., Zhang, Y., Ju, W., Chen, J. M., Ciais, P., Cescatti, A., et al. (2020). Recent global decline of CO2 fertilization effects on vegetation photosynthesis. *Science* 370 (6522), 1295–1300. doi:10.1126/science.abb7772

Wen, Y., Liu, X., Bai, Y., Sun, Y., Yang, J., Lin, K., et al. (2019). Determining the impacts of climate change and urban expansion on terrestrial net primary production in China. *J. Environ. Manage.* 240, 75–83. doi:10.1016/j.jenvman.2019.03.071

Wu, G., Cheng, Z., Alatalo, J. M., Zhao, J., and Liu, Y. (2021). Climate warming consistently reduces grassland ecosystem productivity. *Earths Future* 9 (6). doi:10.1029/2020EF001837

Wu, H., Zhang, J., Bao, Z., Wang, G., Wang, W., Yang, Y., et al. (2022). The impacts of natural and anthropogenic factors on vegetation change in the Yellow-Huai-Hai River Basin. *Front. Earth Sci.* 10, 959403. doi:10.3389/feart.2022.959403

Wu, N., Liu, A., Ye, R., Yu, D., Du, W., Chaolumeng, Q., et al. (2021). Quantitative analysis of relative impacts of climate change and human activities on Xilingol grassland in recent 40 years. *Glob. Ecol. Conserv.* 32, e01884. doi:10.1016/j.gecco.2021.e01884

Wu, S., Zhou, S., Chen, D., Wei, Z., Dai, L., and Li, X. (2014). Determining the contributions of urbanisation and climate change to NPP variations over the last decade in the Yangtze River Delta, China. *Sci. Total Environ.* 472, 397–406. doi:10.1016/j.scitotenv.2013.10.128

Xiao, J., and Zhuang, Q. (2007). Drought effects on large fire activity in Canadian and Alaskan forests. *Environ. Res. Lett.* 2 (4), 044003. doi:10.1088/1748-9326/2/4/044003

Xiong, Q., Pan, K., Zhang, L., Wang, Y., Li, W., He, X., et al. (2016). Warming and nitrogen deposition are interactive in shaping surface soil microbial communities near the alpine timberline zone on the eastern Qinghai-Tibet Plateau, southwestern China. *Appl. Soil Ecol.* 101, 72–83. doi:10.1016/j.apsoil.2016.01.011

Xiong, Q., Xiao, Y., Liang, P., Li, L., Zhang, L., Li, T., et al. (2021). Trends in climate change and human interventions indicate grassland productivity on the Qinghai-Tibetan Plateau from 1980 to 2015. *Ecol. Indic.* 129, 108010. doi:10.1016/j.ecolind.2021.108010

Xu, H., Wang, X., and Zhang, X. (2016). Alpine grasslands response to climatic factors and anthropogenic activities on the Tibetan Plateau from 2000 to 2012. *Ecol. Eng.* 92, 251–259. doi:10.1016/j.ecoleng.2016.04.005

Xu, J., Yin, R., Li, Z., and Liu, C. (2006). China's ecological rehabilitation: Unprecedented efforts, dramatic impacts, and requisite policies. *Ecol. Econ.* 57 (4), 595–607. doi:10.1016/j.ecolecon.2005.05.008

Xu, X., Jiang, H., Guan, M., Wang, L., Huang, Y., Jiang, Y., et al. (2020). Vegetation responses to extreme climatic indices in coastal China from 1986 to 2015. *Sci. Total Environ.* 744, 140784. doi:10.1016/j.scitotenv.2020.140784

Yan, M., Xue, M., Zhang, L., Tian, X., Chen, B., and Dong, Y. (2021). A decade's change in vegetation productivity and its response to climate change over northeast China. *Plants* 10 (5), 821. doi:10.3390/plants10050821

Yan, Y., Liu, X., Wen, Y., and Ou, J. (2019). Quantitative analysis of the contributions of climatic and human factors to grassland productivity in northern China. *Ecol. Indic.* 103, 542–553. doi:10.1016/j.ecolind.2019.04.020

Yang, H., Mu, S., and Li, J. (2014). Effects of ecological restoration projects on land use and land cover change and its influences on territorial NPP in Xinjiang, China. *Catena* 115, 85–95. doi:10.1016/j.catena.2013.11.020

Yang, H., Zhong, X., Deng, S., and Xu, H. (2021). Assessment of the impact of LUCC on NPP and its influencing factors in the Yangtze River basin, China. *Catena* 206, 105542. doi:10.1016/j.catena.2021.105542

Yang, J., Zhang, X., Luo, Z., and Yu, X. (2017). Nonlinear variations of net primary productivity and its relationship with climate and vegetation phenology, China. *Forests* 8 (10), 361. doi:10.3390/f8100361

Yang, Y., Guan, H., Shen, M., Liang, W., and Jiang, L. (2015). Changes in autumn vegetation dormancy onset date and the climate controls across temperate ecosystems in China from 1982 to 2010. *Glob. Change Biol.* 21 (2), 652–665. doi:10.1111/gcb.12778

Yin, L., Dai, E., Zheng, D., Wang, Y., Ma, L., and Tong, M. (2020). What drives the vegetation dynamics in the Hengduan Mountain region, southwest China: Climate change or human activity? *Ecol. Indic.* 112, 106013. doi:10.1016/j.ecolind.2019.106013

Yin, Y., Deng, H., and Ma, D. (2022). Complex effects of moisture conditions and temperature enhanced vegetation growth in the Arid/humid transition zone in Northern China. *Sci. Total Environ.* 805, 150152. doi:10.1016/j.scitotenv.2021.150152

Zeng, B., and Yang, T. (2008). Impacts of climate warming on vegetation in Qaidam Area from 1990 to 2003. *Environ. Monit. Assess.* 144 (1-3), 403–417. doi:10.1007/s10661-007-0003-x

Zhang, C., Wang, X., Li, J., and Hua, T. (2011). Roles of climate changes and human interventions in land degradation: A case study by net primary productivity analysis in China's shiyanghe basin. *Environ. Earth Sci.* 64 (8), 2183–2193. doi:10.1007/s12665-011-1046-4

Zhang, X., Moran, M. S., Zhao, X., Liu, S., Zhou, T., Ponce-Campos, G. E., et al. (2014). Impact of prolonged drought on rainfall use efficiency using MODIS data across China in the early 21st century. *Remote Sens. Environ.* 150, 188–197. doi:10.1016/j.rse.2014.05.003

Zhao, F., Xu, B., Yang, X., Xia, L., Jin, Y., Li, J., et al. (2019). Modelling and analysis of net primary productivity and its response mechanism to climate factors in temperate grassland, northern China. *Int. J. Remote Sens.* 40 (5-6), 2259–2277. doi:10.1080/01431161.2018.1516322

Zhao, L., Dai, A., and Dong, B. (2018). Changes in global vegetation activity and its driving factors during 1982-2013. *Agric. For. Meteorol.* 249, 198–209. doi:10.1016/j.agrformet.2017.11.013

Zhao, M., Heinsch, F. A., Nemani, R. R., and Running, S. W. (2005). Improvements of the MODIS terrestrial gross and net primary production global data set. *Remote Sens. Environ.* 95 (2), 164–176. doi:10.1016/j.rse.2004.12.011

Zhao, M., and Running, S. W. (2010). Drought-Induced reduction in global terrestrial net primary production from 2000 through 2009. *Science* 329 (5994), 940–943. doi:10.1126/science.1192666

Zhou, B., Liao, Z., Chen, S., Jia, H., Zhu, J., and Fei, X. (2022). Net primary productivity of forest ecosystems in the southwest karst region from the perspective of carbon neutralization. *Forests* 13 (9), 1367. doi:10.3390/f13091367

Zhou, W., Gang, C., Zhou, F., Li, J., Dong, X., and Zhao, C. (2015). Quantitative assessment of the individual contribution of climate and human factors to desertification in northwest China using net primary productivity as an indicator. *Ecol. Indic.* 48, 560–569. doi:10.1016/j.ecolind.2014.08.043

Zhou, X., Fei, S., Sherry, R., and Luo, Y. (2012). Root biomass dynamics under experimental warming and doubled precipitation in a tallgrass prairie. *Ecosystems* 15 (4), 542–554. doi:10.1007/s10021-012-9525-3

frontiers | Frontiers in Remote Sensing

TYPE Original Research
PUBLISHED 04 April 2023
DOI 10.3389/frsen.2023.1096000

OPEN ACCESS

EDITED BY
Ram Kumar Singh,
TERI School of Advanced Studies (TERI SAS), India

REVIEWED BY
Patrick Jantz,
Northern Arizona University, United States
Huaguo Huang,
Beijing Forestry University, China

*CORRESPONDENCE
Taejin Park,
tpark@baeri.org
Sunhui Sim,
ssim@una.edu

SPECIALTY SECTION
This article was submitted to Image Analysis and Classification, a section of the journal Frontiers in Remote Sensing

RECEIVED 11 November 2022
ACCEPTED 13 March 2023
PUBLISHED 04 April 2023

CITATION
Park T and Sim S (2023), Characterizing spatial burn severity patterns of 2016 Chimney Tops 2 fire using multi-temporal Landsat and NEON LiDAR data. *Front. Remote Sens.* 4:1096000. doi: 10.3389/frsen.2023.1096000

Characterizing spatial burn severity patterns of 2016 Chimney Tops 2 fire using multi-temporal Landsat and NEON LiDAR data

Taejin Park[1,2]* and Sunhui Sim[3]*

[1]Bay Area Environmental Research Institute, Moffett Field, CA, United States, [2]NASA Ames Research Center, Moffett Field, CA, United States, [3]Geoscience Department, University of North Alabama, Florence, AL, United States

The Chimney Tops 2 wildfire (CT2) in 2016 at Great Smoky Mountains National Park (GSMNP) was recorded as the largest fire in GSMNP history. Understanding spatial patterns of burn severity and its underlying controlling factors is essential for managing the forests affected and reducing future fire risks; however, this has not been well understood. Here, we formulated two research questions: 1) What were the most important factors characterizing the patterns of burn severity in the CT2 fire? 2) Were burn severity measures from passive and active optical remote sensing sensors providing consistent views of fire damage? To address these questions, we used multitemporal Landsat- and lidar-based burn severity measures, i.e., relativized differenced Normalized Burn Ratio (RdNBR) and relativized differenced Mean Tree Height (RdMTH). A random forest approach was used to identify key drivers in characterizing spatial variability of burn severity, and the partial dependence of each explanatory variable was further evaluated. We found that pre-fire vegetation structure and topography both play significant roles in characterizing heterogeneous mixed burn severity patterns in the CT2 fire. Mean tree height, elevation, and topographic position emerged as key factors in explaining burn severity variation. We observed generally consistent spatial patterns from Landsat- and lidar-based burn severity measures. However, vegetation type and structure-dependent relations between RdNBR and RdMTH caused locally inconsistent burn severity patterns, particularly in high RdNBR regions. Our study highlights the important roles of pre-fire vegetation structure and topography in understanding burn severity patterns and urges to integrate both spectral and structural changes to fully map and understand fire impacts on forest ecosystems.

KEYWORDS

fire, burn severity, Landsat, NEON lidar, remote sensing, vegetation structure, topography, great smoky mountains national park

1 Introduction

The Great Smoky Mountains National Park (GSMNP) is situated over the Southern Appalachians between Tennessee and North Carolina. This national park is one of the world's most ecologically rich, diverse, and important protected areas (National Park Service, 2017). Mountainous terrain, complex topography, and rainy temperate climate create unique habitats for diverse flora and fauna (Whittaker, 1956; Jenkins, 2007). Fire in the mountains has been a dynamic and natural process that influences ecosystem function and

the structural and compositional heterogeneity of the forests (Kelly et al., 2020). Yet, since the early 1900 s, fire suppression/prevention and changing climate have significantly increased the fire susceptibility of the forests (Cohen et al., 2007). During the last week of November 2016, a fire began on the Chimney Tops within the GSMNP (National Park Service, 2017). Due to accompanying drought and strong winds, the Chimney Tops 2 wildfire (hereafter, CT2) was recorded as the largest fire in the GSMNP history and caused significant environmental, social, and economic damage (Guthrie et al., 2017; National Park Service, 2017).

In addition to restoring the damaged GSMNP forests, understanding how fire modifies these forests is essential for managing the forests affected (e.g., devising restoration plans) and reducing future fire risks (e.g., prescribed burn) (Harris and Taylor, 2015; Schwartz et al., 2016). Recent advancements of remote sensing and its easier access have promoted various applications for fire monitoring and burn severity mapping (Szpakowski and Jensen, 2019). Temporarily frequent land surface observations from the earth-observing satellites (e.g., Landsat, Sentinel 2a, MODIS, VIIRS, etc.) can timely capture pre- and post-fire conditions and assess fire severity. For instance, Guindon et al. (2021) used historical Landsat data to quantify decades of burn severity over the entire country of Canada; Alonso-Gonzalez and Fernandez-Garcia (2021) quantified burn severity globally using both Aqua and Terra MODIS surface reflectance datasets. In addition to the passive optical sensors, light detection and ranging (lidar) onboard airborne or space-borne platforms can assess vertical forest structure and its change over large areas by providing high-resolution and consistent 3-dimensional measurements of ground and vegetation canopy (Kampe et al., 2010; Jung et al., 2011; Atkins et al., 2020; Park, 2020). For instance, Kane et al. (2015) used bi-temporal lidar observations to characterize mixed fire severity within the 2013 Rim fire, and Alonzo et al. (2017) quantified canopy and surface layer consumption in boreal forests using repeated lidar observations. These demonstrate that both passive and active remote sensing data together can provide unique and complementary information on fire severity as well as pre- and post-fire vegetation conditions.

Fires interact with the existing vegetation (i.e., fuels), topography, and weather conditions (Alexander et al., 2006; Birch et al., 2015; Harris and Taylor, 2015). Such interactions characterize fire behavior, burn severity patterns, and ultimately post-fire regeneration. For instance, depending on the level of burn severity, fires could maintain a vegetation type or mediate forest change (Pyne, 1996), or continuously reshape forest stands by restructuring individual trees and tree patches (Turner and Romme, 1994). Pre-fire forest structure, such as the size and arrangement of individual trees, is also a particularly important factor leading to patterns of fire spread and damage (Perry et al., 2011). Over many mixed forests like the GSMNP, fire severity exhibits a considerable spatial variation within a single fire event. However, the degree to which such mixed-severity fires are a result of existing vegetation (fuels), topography, and weather remains poorly understood. Particularly, quantifying the roles of the pre-fire vegetation conditions has been recognized as a research priority because fuel condition is one of factors that can be addressed by land management.

In this study, we aim to understand spatial variation of remotely sensed burn severity measures across gradients of environmental conditions including pre-fire vegetation type and structure, and topography in the GSMNP. First objective of this study is to identify which biophysical factors are important in determining the patterns of burn severity in the 2016 Chimney Tops 2 wildfire. Second objective is to evaluate consistency and inconsistency of burn severity measures from multitemporal Landsat and National Ecological Observatory Network (NEON) lidar data. Section 2 presents the data and methodology. The results of this study are presented in Section 3, and discussions and concluding remarks are presented in Section 4 and Section 5, respectively.

2 Materials and methods

2.1 Study area

Our study region is defined based on the fire perimeter from the Monitoring Trends in Burn Severity (MTBS) database shown in Figure 1A (Eidenshink et al., 2007). The study region covers the area burned by the CT2 fire in 2016 (Figure 1B), and its extent is about 3,994 ha. The selected area's elevation ranges from 405 m to 1,638 m (Figure 1E). Along the elevation gradient, annual precipitation amounts range from 127 to 203 cm, and they increase with elevation (Shanks, 1954). The mean annual temperature is 13°C varying up to 6.7°C. The GSMNP is ecologically rich and diverse. This park consists of more than 1,600 species of flowering plants, including about 100 native shrub and tree species (Jenkins, 2007). It is one of the largest deciduous, temperate, and old-growth forests that still exist in North America. The distribution of vegetation in the park is strongly influenced by topography, moisture, and other environmental gradients (Whittaker, 1956) (Figure 1C). Before the fire event, most of our study region was densely tree covered (~98 ± 6%), and the mean forest height was 21.6 ± 7.4 m (Figure 1D, see Section 2.4).

2.2 Vegetation type map

The National Park Service developed a seamless and complete GIS vegetation database of GSMNP. Photo interpretation of color infrared aerial photographs (1997–1998), GPS-assisted field observations, and the hierarchical GSM Vegetation Classification System containing over 150 overstory and understory classes were used to create the vegetation database. The vegetation type map is available from https://www.sciencebase.gov/catalog/item/542ecdb6e4b092f17df5ac4a. The overall attribute accuracy of the vegetation type map is 80.4% (Kappa Index = 80.0). The map provides 150 over- and understory forest types, but we only focused on the forest types whose occurrence is more than 5% of the total vegetated area within our study region (Figure 1C). Over the defined study region, Successional Hardwood Forest (SHF), Chestnut Oak Forest (COF), Yellow Pine Forest (YPF), Oak-hickory forest (OHF), Northern hardwood/acid hardwood forest (NHF/AHF), and others occupy 6.4%, 27.8%, 12.8%, 14.9%, 13.9% and 24.2% of the total vegetated regions. We use these six forest types for the following analyses.

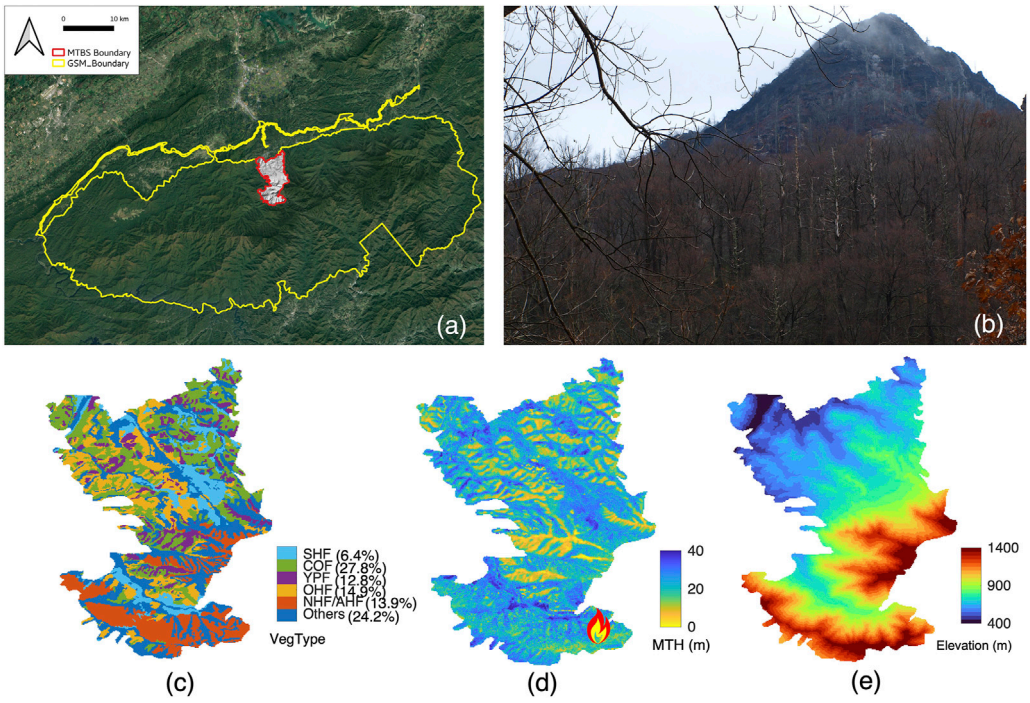

FIGURE 1
Geographical location of 2016 Chimney Tops 2 wildfire in Great Smoky Mountains National Park **(A)** and a view of burnt forest captured during 2018s field trip **(B)**. Spatial distribution of vegetation type **(C)**, mean forest height **(D)**, and digital elevation **(E)** over the study region. A fire marker in panel **(D)** indicates the location of the first fire ignition of the CT2 fire. In panel **(C)**, HF, COF, YPF, OHF, and NHF/AHF stand for successional hardwood forest, chestnut oak forest, yellow pine forest, oak-hickory forest, and northern hardwood/acid hardwood forest, respectively.

2.3 Landsat based burn severity and vegetation indices

To quantify the burn severity of the CT2 fire, we first checked the differenced Normalized Burn Ratio (dNBR) and the burn severity classification from the publicly available MTBS database. In general, Normalized Burn Ratio (NBR, Eq.1) is sensitive to the amount of leaves, moisture, and char or ash in the soil, thus the difference between pre- and post-fire NBR has been often used as a proxy of fire damage. Our initial assessment of MTBS dNBR product showed unexpected biases because of a seasonal mismatch in pre- and post-fire NBR (Eq.2). Also dNBR has been generally considered to have biases due to pre-fire vegetation conditions (Wulder et al., 2009). Thus, in this study, we decided to use the Relativized dNBR, i.e., RdNBR (Eq.3) (Miller and Thode, 2007), and directly compute RdNBR from two cloud-free Landsat 8 OLI L2 surface reflectances collected in 2015 (DOY 257) and 2017 (DOY 246). Note that we alternatively took 2015 as a pre-fire state due to the absence of cloud-free images in 2016. All Landsat data was obtained from Harmonized Landsat and Sentinel (HLS) data archive at https://hls.gsfc.nasa.gov/. The Landsat surface reflectances from HLS are normalized for per-pixel view and per-granule illumination angles (Claverie et al., 2017). View angle is set to nadir and solar zenith is set to a temporally constant value at each tile's center and varies with latitude. Higher values of the satellite-derived burn severity index (e.g., dNBR and RdNBR) indicate a decrease in photosynthetic and surface materials holding water and an increase in ash, carbon, and soil cover (Miller and Thode, 2007).

$$NBR = \frac{\rho_{nir} - \rho_{swir7}}{\rho_{nir} + \rho_{swir7}} \quad (1)$$

$$dNBR = \left(NBR_{pre} - NBR_{post}\right) \times 1000 \quad (2)$$

$$RdNBR = \frac{dNBR}{sqrt\left(abs\left(NBR_{pre}\right)\right)} \quad (3)$$

where ρ_{nir} and ρ_{swir} are surface reflectances at near-infrared (NIR, Band 5) and shortwave infrared (SWIR, Band 7) wavelengths. NBR_{pre} and NBR_{post} stand for pre- and post-fire NBR values.

Additionally, we also calculated the Normalized Difference Vegetation Index (NDVI), Normalized Difference Moisture Index (NDMI), and Land Surface Temperature (LST) from the pre- and post-fire Landsat images. NDVI quantifies the amount of living green plant material and is linearly related to absorbed photosynthetically active radiation (e.g., Sellers, 1985). It is calculated from contrasting reflectances at near-infrared (ρ_{nir}) and red (ρ_{red}) bands (Rouse et al., 1974) (Eq.4):

$$NDVI = \frac{\rho_{nir} - \rho_{red}}{\rho_{nir} + \rho_{red}} \quad (4)$$

The NDMI uses NIR and SWIR bands to create a difference ratio that is sensitive to the moisture levels in vegetation (Eq.5) (Wilson and Sader, 2002). It has been widely used to monitor droughts and

fuel levels in fire-prone areas. Note that SWIR bands for NBR and NDMI are different: Band 7 (2.11–2.29 μm) and 6 (1.57–1.65 μm) were used for NBR and NDMI, respectively.

$$NDMI = \frac{\rho_{nir} - \rho_{swir6}}{\rho_{nir} + \rho_{swir6}} \quad (5)$$

To retrieve Landsat-based LST, we followed the approach proposed by Avdan and Jovanovska (2016). Since temperature is the main controller of fuel moisture content that is associated with fire ignition, spread, and other fire behavior, LST is expected to have some degree of relation with burn severity. We first computed *Pv* from NDVI, which is a measure of vegetation proportion in each pixel (Eq. 6). Based on the computed *Pv*, land surface emissivity (Eq. 7) and LST are sequentially calculated (Eq. 8). Note that the top-of-atmosphere brightness temperature (BT) required in Eq. 8 was directly obtained from the Landsat L2 product.

$$P_v = \frac{NDVI - NDVI_{min}}{(NDVI_{max} - NDVI_{min})^2} \quad (6)$$

$$\varepsilon = 0.004 \times P_v + 0.986 \quad (7)$$

where 0.004 and 0.986 correspond to the average emissivity of bare soil and vegetated areas, respectively (Sobrino and Raissouni, 2000).

$$LST = \left[BT / \left(1 + \lambda \times \frac{BT}{\varrho \times \ln(\varepsilon)} \right) \right] \quad (8)$$

where, BT = brightness temperature; λ = wavelength; ϱ = constant of Boltzmann; and ε = surface emissivity.

2.4 NEON lidar data and vegetation structural variables

NEON Airborne Observation Platform (AOP) has collected lidar data over the GSMNP regions on an annual basis using the Optech ALTM Gemini (Vaughan, ON, Canada) (Kampe et al., 2010; Kane et al., 2014). The AOP has collected full-waveform lidar data over the GSMNP regions since 2016. The lidar produced about 4 laser points per square meter, with a maximum of 5 returns per point. In this study, we used the lidar data collected in June 2016 and June 2018 to investigate changes in pre- and post-fire GSMSP forest structure. Note that we chose 2018 data as a post-fire lidar collection rather than 2017 (October) to avoid a seasonal mismatch between pre- and post-fire lidar data (Calders et al., 2015). The digital terrain model (DTM) and canopy height model (CHM) were generated at 1 m spatial resolution following standard NEON-generated processing algorithms (Kampe et al., 2010). To facilitate analyses of spectral and structural changes derived from Landsat and lidar, we resampled 1 m lidar data into 30 m spatial resolution, which is comparable to Landsat spatial resolution. All lidar-derived structural variables are geometrically co-registered to ensure the same location is assessed by Landat-based land surface variables. Mean tree height (MTH) was used to summarize forest canopy structure in this study, calculated as the average of 1 m canopy heights within 30 m grid cells. We also introduced fractional tree cover (TC) calculated as the percent of 1 m pixels >2 m in height within a 30 m grid cell. Pre- and post-fire MTH were used to quantify forest structural changes induced by the CT2 fire, i.e., RdMTH. The RdMTH is a relativized form by normalizing differences with pre-fire conditions, as below.

$$RdMTH = \frac{MTH_{post} - MTH_{pre}}{MTH_{pre}} \times 100 \quad (9)$$

2.5 Analytical approach for modeling burn severity

Our primary objective is to identify key controlling factors in characterizing burn severity patterns of the CT2 fire. Topographical features and pre-fire vegetation conditions were the main explanatory variables. We used elevation, slope, aspect, and topographic position index (TPI) (Jenness, 2006) as topographical features. TPI is an index showing the morphological characteristics of landscapes. It shows the difference in elevation between a focal cell and all cells in the neighborhood (Jenness, 2006). In the case of plan curvature, negative curvatures illustrate concave, zero curvature represents flat, whereas positive curvatures are known as convex. This index not only can provide important morphological characteristics but also hydrological (e.g., soil wetness, snow accumulation, etc.) variations of the study region (e.g., Choubin et al., 2019).

A random forest regression model was used in this study to quantify the factors explaining the spatial patterns of satellite and lidar observed fire damage over the GSMNP. Random forest regression is a non-parametric statistical method, and it does not require distributional assumptions on covariates in relation to the response variable (Breiman, 2001). In this study, we set 100 binary decision trees in the model, and each node is split using the best break among all variables. Note that we identify the optimal number of decision trees through experimental model runs (not shown here). The explanatory covariates used can be categorized into two groups: topographical features, i.e., Elevation, Aspect, Slope, TPI, and pre-fire vegetation composition and structure, i.e., vegetation type, $NDVI_{pre}$, $NDMI_{pre}$, LST_{pre}, MTH_{pre}, and TC_{pre}. We also computed variable importance from the random forest regression model. The variable importance is a measure based on how much the error increases when the variable is excluded. A larger error before and after permutation means greater importance of the variable in the model and contributes more to predictive accuracy than other variables (Breiman, 2001). The relationship between explanatory variables and target fire severity indices (here, RdNBR and dMTH) was also evaluated using partial dependence plots, which display the marginal effect of an individual predictor on the response variable (Liaw and Wiener, 2002). Additionally, to understand compounding interactions between pre-fire vegetation conditions and topography, we also investigated how topographical features characterize spatial distribution of vegetation type and structure, i.e., MTH_{pre}. All random forest analyses were carried out with the "treebagger" package in Matlab (R2021a).

3 Results

3.1 Burn severity patterns of 2016 Chimney Tops 2 wildfire

Fire severity across our study region was highly variable (Figure 2). Our Landsat- (RdNBR) and lidar- (RdMTH) based analyses show a similar spatial pattern of fire damage during the CT2 fire (Figures 2A,C). In particular, we observed widespread,

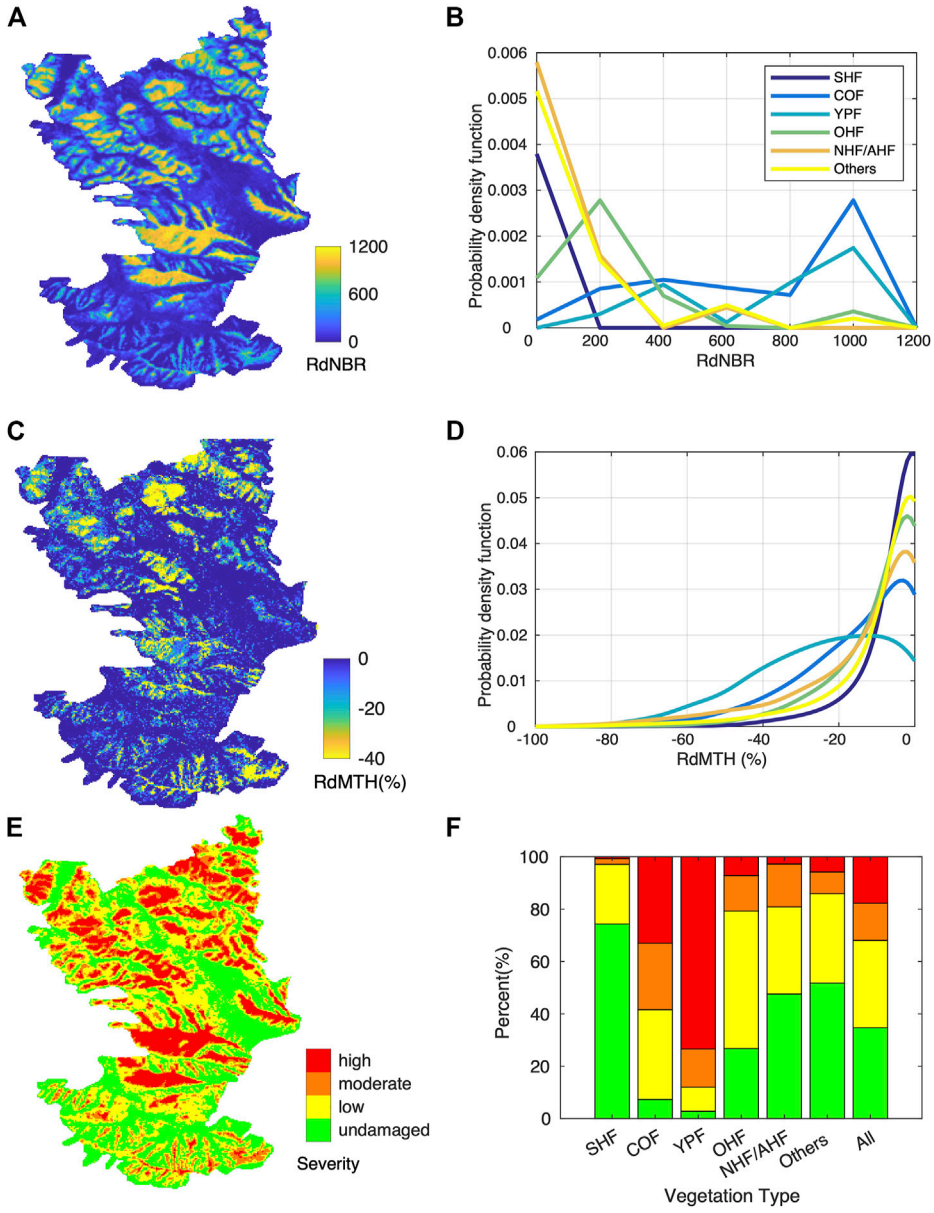

FIGURE 2
Spatial pattern of the relativized differenced Normalized Burn Ratio (RdNBR) **(A)**, relativized mean tree height **(C)**, and burn severity classification based on the RdNBR thresholds defined by Miller and Thode (Miller and Thode, 2007) **(E)**. Probability density function (pdf) of RdNBR **(B)** and RdMTH **(D)** by vegetation type classes. **(F)** Vegetation type specific distribution of burn severity classes. Green, yellow, orange, and red stand for undamaged, low, moderate, and high severity class. HF, COF, YPF, OHF, and NHF/AHF stand for successional hardwood forest, chestnut oak forest, yellow pine forest, oak-hickory forest, and northern hardwood/acid hardwood forest, respectively.

severe, and patchy damaged forests over the central and northeastern parts of the study region. According to the fire severity classification based on RdNBR thresholds defined by Miller and Thode (Miller and Thode, 2007) (Figures 2E,F), the CT2 fire burned approximately 2,608 ha (RdNBR>=69), whereas the rest of the region (1,386 ha) was not likely damaged by the fire. About half (1,333 ha) of the burned regions are damaged with a low degree (69<=RdNBR<=315) of fire severity and the other two one-fourths of the regions are categorized as moderate (566 ha, 22%) (316<=RdNBR<=640) and high (708 ha, 27%) (641<=RdNBR) severity class.

Burn severity varies significantly by forest type. The resulting patterns from both RdNBR and RdMTH indicate that Yellow Pine Forest covered regions were most severely damaged by the CT2 fire and followed by Chestnut Oak Forest (Figures 2B,D). More than 70% and 30% of the Yellow Pine Forest and Chestnut Oak Forest were impacted by high burn severity (based on RdNBR), and it links to about 24% and 15% of MTH reduction respectively. In contrast, most Successional Hardwood Forest and Northern hardwood/acid hardwood forest -covered regions were undamaged or lightly damaged (only −3.9 and −8.7% of RdMTH, respectively). Though both severity measures display a predominant spatial

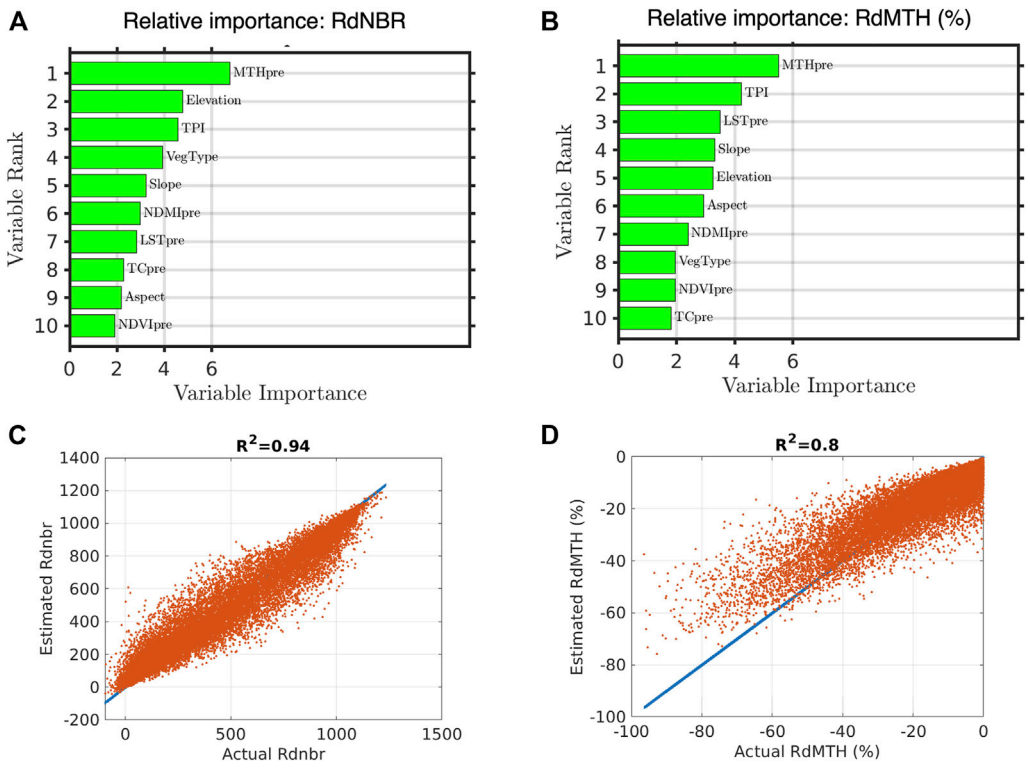

FIGURE 3
Variable importance quantified from the random forest model for the RdNBR **(A)** and RdMTH **(B)**. The performance of the models for the RdNBR **(C)** and RdMTH **(D)** evaluated with independent testing data.

agreement, we found that there is a discernible discrepancy over the central region near the Bull Head peak where relatively shorter Yellow Pine Forest canopies dominated. This discrepancy will be further reported and discussed in the following section (Section 3.3).

3.2 Importance of pre-fire vegetation structure and topography

To identify explanatory variables playing key roles in characterizing spatial patterns of burn severity, we developed RF-models for RdNBR and RdMTH, and quantified the importance of the variables (Figure 3). The RF-based models for both RdNBR and RdMTH reasonably well capture the spatial variation of the CT2 fire induced burn severity. The developed model for RdNBR (N = 6,768) can explain 94% of variation. MTH_{pre}, elevation, TPI, vegetation type, and slope are the five most important variables identified in this model. Interestingly, we also find MTH_{pre}, TPI, slope, and elevation are key variables in explaining forest structural changes, i.e., RdMTH. Our analysis shows that the RF-model for MTH_{pre} (N = 6,768) can capture 80% of variation in the tree height changes in the CT2 fire. In addition, our analysis identifies the pre-fire canopy moisture level ($NDMI_{Pre}$) and land surface temperature (LST_{Pre}) important in the burn severity characterization. However, the RF-model for the RdMTH tends to overestimate severely damaged forests that experienced greater than 40% of MTH reduction. We initially anticipated that vegetation type plays an important role in characterizing burn severity patterns due to species-specific fire flammability and resistance (Popović et al., 2021). However, our results suggest that vegetation type is less important in the CT2 fire likely due to confounding interaction with other variables (e.g., elevation, MTH_{pre}, etc.). We further discuss its importance and relation with other variables in the latter part of this section.

Figure 4 and Figure 5 demonstrate the partial dependence of each explanatory variable on regulating the RdNBR and RdMTH, respectively. First, both partial dependence plots for the RdNBR and RdMTH reveal that fire damage increases with higher elevation and decreases with lower elevation. Despite general agreement in the tendency of partial dependence, we noticed that RdNBR based severity rapidly increases from low to medium elevation whereas RdMTH-based severity increases from medium to high elevation range. Shorter pre-fire canopy heights tend to be more damaged whereas taller trees tend to be less damaged. Higher land surface temperature likely increases the degree of burn severity for both Landsat- and lidar-based burn severity metrics. Other important topographical features identified are slope and TPI. These two features together suggest that burn severity is generally higher in upper and steep hills whereas the bottom of the valley with flat conditions is likely less damaged. In the case of RdNBR, we find an obvious pattern showing that south-facing forest stands experience higher damage while north-facing stands tend to be less damaged. This aspect-dependent relation is also evident in the RdMTH but the severity peaks at south and south-east facing forests. Our partial

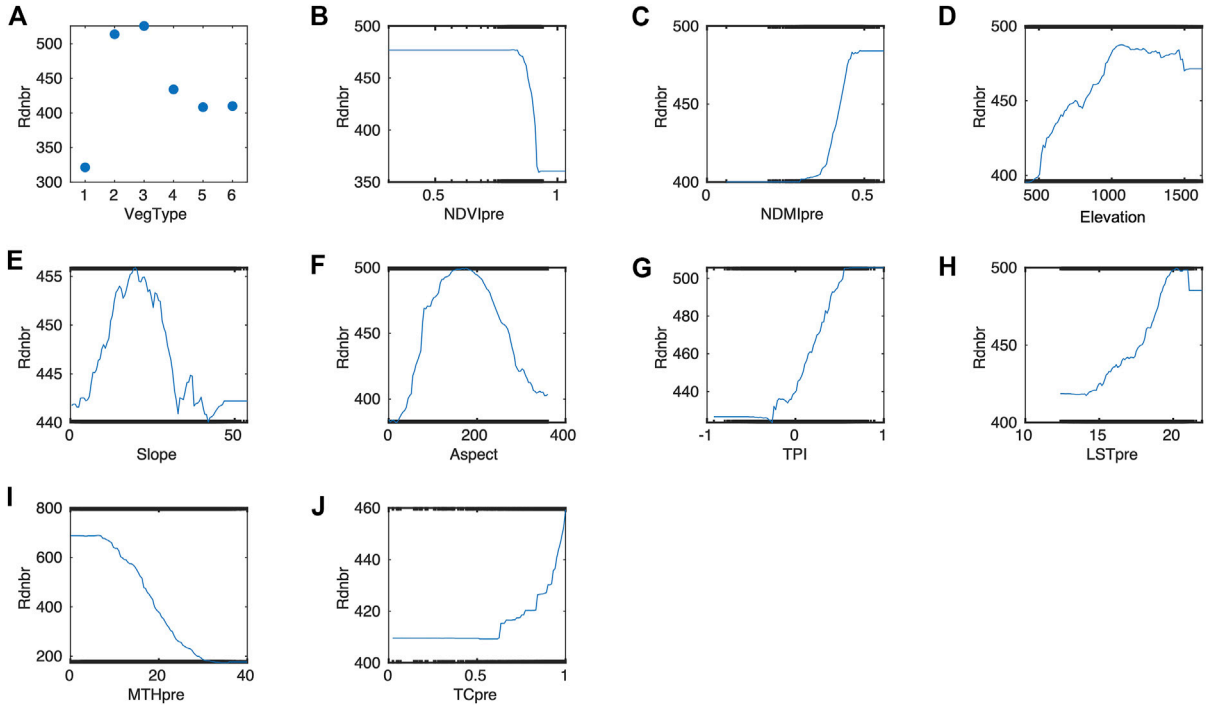

FIGURE 4
Partial dependence plots of explanatory variables (n = 10) on regulating RdNBR of the CT2 fire in Great Smoky Mountains National Park: **(A)** Vegetation type, **(B)** $NDVI_{pre}$, **(C)** $NDMI_{pre}$, **(D)** Elevation, **(E)** Slope, **(F)** Aspect, **(G)** TPI, **(H)** LST_{pre}, **(I)** MTH_{pre}, and **(J)** TC_{pre}. In panel **(A)**, numbers stand for six vegetation type classes, i.e., HF, COF, YPF, OHF, NHF/AHF, and others, respectively.

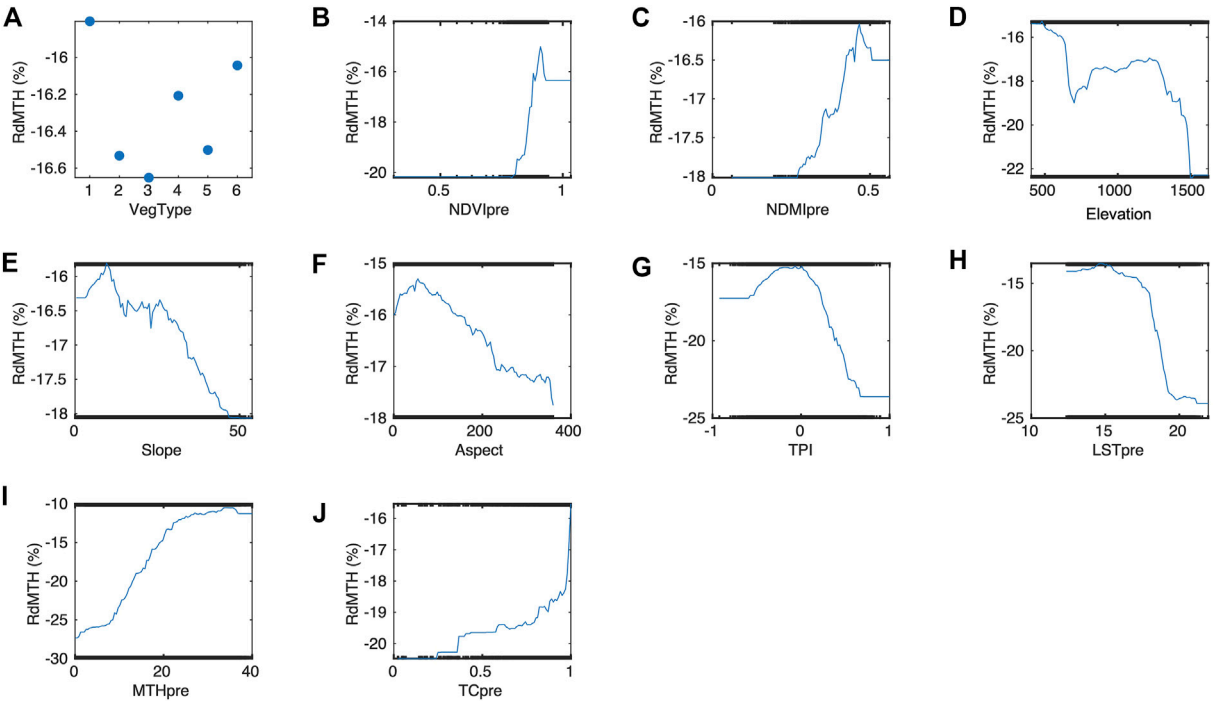

FIGURE 5
Partial dependence plots of explanatory variables (n = 10) on regulating RdMTH of the CT2 fire in Great Smoky Mountains National Park: **(A)** Vegetation type, **(B)** $NDVI_{pre}$, **(C)** $NDMI_{pre}$, **(D)** Elevation, **(E)** Slope, **(F)** Aspect, **(G)** TPI, **(H)** LST_{pre}, **(I)** MTH_{pre}, and **(J)** TC_{pre}. In panel **(A)**, numbers stand for six vegetation type classes, i.e., HF, COF, YPF, OHF, NHF/AHF, and others, respectively.

dependence analysis from both Landsat RdNBR and lidar RdMTH data shows vegetation type dependent burn severity patterns confirming two most severely damaged forests (Yellow Pine Forest and Chestnut Oak Forest) and two least damaged forests (Successional Hardwood Forest and other forest class). For the case of TC, we find opposite patterns in RdNBR and RdMTH indicating an increase of RdNBR and a decrease of RdMTH over higher tree covered regions. In the RF model for RdMTH, lower pre-fire NDMI which is a proxy of vegetation moisture content burned more severely than those with higher $NDMI_{pre}$ but this pattern is not consistent in the RdNBR though it is a less important variable.

The pre-fire vegetation structure and topographical features derived from the NEON AOP lidar data over the GSMNP were identified as key explanatory variables in explaining spatial burn severity patterns measured from both multitemporal Landsat and lidar data (Figure 3). We initially anticipated that vegetation type can be a key variable as species-dependent fire resistance may play a critical role in determining fuel characteristics and severity patterns (Hengst and Dawson, 1994; Fernández-Guisuraga et al., 2021). In contrast, our results suggest that vegetation type is relatively less important in the CT2 fire. We then hypothesized that topographical features govern forest type occurrence and structure, thus these variables are standing out from our analyses. To test this hypothesis, we further investigated how topography alone can explain forest type occurrence and structure. The results shown in Supplementary Figures S1, S2 supported our hypothesis. Particularly, elevation and aspect could reasonably predict spatial distribution of MTH_{pre}. Aspect and TPI were identified as important features of forest type distribution. Supplementary Figure S3 shows distribution of species with respect to environmental conditions. In general, north- and northeast-facing slopes at higher elevation are most likely to have Northern hardwood/acid hardwood forest, and other forest types, whereas we found more Chestnut Oak Forest and Yellow Pine Forest over lower elevation with south- and southwest-facing slopes. Partial dependence of TPI implies that the upper hill is the most favorable location for Chestnut Oak Forest and Yellow Pine Forest and the bottom of the valley is much favorable for the other forest class. These topographical controls on forest type distribution also strongly limit tree growth, i.e., taller trees in north facing, shorter trees in south facing. For instance, trees in the Yellow Pine Forest, that face north and are located at the bottom of the valley, reach ~25 m, but trees facing south are only 10 m tall at the top of the ridge. Topographic associations between valley bottoms and vegetation growth, i.e., MTH_{pre}, likely reflect more favorable edaphic conditions along the channel banks, as well as more sheltered microclimates and available water (Moeslund et al., 2013a; Moeslund et al., 2013b). As a whole, the observed spatial pattern of forest type distribution and their height growth suggest a closely linked biogeographical niche governed by topography-mediated microclimate and forest structure (Moeslund et al., 2013a; Moeslund et al., 2013b). This close association between pre-fire vegetation composition/structure and local topography indicates there are discernible compounding interactions between these factors on burn severity patterns.

3.3 Comparison between Landsat- and lidar-based burn severity measures

Our analyses reveal how two different burn severity measures from Landsat and lidar perform in the CT2 fire case (Figure 6). Complementary analysis reveals that spectral burn severity indices from Landsat including dNDVI (= $NDVI_{pre}$-$NDVI_{post}$), dNBR, and RdNBR tightly share their variations (Supplementary Figure S4). It indicates that they could capture fire-induced damage in a similar manner. Yet, relations between spectral indices and lidar structural variables tend to be linear at low and moderate burn severity levels (based on RdNBR) but their linearity turns to non-linear at higher damage class (>800 RdNBR) (Figure 6). This non-linear relation is even inverted when RdNBR is greater than ~950. This inverted relation explains why RdNBR and RdMTH display inconsistent burn severity patterns in the central part (near the Bull Head peak) of our study region (Figures 2A,C). Interestingly, these relations between RdNBR and RdMTH are invariant across vegetation classes except Northern hardwood/acid hardwood forest stands. We find that about two times less RdNBR changes in Northern hardwood/acid hardwood forest than in the other five classes with respect to the change in MTH. For instance, 20% of MTH reduction in Northern hardwood/acid hardwood forest and other five forest classes mean ~400 and ~800 of RdNBR, respectively. This implies a varying sensitivity of RdNBR to structural changes in different forest types.

In addition to vegetation type dependent varying sensitivity of RdNBR to RdMTH, we also find a varying sensitivity of RdNBR to RdMTH over different pre-fire forest structures (Figure 7). To the increase of RdNBR, taller and old growth forests tend to have less dynamic RdMTH change than shorter and younger forest stands. This structure dependent response likely causes the observed non-linear and inverse relation between RdMTH and RdNBR at high-severity burn (Figure 6).

4 Discussion

The topographical features derived from the NEON AOP lidar data over the GSMNP were identified as key explanatory variables in explaining spatial burn severity patterns. Generally, topography including elevation, topographic position, aspect, and slope plays an important role in determining local patterns of potential incident solar radiation. Topography-induced variation in solar energy can influence local vegetation patterns and flammability through multiple mechanisms: soil moisture, temperature, and light availability (Lydersen and North, 2012; Moeslund et al., 2013a). For instance, southern aspects generally receive more sunlight leading to more xeric and warmer conditions (Stage, 1976) (Supplementary Figures S3A, D) and thus resulting in drier fuels and smaller trees (Supplementary Figure S3G), which may burn with greater severity. Furthermore, topography is also a determinant of fire spread behavior. Fire spreads more readily upslope than downslope, and daytime upslope winds that develop from differential heating in mountainous terrain can drive upslope fire spread (Weng et al., 2004; Werth et al., 2011). Middle and upper slope positions often experience higher fire line intensities because of higher effective wind speeds, lower canopy cover, and

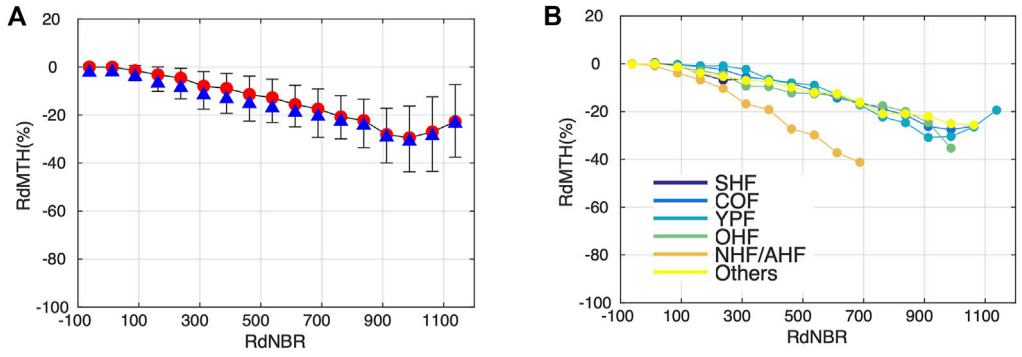

FIGURE 6
Comparison between burn severity measures (RdNBR and dMTH) from passive and active remote sensing sensors. Relations from all vegetation types and each type shown in **(A)** and **(B)** respectively. In panel **(A)**, the red circle and blue triangle represent median and mean values, and error bars stand for the 25th and 75th percentile. In panel **(B)**, the colored circles represent median values of each vegetation type.

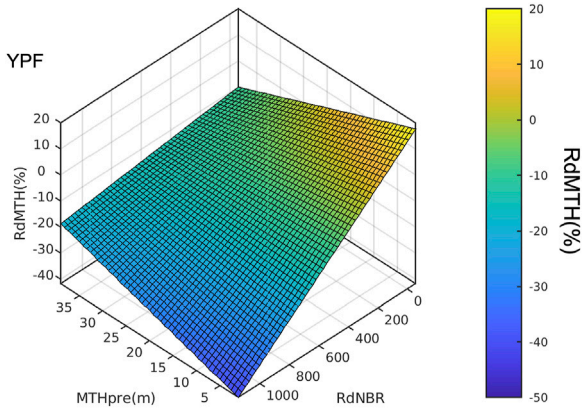

FIGURE 7
Relations between MTH_{pre}, RdMTH, and RdNBR in yellow pine forests (YPF).

preheating of fuels as fires move upslope (Figure 4G; Figure 5G) (Rothermel, 1983).

The association we observed between pre-fire structure (i.e., MTH_{pre}) and fire severity may be linked to several mechanisms. Because taller trees usually have bigger stems and thicker bark, it has been linked to the reduced fire-induced mortality (Hély et al., 2003). Alternatively, fuel characteristics over large tree dominated areas may have been burned less intensely (Figure 4I; Figure 5I). Thus, the patterns we observed may have been created by variation in fire intensity, spreading pattern, variation in the susceptibility of trees to damage and mortality, or a combination of these factors. Another potential confounding issue is that there is a historical disturbance gradient within the fire footprint where higher elevations were minimally disturbed and lower elevations were progressively more disturbed in the early part of the 20th century. This disturbance has likely had a range of effects on vegetation structure and composition, either directly or through changes to soils (Tucker, 1979; Tuttle and White, 2016).

In this study, we did not include weather variables (e.g., temperature, humidity, wind, etc.) in characterizing spatial patterns of burn severity since spatially explicit weather data was not available at a fine scale. According to the regional weather data (Supplementary Figure S5), November of 2016 when the CT2 fire happened was a very dry month (and year) with unprecedented wind gusts (National Park Service, 2017). Under extreme fire conditions, we expect that local weather conditions may play a significant role in determining fire spread and severity patterns (Viedma et al., 2020). Without accounting for fire weather, however, our RF-based analyses could explain a significant portion of the spatial variation of burn severity (R^2 of RdNBR = 0.94, R^2 of RdMTH = 0.8). This is likely because our analysis indirectly accounted for weather-induced burn severity patterns by introducing proxies such as topography, canopy moisture level, and land surface temperature which govern fire spread and microclimate conditions. Our RF-based analysis revealed that LST is an important variable for both RdNBR and RdMTH modeling. Hotter land surfaces in the study region tend to be severely damaged whereas cooler surfaces are less damaged. Further, interactions between topography (and/or pre-fire vegetation) and weather conditions (e.g., wind direction) might reflect fire-weather interaction into the developed RF-models.

In this study, by comparing burn severity measures from Landsat and lidar observations, we confirmed that there is a generally good agreement between spectral (RdNBR) and structural (RdMTH) measures (Wulder et al., 2009; McCarley et al., 2017). However, vegetation type and pre-fire structure dependent RdNBR sensitivities were noticed (Figure 6; Figure 7). We observed unexpected non-linear and inverse relations between RdMTH and RdNBR at highly damaged forests (Figure 6). Possible explanations for the observed pattern are twofold: First, residual structures such as dead standing trees were still measurable from the post-fire lidar observation but its spectral responsiveness is low to the RdNBR (see Figure 1B; Figure 8) (Bolton et al., 2015). Second, understory, subcanopy,

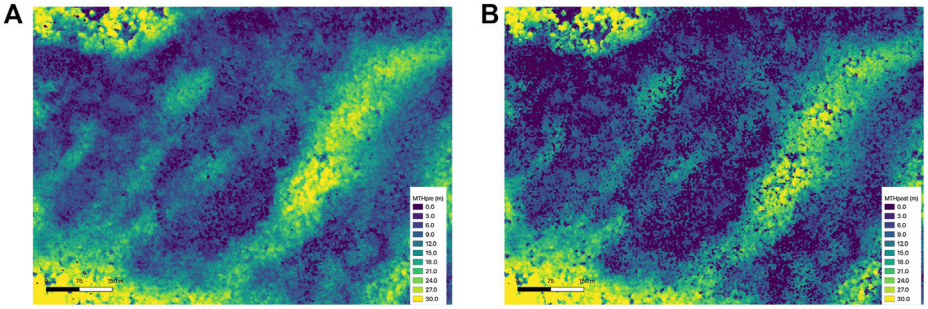

FIGURE 8
Pre- **(A)** and post-fire **(B)** mean tree height near the Bull Head peak where Landsat and lidar based burn severity measures show inconsistent patterns.

and/or soil burning may increase RdNBR significantly but not RdMTH because RdMTH represents more upper canopy status than lower canopy and/or soil. Spectral burn severity indices from Landsat NIR and SWIR bands generally provide how much photosynthetically active vegetation is damaged by fire events. Surface reflectances at different wavelengths are a result of photon interaction with vegetation media and soil, however, the lidar based matrix we used represents mostly changes in upper canopy status rather than lower canopy and near-surface vegetation. This difference may result in the observed discrepancy in burn severity measures.

Over the GSMNP regions, NEON AOP collected lidar data on an annual basis since 2016. The collected multi-temporal lidar observations are fortunate and grant a unique opportunity to understand how the CT2 fire event modified the GSMNP forests and what environmental factors primarily characterize spatial variability of burn severity over the highly mixed severity fire. Furthermore, future repeat lidar data acquisition over the GSMNP can offer insight into processes of forest regeneration after fire events across varying degrees of burn severity, topography, and pre-fire vegetation structure and composition. A growing number of repeat lidar data acquisition allows us to investigate forest structural changes after disturbance by providing multidimensional information. In addition to the GSMNP, the repeating lidar collections over a range of ecosystems and disturbance histories are already available within the NEON sites (Atkins et al., 2020) and other long-term research sites (e.g., G-LiHT, LVIS, etc.) (Leitold et al., 2021). Repetitive spaceborne lidar measurements from NASA Global Ecosystem Dynamics Investigation (GEDI) and ICESat-1and2 also expand our capability to sample multi-temporal forest structure characteristics and its changes (Neuenschwander and Pitts, 2019; Dubayah et al., 2020). Synergistic uses of such high spatial resolution multi-temporal 3-D data with optical passive sensors (e.g., Landsat, Sentinel-2, etc.) and other supporting measurements (e.g., field measurements) will greatly improve our understanding of carbon turnover, the timing and duration of subsequent changes in forest structure, and the associated impacts on productivity, demography, runoff, and nutrient cycling across ecosystems.

5 Concluding remarks

We used multitemporal Landsat and lidar observations to quantify fire severity at the GSMNP. Our analysis revealed that the CT2 fire was a mixed-severity fire, and about 22% and 27% of the burned area was damaged moderately and severely. We found that topography and pre-fire vegetation structure played significant roles in characterizing heterogeneous mixed burn severity patterns. Elevation, mean tree height, and topographic position emerged as key controlling factors. We generally observed consistent spatial patterns from Landsat and lidar-based severity measures. However, vegetation type and pre-fire structure-dependent relations between RdNBR and RdMTH caused locally inconsistent severity, particularly in high RdNBR regions. Our study highlights the critical roles of topography and pre-fire vegetation structure in understanding burn severity patterns and urges to integrate both spectral and structural changes to fully map fire impacts on forests.

Data availability statement

All data used in this study is publicly available. The vegetation type map used in this study is available in https://www.sciencebase.gov/catalog/item/542ecdb6e4b092f17df5ac4a. Landsat and NEON airborne lidar data used in this study are available in https://hls.gsfc.nasa.gov/ and https://data.neonscience.org/, respectively.

Author contributions

TP and SS designed the research; TP performed analysis; TP and SS interpreted the results, wrote the draft, and revised the paper. All authors contributed to the article and approved the submitted version.

Funding

This work is supported by the 2022-2023 College of Arts and Sciences Research Grant Fund at University of North Alabama and

the Ben H. Craig Professorship of Geography, University of North Alabama.

Acknowledgments

TP gratefully acknowledges the support from NASA Earth Science Directorate (ESD).

Conflict of interest

The authors declare that the research was conducted in the absence of any commercial or financial relationships that could be construed as a potential conflict of interest.

Publisher's note

Supplementary material

The Supplementary Material for this article can be found online at: https://www.frontiersin.org/articles/10.3389/frsen.2023.1096000/full#supplementary-material

References

Alexander, J. D., Seavy, N. E., Ralph, C. J., and Hogoboom, B. (2006). Vegetation and topographical correlates of fire severity from two fires in the Klamath-Siskiyou region of Oregon and California. *Int. J. Wildland Fire* 15, 237–245. doi:10.1071/wf05053

Alonso-González, E., and Fernández-García, V. (2021). Mosev: A global burn severity database from MODIS (2000–2020). *Earth Syst. Sci. Data* 13, 1925–1938. doi:10.5194/essd-13-1925-2021

Alonzo, M., Morton, D. C., Cook, B. D., Andersen, H.-E., Babcock, C., and Pattison, R. (2017). Patterns of canopy and surface layer consumption in a boreal forest fire from repeat airborne lidar. *Environ. Res. Lett.* 12, 065004. doi:10.1088/1748-9326/aa6ade

Atkins, J. W., Bond-Lamberty, B., Fahey, R. T., Haber, L. T., Stuart-Haëntjens, E., Hardiman, B. S., et al. (2020). Application of multidimensional structural characterization to detect and describe moderate forest disturbance. *Ecosphere* 11, e03156. doi:10.1002/ecs2.3156

Avdan, U., and Jovanovska, G. (2016). Algorithm for automated mapping of land surface temperature using LANDSAT 8 satellite data. *J. sensors* 2016, 1–8. doi:10.1155/2016/1480307

Birch, D. S., Morgan, P., Kolden, C. A., Abatzoglou, J. T., Dillon, G. K., Hudak, A. T., et al. (2015). Vegetation, topography and daily weather influenced burn severity in central Idaho and Western Montana forests. *Ecosphere* 6, 1–23. doi:10.1890/es14-00213.1

Bolton, D. K., Coops, N. C., and Wulder, M. A. (2015). Characterizing residual structure and forest recovery following high-severity fire in the Western boreal of Canada using Landsat time-series and airborne lidar data. *Remote Sens. Environ.* 163, 48–60. doi:10.1016/j.rse.2015.03.004

Breiman, L. (2001). Random forests. *Mach. Learn.* 45, 5–32. doi:10.1023/a:1010933404324

Calders, K., Schenkels, T., Bartholomeus, H., Armston, J., Verbesselt, J., and Herold, M. (2015). Monitoring spring phenology with high temporal resolution terrestrial LiDAR measurements. *Agric. For. Meteorology* 203, 158–168. doi:10.1016/j.agrformet.2015.01.009

Choubin, B., Borji, M., Mosavi, A., Sajedi-Hosseini, F., Singh, V. P., and Shamshirband, S. (2019). Snow avalanche hazard prediction using machine learning methods. *J. Hydrology* 577, 123929. doi:10.1016/j.jhydrol.2019.123929

Claverie, M., Masek, J. G., Ju, J., and Dungan, J. L. (2017). *Harmonized landsat-8 sentinel-2 (HLS) product user's guide*. Washington, DC, USA: National Aeronautics and Space Administration.

Cohen, D., Dellinger, B., Klein, R., and Buchanan, B. (2007). Patterns in lightning-caused fires at great smoky mountains national park. *Fire Ecol.* 3, 68–82. doi:10.4996/fireecology.0302068

Dubayah, R., Blair, J. B., Goetz, S., Fatoyinbo, L., Hansen, M., Healey, S., et al. (2020). The global ecosystem dynamics investigation: High-resolution laser ranging of the earth's forests and topography. *Sci. remote Sens.* 1, 100002. doi:10.1016/j.srs.2020.100002

Eidenshink, J., Schwind, B., Brewer, K., Zhu, Z.-L., Quayle, B., and Howard, S. (2007). A project for monitoring trends in burn severity. *Fire Ecol.* 3, 3–21. doi:10.4996/fireecology.0301003

Fernández-Guisuraga, J. M., Suárez-Seoane, S., García-Llamas, P., and Calvo, L. (2021). Vegetation structure parameters determine high burn severity likelihood in different ecosystem types: A case study in a burned mediterranean landscape. *J. Environ. Manag.* 288, 112462. doi:10.1016/j.jenvman.2021.112462

Guindon, L., Gauthier, S., Manka, F., Parisien, M.-A., Whitman, E., Bernier, P., et al. (2021). Trends in wildfire burn severity across Canada, 1985 to 2015. *Can. J. For. Res.* 51, 1230–1244. doi:10.1139/cjfr-2020-0353

Guthrie, V., Finucane, M., Keith, P., and Stinnett, D. (2017). *After action review of the november 28, 2016*. United States: Firestorm.

Harris, L., and Taylor, A. H. (2015). Topography, fuels, and fire exclusion drive fire severity of the Rim fire in an old-growth mixed-conifer forest, yosemite national park, USA. *Yosemite Natl. Park, U. S. A. Ecosyst.* 18, 1192–1208. doi:10.1007/s10021-015-9890-9

Hély, C., Flannigan, M., and Bergeron, Y. (2003). Modeling tree mortality following wildfire in the southeastern Canadian mixed-wood boreal forest. *For. Sci.* 49 (4), 566–576. doi:10.1093/forestscience/49.4.566

Hengst, G. E., and Dawson, J. O. (1994). Bark properties and fire resistance of selected tree species from the central hardwood region of North America. *Can. J. For. Res.* 24, 688–696. doi:10.1139/x94-092

Jenkins, M. A. (2007). Vegetation communities of great smoky mountains national park. *Southeast. Nat.* 6, 35–56. doi:10.1656/1528-7092(2007)6[35:vcogsm]2.0.co;2

Jenness, J. (2006). *Topographic Position Index (tpi_jen. avx) extension for ArcView 3. x, v. 1.3 a*. United States: Jenness Enterprises.

Jung, S.-E., Kwak, D.-A., Park, T., Lee, W.-K., and Yoo, S. (2011). Estimating crown variables of individual trees using airborne and terrestrial laser scanners. *Remote Sens.* 3, 2346–2363. doi:10.3390/rs3112346

Kampe, T. U., Johnson, B. R., Kuester, M. A., and Keller, M. (2010). Neon: The first continental-scale ecological observatory with airborne remote sensing of vegetation canopy biochemistry and structure. *J. Appl. Remote Sens.* 4, 043510. doi:10.1117/1.3361375

Kane, V. R., Cansler, C. A., Povak, N. A., Kane, J. T., McGaughey, R. J., Lutz, J. A., et al. (2015). Mixed severity fire effects within the Rim fire: Relative importance of local climate, fire weather, topography, and forest structure. *For. Ecol. Manag.* 358, 62–79. doi:10.1016/j.foreco.2015.09.001

Kane, V. R., North, M. P., Lutz, J. A., Churchill, D. J., Roberts, S. L., Smith, D. F., et al. (2014). Assessing fire effects on forest spatial structure using a fusion of Landsat and airborne LiDAR data in Yosemite National Park. *Remote Sens. Environ.* 151, 89–101. doi:10.1016/j.rse.2013.07.041

Kelly, L. T., Giljohann, K. M., Duane, A., Aquilué, N., Archibald, S., Batllori, E., et al. (2020). Fire and biodiversity in the anthropocene. *Science* 370, eabb0355. doi:10.1126/science.abb0355

Leitold, V., Morton, D. C., Martinuzzi, S., Paynter, I., Uriarte, M., Keller, M., et al. (2021). Tracking the rates and mechanisms of canopy damage and recovery following Hurricane Maria using multitemporal lidar data. bioRxiv.

Liaw, A., and Wiener, M. (2002). Classification and regression by randomForest. *R. news* 2, 18–22.

Lydersen, J., and North, M. (2012). Topographic variation in structure of mixed-conifer forests under an active-fire regime. *Ecosystems* 15, 1134–1146. doi:10.1007/s10021-012-9573-8

McCarley, T. R., Kolden, C. A., Vaillant, N. M., Hudak, A. T., Smith, A. M., Wing, B. M., et al. (2017). Multi-temporal LiDAR and Landsat quantification of fire-induced changes to forest structure. *Remote Sens. Environ.* 191, 419–432. doi:10.1016/j.rse.2016.12.022

Miller, J. D., and Thode, A. E. (2007). Quantifying burn severity in a heterogeneous landscape with a relative version of the delta Normalized Burn Ratio (dNBR). *Remote Sens. Environ.* 109, 66–80. doi:10.1016/j.rse.2006.12.006

Moeslund, J. E., Arge, L., Bøcher, P. K., Dalgaard, T., Odgaard, M. V., Nygaard, B., et al. (2013a). Topographically controlled soil moisture is the primary driver of local vegetation patterns across a lowland region. *Ecosphere* 4, art91–26. doi:10.1890/es13-00134.1

Moeslund, J. E., Arge, L., Bøcher, P. K., Dalgaard, T., and Svenning, J.-C. (2013b). Topography as a driver of local terrestrial vascular plant diversity patterns. *Nordic J. Bot.* 31, 129–144. doi:10.1111/j.1756-1051.2013.00082.x

National Park Service (2017). *Chimney tops 2 fire ReviewIndividual fire review report*. Berlin, Germany: Springer.

Neuenschwander, A., and Pitts, K. (2019). The ATL08 land and vegetation product for the ICESat-2 Mission. *Remote Sens. Environ.* 221, 247–259. doi:10.1016/j.rse.2018.11.005

Park, T. (2020). Potential lidar height, intensity, and ratio parameters for plot dominant species discrimination and volume estimation. *Remote Sens.* 12, 3266. doi:10.3390/rs12193266

Perry, D. A., Hessburg, P. F., Skinner, C. N., Spies, T. A., Stephens, S. L., Taylor, A. H., et al. (2011). The ecology of mixed severity fire regimes in Washington, Oregon, and Northern California. *For. Ecol. Manag.* 262, 703–717. doi:10.1016/j.foreco.2011.05.004

Popović, Z., Bojović, S., Marković, M., and Cerdà, A. (2021). Tree species flammability based on plant traits: A synthesis. *Sci. Total Environ.* 800, 149625. doi:10.1016/j.scitotenv.2021.149625

Pyne, S. J. (1996). "Wild hearth a prolegomenon to the cultural fire history of northern Eurasia," in *Fire in ecosystems of boreal eurasia* (Berlin, Germany: Springer), 21–44.

Rothermel, R. C. (1983). *Field procedures for verification and adjustment of fire behavior predictions*. United States: US Department of Agriculture, Forest Service, Intermountain Forest and Range.

Rouse, J. W., Haas, R. H., Schell, J. A., and Deering, D. W. (1974). "Monitoring vegetation systems in the great plains with ERTS: Proceedings of the third earth resources technology satellite-1 symposium," in NASA SP-351, United States, CA, 01 January 1974, 301–317.

Schwartz, N. B., Urban, D. L., White, P. S., Moody, A., and Klein, R. N. (2016). Vegetation dynamics vary across topographic and fire severity gradients following prescribed burning in Great Smoky Mountains National Park. *For. Ecol. Manag.* 365, 1–11. doi:10.1016/j.foreco.2016.01.027

Sellers, P. J. (1985). Canopy reflectance, photosynthesis and transpiration. *Int. J. remote Sens.* 6 (8), 1335–1372. doi:10.1080/01431168508948283

Shanks, R. E. (1954). Climates of the great smoky mountains. *Ecology* 35, 354–361. doi:10.2307/1930098

Sobrino, J. A., and Raissouni, N. (2000). Toward remote sensing methods for land cover dynamic monitoring: Application to Morocco. *Int. J. remote Sens.* 21 (2), 353–366. doi:10.1080/014311600210876

Stage, A. R. (1976). An expression for the effect of aspect, slope, and habitat type on tree growth. *For. Sci.* 22 (4), 457–460. doi:10.1093/forestscience/22.4.457

Szpakowski, D. M., and Jensen, J. L. (2019). A review of the applications of remote sensing in fire ecology. *Remote Sens.* 11, 2638. doi:10.3390/rs11222638

Tucker, C. J. (1979). Red and photographic infrared linear combinations for monitoring vegetation. *Remote Sens. Environ.* 8, 127–150. doi:10.1016/0034-4257(79)90013-0

Turner, M. G., and Romme, W. H. (1994). Landscape dynamics in crown fire ecosystems. *Landsc. Ecol.* 9, 59–77. doi:10.1007/bf00135079

Tuttle, J. P., and White, P. S. (2016). "Structural and compositional change in great smoky mountains national park since protection, 1930s–2000s," in *Natural disturbances and historic range of variation* (Berlin, Germany: Springer), 263–294.

Viedma, O., Chico, F., Fernández, J. J., Madrigal, C., Safford, H. D., and Moreno, J. M. (2020). Disentangling the role of prefire vegetation vs. burning conditions on fire severity in a large forest fire in SE Spain. *Remote Sens. Environ.* 247, 111891. doi:10.1016/j.rse.2020.111891

Weng, Q., Lu, D., and Schubring, J. (2004). Estimation of land surface temperature–vegetation abundance relationship for urban heat island studies. *Remote Sens. Environ.* 89, 467–483. doi:10.1016/j.rse.2003.11.005

Werth, P. A., Potter, B. E., Clements, C. B., Finney, M. A., Forthofer, J. A., McAllister, S. S., et al. (2011). *Synthesis of knowledge of extreme fire behavior: volume I for fire managers*. United States: US Department of Agriculture, Forest Service, Intermountain Forest and Range.

Whittaker, R. H. (1956). Vegetation of the great smoky mountains. *Ecol. Monogr.* 26, 1–80. doi:10.2307/1943577

Wilson, E. H., and Sader, S. A. (2002). Detection of forest harvest type using multiple dates of Landsat TM imagery. *Remote Sens. Environ.* 80, 385–396. doi:10.1016/s0034-4257(01)00318-2

Wulder, M. A., White, J. C., Alvarez, F., Han, T., Rogan, J., and Hawkes, B. (2009). Characterizing boreal forest wildfire with multi-temporal Landsat and LIDAR data. *Remote Sens. Environ.* 113, 1540–1555. doi:10.1016/j.rse.2009.03.004

frontiers | Frontiers in Environmental Science

TYPE Original Research
PUBLISHED 09 May 2023
DOI 10.3389/fenvs.2023.1154115

OPEN ACCESS

EDITED BY
Meenu Rani,
Kumaun University, India

REVIEWED BY
Jan Kavan,
Masaryk University, Czechia
Himangshu Kalita,
Cotton University, India

*CORRESPONDENCE
Anna Zmarz,
azmarz@uw.edu.pl

RECEIVED 30 January 2023
ACCEPTED 17 April 2023
PUBLISHED 09 May 2023

CITATION
Zmarz A, Karlsen SR, Kycko M, Korczak-Abshire M, Gołębiowska I, Karsznia I and Chwedorzewska K (2023), BVLOS UAV missions for vegetation mapping in maritime Antarctic. *Front. Environ. Sci.* 11:1154115. doi: 10.3389/fenvs.2023.1154115

BVLOS UAV missions for vegetation mapping in maritime Antarctic

Anna Zmarz [1]*, Stein Rune Karlsen [2], Marlena Kycko [1], Małgorzata Korczak-Abshire [3], Izabela Gołębiowska [1], Izabela Karsznia [1] and Katarzyna Chwedorzewska [4]

[1]Department of Geoinformatics, Cartography and Remote Sensing, Faculty of Geography and Regional Studies, University of Warsaw, Warsaw, Poland, [2]NORCE Norwegian Research Centre AS, Tromsø, Norway, [3]Department of Antarctic Biology, Institute of Biochemistry and Biophysics, Polish Academy of Sciences, Warsaw, Poland, [4]Department of Botany, Institute of Biology, Warsaw University of Life Sciences-SGGW, Warsaw, Poland

Polar areas are among the regions where climate change occurs faster than on most of the other areas on Earth. To study the effects of climate change on vegetation, there is a need for knowledge on its current status and properties. Both classic field observation methods and remote sensing methods based on manned aircraft or satellite image analysis have limitations. These include high logistic operation costs, limited research areas, high safety risks, direct human impact, and insufficient resolution of satellite images. Fixed-wing unmanned aerial vehicle beyond the visual line of sight (UAV BVLOS) missions can bridge the scale gap between field-based observations and full-scale airborne or satellite surveys. In this study the two operations of the UAV BVLOS, at an altitude of 350 m ASL, have been successfully performed in Antarctic conditions. Maps of the vegetation of the western shore of Admiralty Bay (King George Island, South Shetlands, Western Antarctic) that included the Antarctic Specially Protected Area No. 128 (ASPA 128) were designed. The vegetation in the 7.5 km^2 area was mapped in ultra-high resolution (<5 cm and DEM of 0.25 m GSD), and from the Normalized Difference Vegetation Index (NDVI), four broad vegetation units were extracted: "dense moss carpets" (covering 0.14 km^2, 0.8% of ASPA 128), "*Sanionia uncinata* moss bed" (0.31 km^2, 1.7% of ASPA 128), "*Deschampsia antarctica* grass meadow" (0.24 km^2, 1.3% of ASPA 128), and "*Deschampsia antarctica*–*Usnea antarctica* heath" (1.66 km^2, 9.4% of ASPA 128). Our results demonstrate that the presented UAV BVLOS–based surveys are time-effective (single flight lasting 2.5 h on a distance of 300 km) and cost-effective when compared to classical field-based observations and are less invasive for the ecosystem. Moreover, unmanned airborne vehicles significantly improve security, which is of particular interest in polar region research. Therefore, their development is highly recommended for monitoring areas in remote and fragile environments.

KEYWORDS

UAV, King George Island, the Antarctic, NDVI, vegetation

1 Introduction

Maritime Antarctic is a region where recent dynamic climate changes are taking place (Siegert et al., 2019), and projections forecast a strong impact of future climate change on Antarctic biodiversity (Koerich et al., 2022). The development of vegetation in maritime Antarctica is limited to scatter ice-free areas located mainly in the coastal zone, which account for only a few percent (2%–5%) of the total area. The productivity and growth of the terrestrial tundra communities in the harsh Antarctic environment are controlled by a set of extreme environmental factors, like sub-zero temperatures, limited liquid water availability, a specific light regime, elevated ultraviolet-B radiation levels, desiccating and destructively strong winds, poorly developed soils with low organic matter and nutrient content, irregular nutrient distribution (from nutrient-deficient habitats to the ones extremely enriched in nutrients by, e.g., breeding colonies of seabirds), high salinity in many locations, and cryogenic processes (e.g., Convey, 1996; Znój et al., 2017; Łachacz et al., 2018). The presence of so many stress factors makes the Antarctic terrestrial ecosystems a mosaic of microhabitats colonized by highly heterogeneous and discontinuous communities (Smith, 1984; Block et al., 2009), currently threatened by biological invasions of alien species (Galera et al., 2018). Although so urgent, the detection and mapping of vegetation remain limited in the Antarctic environment. The mapping of the tundra communities in Antarctica has a short history, and usually small vegetation areas around research stations have been investigated (e.g., Lindsay, 1971; Smith, 1972). The classical field observation methods are laborious, generate a high cost of expeditions, high levels of human impact on the environment, and require specialized botanical knowledge. Also, vegetation mapping by image classification using remote sensing techniques remains limited in the Antarctic environment (Casanovas et al., 2015). Mainly due to the patchiness of terrestrial communities, its surface coverage can be sparse, with isolated individuals interspersed with bare ground and rocks, in small communities forming biocrusts on soil or rocks, or sometimes communities forming more extensive dense patches (Sotille et al., 2020). Obtaining satellite imagery material at the appropriate time of a vegetation stage and in sufficient qualities is still problematic, especially in the Antarctic Peninsula region, due to frequent occurrences of dense cloud cover and mist (Mustafa et al., 2012). Therefore, cost-effective and reliable wide-scale survey methods are required to accelerate assessments of Antarctic biodiversity (Wall et al., 2011; Casanovas et al., 2015).

A high spatial resolution is required to map most of the plant communities, and spectral bands in the short-wave infrared parts are crucial when distinguishing between bryophyte communities. This limits the use of the available satellite-based sensors. For example, Casanovas et al. (2015) used the Normalized Difference Vegetation Index (NDVI) and the matched filtering (MF) approach from Landsat data to study the vegetation distribution, however, they were unable to identify a pattern between the NDVI values and vegetation types. The NDVI is a standard tool in remote sensing monitoring of green biomass (Pettorelli et al., 2005). It takes values ranging from −1 to 1. The higher the value of this indicator, the higher the biomass content and better the condition of the vegetation (Rouse et al., 1974). The NDVI has gained popularity due to its ease of calculation based on two spectral ranges—a standardized range and high correlation with plant properties. The NDVI has found widespread use for assessing chlorophyll content, assessing plant stress, or identifying vegetation types (Geerken et al., 2005; Ozyavuz et al., 2015), and classifying land cover (Defries and Townshend, 1994) and detecting change for vegetation cover (Gandhi et al., 2015; Ju and Bohrer, 2022). It can be also used to estimate the density of green on an area of land (Weier and Herring, 2000).

Fretwell et al. (2011) used data covering Graham Land in the northern part of the Antarctic Peninsula and ground truthing in a test that found that 0.086% of the study area (74,468 km^2) showed a probability of vegetation presence of over 50%. In this study, the authors could not determine whether low NDVI values referred to partial coverage of mosses or a continuous coverage of lichens or algae, or if the pixel contained a significant area of vegetation-free soil. They found out that olivine-rich sub-aerial palagonite tuffs (Middle to Upper Miocene, James Ross Island Volcanic Group) return NDVI ratios that are within the range of values given by sparse vegetation. Detailed information from these studies is not available due to the images' limited spatial and spectral resolution and ground-truthing efforts. In such an environment, where terrestrial communities are dominated by species of low biomass and are characterized by irregular distribution, mid- or low-resolution images have limited use in the analysis of vegetation spatial coverage. Better results were obtained by Murray et al. (2010) and Andrade et al. (2018) who used, respectively, high-resolution IKONOS and QuickBird (four bands) imagery to map Antarctic vegetation, but they could not discriminate between lichens and bare ground and rocks. Whereas, Shin et al. (2014) successfully used linear unmixing of three endmember spectra (snow, rock/soil, and vegetation) extracted from QuickBird and KOMPSAT-2 imagery to map vegetation in Barton Peninsula. Furthermore, multispectral WorldView-2 satellite data having eight bands could capture most of the spectral characteristics of the cryptogam-dominating vegetation. These data have been applied by Power et al. (2020) to estimate microbial mat biomass based on the NDVI in Dry Valleys, Eastern Antarctic, and by Jawak et al. (2019) to map the vegetation of the Larsemann Hills and Schirmacher Oasis, by ensemble merging of the five top-performing methods (mixture-tuned matched filtering, matched filtering, matched filtering/Spectral Angle Mapper ratio, NDVI-2, and NDVI-4).

Sun et al. (2021) using WorldView-2 images and seven SMA models (FCLS, NM, FM, GBM, and three MNM-AVs) extracted vegetation data in the Fildes Peninsula, a part of the Nelson Peninsula (the King George Island) and Ardley Island. The newly proposed models achieved the best performance in abundance estimation of both mosses and lichens when compare to the previous study.

But, all space-borne methodological approaches share a common feature: the classifiers of vegetation communities perform well only when the spectral mixing in each image pixel is low (Calviño-Cancela and Martín-Herrero, 2016; Miranda et al., 2020). Therefore, these techniques do not work well with plant

communities in polar regions where tundra patches are scattered and discontinuous and may provide imagery with undesired degrees of spectral mixing with other classes.

More reliable specific vegetation maps may be provided through the incorporation of the classification procedure of intermediate scales of observation between ground and satellite levels. Obtaining data by the traditional aerial surveys with airplanes or helicopters (Furmańczyk and Ochyra, 1982) and currently unmanned aerial vehicles (UAVs) (e.g., Lucieer et al., 2014; Miranda et al., 2020; Váczi et al., 2020) is the solution. Although, UAV data can cover a much smaller area than do satellite images, their high resolution permits distinguishing many details related to the vegetation that are not evident in satellite images. Moreover, using the far-range UAVs and beyond the visual line of sight method allows exploring sites located away from the operation center. Therefore, the use of small UAVs in the terrestrial regions of Antarctica is increasing steadily. The successful application of the UAV methodology was already implemented in a multitude of objectives (Zmarz et al., 2018), like wildlife inventorying and monitoring (e.g.,: Goebel et al., 2015; Mustafa et al., 2018; Korczak-Abshire et al., 2019), periglacial landform mapping (Dąbski et al., 2017; Pina et al., 2019), glacier forelands (Dąbski et al., 2020; Kreczmer et al., 2021), and monitoring sea ice surface features (Li et al., 2019), among others (Pina and Vieira, 2022). The UAVs based vegetation studies in Antarctica are extremely helpful in providing additional details for mapping procedures (Turner et al., 2014), obtaining the micro-topography of moss beds (Lucieer et al., 2014), assessing the stress (Malenovský et al., 2017) and health status (Turner et al., 2019) of plants, or monitoring the changes taking place in vegetation over time (Jawak et al., 2019; Bollard et al., 2022).

The entire of Antarctica is governed internationally by the decisions of the Antarctic Treaty countries and has the status of a natural reserve (www.ats.aq/e/ep.htm). To protect this unique ecosystem, the Antarctic Specially Protected Area system was established (http://www.ats.aq/documents/recatt/Att004_e.pdf). Unfortunately, there has been no proper long-term monitoring system for these areas (Convey and Peck, 2019). Any conservation actions in Antarctica would depend on robust and reliable baseline information, which is still sparse for most regions. Therefore, the development of an effective and efficient vegetation monitoring system is currently a challenge.

The main aim of this study is to develop a UAV BVLOS–based NDVI map of the Antarctic Specially Protected Area No. 128, located on the west coast of Admiralty Bay on King George Island. A second aim is to relate the NDVI values to broad vegetation units. These maps will become important baseline maps for future studies on changes in vegetation cover.

2 Materials and methods

2.1 Study area

The study area is located on King George Island (62°10′S, 58°28′W), the largest volcanic island in the South Shetlands archipelago, with a surface area of around 1,310 km^2, of which more than 92% is covered by glaciers (Lim et al., 2014). The area covering the west coast of Admiralty Bay: the main body of Point Thomas Oasis with Henryk Arctowski Polish Antarctic Station (Arctowski) and the Antarctic Specially Protected Area No. 128 (ASPA 128) (Figure 1). The Point Thomas Oasis is one of the largest seasonally ice-free areas (approx. 25 km^2) in the maritime Antarctic region with relatively high temperatures during the austral summer (Kejna et al., 2013; Galera et al., 2015) and a constant flow of freshwater (Nędzarek et al., 2014) throughout most of the summer season (Kejna et al., 2013; Sancho et al., 2017). The area is supplied with nutrients by large animal colonies, especially penguins and pinnipeds (Sierakowski et al., 2017), and is under the constant influence of sea aerosols (Łachacz et al., 2018). Apart from temperature (mean annual air temperature is −1.8°C with a minimum of −32.3°C and a maximum of 16.7°C; Kejna, 1999; Kejna et al., 2013) and humidity (average relative humidity is 86.2%, with a monthly average precipitation of 33.0 mm; Kejna, 1999), the driving force that shapes tundra communities is the constantly blowing strong wind (average annual wind speed equals 6.6°ms^{-1}; Marsz and Styszyńska, 2000, with a maximum exceeding 65.0°ms^{-1}; Zwoliński, 2007). Winds cause desiccation stress and act as an abrasion factor. All these conditions favor the development of one of the most diverse tundra communities in maritime Antarctic (Furmańczyk and Ochyra, 1982; Ferrari et al., 2021). The tundra in this region is mainly made up of cryptogams: lichens—ca. 380 species (Øvstedal and Smith, 2001; Olech, 2004), fungi—over 100 species (Malosso et al., 2006), bryophytes—ca. 140 species (Ochyra et al., 2008), and 22 species of liverworts (Bednarek-Ochyra et al., 2000) and algae (Broady, 1996). These terrestrial ecosystems are extremely deficient in Magnoliophyta, of which only two native flowering plant species are found, and these are limited to the coastal parts of the west Antarctic Peninsula and its associating islands and archipelagoes: the Antarctic hairgrass *Deschampsia antarctica* Desv. (Poaceae) and pearlwort *Colobanthus quitensis* (Kunth) Bartl. (Caryophyllaceae) (Chwedorzewska et al., 2004; Androsiuk et al., 2015; Koc et al., 2018). In the study area, some of the plant communities had been described by Zarzycki (1993), Victoria et al. (2006, 2009), and Pereira et al. (2010), showing the spatial distribution of selected vegetation communities at Demay Point, in the southern parts of ASPA 128.

2.2 Data acquisition

BVLOS flights at an altitude of 350 m ASL were implemented by the PW-ZOOM fixed-wing UAV (Goetzendorf-Grabowski and Rodzewicz, 2016; Rodzewicz et al., 2017; Zmarz et al., 2018), which was equipped with an MP autopilot: MicroPilot (Stony Mountain, Canada). The operation was performed by a three-member team: remote control operator (RC), ground control station operator (GCS), and maintenance operator (all had BVLOS licenses issued by national authorities). Two separate flights were implemented to obtain the data that were required to calculate the NDVI: one with the R-G-B camera (Canon EOS 700D + 35 mm lens) and another with the B-G-NIR camera (blue channel, visible blue light—green channel, visible green light—NIR from 680 nm to 800 nm; Canon EOS REBEL T5i + 35 mm lens). The B-G-NIR camera uses blue as the absorption channel and NIR as the reflection channel. The two flights were undertaken on 10–11 November 2016 at an altitude of 350 m ASL and obtained

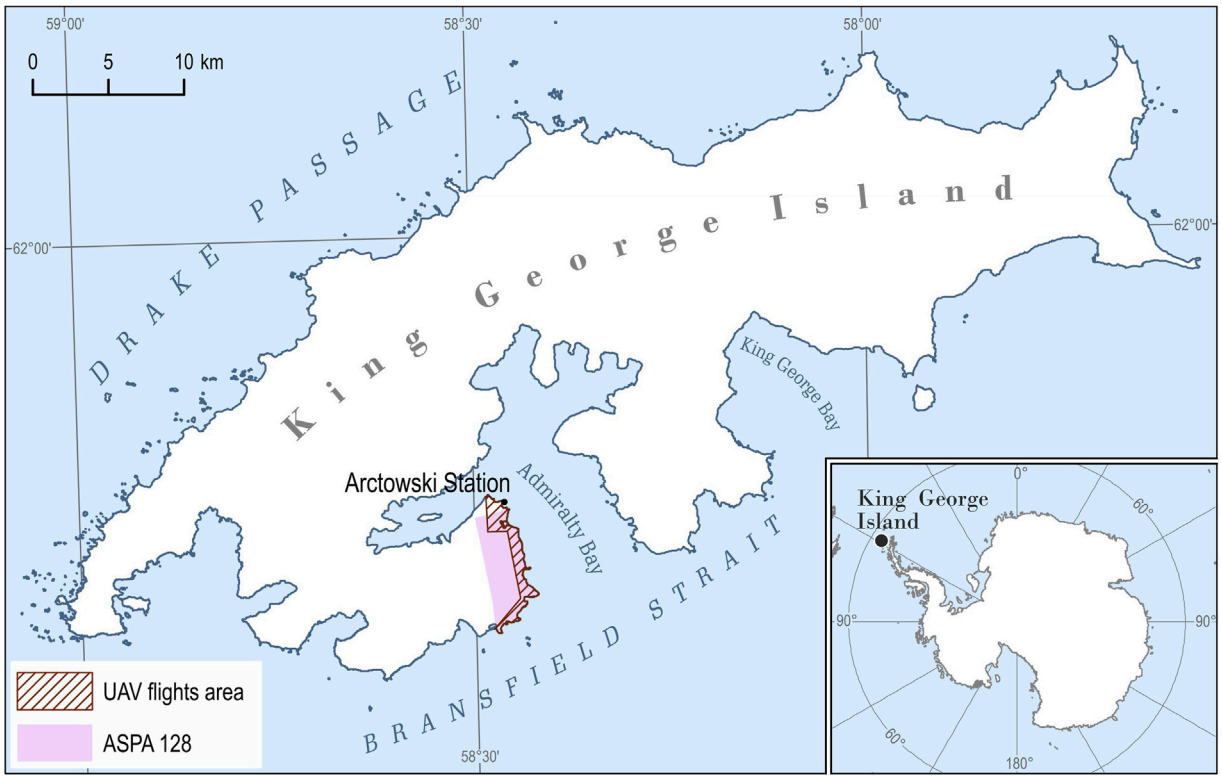

FIGURE 1
The study area located on King George Island, South Shetlands Archipelago, the Western Antarctic; UAV flights area (7.5 km^2) marked in the hatch; and Antarctic Specially Protected Area No. 128 marked in purple [The coastline of the island on the basis of the SCAR King George Island geographic information system project (http://www.kgis.scar.org/)].

data at a spatial resolution of <5 cm GSD and DEM of 0.25 m. The area for which the data was obtained amounted to 7.5 km^2 (Figure 1). The time that each flight took was 2 h and 2.5 h, respectively. All images that were obtained had georeferences (X, Y, and Z) registered by the autopilot logger that was mounted on the UAV. The GPS Receiver GP-E2 was used for the geolocation of images allowing for horizontal accuracy of measurement <5 m. The data in the form of single images were processed into an orthophoto map in the Universal Transverse Mercator system, zone 21 S (EPSG: 32721). The two sensors were matched into a single four-bands file (R-G-B-NIR) using the layer stacking method in the ENVI software. Then, the normalized difference vegetation index (NDVI), which reflects the vegetation coverage and biomass, was calculated.

2.3 Dividing NDVI values to vegetation units

After processing the NDVI map, we aimed to divide the NDVI values into broad vegetation units. The vegetation was studied in January and February 2016, the austral summer before the acquisition of the NDVI image. The percent cover of each species and for impediment was estimated in altogether 99 1 × 1 m^2 phytosociological relevés. The relevés were placed systematically every 10 m in the north–south direction along three transects (Figure 4). Then, to reveal the main vegetation units in the area, the relevés were clustered by Euclidean distances based on the species cover of each relevé and a dendrogram was produced (Figure 2). For the groups separated by the clustering, the number of relevés (n) was taken, and the percentage cover (c) and frequency (f) of the main species were described for each group. We also calculated the mean NDVI value for each relevé and thereby found the NDVI range for each group. This range was used in the main division of the NDVI values into vegetation units.

However, the transects with relevés did not cover a penguin colony and protected wetland, these areas have some differences in vegetation composition when compared with the areas that the transects cover, and validation data for these areas were obtained separately.

In the Point Thomas penguin colony area, east of the Arctowski Station (Rakusa Point), the cliffs and rocks close to the sea are enriched by guano and are dominated by epilithic lichen with orange thallus (mainly, *Caloplaca regalis*, *C. sublobulata*, and *Xanthoria elegans*). A total of 50 polygons of these lichens were identified on the RGB image and the NDVI values were calculated. In this penguin colony, the green algae *Prasiola crispa* locally dominates the ground. Also for these algae, 50 polygons were identified on the RGB image and the NDVI values were calculated.

Furthermore, just east of the Arctowski Station, there is a small (<0.08 km^2) very vulnerable protected wetland (Jasnorzewski Gardens), with a dense vegetation cover in mainly standing waters (Figure 4). To avoid walking in this area, we instead

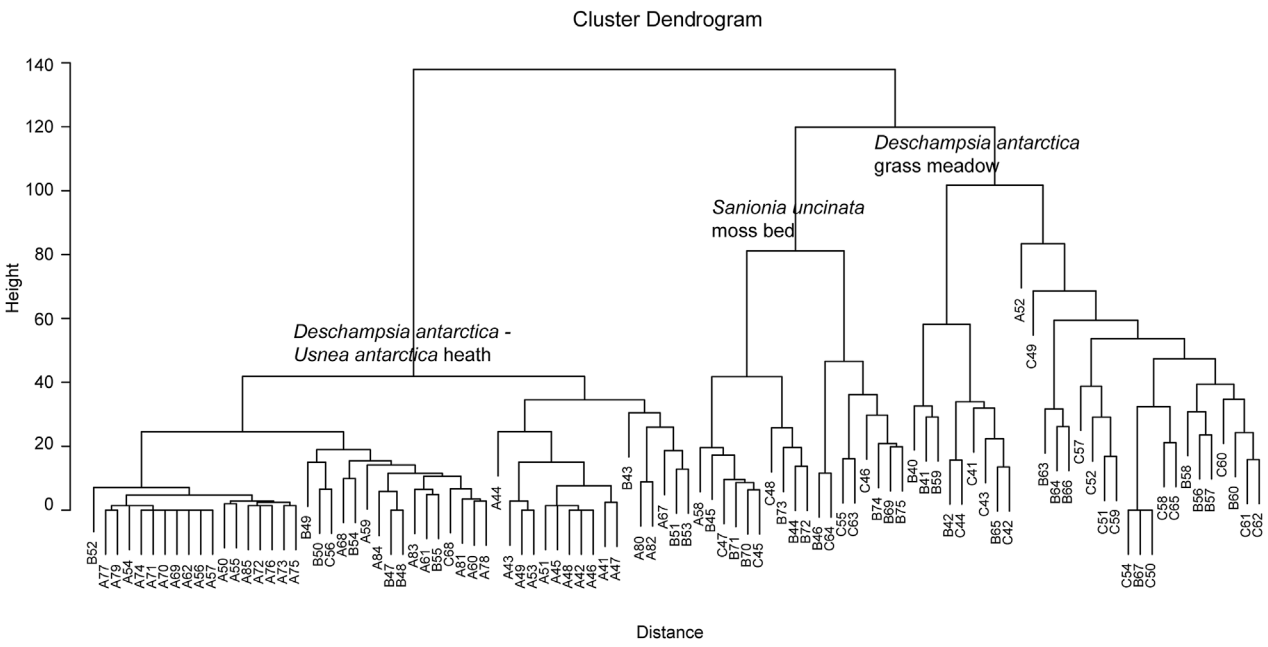

FIGURE 2
Dendrogram. Euclidean distance of 99 relevés.

georeferenced a previous vegetation map interpreted from an ordinary paper of a photo captured from a helicopter back in 1979 (Furmańczyk and Ochyra, 1982). Then, the NDVI values from our flight were extracted for the vegetation types and species composition of the communities in the old map.

3 Results

3.1 NDVI map

Altogether ASPA 128 covers 17.5 km^2, and 9.2 km^2 (53%) is covered by glaciers (Pudełko et al., 2018). The ice-free area of ASPA 128 is 8.2 km^2 (47%) and most of this was mapped with the NDVI (Figure 3). Altogether 7.5 km^2 was mapped with 4 × 4 cm^2 pixel resolution that covered the entire coastline and most of the ice-free areas of the ASPA 128. The map shows that 2.35 km^2 have NDVI values above 0.12, which we use as a threshold for vegetation cover (for details, please refer Section 3.2). Continuous areas with NDVI above 0.12 were mainly found in the southern parts at Demay Point and northern parts closer to the Arctowski.

3.2 Vegetation units

The clustering of the 99 relevés separated three main groups on Euclidian distance of 100 (Figure 4). In the left group (*Deschampsia antarctica—Usnea antarctica* heath) 48 of the 51 relevés had NDVI values in the range of 0.05–0.154. The remaining three relevés had NDVI values of 0.030, 0.234, and 0.286. However, relevés with <5% vegetation cover mainly had NDVI values below 0.120. For the '*Sanionia uncinata* moss bed' group, the 18 relevés had NDVI values in the range of 0.235–0.384, but 14 of these were in the NDVI range of 0.252–0.370. For the '*Deschampsia antarctica* grass meadow' group, 26 of the 30 relevés had NDVI values in the range of 0.163–0.298. The relevés did not cover the penguin colony. A total of 50 polygons from RGB images of the epilithic lichen with orange thallus show NDVI values mainly in the range of 0.25–0.30. In addition, 50 polygons of the green algae (*Prasiola crispa*) had NDVI values in the range of 0.17–0.30.

We also analyzed the NDVI values of the plant communities described in the old vegetation map of the protected wetland (Furmańczyk and Ochyra, 1982), and most of these dense moss carpets that were found had high NDVI values of mainly above 0.37.

Based on the data set mentioned above, we divided the NDVI map into four broad vegetation units, where the exact threshold in NDVI values between the units was subjectively chosen due to some overlaps in relevés NDVI values. The 'dense moss carpet' unit had NDVI values >0.37. However, the NDVI threshold of 0.37 was subjectively chosen, and the group had some overlap with the related unit below. The '*Sanionia uncinata* moss bed' unit occurs in the NDVI range of 0.27–0.37. This unit also has a gradual transition in NDVI values to the group below. The '*Deschampsia antarctica* grass meadow' has NDVI values in the range of 0.22–0.26. The '*Deschampsia antarctica–Usnea antarctica* heath' has NDVI values in the range of 0.12–0.22. The lower values were classified as those without vegetation.

3.2.1 Dense moss carpets

This unit displays different bryophyte plant communities, which make thick, dense moss carpets in moist to wet areas, partly protected from the wind. In more permanently wet (standing water) parts, hydrophilous bryophytes such as *Warnstorfia*

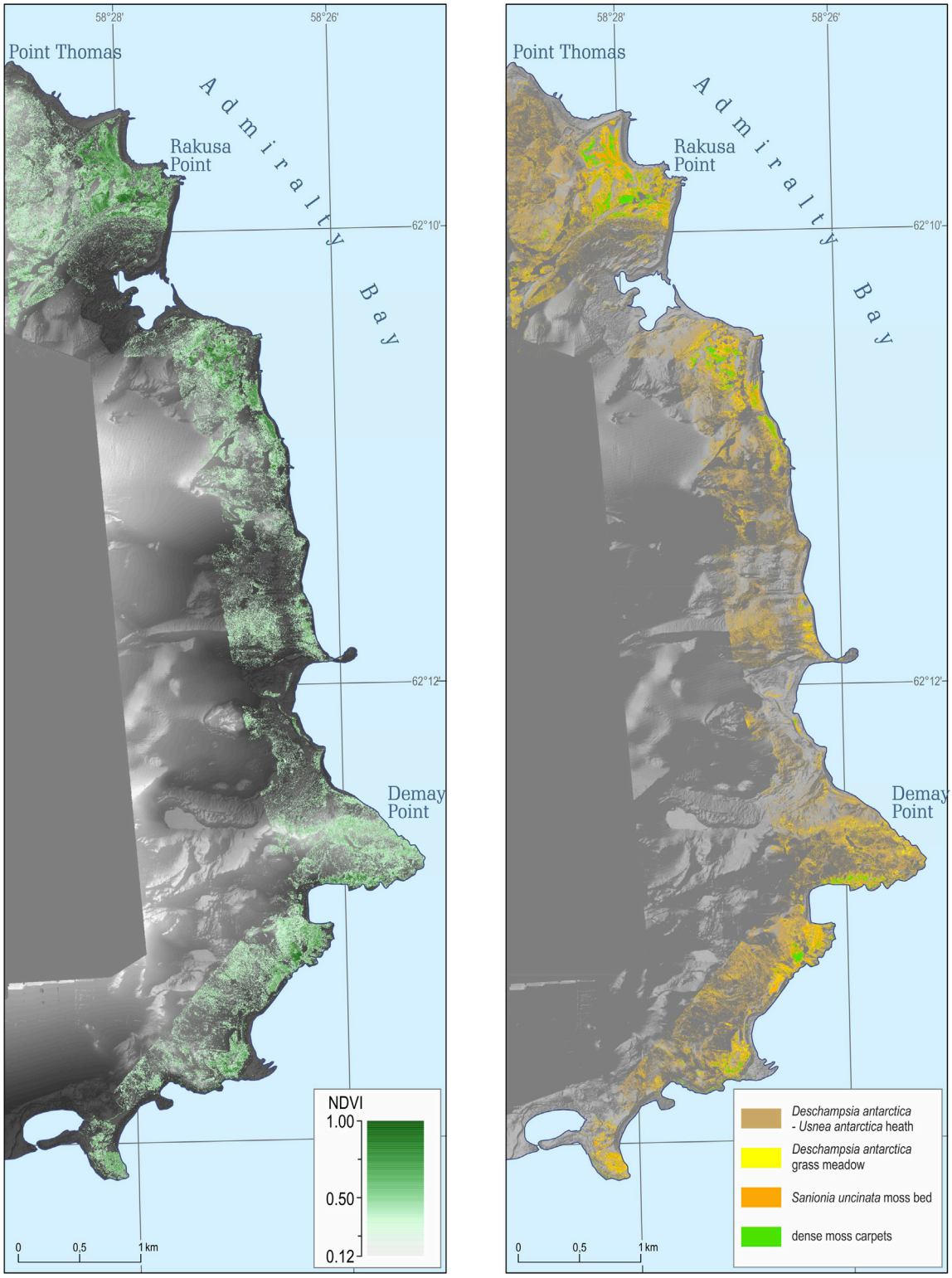

FIGURE 3
NDVI map (left) of the western shore of Admiralty Bay, King George Island, South Shetlands Archipelago, and ultra-high resolution vegetation map (right) covering an area of 7.5 km^2 (Source data: DEM and orthophoto based on the original UAV-derived data).

sarmentosa and *W. fontinaliopsis* locally dominate. *Bryum pseudotriquetrum* is widespread in the study area, particularly along creeks and in concave parts. Some of the thickest carpets of *Sanionia uncinate* are also included in this class. This unit covered 0.14 km^2 (0.8 % ASPA 128) and is mainly found at lower altitudes (<30 m. ASL), and 89% of the unit occurs in flat areas.

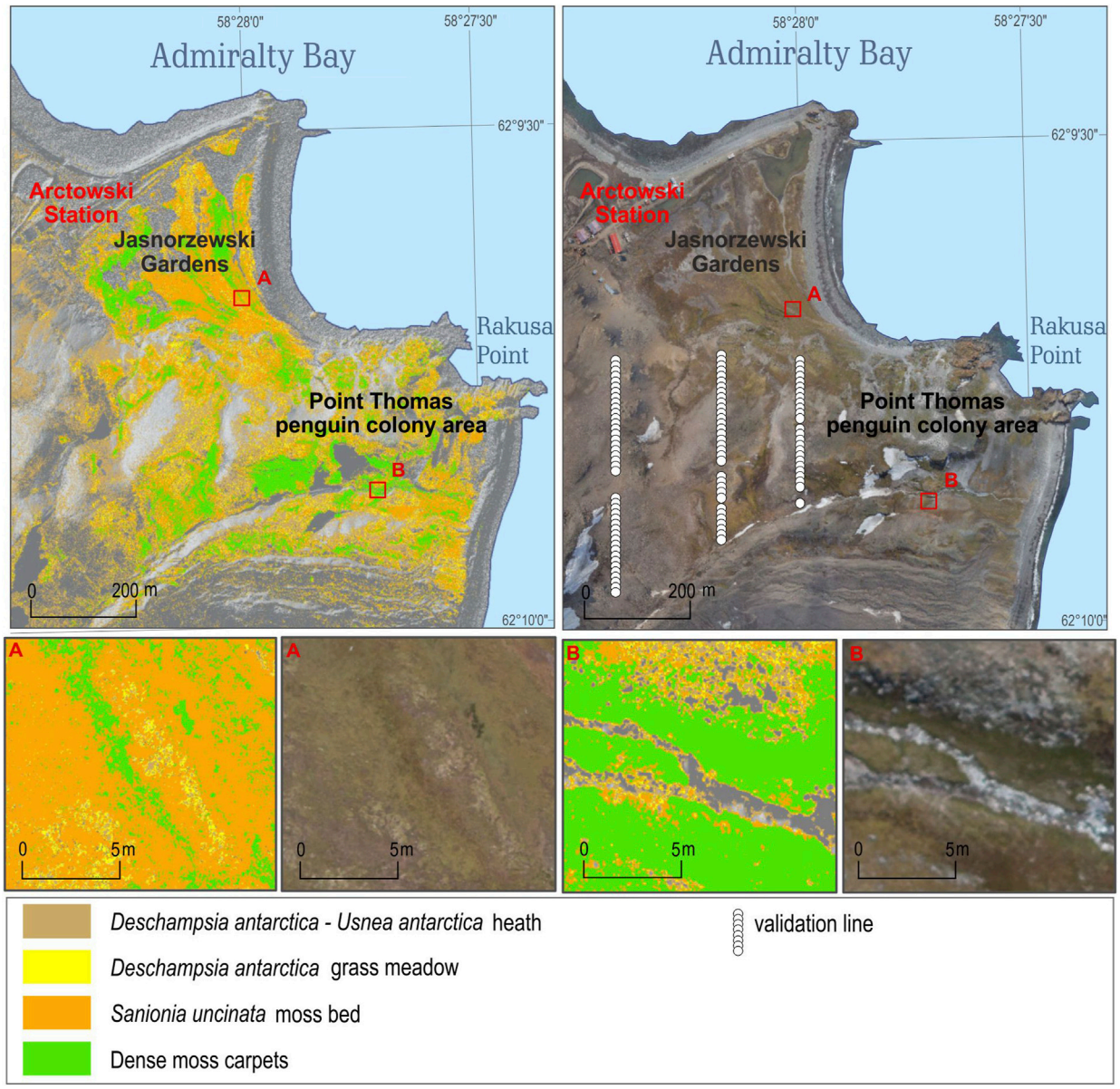

FIGURE 4
Jasnorzewski Gardens and Point Thomas penguin colony vegetation map based on UAV-derived images. The map also shows the location of the 99 relevés (white dots) which were placed systematically every 10 m along three transects.

3.2.2 *Sanionia uncinata* moss bed

This unit is dominated by the widespread bryophyte *Sanionia uncinata*. From the Euclidean clustering, 18 relevés (n = 18) show that *Sanionia uncinata* occurs in every relevé (frequency, f = 100) used to describe this unit and has an average percentage cover (c) of 64%. This bryophyte often forms dense homogeneous carpets, but with a gradual transition to dominants of *Deschampsia antarctica* (f = 80, c = 7%). Also frequently found are the bryophytes *Polytrichastrum alpinum* (f = 50) and *Polytrichum juniperinum* (f = 28), but these cover less than 2% each. The relevés show that some of the moss were classified as dead (c = 14%). The unit is widespread in ASPA 128 and covers 0.31 km^2 (1.7% of ASPA 128, and is often dominated in less wind-exposed areas.

3.2.3 *Deschampsia antarctica* grass meadow

Together with *S. uncinata*, *D. antarctica* is the most widespread species in the study area, and these are often associated with each other. The 30 relevés (n = 30) show a mean cover (c) of 30% of *D. antarctica* in this unit, in addition to dead moss and grass cover altogether covering 15%. The unit is rather homogeneous, but some other species are also found, such as the lichens *Ochrolechia frigida* (f = 63, c = 6%) and *Usnea antarctica* (f = 43, c = 6%), Antarctic pearlwort (*Colobanthus quitensis*) (f = 37, c = 2%), *Sanionia uncinata* (f = 47, c = 6%), the brownish bryophytes *Polytrichastrum alpinum* (f = 20), *Polytrichum juniperinum* (f = 23), and *P. piliferum* (f = 23), but the latter three cover less than 2% each. The unit dominates often in slightly convex, north-facing

slopes. In addition, since *D. antarctica* tolerates high salinity, the unit occurs in the littoral zone, that is, areas directly influenced by marine aerosols and/or over-manured by birds' feces. In the penguin colony area, some of the algae *Prasiola crispa* and epilithic lichen with orange thallus are also included in this unit. The unit covers 0.24 km^2 (1.3% of ASPA 128).

3.2.4 *Deschampsia antarctica–Usnea antarctica* heath

This unit is characterized by high species diversity, sparse vegetation cover, and the visually dominated lichen *Usnea antarctica*. The unit has a discontinued vegetation cover, and gravel and open soil cover altogether of 85%. The unit has a high species diversity of lichens, but only *U. antarctica* (f = 35, c = 5%) and *Ochrolechia frigida* (f = 20, c = 1%) occur frequently. *D. antarctica* is the most frequent species (f = 58, c = 1%), but it covers far less than *U. antarctica* does. *C. quitensis* occurs frequently (f = 24) but has an insignificant cover (c = 0.2%). The unit also has a high diversity of bryophytes, which occurs in all of the 51 (n = 51) relevés, and as in the previous units, the *Sanionia uncinata*, *Polytrichastrum alpinum*, *P. juniperinum,* and *P. piliferum* are among the most frequent bryophytes. This unit is widespread at altitudes above the previously described units (mean height 58 m H ellipse), and mainly occurs in areas characterized by less snow cover which is often slightly convex, dry, and exposed. These areas are rarely influenced by pinnipeds and penguin disturbances. In addition, the unit includes a variety of plant communities at lower altitudes, all with only scattered vegetation cover, and some of the epilithic lichens with orange thallus in the penguin colony. This is the most commonly mapped unit and covers 1.66 km^2 (9.4% of ASPA 128).

4 Discussion

In our work, we laid the foundations for BVLOS UAV–based monitoring vegetation on the western shore of Admiralty Bay of King George Island (South Shetlands). The vegetation in the 7.5 km^2 area was mapped with ultra-high resolution and is to our knowledge among the largest UAV-based vegetation maps in maritime Antarctic.

The 99 relevés used in this study were originally meant for accuracy assessment for a vegetation map based on a UAV-mounted multispectral camera. However, during the 1 month from 23 January to 24 February 2016, not a single day had usable flight conditions (too strong wind), or there was too much fresh snow on the ground. This illustrates the challenges in vegetation mapping in maritime Antarctic. Instead, the relevés were used to interpret the later obtained NDVI map to identify some broad vegetation units, but then without the possibilities for accuracy assessment. However, three of the four mapped units were based on the clustering of relevés, and with the separation of the units at an Euclidean distance of 100, some very distinct units appear. Based on this division, the cover and frequency of the species in these three units were taken. Hence, it is reasonable to believe that in most cases, the four mapped units described in this study are reasonably accurate. However, with some exceptions, within the penguin colony, rocks are covered with ornithocoprophilous, epilithic lichen with orange thallus, and on the ground, the green algae *Prasiola crispa* often dominates. These unusual cases mainly occur within the mapped units '*Deschampsia antarctica* grass meadow' and '*Deschampsia antarctica–Usnea antarctica* heath,' respectively. This is due to the spectral similarities between *P. crispa* and *D. antarctica* in both the red and NIR bands (Calviño-Cancela and Martín-Herrero, 2016) and thereby similarities in the NDVI values, and the relatively high reflectance in the red band to the epilithic lichen with orange thallus *Caloplaca* sp. and *Xanthoria* sp. (Calviño-Cancela and Martín-Herrero, 2016). Furthermore, scattered occurrences of the lichen *Usnea antarctica* have been noted at higher altitudes that did not give any significant signal in the NDVI value and were not mapped, as the NDVI values were below 0.12. This suggests that the NDVI is not useful in mapping spots of brightly colored lichens like *Usnea antarctica*, probably due to the high reflectance in both the visible and NIR bands of such lichens (Calviño-Cancela and Martín-Herrero, 2016; da Rosa et al., 2022).

Moreover, since we used an ordinary GPS for determining the location of the relevés, there is an accuracy issue, and by adding the accuracy error in the NDVI map, the NDVI values extracted from the 1 × 1 m^2 relevés would not fit perfectly with the NDVI map. However, due to the gradual changes in vegetation/NDVI in the rather flat landscape, this inaccuracy does not influence the main results when dividing the NDVI values into vegetation units. The extracted NDVI values from the 6 × 6 m^2 plots correlate significantly with the NDVI values from the 1 × 1 m^2 relevés (r^2 = 0.95, n = 99, and p = 5.34^{-65}), indicating that the inaccuracy in location/NDVI map does not influence the results. Since no other maps of the vegetation in ASPA 128 exist, except for the very small and old vegetation map of the protected wetland (Furmańczyk and Ochyra, 1982) and a coarse vegetation map of Demay Point (Pereira et al., 2010), this is a huge step forward. The presented NDVI map and vegetation map show the current status of the vegetation and will be highly useful in the study of the ongoing environmental change, particularly the changes in vegetation cover, and for the conservation of the ASPA 128. The presented map could also be used as validation, giving a potential baseline for satellite-based vegetation mapping (Miranda et al., 2020), monitoring, and assessment of even larger areas. Future UAV-based vegetation mapping of the area has to use cameras with more spectral bands in order to better separate plant communities at a more detailed level when compared with this level of mapping. Alternatively, a recent geographic object-based image analysis of UAV data in a comparable area in maritime Antarctic has shown promising results (Sotille et al., 2022), although they have not separated the different bryophyte species, which dominate in our study area.

Under the strongest forcing scenario, projections predict not only a tripling (300% increase) of ice-free areas over parts of the Antarctic Peninsula as a result of more than 50 additional-degree days above freezing by the end of the 21st century (Lee et al., 2017) but also the increases in precipitation (Turner et al., 2019), permafrost warming, and active layer thickening (Guglielmin et al., 2014; Hrbăcek et al., 2021). This means that groundwater will remain available in the upper parts of the soil throughout the season. In maritime Antarctic, the development of terrestrial communities is controlled by extreme environmental conditions, with the crucial role of liquid water availability, rather than biotic interactions (Convey & Peck, 2019). Such communities are expected to be very sensitive to changes in climate and consequential processes (Bargagli, 2005; Frenot et al., 2005). Since more cumulative energy is available to terrestrial biota (both in terms of the absolute positive temperature achieved and cumulative degree days) the

consequences are thought to include increased diversity (also by migrating some species from temperate zones to maritime Antarctic), biomass, trophic complexity, and rapid colonization of newly deglaciated terrains, all of which enable the development of a more complex ecosystem (Siegert et al., 2019; Weisleitner et al., 2020). Thus, most likely, further complications will arise from the complexity of those species interactions (Molina-Montenegro et al., 2019). While the contemporary Antarctic biota shows the ability to survive abiotic environmental extremes, its competitive abilities are very poorly developed, and even whole communities are vulnerable to increased competition from opportunistic invaders (Galera et al., 2019; Colesie et al., 2022). These observed changes are an area of concern for the Antarctic Treaty System, whose decisions to protect the Antarctic ecosystem are based on the best available reliable scientific data. As described here, the UAV BVLOS operations proved to be very robust in gathering valuable qualitative and quantitative data that are necessary for monitoring distant and isolated polar environments. It is important to notice the differences between the multi-rotor and fixed-wing platforms, and between the visual line of sight and beyond visual line of sight operations. Multi-rotor and fixed-wing platforms are completely different solutions with extremely different performances, but also with different functional and operational requirements. That is why, it is so important to precisely define tasks in order to choose the optimal system. The factors which significantly affect the efficiency of UAV operations are flight time, flight speed, type of drive (combustion or electric engine), possible distance to be covered by one flight, telemetric range, and payload. Unmanned multi-rotor platforms are mainly used for small, even very small areas located close to the take-off/landing point and in favorable calm weather conditions. For tasks requiring longer flight time and range, fixed-wing platforms turn out to be much more effective especially in the BVLOS operation, as was proved here, as in previous studies (see Zmarz et al., 2018; Korczak-Abshire et al., 2019; Dąbski et al., 2020). Data described here can be applied in the conservation of the protected areas and further studies of environmental changes.

5 Conclusion

The BVLOS operation of the fixed-wing PW-ZOOM UAV, equipped with an R-G-B camera and a B-G-NIR camera allowed obtaining data for the development of a vegetation map in the Antarctic Specially Protected Area No. 128. The flights were made for an area of 7.5 km^2 in a relatively short time (one flight lasted for 2 h and the second flight for 2.5 h). Using BVLOS operations in Antarctic conditions proved to be an effective method of obtaining data in hard-to-reach areas. Advantages include short data acquisition time, long range of BVLOS flights, and few crew members involved in servicing the BVLOS flights. Furthermore, the proposed method of acquiring high-resolution data fills the gap between satellite data and data obtained by traditional field-based methods.

Data availability statement

The data: reléve coordinates, NDVI reléve values, NDVI map as pdf, supporting the conclusion of this article will be made available by the authors, without undue reservation.

Author contributions

AZ and SK conceived the ideas and designed the methodology; AZ, SK, MK-A, and KC collected the data; AZ, SK, MK, MK-A, IG, IK, and KC analyzed the data; AZ, SK, MK, MK-A, and KC led the writing of the manuscript. All authors contributed critically to the drafts and gave final approval for publication.

Funding

The research was conducted as part of the project "A novel approach to monitoring the impact of climate change on Antarctic ecosystems (MONICA)" funded by the Polish–Norwegian Research Programme operated by the National Centre for Research and Development under the Norwegian Financial Mechanism 2009–2014 in the frame of Project Contract No. 197810. The data used in the study were collected at the Henryk Arctowski Polish Antarctic Station.

Conflict of interest

The authors declare that the research was conducted in the absence of any commercial or financial relationships that could be construed as a potential conflict of interest.

Publisher's note

All claims expressed in this article are solely those of the authors and do not necessarily represent those of their affiliated organizations, or those of the publisher, editors, and reviewers. Any product that may be evaluated in this article, or claim that may be made by its manufacturer, is not guaranteed or endorsed by the publisher.

References

Andrade, A. M. De, Michel, R. F. M., Bremer, U. F., Schaefer, C. E. G. R., and Simões, J. C. (2018). Relationship between solar radiation and surface distribution of vegetation in Fildes Peninsula and Ardley Island, maritime Antarctica. *Int. J. Remote Sens.* 39 (8), 2238–2254. doi:10.1080/01431161.2017.1420937

Androsiuk, P., Chwedorzewska, K., Szandar, K., and Giełwanowska, I. (2015). Genetic variability of *Colobanthus quitensis* from King George Island (Antarctica). *Pol. Polar Res.* 36 (3), 281–295. doi:10.1515/popore-2015-0017

Bargagli, R. (2005). *Antarctic ecosystems, environmental contamination, climate change, and human impact. Ecological studies, 175* M. M. Caldwell, G. Heldmaier, R. B. Jackson, O. L. Lange, H. A. Mooney, E. D. Schulze, et al. (Heidelberg, Germany: U., Friedmut Kröner), 393.

Bednarek-Ochyra, H., Váňa, J., Ochyra, R., and Lewis Smith, R. I. (2000). *The liverwort flora of Antarctica*. Cracow: Polish Academy of Sciences, Institute of Botany, 236.

Block, W., Lewis Smith, R. I., and Kennedy, A. D. (2009). Strategies of survival and resource exploitation in the Antarctic fellfield ecosystem. *Biol. Rev.* 84 (3), 449–484. doi:10.1111/j.1469-185X.2009.00084.x

Bollard, B., Doshi, A., Gilbert, N., Poirot, C., and Gillman, L. (2022). Drone technology for monitoring protected areas in remote and fragile environments. *Drones* 6 (2), 42. doi:10.3390/drones6020042

Broady, P. A. (1996). Diversity, distribution and dispersal of Antarctic terrestrial algae. *Biodivers. Conservation* 5 (11), 1307–1335. doi:10.1007/BF00051981

Calviño-Cancela, M., and Martín-Herrero, J. (2016). Spectral discrimination of vegetation classes in ice-free areas of Antarctica. *Remote Sens.* 8 (10), 856–915. doi:10.3390/rs8100856

Casanovas, P., Black, M., Fretwell, P., and Convey, P. (2015). Mapping lichen distribution on the Antarctic Peninsula using remote sensing, lichen spectra and photographic documentation by citizen scientists. *Polar Res.* 34 (1), 25633. doi:10.3402/polar.v34.25633

Chwedorzewska, K. J., Bednarek, P. T., and Puchalski, J. (2004). Molecular variation of antarctic grass *Deschampsia Antarctica* Desv. From King George Island (Antarctica). *Acta Soc. Bot. Pol.* 73 (1), 23–29. doi:10.5586/asbp.2004.004

Colesie, C., Walshaw, C. V., Sancho, L. G., Davey, M. P., and Gray, A. (2022). Antarctica's vegetation in a changing climate. *WIREs Clim. Change* 14, e810. doi:10.1002/wcc.810

Convey, P., and Peck, L. S. (2019). Antarctic environmental change and biological responses. *Sci. Adv.* 5 (11), eaaz0888. doi:10.1126/sciadv.aaz0888

Convey, P. (1996). The influence of environmental characteristics on life history attributes of Antarctic terrestrial biota. *Biol. Rev.* 71, 191–225. doi:10.1111/j.1469-185x.1996.tb00747.x

da Rosa, C. N., Pereira Filho, W., Bremer, U. F., Putzke, J., de Andrade, A. M., Kramer, G., et al. (2022). Spectral behavior of vegetation in Harmony Point, Nelson Island, Antarctica. *Biodivers. Conservation* 31, 1867–1885. doi:10.1007/s10531-022-02408-7

Dąbski, M., Zmarz, A., Pabjanek, P., Korczak-Abshire, M., Karsznia, I., and Chwedorzewska, K. J. (2017). UAV-Based detection and spatial analyses of periglacial landforms on Demay Point (King George Island, South Shetland Islands, Antarctica). *Geomorphology* 290, 29–38. doi:10.1016/j.geomorph.2017.03.033

Dąbski, M., Zmarz, A., Rodzewicz, M., Korczak-Abshire, M., Karsznia, I., Lach, K., et al. (2020). Mapping glacier forelands based on UAV BVLOS operation in Antarctica. *Remote Sens.* 12 (4), 630. doi:10.3390/rs12040630

Defries, R. S., and Townshend, J. R. (1994). NDVI-derived land cover classifications at a global scale. *Int. J. Remote Sens.* 15 (17), 3567–3586. doi:10.1080/01431169408954345

Ferrari, F. R., Schaefer, C. E. G. R., Pereira, A. B., Thomazini, A., Schmitz, D., and Francelino, M. R. (2021). Coupled soil-vegetation changes along a topographic gradient on King George Island, maritime Antarctica. *Catena* 198, 105038. doi:10.1016/j.catena.2020.105038

Frenot, Y., Chown, S. L., Whinam, J., Selkirk, P. M., Convey, P., Skotnicki, M., et al. (2005). Biological invasions in the Antarctic: Extent, impacts and implications. *Biol. Rev.* 80, 45–72. doi:10.1017/s1464793104006542

Fretwell, P. T., Convey, P., Fleming, A. H., Peat, H. J., and Hughes, K. A. (2011). Detecting and mapping vegetation distribution on the Antarctic Peninsula from remote sensing data. *Polar Biol.* 34 (2), 273–281. doi:10.1007/s00300-010-0880-2

Furmańczyk, K., and Ochyra, R. (1982). Plant communities of the Admiralty Bay region (King George Island, South Shetland Islands, Antarctic) I. Jasnorzewski Gardens. *Pol. Polar Res.* 3 (1–2), 25–39.

Galera, H., Chwedorzewska, K. J., Korczak-Abshire, M., and Wódkiewicz, M. (2018). What affects the probability of biological invasions in Antarctica? Using an expanded conceptual framework to anticipate the risk of alien species expansion. *Biodivers. Conservation* 27, 1789–1809. doi:10.1007/s10531-018-1547-5

Galera, H., Chwedorzewska, K. J., and Wódkiewicz, M. (2015). Response of *Poa annua* to extreme conditions: Comparison of morphological traits between populations from cold and temperate climate conditions. *Polar Biol.* 38 (10), 1657–1666. doi:10.1007/s00300-015-1731-y

Galera, H., Rudak, A., Czyż, E. A., Chwedorzewska, K. J., Znój, A., and Wódkiewicz, M. (2019). The role of the soil seed store in the survival of an invasive population of *Poa annua* at Point Thomas Oasis, King George Island, maritime Antarctica. *Glob. Ecol. Conservation* 19, e00679. doi:10.1016/j.gecco.2019.e00679

Gandhi, G. M., Parthiban, S., Thummalu, N., and Christy, A. (2015). NDVI: Vegetation change detection using remote sensing and GIS — a case study of vellore district. *Procedia Comput. Sci.* 57, 1199–1210. doi:10.1016/j.procs.2015.07.415

Geerken, R., Zaitchik, B., and Evans, J. P. (2005). Classifying rangeland vegetation type and coverage from NDVI time series using Fourier Filtered Cycle Similarity. *Int. J. Remote Sens.* 26 (24), 5535–5554. doi:10.1080/01431160500300297

Goebel, M. E., Perryman, W. L., Hinke, J. T., Krause, D. J., Hann, N. A., Gardner, S., et al. (2015). A small unmanned aerial system for estimating abundance and size of Antarctic predators. *Polar Biol.* 38 (5), 619–630. doi:10.1007/s00300-014-1625-4

Goetzendorf-Grabowski, T., and Rodzewicz, M. (2016). Design of UAV for photogrammetric mission in Antarctic area. *Proc. Institution Mech. Eng. Part G J. Aerosp. Eng.* 231 (9), 1660–1675. doi:10.1177/0954410016656881

Guglielmin, M., Dalle Fratte, M., and Cannone, N. (2014). Permafrost warming and vegetation changes in continental Antarctica. *Environ. Res. Lett.* 9 (4), 045001. doi:10.1088/1748-9326/9/4/045001

Hrbăcek, F., Vieira, G., Oliva, M., Balks, M., Guglielmin, M., Pablo, M. A., et al. (2021). Active layer monitoring in Antarctica: An overview of results from 2006 to 2015. *Polar Geogr.* 44 (3), 217–231. doi:10.1080/1088937X.2017.1420105

Jawak, S. D., Luis, A. J., Fretwell, P. T., Convey, P., and Durairajan, U. A. (2019). Semiautomated detection and mapping of vegetation distribution in the Antarctic environment using spatial-spectral characteristics of WorldView-2 imagery. *Remote Sens.* 11 (16), 1909. doi:10.3390/rs11161909

Ju, Y., and Bohrer, G. (2022). Classification of wetland vegetation based on NDVI time series from the HLS dataset. *Remote Sens.* 14 (9), 2107. doi:10.3390/rs14092107

Kejna, M. (1999). Air temperature on King George Island, South Shetland Islands, Antarctica. *Pol. Polar Res.* 20 (3), 183–201.

Kejna, M., Araźny, A., and Sobota, I. (2013). Climatic change on King George Island in the years 1948 – 2011. *Pol. Polar Res.* 34 (2), 213–235. doi:10.2478/popore-2013-0004

Koc, J., Androsiuk, P., Chwedorzewska, K. J., Cuba-Díaz, M., Górecki, R., and Giełwanowska, I. (2018). Range-wide pattern of genetic variation in *Colobanthus quitensis*. *Polar Biol.* 41 (12), 2467–2479. doi:10.1007/s00300-018-2383-5

Koerich, G., Fraser, C. I., Lee, C. K., Morgan, F. J., and Tonkin, J. D. (2022). Forecasting the future of life in Antarctica. *Trends Ecol. Evol.* 38, 24–34. doi:10.1016/j.tree.2022.07.009

Korczak-Abshire, M., Zmarz, A., Rodzewicz, M., Kycko, M., Karsznia, I., and Chwedorzewska, K. J. (2019). Study of fauna population changes on Penguin Island and Turret Point Oasis (King George Island, Antarctica) using an unmanned aerial vehicle. *Polar Biol.* 42 (1), 217–224. doi:10.1007/s00300-018-2379-1

Kreczmer, K., Dąbski, M., and Zmarz, A. (2021). Terrestrial signature of a recently-tidewater glacier and adjacent periglaciation, Windy Glacier (South Shetland Islands, Antarctic). *Front. Earth Sci.* 9, 671985. doi:10.3389/feart.2021.671985

Łachacz, A., Kalisz, B., Giełwanowska, I., Olech, M., Chwedorzewska, K. J., and Kellmann-Sopyła, W. (2018). Nutrient abundance and variability from soils in the coast of King George Island. *J. Soil Sci. Plant Nutr.* 18 (2), 294–311. doi:10.4067/S0718-95162018005001101

Lee, J. R., Raymond, B., Bracegirdle, T. J., Chades, I., Fuller, R. A., Shaw, J. D., et al. (2017). Climate change drives expansion of Antarctic ice-free habitat. *Nature* 547 (7661), 49–54. doi:10.1038/nature22996

Li, T., Zhang, B., Cheng, X., Westoby, M. J., Li, Z., Ma, C., et al. (2019). Resolving fine-scale surface features on polar sea ice: A first assessment of uas photogrammetry without ground control. *Remote Sens.* 11 (7), 784. doi:10.3390/rs11070784

Lim, H. S., Park, Y., Lee, J. Y., and Yoon, H. Il. (2014). Geochemical characteristics of meltwater and pondwater on Barton and Weaver Peninsulas of King George Island, west Antarctica. *Geochem. J.* 48 (4), 409–422. doi:10.2343/geochemj.2.0316

Lindsay, D. C. (1971). Vegetation of the South Shetland Islands. *Br. Antarct. Surv. Bull.* 25, 59–83.

Lucieer, A., Turner, D., King, D. H., and Robinson, S. A. (2014). Using an unmanned aerial vehicle (UAV) to capture micro-topography of Antarctic moss beds. *Int. J. Appl. Earth Observation Geoinformation* 27, 53–62. doi:10.1016/j.jag.2013.05.011

Malenovský, Z., Robinson, S. A., Lucieer, A., King, D. H., Turnbull, J. D., and Robinson, S. A. (2017). Unmanned aircraft system advances health mapping of fragile polar vegetation. *Methods Ecol. Evol.* 8, 1842–1857. doi:10.1111/2041-210X.12833

Malosso, E., Waite, I. S., English, L., Hopkins, D. W., and O'Donnell, A. G. (2006). Fungal diversity in maritime Antarctic soils determined using a combination of culture isolation, molecular fingerprinting and cloning techniques. *Polar Biol.* 29 (7), 552–561. doi:10.1007/s00300-005-0088-z

Marsz, A. A., and Styszyńska, A. (2000). *Główne cechy klimatu rejonu Polskiej Stacji Antarktycznej im. H. Arctowskiego (Antarktyka Zachodnia, Szetlandy Południowe, Wyspa Króla Jerzego. [Main climate characteristics of the region of the Polish Antarctic Station H. Arctowski (West Antarctica, South Shetland Islands, King George Island) - in Polish]*, WSM, Gdynia, pp. 264.

Miranda, V., Pina, P., Heleno, S., Vieira, G., Mora, C., and Schaefer, E. G. R. C. (2020). Monitoring recent changes of vegetation in Fildes Peninsula (King George Island, Antarctica) through satellite imagery guided by UAV surveys. *Sci. Total Environ.* 704, 135295. doi:10.1016/j.scitotenv.2019.135295

Molina-Montenegro, M. A., Bergstrom, D. M., Chwedorzewska, K. J., Convey, P., and Chown, S. L. (2019). Increasing impacts by Antarctica's most widespread invasive plant species as result of direct competition with native vascular plants. *Neobiota* 51, 19–40. doi:10.3897/neobiota.51.37250

Murray, H., Lucieer, A., and Williams, R. (2010). Texture-based classification of sub-Antarctic vegetation communities on Heard Island. *Int. J. Appl. Earth Observation Geoinformation* 12 (3), 138–149. doi:10.1016/j.jag.2010.01.006

Mustafa, O., Barbosa, A., Krause, D. J., Peter, H. U., Vieira, G., and Rümmler, M. C. (2018). State of knowledge: Antarctic wildlife response to unmanned aerial systems. *Polar Biol.* 41 (11), 2387–2398. doi:10.1007/s00300-018-2363-9

Mustafa, O., Pfeifer, C., Peter, H.-U., Kopp, M., and Metzig, R. (2012). Pilot study on monitoring climate-induced changes in penguin colonies in the Antarctic using satellite

images. On behalf of the German Environment Agency. Texte 19/2012. Dessau-Roßlau. Available at: http://www.umweltbundesamt.de/publikationen/pilot-study-on-monitoring-climate-induced

Nędzarek, A., Tórz, A., and Drost, A. (2014). Selected elements in surface waters of Antarctica and their relations with the natural environment. *Polar Res.* 33, 21417. doi:10.3402/polar.v33.21417

Ochyra, R., Lewis Smith, R. I., and Bednarek-Ochyra, H. (2008). *The illustrated moss flora of Antarctica*. Cambridge: Cambridge University Press, 704. doi:10.1093/aob/mcp111

Olech, M. (2004). *Lichens of King George Island, Antarctica*. Kraków: Institute of Botany of The Jagiellonian University, 391.

Øvstedal, D. O., and Lewis Smith, R. I. (2001). *Lichens of Antarctica and South Georgia. A guide to their identification and ecology*. Cambridge: Cambridge University Press, 424. doi:10.1177/1748895811401979

Ozyavuz, M., Bilgili, B. C., and Salici, A. (2015). Determination of vegetation changes with NDVI method. *J. Environ. Prot. Ecol.* 16 (1), 264–273.

Pereira, A. B., Francelino, M. R., Stefenon, V. M., Schünemann, A. L., and Roesch, L. F. W. (2010). Plant communities from ice-free areas of Demay Point, King George Island, Antarctica. *INCT-APA Annu. Act. Rep.* 2, 58–62. doi:10.4322/apa.2014.024

Pettorelli, N., Vik, J. O., Mysterud, A., Gaillard, J.-M., Tucker, C. J., and Stenseth, N. Chr. (2005). Using the satellite-derived NDVI to assess ecological responses to environmental change. *Trends Ecol. Evol.* 20 (9), 503–510. doi:10.1016/j.tree.2005.05.011

Pina, P., Pereira, F., Marques, J. S., and Heleno, S. (2019). "Detection of stone circles in periglacial regions of Antarctica in UAV datasets," in *Pattern recognition and image analysis, lecture notes in computer science* A. Morales, J. Fierrez, J. S. Sánchez, and B. Ribeiro (Germany: Springer Nature Switzerland AG), 279–288. doi:10.1016/0165-1684(94)90196-1

Pina, P., and Vieira, G. (2022). UAVs for science in Antarctica. *Remote Sens.* 14 (7), 1610–1639. doi:10.3390/rs14071610

Power, S. N., Salvatore, M. R., Sokol, E. R., Stanish, L. F., and Barrett, J. E. (2020). Estimating microbial mat biomass in the McMurdo Dry Valleys, Antarctica using satellite imagery and ground surveys. *Polar Biol.* 43 (11), 1753–1767. doi:10.1007/s00300-020-02742-y

Pudełko, R., Angiel, P. J., Potocki, M., Jędrejek, A., and Kozak, M. (2018). Fluctuation of glacial retreat rates in the eastern part of Warszawa Icefield, King George Island, Antarctica, 1979-2018. *Remote Sens.* 10, 892. doi:10.3390/rs10060892

Rodzewicz, M., Głowacki, D., and Hajduk, J. (2017). Some dynamic aspects of photogrammetry missions performed by "PW-ZOOM"-the UAV of Warsaw University of Technology. *Archive Mech. Eng.* 64 (1), 37–55. doi:10.1515/meceng-2017-0003

Rouse, J. W., Haas, R. H., Schell, J. A., and Deering, D. W. (1974). "Monitoring vegetation systems in the great plains with ERTS," in *Third earth resources technology satellite–1 syposium. Volume I: Technical presentations, NASA SP-351* S. C. Freden, E. P. Mercanti, and M. Becker (Washington, D.C.: NASA), 309–317.

Sancho, L. G., Pintado, A., Navarro, F., Ramos, M., De Pablo, M. A., Blanquer, J. M., et al. (2017). Recent warming and cooling in the Antarctic Peninsula region has rapid and large effects on lichen vegetation. *Sci. Rep.* 7, 5689. doi:10.1038/s41598-017-05989-4

Shin, J. Il, Kim, H. C., Kim, S. Il, and Hong, S. G. (2014). Vegetation abundance on the Barton Peninsula, Antarctica: Estimation from high-resolution satellite images. *Polar Biol.* 37 (11), 1579–1588. doi:10.1007/s00300-014-1543-5

Siegert, M., Atkinson, A., Banwell, A., Brandon, M., Convey, P., Davies, B., et al. (2019). The Antarctic Peninsula under a 1.5C global warming scenario. *Front. Environ. Sci.* 1 (102), 1–7. doi:10.3389/fenvs.2019.00102

Sierakowski, K., Korczak-Abshire, M., and Jadwiszczak, P. (2017). Changes in bird communities of Admiralty Bay, King George Island (West Antarctic): Insights from monitoring data (1977-1996). *Pol. Polar Res.* 38 (2), 231–262. doi:10.1515/popore-2017-0010

Smith, R. I. L. (1984). "Terrestrial biology of the Antarctic and sub-Antarctic," in *Antarctic ecology* R. M. Laws (London: Academic Press), 61–162.

Smith, R. I. L. (1972). *Vegetation of the South Orkney Islands with particular reference to Signy Island Scientific Report of the British Antarctic Survey*, 68. London: British Antarctic Survey Scientific Reports.

Sotille, M. E., Bremer, U. F., Vieira, G., Velho, L. F., Petsch, C., Auger, J. D., et al. (2022). UAV-based classification of maritime Antarctic vegetation types using GEOBIA and random forest. *Ecol. Inf.* 71, 101768. doi:10.1016/j.ecoinf.2022.101768

Sotille, M. E., Bremer, U. F., Vieira, G., Velho, L. F., Petsch, C., and Simões, J. C. (2020). Evaluation of UAV and satellite-derived NDVI to map maritime Antarctic vegetation. *Appl. Geogr.* 125, 102322. doi:10.1016/j.apgeog.2020.102322

Sun, X., Wu, W., Li, X., Xu, X., and Li, J. (2021). Vegetation abundance and health mapping over southwestern Antarctica based on WorldView-2 data and a Modified Spectral Mixture Analysis. *Remote Sens.* 13 (2), 166. doi:10.3390/rs13020166

Turner, D. J., Malenovsky, Z., Lucieer, A., Turnbull, J. D., and Robinson, S. A. (2019). Optimizing spectral and spatial resolutions of Unmanned Aerial System imaging sensors for monitoring Antarctic vegetation. *IEEE J. Sel. Top. Appl. Earth Observations Remote Sens.* 12 (10), 3813–3825. doi:10.1109/JSTARS.2019.2938544

Turner, D., Lucieer, A., Malenovský, Z., King, D. H., and Robinson, S. A. (2014). Spatial co-registration of ultra-high resolution visible, multispectral and thermal images acquired with a micro-UAV over Antarctic moss beds. *Remote Sens.* 6 (5), 4003–4024. doi:10.3390/rs6054003

Váczi, P., Barták, M., Bednaříková, M., Hrbáček, F., and Hájek, J. (2020). Spectral properties of Antarctic and Alpine vegetation monitored by multispectral camera: Case studies from James Ross Island and Jeseníky Mts. *Czech Polar Rep.* 10 (2), 297–312. doi:10.5817/CPR2020-2-22

Victoria, F. C., Albuquerque, M. P., and Pereira, A. B. (2006). Lichen-moss associations in plant communities of the southwest Admiralty Bay, King George Island, Antarctica. *Neotropical Biol. Conservation* 1 (2), 84–89.

Victoria, F. C., Pereira, A. B., and Pinheiro-da-Costa, D. (2009). Composition and distribution of moss formations in the ice-free areas adjoining the Arctowski region, Admiralty Bay, King George Island, Antarctica. *Iheringia, Série Botânica* 64 (1), 81–91.

Wall, D. H., Lyons, B. W., Chown, S. L., Convey, P., Howard-Williams, C., Quesada, A., et al. (2011). Long-term ecosystem networks to record change: An international imperative. *Antarct. Sci.* 23 (3), 209. doi:10.1017/S0954102011000319

Weier, J., and Herring, D. (2000). *Measuring vegetation (NDVI and EVI)*. Washington DC: NASA Earth Observatory.

Weisleitner, K., Perras, A. K., Unterberger, S. H., Moissl-Eichinger, C., Andersen, D. T., and Sattler, B. (2020). Cryoconite hole location in East Antarctic Untersee oasis shapes physical and biological diversity. *Front. Microbiol.* 11, 1165. doi:10.3389/fmicb.2020.01165

Zarzycki, K. (1993). "Vascular plants and terrestrial biotopes," in *The maritime antarctic coastal ecosystem of Admiralty Bay* S. Rakusa-Suszczewski (Warsaw: Department of Antarctic Biology, Polish Academy of Sciences), 181–187.

Zmarz, A., Rodzewicz, M., Dąbski, M., Karsznia, I., Korczak-Abshire, M., and Chwedorzewska, K. J. (2018). Application of UAV BVLOS remote sensing data for multi-faceted analysis of Antarctic ecosystem. *Remote Sens. Environ.* 217, 375–388. doi:10.1016/j.rse.2018.08.031

Znój, A., Chwedorzewska, K. J., Androsiuk, P., Cuba-Diaz, M., Giełwanowska, I., Koc, J., et al. (2017). Rapid environmental changes in the Western Antarctic Peninsula region due to climate change and human activity. *Appl. Ecol. Environ. Res.* 15 (4), 525–539. doi:10.15666/aeer/1504_525539

Zwoliński, Z. (2007). "Mobilność materii mineralnej na obszarach paraglacjalnych, Wyspa Króla Jerzego, Antarktyka Zachodnia [the mobility of mineral matter in paraglacial area, King George Island, western Antarctica - in polish," in *Seria geograficzna 74* (Poznań: Adam Mickiewicz University Press), 266.

frontiers | Frontiers in Ecology and Evolution

TYPE Original Research
PUBLISHED 06 June 2023
DOI 10.3389/fevo.2023.1189184

OPEN ACCESS

EDITED BY
Ram Kumar Singh,
TERI School of Advanced Studies (TERI SAS), India

REVIEWED BY
César Marín,
Santo Tomás University, Chile
Pir Mohammad,
Hong Kong Polytechnic University, Hong Kong SAR, China
Pham Viet Hoa,
Vietnam Academy of Science and Technology, Vietnam

*CORRESPONDENCE
Javed Mallick
✉ jmallick@kku.edu.sa

RECEIVED 18 March 2023
ACCEPTED 08 May 2023
PUBLISHED 06 June 2023

CITATION
Alqadhi S, Mallick J, Talukdar S and Alkahtani M (2023) An artificial intelligence-based assessment of soil erosion probability indices and contributing factors in the Abha-Khamis watershed, Saudi Arabia. *Front. Ecol. Evol.* 11:1189184. doi: 10.3389/fevo.2023.1189184

An artificial intelligence-based assessment of soil erosion probability indices and contributing factors in the Abha-Khamis watershed, Saudi Arabia

Saeed Alqadhi[1], Javed Mallick[1]*, Swapan Talukdar[2] and Meshel Alkahtani[1]

[1]Department of Civil Engineering, College of Engineering, King Khalid University, Abha, Saudi Arabia, [2]Department of Geography, Faculty of Natural Science, Jamia Millia Islamia, New Delhi, India

Soil erosion is a major problem in arid regions, including the Abha-Khamis watershed in Saudi Arabia. This research aimed to identify the soil erosional probability using various soil erodibility indices, including clay ratio (CR), modified clay ratio (MCR), Critical Level of Soil Organic Matter (CLOM), and principle component analysis based soil erodibility index (SEI). To achieve these objectives, the study used *t*-tests and an artificial neural network (ANN) model to identify the best SEI model for soil erosion management. The performance of the models were then evaluated using R^2, Root Mean Squared Error (RMSE), Mean Squared Error (MSE), and Mean Absolute Error (MAE), with CLOM identified as the best model for predicting soil erodibility. Additionally, the study used Shapley additive explanations (SHAP) values to identify influential parameters for soil erosion, including sand, clay, silt, soil organic carbon (SOC), moisture, and void ratio. This information can help to develop management strategies oriented to these parameters, which will help prevent soil erosion. The research showed notable distinctions between CR and CLOM, where the 25–27% contribution explained over 89% of the overall diversity. The MCR indicated that 70% of the study area had low erodibility, while 20% had moderate and 10% had high erodibility. CLOM showed a range from low to high erodibility, with 40% of soil showing low CLOM, 40% moderate, and 20% high. Based on the *T*-test results, CR is significantly different from CLOM, MCR, and principal component analysis (PCA), while CLOM is significantly different from MCR and PCA, and MCR is significantly different from PCA. The ANN implementation demonstrated that the CLOM model had the highest accuracy (R^2 of 0.95 for training and 0.92 for testing) for predicting soil erodibility, with SOC, sand, moisture, and void ratio being the most important variables. The SHAP analysis confirmed the importance of these variables for each of the four ANN models. This research provides valuable information for soil erosion management in arid regions. The identification of soil erosional probability and influential parameters will help to develop effective management strategies to prevent soil erosion and promote agricultural production. This research can be used by policymakers and stakeholders to make informed decisions to manage and prevent soil erosion.

KEYWORDS

soil erodibility index (SEI), soil erosion, principle component analysis (PCA), artificial neural network, SHAP

1. Introduction

Soil erosion is aggravated by abrupt climate variability, exploitation of natural resources, land degradation, etc. As a result, soil erosion and its environmental consequences are growing concerns worldwide (Gilani et al., 2022; Tsesmelis et al., 2022). Over the last few decades, it has become increasingly clear that soil erosion poses a significant risk to long-term soil sustainability, leading to soil management scenarios and practical conservation practices to preserve soil against erosive forces (Telak et al., 2021; Tesfahunegn et al., 2021; Khalil and Aslam, 2022). As a deterministic factor in soil erosion, vegetation cover can protect soil from erosive agents. The presence of vegetation in an area contributes significantly to the management of soil and water resources through interception of rainfall and regulation of surface run-off (Zhang et al., 2014). The leaves, stems, and root systems of plants collectively act as a control mechanism for surface water, effectively reducing erosion and conserving soil and water resources (Stagnari et al., 2010; Jiang et al., 2017).

However, in recent decades soils have become increasingly susceptible to water because of the rapid changes in the land use pattern and land composition, mainly due to intense agricultural practices and deforestation. Furthermore, human activities such as urbanization and characteristics such as population growth have accelerated vegetation eradication from the surface and the acceleration of soil displacement (Esa et al., 2018; Gong et al., 2022). Therefore, long-term strategic plans and efficient management are the only ways to protect the environment from rapid decline and keep the soil productive indefinitely. In addition, land degradation directly affects sediment formation and leads to accelerated sedimentation in watersheds. Globally, about 1964.4 million hectares (Mha) of soil were degraded due to anthropogenic activities, with 1903 M ha enhanced by water erosion (Pal, 2016). India is classified as humid subtropical, and one of the most significant threats to the country's fertile topsoil is soil erosion. According to the National Bureau of Soil Survey and Land Use Planning (NBSS&LUP), nearly 146.8 million ha (45%) of land in the country is at risk of soil erosion, most of which is due to surface run-off (Bhattacharyya et al., 2015; Pal et al., 2022; Saha et al., 2022). As a result, appropriate soil management practices must be implemented to prevent accelerated soil erosion through a comprehensive study of area-specific original data sets.

Several empirical and physical models for predicting soil erosion, soil loss, and sediment yield have been used by various researchers, such as the Morgan and Finney (MMF) model (Kumar and Pani, 2022), the European Soil Erosion Model (EUROSEM; Bora et al., 2022), Griffith University Erosion System Template (GUEST; Raza et al., 2021), the Water Erosion Prediction Project (WEPP; Meinen and Robinson, 2021; Mirzaee and Ghorbani-Dashtaki, 2021), Chemicals, Run-off, and Erosion from Agricultural Management System (CREAMS; Shi et al., 2022), Kinematic Runoff and Soil Erosion Model (KINEROS; Duarte et al., 2022), Soil & Water Assessment Tool (SWAT; Naseri et al., 2021), Agricultural Non-Point Source Pollution (AGNPS; Shrestha et al., 2021), Areal Nonpoint Source Watershed Environment Response Simulation (ANSWERS; Pandey et al., 2021), and others. However, insufficient spatial data makes these models ill-suited for fitting with small- to medium-sized watersheds, particularly in developing nations such as India. Hence, a model such as USLE (Universal Soil Loss Equation) was developed to forecast soil losses on agricultural land by Wischmeier and Smith in 1978. Later Revised Universal Soil Loss Equation (RUSLE) model was developed by Renard in 1997. It employs a framework similar to USLE but is more streamlined to best use the available data sources. Since 1990, it has been extensively employed in predicting soil water erosion (Millward and Mersey, 1999; Toy et al., 1999; Nyakatawa et al., 2001; Dissanayake et al., 2019; Kebede et al., 2021). RUSLE employs the same empirical principles as USLE but with more accurate factor calculation (McCool et al., 1987; Nearing et al., 2005; Das et al., 2020).

However, the mentioned methods are mostly qualitative methods based on remote sensing databases, which lack the ground validation and measurement. In the present study, we have planned to use an empirical model. The empirical models consider several elements such as the primary particles, the concentration of organic matter, the permeability, and the structure of the soil. The slope's steepness and concavity or convexity, the amount of pore space filled by air, the residual effects of sod crops, the aggregation, the parent material, and the many interactions between these factors all have a role (Olaniya et al., 2020). There are a number of different indicators of soil erodibility, some of which include the aggregation of soil and the proportion of water stable aggregates (Zuo et al., 2020; Rieke et al., 2022). Soil erodibility is reportedly affected by soil aggregation, which in turn is affected by land use system (Wassie, 2020). Researchers employ a variety of indicators, including quantitative indices for soil erodibility, to better comprehend the susceptibility of soil to erosion. Three of these are particularly popular: the Clay Ratio (CR), the Modified Clay Ratio (MCR), and the Critical Level of Soil Organic Matter (CLOM; Olaniya et al., 2020; Babur et al., 2021; Senanayake and Pradhan, 2022). Soil conservation priorities can be set with the help of indices like the clay ratio, the modified clay ratio, and the CLOM (Vitali et al., 2019; Olaniya et al., 2020; de Almeida Valente et al., 2023).

Despite the availability of various methods for assessing and quantifying soil erosion, some approaches have been limited to incorporating only two or three parameters, while others have included multiple parameters. But no study has been conducted to incorporate both equation-based soil erosion and weighting-based soil erosion models together. In the present study, we used several equation-based indices for quantifying the probability of soil erosion like clay ratio (CR), modified soil erosion (MCR), and CLOM, as well as weighting-based SEI to measure soil erosion probability. However, in the present study, we attempted to merge all the available erodibility indices and provide one erodibility indices with high accuracy.

Soil erosion is a significant environmental problem, which leads to soil degradation, loss of fertile land, and ecological imbalance. Therefore, accurate and reliable soil erodibility indices (SEIs) are necessary for effective soil erosion management. Various methods have been proposed for calculating SEIs, including CR, MCR, CLOM, and PCA-based models. However, identifying the best SEI model among them is challenging due to the complexity of the soil-landscape system and the involvement of numerous variables. To address this issue, researchers proposed using Artificial Neural Network (ANN) models to identify the best SEI for soil erosion prediction. The study utilized ANN to model nonlinear relationships and identify key variables for predicting soil erosion. Four SEI models were compared using ANN, with hyper-parameters optimized via grid search. Model performance was evaluated using R^2, Root Mean Squared Error (RMSE), Mean Squared Error (MSE), and Mean Absolute Error (MAE).

Moreover, the addition of explainable artificial intelligence in the form of SHAP (Shapley Additive Explanations) made a significant

contribution to soil erosion management. After identifying the best SEI model, the researchers introduced explainable artificial intelligence (XAI) techniques to quantify the influence of individual parameters in the model (Arrieta et al., 2020; Vilone and Longo, 2021; Al-Najjar et al., 2022). Specifically, SHAP (Shapley additive explanations) values were used to estimate the contribution of each variable in the model (García and Aznarte, 2020), which can be used to develop management strategies for reducing soil erosion. SHAP is a model-agnostic method that identifies the most influential variables and the magnitude of their influence on the model's output. By utilizing SHAP, it is possible to identify the critical parameters that contribute to soil erosion and develop targeted management strategies. Overall, the combination of ANN and SHAP has great potential for identifying the best SEI model and developing effective soil erosion management strategies. This research has theoretical implications for the development of soil erosion models and practical implications for the implementation of soil erosion management practices.

This study aims to address the issue of identifying the best SEIs for effective soil erosion management. The study utilizes ANN to model nonlinear relationships and identify key variables for predicting soil erosion, with four SEI models compared using ANN. The study's objective is to determine the best SEI model for soil erosion prediction, evaluate the performance of the models, and identify the influential parameters using XAI techniques. The novelty of the study lies in the application of ANN models and XAI techniques to identify the best SEI model and quantify the importance of individual parameters in the model. The addition of XAI in the form of SHAP made a significant contribution to soil erosion management by identifying the most influential variables and the magnitude of their influence on the model's output, which can be used to develop management strategies for reducing soil erosion. Overall, the study's findings have both theoretical implications for the development of soil erosion models and practical implications for the implementation of soil erosion management practices.

2. Materials and methodology

2.1. Study area

Abha-Khamis Watershed, located in the South-Western region of Saudi Arabia, has a semiarid climate and hilly topography. The watershed encompasses an area of 1,773 kilometers (Figure 1). Aseer's terrain is rugged, with high peaks that are about 2,990 meters above sea level. The highest peaks of the watershed are located in Jabal Alsouda. Some small Wadi (valley/riverbed which is either permanently or intermittently dry) occur in the higher mountains because to the great amount of precipitation received by the higher mountains, however none of the Wadi flow for more than 50 kilometers before entering the Wadi plains (Vincent, 2008). The semi-arid South-Western Coast of Saudi Arabia is surrounded by mountainous terrain, where strong rainstorms occur irregularly throughout the year (Mallick, 2016). Wet oceanic currents cause the region to get rainfall from the South-Western monsoon (Vincent, 2008). High summer temperatures over the peninsula have contributed to the formation of tropical continental air, which is a component of the monsoon with low circulation in the northwest of India (Vincent, 2008). From March to June, the regions receive the most precipitation, and flash floods are reported in the downstream regions (Mallick, 2016). April receives the most precipitation, with an annual average of 244 millimeters. In the Aseer region, rainfall originates from orographic convection over the scarp, particularly during the late summer monsoon season. Rainfall over 200 mm per year is restricted to a 20–30 km wide zone along the crest.

2.2. Sampling of soils with laboratory analysis

Using a Global Positioning System (GPS) model GPS 38S, soil samples were gathered from the study region during dry weather conditions using a stratified technique, i.e., an area separated into areas with similar topography, soil moisture, and land cover. A total of one hundred thirty five (135) soil samples were taken from each site, with two replicates separated by 2–3 meters and 0–30 centimeters in depth. After air-drying soil samples at 102°C for 24 h in an oven, they were carefully homogenized, sieved through a 2-mm mesh, and then analyzed for their qualities, including soil texture and organic matter content, according to Carter's standard process (1993). Using a muffle furnace at 350–600°C for 2 h, the organic matter content was determined. The precision of the measurements is specified to be 1.5% of the amount observed, with a detection limit of 0.02% (Hill and Schütt, 2000). Using the hydrometer method and Stokes' law, the soil samples were analyzed for texture (Sheldrick and Wang, 1993).

2.3. Method for computing soil erodibility indices

In the present study, we have computed three conventional SEIs and proposed one PCA based SEI method for investigating the soil erodibility.

2.3.1. Computation of clay ratio

The clay ratio is an evaluation of the quantity of the binding agent clay that securely binds the soil particles, making it difficult for the particle to be detached by the external forces in the presence of a larger number of clay particles (Bouyoucos, 1935). Ten percent minimum clay content is required for any interpretation (Bryan, 1968). Soil erodibility decreases as CR rises. The computation of clay ratio Eq. 1 is mentioned below

$$CR = \left(\%sand + \%silt\right) / \%clay \tag{1}$$

2.3.2. Computation of modified clay ratio

Correlation analyses between soil characteristics have shown that the modified clay ratio may be used as an alternative measure of soil erodibility, as reported by Mukhi (1988) and Tarafdar and Ray (2005). They found that in high-organic-content soil, MCR was a better explanation of erodibility than CR. It can be computed using Eq. 2:

$$MCR = \left(\%sand + \%silt\right) / \left(\%clay + \%OM\right) \tag{2}$$

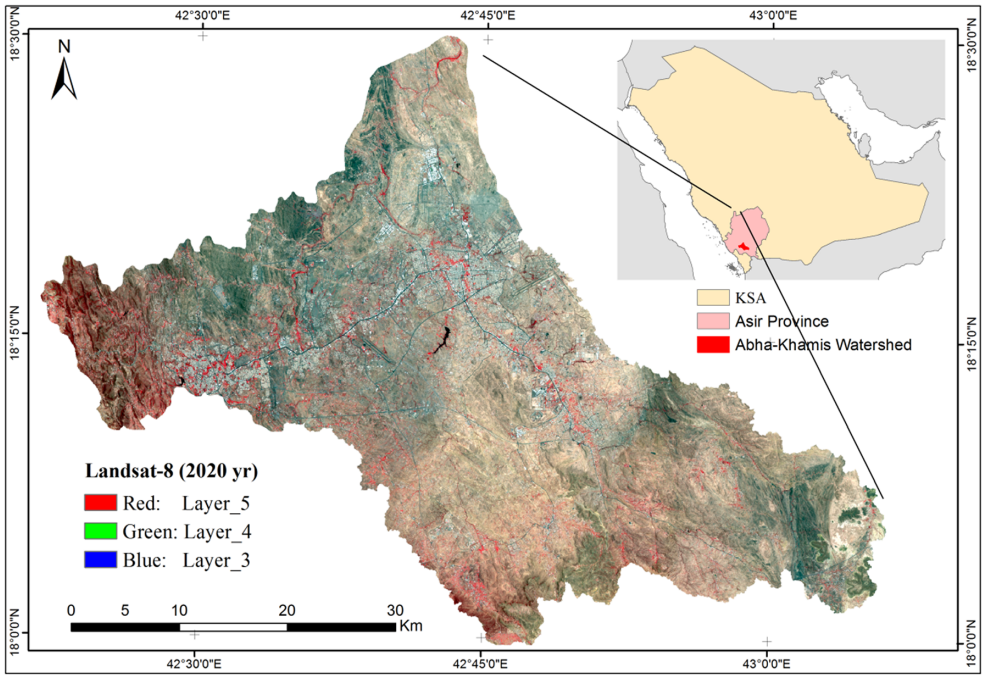

FIGURE 1
Location of the study area as Abha-Khamis watershed, Saudi Arabia.

2.3.3. Computation of critical level of soil organic matter

An indication of how susceptible soil is to erosion is referred to as the critical level of soil organic matter (CLOM). CLOM, according to Pieri (2012), has an effect on soil structure, which provides resistance to erosion. In their research, if CLOM is 5% or below, soil structure is lost and erosion susceptibility is high, 5–7% is moderate, and >9% shows stable soil structure, enabling better erosion resistance. The following Eq. 3 was used to get an estimate for the Critical Soil Organic Matter:

$$CLOM = \frac{OM}{Clay + Silt} \quad (3)$$

2.3.4. Computation of PCA based soil erodibility index

In the present study, we proposed a PCA-based soil erodibility index (PSEI) method for computing robust SEI, where different parameters can contribute. An indexing method was used to determine the SEI which has been shown to work well for small-scale applications, including on-filed studies (Andrews et al., 2002). A SEI is the result of three phases: (i) determination of the minimum dataset (MDS) of indicators with the best representation of the soil structure related to erosion; (ii) standardization of MDS indicators; and (iii) combining the scores of the indicators.

Principal component analysis (PCA) was used to refine indicators suitable for the MDS. PCA reduces dimensionality and minimizes information loss. This is done by constructing unrelated variables called principal components (PCs), which are arranged so that the first few retain most of the volatility of the original data. The 9 previously standardized soil chemical and physical variables were subjected to PCA analysis. Standardized variables contain unit variance, so the PCA variance is equal to the number of observed variables. An eigenvalue is the numerical representation of a PC's proportional contribution to the total variance. Using the eigenvalue criterion one (Kaiser, 1960) and the Scree test, the number of components was reduced (Cattell, 1966). Any component with an eigenvalue greater than 1.00 should be retained. Due to the fact that each of the observed standardized variables contributes one unit of variance, a PC with an eigenvalue less than 1.00 can be said to represent less variation than a single standardized variable. The Scree test plots the eigenvalues of each PC in descending order, picking the PC's up to the bend in the graph.

Component loading or variable weights under a PC have been used to reduce the number of variables. For each PC, we considered only those variables that were in the top 10% in terms of absolute component loading (Wander and Bollero, 1999). Correlation analysis was used to assess whether heavily weighted factors were redundant and could be reduced further. The MDS indicators were converted into unitless combinable values from 0 to 1 to account for their contribution to soil functions. Wymore (1993) provided an equation for constructing three scoring curves: higher is better, lower is better, and optimal (a bell-shaped curve). A thorough knowledge of the relationship between the indicator and the quality of the soil is necessary to determine which function accomplishes what, i.e., the best shape for each indication. More is better should be used when increasing the level of the indicator improves the quality of the soil. The indicators whose increment decreases the quality of the soil correspond to the curve less is better. The optimal curve ranks indicators having a positive relationship with soil quality up to an ideal threshold, above which the SQ decreases.

After determining the type of indicator curve, the baseline, thresholds, and slope of the scoring function should be defined to

account for deviations in the expected ranges due to soil, climate, and crop. The literature review and researchers' opinions were used to determine the function and critical limits of each indicator.

After obtaining the *S* values for all of the indicator parameters, the PCA statistics were used to weight each characteristic. Each PC was responsible for explaining a particular percentage (%) of the whole data set's variance. Once S and W were determined, the PSEI for each location could be computed using Eq. (4). When the index score is higher, it indicates that the erodability of the soil is higher.

$$PSEI = \sum_{i=1}^{n} SE_j \times S \quad (4)$$

2.4. Application of statistical tests for finding out the differences among the soil erodibility indices

The pairwise *t*-test was used to compare the means of each SEI with every other index prepared in this study. A *t*-test is a statistical test that is used to determine if the means of two groups are significantly different from each other. The *t*-test calculates two outputs: the *t*-value and the value of *p*. The *t*-value measures the difference between the means of the two groups relative to the variance within the groups, while the value of *p* measures the probability of observing a *t*-value as extreme as the one calculated if the means of the two groups were actually equal. If the value of *p* is less than a pre-determined significance level (usually 0.05), it is concluded that there is a statistically significant difference between the two indices being compared. By using a pairwise *t*-test, we can identify which indices have significantly different means from each other and thus provide insights into the differences between the soil erodibility indices.

2.5. Application of artificial neural network to find out best SEI

Artificial Neural Networks (ANN) is a class of machine learning algorithms that are inspired by the structure and functioning of the human brain (Boger and Guterman, 1997). ANN models consist of layers of interconnected artificial neurons that process and transmit information. ANN has been widely used in the field of agriculture and soil science for various applications, including soil erosion prediction (Garg et al., 2022; Egbueri et al., 2023).

In this study, TensorFlow and Keras were used to implement an ANN regression model to predict the soil erodibility indices based on the given features. The four soil erodibility indices CR, MCR, CLOM, and PCA were considered as the target variables, and the other relevant soil properties were considered as features. The ANN regression model is trained using a large dataset of soil properties and particular SEI. The process is repeated for four times, because we have four target variables with the same model architecture. During the training process, the model learns to optimize the weights of its connections by minimizing the error between the predicted and actual values (Nouri et al., 2023). The model's performance is evaluated using metrics such as Mean Squared Error (MSE), Root Mean Squared Error (RMSE), *R*-squared (R^2), and Mean Absolute Error (MAE). The ANN model's architecture consists of an input layer, two hidden layers, and an output layer. Each layer contains a set of neurons that perform a specific computation. The input layer receives the input features, and the output layer produces the predicted soil erodibility indices. The hidden layers perform intermediate computations between the input and output layers, and each neuron's output is determined by an activation function. The activation function introduces non-linearity into the model and enables it to learn complex relationships between the input features and the target variables (Nouri et al., 2023).

The model's performance can be improved by tuning its hyperparameters such as the number of hidden layers, number of neurons per layer, learning rate, batch size, and number of epochs. These hyperparameters are optimized using techniques such as Grid Search, Random Search, and Bayesian optimization. Once the model is trained and optimized, it can be used to predict the soil erodibility indices for new soil samples. The model's prediction accuracy can be further improved by using a larger and more diverse dataset for training and by including additional relevant features.

2.6. Improving the soil erosion management decision making using ANN derived SHAP model

Shapley additive explanations is a popular model-agnostic interpretability technique used to explain the predictions of machine learning models, including ANN models (Wieland et al., 2021). The SHAP values are calculated for each input feature and indicate the contribution of each feature to the model's output (Al-Najjar et al., 2022).

In this study, the SHAP values were derived from the ANN model to identify which input features are responsible for soil erosion and their impact on the soil erodibility indices. The SHAP values can be used to generate a summary plot that displays the feature importance rankings in descending order (Tang et al., 2022). This summary plot can be used for soil erosion management purposes to identify the most important features and develop effective strategies to manage soil erosion (Zhang et al., 2020; Mohammadifar et al., 2021). The SHAP values are calculated using game theory concepts and define the contribution of each feature by comparing the model's predictions with and without that feature. The SHAP values are additive, meaning that the sum of the SHAP values for all features equals the difference between the model's output and the baseline prediction (Tang et al., 2022). The summary plot generated from the SHAP values displays the most important features at the top of the plot, with the corresponding SHAP values indicating the feature's impact on the soil erodibility indices. The summary plot can be used to identify the most important features and develop effective strategies to manage soil erosion. For example, if the summary plot shows that rainfall intensity is the most important feature contributing to soil erosion, then soil conservation strategies could focus on reducing runoff and increasing infiltration.

3. Results

3.1. Descriptive assessment and spatial mapping of soil parameters

To assess the impact of land management techniques on soil quality, it is essential to evaluate various physicochemical parameters

of the soil, including sand, silt, clay, soil density, moisture content, porosity, and the status of soil organic matter. The results of the SEI are presented in Figure 2, which confirms that SOC, soil density, porosity, and soil particles exhibit significant differences in soil quality/physicochemical properties at the 95% level of statistical confidence (Figure 2). Without a correlation between soil physicochemical properties, identification of underlying factor patterns would not be possible (Brejda et al., 2000). However, the two-tailed correlation matrix for the soil properties in the samples retrieved from the study area showed several correlations among the variables, with significant relationships ($p < 0.05$) being identified among the maximum number of possible soil properties. This large amount of correlation indicates that they can be grouped into a homogeneous set of variables based on their correlation patterns. Thus, these variables can be used as indicators of soil quality in conjunction with the land use management categories identified in the study area. The correlation between soil properties and SEI suggests that soil quality increased as soil properties such as SOC, porosity, and moisture content increased.

Soil texture is a crucial characteristic that influences the infiltration rates of water from the soil surface (Figures 3A-I). Additionally, soil texture plays a significant role in the soil's capacity to retain water and nutrients. The concentration of sand in the soil remained low in most of the study area, particularly in the northwestern site, while it increased in other areas of the study (Figures 3A,C). The northwestern site showed a high silt content that decreased in other regions of the study area. The textural classification of the northwestern area remained as sandy to silty loam texture. The distribution of clay concentration in the soil of the study area indicated a very low class distributed from the northeastern area to the southeastern area. A slightly higher level of clay content was observed in the northwestern part of the study area. The distribution of clay in soil samples suggested that the studied soils have low erodibility due to the cohesiveness of clay particles that form soil aggregates. This study revealed that clay had a negative correlation with soil erodibility (sand particles). The content of clay varied in the study area due to factors such as parent material, mineral characteristics, and weathering processes.

The soil density was found to be high throughout the study area, as shown in Figures 3D,E. The decrease in soil attributes such as moisture content, porosity, and SOC content, along with an increase in bulk density, indicates that intensive tillage practices and lower plant productivity negatively affected soil compaction, microbial attributes, and soil aggregation. Annual tillage activities can disrupt soil aggregates and reduce physical protection of organic matter content, leading to lower SOC content and labile fractions in tilled soils compared to no-tilled soils (Green et al., 2007). The lower SOC content in cultivated soils can also have a negative impact on soil chemical, physical, and microbial properties (Ding et al., 2013; Zandi et al., 2017; Nabiollahi et al., 2018). Figure 3I shows that some areas have increased SOC content, which may be due to higher plant litter inputs and no-till practices during the restoration period, resulting in greater carbon inputs into the soil (Guo et al., 2017).

3.2. Modeling and proposing of SEIs

3.2.1. Analysis of the conventional SEIs

In this study, we investigated the soil erodibility condition of the study area using three conventional SEIs, namely CR, MCR, and CLOM (Figure 4). The CR values in the study area ranged from moderate to high, with lower values observed in the Western part of

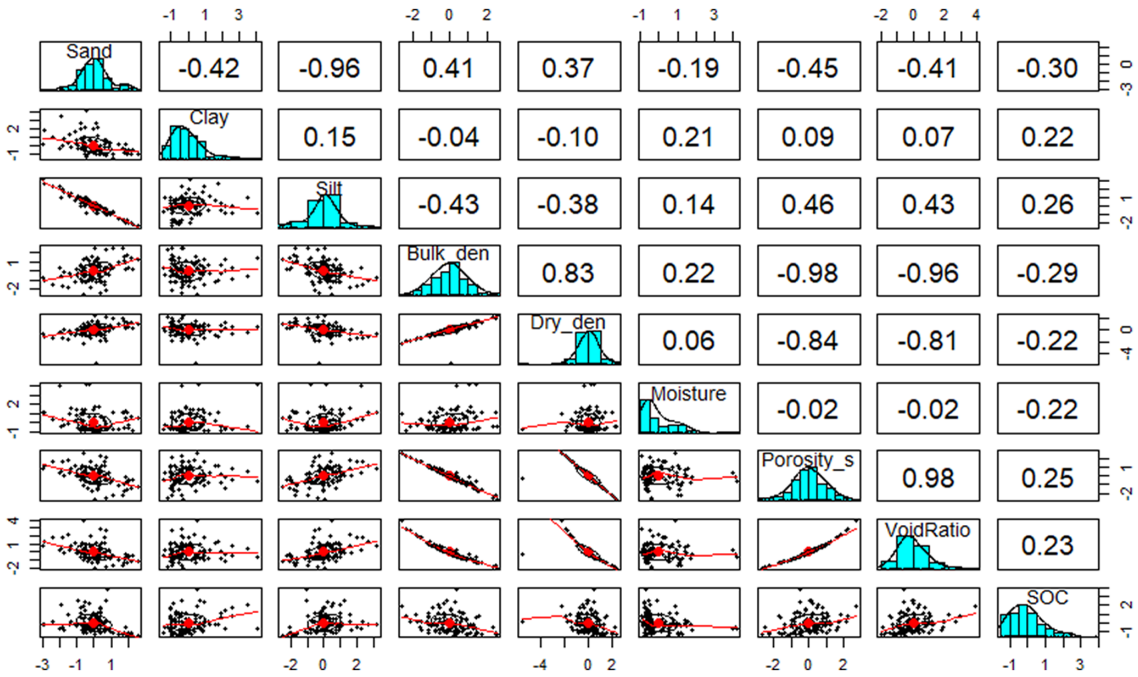

FIGURE 2
Relationship between different soil parameters using Pearson's correlation coefficient technique.

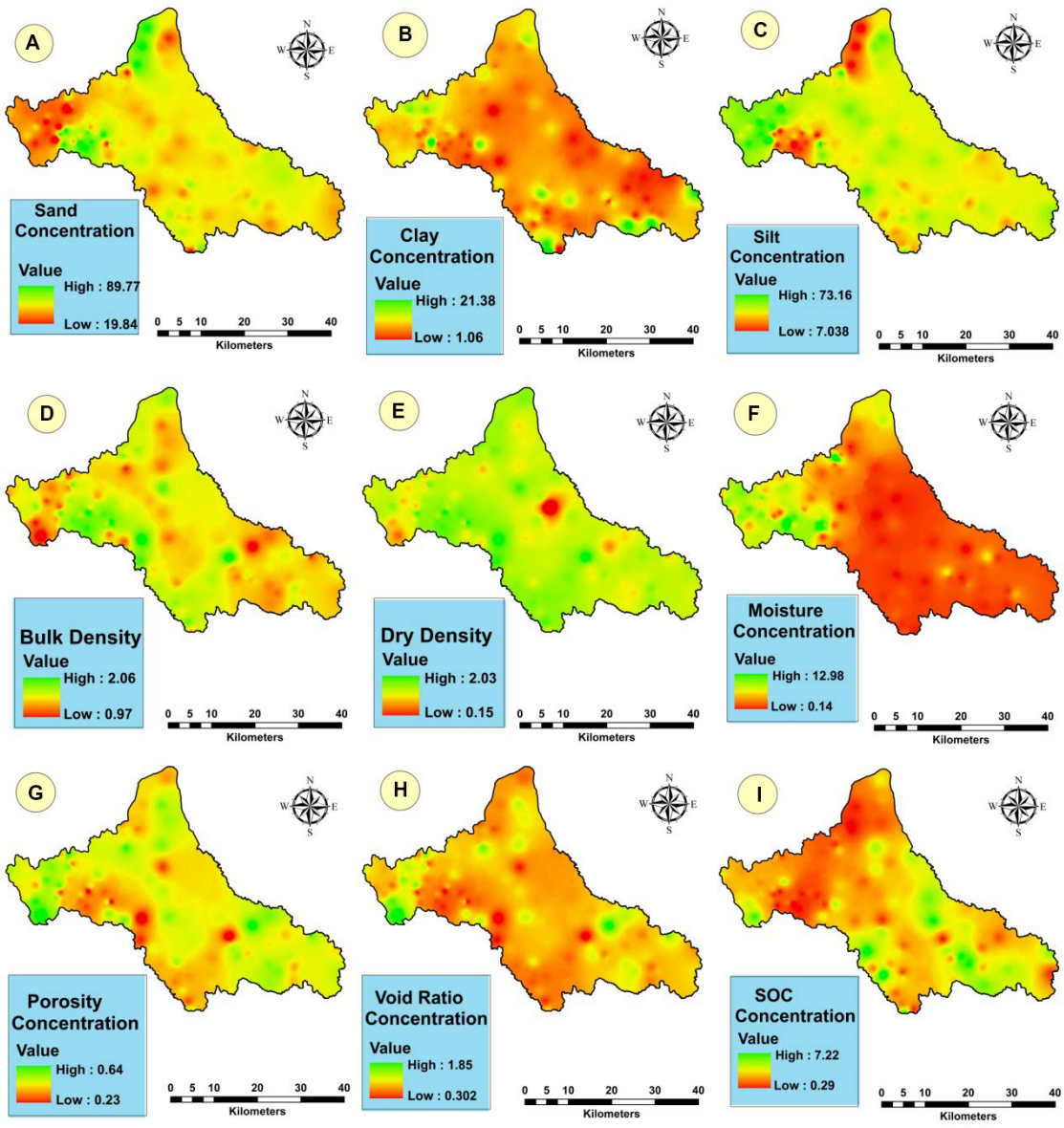

FIGURE 3
Spatial mapping of the concentration of different physical and chemical parameters, such as (A) sand, (B) clay, (C) silt, (D) bulk density, (E) dry density, (F) moisture, (G) porosity, (H) void ratio, (I) SOC.

the area. However, since CR is a ratio between erosion-susceptible primary particles and clay, it cannot provide conclusive information on erosion proneness. To draw meaningful conclusions, it is recommended that the clay content in the cultivated soil be more than 10% (Bryan, 1968), which was the case for all the samples in the study area. However, due to the absence of any scale for erosion proneness, conclusive interpretation could not be drawn for the present study.

Other studies have suggested modified clay ratio (MCR) as another index for soil erosion due to the effects of wind, water, or other natural events (Mukhi, 1988; Tarafdar and Ray, 2005). In this study, the MCR values for the study area ranged from low to high, with most of the soil showing low MCR and a moderate trend of CR. Although the MCR values did not provide conclusive information on the erosion proneness of the soil according to land uses, the low average values indicated that the soils in the study area were not highly susceptible to erosion.

The results showed significant differences among CR and CLOM, with the contribution of 25–27% (Figure 4) accounting for >89% of the total variability. Moreover, significant correlations were observed between the CR and CLOM, with both contributing to the SEI of the study soils.

The CLOM values ranged from low to high, with 40% of the soil showing low CLOM, 40% showing moderate CLOM, and the remaining 20% showing high CLOM (Figure 4). These findings indicate that the soils in the study area had moderate to stable soil structure and offered resistance to erosion. Soil aggregate stability is related to soil organic matter, and the study area showed a range of soil organic carbon levels between 0.29 and 7.22% (Figure 3I). This is consistent with the CLOM findings, which revealed a positive correlation between soil stability and the amount of soil organic matter. However, it is important to note that these methods are entirely based on the developed equation.

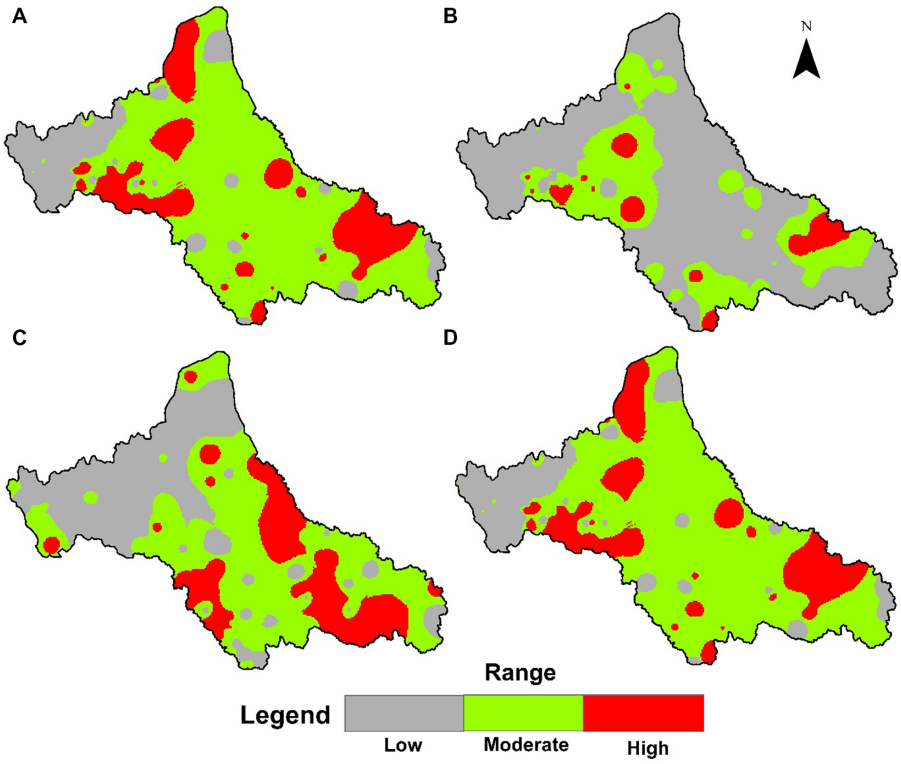

FIGURE 4
Computed soil erodibility indices, such as **(A)** CR, **(B)** MCR, **(C)** CLOM, and **(D)** PCA based SEI model for the Asir.

3.2.2. Proposing PCA based SEI

In this study, instead of relying on equation-based SEIs, we employed a PCA-based weighting technique to develop a new SEI. The PCA analysis indicated that the first three principal components (PCs) accounted for over 10% of the total variance (Figure 5) and explained more than 68.4% of the variability among the various soil properties studied for SEI development. Bulk density is widely recognized as a reliable indicator of soil compaction, and the distribution map revealed a strong correlation between soil density and sand concentration, indicating that higher sand content in soils tends to result in higher bulk density due to the lower total pore space in sandy soils compared to silt or clay soils. Conversely, soils with finer textures, such as silt and clay loams, that display good structure tend to have higher pore space and lower bulk density compared to sandy soils. In our study, we also developed an index based on weights using the first PC of PCA. The weights were computed from the field-based data patterns obtained from Figure 5, rather than relying solely on equations. By using the weights generated from field-based data, we were able to compute erodibility in a more accurate and reliable way. The SEI developed using this approach revealed that 68% of the study area was covered by moderately erosion-prone areas, followed by 9 and 23% of the area being low and high erosion-prone, respectively (Figure 4D).

3.3. Analysis of the difference among SEIs

In this study, the heatmap of correlation shows the correlations between the four soil erodibility indices - CR, MCR, CLOM, and PCA (Figure 6). The correlation coefficients show the strength and direction of the relationship between two variables. According to the heatmap, CR has a relatively strong positive correlation of 0.65 with PCA and an even stronger positive correlation of 0.75 with MCR. On the other hand, the correlation between CR and CLOM is weak with a coefficient of 0.036. This suggests that CR and MCR are likely to be highly related to each other, while CLOM may be less related to the other indices. CLOM has a weak negative correlation with PCA, with a coefficient of −0.047, indicating that these two indices are slightly negatively related to each other. Additionally, CLOM has a moderate negative correlation of −0.28 with MCR, suggesting that these two indices may be somewhat negatively related.

Finally, MCR has a strong positive correlation of 0.74 with PCA, indicating that these two indices are highly related to each other. This correlation is similar in strength to the correlation between CR and MCR, suggesting that both CR and MCR are highly related to PCA.

The results of the *T*-tests provide additional information on the differences between the four soil erodibility indices. A *T*-test is a statistical test used to determine if there is a significant difference between the means of two groups.

The *T*-test results show that there is a significant difference between the means of each pair of soil erodibility indices. The *T*-test for CR vs. CLOM shows a large *t*-value of 43.638 and a value of *p* of 0.00001, indicating a very significant difference between the means of these two indices. Similarly, the *T*-test for CR vs. MCR shows a large *t*-value of 33.643 and a value of *p* of 0.00001, indicating a very significant difference between the means of CR and MCR. The *T*-test for CR vs. PCA also shows a large *t*-value of 48.209 and a value of *p* of

0.00001, indicating a very significant difference between the means of CR and PCA. The *T*-test for CLOM vs. MCR shows a negative *t*-value of −11.072 and a value of *p* of 0.00001, indicating a significant difference between the means of these two indices, with CLOM having a lower mean than MCR. The *T*-test for CLOM vs. PCA shows a positive *t*-value of 14.615 and a value of *p* of 0.00001, indicating a significant difference between the means of these two indices, with PCA having a higher mean than CLOM. Finally, the *T*-test for MCR vs. PCA shows a positive *t*-value of 18.327 and a value of *p* of 0.00001, indicating a significant difference between the means of MCR and PCA, with PCA having a higher mean than MCR.

Based on the *T*-test results, CR is significantly different from CLOM, MCR, and PCA, while CLOM is significantly different from MCR and PCA, and MCR is significantly different from PCA.

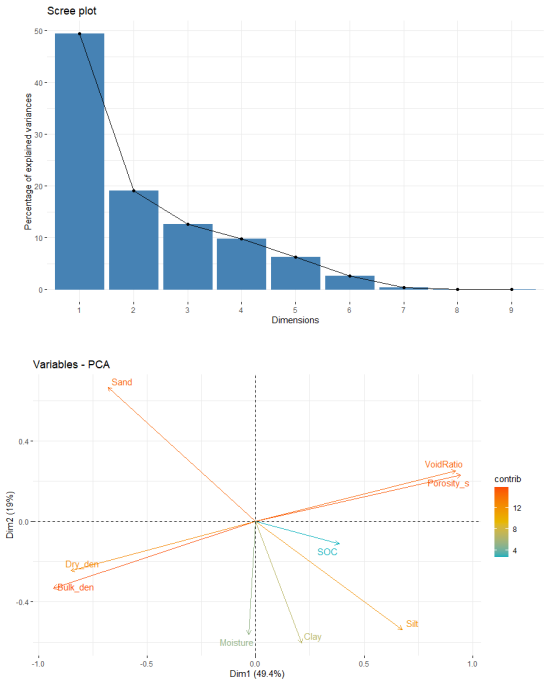

FIGURE 5
Application of PCA for feature selection.

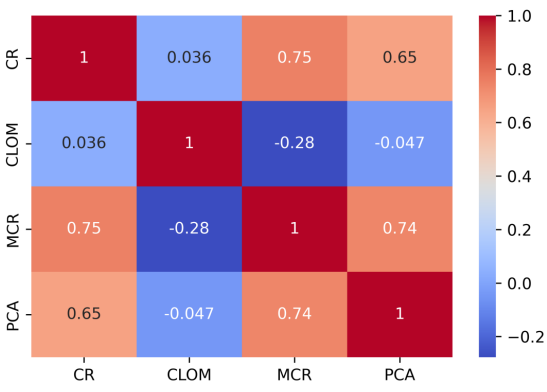

FIGURE 6
Correlation coefficient analysis among four SEIs for understanding the difference among them.

3.4. Best SEI selection using ANN

We optimized the ANN model using grid search to find the best hyper-parameters. The best hyper-parameters are alpha = 0.17060, beta_1 = 0.0001, beta_2 = 0.0289, hidden_layer_sizes = 2, learning_rate_init = 0.0030, max_iter = 971, random_state = 42. These hyper-parameters are fixed for four models means CR with all parameters, MCR with all parameters, CLOM with all parameters, PCA with all parameters.

Figure 7 was used to illustrate the relationship between actual and predicted SEI values for the training and testing datasets for each of the four models. The R^2values for CR were 0.93 and 0.82 for the training and testing datasets, respectively (Figures 7A,B). The R^2 values for MCR were 0.78 and 0.70 for the training and testing datasets, respectively (Figures 7C,D). The R^2 values for CLOM were 0.98 and 0.95 for the training and testing datasets, respectively (Figures 7E,F). The R^2 values for PCA were 0.73 and 0.60 for the training and testing datasets, respectively (Figures 7G,H).

The results of the ANN implementation show that CLOM is the best model for finding out soil erodibility based on the performance indices. This conclusion is based on the evaluation of the four models using R^2, RMSE, MSE, and MAE. The training and testing RMSE, MSE, and MAE values for CLOM were significantly lower than the values for the other models, indicating that the predictions made by the CLOM model are more accurate than those made by the other models.

The CLOM model had lower RMSE values than the other models, with values of 0.4781 for training and 0.5377 for testing. The superior performance of the CLOM model was further confirmed by the MSE and MAE values. Specifically, the MSE values for the CLOM model were 0.2286 for training and 0.2891 for testing, which were significantly lower than the values for the other models. Furthermore, the MAE values for the CLOM model were 0.2998 for training and 0.3489 for testing, which were again significantly lower than the values for the other models.

Therefore, it can be concluded that the CLOM model is the best model for finding out soil erodibility, and this information can be used for soil erosion management practices. The significantly lower values of performance indices indicate that the predictions made by the CLOM model are more accurate, which can help in developing more effective soil erosion management practices.

3.5. Improving decision making using SHAP

In this study, we used Artificial Neural Network (ANN) models to predict the SEI and calculated the SHAP values to identify the most influential variables for each of the four models, namely CR, MCR, CLOM, and PCA (Figure 8). The results showed that sand and silt were the most important variables for CR model, while clay, sand, silt, SOC, and moisture were highly influential for the MCR model. For the CLOM model, SOC, sand, moisture, and void ratio were found to be responsible for soil erosion, while silt and clay played a negative role. These findings have important implications for decision-making in soil erosion management. For example, the study suggests that sand and silt content are crucial factors that need to be monitored and managed to prevent soil erosion. This can be achieved through various management strategies, such as planting vegetation or using

10.3389/fevo.2023.1189184

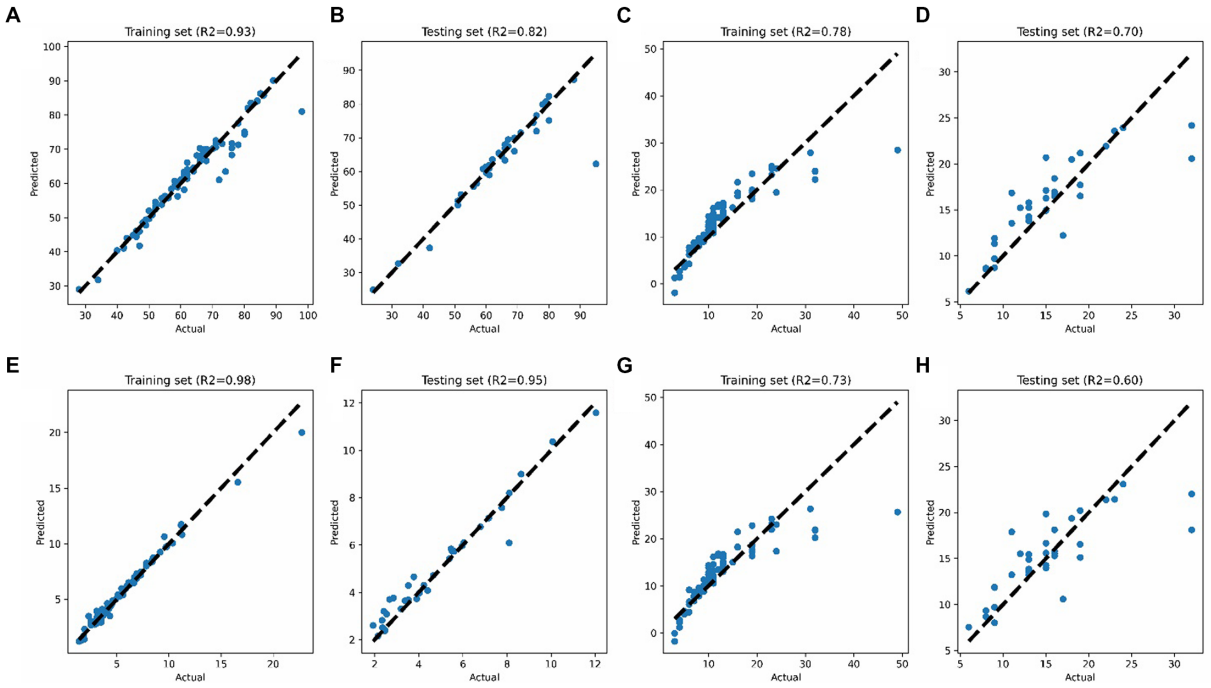

FIGURE 7
Selection of best SEI using optimized ANN model, for **(A)** training of CR, **(B)** testing of CR, **(C)** training of MCR, **(D)** testing of MCR, **(E)** training of CLOM, **(F)** testing of CLOM, **(G)** training of PCA, and **(H)** testing of PCA.

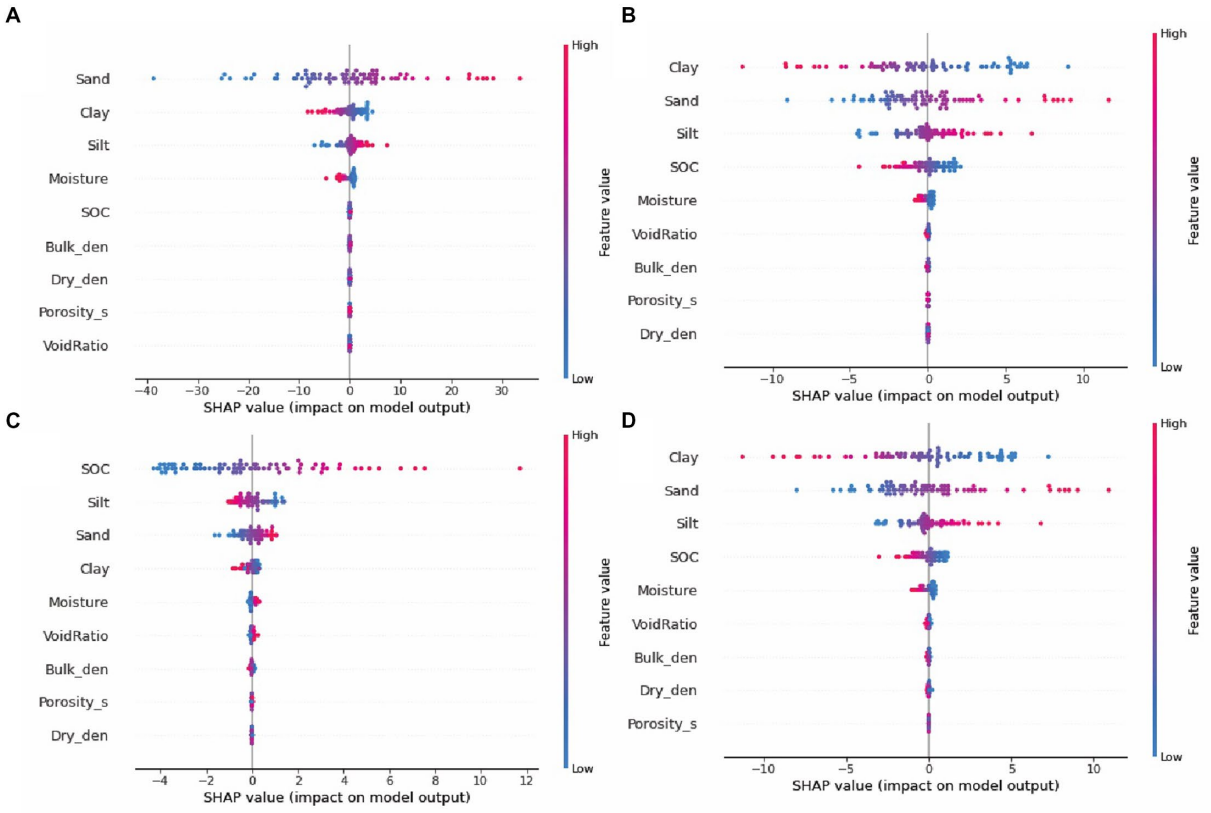

FIGURE 8
SHAP computation for **(A)** CR, **(B)** MCR, **(C)** CLOM, and **(D)** PCA based model.

conservation tillage techniques. Additionally, the study highlights the importance of monitoring the anthropogenic activities that affect the soil properties, such as land use changes or tillage practices, which can have a significant impact on soil erosion.

4. Discussion

The study focused on the use of SEIs to effectively manage soil erosion, which is a significant environmental problem leading to soil degradation, loss of fertile land, and ecological imbalance. Several SEI models were compared using ANN model, and the best model was identified. To further improve soil erosion management, explainable artificial intelligence in the form of SHAP was introduced to quantify the influence of individual parameters in the model.

This study has provided insights into the effects of land use changes on soil recovery in native upland rangeland ecosystems. While soil quality index has been previously used to evaluate soil degradation and the effects of land conversion on soil quality (Li et al., 2013; Raiesi, 2017; Nabiollahi et al., 2018), this approach (use of AI for SEI assessment) has not been used to study the effects of cropland abandonment on soil recovery. The current study has used SEIs to determine soil physicochemical properties after a sequence of land use changes in native rangelands. The results indicated that the long-term activities for crop production on soil had a stronger influence on the quality of these soils, with lower values of SEI, moisture content, void ratio, and SOC observed in the study soils.

Different land use activities can negatively affect the soils, leading to decreases in SOM, soil moisture content, and soil structural stability, which can increase soil erodibility (Harris, 2010; Li et al., 2013; Raiesi and Riahi, 2014). The low values of SEI in soils suggest that the current cropland soils are in a degradation process, primarily due to the loss of soil structure, SOM, soil moisture content, and other physicochemical properties of soil (Raiesi and Salek-Gilani, 2020).

The observed deterioration of soil properties and function is likely due to low SOC input, soil moisture, and soil disturbance by human activities. Consistent with our observations, previous studies have reported soil quality degradation in cropland soils due to frequent tillage practices and little accumulation of plant residues in the surface soils (Raiesi, 2017; Zhang et al., 2019).

Our results showed that SEI values in the North-Western area were higher than those in other areas, which is likely due to the low SOC content at these sites (Figure 3I). In other areas of the study sites, SEI values were slightly higher, suggesting that soil quality can be restored when other physicochemical properties of soils are improved (Raiesi and Salek-Gilani, 2020). Therefore, the addition of SOC through improved cropping systems and the establishment and development of natural vegetation on eroded cropland soils in the study area can switch soil degradation to soil quality, except in the North-Western area.

The study findings indicate that ANN models can be highly accurate in predicting SEI, and the selection of the best model for predicting soil erodibility can be achieved by utilizing four indices, including CR, MCR, CLOM, and PCA. The results of the study showed that CLOM was the best model among the four indices, and the significant factors in predicting soil erodibility included SOC, silt, clay, sand, moisture, and void ratio.

The results of this study suggest that SOC and moisture content are critical variables for the CLOM model, indicating that management practices such as conservation tillage or adding organic matter to the soil can help to increase SOC content and improve soil moisture, thereby reducing soil erosion (Rojas et al., 2016; de Moraes Sa et al., 2018; Yang et al., 2019). Monitoring the void ratio can also help to prevent soil compaction and promote better soil structure. These findings have significant implications for soil erosion management, as soil erosion can lead to severe consequences such as soil degradation, loss of biodiversity, and reduced agricultural productivity.

To address this problem, management strategies should be proposed based on the significant factors identified in this study. Efforts can be made to increase the amount of clay and moisture in the soil, while reducing the amount of sand and silt, to reduce soil erosion. Additionally, anthropogenic activities should be monitored to determine their impact on soil erosion. Overall, the study demonstrates that the use of ANN models and SHAP values can provide valuable insights into the factors that contribute to soil erosion, and the findings can help policymakers and soil management practitioners in developing more effective management strategies to prevent soil erosion and preserve soil health.

This study also highlights the need for further research to assess the applicability of these findings across different soil types and geographic locations. It is important to note that while the study was conducted in a specific area, the results can be used as a foundation for future research in other locations.

The study may also provide valuable insights into the factors that influence soil erodibility, which can be used to develop effective soil erosion management strategies. By implementing these strategies, it is possible to minimize the adverse impact of soil erosion on the environment, agriculture, and society. Therefore, it is crucial for researchers to conduct further studies to validate and expand upon these findings, ultimately leading to better soil erosion management practices globally.

In inference, the study demonstrates the potential of using ANN models and SHAP values to predict soil erodibility with high accuracy. These findings provide significant implications for soil erosion management and suggest that promoting conservation practices and monitoring anthropogenic activities can help prevent soil erosion and preserve soil health. With further research, the findings can be applied globally, leading to more effective soil erosion management practices and a healthier environment.

5. Conclusion

This study provides a comprehensive assessment of different conventional SEI and proposed PCA based SEI with ANN model. Also, the most influencing parameters for SEI have been identified using XAI in the form of SHAP for explaining the interconnection between management practices, soil quality, and crop yields. Significant differences were observed among CR and CLOM with the contribution of 25–27% accounted for >89% of the total variability. The MCR for the 70% of the study area was observed as low, 20% moderate and 10% as high. CLOM for the study area ranged from low to high; where 40% of soil showed low CLOM, 40% of soil showed moderate and remaining 20% of soil fall under high CLOM. Based on the *T*-test results, CR is significantly different from CLOM, MCR, and PCA, while CLOM is significantly different from MCR and PCA, and MCR is

significantly different from PCA. The ANN implementation demonstrated that the CLOM model had the highest accuracy for predicting soil erodibility, with SOC, sand, moisture, and void ratio being the most important variables. The SHAP analysis confirmed the importance of these variables for each of the four ANN models. These results highlight the importance of implementing effective soil erosion management strategies, especially in urban areas where erosion rates are highest. The results also suggest that monitoring and controlling anthropogenic activities that affect these variables, such as land use changes, construction, and irrigation practices, can help reduce soil erosion rates. Overall, these findings can inform policymakers and land managers on effective soil erosion management practices that can help protect soil health and ensure sustainable land use for future generations.

Despite the comprehensive approach used in this study to develop a standard SEI, there are limitations that should be considered. First, the study was conducted in a specific region, and the results may not be applicable to other regions with different soil types and environmental conditions. Second, the study only considered a limited number of soil attributes and did not incorporate biological indicators of soil quality, which are essential for the long-term sustainability of soil health. Finally, while the ANN models showed high accuracy in predicting soil erodibility, further research is needed to validate the results and assess their applicability to other regions.

Future research can build on the findings of this study to improve the accuracy and applicability of SEI models for different regions and soil types. Incorporating biological indicators of soil quality, such as microbial activity and biodiversity, can provide a more comprehensive understanding of soil health and sustainability. Additionally, the use of remote sensing techniques can help in the rapid assessment of soil erosion rates and inform soil erosion management strategies in real-time.

Data availability statement

The raw data supporting the conclusions of this article will be made available by the authors, without undue reservation.

Author contributions

JM, ST, and SA: conceptualization and formal analysis. JM and ST: data curation, methodology, software, and writing – original draft. SA: funding acquisition. JM: project administration, supervision, and validation. MA: resources and writing – review and editing. All authors contributed to the article and approved the submitted version.

Funding

Funding for this research was given under award numbers RGP2/185/43 by the Deanship of Scientific Research; King Khalid University, Ministry of Education, Kingdom of Saudi Arabia.

Acknowledgments

The authors extend their appreciation to the Deanship of Scientific Research at King Khalid University for funding this work through the Research Group under grant number RGP2/185/43. The authors are also thankful to the USGS Earth Explorer for making the LANDSAT data freely available.

Conflict of interest

The authors declare that the research was conducted in the absence of any commercial or financial relationships that could be construed as a potential conflict of interest.

Publisher's note

All claims expressed in this article are solely those of the authors and do not necessarily represent those of their affiliated organizations, or those of the publisher, the editors and the reviewers. Any product that may be evaluated in this article, or claim that may be made by its manufacturer, is not guaranteed or endorsed by the publisher.

References

Al-Najjar, H. A., Pradhan, B., Beydoun, G., Sarkar, R., Park, H. J., and Alamri, A. (2022). A novel method using explainable artificial intelligence (XAI)-based Shapley additive explanations for spatial landslide prediction using time-series SAR dataset. *Gondwana Res.* doi: 10.1016/j.gr.2022.08.004

Andrews, S. S., Karlen, D. L., and Mitchell, J. P. (2002). A comparison of soil quality indexing methods for vegetable production systems in Northern California. *Agric. Ecosyst. Environ.* 90, 25–45. doi: 10.1016/S0167-8809(01)00174-8

Arrieta, A. B., Díaz-Rodríguez, N., Del Ser, J., Bennetot, A., Tabik, S., Barbado, A., et al. (2020). Explainable artificial intelligence (XAI): concepts, taxonomies, opportunities and challenges toward responsible AI. *Inf. Fusion* 58, 82–115. doi: 10.1016/j.inffus.2019.12.012

Babur, E., Kara, O., Fathi, R. A., Susam, Y. E., Riaz, M., Arif, M., et al. (2021). Wattle fencing improved soil aggregate stability, organic carbon stocks and biochemical quality by restoring highly eroded Mountain region soil. *J. Environ. Manag.* 288:112489. doi: 10.1016/j.jenvman.2021.112489

Bhattacharyya, R., Ghosh, B. N., Mishra, P. K., Mandal, B., Rao, C. S., Sarkar, D., et al. (2015). Soil degradation in India: challenges and potential solutions. *Sustainability* 7, 3528–3570. doi: 10.3390/su7043528

Boger, Z., and Guterman, H., (1997) Knowledge extraction from artificial neural network models. In 1997 IEEE International Conference on Systems, Man, and Cybernetics. Computational Cybernetics and Simulation 4, 3030–3035). IEEE.

Bora, M. J., Bordoloi, S., Pekkat, S., Garg, A., Sekharan, S., and Rakesh, R. R. (2022). Assessment of soil erosion models for predicting soil loss in cracked vegetated compacted surface layer. *Acta Geophys.* 1–15. doi: 10.1007/s11600-021-00698-z

Bouyoucos, G. J. (1935). Clay ratio as a criterion of susceptibility of soils to erosion. *J. Am. Soc. Agron.* 27, 738–741.

Brejda, J. J., Karlen, D. L., Smith, J. L., and Allan, D. L. (2000). Identification of regional soil quality factors and indicators II. Northern Mississippi Loess Hills and Palouse Prairie. *Soil Sci. Soc. Am. J.* 64, 2125–2135. doi: 10.2136/sssaj2000.6462125x

Bryan, P. R. (1968). Measures of the degree of chemical weathering of rocks. *J. Geol.* 76, 518–527.

Cattell, R. B. (1966). The Scree test for the number of factors. *Multivar. Behav. Res.* 1, 245–276. doi: 10.1207/s15327906mbr0102_10

Das, S., Deb, P., Bora, P. K., and Katre, P. (2020). Comparison of RUSLE and MMF soil loss models and evaluation of catchment scale best management practices for a mountainous watershed in India. *Sustainability* 13:232. doi: 10.3390/su13010232

de Almeida Valente, F. D., de Castro, M. F., Lustosa Filho, J. F., de Carvalho Gomes, L., Neves, J. C. L., da Silva, I. R., et al. (2023). Native multispecies and fast-growing forest root biomass increase C and N stocks in a reclaimed bauxite mining area. *Environ. Monit. Assess.* 195:129. doi: 10.1007/s10661-022-10720-6

de Moraes Sa, J. C., Potma Goncalves, D. R., Ferreira, L. A., Mishra, U., Inagaki, T. M., Ferreira Furlan, F. J., et al. (2018). Soil carbon fractions and biological activity based indices can be used to study the impact of land management and ecological successions. *Ecol. Indic.* 84, 96–105. doi: 10.1016/j.ecolind.2017.08.029

Ding, F., YL, Y. L. H., Li, L. J., Li, A., Shi, S., Lian, P. Y., et al. (2013). Changes in soil organic carbon and total nitrogen stocks after conversion of meadow to cropland in Northeast China. *Plant Soil* 373, 659–672. doi: 10.1007/s11104-013-1827-5

Dissanayake, D. M. S. L. B., Morimoto, T., and Ranagalage, M. (2019). Accessing the soil erosion rate based on RUSLE model for sustainable land use management: A case study of the Kotmale watershed, Sri Lanka. *Model. Earth Syst. Environ.* 5, 291–306. doi: 10.1007/s40808-018-0534-x

Duarte, A. C., Ferreira, C., and Vitali, G. (2022). "Use of simulation models to aid soil and water conservation actions for sustainable agro-forested systems," in *Natural Resources Conservation and Advances for Sustainability.* Elsevier, 389–412.

Egbueri, J. C., Igwe, O., Omeka, M. E., and Agbasi, J. C. (2023). Development of MLR and variedly optimized ANN models for forecasting the detachability and liquefaction potential index of erodible soils. *Geosyst. Geoenviron.* 2:100104. doi: 10.1016/j.geogeo.2022.100104

Esa, E., Assen, M., and Legass, A. (2018). Implications of land use/cover dynamics on soil erosion potential of agricultural watershed, northwestern highlands of Ethiopia. *Environ. Syst. Res.* 7, 1–14. doi: 10.1186/s40068-018-0122-0

García, M. V., and Aznarte, J. L. (2020). Shapley additive explanations for NO2 forecasting. *Eco. Inform.* 56:101039. doi: 10.1016/j.ecoinf.2019.101039

Garg, A., Wani, I., and Kushvaha, V. (2022). Application of artificial intelligence for predicting erosion of biochar amended soils. *Sustainability* 14:684. doi: 10.3390/su14020684

Gilani, H., Ahmad, A., Younes, I., and Abbas, S. (2022). Impact assessment of land cover and land use changes on soil erosion changes (2005–2015) in Pakistan. *Land Degrad. Dev.* 33, 204–217. doi: 10.1002/ldr.4138

Gong, C., Tan, Q., Liu, G., and Xu, M. (2022). Impacts of mixed forests on controlling soil erosion in China. *Catena* 213:106147. doi: 10.1016/j.catena.2022.106147

Green, V. S., Stott, D. E., Cruz, J. C., and Curi, N. (2007). Tillage impacts on soil biological activity and aggregation in a Brazilian Cerrado Oxisol. *Soil Tillage Res.* 92, 114–121. doi: 10.1016/j.still.2006.01.004

Guo, D., Wang, J., Fu, H., Wen, H., and Luo, Y. (2017). Cropland has higher soil carbon residence time than grassland in the subsurface layer on the Loess Plateau, China. *Soil Tillage Res.* 174, 130–138. doi: 10.1016/j.still.2017.07.003

Harris, R. B. (2010). Rangeland degradation on the Qinghai-Tibetan Plateau: A review of the evidence of its magnitude and causes. *J. Arid Environ.* 74, 1–12. doi: 10.1016/j.jaridenv.2009.06.014

Hill, J., and Schütt, B. (2000). Mapping complex patterns of erosion and stability in dry Mediterranean ecosystems. *Remote Sens. Environ.* 74, 557–569. doi: 10.1016/S0034-4257(00)00146-2

Jiang, X. J., Liu, W., Wu, J., Wang, P., Liu, C., and Yuan, Z. Q. (2017). Land degradation controlled and mitigated by rubber-based agroforestry systems through optimizing soil physical conditions and water supply mechanisms: a case study in Xishuangbanna. *Land Degrad. Develop.* 28, 2277–2289. doi: 10.1002/ldr.2757

Kaiser, H. F. (1960). The application of electronic computers to factor analysis. *Educ. Psychol. Meas.* 20, 141–151. doi: 10.1177/001316446002000116

Kebede, Y. S., Endalamaw, N. T., Sinshaw, B. G., and Atinkut, H. B. (2021). Modeling soil erosion using RUSLE and GIS at watershed level in the Upper Beles, Ethiopia. *Environ. Challenges* 2:100009. doi: 10.1016/j.envc.2020.100009

Khalil, U., and Aslam, B. (2022). Geospatial-based soil management analysis using novel technique for better soil conservation. *Model. Earth Syst. Environ.* 8, 259–275. doi: 10.1007/s40808-020-01078-0

Kumar, H., and Pani, P. (2022). Soil erosion assessment in a part of gully affected Chambal region, Uttar Pradesh (India), using Morgan–Morgan–Finney model. *Model. Earth Syst. Environ.* 8, 5279–5288. doi: 10.1007/s40808-022-01375-w

Li, X., Gao, J., Brierley, G., Qiao, Y., Zhang, J., and Yang, Y. (2013). Rangeland degradation on the Qinghai-Tibet Plateau: implications for rehabilitation. *Land Degrad. Dev.* 24, 72–80. doi: 10.1002/ldr.1108

Mallick, J. (2016). Geospatial-based soil variability and hydrological zones of Abha semi-arid mountainous watershed, Saudi Arabia. *Arab Jour Geosci* 9:281. doi: 10.1007/s12517-015-2302-9

McCool, D. K., Brown, L. C., Foster, G. R., Mutchler, C. K., and Meyer, L. D. (1987). Revised slope steepness factor for the Universal Soil Loss Equation. *Transac ASAE* 30, 1387–1396. doi: 10.13031/2013.30576

Meinen, B. U., and Robinson, D. T. (2021). Agricultural erosion modelling: Evaluating USLE and WEPP field-scale erosion estimates using UAV time-series data. *Environ. Model Softw.* 137:104962. doi: 10.1016/j.envsoft.2021.104962

Millward, A., and Mersey, J. (1999). Adapting the RUSLE to Model Soil Erosion Potential in a Mountainous Tropical Watershed. *Catena* 38, 109–129. doi: 10.1016/S0341-8162(99)00067-3

Mirzaee, S., and Ghorbani-Dashtaki, S. (2021). Calibrating the WEPP model to predict soil loss for some calcareous soils. *Arab. J. Geosci.* 14, 1–10. doi: 10.1007/s12517-021-08646-3

Mohammadifar, A., Gholami, H., Comino, J. R., and Collins, A. L. (2021). Assessment of the interpretability of data mining for the spatial modelling of water erosion using game theory. *Catena* 200:105178. doi: 10.1016/j.catena.2021.105178

Mukhi, A. K. (1988). Credibility of some vertisols. *J. Indian Soc. Soil Sci.* 36, 532–535.

Nabiollahi, K., Golmohamadi, F., Taghizadeh-Mehrjardi, R., Kerry, R., and Davari, M. (2018). Assessing the effects of slope gradient and land use change on soil quality degradation through digital mapping of soil quality indices and soil loss rate. *Geoderma* 318, 16–28. doi: 10.1016/j.geoderma.2017.12.024

Naseri, F., Azari, M., and Dastorani, M. T. (2021). Spatial optimization of soil and water conservation practices using coupled SWAT model and evolutionary algorithm. *Int. Soil Water Conserv. Res.* 9, 566–577. doi: 10.1016/j.iswcr.2021.04.002

Nearing, M. A., Jetten, V., Baffaut, C., Cerdan, O., Couturier, A., Hernandez, M., et al. (2005). Modeling response of soil erosion and runoff to changes in precipitation and cover. *Catena* 61, 131–154. doi: 10.1016/j.catena.2005.03.007

Nouri, A., Esfandiari, M., Eftekhari, K., Torkashvand, A. M., and Ahmadi, A. (2023). Development support vector machine, artificial neural network and artificial neural network–genetic algorithm hybrid models for estimating erodible fraction of soil to wind erosion. *Int. J. River Basin Manage.* 1–10. doi: 10.1080/15715124.2022.2153856

Nyakatawa, E. Z., Reddy, K. C., and Lemunyon, J. L. (2001). Predicting soil erosion in conservation tillage cotton production systems using the revised universal soil loss equation (RUSLE). *Soil Till. Res.* 57, 213–224. doi: 10.1016/S0167-1987(00)00178-1

Olaniya, M., Bora, P. K., Das, S., and Chanu, P. H. (2020). Soil erodibility indices under different land uses in Ri-Bhoi district of Meghalaya (India). *Sci. Rep.* 10, 1–13. doi: 10.1038/s41598-020-72070-y

Pal, S. (2016). Impact of Massanjore dam on hydro-geomorphological modification of Mayurakshi river, Eastern India. *Environ. Dev. Sustain.* 18, 921–944. doi: 10.1007/s10668-015-9679-1

Pal, S., Paul, S., and Debanshi, S. (2022). Identifying sensitivity of factor cluster based gully erosion susceptibility models. *Environ. Sci. Pollut. Res.* 29, 90964–90983. doi: 10.1007/s11356-022-22063-3

Pandey, S., Kumar, P., Zlatic, M., Nautiyal, R., and Panwar, V. P. (2021). Recent advances in assessment of soil erosion vulnerability in a watershed. *Int. Soil Water Conserv. Res.* 9, 305–318. doi: 10.1016/j.iswcr.2021.03.001

Pieri, C. J. (2012). *Fertility of soils: A future for farming in the West African savannah*, *vol. 10.* Springer-Verlag, Berlin: Springer Science & Business Media.

Raiesi, F. (2017). A minimum data set and soil quality index to quantify the effect of land use conversion on soil quality and degradation in native rangelands of upland arid and semiarid regions. *Ecol. Indic.* 75, 307–320. doi: 10.1016/j.ecolind.2016.12.049

Raiesi, F., and Riahi, M. (2014). The influence of grazing exclosure on soil C stocks and dynamics, and ecological indicators in upland arid and semi-arid rangelands. *Ecol. Indic.* 41, 145–154. doi: 10.1016/j.ecolind.2014.01.040

Raiesi, F, and Salek-Gilani, S., (2020). Development of a soil quality index for characterizing effects of land-use changes on degradation and ecological restoration of rangeland soils in a semi-arid ecosystem. *Land Degrad. Dev.* 31, 1533–1544. doi: 10.1002/ldr.3553

Raza, A., Ahrends, H., Habib-Ur-Rahman, M., and Gaiser, T. (2021). Modeling approaches to assess soil erosion by water at the field scale with special emphasis on heterogeneity of soils and crops. *Land* 10:422. doi: 10.3390/land10040422

Rieke, E. L., Bagnall, D. K., Morgan, C. L., Flynn, K. D., Howe, J. A., Greub, K. L., et al. (2022). Evaluation of aggregate stability methods for soil health. *Geoderma* 428:116156. doi: 10.1016/j.geoderma.2022.116156

Rojas, J. M., Prause, J., Sanzano, G. A., Arce, O. E. A., and Sánchez, M. C. (2016). Soil quality indicators selection by mixed models and multivariate techniques in deforested areas for agricultural use in NW of Chaco, Argentina. *Soil Tillage Res.* 155, 250–262. doi: 10.1016/j.still.2015.08.010

Saha, S., Sarkar, D., and Mondal, P. (2022). Assessing and mapping soil erosion risk zone in Ratlam District, Central India. *Reg. Sustain.* 3, 373–390. doi: 10.1016/j.regsus.2022.11.005

Senanayake, S., and Pradhan, B. (2022). Predicting soil erosion susceptibility associated with climate change scenarios in the Central Highlands of Sri Lanka. *J. Environ. Manag.* 308:114589. doi: 10.1016/j.jenvman.2022.114589

Sheldrick, B. H., and Wang, C. (1993). "Particle Size Analysis" in *Soil sampling and methods of analysis.* ed. M. R. Carter (Boca Raton: Lewis Publishers), 499–517.

Shi, P., Li, P., Li, Z., Sun, J., Wang, D., and Min, Z. (2022). Effects of grass vegetation coverage and position on runoff and sediment yields on the slope of Loess Plateau. *Agric Water Manag* 259:107231. doi: 10.1016/j.agwat.2021.107231

Shrestha, N. K., Rudra, R. P., Daggupati, P., Goel, P. K., and Shukla, R. (2021). A comparative evaluation of the continuous and event-based modelling approaches for identifying critical source areas for sediment and phosphorus losses. *J. Environ. Manag.* 277:111427. doi: 10.1016/j.jenvman.2020.111427

Stagnari, F., Ramazzotti, S., and Pisante, M. (2010). "Conservation agriculture: a different approach for crop production through sustainable soil and water management: a review" in *Organic farming, pest control and remediation of soil pollutants*. ed. E. Lichtfouse (Dordrecht: Springer), 55–83.

Tang, Y., Duan, A., Xiao, C., and Xin, Y. (2022). The prediction of the Tibetan Plateau thermal condition with machine learning and Shapley additive explanation. *Remote Sens.* 14:4169. doi: 10.3390/rs14174169

Tarafdar, P. K., and Ray, R. (2005). Effect of trees on improvement of physical environment and fertility in soils of West Bengal. *Bull. Nat. Inst. Ecol.* 16, 129–136.

Telak, L. J., Dugan, I., and Bogunovic, I. (2021). Soil management and slope impacts on soil properties, hydrological response, and erosion in hazelnut orchard. *Soil Syst.* 5:5. doi: 10.3390/soilsystems5010005

Tesfahunegn, G. B., Ayuk, E. T., and Adiku, S. G. K. (2021). Farmers' perception on soil erosion in Ghana: Implication for developing sustainable soil management strategy. *PLoS One* 16:e0242444. doi: 10.1371/journal.pone.0242444

Toy, T. J., Foster, G. R., and Renard, K. G. (1999). RUSLE for mining, construction and reclamation lands. *J. Soil Water Conserv.* 54, 462–467.

Tsesmelis, D. E., Karavitis, C. A., Kalogeropoulos, K., Zervas, E., Vasilakou, C. G., Skondras, N. A., et al. (2022). Evaluating the degradation of natural resources in the Mediterranean environment using the water and land resources degradation index, the case of Crete Island. *Atmos.* 13:135. doi: 10.3390/atmos13010135

Vilone, G., and Longo, L. (2021). Notions of explainability and evaluation approaches for explainable artificial intelligence. *Inform. Fus.* 76, 89–106. doi: 10.1016/j.inffus.2021.05.009

Vincent, P. *Saudi Arabia: an environmental overview* (2008). CRC Press. Available at: https://www.routledge.com/Saudi-Arabia-An-Environmental-Overview/Vincent/p/book/9780367387815

Vitali, F., Mandalakis, M., Chatzinikolaou, E., Dailianis, T., Senatore, G., Casalone, E., et al. (2019). Benthic prokaryotic community response to polycyclic aromatic hydrocarbon chronic exposure: Importance of emission sources in Mediterranean ports. *Front. Mar. Sci.* 6:590. doi: 10.3389/fmars.2019.00590

Wander, M. M., and Bollero, G. A. (1999). Soil quality assessment of tillage impacts in Illinois. *Soil Sci. Soc. Am. J.* 63, 961–971. doi: 10.2136/sssaj1999.634961x

Wassie, S. B. (2020). Natural resource degradation tendencies in Ethiopia: a review. *Environ. Syst. Res.* 9, 1–29. doi: 10.1186/s40068-020-00194-1

Wieland, R., Lakes, T., and Nendel, C. (2021). Using Shapley additive explanations to interpret extreme gradient boosting predictions of grassland degradation in Xilingol. *Geosci. Model Dev.* 14, 1493–1510. doi: 10.5194/gmd-14-1493-2021

Wymore, A.W. (1993) *Model-based systems engineering. 1st*, CRC Press, Boca Raton.

Yang, Y., Tilman, D., Furey, G., and Lehman, C. (2019). Soil carbon sequestration accelerated by restoration of grassland biodiversity. *Nat. Commun.* 10:718. doi: 10.1038/s41467-019-08636-w

Zandi, L., Erfanzadeh, R., and Jafari, H. (2017). Rangeland use change to agriculture has different effects on soil organic matter fractions depending on the type of cultivation. *Land Degrad. Dev.* 28, 175–180. doi: 10.1002/ldr.2589

Zhang, Y., Xu, X., Li, Z., Liu, M., Xu, C., Zhang, R., et al. (2019). Effects of vegetation restoration on soil quality in degraded karst landscapes of southwest China. *Sci. Total Environ.* 650, 2657–2665. doi: 10.1016/j.scitotenv.2018.09.372

Zhang, K., Xu, P., and Zhang, J. (2020). "Explainable AI in deep reinforcement learning models: A shap method applied in power system emergency control" in *In 2020 IEEE 4th Conference on Energy Internet and Energy System Integration (EI2)* (IEEE), 711–716.

Zhang, X., Yu, G. Q., Li, Z. B., and Li, P. (2014). Experimental study on slope runoff, erosion and sediment under different vegetation types. *Water Resour. Manag.* 28, 2415–2433. doi: 10.1007/s11269-014-0603-5

Zuo, F. L., Li, X. Y., Yang, X. F., Wang, Y., Ma, Y. J., Huang, Y. H., et al. (2020). Soil particle-size distribution and aggregate stability of new reconstructed purple soil affected by soil erosion in overland flow. *J. Soils Sediments* 20, 272–283. doi: 10.1007/s11368-019-02408-1

frontiers | Frontiers in Environmental Science

TYPE Original Research
PUBLISHED 15 June 2023
DOI 10.3389/fenvs.2023.1191532

OPEN ACCESS

EDITED BY
Yonghao Xu,
Institute of Advanced Research in Artificial Intelligence (IARAI), Austria

REVIEWED BY
Anlu Zhang,
Huazhong Agricultural University, China
Rina Kumari,
Central University of Gujarat, India

*CORRESPONDENCE
Yong Zhou,
yzhou@ccnu.edu.cn

RECEIVED 22 March 2023
ACCEPTED 05 June 2023
PUBLISHED 15 June 2023

CITATION
Yi S, Zhou Y, Zhang J, Li Q, Liu Y, Guo Y and Chen Y (2023), Spatial-temporal evolution and motivation of ecological vulnerability based on RSEI and GEE in the Jianghan Plain from 2000 to 2020. *Front. Environ. Sci.* 11:1191532. doi: 10.3389/fenvs.2023.1191532

Spatial-temporal evolution and motivation of ecological vulnerability based on RSEI and GEE in the Jianghan Plain from 2000 to 2020

Siqi Yi[1,2], Yong Zhou[1,2]*, Junda Zhang[3], Qing Li[1,2], Yingying Liu[4], Yuting Guo[1,2] and Yaqi Chen[1,2]

[1]Key Laboratory for Geographical Process Analysis and Simulation of Hubei Province, Central China Normal University, Wuhan, China, [2]College of Urban Environmental Sciences, Central China Normal University, Wuhan, China, [3]Cultivated Land Quality Monitoring and Protection and Rural Affairs, PRC, Beijing, China, [4]College of Geography and Environmental Science, Henan University, Kaifeng, China

Recent urbanization and growing food consumption have had a severely detrimental effect on the ecological environment of the Jianghan Plain. The ecological fragility of the Jianghan Plain must be continually monitored for environmental conservation and sustainable development. This study utilized principal component analysis (PCA) to quantitatively assess the ecological vulnerability of the Jianghan Plain based on the remote sensing ecological index (RSEI) and analyzed the space-time changes and drivers in the Jianghan Plain from 2000 to 2020 using the Google Earth Engine Platform (GEE). The findings of this research indicated that the ecological vulnerability of the Jianghan Plain from 2000 to 2020 was predominantly Moderate or Strong level. But still, the EVI displayed a changing decreasing trend, revealing a small development towards a healthier ecological environment. The most significant ecological vulnerability deterioration occurred between 2005 and 2010, accounting for roughly 44.90 percent, whereas the highest improvement occurred between 2000 and 2005, occupying approximately 37.52% of the area. Moran's I of EVI was greater than 0 in Jianghan Plain and displayed a growing and subsequently a falling trend, representing that the spatial distribution of regional ecological vulnerability was strongly correlated and aggregated and that the degree of aggregation has declined. The effects of heat, greenness, wetness, and dryness on the ecological vulnerability of Jianghan Plain were all significant, with greenness and wetness being the primary determinants of the change in Jianghan Plain's ecological vulnerability. The results of this study can offer a theoretical and scientific foundation for ecological protection and restoration in the Jianghan Plain. Meanwhile, this study also provides a practical and rapid method for monitoring regional ecological vulnerability using RSEI, GEE, and PCA, which can be applied elsewhere for ecological vulnerability evaluation.

KEYWORDS

ecological vulnerability, remote sensing ecological index, principal component analysis, Google Earth engine, Geodetector

1 Introduction

With the continuous population growth and rapid economic development, the regional natural environment's carrying capacity and buffer capacity are facing a serve test due to unreasonable resource utilization (Wei and Ye, 2014; Zhang et al., 2022). The contradiction between humans and the environment has become increasingly prominent (Zheng et al., 2021). Ecological degradation has occurred in many regions of the world, and ecological fragility problems are becoming increasingly severe, for example, biodiversity reduction, land desertification, and soil pollution. Therefore, when researching global environmental change and sustainable development, ecological vulnerability has garnered much attention from academics and has emerged as one of the most critical topics to consider (Nguyen et al., 2016; Xu et al., 2018). Conducting ecological vulnerability research is vital for environmental protection and has crucial guiding significance for the efficient management of land resources and long-term growth. (He et al., 2018; Thiault et al., 2018).

With the strengthening of investigations into the consequences of global environmental change, especially for the in-depth exploration of the human-nature relationship, the study of ecological vulnerability has yielded fruitful results in terms of theory and empirical evidence (Beroya-Eitner, 2016; Weißhuhn et al., 2018; Chen et al., 2022). Numerous scholars have used a variety of assessment approaches to perform numerous investigations into various regions. For instance, Cao et al. (2022) constructed the ecological vulnerability index of Shenlongjia thoroughly and quantitatively using the vulnerability scoring diagram (VSD) model during a 22-year period. Hou et al. (2020) combined GIS data with a fuzzy analytic hierarchy method to study hierarchical variations of regional ecological vulnerability. And Boori et al. (2022) proposed a driver-pressure-state-impact-response (DPSIR) framework based on 3S technology and analytical hierarchy process (AHP) to compute the ecological vulnerability index (EVI). However, most assessment systems in previous research are influenced by subjective factors and weighting decisions. The assessment model incorporates all chosen indicators, disregarding the indicators' independence (Zhang et al., 2017; Guo et al., 2019). It increases calculations or inaccurate results (Cai et al., 2021). In recent years, some researchers have increasingly used remote sensing data to construct ecological vulnerability indicators due to their accessibility, objectivity, and accuracy (Liou et al., 2017; Xu et al., 2017). Bai and Ma (2010) established an assessment method of ecological vulnerability using eight indicators extracted from remote sensing data in Qinghai Lake. And Chen et al. (2019) examined ecological vulnerability and discussed its change pattern from 1990 to 2015 in the Amu Darya river basin using image elements as the evaluation object based on multi-source remote sensing data. Therefore, we used a comprehensive index built from Greenness, Wetness, Dryness, and Heat based on the remote sensing ecological index (RSEI). RSEI, as a quantitative measure of regional ecological quality, can not only effectively avoid the subjective influence of human beings in ecological vulnerability studies but also improve the efficiency of evaluation (Hang et al., 2020; Jing et al., 2020; Jiang et al., 2023). RSEI can also be visualized and compared at various spatial and temporal dimensions. Additionally, prior studies have confirmed the validity and credibility of this indicator used in ecological research (Zhu Z. et al., 2015; Kasimu et al., 2019).

As an open-access platform, Google Earth Engine (GEE) significantly simplifies the use of remote sensing data in various research, particularly in large-scale study areas (Gorelick et al., 2017). GEE collects many datasets, such as Landsat, MODIS, ASTER, etc. And GEE allows users to develop interactively and test algorithms and acquire and process shared data in an online or offline programmatic manner, which is advantageous for using remote sensing data in long-term and large-scale studies and dramatically improves the effectiveness of processing remote sensing images (Parastatidis et al., 2017; Ye et al., 2021). Compared to traditional tools, the GEE platform offers significant advantages in the efficiency and accuracy of calculations in research (Kumar and Mutanga, 2018; Xu et al., 2022).

The Jianghan Plain in Hubei Province is a central part of the Yangtze River Plain's middle and lower reaches (Li X. et al., 2022). Due to its unique geographical location and social functions, the Jianghan Plain is one of the prominent carriers of human production and life and assumes essential ecosystem service functions (Jiang et al., 2022). However, as the Jianghan Plain's population and economic development have grown, the dual pressures of increased food production and rapid urbanization have resulted in increasingly serious ecological problems. How to accomplish a win-win goal for socioeconomic growth and environmental protection has come to be a major concern for the region. Thus, long-term monitoring of changes in the Jianghan Plain's ecological vulnerability is required to provide a scientific rationale for future sustainable development decisions. Considering the above facts, we first effectively constructed the EVI using Landsat data on the GEE platform. After that, we visualized the spatial and temporal variation of ecological vulnerability in Jianghan Plain and analyzed the leading impact indicators of changes to reveal the evolution patterns of ecological vulnerability in the region. (Figure 1). The aim is to provide full theoretical support and a scientific foundation for local government to make decisions regarding sustainable development and ecological management in the Jianghan Plain, as well as to offer a workable and efficient method for assessing the regional ecological vulnerability using GEE.

2 Materials and methods

2.1 Study area

The Jianghan Plain is situated in Hubei Province's southernmost region (29°26′-31°37′N, 111°14′-114°36′E). It forms a significant portion of the middle and lower reaches of the Yangtze River Plain, with Jingmen to the north, the Dongting Lake Plain to the south, Wuhan to the east, and Yichang to the west (Figure 2). The overall area is around 29,000 square kilometers and is primarily comprised of 14 counties and cities: Danyang, Zhijiang, Songzi, Jingzhou, Jiangling, Gongan, Shishou, Qianjiang, Jili, Tianmen, Xiantao, Honghu, Yunmeng, Yingcheng, and Hanchuan (Huang et al., 2020). The altitude decreases from the northwest to the

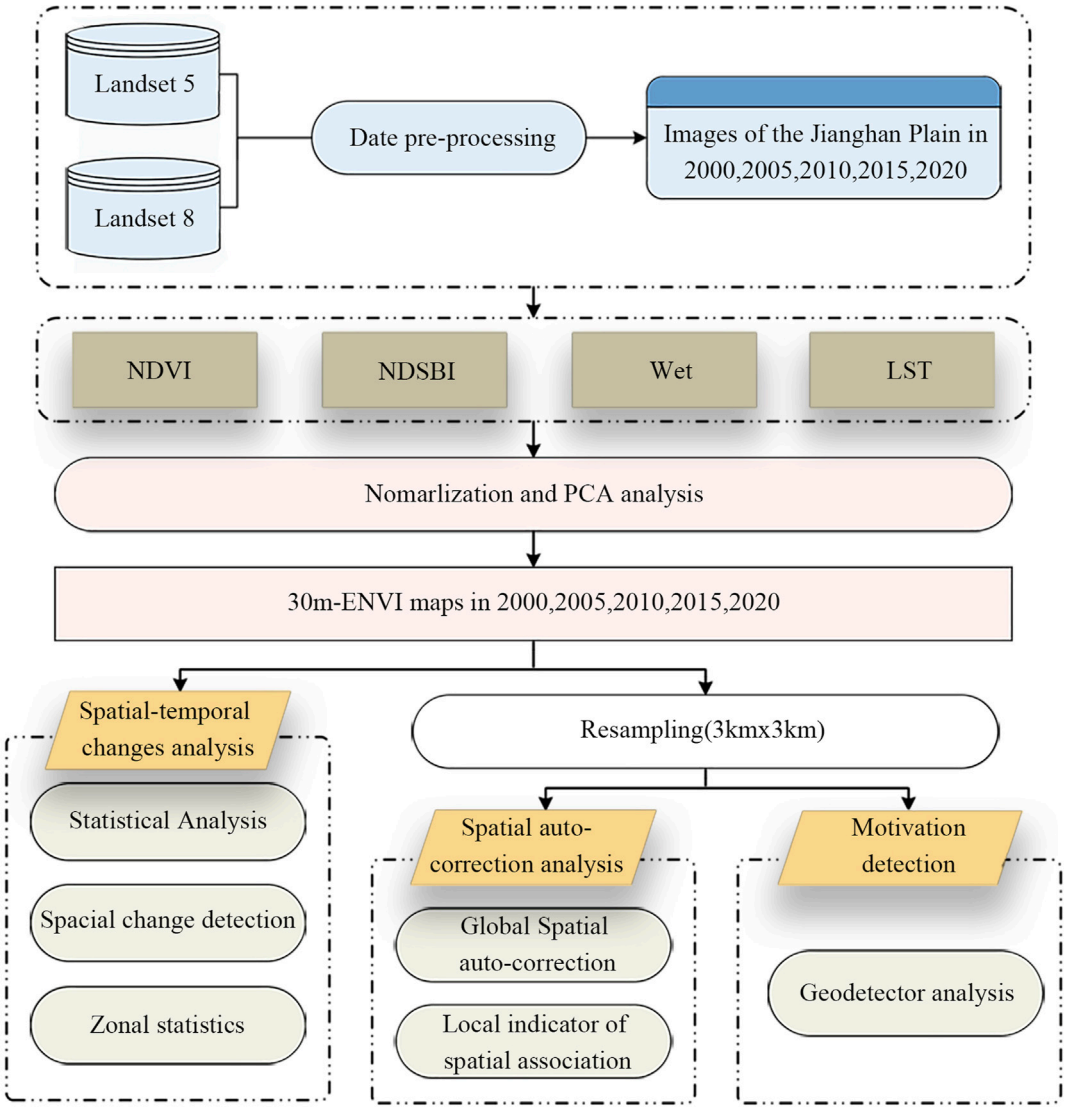

FIGURE 1
Workflow.

southeast. Also, there is predominantly flat, with numerous lakes and rivers. With average annual temperatures between 14 and 18°C and yearly precipitation between 1,100 and 1,300 mm, it has a typical subtropical monsoon climate. Rainfall and high temperatures coincide, and 240 to 260 frost-free days per year are optimal for growing food crops. (Wang et al., 2011). The Jianghan Plain is a critical commodity food base for China because of its advantageous position and food production. And China's food security is also influenced by the state of its ecological ecosystem, which can have both good and adverse effects on the quality of its agricultural output.

2.2 Data and processing

In this study, we employed data from Landsat 5 TM (2000, 2005, 2010) and Landsat 8 OLI/TIRS (2015 and 2020) provided by Google Earth Engine (GEE) to map the spatial and temporal distribution of EVI changes from 2000 to 2020 (Xiao et al., 2019). Because these data have been pre-processed with atmospheric correction, radiometric calibration, and geometric correction, they are immediately usable on the GEE platform (Kumar and Mutanga, 2018; Zhao et al., 2021). To eliminate the effect of clouds, we mean-synthesized the images of the target year and its preceding and following years and applied the corresponding de-clouding algorithm to obtain the required images (Tang et al., 2023). Then, the Normalized Difference Soil Index (NDBSI), the Land Surface Temperature (LST), the Normalized Difference Vegetation Index (NDVI), and Wetness (WET) are calculated based on the de-clouded images, and the specific formulas are shown in Table 2. The processes mentioned above are executed on the GEE platform, and Table 1 displays the image data utilized for this study.

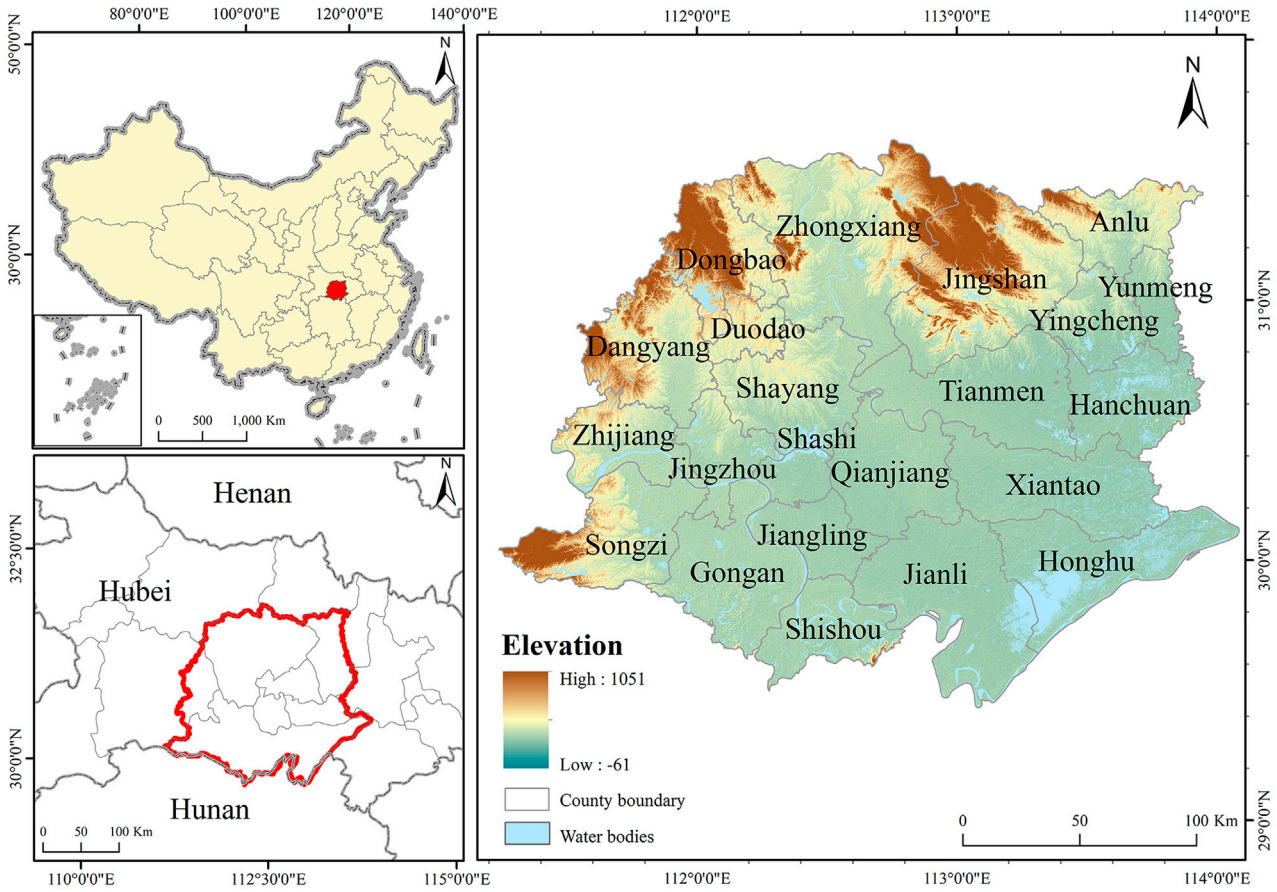

FIGURE 2
The location of the Jianghan Plain.

TABLE 1 Data source.

Data	Source and data details	resolution/m
Landsat5, Surface reflectance Product	Google Earth Engine Platform (product identifier: LANDSAT/L05/C01/T1_SR, used bands:1,2,3,4,5,6)	30
Landsat8, Surface reflectance Product	Google Earth Engine Platform (product identifier: LANDSAT/L08/C01/T1_SR, used bands:2,3,4,5,6,7,10)	30
Land cover	Resources and Environmental Sciences	30

2.3 Methodology

2.3.1 Construction of ecological vulnerability Index (EVI)

Since Xu Qiuhan proposed a comprehensive evaluation of regional ecological quality, researchers have regularly used the four indicators of greenness, moisture, heat, and dryness in regional ecological studies (Xu, 2013a; 2013b). For this reason, we chose four indicators to build the ecological vulnerability index (EVI), and these four indicators are obtained through the standardization of NDVI, Wet, NDBSI, and LST. We also used the modified normalized difference water index (mNDWI) to remove bodies of water from the research region, which further improved the accuracy of the Wet calculation (Xu, 2005). Table 2 lists the relevant calculation equations.

The EVI was constructed using the first, second, and third principal components (PC1, PC2, and PC3) obtained from the principal component analysis (PCA) of four indicators. This is because the combined participation rates of PCs 1, 2, and 3 are higher than 99%. Before using PCA analysis, indicators' values must be normalized because they have various numerical ranges and units. Positive and negative indicators can be distinguished among ecological vulnerability indicators. According to relevant studies (Yao et al., 2016; Wang and Su, 2018), dryness and heat have a detrimental effect on the ecological environment, so they are normalized using Eq. 2. In contrast, greenness and wetness have a beneficial effect, so they are normalized using Eq. 1.

$$SI_i = \frac{I_i - I_{min}}{I_{max} - I_{min}} \quad (1)$$

TABLE 2 Calculation methods of indicators.

Indicators	Formula	Parameters and explanation
NDVI	$\frac{B_{nir}-B_{red}}{B_{nir}+B_{red}}$	B_i indicates the bands of Landsat5 TM and Landsat8 OLI/TIRS bands; β_i are the surface reflectance of each band in different images; SI and IBI respectively denote soil index and building index. Crist. (1985); Xu. (2008), Xu. (2010)
Wet	$\beta_1 B_{blue} + \beta_2 B_{green} + \beta_3 B_{red} + \beta_4 B_{nir} + \beta_5 B_{swir1} + \beta_6 B_{swir2}$	
NDSBI	$SI = \frac{(B_{swir1}+B_{red})-(B_{blue}+B_{nir})}{(B_{swir1}+B_{red})+(B_{blue}+B_{nir})}$	
	$IBI = \frac{(\frac{2B_{swir1}}{B_{swir1}+B_{red}})-(\frac{B_{nir}}{B_{nir}+B_{red}}-\frac{B_{green}}{B_{green}+B_{swir1}})}{(\frac{2B_{swir1}}{B_{swir1}+B_{red}})+(\frac{B_{nir}}{B_{nir}+B_{red}}-\frac{B_{green}}{B_{green}+B_{swir1}})}$	
	$NDBSI = \frac{SI+IBI}{2}$	
LST	$\gamma \times (\frac{\varphi_1 + L_{sensor} + \varphi_2}{\varepsilon} + \varphi_3) + \delta$	ε is the surface specific emissivity; γ is a constant; φ_i based on calculations by Jimenez-Munoz et al. (2009); L_{sensor} is the radiation brightness measured by the sensor
mNDWI	$\frac{B_{green}-B_{swir1}}{B_{green}+B_{swir1}}$	B_i indicates the bands of Landsat5 TM and Landsat8 OLI/TIRS bands Xu (2005)

$$SI_i = \frac{I_{max} - I_i}{I_{max} - I_{min}} \quad (2)$$

Where I_i denotes the standardized value of indicator i, with a value range of [0, 1]; I_{min} denotes the lowest value of indicator i; I_{max} denotes the highest value of indicator i. After normalization of all indicators, we used PCA in Google Earth Engine to calculate PC1, PC2, and PC3. We obtained the value of EVI using Eq. 3 based on the PCA results.

$$EVI = r_1 Y_1 + r_2 Y_2 + r_3 Y_3 \quad (3)$$

Where EVI represents the status and characteristics of the ecological vulnerability; r_i and Y_i represent the ith principal component and the contribution rate of the ith principal component, respectively. We divided the EVI in Jianghan Plain into five levels, each with a 0.2 increment, because the closer the value is to 1, the more fragile the ecosystem is. Among them, Level Ⅰ (Slight): 0–0.2; Level Ⅱ (Light): 0.2–0.4; Level Ⅲ(Moderate): 0.4–0.6; Level Ⅳ (Strong): 0.6–0.8; Level Ⅴ (Extreme): 0.8–1.0.

2.3.2 Geodetector

Geodetector is a quantitative approach to identifying spatial heterogeneity and illuminating the main drivers behind the phenomenon (Zhou X. et al., 2021; Guo et al., 2022). Since Jinfeng Wang and others proposed geodetector in 2004, it has been extensively employed in various fields, including land use, ecology, soil, and regional economy, due to its superiority in being able to be used for both numerical and typological data and immune to covariance (Wang and Xu, 2017; Zhou et al., 2020; Zhou et al., 2021 X.). In this study, using the factor detector, we explored the influence of four indicators (Wet, LST, NDSBI, and NDVI) on EVI.

$$q = 1 - \frac{\sum_{i=1}^{l} N_i \sigma_i^2}{N\sigma^2} = 1 - \frac{SSW}{SST} \quad (4)$$

$$SSW = \sum_{i=1}^{l} N_i \sigma_i^2 \quad (5)$$

$$SST = N\sigma^2 \quad (6)$$

Where i = 1,2⋯l represents the classification or strata of the factor; N_i and σ_i are the number of units and variance at class or strata i; N and σ are the sum of units and variance within the study area; SST and SSW denote the total sum of squares and the within sum of squares, respectively. Higher q values indicate more explanatory power of independent factors on a dependent variable, and the range for q is [0,1].

2.3.3 Spatial auto-correlation

Spatial auto-correlation reflects the degree of correlation between a phenomenon in a region and the same phenomenon in neighboring regional units, including global auto-correlation and local auto-correlation (Fan and Cowley, 1985; Martin, 1996). It is a vital index to test whether an element's ecological vulnerability is correlated with its adjacent space's ecological vulnerability (Jing et al., 2020). For spatial analysis, the main methods applied in numerous studies are the local indicator of spatial association (Local Moran's I) and the global spatial auto-correlation (Global Moran's I).

The Global Moran's I can disclose the regional clustering of the spatial layout of ecological environment vulnerability. Its value is between plus and minus 1. A value above zero denotes a positive spatial correlation, a zero value denotes no spatial correlation at all, and a value below zero denotes one negative (Wan et al., 2011). The following is the calculation formula:

$$Global\ Moran's\ I = \frac{N\sum_{i=1}^{N}\sum_{j=1}^{N} w_{ij}(x_i - \bar{x})(x_j - \bar{x})}{\sum_{i=1}^{N}\sum_{j=1}^{N} w_{ij}(x_i - \bar{x})^2} \quad (7a)$$

Where N is the total of elements; w_{ij} is the spatial weight matrix; x_i represents the ecological vulnerability value of position i; $\bar{x}$ is the average value of all ecological vulnerability values.

Local Moran's I, also known as LISA (Local Indicators of Spatial Association, is a valuable indicator of the geographic correlation of each unit's ecological vulnerability (Anselin, 2010). When the global auto-correlation exits, LISA is able to analyze further whether there is spatial heterogeneity. Therefore, it is necessary to calculate Local Moran's I. The calculation formula is shown in Eq. 8, and the parameters in the formula are consistent with Eq. 7 (Lei et al., 2019; Xiong et al., 2021).

TABLE 3 PCA results in 2000,2005,2010,2015 and 2020.

Year	Indicator	PC1	PC2	PC3	PC4
2000	NDVI	0.758	−0.587	−0.162	0.232
	WET	0.148	0.517	0.030	0.842
	NDBSI	0.632	0.557	0.273	−0.464
	LST	0.057	0.278	−0.947	−0.147
	Eigenvalue	0.009	0.003	0.002	0.000
	Percent eigenvalue	64.42%	20.48%	14.23%	0.87%
2005	NDVI	0.865	0.207	−0.419	−0.179
	WET	0.060	−0.368	0.316	−0.72
	NDBSI	0.480	−0.528	0.536	0.451
	LST	0.131	−0.736	−0.661	0063
	Eigenvalue	0.009	0.002	0.001	0.000
	Percent eigenvalue	78.64%	14.17%	6.66%	0.53%
2010	NDVI	0.561	0.267	0.768	−0.156
	WET	0.077	0.124	−0.291	−0.946
	NDBSI	0.636	0.446	−0.562	0.283
	LST	0.524	0.845	0.097	0.039
	Eigenvalue	0.012	0.005	0.002	0.000
	Percent eigenvalue	63.46%	28.12%	8.22%	0.20%
2015	NDVI	0.801	−0.575	−0.029	0.162
	WET	0.101	0.396	0.003	0.912
	NDBSI	0.589	0.709	0.105	−0.374
	LST	0.039	0.093	−0.994	−0.041
	Eigenvalue	0.015	0.003	0.002	0.000
	Percent eigenvalue	75.22%	12.93%	11.59%	0.27%
2020	NDVI	0.813	−0.555	−0.112	0.136
	WET	0.103	0.353	0.123	0.921
	NDBSI	0.555	0.648	0.376	−0.361
	LST	0.142	0.384	−0.912	−0.041
	Eigenvalue	0.015	0.002	0.002	0.000
	Percent eigenvalue	76.96%	12.12%	10.69%	0.23%

$$\textit{Local Moran's } I = \frac{(x_i - \bar{x})\sum_{j=1}^{N}(x_j - \bar{x})}{\sum_{i=1}^{N}(x_i - \bar{x})^2} \tag{7b}$$

The LISA has five types of spatial aggregation, High-High (HH), High-Low (HL), Low-High (LH), Low-Low (LL), and Not significant (Jing et al., 2020). The HH represents that a region with a high value is accompanied by other areas with a high value. In contrast, the LL means that an area with a low value is accompanied by other sites with a low value. LH denotes that the chosen area's value is low while the surrounding area's value is high. HL denotes that while the value of the selected location is high, the value of the nearby area is low. HH and LL show high positive spatial correlations and regional clustering and similarity.

2.3.4 Coupling coordinative degree model

The coupling coordination degree describes the degree of interaction and coordination among systems or elements, reflecting the strength of each system's interconnectedness and the good or bad coordination between systems. In recent years, the coupling coordination degree model has been widely used to describe the nonlinear interaction between multiple systems in many disciplines, such as biology, geography, ecology, and urbanization (Li et al., 2013; Liu et al., 2022). The coordination coupling degree model (CCDM) is used to evaluate the degree of coordination development between two or more subsystems, and its calculation formula is shown as follows:

$$\begin{cases} C = \dfrac{n\sqrt{X_1 X_2 \ldots X_n}}{X_1 + X_2 + \ldots + X_n} \\ T = \alpha_1 X_1 + \alpha_2 X_2 + \ldots + \alpha_n X_n \\ D = \sqrt{C \times T} \end{cases} \tag{8}$$

Where C denotes the coupling degree between systems, T represents the coordination degree between systems, D denotes the coordination coupling degree between systems, $X_1 X_2 \ldots X_n$ indicates the selected subsystem, $\alpha_1 \alpha_2 \ldots \alpha_n$ represents the coefficients to be determined and $\alpha_1 + \alpha_2 + \ldots + \alpha_n = 1$. C and D take values between 0 and 1.

3 Results

3.1 Overall characteristic of ecological vulnerability

As demonstrated in Table 3, the sum contribution rates of the first, second, and third principal components (PC1, PC2, PC3) were higher than 99%, with 99.13% in 2000, 99.47% in 2005, 99.80% in 2010, 99.73% in 2015, 99.77% in 2020, respectively. It indicated that PC1, PC2, and PC3 concentrated the majority of traits of the four indicators.

Table 4 displays the results of descriptive statistics for the EVI and all data variables used in this study. During the past 2 decades, NDVI and Wet values in the Jianghan Plain have fluctuated upwards. Their mean values increased from −0.096 and 0.445 in 2000 to −0.033 and 0.476 in 2020, with increases of 65.62% and 6.97%. It indicated that water conservation capacity in the Jianghan Plain had improved, and the vegetation cover had shown an increasing trend. The NDBSI had decreased by 20.32 percent, with the average value falling from −0.123 in 2000 to −0.148 in 2020, meaning a reduction in the Jianghan Plain's surface exposure. While the surface temperature, which is strongly tied to water and plant, increased annually, with the average value increasing from 21.226 in 2000 to 22.452 in 2020, a 5.75% increase. It meant that the water-heat balance difference in the Jianghan Plain had increased, which had a substantial impact on the regional ecological vulnerability. Regarding the Minimum, four indicators showed a decreasing and then increasing trend. The turning year of NDVI and WET occurred in 2010, while the turning year of LST and NDBSI was in 2010. And the maximum of NDVI, LST, WET, and NDBSI peaked in 2020. The standard deviations

TABLE 4 Statistics of four indicators and EVI.

Years	Statistics	NDVI	WET	LST	NDBSI	EVI
2000	Minimum	−0.494	−0.703	−0.087	−0.490	0.000
	Maximum	0.830	0.029	30.156	0.410	1.000
	Mean	0.445	−0.096	21.226	−0.123	0.656
	Std Dev	0.103	0.030	1.348	0.061	0.358
2005	Minimum	−0.677	−0.849	−5.185	−0.905	0.000
	Maximum	0.983	0.184	55.49	0.68	1.000
	Mean	0.516	−0.092	21.512	−0.134	0.605
	Std Dev	0.138	0.033	2.239	0.083	0.072
2010	Minimum	−0.788	−0.929	3.235	−0.524	0.000
	Maximum	0.861	0.213	35.142	0.483	1.000
	Mean	0.467	−0.095	21.925	−0.125	0.627
	Std Dev	0.035	0.035	2.720	0.081	0.099
2015	Minimum	−0.226	−0.735	4.851	−0.610	0.000
	Maximum	0.979	0.129	36.779	0.723	1.000
	Mean	0.526	−0.050	22.343	−0.131	0.577
	Std Dev	0.126	0.032	2.336	0.091	0.094
2020	Minimum	−0.345	−0.807	5.153	−0.644	0.000
	Maximum	0.996	0.162	44.597	0.943	1.000
	Mean	0.476	−0.033	22.452	−0.148	0.546
	Std Dev	0.146	0.037	1.678	0.093	0.091

of all four indicators except LST were less than 0.2, indicating that all variables used in this study were discrete to a small extent in 2000,2005, 2010, 2015, and 2020. From 2000 to 2020, the average EVI values in the Jianghan Plain were between 0.5 and 0.7. The ecological vulnerability level of most areas in Jianghan Plain was mainly at Moderate or Extreme levels. During 20 years, the mean EVI value showed a trend of "down—up—down," demonstrating that the ecological vulnerability of Jianghan Plain fluctuated downward. Indirectly, it also side reflected the movement toward enhancing the environmental quality of Jianghan Plain. Moreover, the turning years of the trends of the other three indicators are consistent with the EVI except for LST.

Figure 3 illustrates the proportional change in each ecological vulnerability level. From 2000 to 2020, the majority of ecological vulnerability level was either Moderate or Strong. The proportion of Slight and Light levels increased, whereas the percentage of the Slight level was the lowest each year. Over 20 years, the proportion of Moderate level fluctuating grew, with the highest rate occurring in 2020. The change in the Extreme level was the opposite of the Moderate level, and it showed a fluctuating decrease, with the lowest percentage of 29.06% in 2020. The rate of Extreme level was the largest in 2010 with 9.29%, and only 0.86%, 0.02%, 0.34%, and 0.13% in 2000, 2005, 2015, and 2020, respectively. The temporal changes of the extreme level were generally consistent with the EVI trend in study time.

Dark green, light green, yellow, orange, and brown represent Mild, Light, Moderate, Strong, and Extreme ecological vulnerability, respectively, in Figure 4. From 2000 to 2020, the spatial and temporal patterns of ecological vulnerability in the Jianghan Plain were highly variable and strongly tied to human agricultural production, urban expansion, and some government policies over 20 years. The temporal and spatial patterns of ecological vulnerability in the Jianghan Plain were highly variable from 2000 to 2020 and were deeply associated with human agricultural activities, urbanization, and specific government policies. Ecological vulnerability decreased from south to northwest in the Jianghan Plain in 2000. The region with the lowest ecological vulnerability was Zhongxiang, while Hanchuan was the most vulnerable. In 2005, 2010, 2015, and 2020, the ecological vulnerability decreased from west to east in the Jianghan Plain. In 2010, the area of Extreme level in the Jianghan Plain increased significantly and was mainly distributed in Dongbao, Dangyang, Songzi, Gongan, Shihou, and Jiangling. In 2015 and 2020, Anlu, Yunmeng, Hanchuan, Xiantao, and Honghu in the eastern proportion of the Jianghan Plain and Zhongxiang in the northern part of the Jianghan Plain had low ecological vulnerability levels, while the regions with comparatively high ecological vulnerability levels were primarily situated in the central and northeastern proportion in the Jianghan Plain.

In terms of city scale, from 2000 to 2020, the EVI value of Jingmen was low, which represented the ecological environment was relatively good and the possibility of ecological degradation was relatively low (Figure 5). The relatively high EVI values in Xiaogan indicated high ecological vulnerability. Nonetheless, it displayed a significant downward trend, meaning that the ecological environment in Xiaogan has considerably improved from 2000 to 2020. Jingzhou and Yichang have higher EVI values, and in 2010 the EVI of these two cities was the highest of all cities studied. It suggested that the two cities were more vulnerable to environmental threats. However, after 2010, the EVI values of the two cities also decreased significantly, reflecting that the two cities' ecological environment had become better and was trending in a positive direction.

Regarding the district and county scales, the EVI values of each district and county showed fluctuations and decreases. And in 2010, all other Counties or Districts showed an increasing trend except Honghu, Dongdao, Jingshan, Duodao, Shayang, Yingcheng, Hanchuan, and Anlu. Most Counties or Districts had their maximum values of EVI in 2010, while all Counties or Districts had the lowest EVI values in 2020, which denoted that all counties or districts had improved their ecological environment quality with proper environmental protection measures in 2000–2020.

3.2 Dynamic changes in EVI

Based on the EVI level classification findings in 2000, 2005, 2010, 2015, and 2020, the spatial distributions were mapped in Figure 6, and the area changes were listed in Table 5 to investigate further shifts of ecological vulnerability in the Jianghan Plain over 20 years. We determined the area changes for each EVI level and categorized the results into four categories based on four time periods (2000–2005, 2005–2010, 2010–2015, and 2015–2020). They were, respectively, Obvious Improvement (OI), Slight Improvement (SI), Invariability

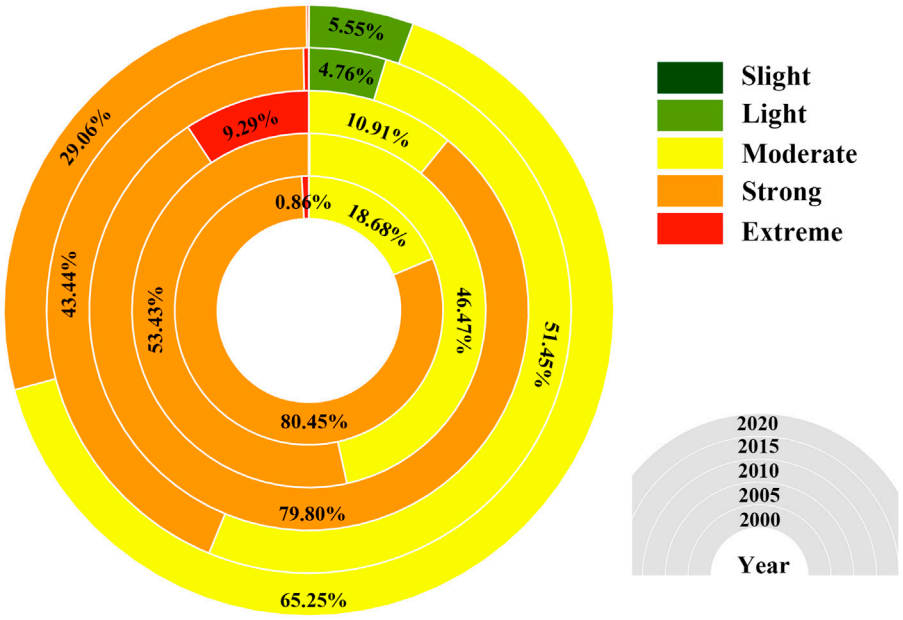

FIGURE 3
The proportion of ecological vulnerability index (EVI) in Jianghan Plain from 2000 to 2020.

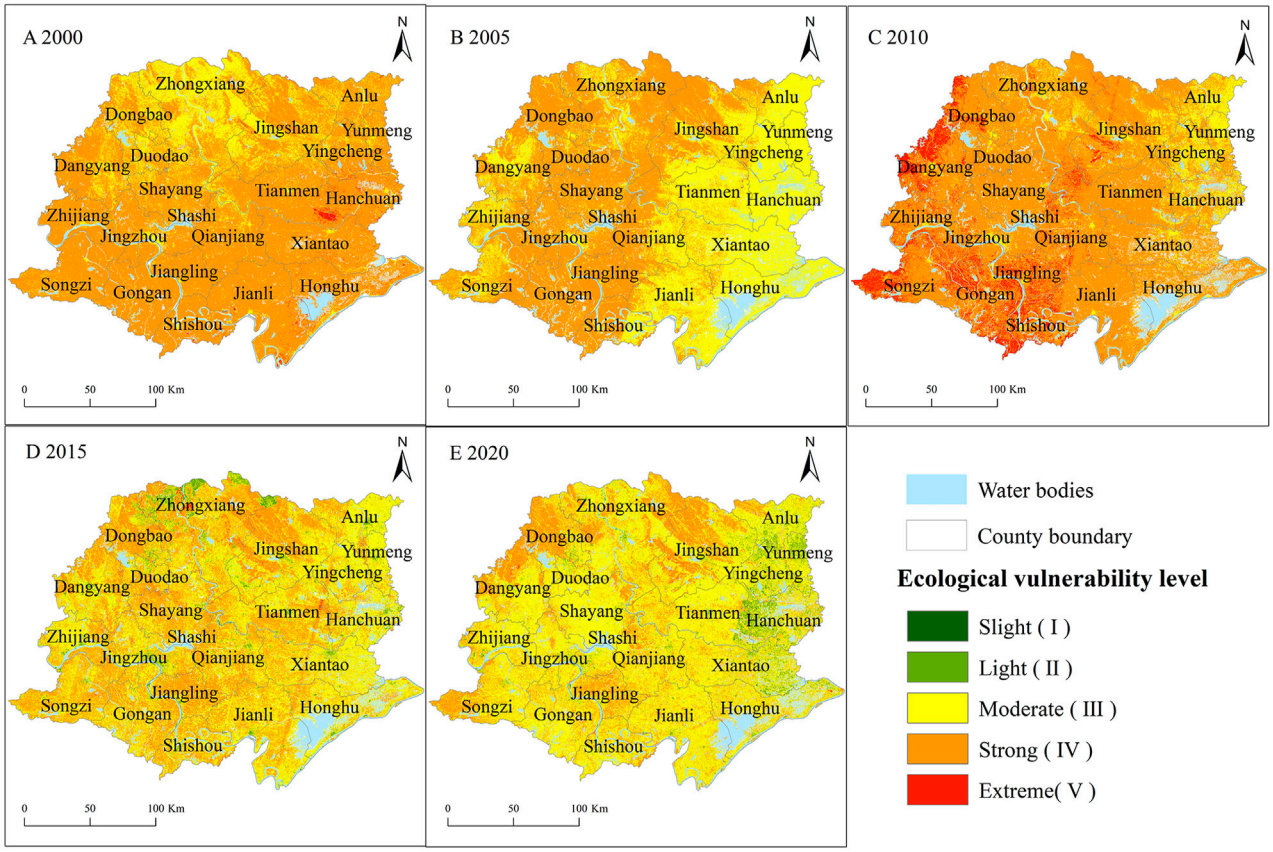

FIGURE 4
Spatial distribution of ecological vulnerability index (EVI) in Jianghan Plain from 2000 to 2020.

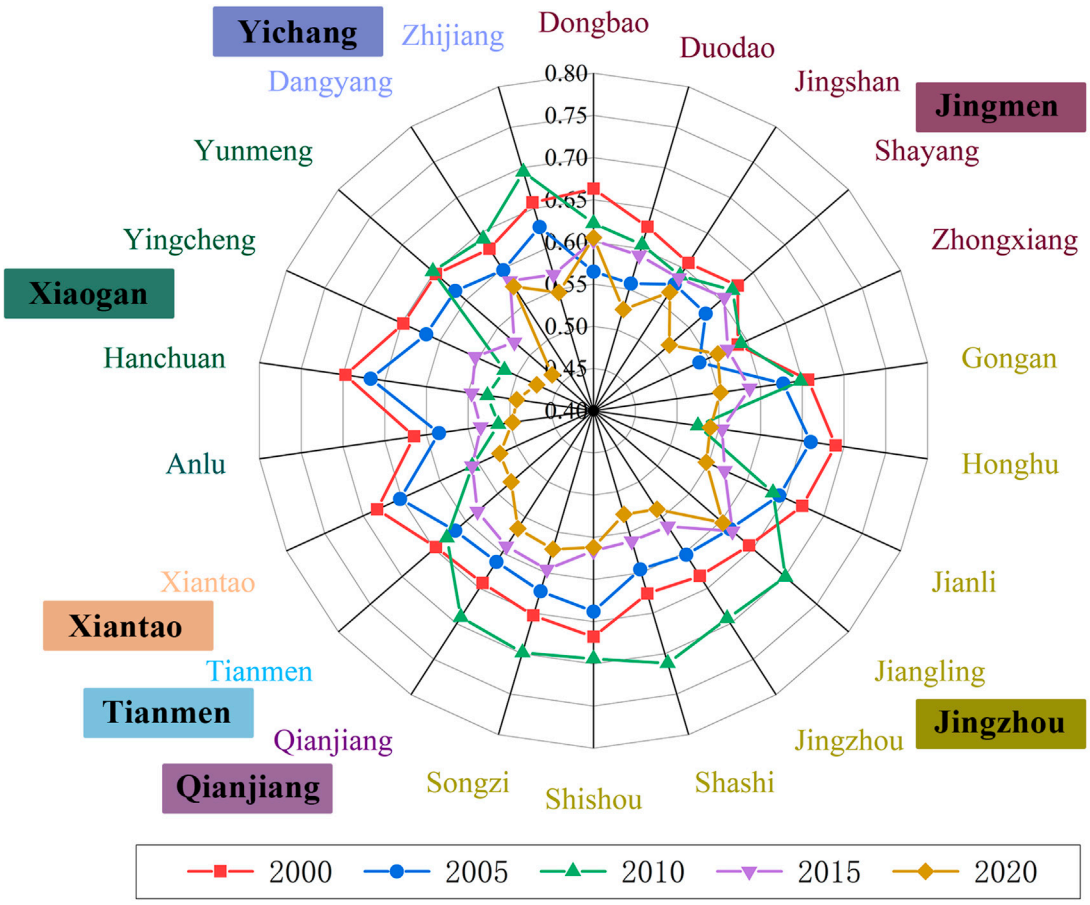

FIGURE 5
The mean ecological vulnerability index (EVI) of each county in Jianghan Plain from 2000 to 2020.

(IN), Slight Deterioration (SD), and Obvious Deterioration (OD). The analysis revealed that ecological vulnerability remained stable in the majority of the Jianghan Plain, with IN accounting for the largest proportion in each period, at 52.04 percent, 53.65 percent, 55.44 percent, and 60.12 percent, respectively. It showed that the construction of ecological civilization in the Jianghan Plain had achieved remarkable achievements, the regional ecological environment had been improving, and the ecological carrying capacity and buffering capacity also had been increasing. The ratio of OI and OD change was less than 0.1%, showing that from 2000 to 2020, there were fewer regions with significant ecological vulnerability changes in the study area. Except for 2005–2010, the proportion of SI was second only to IN, with 37.52%, 1.46%, 29.02%, and 27.53% in the four periods, and the largest proportion in 2010–2015. And the proportion of SD increased and then decreased between 2000 and 2020, with ratios of 10.44%, 44.90%, 14.62%, and 12.34%. Above, it was demonstrated that the degree of ecological vulnerability fluctuated downward in the Jianghan Plain.

Figure 7 illustrates the complex spatial variations in ecological vulnerability levels between 2000 and 2020. From 2000 to 2010, the ecological vulnerability of the Jianghan Plain mainly shifted from levels III and IV to other levels. The areas where the classes remained unchanged were all in the central regions of the Jianghan Plain. From 2000 to 2005, the ecological vulnerability in the northern part of the Jianghan Plain changed mainly from the level III to the level IV and V, indicating a decrease in ecological vulnerability. The north part of the Jianghan Plain is relatively high in elevation, and forests dominate the land use. And China implemented the policy of returning farmland to forest in 1999. The protection of forests increased its area, which influenced the change in regional ecological vulnerability from 2000 to 2005. In the southern portion of the Jianghan Plain, ecological vulnerability decreased from level IV to other levels, whereas ecological vulnerability decreased from level IV to level III in the southeast and southwest, indicating an improvement in ecological fragility. From 2005 to 2010, the ecological vulnerability of the southwest and northwest portions of the Jianghan Plain deteriorated, manifesting a change from level III or IV to level V. However, these deteriorated areas showed an improving trend during 2010–2015, with a shift from the V level to other levels. Most regions' ecological vulnerability levels remain unchanged from 2015 to 2020. Some areas in the north mainly changed from II to III level. The central part of Jianghan Palin showed areas where the III level became II level or IV level, changed to III level, which indicated a decrease in ecological vulnerability level and an improvement in the ecological environment.

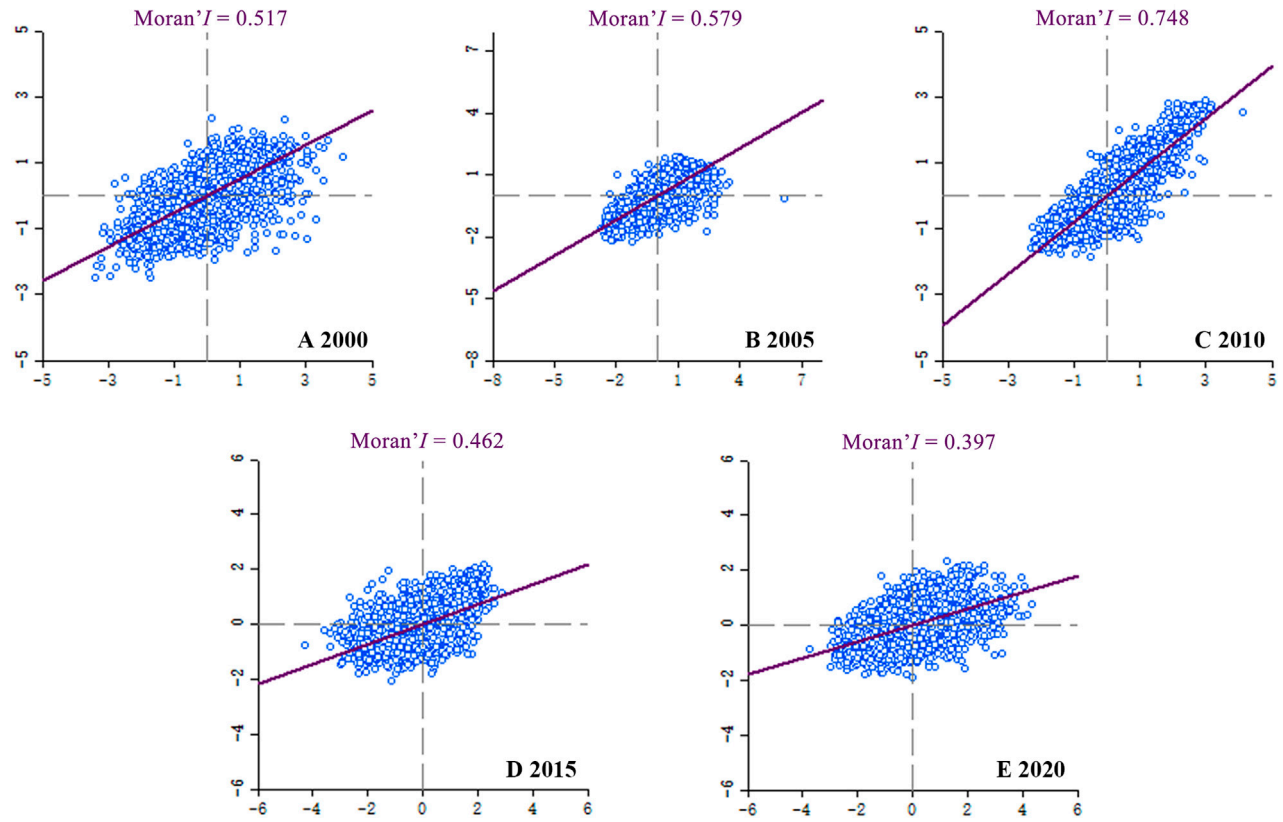

FIGURE 6
Scatter plots of the ecological vulnerability index (EVI) in Jianghan Plain from 2000 to 2020.

TABLE 5 Changes in EVI level from 2000 to 2020.

Year		OI		SI		IN	SD		OD	
2000–2005	Change level	4	3	2	1	0	−1	−2	−3	−4
	Area/km^2	0	0.41	317.05	16676.64	23570.87	4,728.81	0.43	0	0
	Change area/km^2	0.41		16993.69		23570.87	4,729.24		0	
	Percentage	0.00%		37.52%		52.04%	10.44%		0.00%	
2005–2010	Change level	4	3	2	1	0	−1	−2	−3	−4
	Area/km^2	0	0.01	0.4	659.89	24298.41	19941.8	393.35	0.34	0
	Change area/km^2	0.01		660.29		24298.41	20335.15		0.34	
	Percentage	0.00%		1.46%		53.65%	44.90%		0.00%	
2010–2015	Change level	4	3	2	1	0	−1	−2	−3	−4
	Area/km^2	0.02	32.15	216.07	13310.63	25112.2	6580.43	42.68	0.01	0
	Change area/km^2	32.17		13526.70		25112.20	6623.11		0.01	
	Percentage	0.07%		29.87%		55.44%	14.62%		0.00%	
2015–2020	Change level	4	3	2	1	0	−1	−2	−3	−4
	Area/km^2	0.03	4.08	516.55	11952.73	27229.63	5377.11	213.5	0.58	0
	Change area/km^2	4.11		12469.28		27229.63	5590.61		0.58	
	Percentage	0.01%		27.53%		60.12%	12.34%		0.00%	

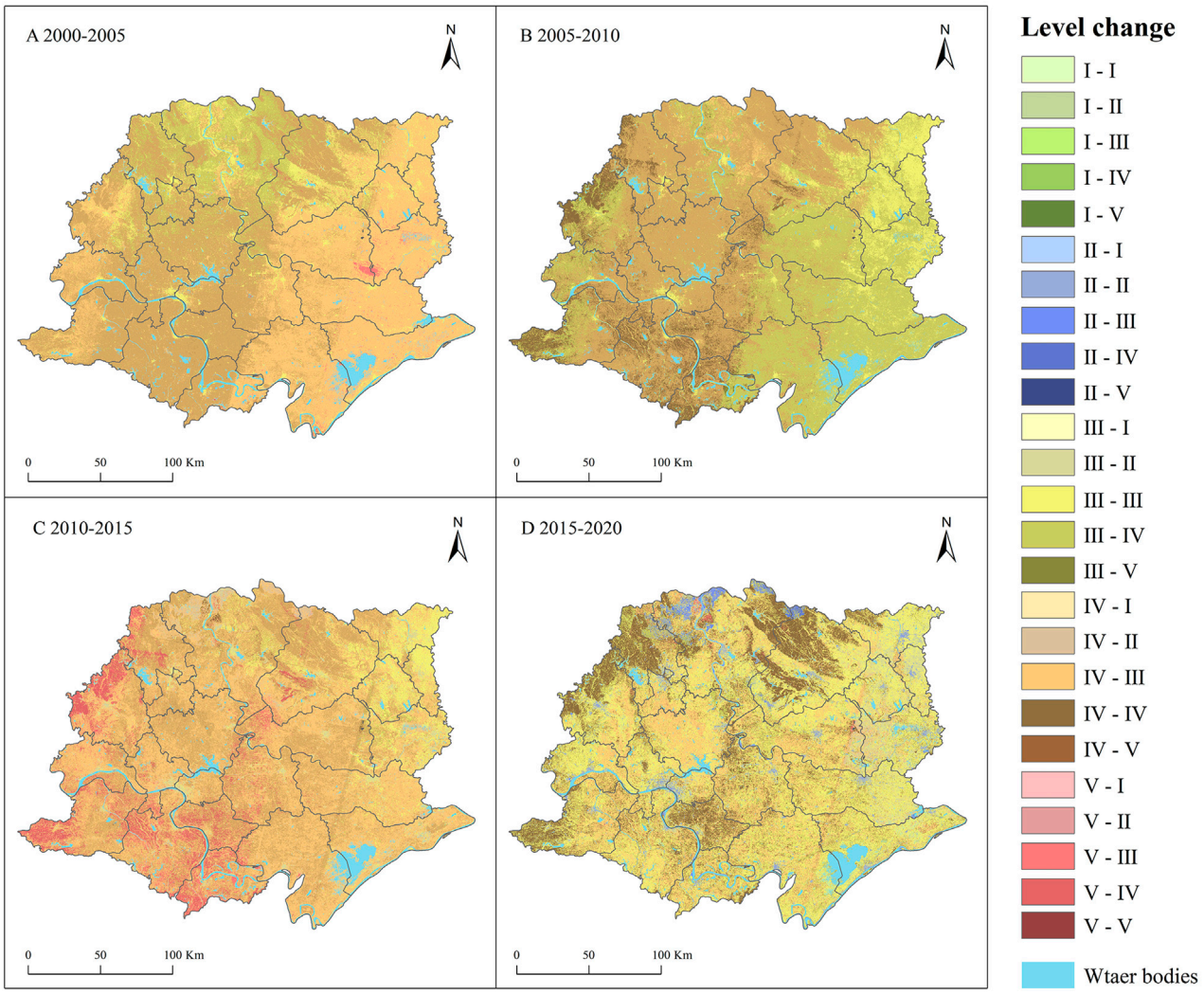

FIGURE 7
Spatial and temporal pattern of ecological vulnerability index (EVI) in Jianghan Plain in four period (A2000-2005, B2005-2010, C2010-2015, D2015-2020).

4 Discussion

4.1 Spatial auto-correlation analysis of EVI

Considering the actual situation of Jianghan Plain, a 3 km × 3 km grid was established to extract the image information in order to ensure the completeness of the details within the scale and the precision of calculation. In this study, we extracted 4,319, 4,337, 4,304, 4,323, and 4,261 sample points from the images of 2000, 2005, 2010, 2015, and 2020 due to the varying extent of water bodies in each year. Moran's I index and LISA were used to conduct a spatial autocorrelation analysis of EVI in the Jianghan Plain using the previously mentioned sample points. Figure 8 depicts the scatter plot of Moran's I for Jianghan Plain's EVI. From 2000 to 2020, the scatter points were primarily dispersed in the first and third quadrants, indicating that the ecological vulnerability in Jianghan Plain had a positive spatial correlation and a clustered instead of random distribution. And the value of Moran's I increased and decreased over the past 2 decades, with values of 0.517, 0.579, 0.748, 0.462, and 0.397, respectively. In 2010, Moran's I had its highest value, implying a significantly positive spatial correlation. With a value of only 0.397, the ecological vulnerability of Jianghan Plain was the weakest spatial correlation in 2020.

By analyzing the local spatial correlation pattern based on the LISA cluster map, we could determine the spatial distribution of 5 cluster types (No Significant, H-H, H-L, L-L, L-H) each year. As depicted in Figure 8, the No Significance was most prevalent in relatively low-elevation regions, including Qianjiang, Jianli, Shishou, and Xiantao. From 2000 to 2020, L-L and H-H were more concentrated and prominent, while HH and LH were more dispersed and fewer. And the spatial spread of L-H and H-L was more variable. In 2000, the H-H dominated the eastern and western parts of the Jianghan Plain, whereas the L-L dominated these regions in 2005 and 2010. In addition, the area of L-L decreased

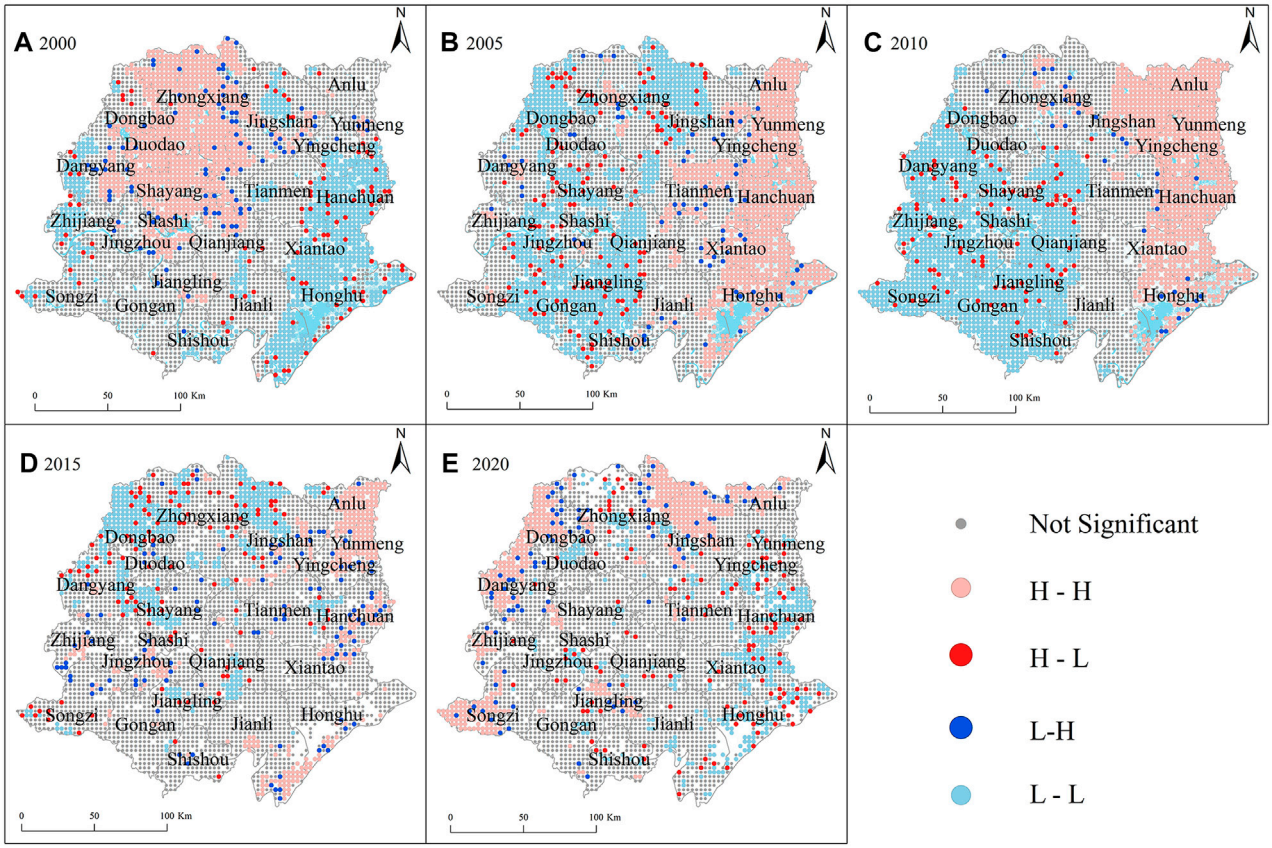

FIGURE 8
Jianghan Plain ecological vulnerability index (EVI) cluster map from 2000 to 2020.

continuously from 2010 to 2020, indicating that the environment quality had enhanced and the degree of ecological vulnerability had declined as a result of the promotion of the development of ecological civilization (Zhu et al., 2022). In conjunction with the preceding, the temporal tendencies of L-L and HH are consistent with the EVI's movements in the Jianghan Plain.

4.2 Driving forces analysis

The ecological vulnerability manifests in the degree of structural and functional integrity of ecosystems. Natural attributes and human activities influence regional ecological vulnerability and lead to spatial and temporal changes (Abd El-Hamid et al., 2020). Natural factors are the material basis for the existence and continued positive role of regional ecosystems, and changes in the natural environment usually affect the structure and function of regional ecosystems, which in turn leads to the emergence of ecological vulnerability problems. However, in contrast to the long-term slow evolution of natural factors, the dramatic disturbance of human activities is more likely to cause sudden changes in the regional ecological environment and create ecological vulnerability problems. It has been proved that ecological vulnerability is directly related to the natural conditions of the regional ecological background. Still, the natural conditions only determine the potential existence of environmental vulnerability. The main factors that cause the further transformation of potential environmental vulnerability to actual ecological vulnerability are the excessive production and living activities of human beings, such as rapid urbanization, irrational exploitation of resources, environmental pollution, and so on (Hou et al., 2016).

The four indicators of Heat, Greenness, Wetness, and Dryness did not simply represent the natural environment but also reflected the impact of human activities on the natural environment from the side. Therefore, we quantified the explanatory power of the indicators in the Geodetector to investigate the major driving forces of the four indicators of changes in ecological vulnerability in the Jianghan Plain. A 3 km × 3 km grid was created using ArcGIS for sampling, and the values of the four indicators and EVI from 2000 to 2020 at the sample sites were extracted and imported into the detector for calculation. As can be seen in Figure 9, the outcomes of the factor detector for four indicators over 20 years demonstrated that $p = 0$, suggesting that each indicator notably affected the change in ecological vulnerability in Jianghan Plain. Every year, NDVI had the highest q value and had the most effect on how ecologically vulnerable the Jianghan Plain was. It was followed by NDBSI, which also had a q value over 0.5. With the accelerating urbanization process, especially from 2005 to 2010, the construction land in Jianghan Plain increased by 18.30%, and the ecological land area decreased sharply, resulting in a decreasing trend of EVI. As

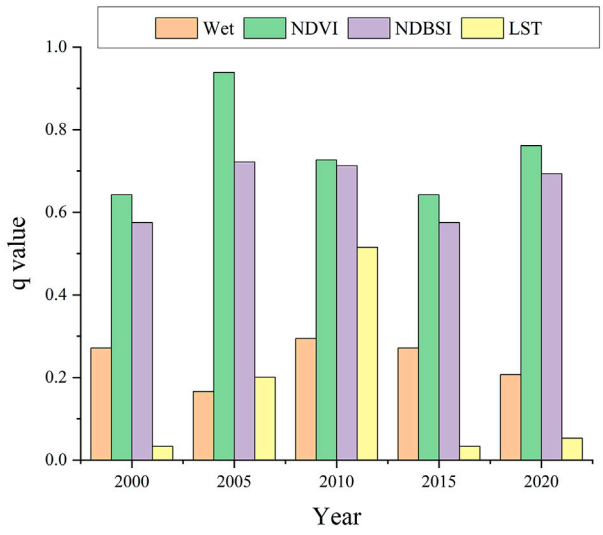

FIGURE 9
The results of the Factor Detector.

confirmed by many studies, urban expansion and over-exploitation of arable land have seriously affected the regional ecological environment (Xie et al., 2013; Liou et al., 2017; Jiang et al., 2022). The q values of Wet changed less over 20 years, remaining between 0.1 and 0.3, indicating that the effect of wetness on the variation in ecological vulnerability in Jianghan Plain was more consistent. From 2000 to 2020, LST q values were lower, exhibiting a first ascending and then descending trend. The effect of human activities, such as environmental pollution and land use change, was still the main driver of regional ecological vulnerability. In response, the local government should improve the policy system, implement the responsibilities of all parties, coordinate the balance between ecological vulnerability management and economic development of residents, and take correct and appropriate measures to halt the deterioration of ecological vulnerability. These were crucial for accelerating the ecological management of the Jianghan Plain, consolidating the achievements of ecological management and construction, and finally achieving the win-win goal of enhancing the region's ecological and economic environments. It is somewhat related to the slight variation in temperature and humidity in the Jianghan Plain over the past 20 years.

In addition, changes in ecological vulnerability are closely related to government policies. Ecological vulnerability in the Jianghan Plain became better from 2000 to 2005, deteriorated from 2005 to 2010, and improved significantly after 2010. In Hubei Province, implementing the policy of returning farmland to the forest in 2000 achieved great ecological benefits, which directly or indirectly caused the improvement of regional ecological vulnerability (Zhao et al., 2023). However, with the rapid development of urbanization, the ecological environment became increasingly fragile from 2005 to 2010. In 2012, with the implementation of the ecological civilization construction strategy and various ecological protection policies, the regional ecological environment was improved again. Therefore, governments at all levels of the Jianghan Plain should give full play to their roles to promote the improvement of the regional ecological environment and the management of ecological problems and ultimately achieve the win-win goal of enhancing the regional ecological and economic environment.

4.2.1 Sustainable development and local government suggestions

The 2030 Agenda for Sustainable Development sets out 17 goals and 169 sub-goals comprising the Sustainable Development Goals (United Nations, 2015). The development of these goals has placed greater emphasis on integrating the intrinsic linkages between social development, economic development, and environmental protection, changing the previous failure to pay sufficient attention to the ecological field and addressing the persistent problems and emerging challenges facing humanity and the planet. China has also been working toward sustainable development goals. With the rapid urbanization of the Jianghan Plain, the urban heat island is profoundly affecting the natural environmental processes on the surface and the sustainable development of human society. Clarifying the relationship between carbon emissions and urban heat islands can inform how to achieve low-carbon and decarbonized sustainable development goals. (Wise et al., 2009). We divided the Jianghan Plain into 4,903 cells using a 3 km × 3 km grid and determined the urban heat island (UHI) area in 2000 and 2020 based on LST > LST_{ave}+0.5 × δ (LST_{ave} denotes the mean value of LST in the Jianghan Plain, and δ denotes the standard deviation of LST in the Jianghan Plain) (Shahfahad et al., 2021). We determined carbon emission coefficients for each land use type in the Jianghan Plain based on the IPCC framework and some studies on carbon emission coefficients (IPCC, 2007; Zhu Q. et al., 2015; Zhou S. et al., 2021). Then, we used the coupling and coordination degree model (CCDM) to measure the relationship between urban heat island density (UHII) and carbon emissions after standardized data (Naikoo et al., 2023). As shown in Figure 10, the UHI area of the Jianghan Plain was mainly located in the central region in 2000 and shifted to the west in 2020, and the urban heat island effect in the eastern part was mitigated. Based on the results of CCDM, the spatial distribution patterns of the coupling and coordination degrees of carbon emissions and urban heat island density in the Jianghan Plain in 2000 and 2020 were generally consistent. The region's area with high coupling and coordination in 2020 increased significantly compared to 2000. In fact, the urban heat island effect and carbon emissions showed high coupling and high coordination in the central urban areas of each city, as has been demonstrated by some scholars (Sharifi et al., 2020; Dewa and Buchori, 2023). Extreme incoordination occurred mainly in the northern part of the Jianghan Plain, which was at a higher elevation and had a less significant urban heat island. The emergence of the urban heat island phenomenon not only has specific effects on human health but also has adverse effects on vegetation growth and climate change. (Heaviside et al., 2017; Shahfahad et al., 2022). Therefore, promoting the implementation of low-carbon emission reduction is conducive to mitigating the negative impacts of the urban heat island effect and reducing the fragility of the regional ecology (Imam and Banerjee, 2016; Chen and You, 2020). This is also the way to improve the ecological environment of Jianghan Plain and achieve sustainable development.

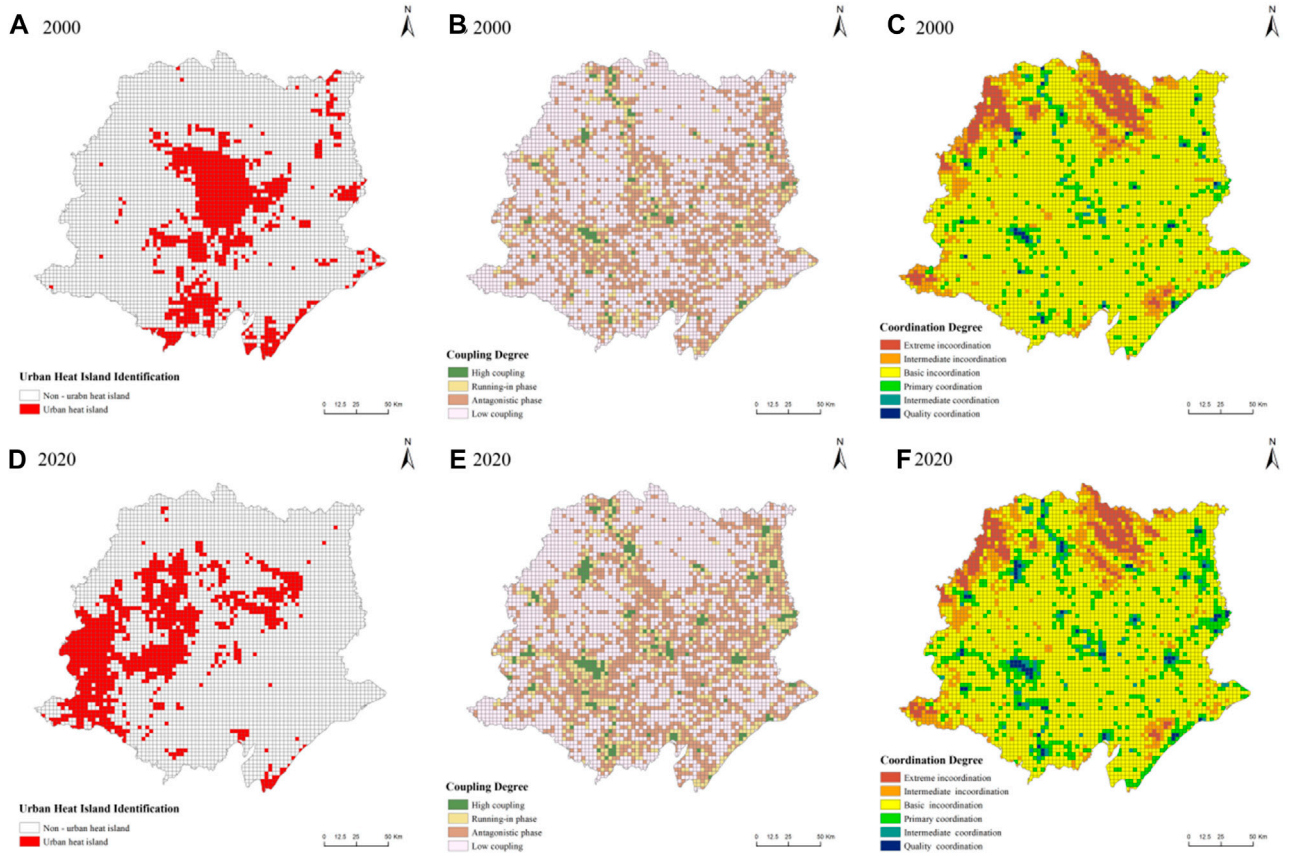

FIGURE 10
(A) Urban heat island in 2000; **(B)** coupling degree in 2000; **(C)** Coordination degree in 2000; **(D)** Urban heat island in 2020; **(E)** coupling degree in 2020; **(F)** Coordination degree in 2020.

Ecological vulnerability monitoring and driving force analysis provide decision-makers with suggestions for environmental improvement to achieve sustainable development (Li F. et al., 2022). In this study, we promoted the following suggestions further to improve the sustainable development of the Jianghan Plain and achieve the win-win goals of economy and ecology.

First, gradually change the urban development model to ensure ecological land use. The rapid expansion of urban land in the Jianghan Plain has led to increasing fragmentation of habitats. Local governments should do reasonable urban planning, especially in Yichang and Jingzhou, to ensure the regional ecological environment is not degraded. They should effectively reduce the inefficient use of urban land, promote urbanization from incremental expansion to stock renewal, improve internal urban greening, and ensure the quality and quantity of regional ecological land. In addition, the governments should promote low-carbon production and living, improve regional carbon emission efficiency, and reduce regional carbon emission levels to enhance environmental quality.

Second, protect arable land and vigorously develop green agriculture. As the Jianghan Plain is a substantial food production base in China, protecting the quality and quantity of basic farmland is a must to protect the regional ecological environment and an inevitable choice to ensure national food security. From the factor results, vegetation cover is the main factor affecting the ecological vulnerability of the Jianghan Plain, so the local government should develop green agriculture and eco-agricultural tourism, ensure the planting of crops and various trees, prevent the emergence of "non-farming" and "non-grain," and improve regional vegetation cover (Zhang et al., 2019). In addition, the government should strictly regulate the use of fertilizers, designate an ecological compensation system to prevent soil pollution, protect the region's natural background from deterioration, and improve the ecological environment's carrying capacity and buffering ability to cope with artificial disturbances.

Third, develop resources rationally and improve their utilization rate. The government should scientifically formulate resource development plans for the Jianghan Plain, improve resource utilization rates, eliminate resource waste, and maximize the value of local ecological resources to achieve sustainable economic development.

Fourth, improve the policy system and play a macro-control role. The relevant departments need to provide reasonable policies to guide local companies, groups, and individuals to participate in ecological protection, such as strengthening

TABLE 6 Results of multicollinearity diagnostics.

Indicators	VIF	TOL	Indicators	VIF	TOL
Wet	7.185	0.139	NDVI	5.122	0.195
NDBSI	6.260	0.160	LST	1.325	0.755

supervision and establishing a sound regulatory mechanism. They also need to implement the responsibilities of all parties, coordinate the balance between ecological vulnerability management and residents' economic development, take correct and appropriate measures to stop the deterioration of ecological vulnerability, and play a macro-regulatory role in the rational use of resources and ecological protection.

4.2.2 Strength and limitation

Considering the ecological vulnerability assessment's complexity and ambiguity, the current methods could not achieve a scientific, objective, and comprehensive evaluation. Combined with previous studies, to avoid subjective consciousness seriously affecting the research results (Li et al., 2012), Due to the complexity and ambiguity of ecological vulnerability assessment, the current methodologies are incapable of producing an exhaustive, scientific, and objective evaluation. This study chose the index system of the RSEI established by Xu Hanqiu in combination with earlier research in order to prevent subjective consciousness from significantly influencing the research findings (Xu, 2013a; Wang et al., 2016). Although there was no further apparent correlation between the indices, this system could correctly represent soil moisture, surface temperature, vegetation, and exposed surface conditions of the study region. We used 2020 as an example to determine the covariance of each indicator in order to confirm the correlation of the indicators further. There are two leading commonly used covariance diagnostic indicators, the variance inflation factor (VIF) and the tolerance level (TOL) (Yao et al., 2016). When VIF>10 (i.e., TOL0.1), the multicollinearity of the chosen index was more severe. A 3 km × 3 km grid was used to encompass the entire image in ArcGIS 10.8, and 4,261 sample points were obtained by excluding the sampling points from the water bodies. Then, the values of the EVI and four indicators were extracted, and SPSS 25.0 was utilized to get the VIF and TOL of each indicator (Table 6). The results of the calculations revealed that the VIF of each indicator was less than 10, and the TOL was greater than 0.1, demonstrating there was not any correlation among the indicators. Therefore, selecting greenness, wetness, dryness and heat as the assessment index system in this study was desirable. In addition, we processed and employed the remote sensing data to construct EVI using the Google Earth Engine. It has certain advantages of multiple data sources, online processing, and fast speed compared with traditional local computer download processing, dramatically improving the efficiency and accuracy of data processing in this study.

However, there were still some shortcomings in this study. This study's primary purpose was to explore a regional ecological vulnerability assessment method using objective models through the idea of a remote sensing index. Firstly, there was still a need for further exploration of the intrinsic mechanisms driving ecological vulnerability changes. Second, multiple natural and human activities influenced regional ecological vulnerability changes, and it was not easy to fully characterize them with a few indicators. This study selected only four indicators to measure regional ecological vulnerability. Simultaneously, the arable land in the Jianghan Plain was widely distributed, and the regional environment affected various human activities. Therefore, further exploration and research were needed to reflect the spatial and temporal changes of ecological vulnerability in the Jianghan Plain more scientifically and comprehensively.

5 Conclusion

This study considered greenness, wetness, dryness, and heat to build an ecological vulnerability assessment index system and then used the GEE platform and principal component analysis to make a macro, objective, and rapid evaluation of the ecological vulnerability in the Jianghan Plain, thereby revealing the evolutionary dynamics of its ecological vulnerability. It provided some reference value for the ecological vulnerability management and food security of the Jianghan Plain and some ideas for researching regional ecological vulnerability. The following are this study's main conclusions.

1) The EVI of the Jianghan Plain showed a fluctuating decline from 2000 to 2020, with an overall improvement in ecological vulnerability and local degradation, especially after 2010, when the ecological vulnerability improved significantly.
2) The average value of EVI in the 20 years was between 0.5 and 0.7, and most areas of the Jianghan Plain were mainly at Moderately level or Strong level. Also, Jingmen City had a more light ecological vulnerability, but the ecological vulnerability of Xiaogan City needed improvement.
3) Most of the areas in Jianghan Plain had the same ecological vulnerability level in each period, accounting for 52.04%, 53.65%, 55.44%, and 60.12%, respectively. The most serious period of degradation was 2005–2010, with about 44.90% of the areas showing degradation, and the period with the highest percentage of improvement was 2000–2005, with approximately 37.52% of the areas showing an improvement.
4) From 2000 to 2020, Moran's I in Jianghan Plain increased and then decreased, with values of 0.517, 0.579, 0.748, 0.462, and 0.397 in 2000, 2005, 2020, 2015, and 2020, respectively. The spatial distribution of ecological vulnerability showed a positive correlation and aggregated distribution rather than random distribution.
5) Regarding the evolutionary drivers, all four indicators significantly affected ecological vulnerability in Jianghan Plain, and greenness and wetness were the greatest driving force for changes in Jianghan Plain.

Data availability statement

The original contributions presented in the study are included in the article/supplementary material, further inquiries can be directed to the corresponding author.

Author contributions

SY: Conceptualization, methodology, software, writing-original draft, writing-review and editing. YZ: supervision, funding acquisition, project administration. JZ: formal analysis, writing-review and editing. QL: software, supervision. YL: resources preparation, writing-review and editing. YG: data analysis. YC: writing-original draft. All authors contributed to the article and approved the submitted version.

Funding

This research was funded by the National Natural Science Foundation of China (NO. 42171061) and the Special Foundation for National Science and Technology Basic Research Program of China (NO. 2021FY100505).

Acknowledgments

We acknowledge all people who contributed to the data collection and processing, as well as the constructive and insightful comments by the editor and reviewers.

Conflict of interest

The authors declare that the research was conducted in the absence of any commercial or financial relationships that could be construed as a potential conflict of interest.

Publisher's note

References

Abd El-Hamid, H. T., Caiyong, W., Hafiz, M. A., and Mustafa, E. K. (2020). Effects of land use/land cover and climatic change on the ecosystem of North Ningxia, China. *Arab. J. Geosci.* 13, 1099. doi:10.1007/s12517-020-06047-6

Anselin, L. (2010). Local indicators of spatial association-LISA. *Geogr. Anal.* 27, 93–115. doi:10.1111/j.1538-4632.1995.tb00338.x

Bai, Y., and Ma, H. (2010). Eco-environmental vlunerability analysis around Qinghai lake based on RS and GIS technology. *Remote Sens. Technol. Apl.* 24, 635–641. doi:10.11873/j.issn.1004-0323.2009.5.635

Beroya-Eitner, M. A. (2016). Ecological vulnerability indicators. *Ecol. Indic.* 60, 329–334. doi:10.1016/j.ecolind.2015.07.001

Boori, M. S., Choudhary, K., Paringer, R., and Kupriyanov, A. (2022). Using RS/GIS for spatiotemporal ecological vulnerability analysis based on DPSIR framework in the Republic of Tatarstan, Russia. *Ecol. Inf.* 67, 101490. doi:10.1016/j.ecoinf.2021.101490

Cai, X., Li, Z., and Liang, Y. (2021). Tempo-spatial changes of ecological vulnerability in the arid area based on ordered weighted average model. *Ecol. Indic.* 133, 108398. doi:10.1016/j.ecolind.2021.108398

Cao, J., Yang, Y., Deng, Z., and Hu, Y. (2022). Spatial and temporal evolution of ecological vulnerability based on vulnerability scoring diagram model in Shennongjia, China. *Sci. Rep.* 12, 5168. doi:10.1038/s41598-022-09205-w

Chen, R., and You, X. (2020). Reduction of urban heat island and associated greenhouse gas emissions. *Mitig. Adapt Strateg. Glob. Change* 25, 689–711. doi:10.1007/s11027-019-09886-1

Chen, T., Bao, A., Guo, H., Zheng, G., Yuan, Y., and Yu, T. (2019). Ecological vulnerability assessment for a transboundary basin in Central Asia and its spatiotemporal characteristic analysis:Taking Amu Darya River Basin as an example. *J. Nat. Resour.* 34, 2643–2657.

Chen, Y., Li, H., Karimian, H., Li, M., Fan, Q., and Xu, Z. (2022). Spatio-temporal variation of ozone pollution risk and its influencing factors in China based on Geodetector and Geospatial models. *Chemosphere* 302, 134843. doi:10.1016/j.chemosphere.2022.134843

Crist, E. P. (1985). A TM Tasseled Cap equivalent transformation for reflectance factor data. *Remote Sens. Environ.* 17, 301–306. doi:10.1016/0034-4257(85)90102-6

Dewa, D. D., and Buchori, I. (2023). Impacts of rapid urbanization on spatial dynamics of land use–based carbon emission and surface temperature changes in the Semarang Metropolitan Region, Indonesia. *Environ. Monit. Assess.* 195, 259. doi:10.1007/s10661-022-10839-6

Fan, G. Y., and Cowley, J. M. (1985). Auto-correlation analysis of high resolution electron micrographs of near-amorphous thin films. *Ultramicroscopy* 17, 345–355. doi:10.1016/0304-3991(85)90201-3

Gorelick, N., Hancher, M., Dixon, M., Ilyushchenko, S., Thau, D., and Moore, R. (2017). Google earth engine: Planetary-scale geospatial analysis for everyone. *Remote Sens. Environ.* 202, 18–27. doi:10.1016/j.rse.2017.06.031

Guo, B., Wei, C., Yu, Y., Liu, Y., Li, J., Meng, C., et al. (2022). The dominant influencing factors of desertification changes in the source region of Yellow River: Climate change or human activity? *Sci. Total Environ.* 813, 152512. doi:10.1016/j.scitotenv.2021.152512

Guo, Z., Wei, W., Pang, S., Li, Z., Zhou, J., and Xie, B. (2019). Spatio-temporal evolution and motivation analysis of ecological vulnerability in arid inland river basin based on spca and remote sensing index: A case study on the shiyang river basin. *Acta Ecol. Sin.* 39, 2558–2572.

Hang, X., Luo, X.-C., Cao, Y., and Li, Y.-C. (2020). Ecological quality assessment and the impact of urbanization based on RSEI model for Nanjing, Jiangsu Province, China. *Ying yong sheng tai xue bao = J. Appl. Ecol.* 31, 219–229. doi:10.13287/j.1001-9332.202001.030

He, L., Shen, J., and Zhang, Y. (2018). Ecological vulnerability assessment for ecological conservation and environmental management. *J. Environ. Manag.* 206, 1115–1125. doi:10.1016/j.jenvman.2017.11.059

Heaviside, C., Macintyre, H., and Vardoulakis, S. (2017). The urban heat island: Implications for health in a changing environment. *Curr. Envir Health Rpt* 4, 296–305. doi:10.1007/s40572-017-0150-3

Hou, K., Li, X., Wang, J., and Zhang, J. (2016). An analysis of the impact on land use and ecological vulnerability of the policy of returning farmland to forest in Yan'an, China. *Environ. Sci. Pollut. Res.* 23, 4670–4680. doi:10.1007/s11356-015-5679-9

Hou, K., Tao, W., Wang, L., and Li, X. (2020). Study on hierarchical transformation mechanisms of regional ecological vulnerability and its applicability. *Ecol. Indic.* 114, 106343. doi:10.1016/j.ecolind.2020.106343

Huang, D., Yan, H., Chi, H., Geng, X., and Shao, Q. (2020). Research on spatiotemporal characteristic of farmland ecosystem NPP in Jianghan Plian from 2000 to 2015. *J. Nat. Resour.* 35, 845–856.

Imam, A. U. K., and Banerjee, U. K. (2016). Urbanisation and greening of Indian cities: Problems, practices, and policies. *Ambio* 45, 442–457. doi:10.1007/s13280-015-0763-4

IPCC (2007). *Summary for policymakers of the synthesis report of the IPCC fourth assessment Report*. Cambridge: Cambridge University Press.

Jiang, X., Guo, X., Wu, Y., Xu, D., Liu, Y., Yang, Y., et al. (2023). Ecological vulnerability assessment based on remote sensing ecological index (RSEI): A case of zhongxian county, chongqing. *Front. Environ. Sci.* 10. Available at: https://www.frontiersin.org/articles/10.3389/fenvs.2022.1074376 (Accessed March 22, 2023).

Jiang, Z., Wu, H., Lin, A., Shariff, A. R. M., Hu, Q., Song, D., et al. (2022). Optimizing the spatial pattern of land use in a prominent grain-producing area: A sustainable development perspective. *Sci. Total Environ.* 843, 156971. doi:10.1016/j.scitotenv.2022.156971

Jimenez-Munoz, J. C., Cristobal, J., Sobrino, J. A., Soria, G., Ninyerola, M., Pons, X., et al. (2009). Revision of the single-channel algorithm for land surface temperature

retrieval from Landsat thermal-infrared data. *IEEE Trans. Geoscience Remote Sens.* 47, 339–349. doi:10.1109/TGRS.2008.2007125

Jing, Y., Zhang, F., He, Y., Kung, H., Johnson, V. C., and Arikena, M. (2020). Assessment of spatial and temporal variation of ecological environment quality in ebinur lake wetland national nature reserve, xinjiang, China. *Ecol. Indic.* 110, 105874. doi:10.1016/j.ecolind.2019.105874

Kasimu, Y., Simayi, Z., Wang, L., and Bayi, X. (2019). Response of ecological environment change to urban construction land expansion in Bole City of Xinjiang. *Nongye Gongcheng Xuebao/Transactions Chin. Soc. Agric. Eng.* 35, 252–259. doi:10.11975/j.issn.1002-6819.2019.01.031

Kumar, L., and Mutanga, O. (2018). Google earth engine applications since inception: Usage, trends, and potential. *Remote Sens.* 10, 1509. doi:10.3390/rs10101509

Lei, J., Chen, Z., Wu, T., Li, Y., Yang, Q., and Chen, X. (2019). Spatial autocorrelation pattern analysis of land use and the value of ecosystem services in northeast Hainan island. *Acta Ecol. Sin.* 39, 2366–2377.

Li, F., Zhou, W., Shao, Z., and Zhou, X. (2022a). Effects of ecological projects on vegetation in the three gorges area of chongqing, China. *J. Mt. Sci.* 19, 121–135. doi:10.1007/s11629-021-6768-5

Li, S., Ge, J., Liang, Y., Liu, Y., Sun, H., Su, W., et al. (2013). An infectious full-length cDNA clone of duck Tembusu virus, a newly emerging flavivirus causing duck egg drop syndrome in China. *Res. Soil Water Conservation* 20, 238–241. doi:10.1016/j.virusres.2012.10.019

Li, X., Xiao, P., Zhou, Y., Xu, J., and Wu, Q. (2022b). The spatiotemporal evolution characteristics of cultivated land multifunction and its trade-off/synergy relationship in the two lake plains. *Int. J. Environ. Res. Public Health* 19, 15040. doi:10.3390/ijerph192215040

Li, Y., Li, Y., Zhou, Y., Shi, Y., and Zhu, X. (2012). Investigation of a coupling model of coordination between urbanization and the environment. *J. Environ. Manag.* 8, 127–133. doi:10.1016/j.jenvman.2011.12.025

Liou, Y.-A., Nguyen, A. K., and Li, M.-H. (2017). Assessing spatiotemporal eco-environmental vulnerability by Landsat data. *Ecol. Indic.* 80, 52–65. doi:10.1016/j.ecolind.2017.04.055

Liu, C., Sun, W., and Li, P. (2022). Characteristics of spatiotemporal variations in coupling coordination between integrated carbon emission and sequestration index: A case study of the Yangtze River delta, China. *Ecol. Indic.* 135, 108520. doi:10.1016/j.ecolind.2021.108520

Martin, D. (1996). An assessment of surface and zonal models of population. *Int. J. Geogr. Inf. Syst.* 10, 973–989. doi:10.1080/02693799608902120

Naikoo, M. W., ShahfahadTalukdar, S., Ishtiaq, M., and Rahman, A. (2023). Modelling built-up land expansion probability using the integrated fuzzy logic and coupling coordination degree model. *J. Environ. Manag.* 325, 116441. doi:10.1016/j.jenvman.2022.116441

Nguyen, A. K., Liou, Y.-A., Li, M.-H., and Tran, T. A. (2016). Zoning eco-environmental vulnerability for environmental management and protection. *Ecol. Indic.* 69, 100–117. doi:10.1016/j.ecolind.2016.03.026

Parastatidis, D., Mitraka, Z., Chrysoulakis, N., and Abrams, M. (2017). Online global land surface temperature estimation from Landsat. *Remote Sens.* 9, 1208. doi:10.3390/rs9121208

ShahfahadNaikoo, M. W., Towfiqul Islam, A. R. Md., Mallick, J., and Rahman, A. (2022). Land use/land cover change and its impact on surface urban heat island and urban thermal comfort in a metropolitan city. *Urban Clim.* 41, 101052. doi:10.1016/j.uclim.2021.101052

ShahfahadRihan, M., Naikoo, M. W., Ali, M. A., Usmani, T. M., and Rahman, A. (2021). Urban heat island dynamics in response to land-use/land-cover change in the coastal city of Mumbai. *J. Indian Soc. Remote Sens.* 49, 2227–2247. doi:10.1007/s12524-021-01394-7

Sharifi, E., Larbi, M., Omrany, H., and Boland, J. (2020). Climate change adaptation and carbon emissions in green urban spaces: Case study of Adelaide. *J. Clean. Prod.* 254, 120035. doi:10.1016/j.jclepro.2020.120035

Tang, L., Kasimu, A., Ma, H., and Eziz, M. (2023). Monitoring multi-scale ecological change and its potential drivers in the economic zone of the tianshan mountains' northern slopes, xinjiang, China. *Int. J. Environ. Res. Public Health* 20, 2844. doi:10.3390/ijerph20042844

Thiault, L., Marshall, P., Gelcich, S., Collin, A., Chlous, F., and Claudet, J. (2018). Space and time matter in social-ecological vulnerability assessments. *Mar. Policy* 88, 213–221. doi:10.1016/j.marpol.2017.11.027

United Nations (2015). *Transforming our world: The 2030 Agenda for sustainable development*. Department of Economic and Social Affairs. New York: United Nations Available at: https://sdgs.un.org/2030agenda (Accessed May 5, 2023).

Wan, L., Wang, S., and Chen, X. (2011). GeoDA-based spatial correlation analysis of GDP in Hadaqi industrial corridor. *Geogr. Res.* 30, 977–984.

Wang, H., Song, M., Li, R., and Yu, G. (2011). Study on spatial-temporal pattern and driving forces of construction land expansion in jianghan plian from 1996 to 2005. *Resour. Environ. Yangtze Basin* 20, 416–421.

Wang, J., and Xu, C. (2017). Instrumental networking and social network building: How horizontal networking and upward networking create social capital. *Acta Geogr. Sin.* 72, 116–134. doi:10.3724/sp.j.1041.2017.00116

Wang, S., Zhang, X., Zhu, T., Yang, W., and Zhao, J. (2016). Assessment of ecological environment quality in the Changbai Mountain Nature Reserve based on remote sensing technology. *Prog. Geogr.* 35, 1269–1278.

Wang, Z., and Su, Y. (2018). Analysis of Eco-environmental vulnerability characteristics of Hanzhong City, near the water source midway along the route of the south-to-north water transfer project, China. *J. Ecol.* 38, 432–442. doi:10.5846/stxb201609261944

Wei, Y. D., and Ye, X. (2014). Urbanization, urban land expansion and environmental change in China. *Stoch. Environ. Res. Risk Assess.* 28, 757–765. doi:10.1007/s00477-013-0840-9

Weißhuhn, P., Müller, F., and Wiggering, H. (2018). Ecosystem vulnerability review: Proposal of an interdisciplinary ecosystem assessment approach. *Environ. Manag.* 61, 904–915. doi:10.1007/s00267-018-1023-8

Wise, M., Calvin, K., Thomson, A., Clarke, L., Bond-Lamberty, B., Sands, R., et al. (2009). Implications of limiting CO2 concentrations for land use and energy. *Science* 324, 1183–1186. doi:10.1126/science.1168475

Xiao, C., Li, P., and Feng, Z. (2019). Monitoring annual dynamics of mature rubber plantations in xishuangbanna during 1987-2018 using Landsat time series data: A multiple normalization approach. *Int. J. Appl. Earth Observation Geoinformation* 77, 30–41. doi:10.1016/j.jag.2018.12.006

Xie, H., Wang, P., and Huang, H. (2013). Ecological risk assessment of land use change in the poyang lake eco-economic zone, China. *Int. J. Environ. Res. Public Health* 10, 328–346. doi:10.3390/ijerph10010328

Xiong, Y., Xu, W., Lu, N., Huang, S., Wu, C., Wang, L., et al. (2021). Assessment of spatial–temporal changes of ecological environment quality based on RSEI and GEE: A case study in erhai lake basin, yunnan province, China. *Ecol. Indic.* 125, 107518. doi:10.1016/j.ecolind.2021.107518

Xu, H. (2008). A new index for delineating built-up land features in satellite imagery. *Int. J. Remote Sens.* 29, 4269–4276. doi:10.1080/01431160802039957

Xu, H. (2013a). A remote sensing index for assessment of region ecological changes. *China Environ. Sci.* 33, 889–897.

Xu, H. (2013b). A remote sensing urban ecological index and its application. *Acta Ecol. Sin.* 33, 7853–7862.

Xu, H. (2005). A study on information extraction of water body with the modified normalized difference water index (MNDWI). *J. Remote Sens.* 9, 589–595.

Xu, H. (2010). Analysis of impervious surface and its impact on urban heat environment using the normalized difference impervious surface index (NDISI). *Photogrammetric Eng. Remote Sens.* 76, 557–565. doi:10.14358/PERS.76.5.557

Xu, H., Li, C., and Shi, T. (2022). Is the z-score standardized RSEI suitable for time-series ecological change detection? Comment on zheng et al. (2022). *Sci. Total Environ.* 853, 158582. doi:10.1016/j.scitotenv.2022.158582

Xu, H., Wang, M., Shi, T., Guan, H., Fang, C., and Lin, Z. (2018). Prediction of ecological effects of potential population and impervious surface increases using a remote sensing based ecological index (RSEI). *Ecol. Indic.* 93, 730–740. doi:10.1016/j.ecolind.2018.05.055

Xu, W., Binbin, H., Aike, K., Cirenluobuand Xiao, Y. (2017). The study of quantitative assessment of regional eco-environmental vulnerability based on multi-source remote sensing. *IOP Conf. Ser. Earth Environ. Sci.* 94, 012141. doi:10.1088/1755-1315/94/1/012141

Yao, X., Yu, K., Liu, J., Yang, S., He, P., Deng, Y., et al. (2016). Spatial and temporal changes of the ecological vulnerability in a serious soil erosion area,Southern China. *Chin. J. Appl. Ecol.* 27, 735–745. doi:10.13287/j.1001-9332.201603.022

Ye, J., Hu, Y., Zhen, L., Wang, H., and Zhang, Y. (2021). Analysis on land-use change and its driving mechanism in xilingol, China, during 2000–2020 using the google earth engine. *Remote Sens.* 13, 5134. doi:10.3390/rs13245134

Zhang, B., Li, P., Xu, Y., and Yue, X. (2019). What affects farmers' ecocompensation expectations? An empirical study of returning farmland to forest in China. *Trop. Conservation Sci.* 12, 194008291985719. doi:10.1177/1940082919857190

Zhang, F., Liu, X., Zhang, J., Wu, R., Ma, Q., and Chen, Y. (2017). Ecological vulnerability assessment based on multi-sources data and SD model in Yinma River Basin, China. *Ecol. Model.* 349, 41–50. doi:10.1016/j.ecolmodel.2017.01.016

Zhang, X., Liu, K., Wang, S., Wu, T., Li, X., Wang, J., et al. (2022). Spatiotemporal evolution of ecological vulnerability in the Yellow River Basin under ecological restoration initiatives. *Ecol. Indic.* 135, 108586. doi:10.1016/j.ecolind.2022.108586

Zhao, Q., Yu, L., Li, X., Peng, D., Zhang, Y., and Gong, P. (2021). Progress and trends in the application of google earth and google earth engine. *Remote Sens.* 13, 3778. doi:10.3390/rs13183778

Zhao, Y., Wang, M., Lan, T., Xu, Z., Wu, J., Liu, Q., et al. (2023). Distinguishing the effects of land use policies on ecosystem services and their trade-offs based on multi-scenario simulations. *Appl. Geogr.* 151, 102864. doi:10.1016/j.apgeog.2022.102864

Zheng, C., Wen, Z., Liu, Y., Guo, Q., Jiang, Y., Ren, H., et al. (2021). Integrating habitat suitability and the near-nature restoration priorities into revegetation plans based on potential vegetation distribution. *Forests* 12, 218. doi:10.3390/f12020218

Zhou, S., Xi, F., Yin, Y., Bing, L., Wang, J., Ma, M., et al. (2021a). Accounting and drivers of carbon emission from cultivated land utilization in Northeast China. *Chin. J. Appl. Ecol.* 32, 3865–3871. doi:10.13287/j.1001-9332.202111.003

Zhou, X., Wen, H., Zhang, Y., Xu, J., and Zhang, W. (2021b). Landslide susceptibility mapping using hybrid random forest with GeoDetector and RFE for factor optimization. *Geosci. Front.* 12, 101211. doi:10.1016/j.gsf.2021.101211

Zhou, Y., Li, X., and Liu, Y. (2020). Land use change and driving factors in rural China during the period 1995-2015. *Land Use Policy* 99, 105048. doi:10.1016/j.landusepol.2020.105048

Zhu, Q., Mei, J., Chen, Y., and Han, X. (2015a). Regional differentiation characteristics and optimization of the structural efficincy of land use in Hubei province based on the carbon emissions. *Econ. Geogr.* 35, 176–184. doi:10.15957/j.cnki.jjdl.2015.12.025

Zhu, Y., Zhang, R., Gu, J., and Gao, Z. (2022). Spatiotemporal evolution and driving mechanism of ecological well-being performance in the urban agglomeration of the middle reaches of the Yangtze River under the carbon peaking and carbon neutrality goals. *Prog. Geogr.* 41, 2231–2243. doi:10.18306/dlkxjz.2022.12.004

Zhu, Z., Wang, S., and Woodcock, C. E. (2015b). Improvement and expansion of the fmask algorithm: Cloud, cloud shadow, and snow detection for landsats 4–7, 8, and sentinel 2 images. *Remote Sens. Environ.* 159, 269–277. doi:10.1016/j.rse.2014.12.014

frontiers | Frontiers in Earth Science

TYPE Original Research
PUBLISHED 31 August 2023
DOI 10.3389/feart.2023.1226795

OPEN ACCESS

EDITED BY
Yonghao Xu,
Linköping University, Sweden

REVIEWED BY
Zhichao Wang,
Beijing Forestry University, China
Klemen Zakšek,
University of Hamburg, Germany

*CORRESPONDENCE
Zhiyong Wang,
wangzhiyong@hust.edu.cn

†These authors have contributed equally to this work

RECEIVED 22 May 2023
ACCEPTED 21 August 2023
PUBLISHED 31 August 2023

CITATION
Hu C, Huang G and Wang Z (2023), Exploring the seasonal relationship between spatial and temporal features of land surface temperature and its potential drivers: the case of Chengdu metropolitan area, China.
Front. Earth Sci. 11:1226795.
doi: 10.3389/feart.2023.1226795

Exploring the seasonal relationship between spatial and temporal features of land surface temperature and its potential drivers: the case of Chengdu metropolitan area, China

Chunguang Hu[1,2†], Gaoliu Huang[1,2†] and Zhiyong Wang[1,2*]

[1]School of Architecture and Urban Planning, Huazhong University of Science and Technology, Wuhan, China, [2]Hubei Engineering and Technology Research Center of Urbanization, Wuhan, China

Global climate change and the process of urbanization have had a significant impact on land surface temperature (LST). This study selects the Chengdu metropolitan area in China as a typical research subject. Based on the seasonal heterogeneity and spatial distribution characteristics of LST, different types of potential influencing factors are selected for Principal Component Analysis (PCA) to determine the categories of these factors. Subsequently, a multiple linear regression analysis is conducted to explore the relationship between LST and the identified potential influencing factors during different seasons. The findings of this study suggest that the regions with high temperatures and secondary high temperatures in the Chengdu metropolitan area are primarily concentrated in Chengdu and its adjacent localities, exhibiting noticeable seasonal variations. In the summer, high-temperature zone and second high-temperature zone of the LST show a central aggregation pattern. In the transition season, the high-temperature zone of the LST presents a "large dispersion, small aggregation" pattern. In the winter, it presents a dispersed pattern. In terms of influencing factors, elevation, slope, wind speed, humidity, and surface vegetation cover related to natural geographical conditions have a significant impact on LST, reaching a peak during the transition season. Factors associated with social and economic conditions, such as population size, nighttime light index, and road density, have a pronounced effect on LST during the summer season. During winter, LST is mainly influenced by landscape pattern-related factors such as Shannon Diversity Index, Edge Density, Largest Patch Index, and Patch Density. This study not only assesses the seasonal and spatial characteristics of LST in the Chengdu metropolitan area but also provides valuable insights for formulating phased measures to mitigate the Urban Heat Island (UHI) in other regions.

KEYWORDS

Chengdu metropolitan area, land surface temperature (LST), urban heat island (UHI), correlation, multiple linear regression

1 Introduction

With the ongoing global climate change and urbanization process, the continuous development of cities worldwide and the concentration of population in urban areas have had a significant impact on the urban ecological environment. The advancing urbanization exerts a strong force on climate change in cities and their surrounding areas. Among these forces, the urban heat island (UHI) effect plays a crucial role. (Grimm et al., 2008). This phenomenon is identified by a considerable rise in air and land surface temperature (LST) within urban regions, contrasting with the adjacent rural surroundings (Thompson and Perry, 1997). The Surface Urban Heat Island (SUHI) effect can be identified using conventional thermal-infrared remote sensing techniques, which can effectively interpret the land-surface energy flow characteristics in terms of numerical values. The SUHI effect exhibits pronounced spatial and temporal variations when compared to the UHI effect described by air temperature. It is also more susceptible to variations in land surface characteristics and human activity. Furthermore, the rise in LST gives rise to an upward movement of air currents, which can provide better insight into the underlying causes of UHI than air temperature-based evaluations (Wang Z. et al., 2022; Hu and Li, 2022). SUHI effect exerts a significant force on human production and living. In recent years, it has drawn attention from various disciplines such as geography, ecology, meteorology, and urban planning. Many scholars have begun to explore the characteristics of LST changes and the mechanisms behind the formation of SUHI(Zakšek and Oštir, 2012). They have been investigating different approaches to mitigate the rise in surface temperature and, consequently, alleviate the impact of UHI on human production and living. Therefore, it is of vital importance to scientifically investigate the spatial and temporal distribution of UHI and its influencing factors to understand the functioning of the urban heat island effect and find ways to mitigate its impact.

Currently, the conventional approach of identifying LST through weather stations has no longer sufficient to meet practical needs. Multivariate remote sensing data, such as Landsat Thematic Mapper, Advanced Very High-Resolution Radiometer (AVHRR) satellite data, Moderate Resolution Imaging Spectroradiometer (Modis), and Advanced Spaceborne Thermal Emission and Radiation (Aster), have revolutionized the field of LST detection. Compared to traditional methods of measuring LST, remote sensing technology has proven to be more reliable and efficient in capturing the complex and dynamic nature of LST variations over time and space (Imhoff et al., 2010). In this study, MODIS11A2 data is utilized, which is captured by long-term surface satellites and processed through techniques such as stitching, projection conversion, and other image processing. This method offers a more accurate and extended detection time range of LST data (Wan, 2008).

Merely examining the spatial distribution of LST might not be adequate in effectively mitigating UHI hazards; it is crucial to investigate the probable factors behind LST changes. Numerous statistical techniques have been utilized for examining the impacts of LST including geographically-weighted regression models to explore the connection between LST variation and its driving forces (Gao et al., 2022), geographic detectors (Geo-detectors) for identifying the impact of surface parameters on LST (Wang W. et al., 2021), and spatial regression models to examine the influence of urban spatial structure on UHI at the community level (Guo A. et al., 2020). The above study explores the spatial characteristics and influencing factors of urban heat islands from different perspectives, providing valuable suggestions for mitigating the urban heat island effect. However, there are several limitations. Firstly, from a temporal perspective, many studies focus on the surface temperature during the summer season, overlooking the seasonal variations and making it difficult to assess the phased characteristics of surface temperature. Secondly, from a spatial perspective, numerous studies concentrate on individual cities or large urban clusters, neglecting the closer connections within urban agglomerations that encompass economic, social, and natural aspects. Furthermore, many studies have focused on the impacts of natural geographical features and human socio-economic activities on urban heat islands (Ward et al., 2016). In recent years, the influence of landscape patterns on urban heat islands has also been gradually addressed. Several studies have indicated a relationship between urban green spaces and urban heat islands (Li et al., 2013). Common landscape indicators are often used to explore the connection between urban thermal environments and landscape pattern factors (Peng et al., 2016; Sun et al., 2022). However, many of these studies overlook the interactions between multiple influencing factors and the seasonal variations in these factors. To address this gap, our research will consider multiple types of influencing factors, emphasizing the elimination of interactions among these factors. This approach allows for a more intuitive identification of the dominant factors influencing urban heat islands at different stages. Additionally, considering the seasonal variability of the driving factors for surface temperature, we will propose tailored mitigation measures. Nevertheless, there are still limitations in the current research regarding this aspect.

Since China's reform and opening-up, cities have developed rapidly. The continuous advancement of urbanization has put forward new requirements for the construction and development of Chinese cities. Urban agglomerations and metropolitan areas have become important models for the development of Chinese cities. Nevertheless, metropolitan areas exhibit more proximate material and spatial linkages compared to urban agglomerations. Furthermore, they play a crucial role in the evolvement of urban agglomerations (Fang, 2021; Wang Q. et al., 2022). In 2021, the Chinese government released the Chengdu Metropolitan Area Development Plan, designating the Chengdu metropolitan area as a significant growth center in southwest China. However, due to its location in the Sichuan Basin, the area faces challenges in heat dissipation and is prone to forming a heat island. In recent years, the UHI effect in Chengdu has had a stronger influence on people's production and life, and at the same time, it has posed challenges to the sustainable development of the city (Guo J. et al., 2020; Wu et al., 2021). Currently, there are multiple perspectives in the research on surface temperature in the Chengdu region to explore the urban heat island phenomenon and the driving factors influencing it. These perspectives include examining the relationship between urban land changes and the urban heat island effect (Zhigang et al., 2016; Yu et al., 2022; Zhe et al., 2022), investigating the relationship between the built environment in the Chengdu region and surface temperature (Sun et al., 2022; Luo et al., 2023), exploring the impact of changes in health indices of urban and rural residents

in China on surface temperature (Ren et al., 2021), studying the influence of landscape patterns on the intensity of the urban heat island (Sun et al., 2022), and using remote sensing satellite products to investigate the impact of meteorological factors on the intensity of the urban heat island (Lai et al., 2018; Liao et al., 2022). However, the current research on the Chengdu region mostly focuses on the urban heat island characteristics within the city itself, while there is relatively little research on the urban heat island effect in the Chengdu metropolitan area, lacking an exploration of the characteristics of the urban heat island effect within the metropolitan area that spans administrative boundaries and has close interconnections among its elements.

Therefore, this study focuses on the Chengdu metropolitan area, aiming to fill the research gap on urban heat islands in the Chengdu metropolitan area and provide recommendations for mitigating the urban heat island effect. In summary, although there are many studies focusing on exploring the characteristics and influencing factors of the urban heat island effect, this study has several key innovations compared to previous research. Firstly, in terms of the choice of research area, this study takes the perspective of the metropolitan area and selects the Chengdu metropolitan area as the research object. As the first approved metropolitan area in Southwest China and an important growth pole in the region, there is relatively limited research on the Chengdu metropolitan area. Therefore, this study focuses on the Chengdu metropolitan area, which has important theoretical value for mitigating the urban heat island effect at the metropolitan scale. Secondly, in terms of research methods, this study examines the characteristics of the urban heat island in different seasons, conducts correlation analysis to explore potential driving factors influencing surface temperature in the Chengdu metropolitan area, and finally utilizes principal component analysis and multiple linear regression to investigate the relationships among the driving factors, thereby identifying the main factors influencing surface temperature in different seasons in the Chengdu metropolitan area. Thirdly, from a theoretical and practical perspective, this study identifies the dominant factors influencing surface temperature in different seasons and proposes seasonal mitigation measures, providing reference and guidance for local governments and urban planners to a certain extent. This study is of theoretical significance and practical relevance to the construction and development of the Chengdu metropolitan area.

2 Research region

The location of the Chengdu metropolitan area lies in the northwestern vicinity of the Sichuan Basin, specifically positioned within the southwestern boundaries of China's Sichuan Province (30°04′-31°42′N; 103°50′-105°27′E). The Chengdu metropolitan area, with a total expanse of 33,100 square kilometers, encompasses various counties and urban zones, including the Jingyang District of Deyang City, Shifang City, and Guanghan City, and is primarily centered around Chengdu City. The topography of the region is predominantly flat, with ranges of mountains situated towards the west. The bulk of the metropolitan zone is located within the central subtropical belt (Liu et al., 2021a), and its unique geographic location results in an average temperature of 16.8°C in Chengdu City. The planning area is selected as the study area (Figure 1) to provide a relevant reference for the planning and construction of Chengdu metropolitan area.

This study is based on the climatic characteristics of the Chengdu metropolitan area and previous research findings (Wang Z. et al., 2022). We also take into account the geographical environment of the Chengdu metropolitan area. On one hand, we analyze the temperature and precipitation data for each month. On the other hand, we consider the continuity of human society's seasonal division, resulting in the categorization of the Chengdu metropolitan area into three seasons: summer, transition season, and winter. The Chengdu metropolitan area exhibits distinct subtropical monsoon humid climate characteristics and is mainly situated in the central subtropical region (Figure 2). During June to September, the average temperatures are relatively high and exhibit a stable distribution. The temperature fluctuations during these 4 months are minimal, thus designating them as the summer season. In comparison, the average temperatures from December to March are lower, especially in January. Although the average temperature and precipitation in March are slightly higher than in November, the seasonal classification pattern considers the coherence in month-to-month division. As a result, these 4 months are defined as the winter season. The average temperatures in April-May and October-November are relatively similar, as these months often serve as transitional periods between summer and winter. Therefore, the study defined March, April, May, and October as the transition seasons.

3 Data and methods

3.1 Data sources and processing

The data utilized in this study comprise LST data and potential driving force that affect LST. These factors include a digital elevation model, wind speed, humidity, slope, Shannon diversity index, edge density, maximum patch area index, patch density, road density, population density, night lighting, and vegetation cover, resulting in a total of 12 potential driving force (Figure 3). Please refer to (Table 1) for more details. To characterize the distribution characteristics of various influencing factors, this study employed the natural breakpoint method to reclassify the potential influencing factors into five levels ranging from 1 to 5. A higher level indicates a higher numerical value, and a more pronounced spatial expression of the corresponding potential influencing factor.

The study utilized MODIS11A2 data obtained from the Terra and Aqua satellites, which are equipped with the important MODIS sensor. The sensor allows for the acquisition of LST data at four daily intervals, it was determined that MODIS11A2 data offers higher accuracy (Wan, 2008). Therefore, for this study, the 2020 MODIS11A2 data was utilized to obtain processed LST data for the Chengdu metropolitan area, which was sourced from LAADS DAAC.

3.2 Research methodology

The logical framework for the research presented is illustrated in the following (Figure 4). The main purpose is to summarize the LST distribution characteristics of Chengdu metropolitan area by using

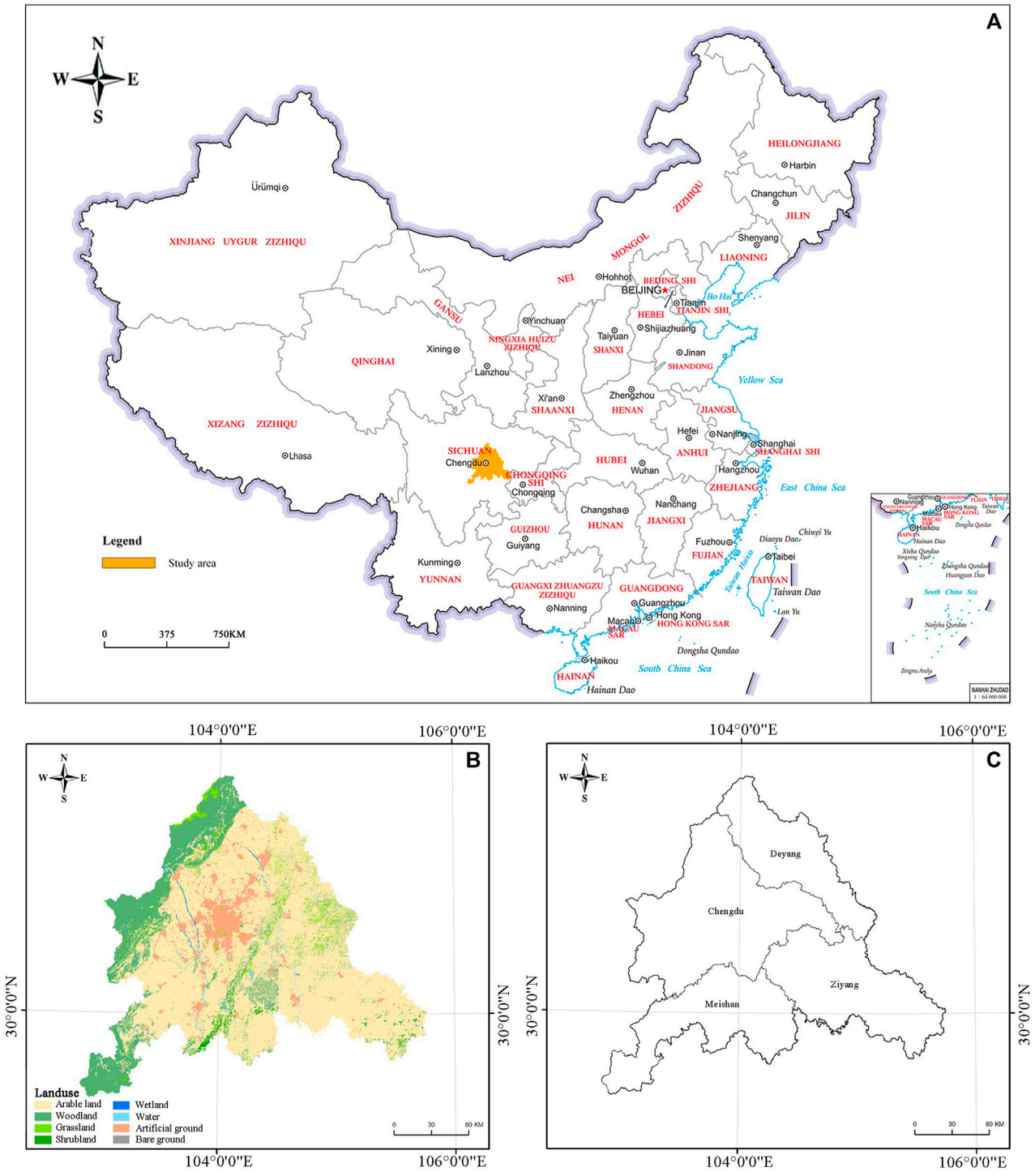

FIGURE 1
(A) Extent of the research region **(B)** Research region land use **(C)** Administrative division of the research region.

LST characteristics in different seasons, and 12 potential driving force are selected to analyze the potential factors affecting the spatial distribution pattern of heat islands in Chengdu metropolitan area, and to establish a season-al mathematical relationship model affecting the LST of Chengdu metropolitan area by correlation analysis, principal component analysis and multiple regression analysis, and finally summarize the analysis results for discussion.

3.2.1 LST division

To investigate the seasonal fluctuations of Land Surface Temperature (LST) throughout the Chengdu metropolitan area, ArcGIS 10.8 was utilized to reclassify the LST data using the mean–standard deviation technique (Table 2). Among them, Ts represents the unit raster value of LST in Chengdu metropolitan area, μ represents the mean value of LST in Chengdu metropolitan

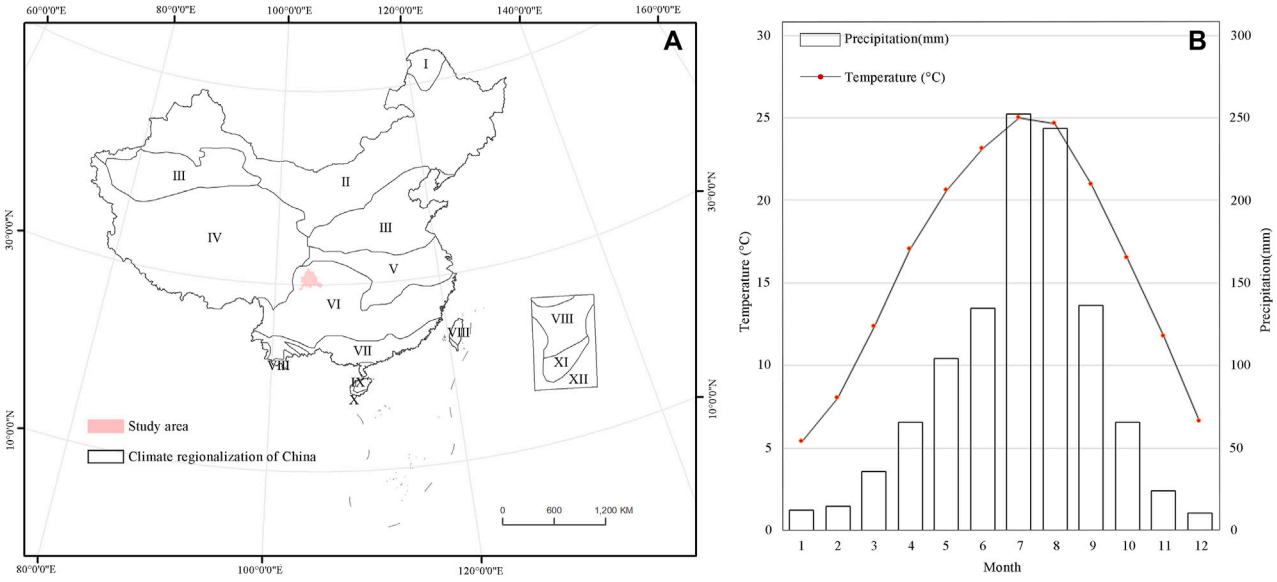

FIGURE 2
(A) The climate zone in which the study area is located (I. Northern Temperate Zone II. Central Temperate Zone III. Southern Temperate Zone IV. Highland climate zone V. Northern Subtropical VI. Central subtropics VII. Southern subtropics VIII. Northern subtropics IX. Northern subtropics X. Central tropics XI. Southern tropics XII. South Sea islands) **(B)** Average monthly temperature and precipitation in the central subtropics.

area in different seasons, and std represents the standard deviation of LST in Chengdu metropolitan area in different seasons. Combining with related studies (Hu et al., 2022a; Hu and Li, 2022), we define the mid-temperature zone, second high-temperature zone and high-temperature zone as UHI regions with high heat sources.

3.2.2 Landscape pattern indices

Landscape pattern index is commonly employed to quantify landscape characteristics and effectively depict the shape and distribution features of various patches within a landscape. Based on previous studies (McGarigal et al., 2012; Zhang et al., 2020), landscape edge density (ED), maximum patch index (LPI), Shannon diversity index (SHDI), and patch density (PD) were selected in this study. And the optimal window size was selected to calculate the landscape pattern index using Fragstats 4.2 software, and the specific formula is shown in the table below (Table 3).

From Table 3, it can be observed that this study selects four different landscape pattern factors to represent distinct meanings. Among them, Edge Density (ED) is the ratio of the total perimeter of all patches to the total landscape area, often used to indicate the degree of landscape fragmentation by boundaries, reflecting the degree of landscape element fragmentation. The Largest Patch Index (LPI) is the ratio of the largest patch area to the total landscape area. It is used to calculate the proportion of the largest patch within the spatial unit, helping identify dominant patch types within the landscape and assessing human disturbance to the landscape. The Shannon Diversity Index (SHDI) is commonly used to measure landscape diversity, reflecting the uneven distribution of patches within the landscape. It can also detect changes in diversity and heterogeneity of the same landscape at different periods. In a landscape system, the more diverse the land use types, the richer the patch types, and correspondingly, the higher the SHDI value. Patch Density (PD) is the ratio of the total number of patches to the total landscape area. It characterizes the degree of landscape fragmentation caused by segmentation and reflects the degree of human disturbance to the landscape. A higher Patch Density index indicates a greater degree of landscape fragmentation within the landscape unit (Zheng et al., 2010; Li et al., 2012).

3.2.3 Standard deviation ellipse

The standard deviation ellipse is commonly used to study the spatial distribution characteristics of geographical elements, displaying their distribution patterns in space and identifying variations in the center of the elements. The long semi-axis of the ellipse represents the main direction of the element distribution, while the size of the short semi-axis indicates the degree of spatial aggregation. The larger the difference between the lengths of the long and short axes, the more pronounced the directional distribution of the element. The azimuth represents the angle in a clockwise direction from the north to the direction of the long axis of the ellipse, indicating the main direction of the element's distribution (Zhao et al., 2022). Therefore, in this study, the standard deviation ellipse is used to quantitatively describe the spatial distribution and evolutionary characteristics of surface temperature in the Chengdu metropolitan area. The calculations are as follows:

$$x' = x_i - x_{ave}, y' = y_i - y_{ave} \tag{1}$$

$$tan\theta = \frac{\left(\sum_{i=1}^{n} w_i^2 x'^2_i - \sum_{i=1}^{n} w_i^2 y'^2_i\right) + \sqrt{\left(\sum_{i=1}^{n} w_i^2 x'^2_i - \sum_{i=1}^{n} w_i^2 y'^2_i\right) + 4\sum_{i=1}^{n} w_i^2 x'_i y'_i}}{2\sum_{i=1}^{n} w_i^2 x'^2_i y'^2_i} \tag{2}$$

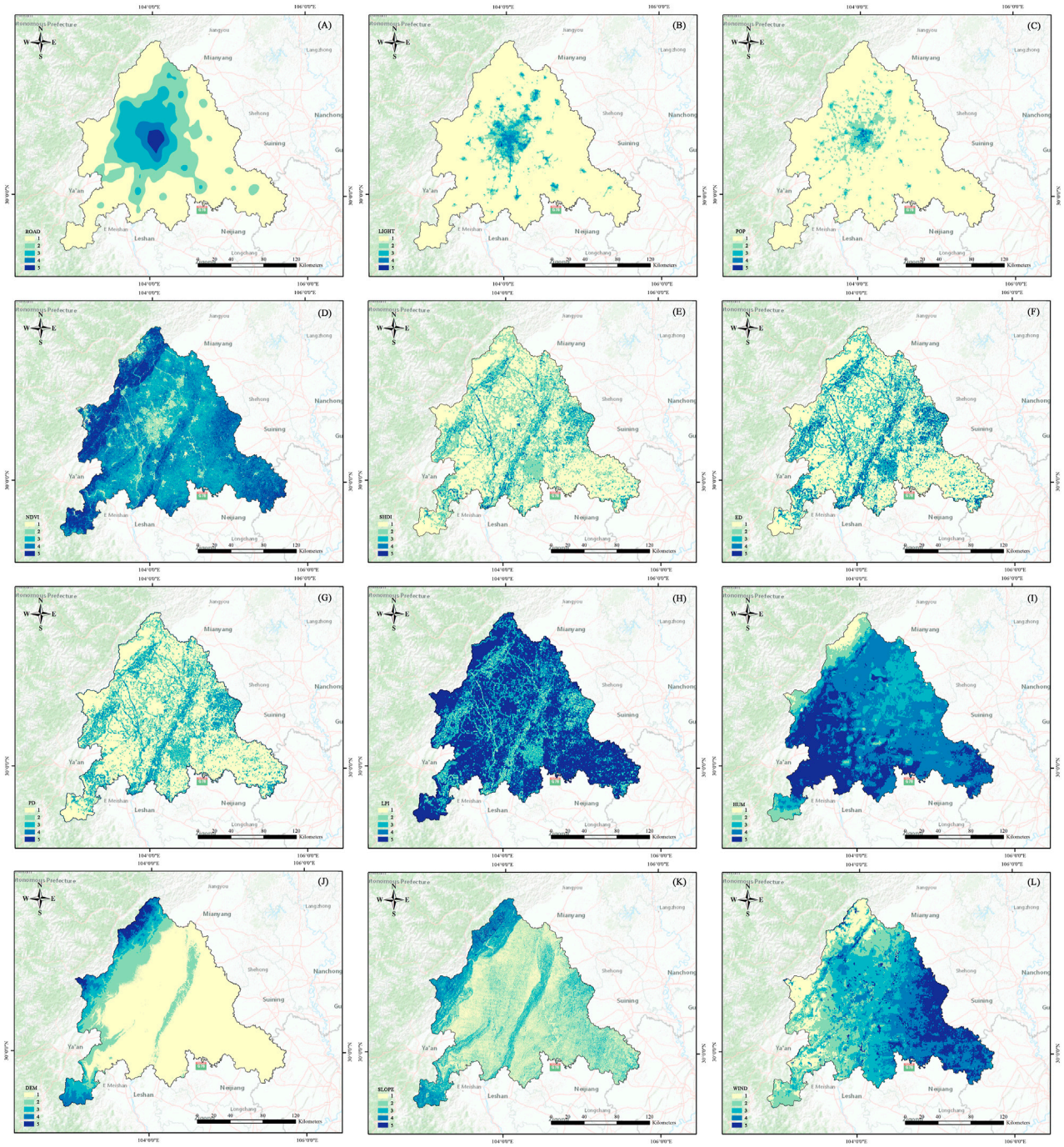

FIGURE 3
Potential driving force affecting LST change in the Chengdu metropolitan area **(A)** ROAD **(B)** LIGHT **(C)** POP **(D)** NDVI **(E)** SHDI **(F)** ED **(G)** PD **(H)** LPI **(I)** HUM **(J)** DEM **(K)** SLOPE **(L)** WIND.

$$\delta_x = \sqrt{\frac{\sum_{i=1}^{n}\left(w_i x_i' \cos\theta - w_i y_i' \sin\theta\right)^2}{\sum_{i=1}^{n} w_i^2}} \tag{3}$$

$$\delta_y = \sqrt{\frac{\sum_{i=1}^{n}\left(w_i x_i' \sin\theta - w_i y_i' \cos\theta\right)^2}{\sum_{i=1}^{n} w_i^2}} \tag{4}$$

In the equation, $(x_{ave}, y_{ave})$is the average center of (x_i, y_i), w_i is the LST, and (x', y') represents the relative coordinates of each point to the centroid of the study area, where $\tan\theta$ can obtain the azimuth angle, and δ_x and δ_y are the standard deviations of the X and Y-axes.

3.2.4 Correlation analysis

Correlation analysis is a statistical method used to assess the strength and direction of the relationship between two variables. In

TABLE 1 Potential driving force of LST.

Potential driving force	Abbreviations	Explanations	Literature basis	Data sources
Digital Elevation Model	DEM	This data is the annual data of 2020 after the calculation and processing of remote sensing satellite data, reflecting the surface elevation in unit space	Wang et al. (2018), Wang Z. et al. (2021)	The geospatial data cloud platform (https://www.gscloud.cn/#page1/1, accessed 16 February 2023)
Slope	SLOPE	This data is the DEM data calculated and processed for the year 2020, responding to the slope value in the unit space	Wang et al. (2018), Wang Z. et al. (2021)	Using DEM elevation data and the slope analysis tool in ArcGIS 10.8, the slope information was obtained
Wind speed	WIND	The data is synthesized by the algorithm for the year 2020, responding to the monthly average wind speed at the surface per unit space	Zhao et al. (2020)	The National Earth System Science Data Center (http://www.nesdc.org.cn/, accessed 3 March 2023)
Humidity	HUM	This data is synthesized by algorithm for the year 2020 and reflects the monthly average humidity value of the surface in the unit space	Zhao et al. (2020)	The National Earth System Science Data Center (http://www.nesdc.org.cn/, accessed 3 March 2023)
Shannon Diversity Index	SHDI	This number was calculated using 2020 land use data and reflects the richness of landscape types	Ren et al. (2016), Peng et al. (2018), Guo G. et al. (2020)	Based on the latest land-use data from the research area, landscape pattern indices were calculated using Fragstats software, Land-use data from Globeland30 (http://www.globallandcover.com/, accessed 3 March 2023)
Edge Density	ED	This number is calculated using 2020 land use data and reflects the edge density of landscape patches	Ren et al. (2016), Peng et al. (2018), Guo G. et al. (2020)	Based on the latest land-use data from the research area, landscape pattern indices were calculated using Fragstats software, Land-use data from Globeland30 (http://www.globallandcover.com/, accessed 3 March 2023)
Largest Patch Index	LPI	This number is calculated using 2020 land use data and reflects the maximum area index of landscape patches	Ren et al. (2016), Peng et al. (2018), Guo G. et al. (2020)	Based on the latest land-use data from the research area, landscape pattern indices were calculated using Fragstats software, Land-use data from Globeland30 (http://www.globallandcover.com/, accessed 3 March 2023)
Patch Density	PD	This number was calculated using 2020 land use data and reflects the density of landscape patches	Ren et al. (2016), Peng et al. (2018), Guo G. et al. (2020)	Based on the latest land-use data from the research area, landscape pattern indices were calculated using Fragstats software, Land-use data from Globeland30 (http://www.globallandcover.com/, accessed 3 March 2023)
Road density	ROAD	This data is obtained after kernel density processing using 2020 road vector data, pre-processed and corrected	Correa et al. (2012)	The non-profit map service platform Open Street Map (http://www.openstreetmap.org/, ac-cessed 27 February 2023)
Population density	POP	This number is the algorithm synthesized data for the year 2020, reflecting the number of people in the unit space	Peng et al. (2018), Geng et al. (2023)	Worldpop (https://www.worldpop.org/, accessed 26 February 2023)
Night light	LIGHT	The data is synthesized by algorithm for the year 2020, reflecting the value of nighttime lighting in the unit space	Peng et al. (2018)	The Resource and Environmental Science and Data Center of the Institute of Geographical Sciences and Resources, Chinese Academy of Sciences (https://www.resdc.cn/, accessed 25 February 2023)
NDVI	NDVI	This data is synthesized by the algorithm for the year 2020 and reflects the amount of vegetation cover per unit space	Yang et al. (2019)	The national ecological data center resource sharing service platform (http://www.nesdc.org.cn/, February 26s, 2023)

this study, this method is used to determine the correlation among various potential factors influencing surface temperature in the Chengdu metropolitan area, with a focus on determining the degree of correlation between surface temperature and factors such as elevation, slope, and humidity. Specifically, a random sampling tool in ArcGIS 10.8 was used to select 20,000 points and obtain their attribute values. Pearson correlation analysis was then conducted using SPSS software to calculate the Pearson

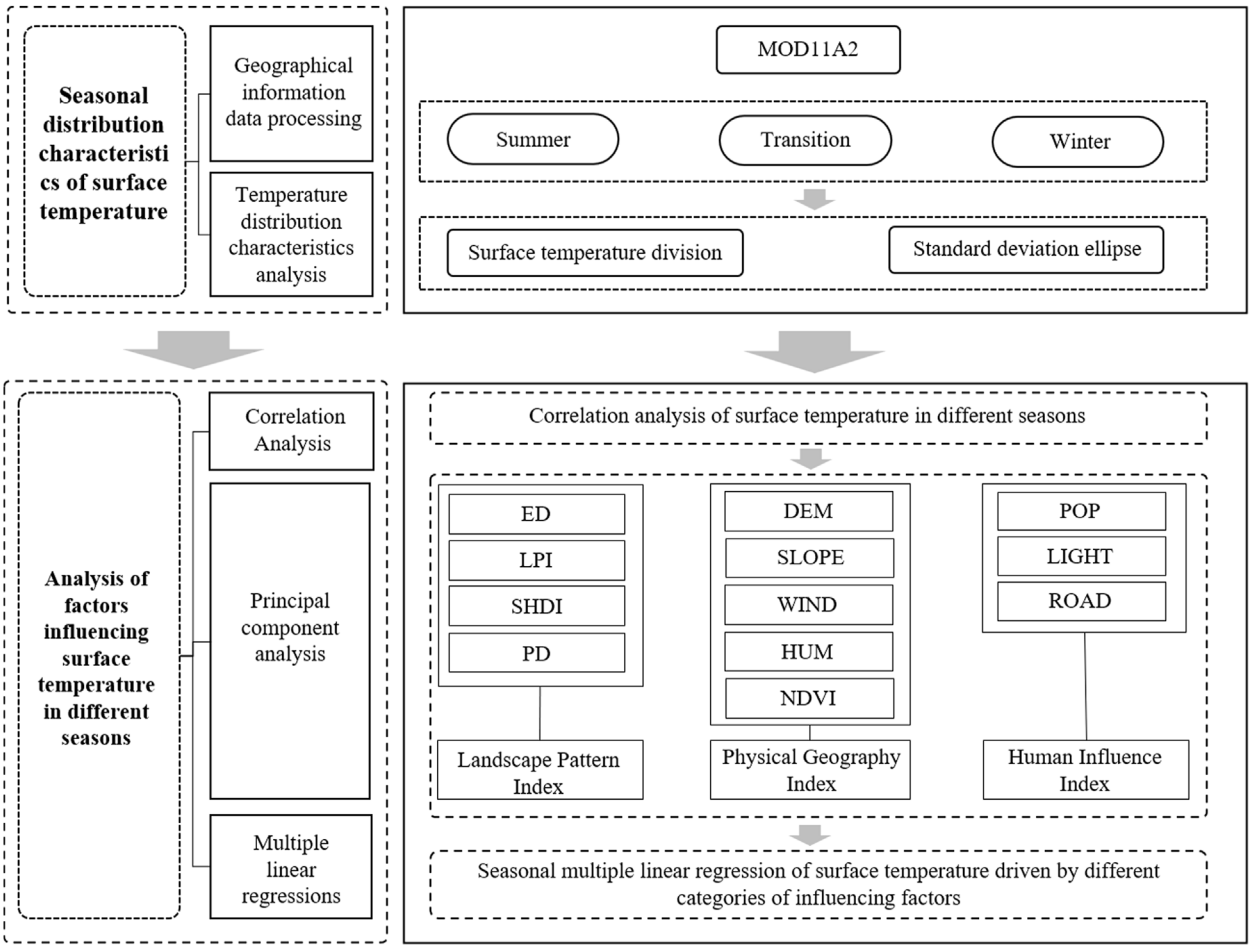

FIGURE 4
The framework for exploring the spatial and temporal distribution patterns of LST and the driving factors.

TABLE 2 Classification criteria for LST classes.

Temperature level	Classification method
High-temperature zone	Ts>μ+std
Second high-temperature zone	μ+0.5std≤Ts≤μ+std
Mid-temperature zone	μ-0.5std≤Ts≤μ+0.5std
Second low-temperature zone	μ-std≤Ts≤μ-0.5std
Low-temperature zone	Ts≤μ-std

correlation coefficients between each factor and surface temperature. Correlation analysis enables the identification of the main factors influencing surface temperature in the Chengdu metropolitan area and the assessment of the interrelationship among potential influencing factors. The correlation coefficient (R) can be expressed using the following formula:

$$R = \frac{\sum_{i=1}^{n}(x_i - \bar{x})(y_i - \bar{y}))}{\sqrt{\sum_{i=1}^{n}(x_i - \bar{x})^2}\sqrt{\sum_{i=1}^{n}(y_i - \bar{y})^2}} \quad (5)$$

In the formula, n represents the number of variables; x_i represents the independent variable (in this case, the potential influencing factor); y_i represents the dependent variable (in this case, the LST value). The range of the correlation coefficient R is $|R| \leq 1$. When the absolute value of R approaches 1, it indicates a stronger correlation between the variables; otherwise, it indicates a weaker correlation.

3.2.5 Principal component analysis

Principal component analysis (PCA) is a statistical method used for dimensionality reduction and data compression. Its main objective is to transform the original variables into a set of uncorrelated principal components to explain the variability in the data. In this study, PCA is employed to identify the main components or factors that explain the variations in surface temperature in the Chengdu metropolitan area. By reducing the number of variables, PCA helps simplify the model and better understand the underlying driving forces. Specifically, the study conducts PCA using SPSS software to analyze the potential influencing factors of surface temperature. The 16 potential influencing factors are subjected to dimensionality reduction based on their contribution rates, with values greater than 0.5 used as grouping criteria to classify them into different categories. This process eliminates the correlation among the factors and categorizes the

TABLE 3 Calculation formulae for landscape indices and their ecological significance.

Indicators	Meaning of indicators	Calculation formula
ED	The density of landscape patches within the spatial unit was measured (m/hm^2). E is the total length of the boundary of all patches in the landscape and A is the total area	$ED = \frac{E}{A}10^6$
LPI	The proportion of the largest patches within the spatial unit was measured. a_{ij} is the area of patch ij and A is the total area	$LPI = \frac{max(a_{ij})}{A}*100$
SHDI	Measurement of landscape diversity within a spatial unit. P_k is the ratio of the total area of category k to the window area	$SHDI = -\sum_{k=1}^{n} P_k \ln(P_k)$
PD	The degree of patch fragmentation was measured, with a larger patch density index indicating a higher degree of landscape fragmentation in that landscape unit. n_i is the number of i patches in the landscape and A is the total landscape area	$PD = \frac{n_i}{A}$

16 potential influencing factors into different groups of latent influencing factors.The calculation proceeded as follows:

Assuming that the original variables have m samples, with each sample having n observations, the matrix of the original variables is:

$$X = \begin{pmatrix} x_{1n} & \cdots & x_{1m} \\ \vdots & \ddots & \vdots \\ x_{m1} & \cdots & x_{nm} \end{pmatrix} \quad (6)$$

In the formula, X represents the potential driving force, n represents the number of potential driving force, and m represents the number of samples.

After obtaining each principal component, the extraction of principal components was performed according to Eq. 7:

$$\alpha_k = \frac{\lambda_k}{\sum_{i=1}^{n} \lambda_i} \quad (7)$$

Where, α_k is the variance contribution of the i-th principal component, indicating the degree of explanation of each component to the information of the original variables; λ_i is the characteristic root of the correlation coefficient matrix.

Expressions for different categories of principal components:

$$\begin{cases} F_1 = a_{11}x_1 + a_{12}x_2 + \ldots + a_{1n}x_n \\ F_2 = a_{21}x_1 + a_{22}x_2 + \ldots + a_{2n}x_n \\ F_3 = a_{31}x_1 + a_{32}x_2 + \ldots + a_{3n}x_n \end{cases} \quad (8)$$

Where, F_1, F_2 ... F_n are the 1st principal component, 2nd principal component ... nth principal component; a_{11}, a_{21} ... a_{nm} are the principal component coefficients.

3.2.6 Multiple linear regression

Multiple regression analysis is a statistical method used to establish the relationship between a dependent variable and multiple independent variables. In order to further investigate whether different categories of potential influencing factors have an impact on surface temperature, this study employs multiple linear regression to determine the effects of different categories of potential influencing factors on surface temperature. It identifies the important role played by each category of factors in the seasonal variation of surface temperature and their relative weights. This helps determine how surface temperature is influenced by different categories of potential influencing factors, and allows for targeted solutions to be proposed.

Assuming that there are independent variables x_1, x_2, x_3 ... x_n and y is the dependent variable, then:

$$y = b_0 + b_1x_1 + b_2x_2 + \ldots b_nx_n \quad (9)$$

And in this study y denotes the LST magnitude and x_1, x_2, x_3...x_n denotes the potential impact factor.

The multiple regression coefficients obtained from the multiple linear regression model need to undergo collinearity diagnosis to determine the severity of collinearity in the multiple linear regression model. The commonly used VIF values are used for this purpose. The calculation formula is as follows:

$$VIF = \frac{1}{1 - R_i^2} \quad (10)$$

R^2 is the coefficient of determination in linear regression, which reflects the percentage of variation in the dependent variable explained by the regression equation. It can be obtained by squaring the multiple correlation coefficient between the dependent variable and the independent variables. If all VIF values are less than 10, it indicates that there is no multicollinearity problem in the model and the model construction is good.

In summary, this study identified 12 potential factors that affect the spatial distribution pattern of the urban heat island in the Chengdu metropolitan area. Through correlation analysis, principal component analysis (PCA), and multiple regression analysis, a seasonal mathematical model was established to explain the influences on surface temperature in the Chengdu metropolitan area. Specifically, correlation analysis was used to determine the relationships between factors, PCA was employed to reduce dimensionality and identify the main components, and multiple regression analysis was utilized to establish a mathematical model explaining the relationship between the dependent and independent variables. Therefore, these three research methods differ in analyzing the influencing factors of the urban heat island's spatial distribution pattern in the Chengdu metropolitan area, and they complement each other. The comprehensive use of these methods provides a comprehensive understanding and modeling of the influencing factors of seasonal variations in surface temperature in the Chengdu metropolitan area.

4 Results

4.1 Temporal-spatial characteristics of LST in Chengdu metropolitan area

Figure 5 presents the annual LST patterns of Chengdu metropolitan area, which were extracted from MOD11A2 data

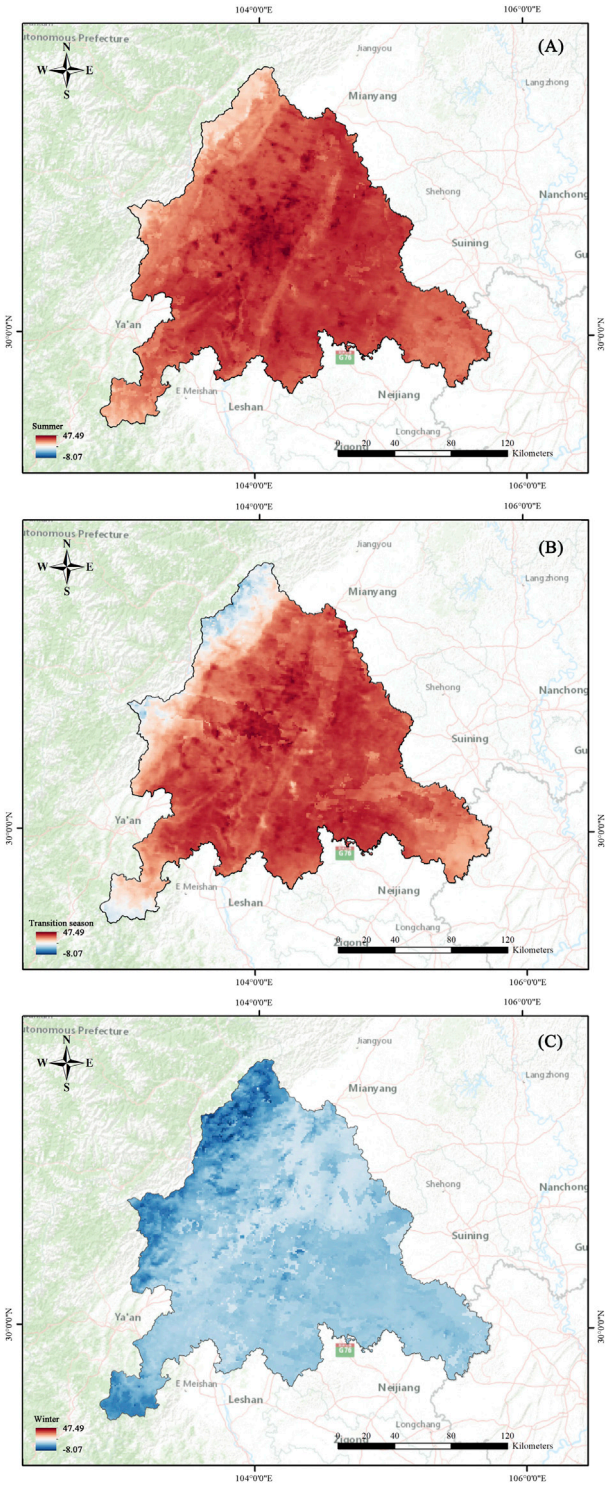

FIGURE 5
Spatial pattern of LST in Chengdu metropolitan area in different seasons: **(A)** summer **(B)** transition season **(C)** winter.

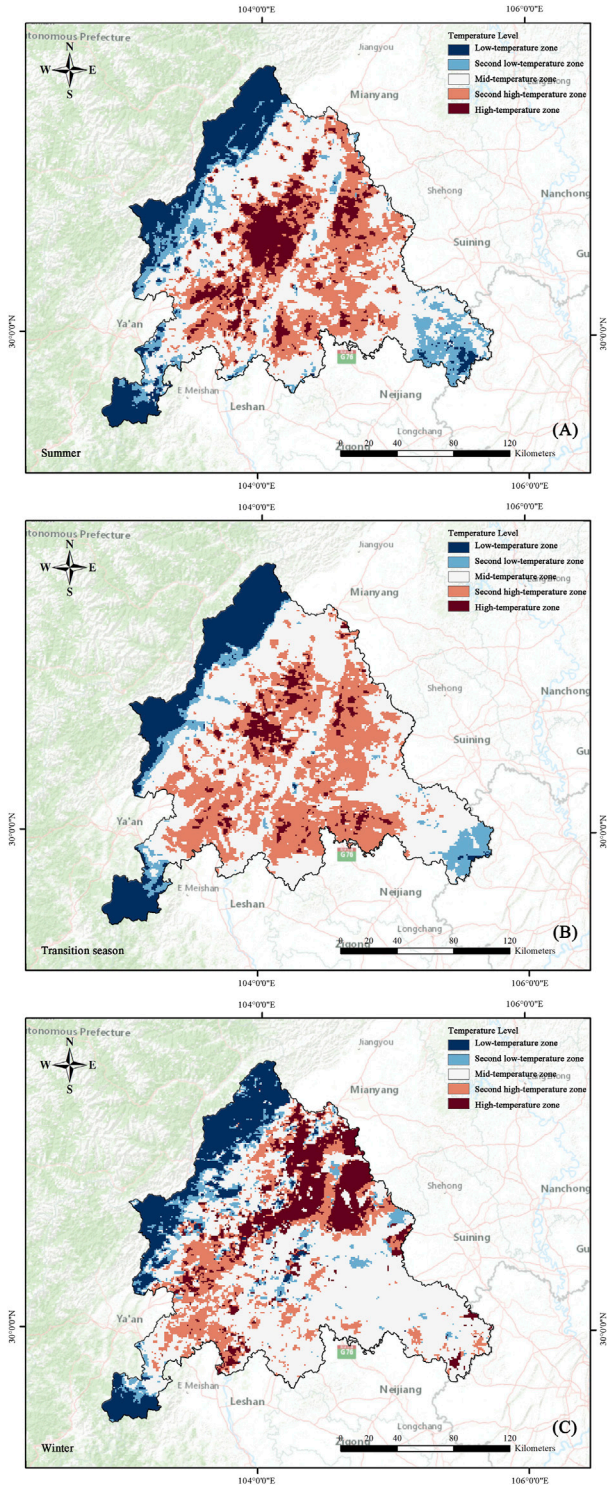

FIGURE 6
Spatial distribution of heat islands in Chengdu metropolitan area in different seasons: **(A)** summer **(B)** transition season **(C)** winter.

and categorized into three phases: summer, transition season, and winter. During summer, the monthly mean LST was 35.3°C, with a maximum value of 46.5°C, a minimum of 19.4°C, and a standard deviation of 3.66. In the transition season, the monthly average LST reached 37.1°C, with a maximum value of 47.5°C, a minimum of 10.4°C, and a standard deviation of 5.09. As for winter, the monthly average LST was 9.3°C, with a maximum value of 17.4°C, a minimum of −8.1°C, and a standard deviation of 3.54.

In order to obtain different characteristics of temporal and spatial changes of the UHI in the Chengdu metropolitan area,

the study used the mean−standard deviation method to reclassify the LST into five zones: "high temperature zone, medium-high temperature zone, medium temperature zone, medium-low temperature zone, and low temperature zone" (Figure 6), in order to investigate the changes in area and space of the LST in different seasons.

Based on the level values of LST in Chengdu metropolitan area after division, the area values of different temperature zones in Chengdu metropolitan area during the transition season, summer, and winter could be obtained. Based on the classification criteria in Table 3, as shown in Table 4: it could be found that the high-temperature zone and the second high-temperature zone of the Chengdu metropolitan area in summer have an area of 3328.25 km^2 and 7778.57 km^2 respectively, accounting for 10.06% and 23.50% of the total area of the Chengdu metropolitan area. Compared with the transition season, the area of high-temperature zones in summer is significantly higher, while compared with winter, the total area of high-temperature zones and the second high-temperature zones is significantly higher than in winter. From a seasonal perspective, the temperature in the Chengdu metropolitan area is generally high throughout the year, with relatively large areas of high-temperature zones and the second high-temperature zones in summer. In the transition season, the second high-temperature zone reaches its peak, accounting for the highest proportion (31.18%) among the three seasons; in winter, the high-temperature zone reaches its peak, accounting for the highest proportion (12.98%) among the three seasons (Figure 7).

In order to explore the spatial characteristics of surface temperature variations in the Chengdu metropolitan area, a standard deviation ellipse analysis was conducted. The analysis results (see Figure 8) show significant differences in the length of the major and minor axes of the ellipses for the three seasons. It can be observed that the temperature variations in the Chengdu metropolitan area exhibit a strong directional pattern in different seasons. From the figure, it can be seen that the temperature variations in the Chengdu metropolitan area follow a northeast-southwest direction. In the summer season, the length of the minor axis of the ellipse is significantly smaller than that in the transitional and winter seasons. The transitional season also shows a relatively smaller value compared to the winter season. Therefore, it can be inferred that the temperature variations in the summer season exhibit the most significant clustering characteristics, followed by the transitional and winter seasons. From winter to transition season, the heat island center moved southeastward by 49.3 km at a deviation angle of 7.5. From transition season to summer, the heat island center shifted northwest by 22.4 km with a deviation angle of 6.3°. Overall, the LST in Chengdu metropolitan area changed significantly with the seasons. In summer, the high-temperature zone was concentrated in the central area. In the transition season, the dispersion of the high-temperature zone caused the center of the heat island to move towards the plain area. In winter, most areas were normal, with low-temperature zones and second low temperature zones located in the northern mountainous areas, causing the center of the heat island to move towards the northern mountainous areas.

4.2 Potential drivers of LST in the Chengdu metropolitan area

To identify the factors influencing LST, the study considered various potential drivers, including POP, LIGHT, DEM, SLOPE, HUM, WIND, ROAD, ED, LPI, PD, SHDI, and NDVI. These factors were analyzed using SPSS and ArcGIS 10.8 to determine their correlation with LST in different seasons. The Spearman correlation analysis method was employed to calculate correlation coefficients between the potential factors and LST (Figure 9), and the results passed the significance test. Specifically, LPI, NDVI, DEM, and SLOPE were negatively correlated with LST in different seasons, indicating that they can significantly reduce LST. On the other hand, ED, PD, SHDI, WIND, HUM, ROAD, POP, and LIGHT were positively correlated with LST in different seasons, indicating that they can significantly increase LST. Meanwhile, the degree of influence on LST varies in different seasons, with slight differences observed in different seasons.

In order to further explore the differences in the driving factors of land surface temperature in different seasons, this study used principal component analysis to further investigate them. Based on the findings presented in Tables 5, 6, principal component analysis (PCA) was employed to reduce the dimensionality of the twelve potential factors. The PCA results revealed that the first three principal components possessed eigenvalues greater than 1, suggesting that they accurately captured the variations in LST. Based on the component matrix after four iterations of rotation, we identified the three main factors affecting LST changes in Chengdu metropolitan area: landscape pattern, natural geography, and human influence factors.

4.3 Seasonal relationship between LST and potential drivers in Chengdu metropolitan area

The study further explored the potential factors affecting LST in Chengdu metropolitan area by using the three principal components identified through principal component analysis, and established regression equations based on seasonal LST. From Tables 6, 7, it can be observed that the linear regression coefficients (R^2) between the independent variables and dependent variables have different values in different seasons. When analyzing the temperature data for summer, the R^2 is 0.621, indicating that the regression equation can explain 62.1% of the sample data. When analyzing the temperature data for the transitional season, the R^2 is 0.746, indicating that the regression equation can explain 74.6% of the sample data. When analyzing the temperature data for winter, the R^2 is 0.497, indicating that the regression equation can explain 49.7% of the sample data. Furthermore, in the collinearity analysis, the VIF (variance inflation factor) and TLR (tolerance limit ratio) values of Principal Component 1 are 9.7408 and 0.1027, respectively. For Principal Component 2, the VIF and TLR values are 3.6464 and 0.2742, respectively. For Principal Component 3, the VIF and TLR values are 7.2896 and 0.1372, respectively. It can be seen that the VIF and TLR values of Principal Component 2 (natural geography) are relatively good, indicating that the regression equation does not have a serious collinearity

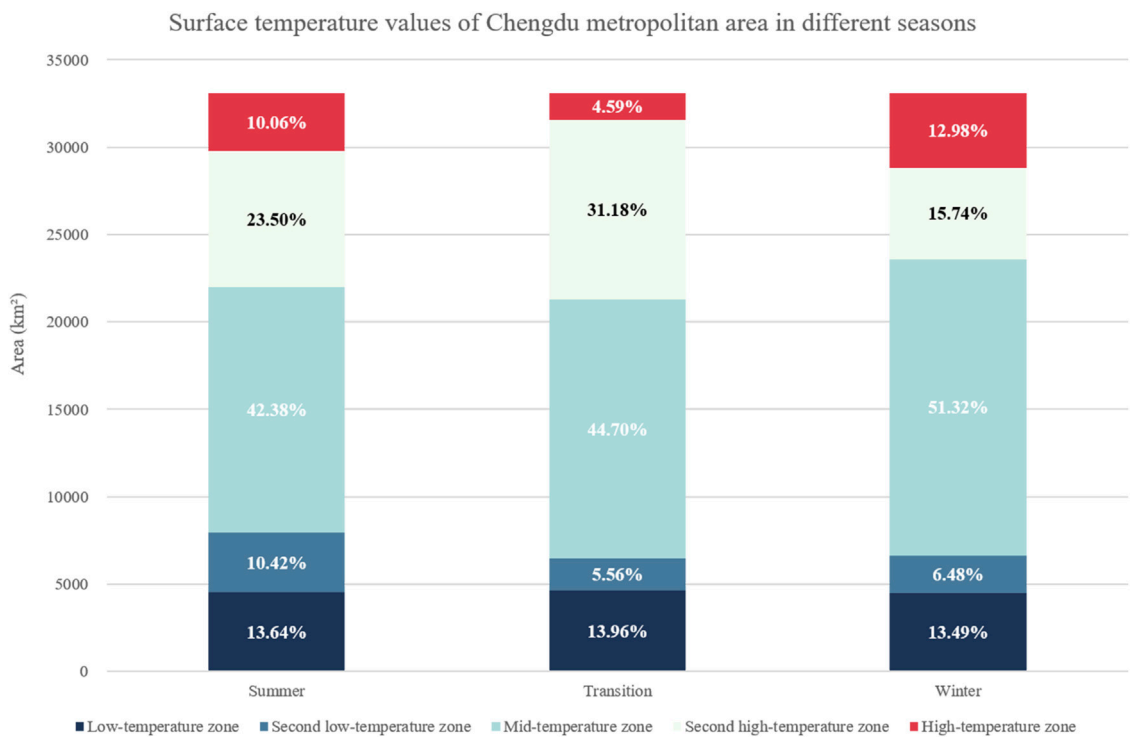

FIGURE 7
Seasonal urban heat island area in Chengdu metropolitan area.

problem. However, the VIF and TLR values of Principal Component 1 (landscape pattern) and Principal Component 3 (socio-economics) are relatively poor. Based on the VIF and Tolerance values, it can be concluded that the regression equation does not have a serious collinearity problem.

Specifically, from Table 8, it can be seen that ED, PD, SHDI, NDVI, DEM, and SLOPE are negatively correlated with land surface temperature, while WIND, HUM, ROAD, POP, and LIGHT are positively correlated with land surface temperature. Overall, natural geographical factors such as WIND, HUM, DEM, and SLOPE have a greater impact on land surface temperature, followed by social and economic factors such as POP, LIGHT, NDVI, and ROAD. Landscape pattern factors such as ED, LPI, PD, and SHDI have the weakest impact on land surface temperature. In terms of seasonality, POP (0.125) and LIGHT (0.16) reach their maximum values in summer, while DEM (−0.857), SLOPE (−0.739), NDVI (−0.203), HUM (0.747), WIND (0.453), and ROAD (0.298) reach their maximum values in the transition season. ED (−0.08), LPI (0.089), PD (−0.076), and SHDI (−0.08) reach their maximum values in winter.

5 Discussion

5.1 Temporal-spatial characteristics of seasonal LST in Chengdu metropolitan area

The study area is situated in a basin typical of its kind, bounded by the Chengdu Plain to the east, the Minshan Mountains to the north, and the Emei Mountains to the southwest. Results from the analysis of LST reveal conspicuous spatial disparities in the UHI effect across the Chengdu metropolitan area. Specifically, areas with relatively low temperatures have formed in proximity to the Minshan Mountains and the Emei Mountains, situated in the north and southwest regions of the study area, respectively, while regions with high temperatures have emerged in the central plain. Collectively, these observations indicate that the thermal environment of the Chengdu metropolitan area exhibits a distinctive feature characterized by high temperatures in the southeast and low temperatures in the northwest.

By considering the spatiotemporal characteristics, it is observed that during summer, the regions with high and second high temperatures are predominantly located in the Chengdu, Deyang, Meishan, and Ziyang areas, with few other cities and counties also exhibiting localized hotspots. Meanwhile, the areas with low and second low temperatures are distributed mainly in the northern mountainous regions of Dujiangyan and the southwestern areas of the study region. In the transitional season, high and second high temperature regions exhibit more dispersed patterns with reduced regional coherence, whereas, low and second low temperature areas have a more concentrated distribution in the northwestern and southwestern sectors of the Chengdu metropolitan area. In winter, the high-temperature zone and the second high-temperature zone are mainly distributed in the northeast of the Chengdu metropolitan area, and are divided by the Longquan Mountains in a northeast-southwest direction. The low-temperature zone and the second low-temperature zone are distributed in the mountains in the northwest of the Chengdu

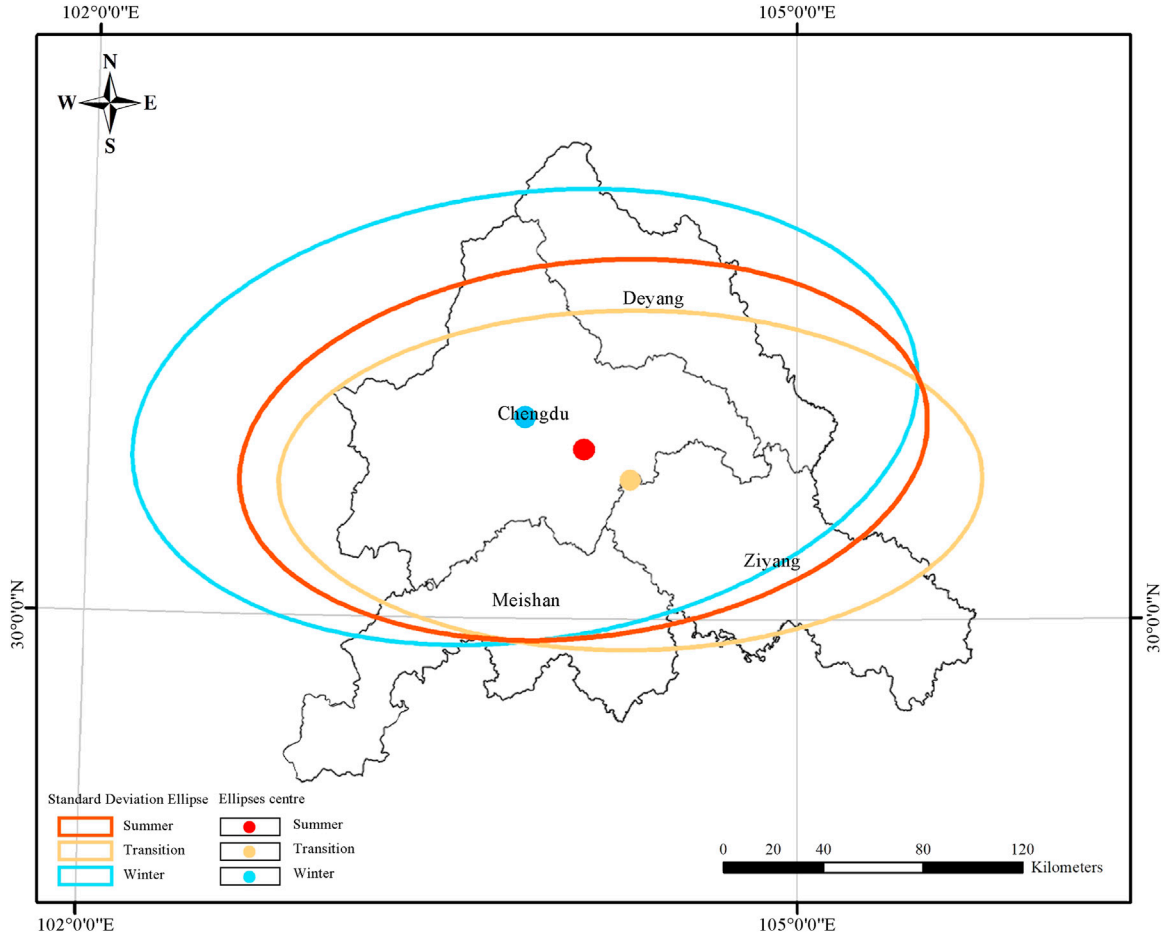

FIGURE 8
Direction of heat island development in Chengdu metropolitan area.

metropolitan area and the Longquan Mountains in the southeast of Chengdu city. These results are consistent with previous research (Zhou et al., 2014).

Considering the distribution of cities, high-temperature areas are mainly concentrated in cities such as Chengdu, Deyang, Ziyang, Guanghan, and Meishan. These cities are located in the plain area, with dense population, developed economy, high level of urban construction, and compact distribution of buildings, which cause the LST to rise (Zhao et al., 2018; Hu et al., 2022b; Ren et al., 2022). And the study area is located inside the Sichuan Basin, surrounded by high-altitude mountains, which cannot disperse the heat airflow, resulting in the accumulation of heat island in the basin area between the mountains. This exacerbates the urban heat island effect (Wang Z. et al., 2022). Concentrated regions of low temperature are found primarily in the mountainous zones located in the northwestern and southwestern sectors. These areas are characterized by high-altitude mountainous terrain with abundant water systems and lush vegetation. Water systems and vegetation cover density can significantly contribute to mitigating the UHI effect. Water systems can directly cool the surface, while vegetation can reduce LST through transpiration (Jin, 2012; Hu et al., 2022c).

5.2 Exploring the driving relationship of seasonal LST in Chengdu metropolitan area

Based on the principal component analysis and judgment of the content of potential influencing factors, the factors affecting surface temperature in the Chengdu metropolitan area are categorized into three groups: landscape pattern factors, natural geographic factors, and socioeconomic factors. Current research indicates that socioeconomic factors play a dominant role in the urban heat island effect in plain areas (Zhou et al., 2016; Sun et al., 2019). However, through the correlation coefficient analysis of multiple linear regression, it is revealed that natural geographic factors have a significant advantage in the formation process of the urban heat island in the Chengdu metropolitan area. It is worth noting that the current research findings may not be quantitatively refutable due to differences in study design, data sources, and methods, which lead to certain limitations. On the one hand, the selection of influencing factors has a significant impact on research results. In this study, typical driving factors were selected as independent variables in the regression analysis, covering different aspects of variables as much as possible. However, it is still challenging to fully consider all possible factors. On the other hand, spatial and temporal scales also influence research outcomes. The urban heat island effect exhibits different

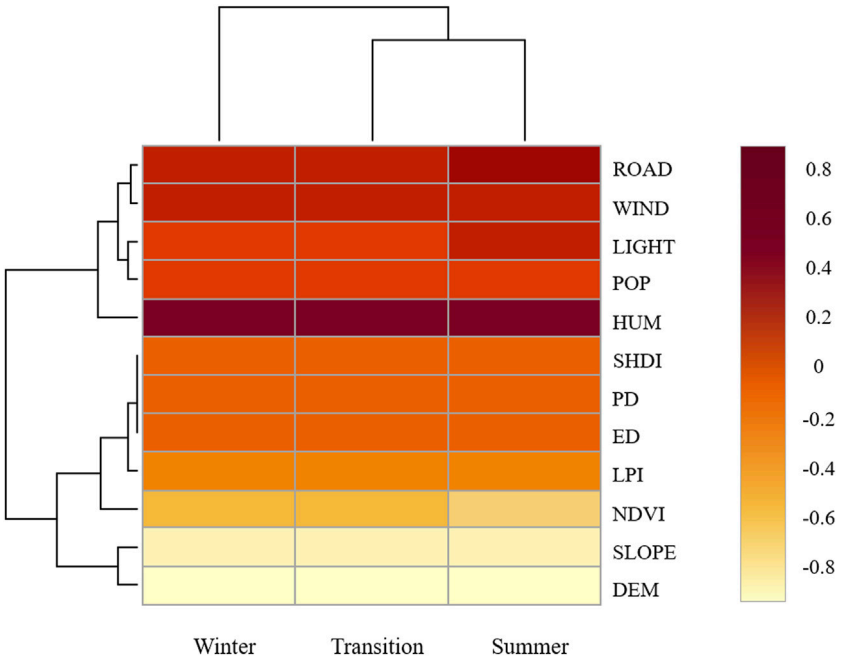

FIGURE 9
The Spearman's rank correlation coefficient was utilized to analyze the influence of various potential factors on LST across diverse seasons.

TABLE 4 Size of heat island area in Chengdu metropolitan area in different seasons.

Season		Low-temperature area	Medium-low temperature zone	Medium temperature zone	Medium-high temperature zone	High temperature zone
Summer	Area (km^2)	2228.07	1649.42	24,048.09	2611.91	2555.81
	Ratio (%)	6.73%	4.98%	72.67%	7.89%	7.72%
Transition	Area (km^2)	3413.73	2195.63	20,845.96	3909.79	2728.19
	Ratio (%)	10.32%	6.63%	62.99%	11.81%	8.24%
Winter	Area (km^2)	1560.97	3911.65	24,901.44	0.00	2719.25
	Ratio (%)	4.72%	11.82%	75.25%	0.00%	8.22%

patterns at different spatial scales (such as within cities and surrounding areas) and temporal scales (such as different seasons and time periods).

The research findings of this study may be related to the geographical environment of the study area, in which the Chengdu plain in the Sichuan Basin is surrounded by large mountains to the north and west. As a result, hot air is inhibited from rising, leading to sinking and resulting in warmer temperatures in the plain area. Moreover, in areas with higher elevations in the study area, a large number of vegetation trees are planted, and the increase in vegetation can effectively reduce the LST (Wang and Akbari, 2016). Among the landscape pattern factors, ED, PD, and SHDI are negatively correlated with LST, while only LPI has a positive correlation with LST, which indicates that most landscape pattern factors can reduce LST. Wind speed and humidity have a positive correlation with LST, indicating that wind speed and humidity can increase LST (Zhou et al., 2016). The location of the Chengdu metropolitan area, situated within a basin characterized by low wind speed and high humidity, is a determining factor. Corroborating the positive correlation between wind speed and LST, higher LST values are observed when wind speed is low. In the plain areas within the basin, the prevailing winds often come from inland regions. According to previous research (Al-Obaidi et al., 2021), when the winds originate from inland areas, they tend to generate a strong urban heat island effect. The presence of water in the atmosphere is known to exert a

TABLE 5 Total variance explained by principal components of potential influences.

Component	Initial eigenvalues			Extracted square sum of loads		
	Total	Percentage of variance %	Cumulative%	Total	Percentage of variance %	Cumulative%
1	3.870	32.246	32.246	3.870	32.246	32.246
2	2.832	23.597	55.843	2.832	23.597	55.843
3	2.001	16.678	72.521	2.001	16.678	72.521
4	0.908	7.567	80.088			
5	0.804	6.699	86.787			
6	0.539	4.491	91.278			
7	0.427	3.559	94.837			
8	0.274	2.280	97.117			
9	0.141	1.175	98.292			
10	0.114	0.948	99.239			
11	0.061	0.511	99.750			
12	0.030	0.250	100.000			

The higher the coefficients of the principal components, the more original variables are included in the components. Dimensionality reduction through filtering of principal component coefficients enables the examination of principal component composition under varying circumstances. The first major component reflected the influence of landscape pattern index on LST, including ED, LPI, PD, and SHDI., The second major component reflected the influence of natural geographical factors on LST, including WIND, HUM, DEM, and SLOPE., The third major component reflected the influence of human factors on LST, including ROAD, NDVI, POP, and LIGHT. NDVI, was easily influenced by human activities and could be reasonably explained as belonging to human factors along with POP, LIGHT, and ROAD (Liu et al., 2021b).

TABLE 6 Contribution of potential driving force affecting the magnitude of LST in Chengdu metropolitan area.

Potential driving force	Principal component 1	Principal component 2	Principal component 3
ED	0.975	−0.057	−0.021
LPI	−0.968	0.041	−0.016
PD	0.958	−0.059	−0.023
SHDI	0.986	−0.057	0.008
WIND	0.080	−0.522	−0.037
HUM	0.050	−0.841	−0.016
ROAD	−0.011	−0.149	0.846
NDVI	−0.004	0.094	−0.618
POP	−0.022	0.017	0.709
LIGHT	0.015	0.008	0.867
DEM	−0.065	0.935	−0.124
SLOPE	0.048	0.768	−0.222

warming effect during periods of falling temperatures and a cooling effect during periods of rising temperatures, which are referred to as the "constant temperature effect," ultimately leading to the maintenance of the surrounding temperature. However, the perpetual low wind speed in the Chengdu area impedes the cooling effect, thereby causing the land surface temperature (LST) to remain persistently high (Zong et al., 2019; Wu et al., 2021). Furthermore, the positive correlation identified between human-influenced factors and LST indicates that anthropogenic activities have a notable enhancing impact on the urban heat island phenomenon. Human construction activities will significantly affect the changes in urban climate (Ren et al., 2022), and the continuous expansion of cities and human energy consumption will generate a large amount of heat, resulting in an increase in LST.

In addition to the overall impact of indicators related to human activities leading to an increase in surface temperature, our further research has revealed that human activities are influenced by seasonal variations, showing varying degrees of impact on

TABLE 7 Results of regression analysis of potential driving force.

		Unstandardized coefficients		Standardization coefficients	t	Significance	Relevance	Collinearity statistics	
		B	Standard error	Beta				Tolerances	VIF
Principal component 1	Summer	−0.0032	0.0006	−0.0717	−5.2733	0.0000	0.1669	0.1027	9.7408
	Transition	−0.0068	0.0007	−0.1096	−9.8496	0.0000	0.2758	0.1027	9.7408
	Winter	−0.1245	0.0007	−0.1096	−9.8496	0.0000	0.2758	0.1027	9.7408
Principal component 2	Summer	−0.0051	0.0001	−0.7782	−93.5535	0.0000	−0.7468	0.2742	3.6464
	Transition	−0.0083	0.0001	−0.8987	−131.9637	0.0000	−0.8456	0.2742	3.6464
	Winter	−0.7510	0.0001	−0.8987	−131.9637	0.0000	−0.8456	0.2742	3.6464
Principal component 3	Summer	0.0003	0.0000	0.1922	16.3434	0.0000	0.2674	0.1372	7.2896
	Transition	0.0002	0.0000	0.0832	8.6406	0.0000	0.1913	0.1372	7.2896
	Winter	0.0410	0.0000	0.0832	8.6406	0.0000	0.1913	0.1372	7.2896

TABLE 8 Regression coefficients of potential influencing factors.

Potential driving force	Principal component 1	Principal component 2	Principal component 3
ED	0.975	−0.057	−0.021
LPI	−0.968	0.041	−0.016
PD	0.958	−0.059	−0.023
SHDI	0.986	−0.057	0.008
WIND	0.080	−0.522	−0.037
HUM	0.050	−0.841	−0.016
ROAD	−0.011	−0.149	0.846
NDVI	−0.004	0.094	−0.618
POP	−0.022	0.017	0.709
LIGHT	0.015	0.008	0.867
DEM	−0.065	0.935	−0.124
SLOPE	0.048	0.768	−0.222

surface temperature. The effects of potential influencing factors on surface temperature also vary across different seasons. Specifically, during the summer season, social-economic factors such as population (POP) and nighttime light (LIGHT) exert a strong influence on surface temperature, which is more significant than during the transitional and winter seasons. On the other hand, road density (ROAD) shows a lower impact during the transitional season compared to the winter season. Additionally, there is a positive correlation between road density, nighttime light, population, and surface temperature, indicating that human activities have a more pronounced effect on surface temperature during the summer, leading to an increase in surface temperature. In the transitional season, natural geographical factors (WIND, HUM, DEM, SLOPE) have a greater impact on surface temperature compared to the summer and winter seasons, suggesting that natural geographical factors have a more significant influence on surface temperature during the transitional season. Moreover, the normalized difference vegetation index (NDVI) exhibits a more pronounced impact on surface temperature during the transitional season.

At the same time, besides human activities and natural factors, this study also considers other potential factors that may influence surface temperature, including landscape pattern indices. On one hand, changes in surface temperature can be influenced by the combined effects of multiple potential driving factors. On the other hand, the study of the aforementioned factors reveals that landscape pattern factors have a greater impact on surface temperature during the winter season compared to the transitional and summer seasons, indicating that landscape pattern factors have a more pronounced effect on surface temperature during the winter season. In summary, different categories of potential influencing factors have significant differences in their effects on surface temperature. Social-economic factors have the most significant impact during the summer season, natural geographical factors have the most significant impact during the transitional season, and landscape pattern factors have the most significant impact during the winter season.

5.3 Seasonal guidance strategies to mitigate urban heat island phenomenon in Chengdu metropolitan area

By examining the determinants of UHI, it becomes evident that both human activities and natural geographical characteristics exhibit seasonally-specific influences on UHI intensity in built environments. In light of these findings, several potential strategies may be recommended to mitigate the adverse consequences of UHI phenomena: 1) During the summer season, a key focus is placed on the significant impact of socio-economic factors, particularly in the urban development process. Adjusting urban land-use patterns is emphasized to alleviate population

concentration. This entails optimizing and enhancing Chengdu's role as the central urban area, leading to the development of surrounding small towns. It also involves extending the reach of public service facilities to the periphery, and rational control of development intensity and population density within the metropolitan area. These measures aim to mitigate the rise in surface temperature caused by population agglomeration. Furthermore, aligning with the direction of urban wind corridors, adjustments are made to the arrangement of buildings and road networks. This aims to prevent blockages in the urban wind corridors due to issues with urban road and building layouts. The goal is to ensure the ventilation pathways in the city are unobstructed, effectively mitigating the urban heat island effect during the summer season (Gedzelman et al., 2003; Ngarambe et al., 2021). 2) During the transitional season, a focus is placed on the critical influence of natural geographical factors. This involves establishing an urban ecological engineering network and an urban park green space system to enhance the city's green environment. The primary framework of this ecological network is centered around the Chengdu Tianfu Greenway, creating an ecological network system. Additionally, the Chengdu Urban Ecological Zone is developed, accompanied by the optimization of the city's landscape spatial structure. This optimization aims to interconnect the city's lake water systems and vegetation green spaces, thereby enhancing the overall continuity of the urban landscape. Emphasis is placed on the ecological protection and restoration of rivers, lakes, and water systems, as well as mountainous vegetation within the metropolitan area. This effort extends to promoting ecological conservation and restoration in river basins like the Min River Basin, as well as strengthening ecological development in regions such as the Min Mountains and Qionglai Mountains. Through these initiatives, adjustments are made to the internal ecological and climatic features of the metropolitan area, aiming to optimize the Humidity (HUM) and Wind (WIND) patterns within the metropolitan area. This strategy contributes to alleviating the rise in urban surface temperature (Das et al., 2020; Hu et al., 2022a; Ren et al., 2022). 3) During the winter season, a key emphasis should be placed on the influence of landscape pattern factors. On one hand, it involves establishing comprehensive landscape elements to ensure the integrity of the urban ecological spaces. This includes advancing the ecological protection and restoration of Longquan Mountain, located at the central position of the metropolitan area, and increasing the edge density of landscapes within the urban spatial scope. This is to prevent human-induced disruptions to urban landscape spaces. Simultaneously, attention should be given to the arrangement of various types of landscape elements, enhancing the preservation of ecological diversity within the metropolitan area, diversifying landscape patches, and increasing the Spatial Heterogeneity Diversity Index (SHDI) value. These efforts aim to alleviate urban surface temperatures (Yu et al., 2019; Han et al., 2022). On the other hand, it involves constructing a network of urban ecological corridors, with mountain formations like Longquan Mountain, Longmen Mountain, and Qionglai Mountain serving as ecological barriers, and river systems such as the Minjiang River and Tuojiang River serving as green ecological corridors. This aims to establish an interconnected ecological system pattern. Through ecosystem restoration and optimization of various branch nodes, the goal is to link landscape nodes into a network, integrate fragmented landscape spaces, and form extensive ecological landscape patches. This approach also aims to reduce the Maximum Patch Area Index of landscapes within the urban spatial scope. Furthermore, it involves proposing corresponding network structure optimization strategies based on evaluating the potential ecological benefits of nodes and corridors within the network structure (Hu et al., 2022a; 2022c).

It is worth noting that the diverse guiding strategies mentioned above are based on an analysis of seasonal driving relationships. They inherently allow for the simultaneous implementation of various measures. However, emphasizing phased measures can accurately and effectively reduce urban surface temperatures, thus establishing a scientific and feasible theoretical basis for the formulation of relevant phased policies.

5.4 The limitations of the study

The limitations of this study are as follows: Firstly, the division of seasons in this study was based on monthly average temperature and precipitation, which may not accurately reflect the seasonal variations. Using alternative data sources for season delineation could improve the accuracy of seasonal changes. Secondly, the study employed multiple linear regression analysis to identify the impact of different factors on surface temperature, but incorporating other methods such as geographic detectors, random forests, and geographically weighted regression models could enhance the model construction and analysis process. Additionally, the study only collected data on 12 influencing factors on surface temperature. Collecting data on additional factors such as floor area ratio, building density, building height, haze pollution, and coastal wind circulation would contribute to a more comprehensive and scientifically grounded study. Lastly, the research primarily focused on the seasonal and spatial variations of surface temperature in the study area in 2020 due to the feasibility of obtaining corresponding data on influencing factors for that specific year. However, for studying the cross-year seasonal and spatial variations of surface temperature, acquiring data on influencing factors for different years poses challenges. Therefore, future research should explore the characteristics of cross-year variations in surface temperature and differences in driving factors, taking into consideration the feasibility of data acquisition.

6 Conclusion

Since the Industrial Revolution, human society has undergone rapid development, and the rate of urbanization has also increased significantly. However, as a result, there has been a significant increase in global LST. This rise in temperature has already had a huge impact on human production and life. Therefore, how to mitigate the increase in LST has become an important topic that urgently needs to be explored across various disciplines. The investigation of the Chengdu metropolitan area revealed a distinct spatial pattern of LST, characterized by a concentration of high temperatures in the central regions and

lower temperatures in the western regions. Both natural geographical factors and human activities factors play a greater role in the size of LST. Among these variables, DEM and SLOPE exhibit an inverse relationship with LST, whereas WIND and HUM demonstrate a positive association with LST. In terms of human activities factors, POP, LIGHT, and ROAD are positively correlated with LST, while the impact of landscape pattern factors on LST is relatively small. Simultaneously, the influence of potential driving force on LST shows marked seasonal variation. In summer, the impact of POP, ROAD, and LIGHT on LST is significantly higher than in other seasons, while in the transitional season, the impact of WIND, HUM, DEM, SLOPE, and NDVI on LST is significantly higher than in other seasons. In winter, the impact of landscape pattern factors on LST is relatively large. Therefore, seasonal guidance strategies need to be adopted to effectively alleviate the rise in urban LST, including the rational use of terrain and topography, the increase of green vegetation within the city, and the regulation of human activities. It is hoped that this study can provide valuable reference and guidance for the future urban planning, design, and operational management of the research area, and lay a research basis for guiding other regions to develop phased measures to alleviate UHI.

Data availability statement

The original contributions presented in the study are included in the article/Supplementary material, further inquiries can be directed to the corresponding author.

Author contributions

CH; writing–revision of articles, software, supervision. GH; writing–original draft, software, data curation. ZW; data curation, software, supervision. All authors contributed to the article and approved the submitted version.

Funding

Key Project of National Social Science Foundation of China (21AZD048), National Natural Science Foundation of China (41901390, 51408248), Natural Science Foundation of Hubei Province (2021CFB012).

Conflict of interest

The authors declare that the research was conducted in the absence of any commercial or financial relationships that could be construed as a potential conflict of interest.

Publisher's note

All claims expressed in this article are solely those of the authors and do not necessarily represent those of their affiliated organizations, or those of the publisher, the editors and the reviewers. Any product that may be evaluated in this article, or claim that may be made by its manufacturer, is not guaranteed or endorsed by the publisher.

References

Al-Obaidi, I., Rayburg, S., Półrolniczak, M., and Neave, M. (2021). Assessing the impact of wind conditions on urban heat islands in large Australian cities. *J. Ecol. Eng.* 22, 1–15. doi:10.12911/22998993/142967

Correa, E., Ruiz, M. A., Canton, A., and Lesino, G. (2012). Thermal comfort in forested urban canyons of low building density. An assessment for the city of Mendoza, Argentina. *Build. Environ.* 58, 219–230. doi:10.1016/j.buildenv.2012.06.007

Das, D. N., Chakraborti, S., Saha, G., Banerjee, A., and Singh, D. (2020). Analysing the dynamic relationship of land surface temperature and landuse pattern: A city level analysis of two climatic regions in India. *City Environ. Interact.* 8, 100046. doi:10.1016/j.cacint.2020.100046

Fang, C., Yin, H., Han, L., Ma, S., He, X., and Huang, G. (2021). Effects of semi-permeable membrane covering coupled with intermittent aeration on gas emissions during aerobic composting from the solid fraction of dairy manure at industrial scale. *Econ. Geogr.* 41, 1–9. doi:10.1016/j.wasman.2021.05.030

Gao, Y., Zhao, J., and Han, L. (2022). Exploring the spatial heterogeneity of urban heat island effect and its relationship to block morphology with the geographically weighted regression model. *Sustain. Cities Soc.* 76, 103431. doi:10.1016/j.scs.2021.103431

Gedzelman, S. D., Austin, S., Cermak, R., Stefano, N., Partridge, S., Quesenberry, S., et al. (2003). Mesoscale aspects of the urban heat island around New York city. *Theor. Appl. Climatol.* 75, 29–42. doi:10.1007/s00704-002-0724-2

Geng, X., Zhang, D., Li, C., Yuan, Y., Yu, Z., and Wang, X. (2023). Impacts of climatic zones on urban heat island: spatiotemporal variations, trends, and drivers in China from 2001–2020. *Sustain. Cities Soc.* 89, 104303. doi:10.1016/j.scs.2022.104303

Grimm, N. B., Faeth, S. H., Golubiewski, N. E., Redman, C. L., Wu, J., Bai, X., et al. (2008). Global change and the ecology of cities. *Science* 319, 756–760. doi:10.1126/science.1150195

Guo, A., Yang, J., Xiao, X., Xia (Cecilia), J., Jin, C., and Li, X. (2020). Influences of urban spatial form on urban heat island effects at the community level in China. *Sustain. Cities Soc.* 53, 101972. doi:10.1016/j.scs.2019.101972

Guo, G., Wu, Z., and Chen, Y. (2020). Evaluation of spatially heterogeneous driving forces of the urban heat environment based on a regression tree model. *Sustain. Cities Soc.* 54, 101960. doi:10.1016/j.scs.2019.101960

Guo, J., Han, G., Xie, Y., Cai, Z., and Zhao, Y. (2020). Exploring the relationships between urban spatial form factors and land surface temperature in mountainous area: a case study in chongqing city, China. *Sustain. Cities Soc.* 61, 102286. doi:10.1016/j.scs.2020.102286

Han, S., Li, W., Kwan, M.-P., Miao, C., and Sun, B. (2022). Do polycentric structures reduce surface urban heat island intensity? *Appl. Geogr.* 146, 102766. doi:10.1016/j.apgeog.2022.102766

Hu, C., and Li, H. (2022). Reverse thinking: the logical system research method of urban thermal safety pattern construction, evaluation, and optimization. *Remote Sens.* 14, 6036. doi:10.3390/rs14236036

Hu, C., Wang, Z., Huang, G., and Ding, Y. (2022a). Construction, evaluation, and optimization of a regional ecological security pattern based on MSPA–circuit theory approach. *Int. J. Environ. Res. Public Health* 19, 16184. doi:10.3390/ijerph192316184

Hu, C., Wang, Z., Li, J., Liu, H., and Sun, D. (2022b). Quantifying the temporal and spatial patterns of ecosystem services and exploring the spatial differentiation of driving factors: A case study of Sichuan Basin, China. *Front. Environ. Sci.* 10, 927818. doi:10.3389/fenvs.2022.927818

Hu, C., Wang, Z., Wang, Y., Sun, D., and Zhang, J. (2022c). Combining MSPA-MCR model to evaluate the ecological network in wuhan, China. *Land* 11, 213. doi:10.3390/land11020213

Imhoff, M. L., Zhang, P., Wolfe, R. E., and Bounoua, L. (2010). Remote sensing of the urban heat island effect across biomes in the continental USA. *Remote Sens. Environ.* 114, 504–513. doi:10.1016/j.rse.2009.10.008

Jin, M. S. (2012). Developing an index to measure urban heat island effect using satellite land skin temperature and land cover observations. *J. Clim.* 25, 6193–6201. doi:10.1175/JCLI-D-11-00509.1

Lai, J., Zhan, W., Huang, F., Quan, J., Hu, L., Gao, L., et al. (2018). Does quality control matter? Surface urban heat island intensity variations estimated by satellite-derived land surface temperature products. *ISPRS J. Photogrammetry Remote Sens.* 139, 212–227. doi:10.1016/j.isprsjprs.2018.03.012

Li, X., Zhou, W., Ouyang, Z., Xu, W., and Zheng, H. (2012). Spatial pattern of greenspace affects land surface temperature: evidence from the heavily urbanized

Beijing metropolitan area, China. *Landsc. Ecol.* 27, 887–898. doi:10.1007/s10980-012-9731-6

Li, X., Zhou, W., and Ouyang, Z. (2013). Relationship between land surface temperature and spatial pattern of greenspace: what are the effects of spatial resolution? *Landsc. Urban Plan.* 114, 1–8. doi:10.1016/j.landurbplan.2013.02.005

Liao, Y., Shen, X., Zhou, J., Ma, J., Zhang, X., Tang, W., et al. (2022). Surface urban heat island detected by all-weather satellite land surface temperature. *Sci. Total Environ.* 811, 151405. doi:10.1016/j.scitotenv.2021.151405

Liu, H., Huang, B., Zhan, Q., Gao, S., Li, R., and Fan, Z. (2021a). The influence of urban form on surface urban heat island and its planning implications: evidence from 1288 urban clusters in China. *Sustain. Cities Soc.* 71, 102987. doi:10.1016/j.scs.2021.102987

Liu, H., Zheng, L., and Liao, M. (2021b). Dynamics of vegetation change and its relationship with nature and human activities — a case study of poyang lake basin, China. *J. Sustain. For.* 40, 47–67. doi:10.1080/10549811.2020.1738947

Luo, P., Yu, B., Li, P., Liang, P., Liang, Y., and Yang, L. (2023). How 2D and 3D built environments impact urban surface temperature under extreme heat: A study in Chengdu, China. *Build. Environ.* 231, 110035. doi:10.1016/j.buildenv.2023.110035

McGarigal, K., Cushman, S. A., and Ene, E. (2012). "FRAGSTATS v4: spatial pattern analysis program for categorical and continuous maps," in *Computer software program produced by the authors at the University of Massachusetts* (Amherst), 15.

Ngarambe, J., Oh, J. W., Su, M. A., Santamouris, M., and Yun, G. Y. (2021). Influences of wind speed, sky conditions, land use and land cover characteristics on the magnitude of the urban heat island in seoul: an exploratory analysis. *Sustain. Cities Soc.* 71, 102953. doi:10.1016/j.scs.2021.102953

Peng, J., Xie, P., Liu, Y., and Ma, J. (2016). Urban thermal environment dynamics and associated landscape pattern factors: A case study in the Beijing metropolitan region. *Remote Sens. Environ.* 173, 145–155. doi:10.1016/j.rse.2015.11.027

Peng, J., Jia, J., Liu, Y., Li, H., and Wu, J. (2018). Seasonal contrast of the dominant factors for spatial distribution of land surface temperature in urban areas. *Remote Sens. Environ.* 215, 255–267. doi:10.1016/j.rse.2018.06.010

Ren, Y., Deng, L.-Y., Zuo, S.-D., Song, X.-D., Liao, Y.-L., Xu, C.-D., et al. (2016). Quantifying the influences of various ecological factors on land surface temperature of urban forests. *Environ. Pollut.* 216, 519–529. doi:10.1016/j.envpol.2016.06.004

Ren, T., Zhou, W., and Wang, J. (2021). Beyond intensity of urban heat island effect: a continental scale analysis on land surface temperature in major Chinese cities. *Sci. Total Environ.* 791, 148334. doi:10.1016/j.scitotenv.2021.148334

Ren, J., Yang, J., Zhang, Y., Xiao, X., Xia, J. C., Li, X., et al. (2022). Exploring thermal comfort of urban buildings based on local climate zones. *J. Clean. Prod.* 340, 130744. doi:10.1016/j.jclepro.2022.130744

Sun, R., Lü, Y., Yang, X., and Chen, L. (2019). Understanding the variability of urban heat islands from local background climate and urbanization. *J. Clean. Prod.* 208, 743–752. doi:10.1016/j.jclepro.2018.10.178

Sun, Z., Li, Z., and Zhong, J. (2022). Analysis of the impact of landscape patterns on urban heat islands: A case study of Chengdu, China. *Int. J. Environ. Res. Public Health* 19, 13297. doi:10.3390/ijerph192013297

Thompson, R. D., and Perry, A. H. (1997). *Applied climatology: principles and practice*. Psychology Press.

Wan, Z. (2008). New refinements and validation of the MODIS Land-Surface Temperature/Emissivity products. *Remote Sens. Environ.* 112, 59–74. doi:10.1016/j.rse.2006.06.026

Wang, Y., and Akbari, H. (2016). The effects of street tree planting on Urban Heat Island mitigation in Montreal. *Sustain. Cities Soc.* 27, 122–128. doi:10.1016/j.scs.2016.04.013

Wang, Y., Du, H., Xu, Y., Lu, D., Wang, X., and Guo, Z. (2018). Temporal and spatial variation relationship and influence factors on surface urban heat island and ozone pollution in the Yangtze River Delta, China. *Sci. Total Environ.* 631–632, 921–933. doi:10.1016/j.scitotenv.2018.03.050

Wang, W., Samat, A., Abuduwaili, J., and Ge, Y. (2021). Quantifying the influences of land surface parameters on LST variations based on GeoDetector model in Syr Darya Basin, Central Asia. *J. Arid Environ.* 186, 104415. doi:10.1016/j.jaridenv.2020.104415

Wang, Z., Meng, Q., Allam, M., Hu, D., Zhang, L., and Menenti, M. (2021). Environmental and anthropogenic drivers of surface urban heat island intensity: A case-study in the yangtze river delta, China. *Ecol. Indic.* 128, 107845. doi:10.1016/j.ecolind.2021.107845

Wang, Q., Wang, H., Chang, R., Zeng, H., and Bai, X. (2022). Dynamic simulation patterns and spatiotemporal analysis of land-use/land-cover changes in the Wuhan metropolitan area, China. *Ecol. Model.* 464, 109850. doi:10.1016/j.ecolmodel.2021.109850

Wang, Z., Sun, D., Hu, C., Wang, Y., and Zhang, J. (2022). Seasonal contrast and interactive effects of potential drivers on land surface temperature in the Sichuan Basin, China. *Remote Sens.* 14, 1292. doi:10.3390/rs14051292

Ward, K., Lauf, S., Kleinschmit, B., and Endlicher, W. (2016). Heat waves and urban heat islands in europe: a review of relevant drivers. *Sci. Total Environ.* 569, 527–539. doi:10.1016/j.scitotenv.2016.06.119

Wu, S., Yang, H., Luo, P., Luo, C., Li, H., Liu, M., et al. (2021). The effects of the cooling efficiency of urban wetlands in an inland megacity: a case study of Chengdu, southwest China. *Build. Environ.* 204, 108128. doi:10.1016/j.buildenv.2021.108128

Yang, J., Dong, J., Xiao, X., Dai, J., Wu, C., Xia, J., et al. (2019). Divergent shifts in peak photosynthesis timing of temperate and alpine grasslands in China. *Remote Sens. Environ.* 233, 111395. doi:10.1016/j.rse.2019.111395

Yu, Z., Yao, Y., Yang, G., Wang, X., and Vejre, H. (2019). Spatiotemporal patterns and characteristics of remotely sensed region heat islands during the rapid urbanization (1995–2015) of Southern China. *Sci. Total Environ.* 674, 242–254. doi:10.1016/j.scitotenv.2019.04.088

Yu, W., Shi, J., Fang, Y., Xiang, A., Li, X., Hu, C., et al. (2022). Exploration of urbanization characteristics and their effect on the urban thermal environment in Chengdu, China. *Build. Environ.* 219, 109150. doi:10.1016/j.buildenv.2022.109150

Zakšek, K., and Oštir, K. (2012). Downscaling land surface temperature for urban heat island diurnal cycle analysis. *Remote Sens. Environ.* 117, 114–124. doi:10.1016/j.rse.2011.05.027

Zhang, L., Hou, G., and Li, F. (2020). Dynamics of landscape pattern and connectivity of wetlands in western Jilin Province, China. *Environ. Dev. Sustain* 22, 2517–2528. doi:10.1007/s10668-018-00306-z

Zhao, C., Jensen, J., Weng, Q., and Weaver, R. (2018). A geographically weighted regression analysis of the underlying factors related to the surface urban heat island phenomenon. *Remote Sens.* 10, 1428. doi:10.3390/rs10091428

Zhao, Z., Shen, L., Li, L., Wang, H., and He, B.-J. (2020). Local climate zone classification scheme can also indicate local-scale urban ventilation performance: an evidence-based study. *Atmosphere* 11, 776. doi:10.3390/atmos11080776

Zhao, Y., Wu, Q., Wei, P., Zhao, H., Zhang, X., and Pang, C. (2022). Explore the mitigation mechanism of urban thermal environment by integrating geographic detector and standard deviation ellipse (SDE). *Remote Sens.* 14, 3411. doi:10.3390/rs14143411

Zhe, L. I., Shengbin, C., and Zhiyang, C. (2022). Spatial scale dependence between land surface temperature and land use types: A case study of Chengdu city. *Ecol. Environ.* 31, 999. doi:10.16258/j.cnki.1674-5906.2022.05.015

Zheng, X., Fu, M. C., and Yao, C. (2010). *Landscape pattern spatial analysis technology and its application*. Beijing, China: Science press.

Zhigang, C., Xinyue, Y., Chen, S., and Yajin, X. (2016). The trend of summer urban heat island effect and its relationship with urban development in Chengdu. *Adv. Clim. Change Res.* 12, 322. doi:10.12006/j.issn.1673-1719.2015.176

Zhou, D., Zhao, S., Liu, S., Zhang, L., and Zhu, C. (2014). Surface urban heat island in China's 32 major cities: spatial patterns and drivers. *Remote Sens. Environ.* 152, 51–61. doi:10.1016/j.rse.2014.05.017

Zhou, D., Zhang, L., Li, D., Huang, D., and Zhu, C. (2016). Climate–vegetation control on the diurnal and seasonal variations of surface urban heat islands in China. *Environ. Res. Lett.* 11, 074009. doi:10.1088/1748-9326/11/7/074009

Zong, H., Liu, Y., Wang, Q., Liu, M., and Chen, H. (2019). Usage patterns and comfort of gardens: a seasonal survey of internal garden microclimate in the aged care homes of Chengdu city. *Int. J. Biometeorol.* 63, 1181–1192. doi:10.1007/s00484-019-01733-x

frontiers | Frontiers in Earth Science

TYPE Original Research
PUBLISHED 01 September 2023
DOI 10.3389/feart.2023.1168384

OPEN ACCESS

EDITED BY
Ram Kumar Singh,
TERI School of Advanced Studies (TERI SAS), India

REVIEWED BY
Kai Zhu,
Hubei University, China
Zhenhua Zou,
University of Maryland, College Park, United States

*CORRESPONDENCE
Anning Cai,
caianning@njxzc.edu.cn

RECEIVED 17 February 2023
ACCEPTED 26 July 2023
PUBLISHED 01 September 2023

CITATION
Guo R, Cai A and Chen X (2023), The quantitative effects of climate change and human activity on the vegetation growth in the Yangtze River Basin. *Front. Earth Sci.* 11:1168384. doi: 10.3389/feart.2023.1168384

The quantitative effects of climate change and human activity on the vegetation growth in the Yangtze River Basin

Renjie Guo[1], Anning Cai[2]* and Xin Chen[3]

[1]Faculty of Geographical Science, Beijing Normal University, Beijing, China, [2]Tourism and Social Administration College, Nanjing Xiaozhuang University, Nanjing, Jiangsu, China, [3]School of Geographical Sciences, Nanjing University of Information Science & Technology, Nanjing, Jiangsu, China

Vegetation has changed dramatically in recent years as a result of various disturbances, but the factors influencing vegetation growth vary geographically. We looked into the impact of climate change and human activity on vegetation growth in the Yangtze River Basin (YRB). We characterized vegetation growth in the YRB using gross primary production (GPP) and the leaf area index (LAI), analyzed the relationship between vegetation growth and climate change using the standardized precipitation evapotranspiration index (SPEI), and quantified the relative contribution rate of climate change and human activity to vegetation growth in the YRB by using residual trend method. The findings revealed that: 1) From 2000 to 2018, the YRB showed an increasing trend of temperature (0.03°C yr^{-1}) and precipitation (4.02 mm yr^{-1}) and that the entire area was gradually becoming warmer and wetter; 2) Vegetation growth in the YRB showed a significant increasing trend (GPP: 7.83 g C m^{-2} yr^{-2}, LAI: 0.02 $years^{-1}$). Among them, 87.40% of the YRB showed an increasing trend, primarily in the northern, eastern, and southern parts, while decreasing areas were primarily found in the Yangtze River Delta (YRD) and the YRB's west region. 3) Vegetation had a significant positive correlation with SPEI in most areas of the YRB, and it was more sensitive to SPEI over a long time scale. The effects of climate change and human activity on vegetation growth in the YRB were spatially heterogeneous, and climate change was the primary driving factors of vegetation change in the YRB (accounting for 61.28%). A large number of grass were converted into forest, crop and urban. Overall, climate change and human activity promoted the growth of vegetation in the middle and upper reaches of YRB (MUYRB) while inhibited the growth of vegetation in the YRD. The findings of this study will contribute to a better understanding of the effects of climate change and human activity on vegetation growth in the YRB, as well as provide a scientific foundation for future ecological restoration in humid and semi-humid areas.

KEYWORDS

climate change, human activity, gross primary production, leaf area index, remote sensing, Yangtze River Basin

1 Introduction

Research focusing on long-term changes in large-scale terrestrial vegetation has demonstrated that vegetation serves as an accurate indicator of the impacts caused by various disturbance factors on regional terrestrial ecosystems. Moreover, it plays a crucial role as an ecological indicator in response to global changes (Forkel et al., 2016). In large-scale terrestrial ecological research, the intricate dynamics of vegetation development are significantly influenced by a combination of climate and human factors (Suzuki et al., 2007; Metcalfe et al., 2010). With the deepening of global change research, it is becoming more and more important to accurately quantify the effects of climate change and human activity on vegetation growth (Liu et al., 2015; Piao et al., 2020).

The impacts of climate change on terrestrial ecosystems are expected to alter the temperature, light availability, and water conditions necessary for vegetation growth. Consequently, these changes will have implications for the stability of terrestrial ecosystems, particularly manifested through variations in vegetation leaf area and productivity (Piao et al., 2020). Many studies have shown that vegetation growth under different temperature and humidity conditions has different sensitivity to meteorological conditions (Jiao et al., 2019; Rahmani and Fattahi, 2021). In the middle and high latitudes of the northern hemisphere, increasing temperatures have been found to promote vegetation growth (Mao et al., 2012). In arid regions, vegetation has a significant correlation with precipitation (Li et al., 2015), while in most other areas, it has a high correlation with temperature (Piao et al., 2015). In humid regions, vegetation growth is highly responsive to temperature fluctuations (Ma et al., 2019). Changes in temperature can influence various physiological processes within plants, such as photosynthesis and transpiration, ultimately affecting the overall productivity and health of vegetation in humid environments (Mathur et al., 2014). The responsiveness of vegetation to temperature fluctuations highlights the intricate relationship between climate conditions and the dynamic nature of plant ecosystems in humid regions. It should be noted that the growth of vegetation is also affected by a variety of meteorological factors, including light, humidity, etc., so multiple factors need to be considered comprehensively in research and monitoring. It is worth noting human activity is an important contributor to both climate change and the growth of vegetation (Li et al., 2022). China and India are crucial to the greening of the world's terrestrial vegetation, which is greatly impacted by human activity through afforestation projects and increased agricultural efficiency (Chen et al., 2019). Urbanization brought by human activity will lead to a sizable portion of crop and grass being taken up by urban land, and vegetation coverage will decrease significantly (Jin et al., 2018). With the implementation of the carbon neutral strategy, regional vegetation growth will benefit from initiatives like converting crop back to grass and forest (Zhao et al., 2018). Therefore, regional and even global vegetation growth processes will be strongly affected by human activity and climate change (Liu et al., 2015).

Many studies have quantified the effects of climate change and human activity on vegetation at a regional scale. It is found that the warm and wet climate in North China has a significant positive correlation with regional greening, in which climate change has a more significant impact on vegetation cover than human activity (Cao et al., 2021). The trend of warm and humid climate was favorable to grass growth, in which the relatively dry and warm climate had a more significant effect on vegetation growth (Han et al., 2018). However, Economic development and population growth had hampered grass growth (Han et al., 2018). In the Loess Plateau, long-term water availability is the dominant climate factor influencing vegetation growth, with the long-term NDVI trend being more sensitive to climate change compared to the short-term trend (Shi et al., 2021). Moreover, in areas experiencing vegetation degradation, human activity has a significantly greater impact on vegetation compared to climate change (Shi et al., 2021). However, studies mainly focus on arid and semi-arid areas, while there are few analyses on humid and semi-humid areas, and most studies only focus on the effects of precipitation and temperature on vegetation growth, which may be insufficient.

The Yangtze River Basin (YRB) is the third largest basin in the world and the main humid and semi-humid region in China. The vegetation in the YRB is very important to maintain the regional carbon and water balance (Qu et al., 2018). In addition, the YRB is one of China's representative regions with a thriving economy and dense population (Yang et al., 2022). The YRB's terrestrial ecosystem has been severely hampered in recent years by environmental issues brought on by population increase, climate change, and economic growth (Zhang et al., 2020). It is crucial to understand the characteristics of vegetation change in the YRB and to separate and estimate the relative contributions of climate change and human activity to vegetation growth in light of the dual impacts of climate change and human activity.

This study used meteorological data, GPP, LAI, and SPEI to examine the effects of climate change and human activity on vegetation in the YRB from 2000 to 2018. To be more precise, it mostly consists of three contents: 1) To determine the characteristics of climate change in the YRB by analyzing changes in temperature, precipitation, radiation and SPEI; 2) To determine the characteristics of vegetation change in the YRB by analyzing the state of vegetation growth and the transfer of land cover; and 3) To distinguish between the effects of climate change and human activity on vegetation growth by residual trend method and to quantify the relative contributions.

2 Data and methods

2.1 Study area

The YRB covers an area of approximately 1.8 million square kilometers. It is located between approximately 24°N and 37°N latitude and 90°E and 122°E longitude. The YRB benefits from a subtropical monsoon climate, characterized by a wet and hot season that creates favorable conditions for vegetation growth (Qu et al., 2018). As shown in Figure 1A, the YRB has a variety of land cover types, with forest predominating in the basin's southwest, southeast, and north. The Sichuan Basin and the middle and lower reaches of the YRB (MLYRB) are the primary regions where most crops are cultivated. The central, western, and southern regions of the YRB, along with the high-altitude regions of the Qinghai-Tibet Plateau, are predominantly covered by grass. The Yangtze River Delta (YRD) and the MLYRB contain the majority of China's urban land. The

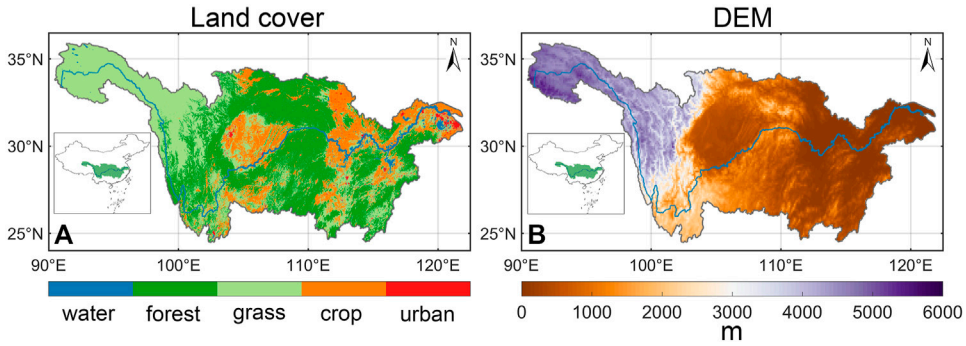

FIGURE 1
Regional overview of the YRB. **(A)**Land cover types in 2018 (water, forest, grass, crop, and urban). **(B)** Elevation.

YRB's topography is uneven, and it has a stepped distribution as the elevation gradually drops from west to east (Figure 1B). With its elevated western regions and lower eastern areas, the Yangtze River gracefully meanders from west to east, eventually emptying into the Pacific Ocean.

2.2 Meteorological data

China Meteorological Forcing Dataset (CMFD) datasets combine multiple sets of reanalysis data and site-level data, and has undergone strict quality control and calibration, with high data quality and accuracy (Yang et al., 2010; He et al., 2020). In order to study the climatic change in the YRB, we picked the monthly temperature, precipitation and downward shortwave radiation data with a spatial resolution of 0.1°.

2.3 Vegetation data

GPP is usually used to characterize the photosynthetic capacity of an ecosystem (Anav et al., 2015). LAI is an index to measure vegetation density and coverage degree, which can reflect the number and distribution of plant leaves, and is usually used to represent the inter-annual dynamic changes of vegetation (Sun and Qin, 2016). In order to study the change of vegetation in the YRB, LAI dataset of GEOV2 and GPP dataset based on NIRv vegetation index were used (Vickers et al., 2016; Wang et al., 2021). The spatial resolutions of GEOV2_LAI and NIRv_GPP are 1 km and 0.05°, respectively, and the temporal resolutions are 10 days and monthly, respectively. We uniformly converted GPP and LAI data into 0.1°, month-scale spatio-temporal resolution to match meteorological data, and analyzed vegetation change in the YRB.

2.4 Drought index

SPEI is useful for identifying how variations in wet and dry conditions affect vegetation (Vicente-Serrano et al., 2010). To study the dry and wet fluctuations in the YRB, SPEI is typically utilized as the drought index (Wang et al., 2020). The SPEI dataset (Global SPEI database) we used has a spatiotemporal resolution of 0.5° and monthly scales (Beguería et al., 2010; Beguería et al., 2014). When examining how various vegetation types respond to drought, the time scale of the drought index is crucial. SPEI at various time scales is a representation of the cumulative water balance over time. SPEI of 1–2 month-scales is often used to characterize agricultural drought (Mishra and Desai, 2005), and SPEI of 3–6 month-scales is often used to study soil water loss (Ji and Peters, 2003; Lotsch et al., 2003; Hirschi et al., 2011). In order to assess the dry and wet changes in the YRB, we employed SPEI with time scales of 1, 6, and 12 months, labeling them as SPEI01, SPEI06, and SPEI12, respectively. We converted 0.5° SPEI data to 0.1° for dry and wet analysis to match the spatial resolution of meteorological data.

2.5 Land cover data

The MCD12Q1 and MCD12C1 Version 6 dataset are derived using a supervised classification of MODIS Terra and Aqua reflectance, which are then subjected to additional post-processing, incorporating prior knowledge and auxiliary information to further refine a particular category. Therefore, we used MCD12Q1 data with a spatial resolution of 500 m from 2001 to 2018 to describe the land cover change of YRB. Additionally, we employed MCD12C1 to quantify the impacts of climate change and human activity on various vegetation types (Friedl and Sulla-Menashe, 2015). Land cover was categorized using the International Geosphere Biosphere Programme (IGBP) guidelines (Friedl et al., 2010). Land cover was categorized into water, forest, grass, crop, and urban by merging the primary vegetation types in the YRB. Since MCD12Q1 and MCD12C1 lack 2000 land cover data, we used 2001 land cover data instead for land cover conversion analysis.

2.6 Residual trend analysis and relative contribution calculation

We separated and measured the effects of human activity and climate change on vegetation using the residual trend method (Evans and Geerken, 2004; Jiang et al., 2017). The residual trend

method was divided into three steps: 1) Combined with the idea of binary linear regression, temperature and precipitation were considered the independent variables, and vegetation was chosen as the dependent variable, and linear regression parameters are calculated by establishing regression models; 2) The estimated vegetation (*VBcc*), which represented how the vegetation would be affected by climate change, was derived based on the regression model's parameters; 3) In order to get vegetation residual (*VBha*), which may be utilized to reflect the impact of human activity on vegetation, the difference between remote sensing vegetation data and *VBcc* was calculated. The specific calculation formula is as follows:

$$VBcc = a \times T + b \times P + c \times R + d \quad (1)$$

$$VBha = VBrs - VBcc \quad (2)$$

Estimated vegetation and remote sensing vegetation data were denoted in the formula by the letters *VBcc* and *VBrs*, respectively. *T*, *P* and *R* stand for temperature, precipitation and radiation, measured in °C, millimeters and W m^{-2}, respectively. *VBha* was the residual, representing the effect of human activity on vegetation. The use of residual has certain conditions of use, requiring the goodness of fit R^2 between the independent variable and the dependent variable to be greater than 0.3 and the significance *p*-value to be less than 0.05. Only regions that meet this requirement can effectively separate human activity from climate change for subsequent analysis.

Utilizing the residual trend approach, we distinguished between the effects of climate change and human activity on vegetation, and then, using the following formula in combination (Table 1), we computed the relative contribution rates of climate change and human activity on vegetation (Shi et al., 2021).

2.7 Land cover transfer matrix

The land cover transfer matrix shows the alterations and directions of all types of land cover in the research region before and after conversion, as well as the area where each type of land cover will be converted (Wang and Bao, 1999). The expression is as follows:

$$S_{ij} = \begin{bmatrix} S_{11} & \cdots & S_{1n} \\ \vdots & \ddots & \vdots \\ S_{n1} & \cdots & S_{nn} \end{bmatrix} \quad (3)$$

The land cover types at the start and end of the study, respectively, were represented by *i* and *j* in the formula; *n* represented the overall number; S_{ij} was the total area before and after the transition of the study period.

3 Results

3.1 Climate change

With high temperatures in the east and low temperatures in the west, as well as high temperatures in the south and low temperatures in the north, the spatial distribution of air temperature in the YRB displayed a spatial heterogeneity pattern (Figure 2A). As a whole, the temperature increasing rate in the west was higher than that in the east, and the rate of increase in the south was faster than in the north. The fastest-growing and significant regions were located in the middle and upper reaches of YRB (MUYRB) and YRD (Figures 2B, C). In the YRB, the yearly precipitation variation trend showed a sizable geographical disparity. The YRB's eastern, middle, and southern regions experienced about 1,500 mm of precipitation, compared to barely 500 mm in the western and the Yangtze River Source region (YRS) (Figure 2D). The southern and northern regions of China experienced a drop in annual precipitation. The YRS exhibited the largest decreasing trend, reaching −40 mm yr^{-1}. Precipitation in the eastern coastal areas showed an obvious increasing trend, and some areas showed inter-annual variation of precipitation greater than 40 mm yr^{-1} (Figures 2E, F). Contrary to the distribution of precipitation and temperature, the radiation distribution in the west is higher than that in the east (Figure 2G). As shown in Figures 2H, I, the spatial variation of radiation is high in the west and low in the east. On the whole, the temperature in most areas of the YRB showed a significant upward trend, the precipitation increased in the east and decreased in the west, and the radiation variation was relatively low.

The YRB's average annual temperature from 2000 to 2018 was 12.41°C, and it increased at a significant rate of 0.03°C yr^{-1} ($p < 0.05$) (Figure 3A). The YRB experienced strong summer and low winter temperature variations, with the peak temperature reaching 22.28°C in July (Figure 3D). The YRB's average annual precipitation from 2000 to 2018 was 1,052.16 mm, with a 4.02 mm yr^{-1} overall increase, however this trend was not statistically significant ($p = 0.33$) (Figure 3B). The maximum precipitation (1,204.54 mm) occurred in 2016, while the minimum precipitation (892.03 mm) occurred in 2011. Consistent with temperature, the monthly precipitation showed obvious seasonal changes in Figure 3E, with little precipitation in winter and more precipitation in summer, and the peak value appeared in June (170.04 mm). In Figure 3C, the inter-annual variation of radiation was low, showing a decreasing trend of −1.08 kWh yr^{-1} ($p = 0.40$). On the monthly scale, the overall change is similar to temperature and precipitation, but it is worth mentioning that there is a decline of about 20 kWh in June (Figure 3F). Therefore, climate change in the YRB was observed to present a trend of warming and wetting.

Figure 4 shows that the SPEI in the northern and southwestern parts of the YRB is less than 0, showing a slight drought. The SPEI in the YRB displayed a more significant spatial variation trend as time scale increased, and the SPEI in the majority of locations displayed an increasing trend. By averaging SPEI of different time scales, it could be found that 69.76% of the grid points were positive and 30.24% of the grid points were negative, indicating that the majority of the YRB became wetter. The YRB's central and eastern regions had an increase in SPEI, indicating a tendency toward a progressive wetness with an increase in precipitation. The SPEI displayed a decreasing tendency in the western and northern regions of the YRB, which was consistent with the local temperature's upward and downward trends. It was clear that the SPEI could accurately capture the impact of temperature and precipitation together.

Overall, through the calculation of the SPEI in the YRB, we observed a consistent and increasing trend in the inter-annual

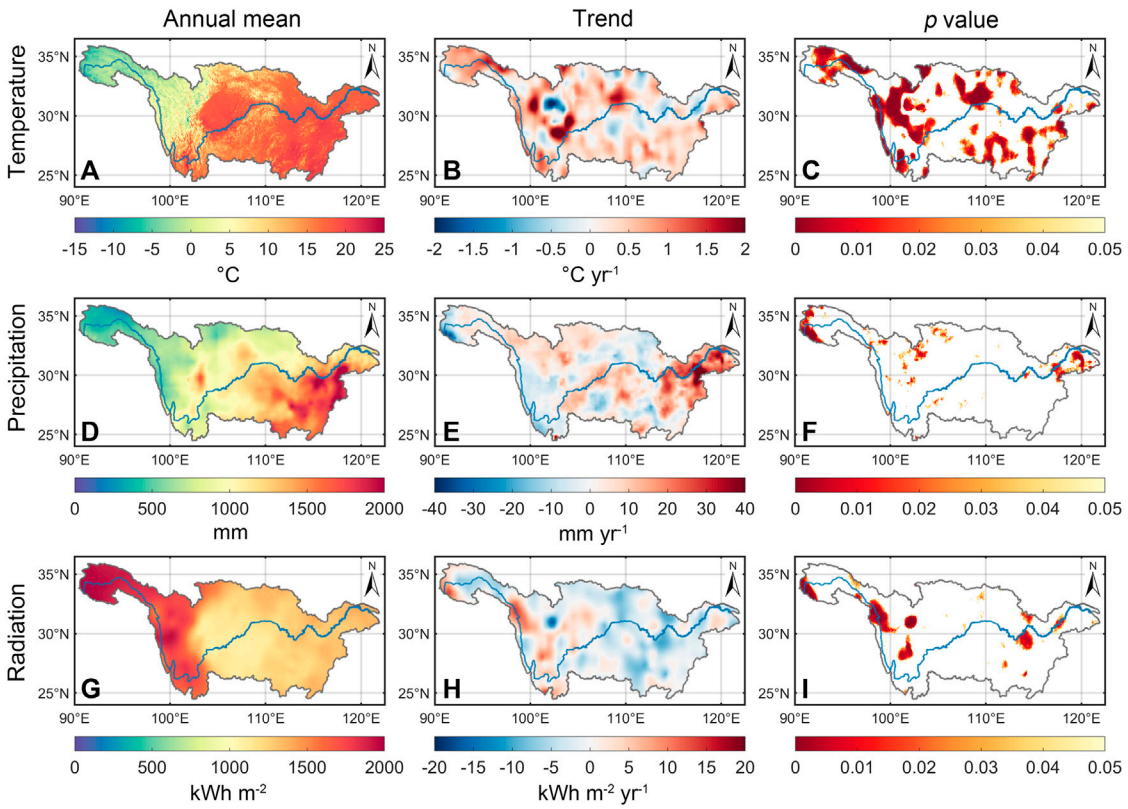

FIGURE 2
Temperature, precipitation and radiation distributions in the YRB from 2000 to 2018. **(A,D,G)** Annual mean value, respectively. **(B,E,H)** Annual trend, respectively. **(C,F,I)** Significance *p*-value ($p < 0.05$), respectively.

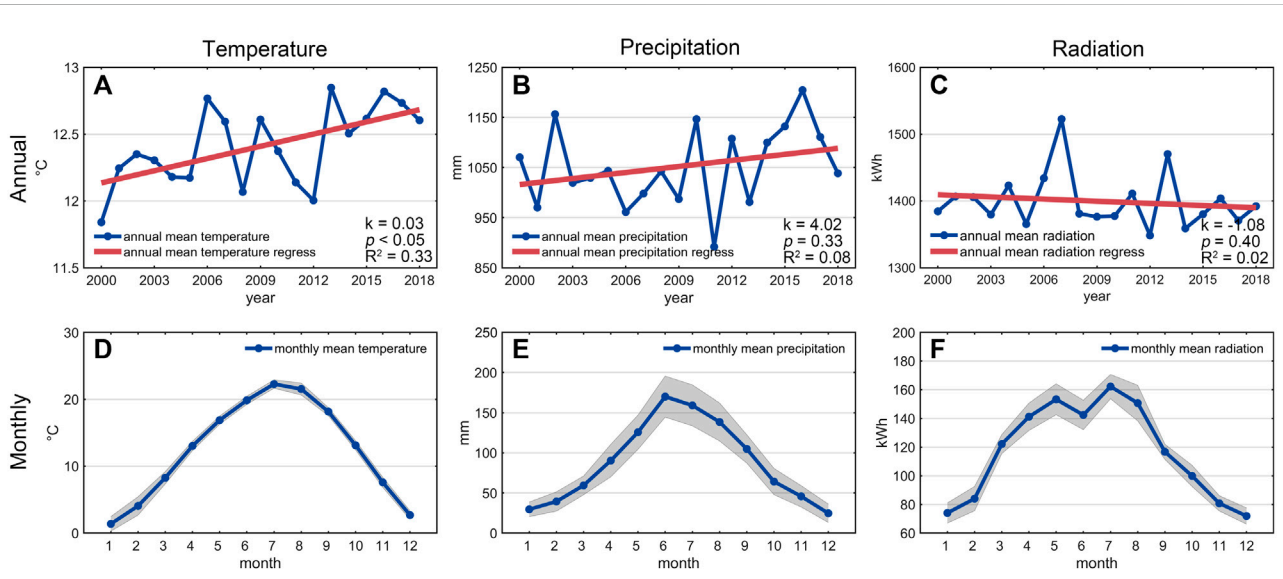

FIGURE 3
Temperature and precipitation changes in the YRB from 2000 to 2018. **(A,D)** Temperature annual and monthly changes, respectively. **(B,E)** Precipitation annual and monthly changes, respectively. **(C,F)** Radiation annual and monthly changes, respectively.

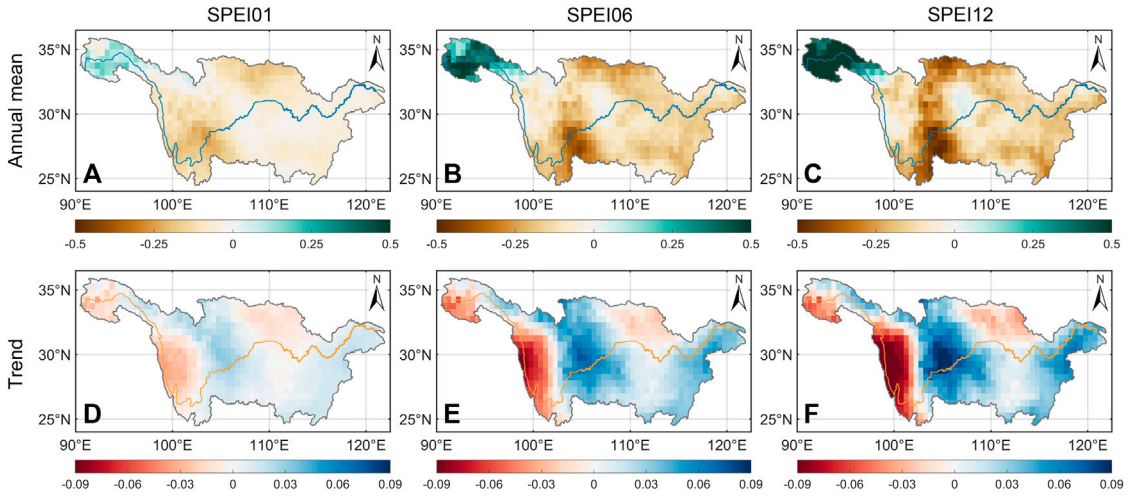

FIGURE 4
SPEI (1, 6, and 12 month-scales) spatial distribution in the YRB from 2000 to 2018. **(A–C)** Annual mean value, respectively. **(D–F)** Annual trend, respectively.

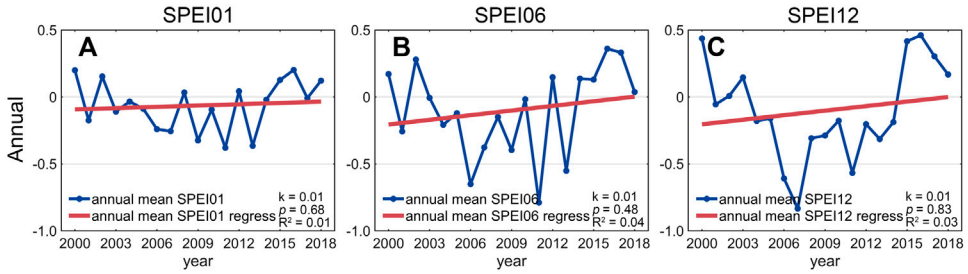

FIGURE 5
Changes of SPEI in the YRB from 2000 to 2018. **(A–C)** Annual trends of SPEI in 1, 6, and 12 month-scales, respectively.

variation of SPEI at the 1, 6, and 12 month-scales (0.01 years^{-1}). This trend indicates that the YRB has been experiencing a progressive increase in moisture levels over time, as depicted in Figure 5. The consistent pattern observed across the 1, 6, and 12 month-scales implies a sustained influence of climate factors on the basin's hydrological conditions.

3.2 Vegetation and land cover change

As shown in Figure 6A, GPP value was higher in the eastern and southern parts of the YRB, with an annual mean value of around 2,000 g C m^{-2} yr^{-1}. However, only about 500 g C m^{-2} yr^{-1} of GPP was produced on average annually in the YRD and the YRS. Figure 6B demonstrated that the GPP in the middle of the YRB increased at a rate of around 10 g C m^{-2} yr^{-2} while decreasing at a rate of about 10 g C m^{-2} yr^{-2} in the YRD and the MLYRB. The YRS remained largely constant and shown a decreasing tendency in some parts, while the MUYRB and northern regions of the YRB showed an increasing trend. Figure 6C showed a similar regional distribution of multi-year LAI mean values in the YRB as Figure 6A, indicating that LAI values in the YRS and the YRD were low. In Figure 6D, LAI decreasing regions were mostly found in the YRD and the MLYRB. It is important to note that while LAI in the majority of the western regions showed little change, LAI in the north, south, and southeast of the YRB exhibited an increasing trend of more than 0.06 years^{-1}. In the western YRB, GPP showed a decreasing trend, while LAI did not change significantly. Overall, from 2000 to 2018, the increasing trend in GPP accounted for 83.78% and the increasing trend in LAI accounted for 91.02%. Only 16.22% of the GPP and 8.98% of the LAI showed a declining trend in the YRB. From 2000 to 2018, most vegetation in the YRB showed continuous greening.

By calculating the total amount of vegetation in the YRB, we could find the inter-annual variation trend of GPP in the YRB increased significantly, reaching 7.83 g C m^{-2} yr^{-2} ($p < 0.01$) (Figure 7A). The annual average GPP increased by 115.92 g C m^{-2} yr^{-1} from 804.20 g C m^{-2} yr^{-1} in 2000 to 920.12 g C m^{-2} yr^{-1} in 2018. The monthly pattern of vegetation growth shown by GPP peaked at 162.93 g C m^{-2} yr^{-1} in July (Figure 7B). The LAI inter-annual trend was 0.02 years^{-1} ($p < 0.01$), the same as the GPP inter-annual trend (Figure 7C). With a growth rate of 0.02 years^{-1} ($p < 0.01$), the monthly mean LAI values in the YRB increased from 1.38

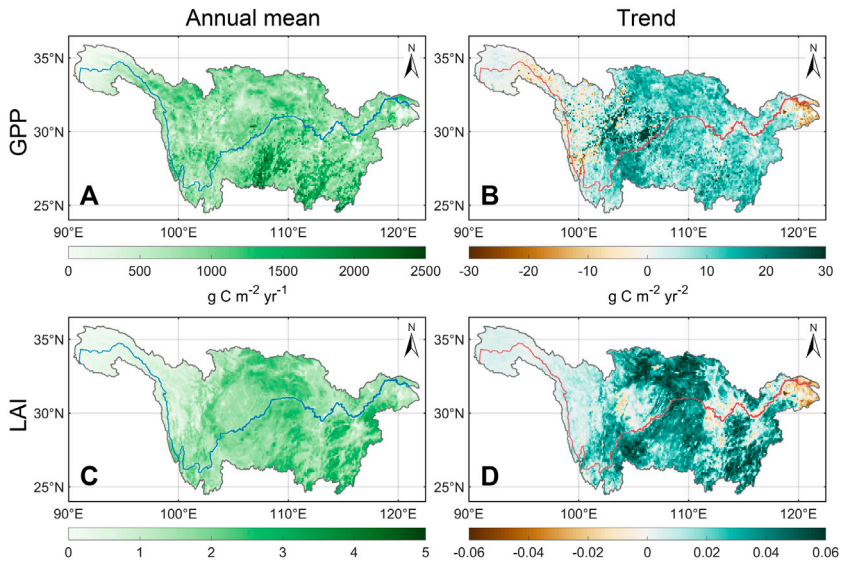

FIGURE 6
GPP and LAI spatial distribution in the YRB from 2000 to 2018. **(A,C)** Annual mean value, respectively. **(B,D)** Annual trend, respectively.

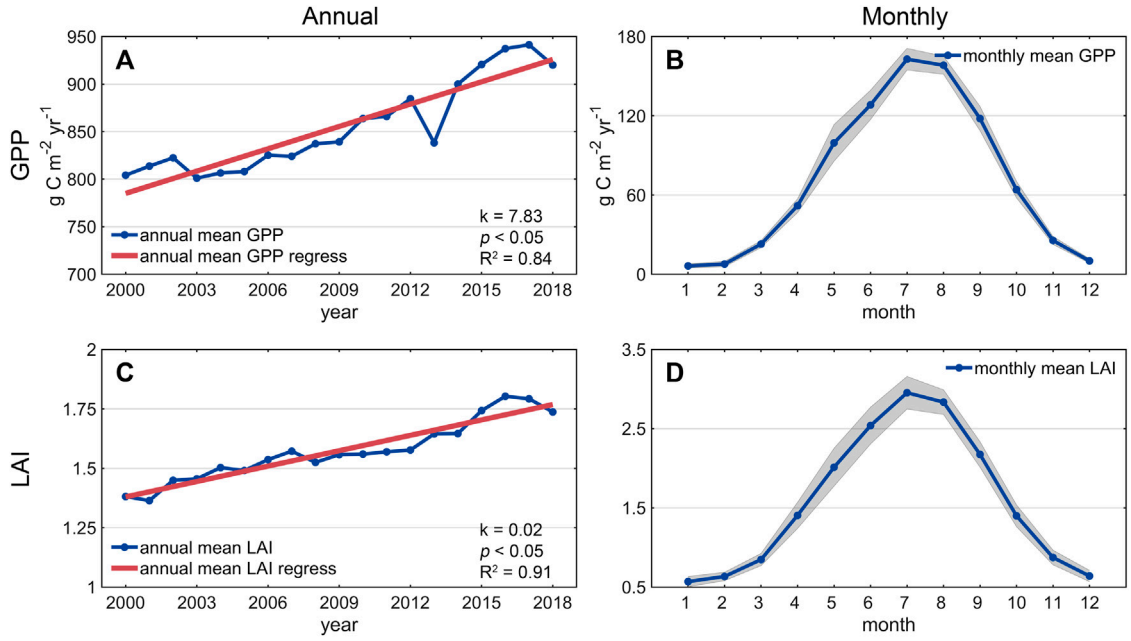

FIGURE 7
Changes of GPP and LAI in the YRB from 2000 to 2018. **(A,C)** GPP and LAI annual trends, respectively. **(B,D)** GPP and LAI monthly changes, respectively.

in 2000 to 1.74 in 2018, and peaked in July, consistent with the monthly variation pattern of GPP (Figure 7D). Therefore, we could find that the overall vegetation in the YRB is gradually turning green.

As shown in Table 2, significant spatial changes had taken place in land cover during 2001–2018. A total of 287,842 pixels of grass were converted into forest, making up 90.28% of the total gain in forest, which resulted in a net increase of 58,050 pixels in forest. Next came the contribution from crop, with 30,974 converted pixels, comprising 9.71% of the area increase overall. In the YRB, forest had the largest vegetation increase, with a net increase of 58,050 pixels, comprising 38.95% of the research region's total increasing area. The grass decreased by 149,041 pixels net, accounting for 1.75% of the basin's total area, and was primarily converted to forest, urban and crop. It could be seen that the mutual conversion of grass, forest and crop is the main mode of vegetation conversion in the YRB. The net increase of 1,857 pixels in the water represented the gradual

TABLE 1 Calculation table of the rate at which climate change and human activity contribute to vegetation.

Remote sensing data trend	Climate change trend	Human activity trend	Relative contribution of climate change	Relative contribution of human activity	Explanation
Increasing	>0	>0	$\frac{slope_{cc}}{slope_{rs}} \times 100$	$\frac{slope_{ha}}{slope_{rs}} \times 100$	Climate change and human activity together promoted vegetation growth
	>0	<0	100	0	Climate change promoted vegetation growth
	<0	>0	0	100	Human activity promoted vegetation growth
Decreasing	<0	<0	$\frac{slope_{cc}}{slope_{rs}} \times 100$	$\frac{slope_{ha}}{slope_{rs}} \times 100$	Climate change and human activity together inhibited vegetation growth
	<0	>0	100	0	Climate change inhibited vegetation growth
	>0	<0	0	100	Human activity inhibited vegetation growth

Note: In the formula, $slope_{rs}$, $slope_{cc}$ and $slope_{ha}$ depicted the varying trends in the remote sensing data, climate change and human activity, respectively.

TABLE 2 The YRB's land cover transfer matrix from 2000 to 2018.

	Water	Forest	Grass	Crop	Urban
Water	107,910	4	886	0	0
Forest	19	3,761,405	239,958	20,174	619
Grass	2,397	287,842	3,208,230	311,427	29,950
Crop	331	30,974	241,731	1,304,603	24,859
Urban	0	0	0	0	131,728
Change	1857	58,050	−149041	33,706	55,428

Note: The unit is 0.25 square kilometer (one pixel). The vertical axis is 2,000 and the horizontal axis is 2018.

expansion of the river and lake area in the humid state of the YRB. The urban expanded by 55,428 pixels, of which crop and grass contributed 98.88%. As a result of the YRB's ongoing urbanization, a large amount of crop and grass has been converted into urban.

3.3 Relative contributions of climate change and human activity to vegetation growth

In Figure 8, the correlation coefficient and time scale between vegetation and SPEI respectively represented the vegetation's response and sensitivity to climate change. The spatial distribution of the maximum correlation between vegetation and SPEI01, SPEI06, and SPEI12 was depicted in Figures 8A, E, respectively. The majority of the YRB (79.93%) showed a positive correlation between climate change and vegetation growth, and 48.33% of those areas showed a significant positive correlation. This was particularly true in the central and southern regions of the YRB, where the correlation coefficient was greater than 0.5, demonstrating that climate change was a significant factor influencing YRB vegetation growth. The negative correlation was mainly concentrated in the YRS, western and northern part of the YRB, which were the main artificial ecological construction protection areas of the YRB, while the YRD was a rapidly developing area of urbanization (Figure 1A). According to Figures 8B, F, vegetation was most sensitive to SPEI12 (41.39%), which was mostly dispersed in the eastern and central portions of the YRB and the YRS. SPEI06 (30.50%) and SPEI01 (28.11%) were the next two most sensitive SPEIs to vegetation. Through the classification analysis of different vegetation can be found that the mean correlation of different vegetation types and time scales is positive (Figures 8C, G). In addition, there was a significant positive correlation between forest (0.31) and crop (0.28). Grass had the lowest sensitivity to SPEI, with an average correlation coefficient of 0.20 and a standard deviation of 0.28. The mean correlations of forest and crop were similar, but they were dispersed differently. The correlation standard deviations for forest and crop were 0.23 and 0.25, respectively, indicating that forest responded to climate change more evenly than crop. In descending order, the average correlation between SPEI and vegetation at different time periods was 0.21 for vegetation at 12 month-scale, 0.20 for vegetation at 6 month-scale, and 0.18 for vegetation at 1 month-scale, demonstrating that long-term climate change had a higher impact on vegetation growth (Figures 8D, H).

The findings of residual trend analysis demonstrated the significant regional variability of the effects of human activity and climate change on vegetation in the YRB (Figure 9). We could find that not all regions meet the use conditions of residual analysis ($R^2 > 0.3$, $p < 0.05$). Therefore, we analyzed the regions that meet the criteria. Most frequently seen in the northern and southern regions of the YRB,

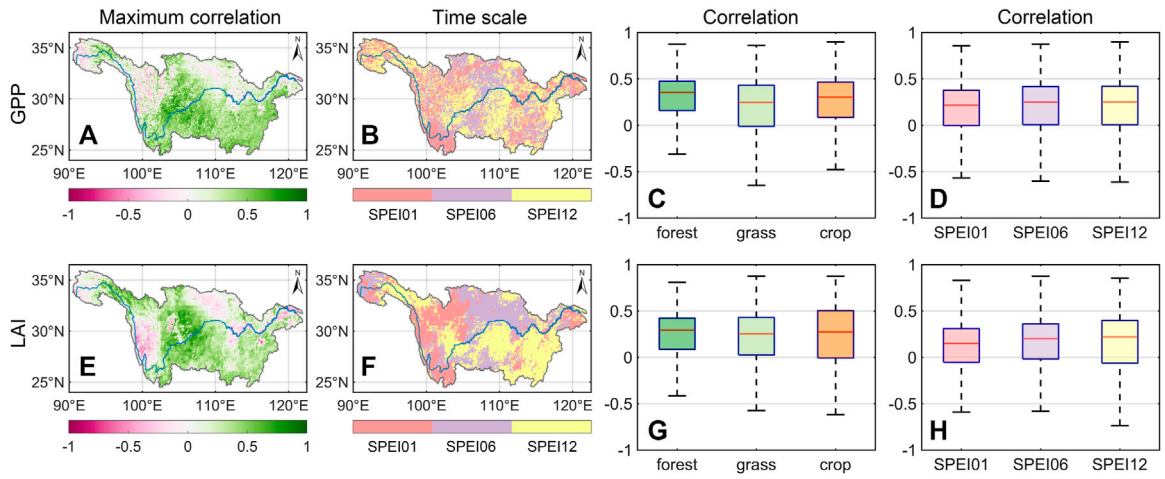

FIGURE 8
Correlation between SPEI and vegetation. **(A,E)** The maximum correlation between GPP, LAI, and SPEI, respectively. **(B,F)** The time scale corresponding to SPEI, respectively. **(C,G)** Correlation of different land cover types, respectively. **(D,H)** Correlation of different SPEI time scales, respectively.

roughly 92.01% of the regions in the YRB demonstrated that climate change contributed to the rise in GPP. The region where climatic change prevented an increase in GPP accounted for 7.99% of the total area, and was primarily spread in the YRD (Figure 9A). Compared with GPP, LAI showed a similar spatial distribution of climate change impacts, in which 86.13% of the regions showed that climate change promoted the increase of GPP, while 13.87% of the regions showed that climate change inhibited vegetation growth (Figure 9E). Figure 9B shows that approximately 90.49% of GPP growth is influenced by human activity. The region where climate change increased GPP increased by 1.52% when compared to the impact of human activity, primarily in the central and northern regions of the YRB. The inhibition of human activity on the growth of GPP accounted for 9.51% of the total area, mainly concentrated in the YRD. The spatial area of LAI influenced by human activity and climate change was larger than that of GPP, but the distribution pattern was similar to that of GPP (Figures 9E, F).

By comparing the proportional rates of climate change and human activity, it was discovered that climate change contributed up to 61.28% of the YRB's vegetation growth, while human activity contributed 38.72%. Only 26.87% of the YRB's vegetative area was less impacted by climate change than by human activity, and it was primarily concentrated in the region's center and southern (Figures 9C, D, G, H). It was evident that vegetation growth in the YRB was mainly driven by climate change, and human activity was mainly auxiliary.

Additionally, the contribution rates of climate change and human activity to various vegetation types varied (Table 3). The average relative contribution of human activity to crops reached the highest value (43.62%), while that of climate change reached the lowest value (56.38%). Climate change and human activity each contributed on average 60.71% and 39.29% of forest, respectively. In grass, climate change and human activity had contributed 63.66% and 36.34%, respectively. Therefore, in all vegetation, climate change dominated the vegetation growth process, and human activity contributed more to crop growth than other vegetation.

4 Discussion

For the investigation and measurement of the natural drivers of ecosystems, the vegetation is sensitive to the influence of climate (Knapp and Smith, 2001; Piao et al., 2020). From 2000 to 2018, the YRB showed a climate change characteristic of warming and wetting (Figure 2; Figure 3). As a typical humid and semi-humid region, temperature has the greatest effect on vegetation growth (Zhang et al., 2020). Since vegetation growth in the YRB was easily affected by temperature change, the correlation between SPEI and vegetation was mostly positive (Figure 8), which is consistent with other research results in the YRB (Chen et al., 2018; Shi et al., 2022). The negative correlation accounted for only 20.07% of the YRB area and was concentrated in northern crop, the urban of the YRD and the western alpine grass (Figure 8). In these areas, the radiation amount is large and the temperature is high (Figure 2), resulting in low precipitation and large surface evapotranspiration, which makes SPEI show a downward trend and show the characteristics of gradual drought (Pan et al., 2015).

Human activity has transformed vast amounts of grass into urban, crop and forest in the YRB (Table 2). Since crop growth is still mainly affected by climate change and is more affected by human land management than other vegetation types, the contribution rate of human activity to crop growth is relatively high (Table 3), resulting in a decrease in the sensitivity of crop growth to climate change (Xin et al., 2008; Piao et al., 2010). The climate in the high altitude area changes with the increase of altitude, the radiation increases, and the temperature and precipitation decreased gradually. Due to the high sensitivity of grass to climate change, the growth of western alpine grass was limited (Nemani et al., 2003; Páscoa et al., 2018; Gao et al., 2019), thus shrinking the grass area in the western YRB (Table 2). With the gradual decrease of altitude, temperature and precipitation gradually increased as controlling factors influencing vegetation growth, and the change rate of temperature and precipitation would also gradually increase

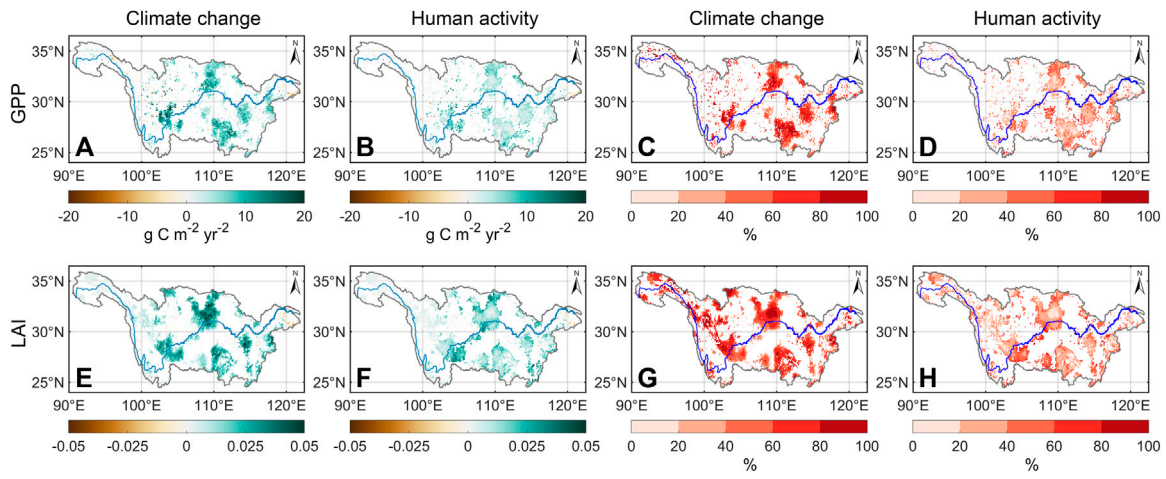

FIGURE 9
Effects of human activity and climate change on vegetation growth. **(A,B)** Trends of climate change and human activity impact on GPP. **(C,D)** Relative contributions of climate change and human activity impact on GPP. **(E,F)** Trends of climate change and human activity impact on LAI. **(G,H)** Relative contributions of climate change and human activity impact on LAI.

TABLE 3 Different vegetation types' relative contributions from human activity and climate change.

	Forest (%)	Grass (%)	Crop (%)
GPP (climate change)	61.12	62.48	57.75
GPP (human activity)	38.88	37.52	42.25
LAI (climate change)	60.30	64.83	55.01
LAI (human activity)	39.70	35.17	44.99

(Figure 2). However, long-term climate change had a higher impact on vegetation than short-term climate change (Figure 8), which is in line with other research findings (Wu et al., 2015; Chen et al., 2020).

The climate of the YRB had become warmer and wetter (Figure 3), which effectively promoted the growth of vegetation. However, the direct and indirect influences of human activity on vegetation growth should also be considered (Piao et al., 2015; Piao et al., 2020). Both climate change and human activity were discovered to have an impact on vegetation change in the YRB, but the relative proportions were very different. As shown in Figure 9, climate change and human activity mainly promoted vegetation growth, and there were few areas that inhibited vegetation growth. Among them, the YRD is the main area where human activity inhibited vegetation growth. A large amount of crop and forest around urban was converted into urban to meet the needs of urban development, leading to a significant reduction of vegetation around urban land (Table 2). It could be seen that urbanization progress is an important cause of vegetation degradation (Fu et al., 2018). The MUYRB is an important ecological area in China, as well as key area for the implementation of the project of returning crop to forest and the construction of artificial forests. Human activity had shown that they promote vegetation growth and increase forest (Table 2). In Figure 9, It could be seen that the project of returning crop to forest effectively improved the human-land relationship and promoted the growth of vegetation in the MUYRB (Wang et al., 2015). Although human activity were important drivers of crop cultivation (Chen et al., 2019; Wang et al., 2023), but some vegetation in the YRD still showed negative growth (Figure 9), which was caused by the conversion of a large number of grass areas into crop and urban (Table 2), which reduced the vegetation coverage area and weakened the carbon sequestration ability of vegetation, thus showing the inhibition effect of human activity on vegetation growth (Yang et al., 2022).

By comparing relative contribution rates, it could be found that human activity was an important influence on vegetation growth in the YRB, but climate change lead vegetation change in all vegetation types (Figure 9; Table 3). Therefore, studying the interaction between YRB vegetation and climate change and understanding the response of ecosystem to human activity will provide an important reference for the future construction of YRB ecological conservation projects.

At present, the use of residual analysis method to study the typical humid and semi-humid YRB has certain limitations in the quantitative assessment of the impacts of climate change and human activity on vegetation. The residual analysis method relies on reliable remote sensing data and climate data. However, the widely used CMFD data sets in China have low spatial resolution. Therefore, obtaining high-quality, high spatio-temporal resolution data remains a challenge. The residual analysis method mainly focuses on the modeling and analysis of linear relationships, while the response of vegetation to climate change and human activity may have nonlinear characteristics. Therefore, it is of great significance to further study the mechanism and method of vegetation nonlinear response for more accurate interpretation of vegetation dynamic change.

In general, the use of residual analysis method to study the impact of vegetation on the typical humid and semi-humid YRB has limitations in data availability, model complexity, research comprehensiveness and nonlinear response challenges. The future development direction should focus on improving the quality and availability of data, improving the accuracy of the model,

considering the influence of multiple factors, and deeply studying the nonlinear response. This will help to evaluate the driving mechanism of dynamic vegetation change in the YRB more comprehensively and accurately, and predict the future vegetation change trend.

5 Conclusion

This study looked at how climate change and human activity affected vegetation growth from 2000 to 2018. The SPEI was used to examine how vegetation responded to climate change in the YRB. Additionally, the relative contribution rate was calculated to examine the effects of climate change and human activity on vegetation growth. Quantitative analysis of the effects of climate change and human activity on vegetation change in humid and sub-humid areas is novel in this study.

The YRB experienced an annual average temperature warming rate of 0.03°C yr^{-1} and an increase in precipitation of 4.02 mm yr^{-1}, presenting a gradually warm and wet state. There was a significant positive correlation between vegetation and SPEI in most areas of the YRB (79.93%), indicating that climate change has significantly affected vegetation growth. Vegetation in the YRB was more susceptible to SPEI over a long time scale. The forest cover has significantly increased during 2000–2018, on the YRB. The vegetation of the YRB showed a significant increasing trend (7.83 g C m^{-2} yr^{-2}). With the continuous development of urbanization, a large number of crop and grass were converted into urban. It reduced the area covered by vegetation and weakened the carbon sequestration ability of vegetation. Climate change and human activity were both driving factors affecting vegetation changes. Among all vegetation changes in the YRB, the relative effect of climate change accounted for 61.28%, and the relative effect of human activity accounted for 38.72%, among which crops were most affected by human activity and the average relative contribution rate of human activity reached the maximum (43.62%), indicating that agricultural management was the important driving factor of crop change. Human activity not only promoted the growth of crop, but also inhibited YRD vegetation growth. Nevertheless, human activity has played a crucial role in promoting vegetation growth in the YRB, with the extent of promotion covering approximately 90.49% of the area. In general, vegetation growth in the YRB is positively influenced by both climate change and human activity, with climate change playing a prominent role. Therefore, coordinating climate change with reducing intensive human activity was a reasonable way to restore the ecosystem in the YRB.

Data availability statement

The original contributions presented in the study are included in the article material, further inquiries can be directed to the corresponding author.

Author contributions

The authorship of this research was divided among RG, AC, and XC. RG and AC contributing to the conceptualization and writing of the original draft, and all authors being involved in the data curation and visualization. XC provided additional support in writing, review, and editing. All authors contributed to the article and approved the submitted version.

Funding

This study was financially supported by the National Natural Science Foundation of China (Grant No. 52078237) and the Jiangsu Province Postgraduate Research and Practice Innovation Plan Project (Grant No. KYCX23_1322) in 2023.

Acknowledgments

The authors extend their gratitude to the editorial team and reviewers for their insightful comments and suggestions, which significantly contributed to the enhancement of the present article.

Conflict of interest

The authors declare that the research was conducted in the absence of any commercial or financial relationships that could be construed as a potential conflict of interest.

Publisher's note

References

Anav, A., Friedlingstein, P., Beer, C., Ciais, P., Harper, A., Jones, C., et al. (2015). Spatiotemporal patterns of terrestrial gross primary production: a review. *Rev. Geophys.* 53, 785–818. doi:10.1002/2015rg000483

Beguería, S., Vicente-Serrano, S. M., and Angulo-Martínez, M. (2010). A multiscalar global drought dataset: the SPEIbase: a new gridded product for the analysis of drought variability and impacts. *Bull. Am. Meteorological Soc.* 91, 1351–1356. doi:10.1175/2010bams2988.1

Beguería, S., Vicente-Serrano, S. M., Reig, F., and Latorre, B. (2014). Standardized precipitation evapotranspiration index (SPEI) revisited: parameter fitting, evapotranspiration models, tools, datasets and drought monitoring. *Int. J. Climatol.* 34, 3001–3023. doi:10.1002/joc.3887

Cao, W., Wu, D., Huang, L., Pan, M., and Huhe, T. (2021). Determinizing the contributions of human activities and climate change on greening in the Beijing–Tianjin–Hebei Region, China. *Sci. Rep.* 11, 21201. doi:10.1038/s41598-021-00788-4

Chen, C., Park, T., Wang, X., Piao, S., Xu, B., Chaturvedi, R. K., et al. (2019). China and India lead in greening of the world through land-use management. *Nat. Sustain.* 2, 122–129. doi:10.1038/s41893-019-0220-7

Chen, S., Zhang, L., Liu, X., Guo, M., and She, D. (2018). The use of SPEI and TVDI to assess temporal-spatial variations in drought conditions in the middle and lower reaches of the Yangtze River basin, China. *Adv. Meteorology* 2018, 1–11. doi:10.1155/2018/9362041

Chen, Z., Wang, W., and Fu, J. (2020). Vegetation response to precipitation anomalies under different climatic and biogeographical conditions in China. *Sci. Rep.* 10, 830. doi:10.1038/s41598-020-57910-1

Evans, J., and Geerken, R. (2004). Discrimination between climate and human-induced dryland degradation. *J. arid Environ.* 57, 535–554. doi:10.1016/s0140-1963(03)00121-6

Forkel, M., Carvalhais, N., Rödenbeck, C., Keeling, R., Heimann, M., Thonicke, K., et al. (2016). Enhanced seasonal CO2 exchange caused by amplified plant productivity in northern ecosystems. *Science* 351, 696–699. doi:10.1126/science.aac4971

Friedl, M. A., Sulla-Menashe, D., Tan, B., Schneider, A., Ramankutty, N., Sibley, A., et al. (2010). MODIS Collection 5 global land cover: algorithm refinements and characterization of new datasets. *Remote Sens. Environ.* 114, 168–182. doi:10.1016/j.rse.2009.08.016

Friedl, M., and Sulla-Menashe, D. (2015). "MCD12C1 MODIS/Terra+ Aqua land cover type yearly L3 global 0.05 Deg CMG V006," in *NASA EOSDIS land processes DAAC* (Washington, United States: NASA).

Fu, W., Lü, Y., Harris, P., Comber, A., and Wu, L. (2018). Peri-urbanization may vary with vegetation restoration: a large scale regional analysis. *Urban For. Urban Green.* 29, 77–87. doi:10.1016/j.ufug.2017.11.006

Gao, M., Piao, S., Chen, A., Yang, H., Liu, Q., Fu, Y. H., et al. (2019). Divergent changes in the elevational gradient of vegetation activities over the last 30 years. *Nat. Commun.* 10, 2970. doi:10.1038/s41467-019-11035-w

Han, Z., Song, W., Deng, X., and Xu, X. (2018). Grassland ecosystem responses to climate change and human activities within the Three-River Headwaters region of China. *Sci. Rep.* 8, 9079. doi:10.1038/s41598-018-27150-5

He, J., Yang, K., Tang, W., Lu, H., Qin, J., Chen, Y., et al. (2020). The first high-resolution meteorological forcing dataset for land process studies over China. *Sci. data* 7, 25. doi:10.1038/s41597-020-0369-y

Hirschi, M., Seneviratne, S. I., Alexandrov, V., Boberg, F., Boroneant, C., Christensen, O. B., et al. (2011). Observational evidence for soil-moisture impact on hot extremes in southeastern Europe. *Nat. Geosci.* 4, 17–21. doi:10.1038/ngeo1032

Ji, L., and Peters, A. J. (2003). Assessing vegetation response to drought in the northern Great Plains using vegetation and drought indices. *Remote Sens. Environ.* 87, 85–98. doi:10.1016/s0034-4257(03)00174-3

Jiang, L., Bao, A., Guo, H., and Ndayisaba, F. (2017). Vegetation dynamics and responses to climate change and human activities in Central Asia. *Sci. Total Environ.* 599, 967–980. doi:10.1016/j.scitotenv.2017.05.012

Jiao, W., Chang, Q., and Wang, L. (2019). The sensitivity of satellite solar-induced chlorophyll fluorescence to meteorological drought. *Earth's Future* 7, 558–573. doi:10.1029/2018ef001087

Jin, K., Wang, F., and Li, P. (2018). Responses of vegetation cover to environmental change in large cities of China. *Sustainability* 10, 270. doi:10.3390/su10010270

Knapp, A. K., and Smith, M. D. (2001). Variation among biomes in temporal dynamics of aboveground primary production. *Science* 291, 481–484. doi:10.1126/science.291.5503.481

Li, S., Yang, S., Liu, X., Liu, Y., and Shi, M. (2015). NDVI-based analysis on the influence of climate change and human activities on vegetation restoration in the Shaanxi-Gansu-Ningxia Region, Central China. *Remote Sens.* 7, 11163–11182. doi:10.3390/rs70911163

Li, X., Du, L., Li, X., Yao, P., Luo, Z., and Wu, Z. (2022). Effects of human activities on urban vegetation: explorative analysis of spatial characteristics and potential impact factors. *Remote Sens.* 14, 2999. doi:10.3390/rs14132999

Liu, Y., Li, Y., Li, S., and Motesharrei, S. (2015). Spatial and temporal patterns of global NDVI trends: correlations with climate and human factors. *Remote Sens.* 7, 13233–13250. doi:10.3390/rs71013233

Lotsch, A., Friedl, M. A., Anderson, B. T., and Tucker, C. J. (2003). Coupled vegetation-precipitation variability observed from satellite and climate records. *Geophys. Res. Lett.* 30. doi:10.1029/2003gl017506

Ma, D., Deng, H., Yin, Y., Wu, S., and Zheng, D. (2019). Sensitivity of arid/humid patterns in China to future climate change under a high-emissions scenario. *J. Geogr. Sci.* 29, 29–48. doi:10.1007/s11442-019-1582-5

Mao, J., Shi, X., Thornton, P. E., Piao, S., and Wang, X. (2012). Causes of spring vegetation growth trends in the northern mid–high latitudes from 1982 to 2004. *Environ. Res. Lett.* 7, 014010. doi:10.1088/1748-9326/7/1/014010

Mathur, S., Agrawal, D., and Jajoo, A. (2014). Photosynthesis: response to high temperature stress. *J. Photochem. Photobiol. B Biol.* 137, 116–126. doi:10.1016/j.jphotobiol.2014.01.010

Metcalfe, D. B., Meir, P., Aragão, L. E., Lobo-Do-Vale, R., Galbraith, D., Fisher, R., et al. (2010). Shifts in plant respiration and carbon use efficiency at a large-scale drought experiment in the eastern Amazon. *New Phytol.* 187, 608–621. doi:10.1111/j.1469-8137.2010.03319.x

Mishra, A., and Desai, V. (2005). Drought forecasting using stochastic models. *Stoch. Environ. Res. risk Assess.* 19, 326–339. doi:10.1007/s00477-005-0238-4

Nemani, R. R., Keeling, C. D., Hashimoto, H., Jolly, W. M., Piper, S. C., Tucker, C. J., et al. (2003). Climate-driven increases in global terrestrial net primary production from 1982 to 1999. *science* 300, 1560–1563. doi:10.1126/science.1082750

Pan, S., Tian, H., Dangal, S. R., Yang, Q., Yang, J., Lu, C., et al. (2015). Responses of global terrestrial evapotranspiration to climate change and increasing atmospheric CO_2 in the 21st century. *Earth's Future* 3, 15–35. doi:10.1002/2014ef000263

Páscoa, P., Gouveia, C. M., Russo, A. C., Bojariu, R., Vicente-Serrano, S. M., and Trigo, R. M. (2018). Vegetation vulnerability to drought on southeastern Europe. *Hydrology Earth Syst. Sci. Discuss.*, 1–29.

Piao, S., Ciais, P., Huang, Y., Shen, Z., Peng, S., Li, J., et al. (2010). The impacts of climate change on water resources and agriculture in China. *Nature* 467, 43–51. doi:10.1038/nature09364

Piao, S., Wang, X., Park, T., Chen, C., Lian, X., He, Y., et al. (2020). Characteristics, drivers and feedbacks of global greening. *Nat. Rev. Earth Environ.* 1, 14–27. doi:10.1038/s43017-019-0001-x

Piao, S., Yin, G., Tan, J., Cheng, L., Huang, M., Li, Y., et al. (2015). Detection and attribution of vegetation greening trend in China over the last 30 years. *Glob. change Biol.* 21, 1601–1609. doi:10.1111/gcb.12795

Qu, S., Wang, L., Lin, A., Zhu, H., and Yuan, M. (2018). What drives the vegetation restoration in Yangtze River basin, China: climate change or anthropogenic factors? *Ecol. Indic.* 90, 438–450. doi:10.1016/j.ecolind.2018.03.029

Rahmani, F., and Fattahi, M. H. (2021). A multifractal cross-correlation investigation into sensitivity and dependence of meteorological and hydrological droughts on precipitation and temperature. *Nat. Hazards* 109, 2197–2219. doi:10.1007/s11069-021-04916-1

Shi, M., Yuan, Z., Shi, X., Li, M., Chen, F., and Li, Y. (2022). Drought assessment of terrestrial ecosystems in the Yangtze River Basin, China. *J. Clean. Prod.* 362, 132234. doi:10.1016/j.jclepro.2022.132234

Shi, S., Yu, J., Wang, F., Wang, P., Zhang, Y., and Jin, K. (2021). Quantitative contributions of climate change and human activities to vegetation changes over multiple time scales on the Loess Plateau. *Sci. Total Environ.* 755, 142419. doi:10.1016/j.scitotenv.2020.142419

Sun, J., and Qin, X. (2016). Precipitation and temperature regulate the seasonal changes of NDVI across the Tibetan Plateau. *Environ. Earth Sci.* 75, 291–299. doi:10.1007/s12665-015-5177-x

Suzuki, R., Masuda, K., and Dye, D. G. (2007). Interannual covariability between actual evapotranspiration and PAL and GIMMS NDVIs of northern Asia. *Remote Sens. Environ.* 106, 387–398. doi:10.1016/j.rse.2006.10.016

Vicente-Serrano, S. M., Beguería, S., and López-Moreno, J. I. (2010). A multiscalar drought index sensitive to global warming: the standardized precipitation evapotranspiration index. *J. Clim.* 23, 1696–1718. doi:10.1175/2009jcli2909.1

Vickers, H., Høgda, K. A., Solbø, S., Karlsen, S. R., Tømmervik, H., Aanes, R., et al. (2016). Changes in greening in the high arctic: insights from a 30 year AVHRR max NDVI dataset for svalbard. *Environ. Res. Lett.* 11, 105004. doi:10.1088/1748-9326/11/10/105004

Wang, J., Wang, K., Zhang, M., and Zhang, C. (2015). Impacts of climate change and human activities on vegetation cover in hilly southern China. *Ecol. Eng.* 81, 451–461. doi:10.1016/j.ecoleng.2015.04.022

Wang, Q., Huang, K., Liu, H., and Yu, Y. (2023). Factors affecting crop production water footprint: A review and meta-analysis. *Sustain. Prod. Consum.* 36, 207–216. doi:10.1016/j.spc.2023.01.008

Wang, S., Zhang, Y., Ju, W., Qiu, B., and Zhang, Z. (2021). Tracking the seasonal and inter-annual variations of global gross primary production during last four decades using satellite near-infrared reflectance data. *Sci. Total Environ.* 755, 142569. doi:10.1016/j.scitotenv.2020.142569

Wang, X., and Bao, Y. (1999). Study on the methods of land use dynamic change research. *Prog. Geogr.* 18, 81–87. doi:10.1007/s41748-017-0029-3

Wang, Y., Li, H., Sun, B., Chen, H., Li, H., and Luo, Y. (2020). Drought impacts on hydropower capacity over the Yangtze River basin and their future projections under 1.5/2° C warming scenarios. *Front. Earth Sci.* 8, 578132. doi:10.3389/feart.2020.578132

Wu, D., Zhao, X., Liang, S., Zhou, T., Huang, K., Tang, B., et al. (2015). Time-lag effects of global vegetation responses to climate change. *Glob. change Biol.* 21, 3520–3531. doi:10.1111/gcb.12945

Xin, Z., Xu, J., and Zheng, W. (2008). Spatiotemporal variations of vegetation cover on the Chinese Loess Plateau (1981–2006): impacts of climate changes and human activities. *Sci. China Ser. D Earth Sci.* 51, 67–78. doi:10.1007/s11430-007-0137-2

Yang, H., Zhong, X., Deng, S., and Nie, S. (2022). Impact of LUCC on landscape pattern in the Yangtze River Basin during 2001–2019. *Ecol. Inf.* 69, 101631. doi:10.1016/j.ecoinf.2022.101631

Yang, K., He, J., Tang, W., Qin, J., and Cheng, C. C. (2010). On downward shortwave and longwave radiations over high altitude regions: observation and modeling in the Tibetan Plateau. *Agric. For. Meteorology* 150, 38–46. doi:10.1016/j.agrformet.2009.08.004

Zhang, Y.-X., Wang, Y.-K., Fu, B., Dixit, A. M., Chaudhary, S., and Wang, S. (2020). Impact of climatic factors on vegetation dynamics in the upper Yangtze River basin in China. *J. Mt. Sci.* 17, 1235–1250. doi:10.1007/s11629-019-5649-7

Zhao, A., Zhang, A., Liu, X., and Cao, S. (2018). Spatiotemporal changes of normalized difference vegetation index (NDVI) and response to climate extremes and ecological restoration in the Loess Plateau, China. *Theor. Appl. Climatol.* 132, 555–567. doi:10.1007/s00704-017-2107-8

frontiers | Frontiers in Ecology and Evolution

TYPE Original Research
PUBLISHED 21 September 2023
DOI 10.3389/fevo.2023.1228558

OPEN ACCESS

EDITED BY
Pavan Kumar,
Rani Lakshmi Bai Central Agricultural University, India

REVIEWED BY
Houlang Duan,
Chinese Academy of Sciences (CAS), China
Tian Xie,
Beijing Normal University, China

*CORRESPONDENCE
Jie Yang
yang_jie@gsau.edu.cn

RECEIVED 25 May 2023
ACCEPTED 05 September 2023
PUBLISHED 21 September 2023

CITATION
Yang J, Xie B, Zhang D, Mak-Mensah E and Pei T (2023) Habitat quality assessment and multi-scenario prediction of the Gansu-Qinghai section of the Yellow River Basin based on the FLUS-InVEST model. *Front. Ecol. Evol.* 11:1228558. doi: 10.3389/fevo.2023.1228558

Habitat quality assessment and multi-scenario prediction of the Gansu-Qinghai section of the Yellow River Basin based on the FLUS-InVEST model

Jie Yang[1]*, Baopeng Xie[2], Degang Zhang[1], Erastus Mak-Mensah[1] and Tingting Pei[2]

[1]College of Pratacultural Science, Gansu Agricultural University, Lanzhou, China, [2]School of Management, Gansu Agricultural University, Lanzhou, China

Research on the impact of land use change on regional habitat quality, in various future scenarios, can effectively aid planning and decision-making for sustainable development at a regional level. The study conducted its research in the Gansu-Qinghai Yellow River section and used ArcGIS and a land use transfer matrix to analyze the spatiotemporal pattern of land use and land cover changes. The study assessed the changes in habitat quality in the Gansu-Qinghai Yellow River region between 1990 and 2020, using the Integrated Valuation of Ecosystem Services and Trade-offs (InVEST) model, by evaluating the gains and losses. Simultaneously, 15 elements of the natural economy were chosen and examined for their temporal and spatial impact on habitat quality using the random forest model and spatially weighted regression model. To forecast land use changes in the Gansu-Qinghai Yellow River section for 2030, the Future Land Use Simulation Model (FLUS) model was utilized and a series of four scenarios (cultivated land protection scenario, ecological protection scenario, natural development scenario, and rapid development scenario) were employed. The research results indicate that over 70% of the Gansu-Qinghai Yellow River is occupied by grasslands, and only a small portion of the area, about 0.22%, is developed for construction purposes. The quality of the habitat in the Gansu-Qinghai Yellow River had a minor drop between 1990 and 2020, followed by an improvement. Habitat quality changes are primarily attributed to improvements, with variations across different areas, i.e., enhanced in the east and reduced in the central and western parts. The habitat quality of the Gansu-Qinghai Yellow River has improved in all four scenarios compared to 2020, as evidenced by the decrease in low-value habitats and increase in high-value areas. The ecological protection scenario has the highest average habitat quality value. These research results can be used to support policy development and ecological restoration initiatives in the Gansu-Qinghai Yellow River.

KEYWORDS

Gansu-Qinghai section of the Yellow River Basin, habitat quality, land use change, multi-scenario, FLUS-InVEST model

1 Introduction

Human survival and development are guaranteed by biodiversity, which also serves as a major engine for ecosystem services (Zhang et al., 2022). The quality of habitat represents the ecosystem's ability to provide suitable conditions for the survival of individuals and populations. Land use change is a major threat to habitat quality, and biodiversity is declining at an alarming rate, according to Bongaarts, (2019).Such as rapid urbanization and large-scale agricultural development activities, have exacerbated species extinction, habitat fragmentation, and habitat degradation, as biodiversity has been destroyed to varying degrees, thereby changing the habitat distribution pattern of habitats. The connectivity of habitat patches is increasingly reduced and fragmented, altering the habitats' structure and composition will ultimately have an impact on how energy and materials move between various ecological fragments (Liu et al., 2014; Wilson et al., 2016). Thoroughly researching the impacts of changes in land use on habitats is crucial for developing effective policies that protect biodiversity and promote coordinated development between humans and ecology, according to Yohannes et al. (2021).

The Maxent model (Wu et al., 2016), Artificial intelligence for ecosystem services (ARIES) model (Vigerstol and Aukema, 2011), Social values for ecosystem services (SoLVES) model (Wang et al., 2016), Habitat suitability index (HSI) model (Liu et al., 2017), and InVEST model are just a few of the current methods for evaluating ecosystem services. The InVEST model is frequently used in habitat quality assessments because of its ease of use, minimal data requirements, and potent spatial expression capabilities (Karimi et al., 2018). Yohannes et al. (2021) explored the habitat quality of Beresa Basin in Ethiopia.Gomes et al. (2021) investigated Lithuania's habitat quality using the InVEST model and examined the effects of various scenarios on land use change.

Based on simulating various scenarios during a certain historical period, land use and regional habitat quality evaluation can obtain the evolution laws of habitat quality over a long time. The evaluation of future habitat quality can better propose ecological environment protection strategies and has extremely important significance for the construction of ecological civilization. Because land use changes are affected by human activities, which are crucial when evaluating habitat quality. The most widely used simulation models, including the Cellular Automata (CA) model, are previously employed to imitate or replicate spatial layout both domestically and internationally (Tang et al., 2022), Markov Model (Liang et al., 2021), Artificial Neural Network (ANN) model, Multi-Agent-System (MAS) model (Gao et al., 2022), system simulation (System Dynamics, SD) model, and effects of changing land use Model (CLUE-S: Conversion of Land Use and its Effects at Small Region Extent) (Bai et al., 2019), but there are certain deficiencies in many of these models. Among them, the system simulation (SD) model does not reflect the spatial elements. Emphasis on the impact of economic benefits and the selection of network structure of the neural network model is different. the influence of various macro factors of the cellular automaton (CA) model on the simulation results is insufficient. The multi-scenario model overemphasizes the impact of actions carried out by humans on the simulation results and ignores the influence of natural elements, although there is still a significant dissimilarity between the outcomes obtained through simulation and those obtained in reality (Yu et al., 2014; Bai et al., 2019).

The FLUS model uses a combination of the CA model and ANN algorithm to demonstrate the spatial paths of different land use categories in different situations while considering both natural environmental and human-related impacts. It incorporates adaptive inertia and competition mechanisms and performs better in model simulations. Future land use patterns have been simulated in several studies using the FLUS model.

The Gansu-Qinghai Yellow River region is unique. It is located in the middle and upper sections of the Yellow River Basin. It is dominated by mountains and has large terrain fluctuations. The Qinghai-Tibet and Loess Plateaus meet in the Gansu-Qinghai Yellow River region. It is also one of the areas that are relatively vulnerable to climate change on a global scale. The special geographical location makes it a key area for ecological restoration (Yang et al., 2020). There are ecological and environmental issues in this region, such as soil erosion, biodiversity loss, a reduction in the area of wetlands, and degradation of grasslands, due to the interplay between elements of nature and actions taken by humans. Huge pressure is put on quality. To analyze the spatiotemporal pattern of land use change in the watershed. Exploring the spatiotemporal changes of habitat quality in the region and predicting future trends can provide important references for regional sustainable development and habitat protection.

This study used the InVEST (Integrated Valuation of Ecosystem Services and Trade-offs) model to evaluate the habitat quality of the Gansu-Qinghai Yellow River basin from 1990 to 2020. The impact of each factor on habitat quality was analyzed using both random forest models, taking into account temporal and spatial changes. A total of 15 factors were selected for analysis, such as the natural economy; and used the FLUS model, four set scenarios of cultivated land protection scenario, natural development scenario, rapid development scenario, and predicted the habitat quality of the above four scenarios.

2 Materials and methods

2.1 The study area

The Gansu-Qinghai Yellow River section can be found in the upper reaches of the Yellow River Basin (Figure 1), with a total area of 29.31×10^4 km^2, accounting for 39.0% of the total area of the Yellow River Basin. The total area of the Gansu section is 14.30×10^4 km^2 and includes Lanzhou City, Wuwei City, Baiyin City, Dingxi City, Linxia Prefecture, Longnan City, Gannan Prefecture, Qingyang City, Tianshui City, Pingliang City and other 10 cities (prefectures). While the total area of the Qinghai section is 15.01×10^4 km^2, including Xining City, Haibei, Haidong area, Huangnan, Guoluo, Hainan, Yushu, Haixi Mongolian and 5 Tibetan autonomous prefectures, and Tibetan Autonomous Prefecture and other 8 cities (prefectures). The altitude of the Gansu-

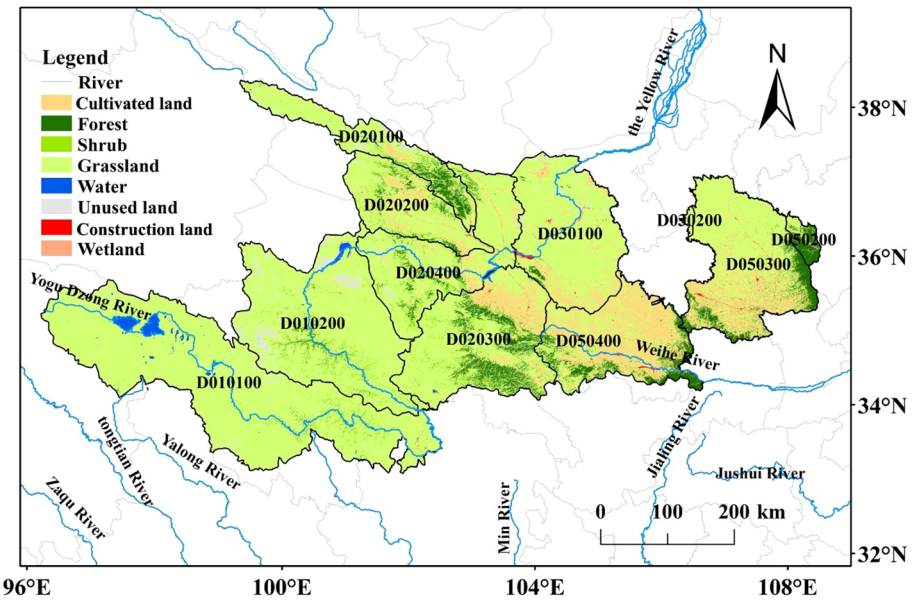

FIGURE 1
The location of the research area.

Qinghai Yellow River section is 3 000~5 000m, the terrain is high in the west and low in the east across the Qinghai-Tibet Plateau and Loess Plateau, belonging to the continental climate area.

D010100: Heyuan to Maqu D010200: Maqu to Longyangxia D020100: Above the Xiangtang of Datong River D020200: Huangshui D020300: Daxia River and Taohe River D020400: Main stream section of Longyangxia to Lanzhou D030100: Lanzhou to the Xiaheyan D030200: Qingshui River and Kushui River D050200: Above the Zhuangtou of Beiluo River D050300: Above the Zhangjiashan of Jinghe River D050400: Above the Baoji Gorge of Weihe River.

2.2 Data sources

The first annual China Land Cover Dataset (CLCD) from Landsat (Yang and Huang, 2021), created by Professors Yang and Huang of Wuhan University on the GEE platform, was used to obtain the land use data for the years 1990 to 2020. It covered 30 continuous years. The 30 m × 30 m represented the spatial resolution.

Selected normalized different indices were, vegetation, precipitation, temperature, elevation, slope, aspect, terrain relief, topographic position index, distance from the river, soil type, gross domestic product, population density, distance from railway, and road. The distance from the government residence and the nighttime light index included 10 natural factors and 6 socioeconomic factors as the driving factors of habitat quality and the factor data of the model simulation. For the data sources of specific factors, refer to Table 1. The data on China's nature reserves came from the Environment Data Sharing Center of the Chinese Academy of Sciences (http://www.resdc.cn/) and Resource.

2.3 Methods

2.3.1 Habitat quality analysis

This study assessed the habitat quality index using the InVEST model's Habitat Quality module. This module is a map that was created by combining different land use types with threats to biodiversity in the habitat with the degree of habitat degradation and habitat quality in a given area. According to this model, habitat quality is a continuous variable that can be anywhere between low and high (Hall et al., 1997). In general, habitat quality is influenced by how close it is to human land use, whereas habitat degradation is influenced by how intense nearby land use is (Nellemann, 2001). The more severe the danger to the natural environment posed by the threat factor and the greater the degree of habitat degradation, the higher the score. Calculated as follows:

$$\sum_{r=1}^{R}\sum_{y=1}^{y_r}\left(\frac{w_r}{\sum_{r=1}^{R}W_r}\right)r_y i_{rxy}\beta_x S_{jr} \quad (1)$$

In the formula, D_{xj}, R, w_x, Y_r and ry represent the habitat degradation degree, (degradation risk index), the number of stress factors, the weight of stress factor r, and the weight of stress factor and the number of grids and the value of the stress factor on the grid, respectively; the distance between the habitat and the source of danger, as well as the effect of the danger on the environment, are represented by the variable "i_{rxy}". Meanwhile, the mitigating effect of protective measures on the impact of the threat on the habitat is indicated by the factor "β_x" (that is, legal degree of protection, the range is 0–1, 1 is complete accessibility); the measure of how much a particular stress factor r affects the habitat type j is indicated by S_{jr}.

$$i_{rxy} = 1 - \left(\frac{d_{xy}}{d_{rmax}}\right) \text{(linear decay)} \quad (2)$$

TABLE 1 Driving factors of habitat quality.

Driving factor			Data sources
Natural factor	NDVI	Normalized Difference Vegetation Index	National Qinghai-Tibet Plateau Scientific Data Center (https://data.tpdc.ac.cn)
	PRE	Precipitation	NASA Dataset (https://appeears.earthdatacloud.nasa.gov/)
	TEM	Temperature	NASA Dataset (https://appeears.earthdatacloud.nasa.gov/)
	DEM	Elevation	Resource and Environmental Data Sharing Center of Chinese Academy of Sciences (http://www.resdc.cn/)
	Slope	Slope	Elevation data was obtained after slope processing in GIS
	PX	Aspect	Elevation data was obtained after slope processing in GIS
	TR	Terrain relief	Elevation data was obtained after slope processing in GIS
	TI	Topographic index	Elevation and slope data were obtained after slope processing in GIS
	DFR	Distance from river	Resource and Environmental Data Sharing Center of Chinese Academy of Sciences (http://www.resdc.cn/)
	ST	Soil type	Resource and Environmental Data Sharing Center of Chinese Academy of Sciences (http://www.resdc.cn/)
Socioeconomic factors	GDP	Gross domestic product	Resource and Environmental Data Sharing Center of Chinese Academy of Sciences (http://www.resdc.cn/)
	POP	Population density	Resource and Environmental Data Sharing Center of Chinese Academy of Sciences (http://www.resdc.cn/)
	DFRO	Distance from road	Openstreetmap dataset (https://www.openstreetmap.org)
	DFR	Distance from railway	Openstreetmap dataset (https://www.openstreetmap.org)
	OLS	DMSP-OLS night light data	Resource and Environmental Data Sharing Center of Chinese Academy of Sciences (http://www.resdc.cn/)

$$i_{rxy} = \exp\left(\frac{-2.99 d_{xy}}{d_{rmax}}\right) (\text{exponential decay}) \quad (3)$$

The equation involves the measurement of d_{xy}, which represents the straight-line distance between the x and y coordinates on the grid. Additionally, the maximum distance of potential danger from the threat source r is referred to as d_{rmax}.

Therefore, the habitat quality in grid cell x in land use type j is:

$$Q_{xj} = H_j\left(1 - \left(\frac{D_{xj}^z}{D_{xj}^z + k^2}\right)\right) \quad (4)$$

The equation uses various parameters. Q_{xj} represents the quality of the habitat in a specific location and land use, while H_j is the suitability of the habitat type, ranging from 0 to 1. The half-saturation constant, denoted as k, is typically equal to half of the highest possible habitat value. Another parameter, z, is a normalization constant and is usually set to 2.5.

In this paper, the parameters of the model are set by referring to the InVEST model User Guide manual (Sharp et al., 2015) and existing literature (Zhang et al., 2020; Zhang et al., 2020), including land use type map and threat source factors (based on the actual land cover situation in the study area, construction land is the most disturbed type by human activities, and cultivated land is the type with more concentrated human activities.

The unused land is basically uncovered by vegetation and has a bad ecological environment. Therefore, the three categories are defined as threat sources and threat factor weights (Table 2) and sensitivity index (Table 3).

2.3.2 Scenario simulation of land use pattern

In 2017, the FLUS model was introduced by Liu et al. (2017). This model is founded on the Geo-SOS theory and utilizes data on land use and its determinants to forecast the future spatial arrangement of land utilization, taking into account both natural

TABLE 2 The weight and the maximum influence distance of the threat source.

Threat factor	Longest threat distance (km)	Weight	Spatial decay type
Cultivated land	8	0.7	linear
Construction land	10	0.9	exponential
Unused land	5	0.2	exponential

TABLE 3 Sensitivity index of land use type to habitat threat factors .

Land use type	Habitat adaptability	Sensitivity index				
		Urban land	Rural land	Construction land	Cultivated land	Unused land
Cultivated Land	0.4	0	0.7	0.5	0.4	0
Forest land	1	0.8	0.5	0.2	1	0.8
Shrub	1	0.6	0.6	0.3	1	0.6
Grassland	0.8	0.5	0.6	0.4	0.8	0.5
Water	1	0.7	0.9	0.1	1	0.7
Unused land	0	0	0	0	0	0
Construction land	0	0	0	0	0	0
Wetland	0.9	0.5	0.8	0.2	0.9	0.5

and human factors. This approach has been further explored by Liang et al. (2018) and by Liu et al. (2017). The driving factors selected in this paper include normalized difference vegetation index, precipitation, temperature, elevation, slope, aspect, terrain relief, distance from river, soil type, GDP, population density, distance from road, and railway. There are 15 natural economic factors in total, including distance, distance from the government residence, and night light index. The simulation process primarily entails scenario setting, adaptive inertia coefficient calculation, model testing, neighborhood factor setting, comprehensive probability calculation, and suitability probability calculation as follows.

2.3.2.1 Suitability probability calculation

Neural networks are the foundation for suitability probability calculations. The probability of a k-type land use type occurring on a particular grid p at time t is calculated using an artificial neural network (ANN) with multiple input and output neurons as p(p,k,t) (Liu et al., 2017):

$$p(p,k,t) = \sum_j w_{j,k} \times \frac{1}{1+e^{-net_j}(p,t)} \quad (5)$$

The suitability probability of land use type k on grid p at time t is given by the formula: p(p,k,t). The adaptive weight between the output layer and hidden layer is given by the formula: w j,k. The signal that neuron j receives from all of the input neurons on grid cell p at time t in the hidden layer is given by the formula: net j(p,t).

The neural network-based probability-of-occurrence calculation module was used to determine the driving force behind land use change. Using this module, the probability of each type of land use in every pixel of the study area was calculated through the neural network algorithm (ANN). The suitability probability calculation module was selected based on the neural network by the startup model. This study used a uniform sampling strategy as its sampling method. The multi-layer feedforward neural network algorithm's hidden layer count was set to 12, and the sampling parameter's value was 20. Then import the variables that may affect changes, like the terrain and the location of traffic, and determine the likelihood of various events occurring in each pixel of the Gansu-Qinghai Yellow River region. and the root mean square error (RMSE) of this model training is 0.153201.

Different colors were selected to represent the probability of occurrence. When the color of suitability probability is closer to blue, it means that the probability of occurrence is higher. Consequently, cultivated land is suitable for distribution in low-slope areas, forest land is suitable for distribution in high-lying mountainous areas, shrub land is suitable for distribution in middle-level terrain and interspersed with grassland, grassland is suitable for distribution in flat areas, and construction land is suitable for distribution in flat terrain and close to the river zone, water areas are suitable for distribution in low-lying areas, unused land is suitable for distribution in soil desertification desert areas, and wetlands are suitable for distribution near water sources. From the adaptive probability distribution, it can be seen that it is consistent with the natural conditions of the Gansu-Qinghai Yellow River, and the result is more reasonable.

The change of land use type is easily affected by many aspects such as nature, society and economy. Generally speaking, the factors affected by the outside world can be classified into three types, namely, natural factors, socioeconomic factors and accessibility factors. Natural factors represent the impact of the natural environment on land use types; socioeconomic factors represent the impact of social and economic development on land use type changes; and accessibility factors refer to the impact of traffic location factors on land use type changes. For urban form and its development, this paper selects 15 driving factors, as shown in Figure 2.

2.3.2.2 Neighborhood factor setting and model testing

The simulation accuracy is evaluated by the kappa coefficient. Closer to 1 signifies higher consistency. The predictions are regarded as credible when the kappa coefficient exceeds 0.75. The neighborhood factor's parameters range from 0 to 1, and a value that is closer to 1 indicates that the land type has a greater capacity for expansion. According to the findings of previous studies, water area, forest land, shrubs, grassland, and cultivated land had the

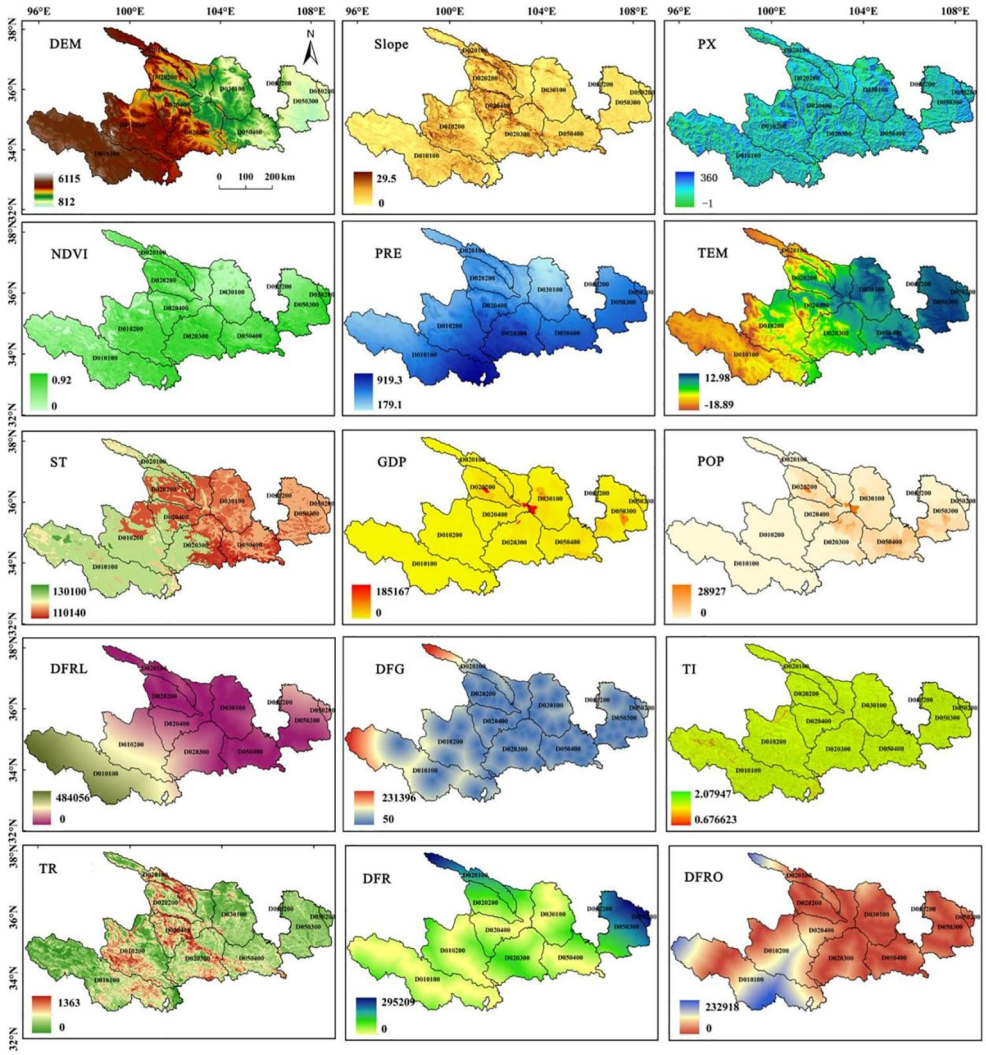

FIGURE 2
Driving factors of land use types in the Gansu-Qinghai section of the Yellow River Basin in 2010.

greatest potential for expansion. The unused land, construction land, and wetland neighborhood factors are set at 0.7, 0.7, 0.6, 0.4, 0.6, 0.5, 0.8, and 0.7. The outcomes of the simulation regarding the utilization of land in 2020 using the neighborhood factor simulation had a Kappa coefficient of 84.88%.

2.3.2.3 Calculation of adaptive inertia coefficient

The inertia coefficient, which is capable of adapting to changes, modifies itself throughout the iterative process. Its purpose is to minimize the difference between the actual supply and expected demand for each type of land use. Consequently, it increases the quantity of land use towards the target value and facilitates the simulation of spatial changes in land use. The equation reads as follows:

$$\text{Interia}_k^t \begin{cases} \text{Interia}_k^{t-1} & |D_k^{t-2}| \le |D_k^{t-1}| \\ \text{Interia}_k^{t-1} \times \frac{|D_k^{t-2}|}{|D_k^{t-1}|} & 0 > |D_k^{t-2}| > |D_k^{t-1}| \\ \text{Interia}_k^{t-1} \times \frac{|D_k^{t-1}|}{|D_k^{t-2}|} & |D_k^{t-1}| > |D_k^{t-2}| > 0 \end{cases} \quad (6)$$

In the formula: Interia_k^t is the inertia coefficient t of type k land during iteration; at iteration t−1, D_k^{t-1} denotes the discrepancy between the requested land quantity for a specific type of land (k) and the actual amount of that land available.

2.3.2.4 Scenario setting

The Gansu-Qinghai Yellow River section has diverse natural conditions, as well as economic and social development, which has led to different control modes for various development and utilization. To simulate the future land under various scenarios based on the traits of each scenario model, we use the scenario analysis method using the present state of social progress as a reference point.

Changes in utilization: Four scenarios were created for land use change simulation in this research based on various development objectives and potential disturbance scenarios in the watershed. These scenarios include rapid development, cultivated land protection, ecological protection, and natural development. Additionally, this setup was created to give managers a guide for

determining the equilibrium of sensible utilization of land in these situations. Here are the 4 possible scenarios for changing land use:

Natural development scenario (NADS): The Markov model is utilized to simulate the land demand, and all land types are convertible to each other, under the assumption that the future land change rate is consistent with the change from 2000 to 2015 and that the natural conditions and economic development conditions of the study area remain unaltered.

Cultivated land protection scenario (COPS): Focusing on the protection of basic farmland, it is strictly forbidden to transfer out cultivated land, except for construction land, which can be used as agricultural land.

Ecological protection scenario (ECPS): sort according to the ecological benefits of various types of land; water area, forest land, wetland, shrub land, cultivated land, construction land, grassland, and unused land.

Rapid development scenario (RADS): Sorted according to development needs; water area, construction, shrub, cultivated, forest land, grassland, wetland, unused land, the conversion principle is not to allow the change of land categories with a high ranking to low ranking.

2.3.2.5 Comprehensive probability calculation

The overall conversion probability of units occupied by the specified land type is estimated using the aforementioned factors, including suitability probability, neighborhood influence factor, suitability matrix, and inertia coefficient, and the formula is as follows:

$$TP_{p,k}^{t} = P_{p,k}^{t} \times \Omega_{p,k}^{t} \times I_{k}^{t} \times (1 - sc_{c \to k}) \tag{7}$$

In the formula: $TP_{p,k}^{t}$ represents the comprehensive probability that element p changes from initial land use type to land use type k at time t; $P_{p,k}^{t}$ represents the suitability probability of converting pixel p to land type k at time $\Omega_{p,k}^{t}$t; The conversion of cell p to land type k is affected by the neighborhood factor. The inertia coefficient of type k at time t is denoted by I. The conversion cost from land type c to land type k is represented by $SC_{c \to k}$. The land use data for different scenarios is obtained by calculating the probability of each iteration, and the accuracy is verified to finalize the results.

2.3.3 Random forest model

Multiple decision trees are used in the Random Forest (RF) classifier, and the majority of the individual output categories determine the output category (Liu et al., 2020). To classify or regress through repeated binary data in the 1980s, Breiman and others used the classification tree algorithm, which significantly decreased the amount of calculation. According to Mansoor et al. (2013), Breiman combined the classification tree into a random forest in 2001. The technique entails creating multiple classification trees randomly from data rows and variables columns, followed by summarizing the outcomes.

Typically, a random forest creates hundreds to thousands of classification trees at random before choosing the tree with the highest level of repetition as the outcome. The random forest algorithm evaluates the impact of each variable on the dependent variable by measuring the increase in the mean square error as a percentage at every level (% Inc MSE). Consequently, greater value implies greater importance of the variable. First, construct the ntree decision tree model and estimate the OBB mean square error of random replacement (ntree out-of-bag data composed of unsampled samples), and construct the following matrix:

$$\begin{bmatrix} MSE_{11} & MSE_{12} & \cdots & MSE_{1ntree} \\ MSE_{21} & MSE_{22} & \ldots & MSE_{1ntree} \\ \vdots & \vdots & \vdots & \vdots \\ MSE_{m1} & MSE_{m2} & \ldots & MSE_{mntree} \end{bmatrix} \tag{8}$$

Then calculate the importance score using the following formula:

$$scoreX_{j} = S_{E}^{-1} \frac{\sum_{r=1}^{n_{tree}} MSE_{r} - MSE_{pr}}{n_{tree}}, \ (1 \le p \le m) \tag{9}$$

The formula involves two variables, namely m which represents the number of variables, and n which represents the number of original data samples.

3 Results and analysis

3.1 Spatiotemporal changes of land use from 1990 to 2020

Grassland dominates the land use in the Gansu-Qinghai Yellow River region, making up more than 70% of the total area. Figure 3 shows that during the 30 years (1990–2020), the variation trend of different regions in the Ganqing section of the Yellow River Basin is shown in Figure 3. The cultivated land increases first and then decreases. In 2000, the cultivated land area is the largest, 434.35 × 104 km^2, and in 2017, the area is the least, 358.44 × 104 km^2. The area of forest land increased steadily in the past 30 years, with a total increase of 40.03 × 104 km^2. The overall shrub land showed a trend of fluctuation decline, the largest in 1990, and the least in 2016 was 29.97 × 104 km^2. The area of grassland fluctuated and then decreased significantly. In 2017, the area of grassland was the largest (2281.58 × 104 km^2), and in 2000, the area of grassland was the smallest (2233.12 × 104 km^2). During the past 30 years, the water area has shown a fluctuating upward trend. In 2020, the area was the largest at 25.01 × 104 km^2, and in 1997 the area was the smallest at 20.13 × 104 km^2. Unused land showed a fluctuating upward trend. The amount of unutilized land was the greatest in the year 2020, measuring 56.71 × 10^4 km^2, and the area was the lowest in 1992 at 39.43 × 104 km^2. The area of water has increased by 17.27 × 104 km^2 in 30 years. From 1990 to 2020, construction land increased year by year. In 2020, the largest area was 6.43 × 104 km^2, and the lowest area was 2.74 × 104 km^2 in 1990, for 30 years, there was a net growth of 3.68 × 10^4 km^2. The area of wetlands fluctuated first and then increased. In 1993, the area of wetlands was the largest at 1.98 × 104 km^2. In 2015, the area of wetlands was the smallest at 0.22 × 104 km^2. In 2000, the area of wetlands decreased the most at 0.63 × 104 km^2.

As shown in Figure 4, the main transfer direction and types of land use categories between years are depicted in the Sangki diagram. The

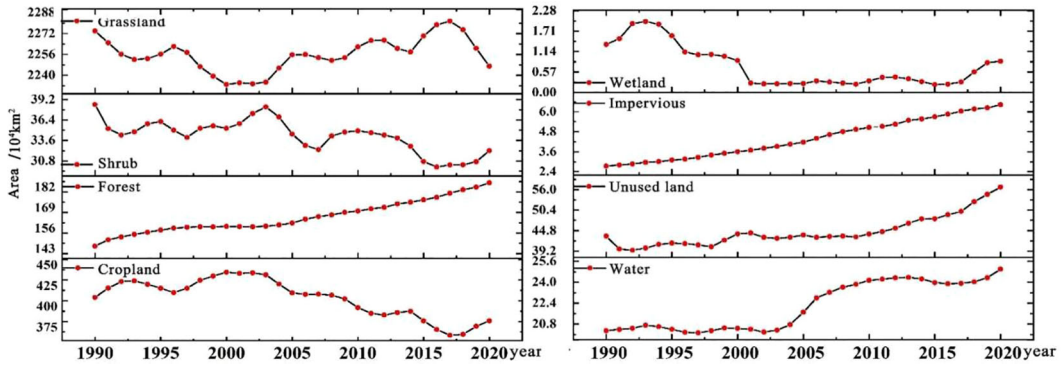

FIGURE 3
Area of land use types in the Gansu-Qinghai section of the Yellow River Basin from 1990 to 2020.

area of land use types moved outward by a total of 2.45 × 10^4 km^2 between 1990 and 2000 (Figure 4A), making up 8.36% of the total area. With a total transfer area of 9.19 × 10^3 km^2, the conversion of grassland into agricultural land was the most significant in terms of size. The conversion of farmland to a grassy area came after that, with a total transfer area of 6.08 × 10^3 km^2. The transfer from wetland to forest land had the smallest total transfer area, at 0.08 km^2. From 2000 to 2010 (Figure 4B), a total of 1.89 × 10^4 km^2 of various types of land were transferred outward, accounting for 6.46% of the total area, and the largest transferred area was still uncultivated land transferred to grassland, with a total transfer of 8.73 × 10^3 km^2, and the transfer area from water to wetland was the smallest, with a total transfer of 0.04 km^2. From 2010 to 2020 (Figure 4C), a total of 2.22 × 104 km^2 was transferred outward, accounting for 7.57% of the total area. This showed that grassland area transferred from cultivated land was the largest, with a total transfer of 8.18 × 10^3 km^2, then the process of transforming a grassy terrain into an area suitable for agriculture, with a total transfer of 6.88 × 10^3 km^2, and the conversion of land from construction to forest was the least significant, with a total transfer of 0.04 km^2.

Between 1990 and 2020 (Figure 4D), there was a transfer of different types of land use amounting to 3.36 × 10^4 km^2, which is

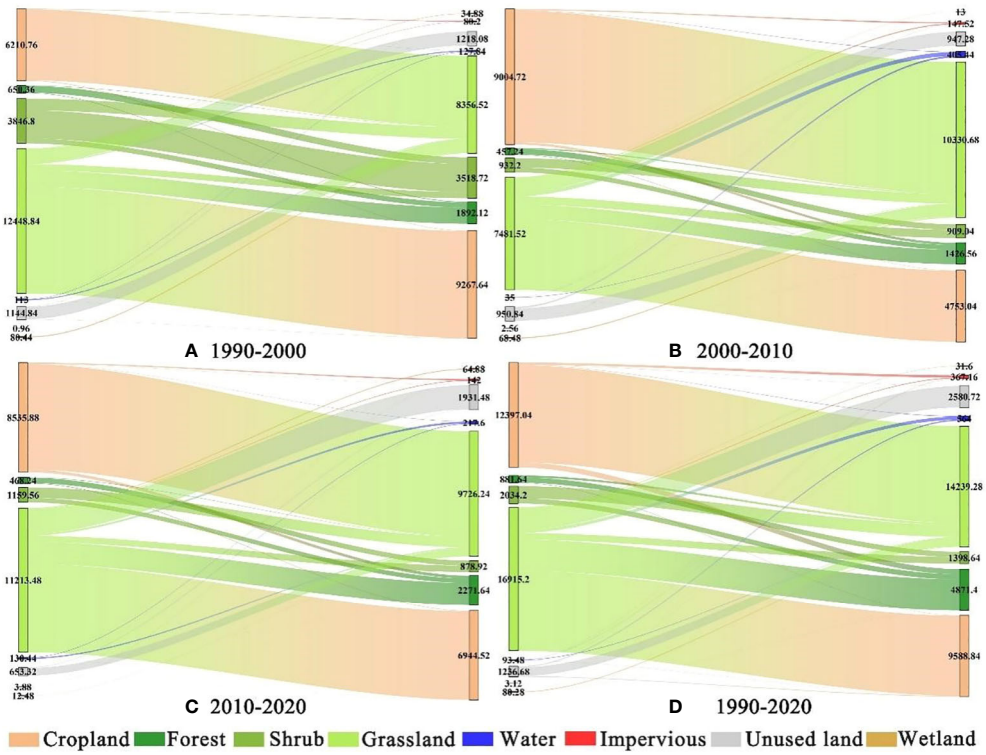

FIGURE 4
Sangki map of land use transfer in the Gansu-Qinghai section of the Yellow River Basin from 1990 to 2020 (**A**. land use transfer of 1990–2000; **B**. land use transfer of 2000–2010; **C**. land use transfer of 2010–2020; **D**. land use transfer of 1990–2020).

equivalent to 11.48% of the total area. The largest area that was transferred was cultivated land, measuring 1.14×10^4 km^2, while the smallest area was undeveloped land converted to construction land, which was only 0.04 km^2.

According to Figure 5, the Gan-Qing section of the Yellow River Basin is divided by the Qinghai-Tibet Plateau and the Loess Plateau excess zone. The main land use type in the west is forest and grass land, and the main land use type in the east is cultivated land and construction land. From 1990 to 2020, the construction land exhibited a point-line expansion trend, mainly concentrated in in Lanzhou and Xining, the provincial capitals of Gansu and Qinghai provinces The cultivated land is mainly distributed in the Loess Plateau area of Gansu Province. It is concentrated in the Above the Baoji Gorge of Weihe River basin and Above the Zhangjiashan of Jinghe River and the east area of Daxia River and Taohe River. In the past 30 years, the cultivated land showed a decreasing trend, this was because urban construction land was rapidly expanding, causing a substantial amount of cultivated land to be occupied, and significant changes in land use patterns. The main land use type in the Ganqing section of the Yellow River Basin is grassland. It is widely distributed in Heyuan to Maqu basin, Maqu to Longyangxia basin, Above the Xiangtang of Datong River basin, Huangshui River basin, Daxia River and Taohe River basin The River basin. The forest land is distributed in the form of sheet or line. It is mainly located in the Above the Xiangtang of Datong River basin, Huangshui River basin, Daxia River and Taohe River basin, and the Main stream section of the transitional zone between the Qinghai-Tibet Plateau and the Loess Plateau Longyangxia to Lanzhou and Above the Zhuangtou of Beiluo River basin, mainly distributed in Heyuan to Maqu Basin and Maqu to Longyangxia Basin, Qinghai Province. It mainly includes Qinghai Lake, Zhaling Lake, Eling Lake, Longyangxia Reservoir and Liujiaxia Reservoir. The unused land is mainly distributed in the Maqu to Longyangxia basin.

3.2 Temporal and spatial changes of habitat quality in the Ganqing section of the Yellow River Basin from 1990 to 2020

The average values of habitat quality from 1990 to 2020 were obtained by using the weighted average, which was 0.745, 0.744, 0.741, 0.743, 0.747, 0.748, and 0.747 (Table 4). This result showed that the overall habitat quality in the Gansu-Qinghai Yellow River is constantly increasing, and the changing trend is initially decreasing, then increasing, and subsequently decreasing. According to research, the habitat quality in various years is categorized into five grades based on the InVEST model: higher (0.8–1), high (0.6–0.8), medium (0.4–0.6), low (0.2–0.4), and lower (0–0.2). The overall habitat quality in the Ganqing section of the Yellow River Basin was in a higher grade (> 0.7). From 1990 to 2020, the ratios of lower, low, and high-grade habitat quality in the Gansu-Qinghai Yellow River have been increasing, with an increase of 0.579%, 2.615%, and 2.105%, respectively, in the past 30 years. The ratios of medium and high grades of habitat quality decreased continuously, by 3.568% and 1.740%, respectively. Among them, the areas with

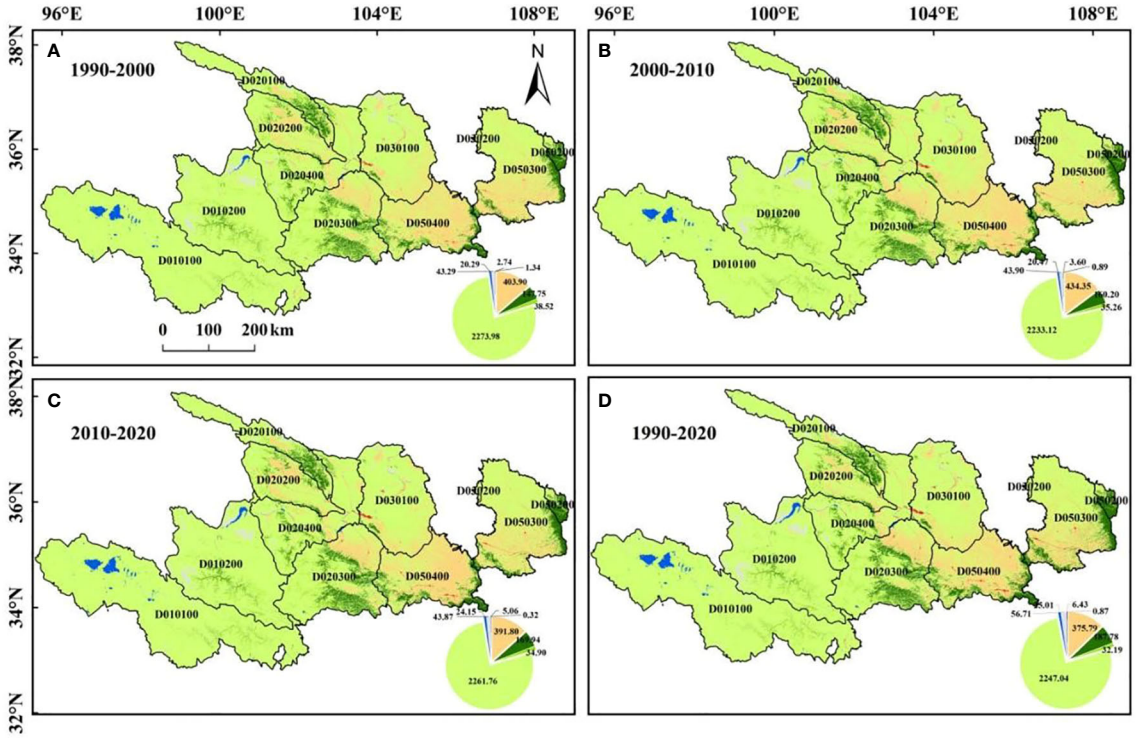

FIGURE 5
Land use types in the Gansu-Qinghai section of the Yellow River Basin from 1990 to 2020.(**A**. land use type of 1990–2000; **B**. land use of type of 2000–2010; **C**. land use type of 2010–2020; **D**. land use type of 1990–2020).

10.3389/fevo.2023.1228558

TABLE 4 Ratio of Habitat quality Grade in Gansu-Qinghai Reach of the Yellow River Basin from 1990 to 2020 (%).

Grade	Domain	1990	1995	2000	2005	2010	2015	2020
		ratio/%	ratio/%	ratio/%	ratio/%	ratio/%	ratio/%	ratio/%
Low	0–0.2	1.56	1.51	1.61	1.62	1.66	1.82	2.14
Lower	0.2–0.4	6.97	7.69	7.78	8.11	8.63	8.93	9.59
Medium	0.4–0.6	6.71	6.37	6.93	5.76	4.64	3.80	3.14
Higher	0.6–0.8	45.30	44.75	44.96	44.87	45.10	46.13	47.40
High	0.8–1	38.79	39.00	38.04	38.96	39.29	38.63	37.05
Mean		0.745	0.744	0.741	0.743	0.747	0.748	0.746

low habitat quality continue to increase, indicating that with the intensification of urbanization, the habitat quality in some areas continues to deteriorate. In addition, the continuous increase of higher-level areas shows that China's conversion of farmland to forests and grassland projects and other ecological restoration projects have achieved significant results.

In terms of time (Figure 6), the general habitat quality of the Gansu-Qinghai Yellow River showed a fluctuating upward movement from 1990 to 2020, with the lowest habitat quality in 2000 at 0.741 and the highest in 2017 at 0.751. Within the tertiary river systems of the Yellow River Basin (as depicted in Figures 6B–D), the watershed with the highest habitat quality is above the Beiluo River Zhuangtou, with a habitat quality of around 0.9, whereas the watershed with the lowest habitat quality is the watershed above the Baoji Gorge of the Weihe River, with habitat quality around 0.6. The watersheds of Qingshui River and Kushui River had obvious habitat quality modifications that occurred 30 years ago, and the transformation pattern was fluctuating initially and then increased with an obvious rising trend. The habitat quality of the watershed from Lanzhou to Xiaheyan and the watershed above Zhangjiashan of the Jinghe River showed a fluctuating upward trend, while the habitat quality of the other sub-basins did not change much in the past 30 years.

In terms of space, the overall habitat quality of the study area presents a spatial feature of high in the west and low in the east, with the transitional zone between the Qinghai-Tibet Plateau and the Loess Plateau as the dividing line. The overall habitat quality of the east region is lower, while that of the west region is higher

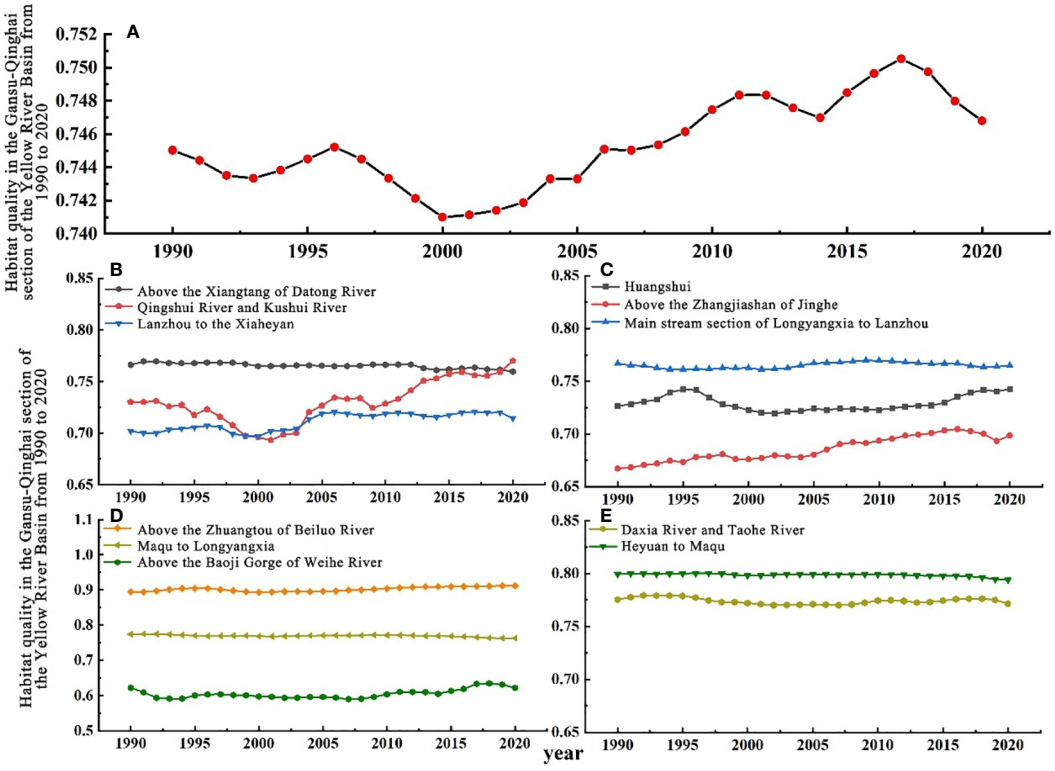

FIGURE 6
Habitat quality in the Gansu-Qinghai section of the Yellow River Basin from 1990 to 2020 **(A)** and habitat quality changes in different sub-basins **(B–E)**.

(Figure 7), which is basically consistent with the spatial characteristics of land use type. The low grade habitat quality areas were concentrated in Lanzhou City of Gansu Province and Xining City of Qinghai Province. This region is the capital city of Gansu Province and Qinghai Province, with high population and economic density, frequent human activities, large construction land area, and poor habitat quality. The lower grade and medium grade habitat quality areas were concentrated in the northeast of the study area. Including the Above the Zhangjiashan of Jinghe basin, the Above the Baoji Gorge of Weihe River basin and the area east of the Daxia River and Taohe River, The overall level of economic development in this region is relatively high, the main land type is cultivated land, and human activities have a great disturbance to the habitat. The regions with high habitat quality are mainly distributed in the Heyuan to Maqu and Maqu to Longyangxi basins in the upper reaches of the Yellow River Basin, and the distribution is relatively concentrated. In the Maqu to Longyangxia Basin, there are scattered areas with lower grade habitat quality. The ecological fragility in this region makes the habitat quality easily disturbed and destroyed, especially the distribution of unused land in this region, which is the main reason for the low habitat quality. In this region, the quality of habitat changed from higher grade to high grade and from lower grade to middle and high grade.

From 1990 to 2020, habitat quality change in the Gansu-Qinghai Yellow River section showed that the gain area was slightly smaller than the loss area. The gain area was 12.55 × 10^4 km^2 and the loss area was 16.76 × 10^4 km^2. There is a lot of spatial heterogeneity as evidenced by the alteration in the quality of the living environment. While the quality of habitat in the central and western regions is declining, it has improved significantly in the east (Figure 8D). the areas with significant loss of habitat quality were mainly distributed in the Daxia River and Taohe River basins and Above the Baoji Gorge of Weihe River basins, which were the areas with faster urbanization. Loss predominated the alteration in the quality of the living environment between 1990 and 2000 (Figure 8A), with the loss area reaching 20.27 × 10^4 km^2 or 75.31% of the total area. It was concentrated in Gansu Province in space, including the southern part of the Lanzhou to the Xiaheyan Basin, the eastern part of the Daxia River and Taohe River basin, and most of the Above the Baoji Gorge of Weihe River basin. The gain area is scattered., with a total area of 9.04 × 10^4 km^2. Habitat quality increased significantly between 2000 and 2010 (Figure 8B), with a gain area of 20.38 × 10^4 km^2 compared to a loss area of 8.93 × 10^4 km^2. It is distributed in the upper reaches of the Yellow River basin, Huangshui Basin, Above the Baoji Gorge of Weihe River basin and other river basins. From 2010 to 2020 (Figure 8C), the habitat quality declined significantly, with the gain area reaching 10.41 × 10^4 km^2 and the loss area reaching 18.90 × 10^4 km^2. From a spatial point of view, the western portion of the study region's overall habitat quality is declining, but the degree of loss is not high, as the loss in the central area is relatively high and mainly concentrated in the surrounding cities of Lanzhou City,

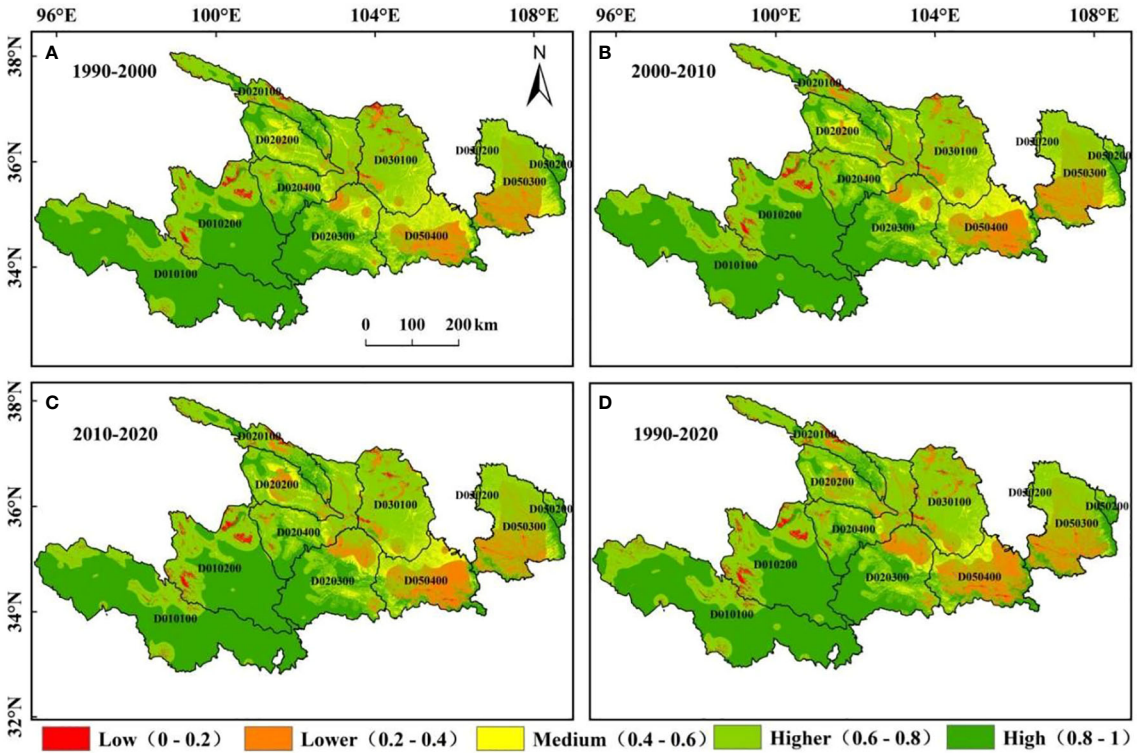

FIGURE 7
Spatial distribution of habitat quality in Gansu-Qinghai section of theYellow River Basin from 1990 to 2020 (**A**. spatial distribution of habitat quality 1990–2000; **B**. spatial distribution of habitat quality 2000–2010; **C**. spatial distribution of habitat quality 2010–2020; **D**. spatial distribution of habitat quality 1990–2020)

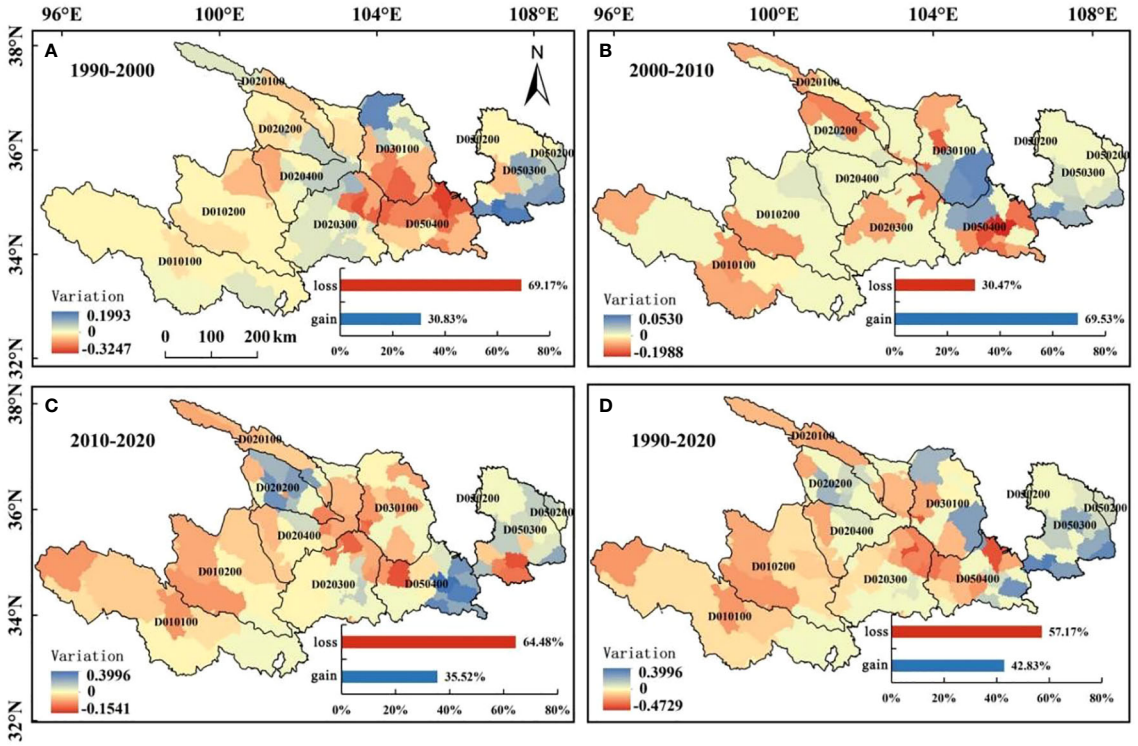

FIGURE 8
Spatial distribution of habitat quality changes in the Gansu-Qinghai section of the Yellow River Basin from 1990 to 2020. (**A**. habitat quality change of 1990–2000; **B**. habitat quality change of 2000–2010; **C**. habitat quality change of 2010–2020; **D**. habitat quality change of 1990–2020).

Gansu Province. Areas with obvious gains include Tianshui City and the eastern part of Qinghai Province.

3.3 Simulation of land use change in the Gansu-Qinghai section of the Yellow River Basin under multiple scenarios

The simulation effect of land use change in the Gansu-Qinghai Yellow River section in 2020 was enhanced. As a result, the spatial distribution pattern of land use in Gansu-Qinghai Yellow River in 2030 was simulated using the land use types in the Gansu-Qinghai Yellow River in 2020.

Therefore, construct natural development scenarios (NADS), cultivated land protection scenarios (COPS), ecological protection scenarios (ECPS), and rapid development scenarios (RADS), respectively set up different transition matrices, and combine the land use type files of the Gansu-Qinghai Yellow River in 2020 to conduct cellular automaton analysis, and then predict 2030 Spatial pattern of land use in the Gansu-Qinghai Yellow River.

Based on the settings of the above four development scenarios, the land use distribution in the Gansu-Qinghai Yellow River in 2030 was simulated, and the land use structure in 2030 and the difference between the land use area in 2020 and the land use area in 2020 under the four scenarios were obtained through the spatial module of ArcGIS. It can be seen from Table 5 that under the natural development scenario, the area of simulated grassland, shrubland, and unused land in 2030 decreased by 1321.72 km^2, 254.62 km^2, and 256.23 km^2 compared to 2020; the area of construction land decreased by 99.72 km^2, and the wetland area decreased by 1.08 km^2. The areas of water area, forest land, and cultivated land increased by 1171.30 km^2, and 82.81 km^2, 679.26 km^2, respectively, and the condition of the ecosystem in the river basin appeared to have been enhanced.

According to the scenario of protecting cultivated land, the area of cultivated land increased by 679.34 km^2, with a corresponding increase in its proportion by 1.80%. Moreover, there were increases in the areas of forest and water by 82.81 km^2 and 1097.63 km^2 respectively. However, the area of construction land only slightly increased by 28.49 km^2. Grassland, water area, wetland, and shrubland all saw decreases in the area of 822.88 km^2, 1321.72 km^2, 310.68 km^2, and 1.27 km^2, respectively.

In the scenario of ecological protection, the protection of ecological land (that is, forest land, water area, grassland, and wetland) is the most important goal, thus the simulated forest land area in 2030 increased by 1675.83 km^2, and grassland, water area, and wetland increased by 448.32 km^2, 82.81 km^2, and 3.25 km^2, and in total, there was a reduction of 257.08 km^2 in the amount of land designated for construction. The primary reason for the expansion of ecological land was the transfer of farmland and undeveloped land, which decreased by 1358.55 km^2 and 546.67 km^2, respectively.

Under the scenario of rapid development, the extension of construction land is the basic symbol of rapid economic

TABLE 5 Land use area under four scenarios in the Gansu-Qinghai section of the Yellow River Basin in 2030 and the difference between land use area in 1990 and 2020/km ^{2}.

Land use type	NADS		COPS		ECPS		RAPS	
	2030	2020–2030	2030	2020–2030	2030	2020–2030	2030	2020–2030
Cultivated land	38465	679.26	38465.12	679.34	36427.23	−1358.55	38465.13	679.35
Forest land	19543.1	1171.3	19469.44	1097.63	20047.64	1675.83	19791.63	1419.82
Shrub	3029.44	−254.62	3029.46	−254.6	3236.16	−47.9	3029.46	−254.6
Grassland	223944	−1321.72	223943.84	−1321.72	225713.88	448.32	223943.77	−1321.78
Water	2626.11	82.81	2626.11	82.81	2626.11	82.81	2554.89	11.6
Unused	4934.94	−256.23	4880.48	−310.68	4644.49	−546.67	4644.48	−546.68
Construction land	550.74	−99.72	678.95	28.49	393.38	−257.08	664.3	13.83
Wetland	87.8	−1.08	87.62	−1.27	92.14	3.25	87.35	−1.53

development. Construction land now covers a larger area of 13.83 km^2. The arable land area increased by 679.35 km^2, while the shrub land area shrank by 254.60 km^2. Wetland area and undeveloped land area both fell by 546.68 km^2 and 1.53 km^2, respectively.

The Gansu-Qinghai Yellow River's land use simulation results for 2030 under each of the four scenarios revealed an increase in the area of ecologically beneficial land, such as water area, forest land, and wetland, while a decrease in the area of economically beneficial land, such as cultivated land and unused land. The river basin's ecological environment is steadily improving into a healthy state.

3.4 Characteristics of habitat quality changes in the Gansu-Qinghai section of the Yellow River Basin under multiple scenarios

With regards to the process of growth that occurs without human intervention, the mean values of habitat quality in 1990, 2020, and 2030 are 0.745, 0.747, and 0.748, showing a rising trend. Compared with 2020 (Table 6), the ratios of lower, low, and high grades of habitat quality in the Gansu-Qinghai Yellow River section have been decreasing and then increased by 0.27%, 0.10%, and 2.00% respectively in the past 10 years. The ratios of medium and high grades increased continuously, increasing by 0.49% and 2.56% respectively. The area with low habitat quality has increased, suggesting that the natural environment in the majority of the watershed's locations tends to be better as time goes by, indicating that various ecological restoration projects in China will achieve significant results in the study area. Compared with 1990, the ratios of low, lower, higher, and high grades are all increasing by 0.31%, 2.52%, 0.10%, and 0.82%, respectively. The proportion of the middle class is decreasing, by 3.08% in 40 years.

The average habitat quality values for the three scenarios—cultivated land protection, ecological protection, and rapid development—were, in that order, 0.748, 0.753, and 0.748. On average, the ecological protection scenario had the best quality of habitat, whereas the rapid development and cultivated land protection scenarios had the lower average quality of habitat. The mean value of habitat quality under the protection of cultivated land scenario and the rapid development scenario is not significantly different because, under the rapid development scenario, the demand for cultivated land is second only to that of construction land, and the area of construction land in the study area is small. According to the ecological protection scenario, only 9.01% of the watershed's total area is made up of low and lower grades in the study area, while 39.53% of the watershed's total area is made up of high grades. Under the ecological protection scenario, the watershed has a high level of habitat quality.

TABLE 6 Ratio of habitat quality levels (%) in Gansu-Qinghai section of the Yellow River Basin under four scenarios.

Grade	Domain	1990	2020	NADS	COPS	ECPS	RAPS
		ratio/%	ratio/%	ratio/%	ratio/%	ratio/%	ratio/%
Low	0–0.2	1.56	2.14	1.87	1.9	1.72	1.89
Lower	0.2–0.4	6.97	9.59	9.49	9.91	7.29	9.85
Medium	0.4–0.6	6.71	3.14	3.63	3.21	5.13	3.29
Higher	0.6–0.8	45.3	47.4	45.4	45.46	46.11	45.47
High	0.8–1	38.79	37.05	39.61	39.53	39.75	39.5
Mean		0.74503	0.7468	0.74829	0.74802	0.75287	0.74817

Under the four scenarios from 2020 to 2030, habitat quality changes in the Gansu-Qinghai Yellow River section showed that the gain area is greater than the loss area. In the NADS (Figure 9A), the gain area occupies 57.23% of the entire watershed area, totaling 16.77×10^4 km^2, while the loss area accounts for 42.77% of the watershed area, amounting to 12.54×10^4 km^2. Significant spatial heterogeneity in habitat quality was evident. While it decreased in the western and central regions, habitat quality in the northeast was noticeably improved. The habitat quality of Above the Baoji Gorge of Weihe River basin, Daxia River and Taohe River basin have significant loss. This area is a densely populated area in Gansu and Qinghai provinces, and the increase of construction land is relatively obvious, which reduces the quality of habitat. In the COPS (Figure 9B), the change in habitat quality was dominated by gain, and the gain area accounts for 53.49% of the total area. The change in habitat quality under the ECPS (Figure 9C) was a result of all gains. In terms of space, the areas with a higher degree of gain is the Loess Plateau region. Including Lanzhou to the Xiaheyan Basin, Above the Baoji Gorge of Weihe River basin, Above the Zhangjiashan of Jinghe basin, Huangshui basin. During the fast development period depicted in Figure 9D, 80.27% of the entire watershed area experienced an improvement in habitat quality, while the remaining 19.73% suffered a decline in habitat quality. From a spatial point of view, although most regions within the examined territory are experiencing growth, the degree of gaining is not high. The areas with the most obvious gains is in the northern part of Lanzhou to the Xiaheyan Basin.

4 Discussion

4.1 Analysis of influencing factors of habitat quality

In this paper, 10 natural factors and 6 socioeconomic factors were selected, and the influence degree of 16 factors on habitat quality was explored through a random forest model, and the spatial resolution of each factor and habitat quality was unified as 100 m × 100 m. According to Figure 10, the Gansu-Qinghai Yellow River region is more affected by natural factors than socioeconomic ones when it comes to habitat quality. The most significant factor that affects habitat quality is NDVI, and its impact is significantly greater than other factors. In addition to NDVI, the higher degree of impact on habitat quality was as follows: PRE, DEM, DFG, TEM, POP, TR, DFRL, DFRO, GDP, TI, ST, Slope, and the degree of influence was not much different. Factors with low impact on habitat quality are slope, PX and OLS.

4.2 Comparative analysis of the results of related studies

To solve the ecological problems of the Gansu-Qinghai Yellow River section, China has introduced many policies and renovation projects. For example, in 2005, the State Council approved the implementation of the "Overall Plan for Ecological Protection and

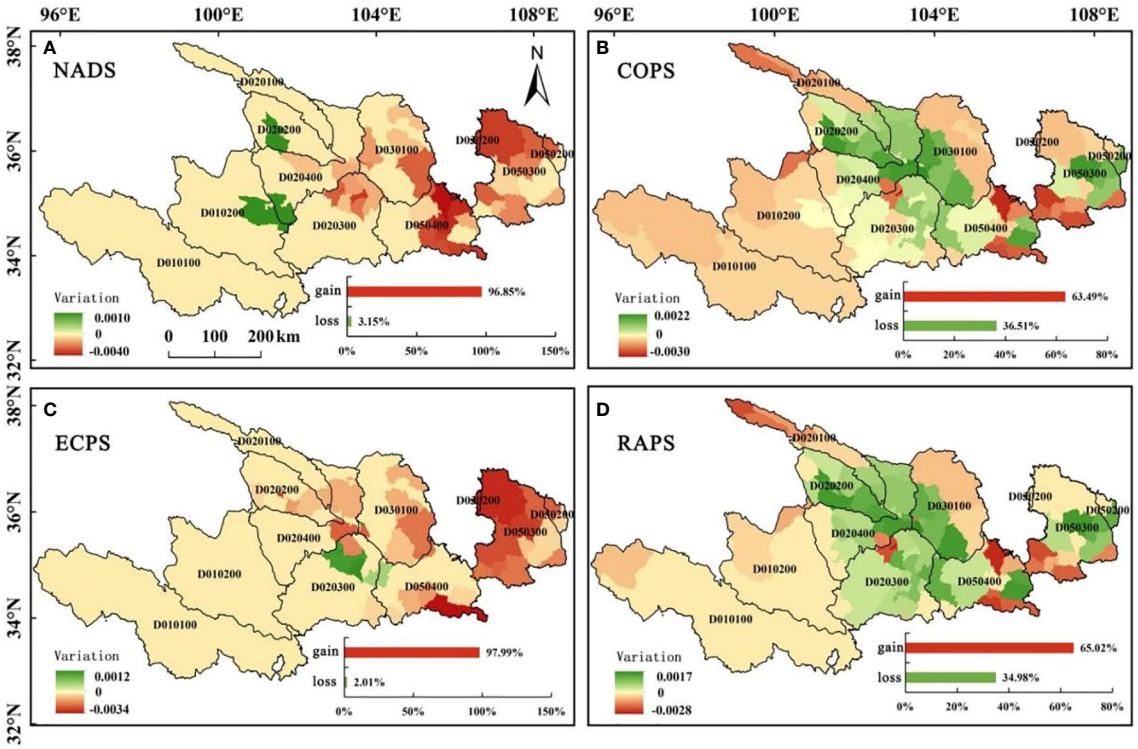

FIGURE 9
Changes in habitat quality in Gansu-Qinghai section of the Yellow River Basin from 2020 to 2030. (**A**. habitat quality of Natural development scenario; **B**. habitat quality of Ecological protection scenario; **C**. habitat quality of Ecological protection scenario; **D**. habitat quality of Rapid development scenario).

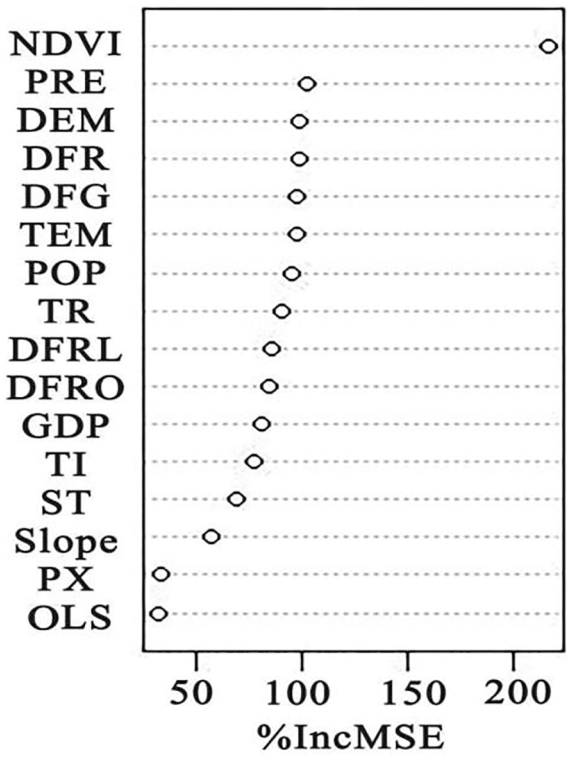

FIGURE 10
Extent of impact of habitat quality drivers.

Construction of the Sanjiangyuan Nature Reserve in Qinghai" to rectify the ecological problems in the Sanjiangyuan area. The implementation of the "Three North Project" on the Loess Plateau (LP) has improved the natural environment of the LP area, increased forest coverage, and solved ecological problems such as soil erosion on the LP. It is precise because of the implementation of these renovation projects and the continuous strengthening of human protection of the ecological environment that the habitat quality of the Gansu-Qinghai Yellow River section has been significantly improved, which is the lowest inflection point of habitat quality in 2000 in this study. This is consistent with the improved results and also reflects the significant achievements China has made in the governance of the region. The findings are comparable to the study conducted by Zhang et al. (2021) that examined the changes in the ecological conditions within the Yellow River Basin.

According to the results of this investigation, it was observed that there was a noteworthy reduction in the standard of living in the research zone during 2017 and that the change in habitat quality from 1990 to 2020 generally showed that the area of the degraded area was greater than that of the gaining area, and the area of the habitat degraded area was higher than that of the optimized area. This research result is similar to the result that Ren et al. (2022) pointed out that the habitat quality will decline from 2015 to 2020 in the study of ecosystem services in the Yellow River Basin's middle reaches. The reason for this phenomenon may be that although projects such as returning farmland to grasslands and forests have played a crucial part in enhancing the ecological environment's quality in the early stage, as time goes by, some disadvantages will also occur. Excessive vegetation restoration may not bring continuous optimization of the ecological environment but will cause unfavorable competition among various vegetation types, resulting in the death of a large number of understory vegetation and the reduction of habitat quality according to Lin et al. (2020). This study also confirmed that ecological environmental problems may occur in the long-term project of converting farmland to grass (forest). As a result, it's crucial to develop a sensible plan for land use that is founded on the utilization of land, to enhance the quality of the Gansu-Qinghai Yellow River's habitat, reduce the damage to natural landscapes such as grassland, forest land, and lake wetlands, increase investment in wetland restoration, and form a scientific effective ecological protection mechanism, but at the same time, it is necessary to eliminate the negative effects caused by over-protection.

The habitat quality level in 2030 under the four scenarios of the Gansu-Qinghai Yellow River section will be ECPS > NADS > RADS > COPS. The variation in land use within the study area could be responsible for the slightly higher average habitat quality in the fast-paced development scenario compared to the scenario where land is protected for cultivation. Conversely, 0.22% of the Yellow River Basin's total area is made up of construction land in the Gansu-Qinghai section, while 10% of the basin's total area is made up of cultivated land. Thus, the expansion of the RADS is not strong. Judging from the coupling results of habitat quality and land use change in various simulated scenarios, the ECPS has the best coupling and coordination improvement effect. The RADS can be selected for the development model of the stage, but the conversion of different land uses must be strictly implemented according to the conversion principle matrix established in the simulation scenario; if the future policy guidance of the basin focuses on ecological benefits, the ECPS can be selected.

4.3 The limitations of this research

This study has shortcomings. First of all, it is the first attempt to estimate the habitat quality based on the annual China Land Cover Dataset (CLCD) produced by two professors Yang and Huang of Wuhan University on the GEE platform. The determination of the sensitivity coefficient of the threat source is obtained by referring to several works of literature, and it is not a specific coefficient obtained for this research area. Additionally, the intricate procedure of altering the purpose of the land is impacted by various natural and socio-economic factors that propel it forward. Even though a variety of land use types are affected significantly by these factors, in this study, a total of 15 natural socio-economic factors were chosen as the driving factors for simulating the future land use pattern. The final simulation result is highly accurate and the land use type has a good fitting effect, but it ignores the influence of policy factors like the ecological protection red line, the permanent basic farmland boundary, and the urban development boundary on land use change.

5 Conclusions

This study investigates the characteristics of land use change and spatial and temporal patterns of habitat quality in ecologically fragile areas on a long-term scale. At the same time, 15 factors such as natural society are selected to influence the habitat quality, and finally explore the features of future land use and habitat quality changes in the study area from four perspectives: cultivated land protection scenario, natural development scenario, rapid development scenario, and ecological protection scenario. The main conclusions obtained were:

(1) Grassland is the main land use type in the Ganqing section of the Yellow River Basin, accounting for over 70% of the total area. Cultivated land and forest land respectively account for about 13% and 6% of the basin. From 1990 to 2020, the area of construction land and forest land showed an increasing trend year by year, while the area of unused land and water area showed a fluctuating increasing trend. The overall area of cultivated land, wetlands, grasslands, and shrublands showed a fluctuating decreasing trend. The Ganqing section of the Yellow River Basin is roughly divided by the transitional zone between the Qinghai Tibet Plateau and the Loess Plateau in space. The main land use types to the west are forests and grasslands, and to the east are farmland and construction land.

(2) The habitat quality of forests, grasslands, and water bodies in the Ganqing section of the Yellow River Basin is high, while the habitat quality of cultivated land and construction land is low. From 1990 to 2020, the habitat quality of the Ganqing section of the Yellow River Basin decreased slightly and then increased. Over the past 30 years, the change in habitat quality showed that the gain area was slightly smaller than the loss area, and the overall habitat quality improved, showing spatial heterogeneity of "enhanced in the east and weakened in the central and western regions".

(3) Compared to 2020, under the four scenarios, the area of arable land, forest land, and water area significantly increased in 2030, while the area of grassland and unused land decreased. Among them, the increase in construction land was significant under the scenarios of arable land protection and rapid development. Under the four scenarios, the habitat quality of the Ganqing section of the Yellow River Basin continues to improve, manifested as a decrease in the area of low value areas and a significant increase in the area of high value areas. Among them, the average habitat quality is the highest under the ECPS, while it is relatively low under the COPS and the RAPS.

Data availability statement

The original contributions presented in the study are included in the article/supplementary material. Further inquiries can be directed to the corresponding author.

Author contributions

JY: conceptualization, methodology, software, and writing—original draft preparation. BX: reviewing and editing. DZ: visualization and supervision. EM-M: Language proofreading. TP: Funding acquisition, Writing—review and editing. All authors contributed to the article and approved the submitted version.

Funding

This research was funded by the Gansu Agricultural University publicly introduced doctoral research start-up fund (GAU-KYQD-2017-35).

Conflict of interest

The authors declare that the research was conducted in the absence of any commercial or financial relationships that could be construed as a potential conflict of interest.

Publisher's note

References

Bai, L., Xiu, C., Feng, X., and Liu, D. (2019). Influence of urbanization on regional habitat quality:a case study of Changchun City. *Habitat Int* 93, 102042. doi: 10.1016/j.habitatint.2019.102042

Bongaarts, J. (2019). Summary for policymakers of the global assessment report on biodiversity and ecosystem services of the Intergovernmental SciencePolicy Platform on Biodiversity and Ecosystem Services. *Popul. Dev. Rev.* 45, 680–681. doi: 10.1111/padr.12283

Gao, L., Tao, F., Liu, R., Wang, Z., Leng, H., and Zhou, T. (2022). Multi-scenario simulation and ecological risk analysis of land use based on the PLUS model: a case study of Nanjing, Sustain. *Cities Soc* 85, 104055. doi: 10.1016/j.scs.2022.104055

Gomes, E., Inácio, M., Bogdzevi, K., Kalinauskas, M., Karnauskaitė, D., and Pereira, P. (2021). Future land use changes and its impacts on terrestrial ecosystem services: a review. *Sci. Total Environ.* 781, 147716. doi: 10.1016/j.scitotenv.2021.146716

Hall, L., Krausman, P., and Morrison, M. (1997). The habitat concept and a plea for standard technology. *Wildlife Soc. Bull.* 25 (1), 173–182. doi: 10.2307/3783301

Karimi, H., Jafarnezhad, J., Khaledi, J., and Ahmadi, A. (2018). Monitoring and prediction of land use/land cover changes using CA-Markov model: a case study of Ravansar County in Iran. *Arab. J. Geosci.* 11 (19), 592. doi:10.1007/s12517-018-3940-5

Liang, X., Guan, Q., Clarke, K., Liu, S., Wang, B., and Yao, Y. (2021). Understanding the drivers of sustainable land expansion using a patch-generating land use simulation (PLUS) model: a case study in Wuhan, China, Environ. *Urban Syst.* 85, 101569. doi: 10.1016/j.compenvurbsys.2020.101569

Liang, X., Liu, X., Li, X., Chen, Y., Tian, H., and Yao, Y. (2018). Delineating multi-scenario urban growth boundaries with a CA-based FLUS model and morphological method. *Landsc. Urban Plan.* 177, 47–63. doi: 10.1016/j.landurbplan.2018.04.016

Lin, Y., Li, Y., Yu, W., Bu, T., and Huang, R. (2020). Quantitative assessment of the impact of the vegetation restoration project on water-energy balance in 12 typical basins of the middle Yellow River. *Geographical Res.* 39 (11), 2593–2606. doi: 10.11821/dlyj020190744

Liu, Y., Huang, X., Yang, H., and Zhong, T. (2014). Environmental effects of land-use/cover change caused by urbanization and policies in Southwest China Karst area-A case study of Guiyang. *Habitat Int.* 44, 339–348. doi: 10.1016/j.habitatint.2014.07.009

Liu, X., Liang, X., Li, X., Xu, X., Ou, J., Chen, Y., et al. (2017). A future land use simulation model (FLUS) for simulating multiple land use scenarios by coupling human and natural effects. *Land. Urban Plann.* 168, 94–116. doi: 10.1016/j.landurbplan.2017.09.019

Liu, M., Zhang, Z., Sun., J., Li, Y., Liu., Yu, Ming, X., et al. (2020). Restoration efficiency of short-term grazing exclusion is the highest at the stage shifting from light to moderate degradation at Zoige, Tibetan Plateau. *Ecol. Indic.* 114, 106323. doi: 10.1016/j.ecolind.2020.106323

Mansoor, D. K., Leh, Marty, D., Eric, C., and Nalley, L. L. (2013). Quantifying and mapping multiple ecosystem services change in West Africa. *Agriculture Ecosyst. Environ.* 165, 6–18. doi: 10.1016/j.agee.2012.12.001

Nellemann, C. (2001). Global methodology for mapping human impacts on the biosphere. *UNEP/GRID-Arendal, United Nations Environment Programme*.

Ren, J., Zhao, X., Xu, X., Ma, P., and Du, Y. (2022). Spatial-temporal evolution, tradeoffs and synergies of ecosystem services in the middle Yellow River. *J. Earth Environ.* 13 (4), 477–490. doi: 10.7515/JEE222019

Sharp, R., Tallis, H. T., Ricketts, T., Guerry, A. D., Wood, S. A., Chapin-Kramer, R., et al. (2015). *InVEST 3.2.0 user's guide. The natural capital project, stanford university, university of minnesota, the nature conservanvy, and world wildlife fund*. Available at: http://www.naturalcapitalproject.org.

Tang, F., Wang, L., Guo, Y., Fu, M., Huang, N., Duan, W., et al. (2022). Spatio-temporal variation and coupling coordination relationship between urbanisation and habitat quality in the Grand Canal, China. *Land Use Pol.* 117, 106119. doi: 10.1016/j.landusepol.2022.106119

Vigerstol, K. L., and Aukema, J. E. (2011). A comparison of tools for modeling freshwater ecosystem services. *J. Environ. Manage.* 92 (10), 2403–2409. doi: 10.1016/j.jenvman.2011.06.040

Wang, Y., Fu, B., Luy, Y., Yang, K., and Che, Y. (2016). Aessment of the social values of ecosystem services based on SolVES model: a case study of Wusong PaoTaiwan Wetland Forest Park, Shanghai, China. *Chin. J. Appl. Ecol.* 27, 1767–1774. doi: 10.13287/j.1001-9332.201606.011

Wilson, M. C., Chen, X., Corlett, R. T., Didham, R. K., Ding, P., Holt, R. D., et al. (2016). Habitat fragmentation and biodiversity conservation: key findings and future challenges. *Landscape Ecol.* 31, 219–227. doi: 10.16251/j.cnki.1009-2307.2016.09.013

Wu, Q., Wang, L., Zhu, Y., Jin, H. Y., and Zhou, H. F. (2016). Nesting habitat suitability analysis of red-crowned crane in Zhalong Nature Reserve based on MAXENT modeling. *Acta Ecologica Sin.* 36 (12), 3758–3764. doi: 10.5846/stxb201410101997

Yang, J., and Huang, X. (2021). The 30 m annual land cover dataset and its dynamics in China from 1990 to 2019. *Earth Syst. Sci. Data* 13, 3907–3925. doi: 10.5194/essd-13-3907-2021,2021

Yang, Z., Zhang, F., and Wang, H. (2020). Analysis on the differences and its green development ways of ecologically fragile areas in China. *Ecol. Environ. Sci.* 29 (6), 1071–1077. doi: 10.16258/j.cnki.1674-5906.2020.06.001

Yohannes, H., Soromessa, T., Argaw, M., and Dewan, A. (2021). Spatio-temporal changes in habitat quality and linkage with landscape characteristics in the Beressa watershed, Blue Nile basin of Ethiopian highland. *J. Environ. Manage.* 281, 111885. doi: 10.1016/j.jenvman.2020.111885

Yu, J., Dong, H., Li, Y., Wu, H., Guan, B., Gao, Y., et al. (2014). Spatiotemporal distribution characteristics of soil organic carbon in newborn coastal wetlands of the Yellow River delta estuary: spatiotemporal distribution characteristics of soil organic carbon. *Clean: Soil Air Water* 42, 311–318. doi: 10.1002/clen.201100511

Zhang, J., Chen, K., Zhang, C., and Guo, P. (2021). The change characteristics of eco-environment in the Yellow River Basin based on entropy weights. *China Environ. Sci.* 41 (8), 3767–3774. doi: 10.19674/j.cnki.issn1000-6923.20210331.013

Zhang, X. R., Zhou, J., Li, G. N., Chen, C., Li, M. M., and Luo, J. M. (2020). Spatial pattern reconstruction of regional habitat quality based on the simulation of land use changes from 1975 to 2010. *J. Geographical Sci.* 30 (12), 601–620. doi: 10.1007/s11442-020-1745-4

Zhang, S., Zhou, Y., Yu, R., Xu, X., Xu, M., Li, G., et al. (2022). China's biodiversity conservation in the process of implementing the sustainable development goals (SDGs). *J. Clean. Prod.* 338, 130595. doi: 10.1016/J.JCLEPRO.2022.130595

frontiers | Frontiers in Ecology and Evolution

TYPE Original Research
PUBLISHED 28 September 2023
DOI 10.3389/fevo.2023.1208601

OPEN ACCESS

EDITED BY
Manoj Kumar,
Forest Research Institute (FRI), India

REVIEWED BY
Keshav Tyagi,
Forest Research Institute (FRI), India
Lingxue Yu,
Chinese Academy of Sciences (CAS), China

*CORRESPONDENCE
Quansheng Hai
66063@bttc.edu.cn

RECEIVED 03 May 2023
ACCEPTED 23 August 2023
PUBLISHED 28 September 2023

CITATION
Li X, Hai Q, Xia K, Vandansambuu B and Bao Y (2023) The biophysical effects of potential changes in irrigated crops on diurnal land surface temperature in Northeast China.
Front. Ecol. Evol. 11:1208601.
doi: 10.3389/fevo.2023.1208601

The biophysical effects of potential changes in irrigated crops on diurnal land surface temperature in Northeast China

Xintao Li[1], Quansheng Hai[2,3]*, Ke Xia[1], Battsengel Vandansambuu[2] and Yuhai Bao[4,5]

[1]School of Earth Sciences and Engineering, Hohai University, Nanjing, China, [2]Department of Geography, School of Arts and Sciences, National University of Mongolia, Ulaanbaatar, Mongolia, [3]Baotou Normal College, Inner Mongolia University of Science & Technology, Baotou, China, [4]College of Geographical Science, Inner Mongolia Normal University, Hohhot, China, [5]Inner Mongolia Key Laboratory of Remote Sensing & Geography Information System, Inner Mongolia Normal University, Hohhot, China

Irrigated crops have experienced a significant global expansion. The biophysical response of climate change to irrigated crop expansion in different regions, particularly in terms of monitoring the influence mechanism of nighttime land surface temperature (LST) change, however, remains insufficiently explored. Taking the three northeastern provinces of China as our study area, we apply window analysis, partial correlation analysis, and geographical detector to quantitatively characterize the spatial and temporal distribution pattern of daytime and nighttime LST (diurnal LST) and biophysical parameters, and the main driving mechanism of diurnal LST change. The results showed that irrigated crop expansion led to asymmetric changes in daytime (–2.11 ± 0.2°C, 97.4%) and nighttime (0.64 ± 0.2°C, 79.9%) LST. ΔLST_{DT} had a negative correlation with ΔLE (63%), but a positive correlation with ΔSSR and ΔH (91% and 77%). This revealed that the cooling effect caused by the superposition of the output latent heat flux and the absorbed solar shortwave radiation was greater than its heating effect. ΔLST_{NT} and ΔLE had a positive connection across 69% of the region. ΔLST_{NT} demonstrated a negative correlation with ΔSSR and ΔH in 82% and 75% of the regions, respectively. At this time, the superposition of latent heat flux and heating potential term produces a greater heating effect. The explanatory power of the single factor (the mean of q<0.50) of biophysical parameters for diurnal LST variation was significantly smaller than that of the interaction factor (the mean of q>0.50, p<0.01). This study shows more detailed dynamic information of diurnal LST and biophysical parameters from 8day scale. The findings highlighted the critical role of asymmetric changes in the diurnal surface thermal environment caused by irrigated crop expansion in the global climate from a land surface hydrothermal energy balance perspective.

KEYWORDS

biophysical parameters, water thermal energy balance, regional climate change, land use and cover, geo-detector model

1 Introduction

By 2050, the world population is expected to reach 9.2 billion, increasing the food demand by 70–110% (Bajželj et al., 2014; van Dijk et al., 2021). To ensure an adequate food supply in the future, intensive irrigated agriculture has been developing rapidly. The Food and Agriculture Organization of the United Nations (FAO) reports that as of 2017, there are approximately 167 million hectares of irrigated crops globally, of which more than 90% are located in Northeast Asia (Delzeit et al., 2017; FAO, 2018). The expansion of irrigated crops fundamentally alters the biogeochemical and biophysical (albedo, sensible heat flux, and latent heat flux) processes between the atmosphere and the land surface. It indirectly alters the seasonal cycle of carbon–water–energy of the land–atmosphere interface and plays a critical role in regulating the regional and global climate (Feddema et al., 2005; Windisch et al., 2021). Among these changes, the influence of biophysical processes on climate is more prominent at regional and short-time series scales (Arora and Montenegro, 2011; Zhang et al., 2014a), and these persistent changes in regional climates will threaten future grain yield (Liang et al., 2018; Gaupp et al., 2020). Therefore, understanding the regional climate effects of irrigated crop expansion from a mechanism perspective will provide a scientific basis for sustainable regional agriculture and food development.

Currently, observation data and model simulation are used mainly to study the influence of irrigated crop expansion on climate (Zhao et al., 2012; Zhu et al., 2012). Observational data, the most reliable *in situ* measurement method, are used to quantify the climate's response to irrigated crop expansion by comparing temperature differences between irrigated and rainfed crops or the differences before and after the conversion of rainfed crops to irrigated crops. However, the data essentially provide point information (Christy et al., 2006). Because of the complex land surface coverage conditions and significant terrain differences, point information cannot fully represent the large-scale situation of a region. In addition, the background information (e.g., the characteristics of the surrounding features) of irrigated crops of different sites is different. Therefore, it is difficult to distinguish temperature differences caused by a combination of irrigated crop expansion and other surrounding instabilities. Model research has compared the differences between the simulation results of different models (coupled or uncoupled) and the results of control experiments (Huang et al., 2009; Wei et al., 2016). Therefore, accurately simulating each sector of irrigation experiments is a crucial step toward achieving effective results. For example, the use of a climate-coupled model to simulate the response of temperature to global irrigation indicated that the intensity of irrigation cooling varied considerably regionally, which may have been caused by factors such as irrigation range and irrigation amount (Lobell et al., 2009). However, the quantitative description of the location, time, method, and number of irrigated crops remains uncertain. Therefore, we used the window-searching strategy proposed by previous studies to eliminate issues like inconsistent background information of climate observation data and uncertainties in the attribution of temperature changes caused by model simulations (Li et al., 2016). Within the same moving window, pairs can be used to calculate differences in land surface parameters between the study object and its surrounding land cover types. It is possible to ensure the consistency of climate background, environment, and topography of different land use and cover types within the window by setting up appropriately sized moving windows (Malyshev et al., 2015; Schultz et al., 2016; Winckler et al., 2017). This method, as a complementary method for investigating temperature change, is used to identify the effects of irrigated crop expansion on local land surface temperature (LST).

Previous studies have simulated the effect of irrigated crop expansion on contemporary climate using models and have concluded that the effect of irrigated crop expansion is negligible on a global average scale (Sacks et al., 2009). However, the effect of irrigated crop expansion has been significant on a regional scale, with varying results. In the humid tropics, for example, the expansion of irrigated crops has caused thermal effects both during the day and at night, whereas it is a source of cold during the day and a source of warmth during the night in arid and semi-arid areas, especially during the dry season (Adegoke et al., 2003; Yang et al., 2020). However, the relative magnitude of daytime cooling and nighttime warming varies by region(Zhu et al., 2011). In the North China Plain, the nighttime warming effect of irrigated crops is greater than the daytime cooling effect, which has increase the regional temperature (Chen and Jeong, 2018). Conversely, in Northeast China, the expansion of irrigated crops has led to more significant daytime cooling effect than the nighttime warming effect during the growing season, resulting in a cooler local region (Liu et al., 2018; Yu and Liu, 2019).

Current research focuses on the influence mechanism of LST change from two aspects: biogeochemical processes and biophysical parameters (Bonan et al., 1992). The former emits or absorbs greenhouse gases, such as carbon dioxide, methane, and nitrous oxide, directly affecting carbon emissions and sequestration in the atmosphere (Pongratz et al., 2010). Studies have revealed that the expansion of irrigated crops has increased greenhouse gas concentrations in the atmosphere, eventually leading to a rise in the average temperature during the growing season (Chen et al., 2013; Sun et al., 2017). The latter directly disturbs the surface energy and water balance by changing the surface albedo, evapotranspiration, roughness, and specific emissivity (Moon et al., 2020). The study of the response of biophysical parameters to irrigated crop expansion, however, remains limited, which is reflected mainly in the trade-off effect between the degree of influence of radiative and nonradiative processes during different growing seasons. It is generally accepted that albedo, latent heat flux, and sensible heat flux are the dominant factors of LST variation (Du et al., 2017; He et al., 2020). Daytime LST decreases during the early growing season (May–June), and this is mainly because the cooling effect of latent heat flux is greater than the warming effect of albedo. Daytime LST variation in July–September is influenced by the synergistic effect of albedo and latent heat flux (Liu et al., 2018; Liu et al., 2019b; Pan et al., 2020; Liu et al., 2022). Through temperature response models, it has been found that local nonradiative processes (i.e., evapotranspiration and sensible heat) dominate the daytime cooling of irrigated crops and that radiation processes (i.e., albedo) play a secondary role (Zhang et al., 2022). The contribution of nonradiative processes to the daytime LST variation had seasonal

characteristics. However, previous studies have only made a qualitative comparison of the relative contributions of radiative and nonradiative mechanisms to LST changes and the seasonal response of LST changes to energy factors remains controversial (Xin et al., 2020). Meanwhile, these studies have ignored the influence of superposition of energy factors (e.g., latent heat flux, solar incident shortwave radiation) on LST. Furthermore, the influence mechanism of nighttime LST change is more complex (Chen et al., 2022; Lian et al., 2022), and it has not been thoroughly discussed in prior research. We assessed the potential influencing factors of nighttime LST increase in terms of thermal inertia generated by net surface energy during the day and atmospheric inverse radiation at night caused by latent heat flux in this study.

The three eastern provinces of China are located in the hinterland of Northeast Asia, characterized by flat topography and abundant water and soil resources. Since the economic reforms in 1978, a large area of wetlands has been reclaimed to ensure the supply of national food production and to meet the demands of local economic development (Dong et al., 2016). A combination of these factors provided a natural experimental site for studying the mechanisms of climate change caused by the expansion of irrigated crops. In this study, we used the window-searching strategy to calculate the differences in surface parameters between irrigated crop and non irrigated crop to remove the influence of climatic background and topographic factors on LST changes. Then, we portrayed the spatial–temporal responses of daytime and nighttime land surface temperature (diurnal LST) changes to surface radiant energy (e.g., incident radiant energy, outgoing radiant energy, and net effect) quantitatively and comprehensively, from the perspective of surface energy superposition. This information has enriched the research system on the mechanism of the climate impact of irrigated crop expansion. Specifically, we examined the following: (1) How do latent heat flux, solar shortwave radiation energy, and heating potential term lead to the decrease of average daytime LST during the growing season? (2) What are the main controlling factors of the increase in nighttime LST? Are they direct effects on the nighttime LST increase? (3) On the spatial scale, which of the interaction effects of single-energy factor (first order) and double-energy factor (second order) has a higher degree of explanation for LST changes?

2 Materials and methods

2.1 Study area

The study area is located in high-latitudes of Northeast Asia, which cover Heilongjiang, Jilin, and Liaoning provinces (38.7–53.5°N, 121.1–123.6°E) (Figures 1A, B), with a total area of about 7.9×10^5 km^2. This region is at the junction of the cold temperate zone, mid-temperate zone, humid and semi-humid climate. This area is cold-dry in winter and warm-humid in summer. The annual average temperature is −3–10°C. The maximum temperature decreases each

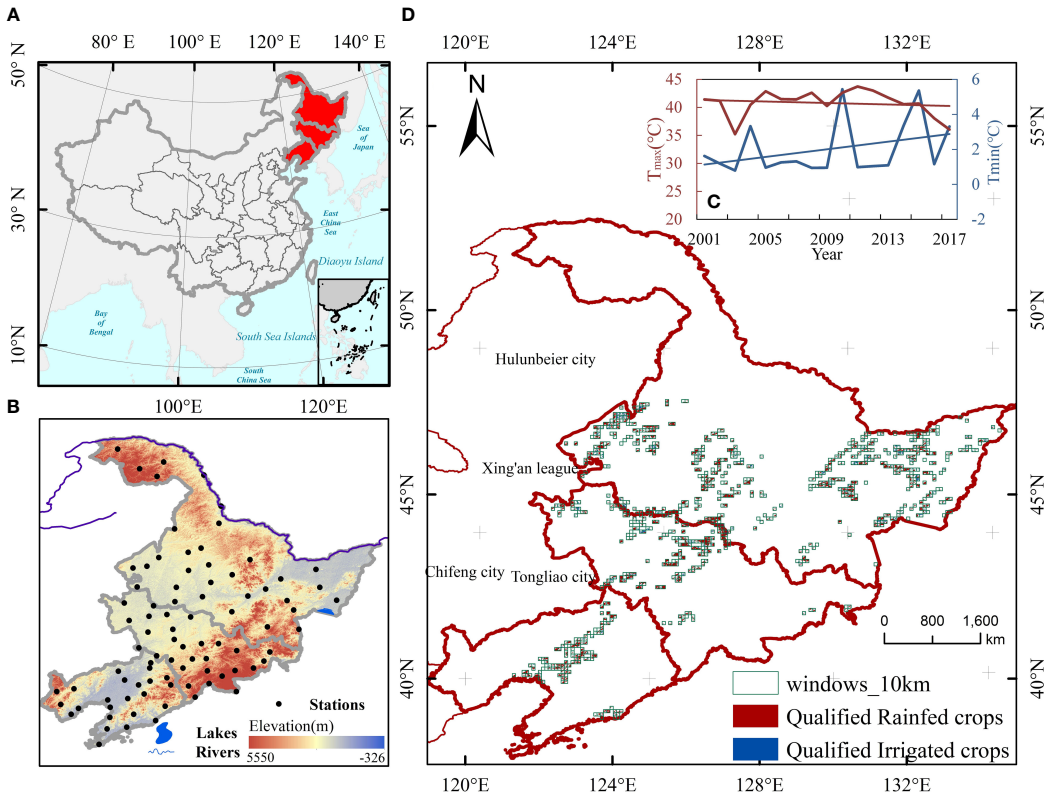

FIGURE 1
(A, B) Geographic location and elevation of Northeast China. **(C)** Climate situation of Northeast China since 2001. **(D)** Spatial distribution map of Irrigated crops expansion from 2015 to 2020.

year, while the minimum temperature increases during the period 2000–2020 (Figure 1C). The annual precipitation ranges between 400 and 1100 mm, with the majority falling between July and September. Its vast plains, fertile soil and sufficient water-heat state provide excellent natural conditions for the growth of single-season rice. The expansion rate of rice area during 2015–2020 is as high as 1.76×10^3 km^2/a (Figure 1D). The rapid development of intensive irrigated agriculture has made it an important commercial grain base in China.

2.2 Data and data processing

Land surface temperature (LST) data from the 8-day 1-km Terra/MODIS products (MOD11A2). As Terra/MODIS overpasses at around 10:30 and 22:30, which are close to the time of daily maximum and minimum air temperatures, so MOD11A2 LSTs at 10:30 and 22:30 were defined daytime LST (LST_{DT}) and nighttime LST (LST_{NT}), accordingly (Wan et al., 2015).

Latent heat flux (LE) is the flux of heat from the Earth's surface to the atmosphere that is associated with evaporation of water at the surface, and is estimated by Terra/MODIS Evapotranspiration/ Latent Heat Flux product (MOD16A2) that includes 500 m 8-day Evapotranspiration (ET), Latent Heat Flux (LE), Potential ET (PET) and Potential LE (PLE). MOD16A2 calculates global LE based on the Penman-Monteith (PM) equation, and its mean absolute bias is within 0.31–0.33 mm day^{-1} (Mu et al., 2011).

Albedo data are derived from 500 m daily albedo Model dataset (MCD43A3). The data include white-sky (directional hemispherical reflectance) and black-sky (dual hemispherical reflectance) albedos for seven MODIS individual bands and three broad bands (0.3–0.7 μm, 0.7–5.0 μm, and 0.3–5.0 μm) (Schaaf et al., 2002). As black-sky and white-sky albedo are highly correlated and have small difference, this study simply chooses white-sky albedo for 0.3–5.0 μm to indicate the total energy reflected by the earth surface.

Downward Shortwave Radiation (DSR) from Global Land Surface Satellite (GLASS), which is the world's first high spatial-temporal resolution radiation product (daily, 0.05°). It mainly uses multiple polar orbits and geostationary satellite data to establish cloudy and cloudless radiative transfer models based on the look-up table algorithm. Using MODIS band data and cloud products, the inversion results of two MODIS observation sensors are combined. The measured coefficient is good 0.83 and the root mean square error is 115.0 W m^{-2} (Zhang et al., 2014b).

The land use/cover data from 2015 to 2020 are derived from the China Cropping Pattern Map. This data is based on GlobeLand30 global cultivated land data, which use mapping algorithm of phenological and threshold of pixel purity, the first planting map of three major crops (rice, maize and wheat) in China based on 500 m MODIS was obtained. The overall classification accuracy was 89%, the kappa coefficient was 0.85, the rice producer accuracy was 93%, and the dryland was 83%–90% (Qiu et al., 2022). We mainly selected irrigated and rainfed crops by the following criteria, as described in the literature (Abera et al., 2019). Assuming six layers for 2015–2020, the dominant land cover type was assigned to each pixel through an automatic selection method, i.e., the ones in the six 500 m pixels should all belong to the same category, or else removed from our analysis. Ultimately, pixels with rice in all six layers for 2015–2020 were defined as irrigated crops, and pixels with corn in a single pixel in all six layers, wheat, or a pixel with both corn and wheat were defined as rainfed crops. Eventually, all products' temporal and spatial resolutions were unified to 1 km and 8-day scales, respectively. Additionally, the projection was unified to match the original projection of MODIS data to facilitate the calculation between products. See Table 1 for details of data products.

2.3 Methodology

This paper is mostly based on data from multiple remote sensing sources. Window-searching strategy is used to find irrigated crops and rainfed crops that have the same climate setting. On the basis of this, the spatial and temporal characteristics of diurnal land surface temperature and land surface biophysical parameters of rainfed crops and irrigated crops are examined. Lastly, by combining the pearson partial correlation analysis and the geo-detector model, the main

TABLE 1 Datasets summery and quality control.

Datasets	Description	Quality control	Resolution	Time
MOD11A2	Land surface temperature (LST at 10:30 and 22:30 local time)	Mandatory QA = 0, indicating good quality; Emiserror = 0, indicating average emissivity error ≤ 0.01; LST error=0, indicating average LST error ≤1K	1 km, 8-day	2015–2020
MOD16A2	Evapotranspiration (ET)	Quality control = 0, indicating good quality	500 m, 8-day	2015–2020
MCD43A1	Shortwave white sky Albedo	Mandatory QA = 0, indicating good quality with full BRDF inversions	500 m, Daily	2015–2020
GLASS	DSR	Overall coefficient of determination = 0.83 Bias = −6.5W m^{-2}, RMSE = 115.0W m^{-2}	0.05°, Daily	2015–2020
Maps of cropping patterns in China	Land use and cover	Overall accuracy = 89% Accuracy of paddy field = 93% Accuracy of rainfed crops = 83%–90%	500 m, year	2015–2020

biophysical mechanisms that cause the diurnal land surface temperature to change were studied on both the spatial and temporal scales. The exact process is shown in Figure 2.

2.3.1 Quantization impacts of irrigated crop expansion on land surface parameters

Land surface temperature: We assessed the biophysical impact on LST changes through hypothetical irrigated crop expansion, which does not happen in reality. This methodology was developed by evaluating the temperature change induced by afforestation and deforestation (Li et al., 2015). The potential impact of irrigated crops on LST was expressed as the LST difference between irrigated crops and nearby rainfed crops in 2015–2020:

$$\Delta LST_i = LST_{IC} - LST_{RC} \quad (1)$$

$$\Delta\overline{LST}_i = \overline{LST}_{IC} - \overline{LST}_{RC} \quad (2)$$

$$\delta LST = \Delta LST_{IC} - \Delta LST_{RC} \quad (3)$$

where i represents daytime (DT) or nighttime (NT); ΔLST_i ($\Delta\overline{LST}_i$) represents ΔLST_{DT}($\Delta\overline{LST}_{DT}$) or ΔLST_{NT}($\Delta\overline{LST}_{NT}$); LST_{IC} and LST_{RC} represent average daytime and nighttime LSTs in 2015–2020 for irrigated crops and rainfed crops, respectively (8 days in growing season); $\overline{LST}_{IC}$ and $\overline{LST}_{RC}$ represent monthly average (mean of ΔLST_i from May to October) daytime and nighttime LST in 2015–2020, respectively, and ΔLST_{IC} and ΔLST_{RC} represent the diurnal LST difference in irrigated crops and the diurnal LST difference in rainfed crops, respectively. Negative ΔLST_i ($\Delta\overline{LST}_i$) indicated the cooling effect of irrigated crops; otherwise, it indicated a warming effect. A negative δLST suggested that the diurnal LST difference was smaller in the irrigated crops compared to non-irrigated crops, and vice versa.

Intrinsic biophysical mechanics: We calculated the biophysical differences in solar shortwave radiation (SSR), latent heat flux (LE), and heating potential term (ΔH) between irrigated crops and nearby non-irrigated crops in the same way as the previous calculation. To directly compare the relative effects of surface radiant energy changes on ΔLST_i, which were caused by the difference between albedo and latent heat flux, we introduced the downward shortwave radiation (DSR). The solar shortwave radiation energy SSR (SSR = DSR (1-Albedo)), which was absorbed by the land surface, was calculated by DSR and albedo (Schultz et al., 2017). We refer to (Li et al., 2015) for the definition of a heating potential term as the difference in absorbed solar shortwave radiation and latent heat fluxes between irrigated crops and nearby non-irrigated crops in 2015–2020 is given by

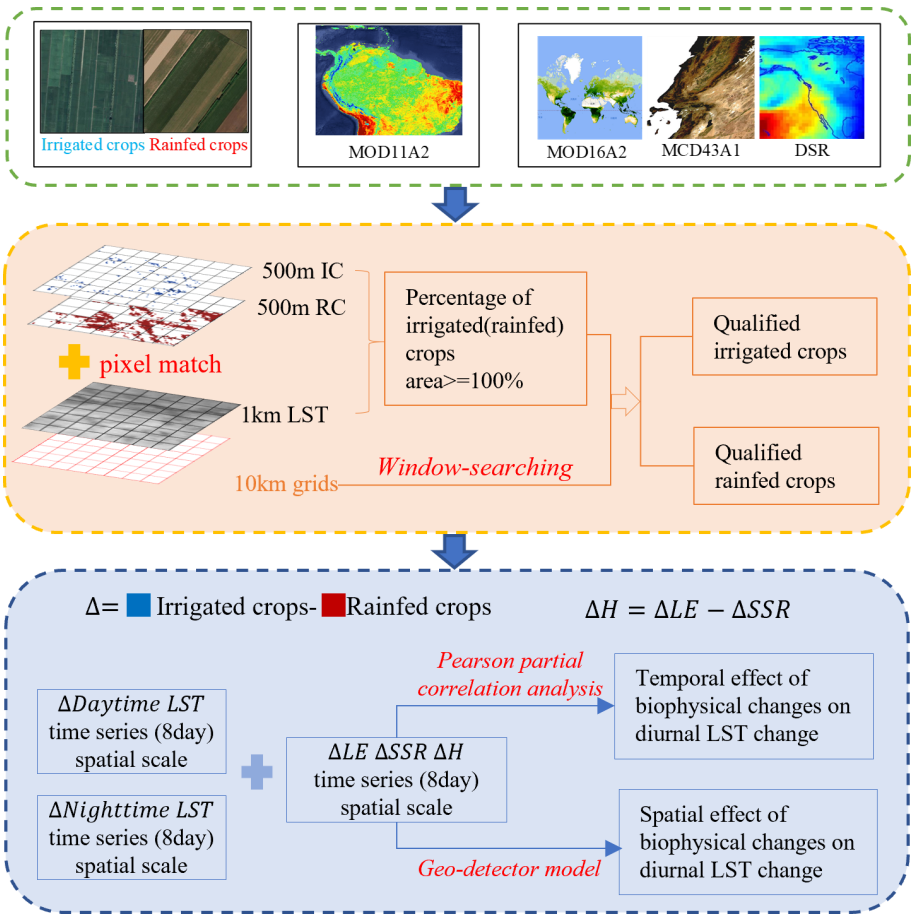

FIGURE 2
Flowchart of this study. IC, irrigated crops; RC, rainfed crops; LE, latent heat flux; SSR, solar shortwave radiation; H, heating potential term.

$$\Delta H = \Delta SSR - \Delta LE \quad (4)$$

$$\Delta \overline{H} = \Delta \overline{SSR} - \Delta \overline{LE} \quad (5)$$

where ΔSSR and ΔLE represent the difference in solar shortwave radiation energy and latent heat flux on the 8-day scale for irrigated crops and rainfed crops in 2015–2020, respectively; $\Delta \overline{SSR}$ and $\Delta \overline{LE}$ represent the monthly average (mean of ΔSSR and ΔLE from May to October) solar shortwave radiation energy and latent heat flux for irrigated crops and rainfed crops in 2015–2020, respectively. Negative ΔH ($\Delta \overline{H}$) indicated that the heating potential term absorbed and released by the irrigated crops was greater than that of the surrounding non-irrigated crops, and vice versa.

2.3.2 Window-searching strategy

Because the 1-km spatial resolution of MODIS products is relatively coarse, it might cause "mixed pixels" and add uncertainties of land surface parameters. To extract relatively pure MODIS pixels, we aggregated the 500-m land use and cover data with the 1-km MODIS LST resolution by calculating the area percentage of irrigated crops and rainfed crops within 1 km × 1 km grids and chose "pure" grids with an area percentage of 100% for irrigated crops (46,163 grids) and rainfed crops (34,797 grids).

We used the "window-searching strategy" to identify the relationship between surface energy parameters of irrigated crops and rainfed crops over a valid geospatial space range (Li et al., 2016; Shen et al., 2019). We defined a 10 km × 10 km moving window covering 100 1 km × 1 km pixels. If both the paddy field and rainfed crop pixels were located within one moving window, this was defined as a valid comparison sample, within which we could calculate the average ΔLST_{DT}, ΔLST_{NT}, ΔLE, ΔSSR, and ΔH.

For the potential impact of irrigated crop expansion, the total number of valid windows was 802 (Figure 1C). The window-searching strategy guaranteed that irrigated crop and rainfed crop pixels within the surrounding neighborhood were under similar climate forcing and minimized the uncertainties of local environment backgrounds (e.g., terrain, elevation wind, MODIS viewing zenith angle).

2.3.3 Spatio-temporal correlation analysis

Pearson partial correlation analysis: The variation of land surface biophysical parameters was the main factor affecting the variation of diurnal LST at the local scale. We used the Pearson partial correlation analysis method to explore the individual effects of latent heat flux, solar shortwave radiation energy, and heating potential term changes on diurnal LST changes on the temporal scale during the growing season. These results revealed the essential characteristics of diurnal LST warming and cooling changes (Umair et al., 2020).

Geo-detector model: Geo-detector is a statistical method used to reveal the driving factors behind by spatial heterogeneity. In this study, our core idea was that the spatial distribution of the two factors with correlation would be similar and mainly runs the model in R studio environment. We used the factor detector and the interactive detector to judge the spatial effect of the change of a single-surface energy factor and the interaction of the change of two-surface energy factors on the diurnal LST changes (Zhu et al., 2020). This degree of explanation is measured by the q-value, and the statistical model is as follows:

$$q = 1 - \sum_{n=1}^{m} N_n \sigma_n^2 / \sum_{n=1}^{m} N_n \sigma_n^2, \quad (6)$$

where n = 1, …, m indicates the subregions (irrigated crops (46163 grids) and rainfed crops (34797 grids)) of variable ΔLST_{DT} (ΔLST_{NT}) or ΔLE (ΔSSR and ΔH); $N_n$was the number of moving windows for the entire region (802); σ_n^2 and σ^2 indicate the variances of n of subregions and the whole area, respectively. Larger q-values indicate a stronger explanatory power of driver variation on diurnal LST variations, while the opposite indicates that the explanatory power is weaker; $q = 1$ indicates that the change of driving factors completely controls the spatial distribution of diurnal LST variations, and the explanatory power reaches 100%.

The factor detector determined the main controlling factor of LST changes mainly by judging the relative magnitude of q-values of multiple single factors. The interaction detector compared the relative magnitudes of q-values of two single factors (e.g., ΔLE, ΔSSR) and two single-factor interactions (e.g., $\Delta LE \cap \Delta SSR$) to determine the type of interaction (divided into five categories) Table 2.

3 Results

3.1 Temporal response of LST and biophysical parameters to irrigation crop expansion

We identified the differences between irrigated crops and rainfed crops in the process when the underlying surface releases latent heat flux and absorbs solar shortwave radiation energy. To reflect the change in the surface energy signal of the prospective growth of irrigated crops, we quantitatively assessed the differences in diurnal LST, latent heat flux, net solar shortwave radiation energy, and

TABLE 2 Interaction detector classifications.

q Value comparison	Interaction	Defined of interaction
q(X1∩X2) <Min(q(X1), (X2))	Non-linear weakening	NLW
Min(q(X1), (X2)) <q(X1∩X2) <Max(q(X1), (X2))	Single-factor nonlinear attenuation	SFNA
Max(q(X1), (X2)) <q(X1∩X2)	Two-factor enhancement	TFE
q(X1∩X2) =q(X1) + (X2)	Independent	IE
q(X1) + (X2) <q(X1∩X2)	Non-linear enhancement	NIE

10.3389/fevo.2023.1208601

heating potential term of irrigated crops and rainfed crops in 2015–2020. During the growing season, the daytime (10:30) and nighttime (22:30) LST differences showed asymmetry (Figures 3A, B). Among these differences, the daytime LST average decreased by 2.11 ± 0.21°C, whereas it increased by 0.64 ± 0.19°C at nighttime, and the daytime cooling range was significantly bigger than the nightly warming range (1.47°C). The order of ΔLST_{DT} was as follows: the early growing season (−3.56 ± 0.27°C) > the mid-growing season (−1.35 ± 0.21°C) > the late-growing season (−1.34 ± 0.16°C). The temporal variation characteristics of ΔLST_{NT}were consistent with those of ΔLST_{DT}, which reached the maximum value (1.98 ± 0.25°C) in the early growing season and the minimum value (−0.76 ± 0.15°C) in the late-growing season. The average values of ΔLST_{IC} and ΔLST_{RC} were 9.03°C and 11.78°C, respectively, and the average value of δ *LST* was −2.75 ± 0.23°C. The main reason for the decrease in ΔLST_{IC} was that irrigated crops were subjected to both daytime cooling and nighttime warming (Figure 3C).

The average difference of latent heat fluxes was 4.05 ± 1.01 W m^{-2} (Figure 3D). This reached its maximum during the mid-growing season (10.35 ± 1.02 W m^{-2}), and the sign of average values of the early growing season (6.01 ± 0.78W m^{-2}) and late-growing season (−3.50 ± 0.92 W m^{-2}) were opposite. The average difference of solar shortwave radiation energy was 2.49 ± 3.12 W m^{-2}. The maximum difference (11.23 ± 3.44 W m^{-2}) in the early growing season was significantly larger than the average value of the entire growing season, whereas the average difference in other months was −2.18 ± 3.02 W m^{-2}. The mean value of the difference of SSR during the whole growing season was greater than zero (Figure 3E). The average difference in heating potential term for DOY = 121–177, was 5.22 ± 2.17 W m^{-2}. The difference of surface heating potential term was the smallest in the late-growing season (0.01 ± 2.94 W m^{-2}; Figure 3F), because the absorbed solar shortwave radiation and the latent heat flux that was released by the surface were similar.

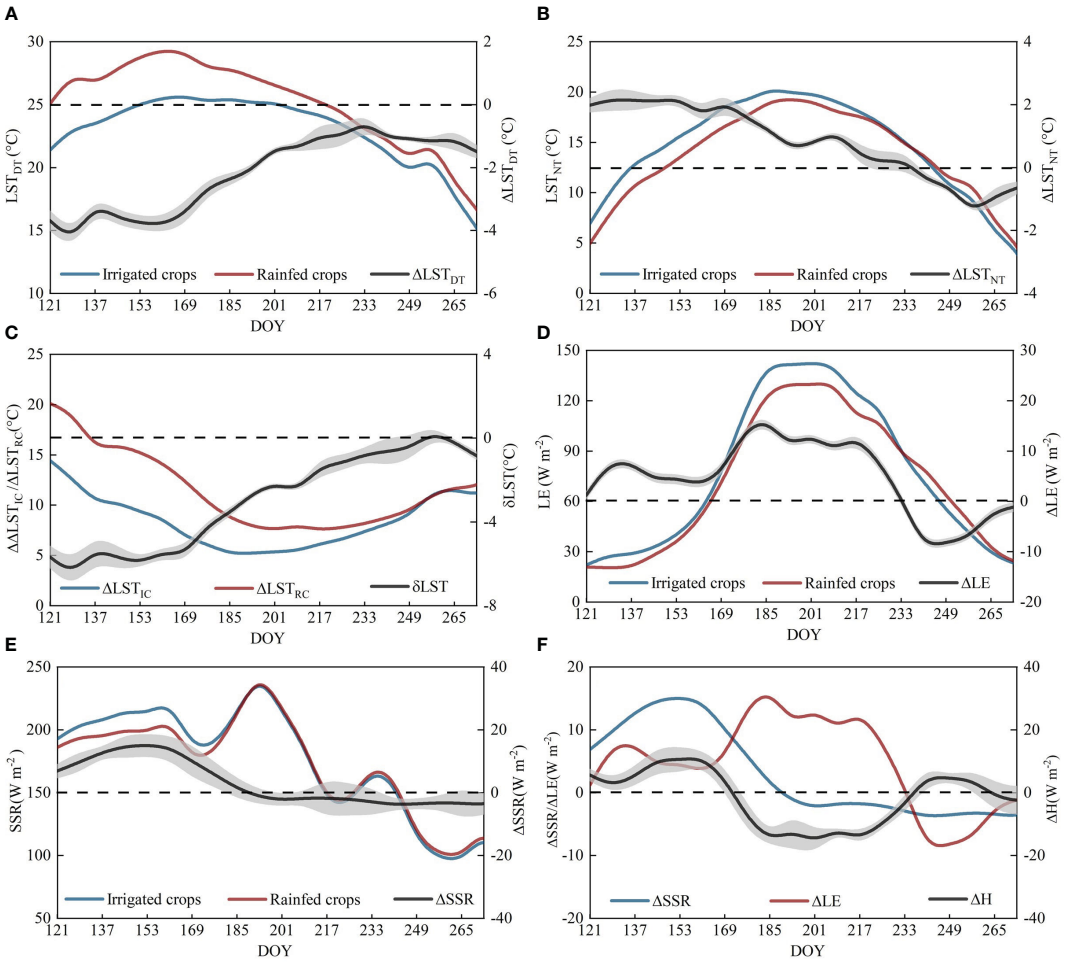

FIGURE 3
Mean 8-day cycle of land surface parameters of irrigated crops and the adjacent rainfed crops, and their differences during the growing season of 2015–2020. **(A)** Daytime LST, **(B)** nighttime LST, **(C)** diurnal LST, **(D)** latent heat flux (LE), **(E)** solar shortwave radiation (SSR), **(F)** heating potential term (H). Grey shadows represent standard deviation.

3.2 Spatial response of LST and biophysical parameters to irrigation crop expansion

We observed significant spatial differences in multiyear mean daytime and nighttime LST of irrigated and rainfed crops in 2015–2020. $\Delta\overline{LST}_{DT}$showed an overall high in the west and low in the east (Figure 4A), with a mean value of −2.11°C, which was concentrated in the range of −3°C to 1°C (Figure 4B). In more than 62% of the regions, the $\Delta\overline{LST}_{DT}$was between −2°C and −5°C. Compared with low latitudes, the daytime LST of irrigated crops decreased significantly at high latitudes. The $\Delta\overline{LST}_{NT}$in the eastern region was slightly lower than that in the western region (Figure 4C), with a mean value of 0.64°C, which was concentrated in the range of −2°C to 2°C. In more than 77% of the regions, the $\Delta\overline{LST}_{NT}$ was between 0°C and 1°C (Figure 4D). Similarly, $\Delta\overline{LST}_{NT}$was bigger in the high latitudes than that in the low latitudes, which mainly showed a warming effect. Because of the low temperature at high latitudes, the non-irrigated crops entered the growing season late. Low latitudes, on the other hand, are close to the ocean, and heavy rainfall during the growing season reduces the surface heat difference between paddy fields and drylands.

From May to October, the ΔLST_{DT} showed a gradual decrease (Table 3), with a maximum difference (−3.7±0.3) in May (the early irrigation period) and a minimum difference (−0.9±0.3) in August (the vegetation bloom period). The ΔLST_{NT}trended upward and then downward, with the greatest difference in June and the smallest difference in September.

We also observed differences in the spatial distribution of $\Delta\overline{LE}$, $\Delta\overline{SSR}$, and $\Delta\bar{H}$ of irrigated crops and rainfed crops in 2015–2020 (Figures 5A, C, E). The change patterns of $\Delta\overline{LE}$, $\Delta\overline{SSR}$ and $\Delta\bar{H}$ were similar, and all showed a weak decreasing trend with an increase in latitude. $\Delta\overline{LE}$ was more than zero in 70.2% of the locations, and $\Delta\overline{SSR}$ was more than zero in 80.6% of the areas. During the entire growing season, irrigated crops released and absorbed less heating potential term than rainfed crops, and the percentage of heating potential term reduction regions was 53.2% (Figures 5B, D, F).

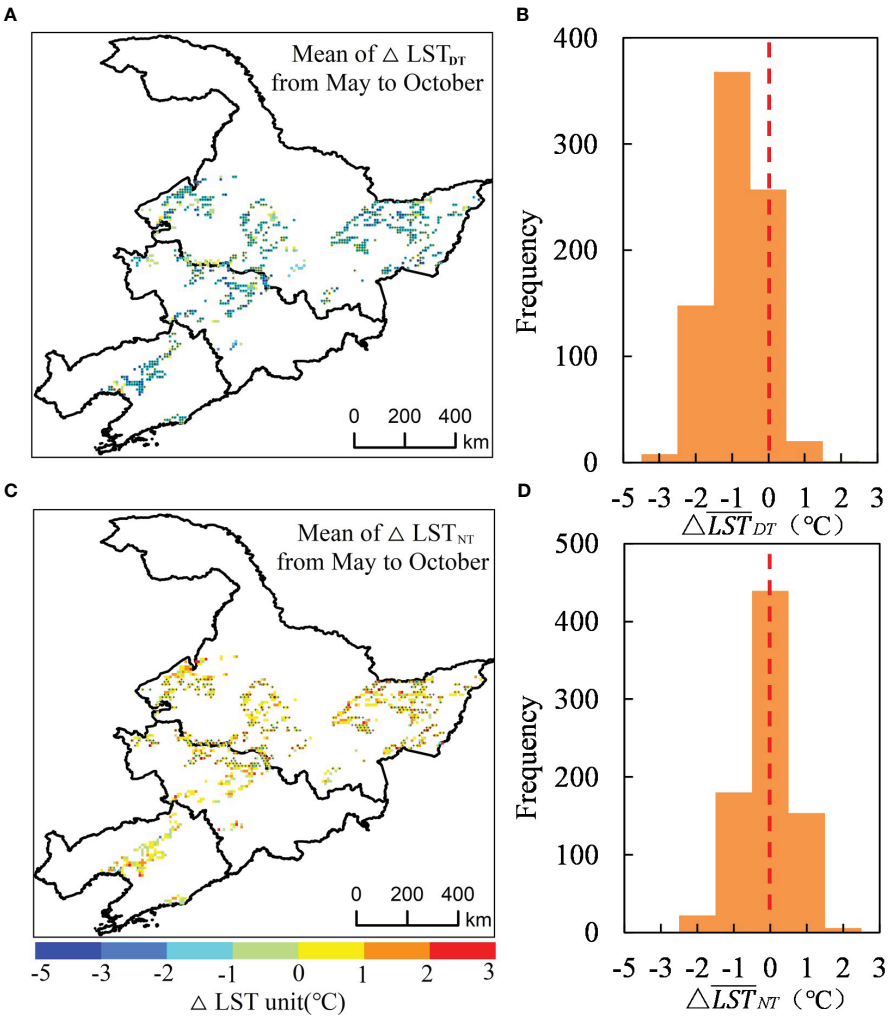

FIGURE 4
The land surface temperature differences of spatial patterns, latitudinal distributions, and frequency histograms of irrigated crops and the adjacent rainfed crops during the growing season of 2015–2020. **(A, B)** The spatial distribution map and the histogram of $\Delta\overline{LST}_{DT}$. **(C, D)** The spatial distribution map and the histogram of $\Delta\overline{LST}_{NT}$. Grids with crosses indicate that the differences are significant at 95% by t-test, grey shadows represent standard deviation.

TABLE 3 The monthly average of ΔLST_{DT} and ΔLST_{NT} ($\pm SD$°C).

	May	June	July	August	September	October
ΔLST_{DT}	−3.7±0.3	−3.4±0.3	−1.8±0.1	−0.9±0.3	−1.2±0.2	−1.5±0.1
ΔLST_{NT}	2.1±0.3	1.9±0.2	0.9±0.1	0.1±0.3	−0.9±0.2	−0.6±0.1

The extreme values of ΔLE and ΔSSR appeared in opposite months (Table 4). ΔLE reached the maximum in July (12.7± 0.9 W m^{-2}) and the minimum in October (0.2±0.9 W m^{-2}). The value of ΔSSR reached its highest point in June (11.4±4.2 W m^{-2}) and its lowest point in July (−1±2.4 W m^{-2}). The heating potential term difference was determined by a combination of latent heat flux and solar shortwave radiation energy.

3.3 Biophysical spatiotemporal driving mechanism of diurnal LST change

3.3.1 Temporal effect of biophysical changes on diurnal LST change

We used latent heat flux and solar shortwave radiation energy and their summation to directly determine the change characteristics of LST. On the seasonal scale, ΔLE was negatively correlated with ΔLST_{DT} , which accounted for 63% of the area (Figure 6A); furthermore, 15% of the regions had highly significant negative correlation. This research demonstrated that when ΔLE between irrigated and rainfed crops grew, so did ΔLST_{DT}. In May–August, the latent heat flux released by irrigated crops was much greater than that released by rainfed crops ($\Delta LE > 0$), resulting in a cool effect, while $\Delta LE < 0$ from September to October. Finally, the average daytime LST of irrigated crops was lower than that of rainfed crops during the growing season. Thus, it indicates that the strong cooling effect of latent heat flux in May–August offsets the weak heating effect in September–October. We observed a positive correlation between ΔSSR and ΔLST_{DT}, which accounted for 91% of the area (Figure 6B), and indicated that the greater the difference in solar shortwave radiation energy, the greater the difference in daytime LST. Compared with rainfed crops, irrigated crops absorbed more solar shortwave radiation energy in May–June, and less in July–October. However, the ΔLST_{DT} was still less than zero, indicating that the cooling effect of high latent heat flux offset the weak warming effect of low solar shortwave radiant energy. ΔH was positively correlated with ΔLST_{DT}(Figure 6C), which accounted for 77% of the area. The $\Delta H < 0$ in entire growing season, eventually produced a cooling effect. This finding revealed that there was a lag effect in the impact of land surface energy.

On the seasonal scale, ΔLE was positively correlated with ΔLST_{NT}, and its area accounted for 69% of the total (Figure 6D). Highly significant positive correlation and substantial positive correlation accounted for 44.6% and 24.4% of the total. This result indicated that with an increase in ΔLE, its ΔLST_{NT} gradually increased. ΔSSR and ΔLST_{NT} were inversely associated, as were ΔH and ΔLST_{NT}, and their regions accounted for 82% and 75%, respectively (Figures 6E, F). Thus, as ΔSSR and ΔH increased, the ΔLST_{NT} decreased steadily. From May to October, irrigated crops had a higher average latent heat flux and a lower average cumulative heating potential term throughout the day than rainfed crops. Finally, irrigated crops provided nighttime warmth. This result showed that the warming effect of latent heat flux was greater than the cooling effect of daytime-accumulated heating potential term. Therefore, the asymmetry of daytime and nighttime LST variation was caused mainly by the different controlling factors of land surface energy.

3.3.2 Spatial effect of biophysical changes on diurnal LST change

The physical energy of surface components and surrounding ground types underwent lateral exchange. Changes in latent heat flux, solar shortwave radiant energy, and heating potential term factor and their interactions on spatial scales directly determined the spatial distribution patterns of daytime LST changes. As shown in Table 5, the single-factor ΔLE and ΔSSR had the strongest explanatory power for the spatial distribution of ΔLST_{DT}in September (q=0.57, p<0.01) and October (q=0.43, p<0.01), respectively, whereas ΔH had significant explanatory power in all of May–October; the mean of the q-value was 0.45.

The latent heat flux, solar shortwave radiant energy, and heating potential term were superimposed, and their interaction also determined ΔLST_{DT}. The effect of interaction factors was significantly greater than the single factor effect (Table 5, Figure 7A), and their q-values were all greater than 0.5. Overall, $\Delta LE \cap \Delta H$ had a more significant effect on ΔLST_{DT} than $\Delta LE \cap \Delta SSR$, whereas $\Delta SSR \cap \Delta H$ had the slightest impact. The trends of the monthly variation of the explanatory power of interaction factors on ΔLST_{DT} were consistent, and all of them peaked in August (q=0.92, 0.85, and 0.84). Among these factors, $\Delta LE \cap \Delta SSR$ had non-linear enhancement throughout the growing season, whereas both $\Delta LE \cap \Delta H$ and $\Delta SSR \cap \Delta H$ had two-factor and non-linear enhancements over the growing season (Figure 7B).

Corresponding to the time scale, at the spatial scale, changes in the land surface energy factor affected the $\Delta LST_{NT}$to a lesser extent than the ΔLST_{DT}, due to the cumulative transfer in time weakened the effects of land surface energy factor. The explanatory power of the single components ΔLE, ΔSSR, and ΔH for the nighttime LST rise was best in August (q = 0.39, 0.3, and 0.56) and poorest in September, all with a q-value of 0.1. (Table 6). The ΔH at the surface was also the primary determining element for nighttime irrigated crop warming.

The explanatory power of the interaction factor on the ΔLST_{NT} was significantly greater than the single-factor effect (Table 6, Figure 8A). Consistent with the influence mechanism of the ΔLST_{DT}, $\Delta LE \cap \Delta H$ had a greater degree of action on ΔLST_{NT} than $\Delta LE \cap \Delta SSR$. The explanatory power of the interaction factors was the strongest in August (q=0.71, 0.82, and 0.80) and the weakest in June

10.3389/fevo.2023.1208601

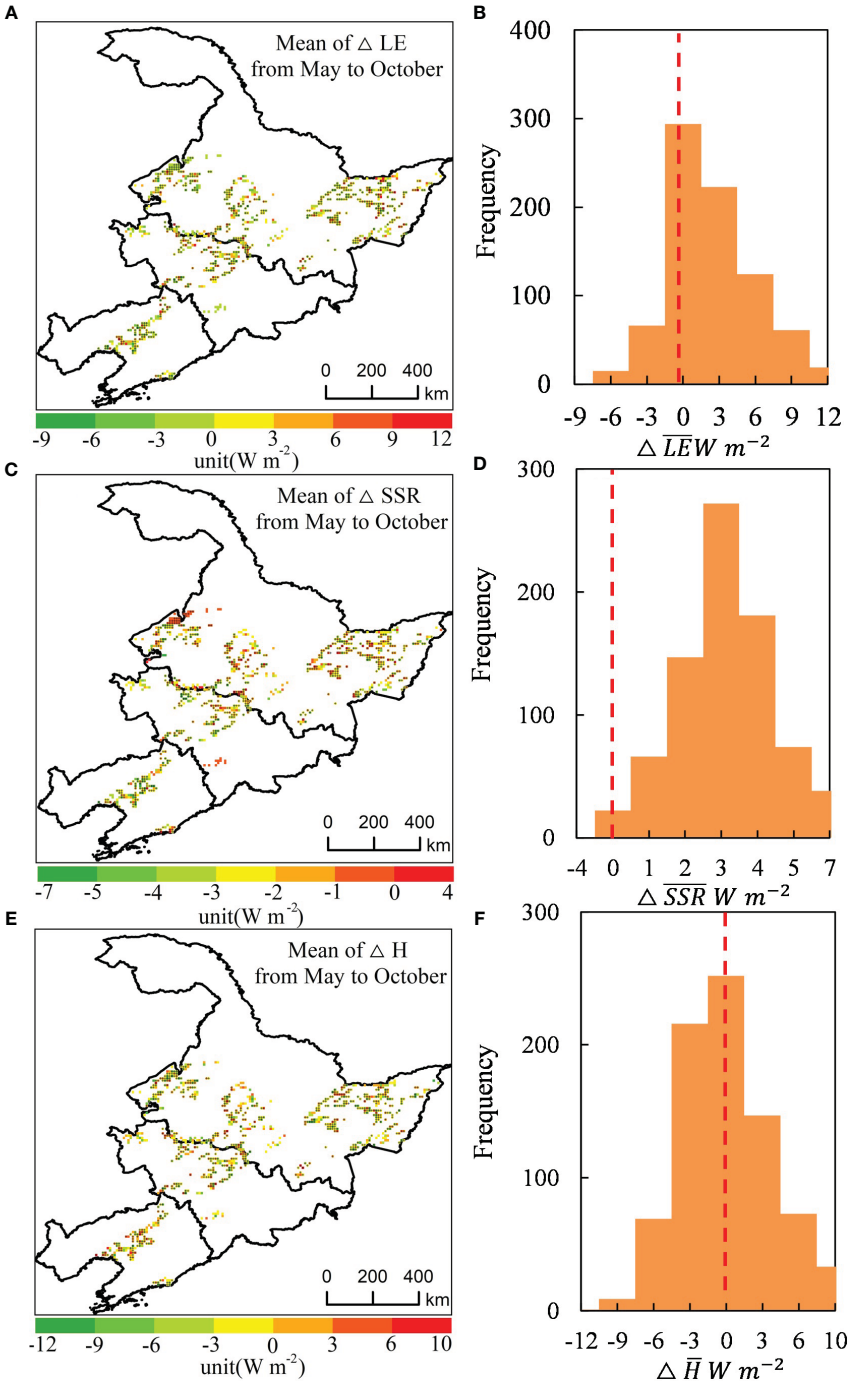

FIGURE 5
The land surface radiation energy differences of spatial patterns, latitudinal distributions, and frequency histograms of irrigated crops and the adjacent rainfed crops during the growing season of 2015–2020. **(A, B)** The spatial distribution map and the histogram of $\Delta\overline{LE}$. **(C, D)** The spatial distribution map and the histogram of $\Delta\overline{SSR}$. **(E, F)** The spatial distribution map and the histogram of $\Delta\bar{H}$. Grids with crosses indicate that the differences are significant at 95% by t-test, grey shadows represent standard deviation.

TABLE 4 The monthly average of ΔLE, ΔSSR and ΔH ($\pm SD$ W m^{-2}).

	May	June	July	August	September	October
ΔLE	5.2 ±0.9	6.8 ±1.0	12.7 ±0.9	3.2 ±1.1	−4.7 ±0.9	0.2 ±0.9
ΔSSR	11.1 ±2.7	11.4 ±4.2	−1 ±2.4	−2.6 ±4.3	−3.5 ±3.0	−1.4 ±2.3
ΔH	5.9 ±2.8	4.6 ±3.7	−13.7 ±2.9	−5.8 ±2.3	1.2 ±3.2	−1.6 ±2.6

10.3389/fevo.2023.1208601

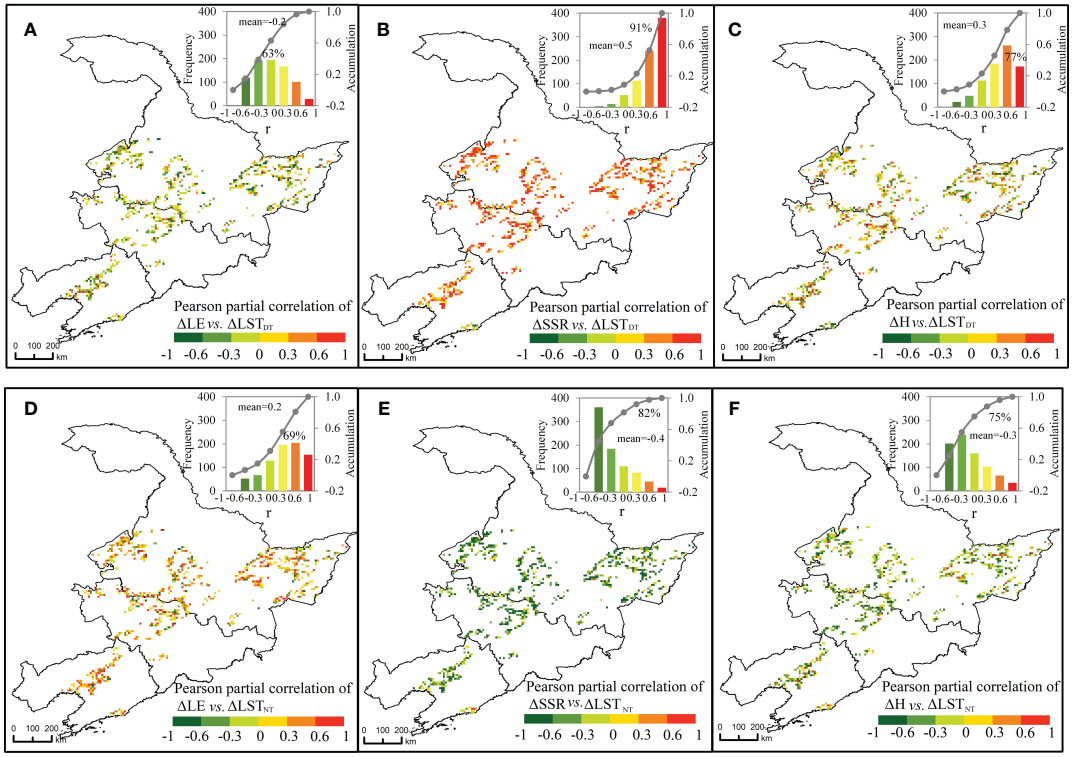

FIGURE 6
Spatial distribution of time scale correlation and their frequency histograms between diurnal LST change and biophysical parameters change during growing seasons. **(A–C)** Correlation between ΔLST_{DT} and ΔLE, ΔSSR, ΔH. **(D–F)** Correlation between ΔLST_{NT} and ΔLE, ΔSSR, ΔH.

TABLE 5 The *q*-value of the single effects for different driving mechanism on ΔLST_{DT}, *representing $p<0.05$, **representing $p<0.01$.

	May	June	July	August	September	October
ΔLE *vs.* ΔLST_{DT}	0.18	0.10	0.48**	0.24	0.57**	0.10
ΔSSR *vs.* ΔLST_{DT}	0.25*	0.17	0.1	0.38*	0.10	0.43*
ΔH *vs.* ΔLST_{DT}	0.29*	0.22*	0.47**	0.41*	0.81**	0.51**

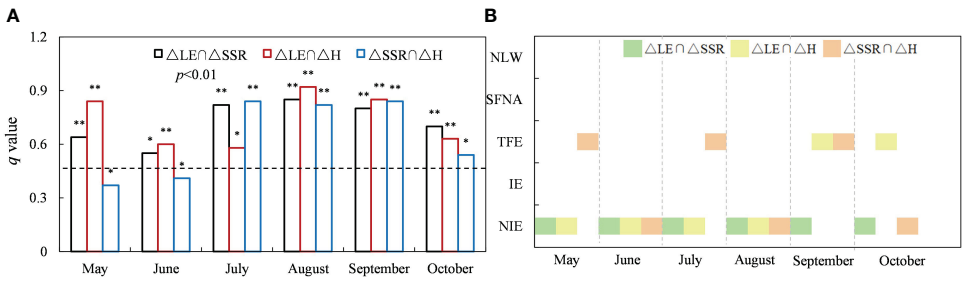

FIGURE 7
The spatial correlation between ΔLE (ΔSSR and ΔH) and ΔLST_{DT} from May to October. **(A)** Interaction detection results (*q*-value). **(B)** Interaction detector classifications. *representing $p<0.05$, **representing $p<0.01$.

TABLE 6 The *q*-value of the single effects for different driving mechanism on ΔLST_{NT}. *representing $p<0.05$, **representing $p<0.01$.

	May	June	July	August	September	October
ΔLEvs ΔLST_{NT}	0.27	0.15	0.28	0.39*	0.1	0.23
ΔSSRvs ΔLST_{NT}	0.16	0.1	0.1	0.3	0.10	0.12
ΔHvs ΔLST_{NT}	0.29	0.12	0.18	0.65**	0.1	0.1

($q<0.5$). The interaction effects of $\Delta LE \cap \Delta H$ and $\Delta SSR \cap \Delta H$ were non-linear enhancements, except for August (two-factor enhancement), but $\Delta LE \cap \Delta SSR$ was all non-linear enhancements throughout the growing season (Figure 8B).

4 Discussion

4.1 Analysis of the time variation of LST and biophysical parameters

The effect of the expansion of irrigated crops on land surface temperature in cold regions China has attracted widespread attention. It is generally believed that during the growing season, the change range of LST is between 1.3°C and 2.0°C during daytime and between 0.8°C and 1.1°C during nighttime (Liu et al., 2018; Liu et al., 2019a; Yu and Liu, 2019; Liu et al., 2022). Previous researches have explored the state of surface temperature variation on a seasonal or interannual scale. This work, we gathered more detailed dynamic information through a fine time scale in 8 day (Figures 9A, B). In addition, we averaged the time series information over nearly 5 years to prevent extreme climate disturbances, such as extreme heat, heat waves, and droughts. Previous studies analyzing the response mechanisms of land surface temperature changes have divided the growing season into different stages (e.g., early growing season, late-growing season) on a monthly scale, and thus, the details of LST time series changes were weakened. Because of the high sensitivity of land surface temperature, the inconsistency of surrounding features (urban, farmland) and climatic conditions (wind speed, wind direction) significantly affected the regional scale LST (Li et al., 2013; Ma et al., 2022). Therefore, when exploring the influence mechanism of LST changes in different process frameworks as well as different research areas, the growing season should be accurately divided according to the crop farming time in the study area. To effectively capture the response mechanism's temporal dynamic characteristics (Figures 9C–F).

4.2 Analysis of the spatial variation of LST and biophysical parameters

We found significant spatial heterogeneity in the diurnal LST differences from May to October. Among these distinctions was the irrigation time for paddy fields in early May, when the water content of the subsurface was much higher than that of non-irrigated crops (Figures 10A, 11B). During the day, irrigation crops had a high evapotranspiration capacity, but at night, the specific heat capacity of water was greater than that of bare soil, which played a role in heat preservation (Jin et al., 2016). The paddy fields were tillered in mid-June, when the surrounding crops were cultivated, and the difference in surface water-heat energy between low vegetation and bare soil was large (Figures 10B, 11B), which eventually led to a significant variation in LST between the irrigated and non-irrigated crops (Dong et al., 2014). July–August was the booting period of irrigated crops, when the land surfaces of irrigated and non-irrigated crops were covered with a large amount of vegetation at the same time. The land surface evapotranspiration capacity, water consumption-renewal capacity, and solar shortwave radiation absorption capacity of irrigated crops were comparable to non-irrigated crops (Figures 10C, D, 11C, D) (Gorguner and Kavvas, 2020; Jiang et al., 2021). September–October was the crop harvesting period, when bare soil was the major land surface cover type and the soil moisture content of irrigated and non-irrigated crops was similar (Cierniewski and Ceglarek, 2018; Rojas et al., 2020), and eventually, the difference in harvesting time-points led to heterogeneity in their diurnal LST differences on a spatial scale (Figures 10E, F, 11E, F). Moreover, the cold regions of China had a

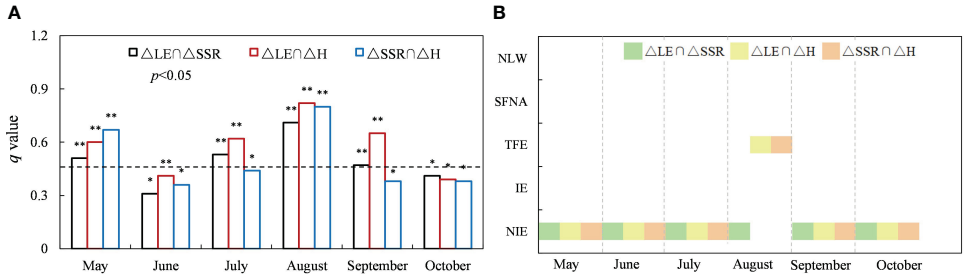

FIGURE 8
The spatial correlation between ΔLE (ΔSSR and ΔH) and ΔLST_{NT} from May to October. **(A)** Interaction detection results (q-value). **(B)** Interaction detector classifications. *representing $p<0.05$, **representing $p<0.01$.

10.3389/fevo.2023.1208601

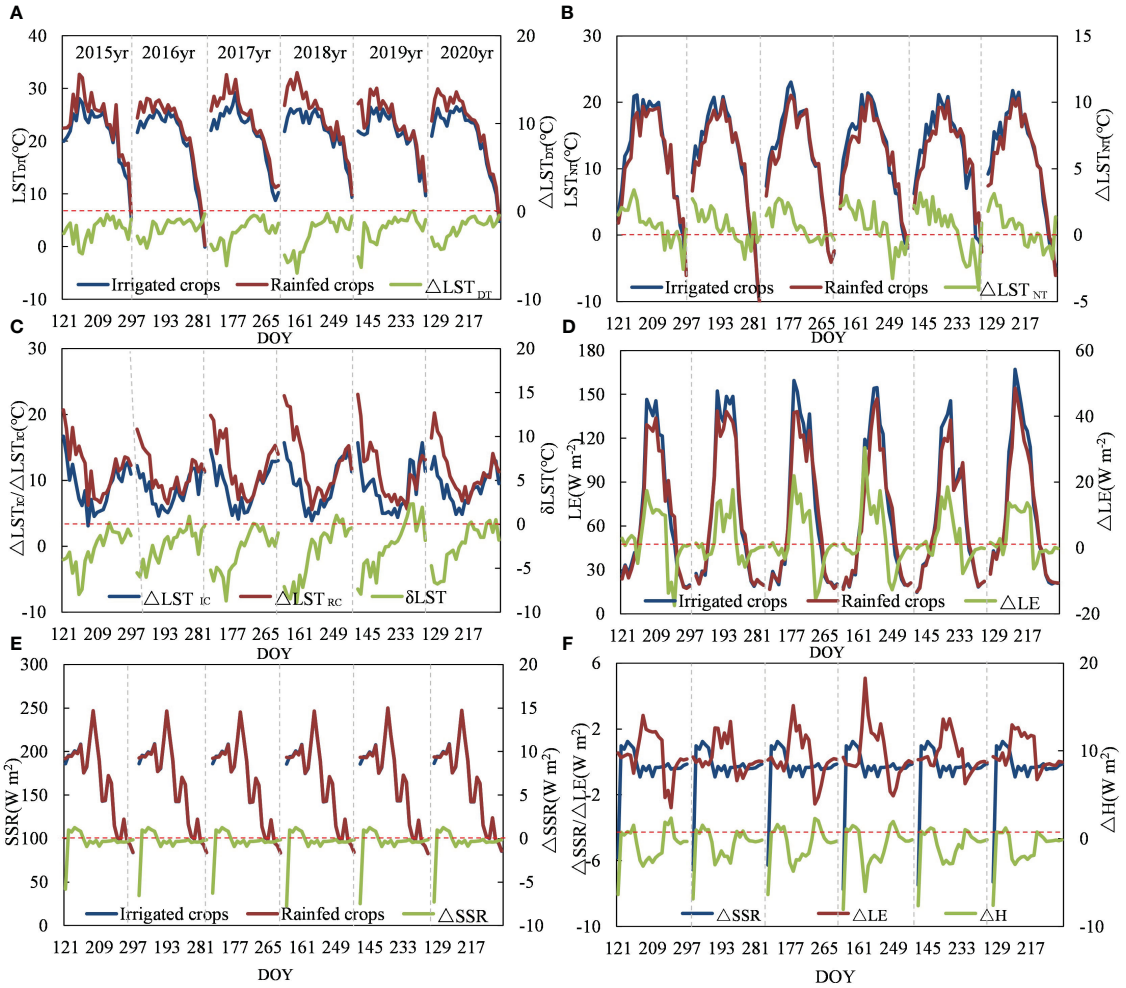

FIGURE 9
Temporal variation of land surface parameters of irrigated crops and the adjacent rainfed crops, and their differences from 2015 to 2020 (DOY=121–297). **(A)** Daytime LST, **(B)** nighttime LST, **(C)** diurnal LST, **(D)** latent heat flux, **(E)** solar shortwave radiation, **(F)** heating potential term.

vast north–south span, and the distribution of solar shortwave radiation varied substantially across latitudes, resulting in a climate with significant latitudinal zonality. As a result, the study area is spatially split based on crop harvest time points and climate variances to investigate the interpretation of surface water-heat energy balance to surface temperature changes in different regions and at different harvesting time points.

4.3 Exploring the effect mechanism of diurnal LST change

Numerous studies have found that irrigation crop expansion influence the spatial–temporal distribution of regional and even global climate primarily through biogeochemical processes and biophysical parameters. Among them, biophysical parameters play a larger role at regional scales than biogeochemical processes, such as the high latitudes of the Northern Hemisphere (Brovkin et al., 2006; Alkama and Cescatti, 2016). Many studies have investigated the effects of land use/cover changes (wetland to cropland or dryland to artificial wetland) on LST in the high-latitude regions, and most of them have explored the main influencing mechanisms of daytime on irrigated farmland changes from the perspectives of non-radiative mechanisms (evapotranspiration) and radiative mechanisms (albedo) (Liu et al., 2018; Liu et al., 2019a; Yu and Liu, 2019). In contrast, our study focuses on analyzing how the heating potential term responds to diurnal LST variations and finds that the LST variations are mainly due to the relative magnitudes of the surface energy income term (solar incident shortwave radiation), and the surface energy expenditure term (latent heat flux). Among them, irrigated crops ultimately lead to a decrease in the heating potential term during the growing season due to more latent heat flux exported from the surface and less solar shortwave radiation absorbed, which is consistent with the findings of the existing studies that there is a cooling effect on irrigated crops (Zhu et al., 2011; Yang et al., 2020; Zhang et al., 2022).

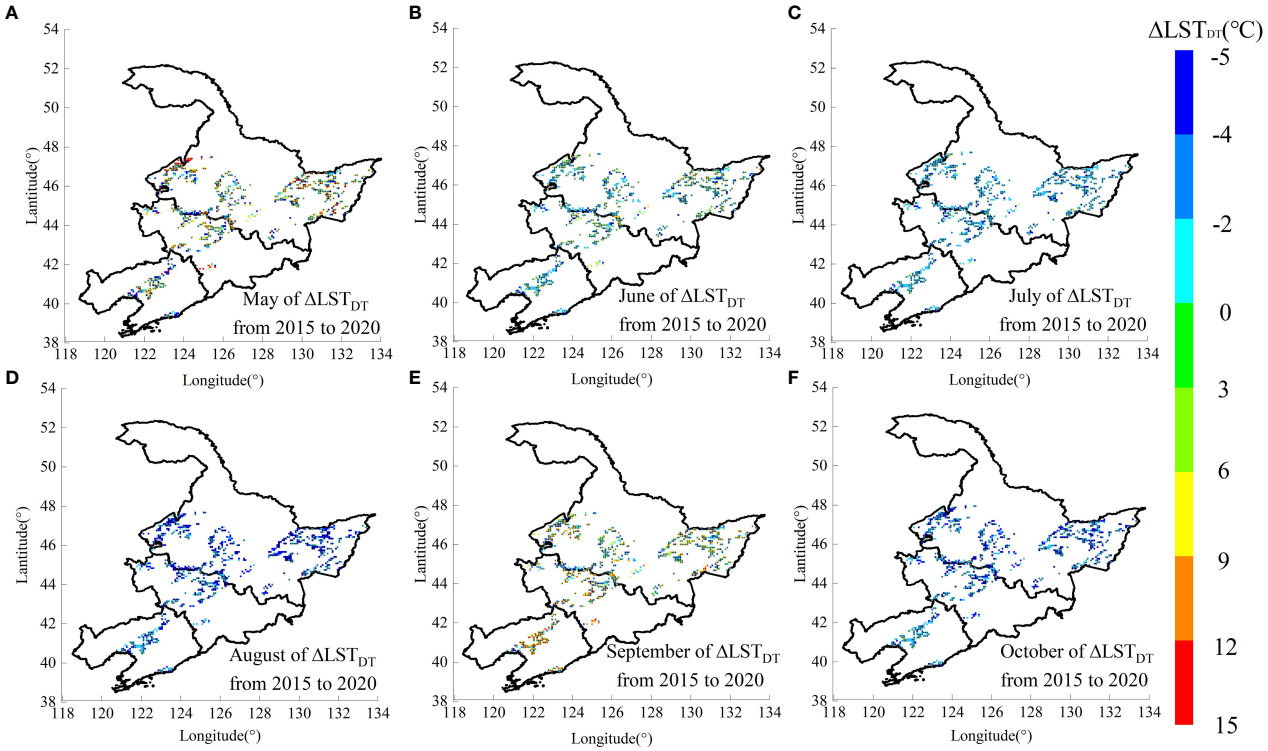

FIGURE 10
Monthly spatial variation of mean daytime land surface temperature from 2015 to 2020. **(A)** Daytime LST in May, **(B)** daytime LST in June, **(C)** daytime LST in July, **(D)** daytime LST in August, **(E)** daytime LST in September, **(F)** daytime LST in October.

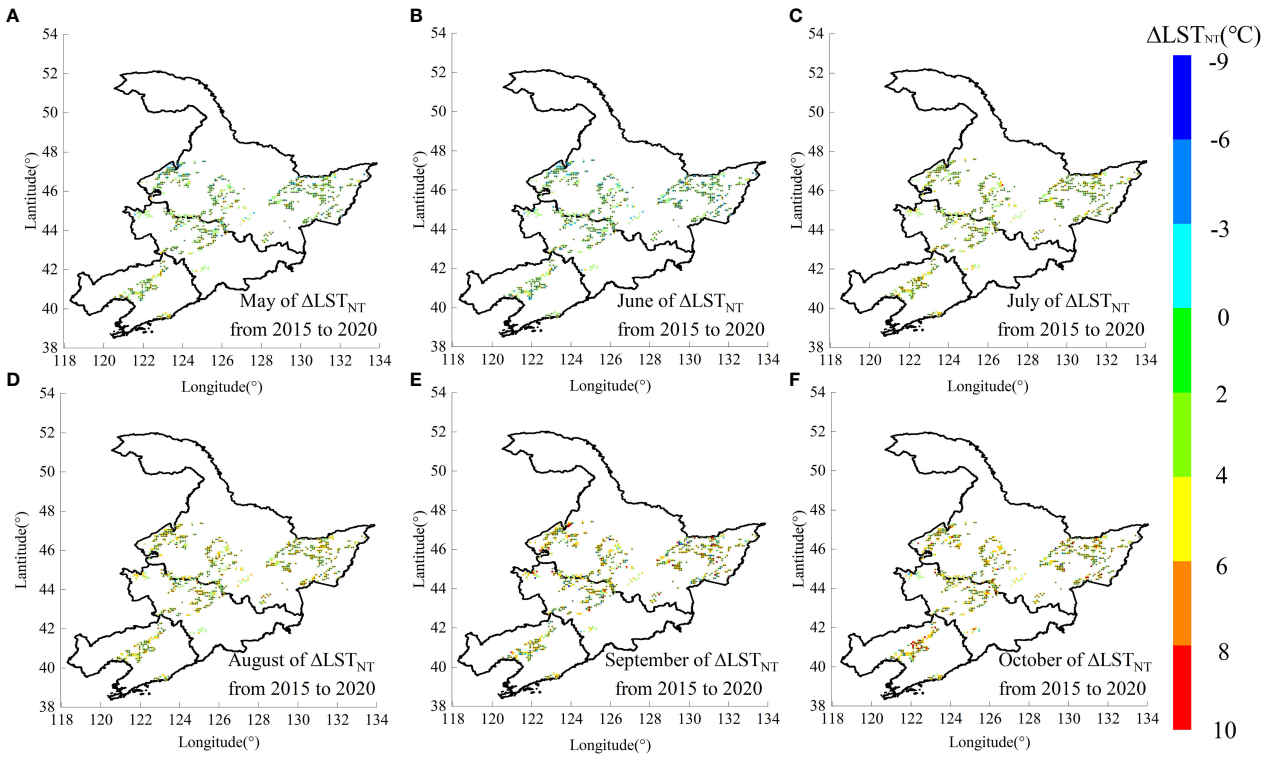

FIGURE 11
Monthly spatial variation of mean daytime land surface temperature from 2015 to 2020. **(A)** Nighttime LST in May, **(B)** nighttime LST in June, **(C)** nighttime LST in July, **(D)** nighttime LST in August, **(E)** nighttime LST in September, **(F)** nighttime LST in October.

As the influencing factors of nighttime LST were complex, the results of current studies on the influencing mechanism of nighttime LST change have not been fully proved (Yuan et al., 2022). Therefore, it remains challenging to explore the main influencing mechanism of nighttime LST, which is an issue for both afforestation and deforestation. (Peng et al., 2014; Li et al., 2016; Shen et al., 2019; Yuan et al., 2022). Existing studies have found that land use/cover changes in northeastern China enhance atmospheric water vapor mainly through evapotranspiration, which enhances downward atmospheric longwave radiation and strengthens the nighttime greenhouse warming effect through measured data (Li et al., 2017). We focused on the effect of the interaction between nighttime atmospheric inverse radiation as well as daytime thermal inertia on nighttime LST changes. However, it has also been suggested that the magnitude of the specific heat capacity of surface components is also a major mechanism influencing the nighttime LST, especially between regions with large differences in surface water content (Cao et al., 2019; Shen et al., 2022). Therefore, to accurately evaluate the main controlling factors of nighttime LST warming, we should comprehensively analyze the potential impact mechanism of warming from the multifactor perspective.

4.4 Uncertainties and future work

In this work, we assumed that irrigated crop expansion occurred in the region during 2015–2020. We emphasized the biophysical effects of "potential" changes in irrigated crops (paired comparison with surrounding non-irrigated crops) on diurnal LST change to accurately obtain more valid window samples and remove the climate background differences caused by long time series and large spans. Another concept that corresponds to "potential" change, namely the application of "actual" change, was reflected in a typical land use and cover changes (afforestation or deforestation.) study. They found that the effects of "potential" and "actual" changes in deforestation (afforestation) on diurnal LST were similar in most regions. So whether the impacts of potential and actual changes in irrigated crops on diurnal LST are consistent. We also wondered how the biophysical mechanisms affected the diurnal LST in the actual changes of irrigated crops. This study showed that the expansion of irrigated crops produced a cooling effect during the daytime and whether its effect could offset global warming caused by long-term human activities. In addition, the cooling effect of irrigated crops with different planting patterns was different, which raised the question of whether or not the cooling effect of high-density irrigated crops lasted longer than low-density. These issues require further exploration.

Because the input parameters of the observed MODIS LST products were not refined between irrigated and non-irrigated crops, they did not consider the species specificity between different crops. As a result, the differences in LST between crops were underestimated. Furthermore, the current thermal infrared remote-sensing satellites are characterized by mutually exclusive spatial–temporal resolutions, and it is difficult for a single remote-sensing sensor to obtain LST data with high spatial–temporal resolutions. Following that, we used a multisource data fusion approach to obtain an all-weather, high-spatial-resolution LST dataset to meet the needs for fine monitoring of LST.

5 Conclusions

The expansion of irrigated crops in the Northeast China significantly altered regional climate, as revealed by our synergetic investigation based on multi-source remote sensing satellite data and the pairwise comparison method. We found an asymmetric variation in diurnal LST, with daytime LST varying more than nighttime LST. The daytime cooling and nighttime warming effects were mainly due to the fact that latent heat fluxes released from irrigated crops is greater than the solar shortwave radiation absorbed, resulting in less heating potential term. The variation in the average land surface parameters had spatial heterogeneity during the growing season. The diurnal LST variation was affected by different energy factors, and its response to land surface energy was accompanied by a lag effect. ΔLST_{DT} followed a decreasing trend as ΔLE increased, but it followed an increasing trend as ΔSSR and ΔH increased. This result indicated that the decrease in LST_{DT} was mainly due to the cooling effect of thermal energy of output and input of irrigated crops to offset the warming effect. ΔLST_{NT} showed an increasing trend with increasing ΔLE and a decreasing trend with increasing ΔSSR and ΔH. This result demonstrated that the increase in the LST_{NT} was due to the fact that the latent heat flux of irrigated crops and the accumulated daytime heating potential term had a greater warming effect than the cooling effect at night from May to October. The degree of influence of the interaction factor on the difference of diurnal LST was significantly greater than the single factor effect. Our study provided a new perspective for comprehending how human activities have an impact on regional, and even global climate change by revealing the spatiotemporal pattern of the biophysical effects of irrigated crop expansion.

Data availability statement

The original contributions presented in the study are included in the article/supplementary material. Further inquiries can be directed to the corresponding author.

Author contributions

XL: Conceptualization, Methodology, Validation, Formal analysis, Investigation, Data Curation, Writing – Original Draft,

Visualization. QH: Writing – Review & Editing, Supervision, Funding acquisition. KX: Writing – Review & Editing, Visualization. BV: Supervision, Funding acquisition. YB: Supervision, Project administration. All authors contributed to the article and approved the submitted version.

Funding

All authors appreciated the financially support for the present study which was founded by the International Cooperation and Exchange Program of National Natural Science Foundation of China (41961144019) and key research base of humanities and social sciences in universities of Inner Mongolia Autonomous Region-Yinshan Cultural Research Center research project (23YSYJ00014).

Conflict of interest

The authors declare that the research was conducted in the absence of any commercial or financial relationships that could be construed as a potential conflict of interest.

Publisher's note

References

Abera, T. A., Heiskanen, J., Pellikka, P., Rautiainen, M., and Maeda, E. E. (2019). Clarifying the role of radiative mechanisms in the spatio-temporal changes of land surface temperature across the Horn of Africa. *Remote Sens. Environ.* 221, 210–224. doi: 10.1016/j.rse.2018.11.024

Adegoke, J. O., Pielke, R. A. Sr., Eastman, J., Mahmood, R., and Hubbard, K. G. (2003). Impact of irrigation on midsummer surface fluxes and temperature under dry synoptic conditions: A regional atmospheric model study of the US High Plains. *Monthly Weather Rev.* 131 (3), 556–564. doi: 10.1175/1520-0493(2003)131<0556:IOIOMS>2.0.CO;2

Alkama, R., and Cescatti, A. J. S. (2016). Biophysical climate impacts of recent changes in global forest cover. *Science* 351, 600–6046273. doi: 10.1126/science.aac8083

Arora, V. K., and Montenegro, A. J. N. G. (2011). Small temperature benefits provided by realistic afforestation efforts. *Nat. Geosci.* 4 (8), 514–518. doi: 10.1038/ngeo1182

Bajželj, B., Richards, K. S., Allwood, J. M., Smith, P., Dennis, J. S., Curmi, E., et al. (2014). Importance of food-demand management for climate mitigation. *Nat. Climate Change* 4 (10), 924–929.

Bonan, G. B., Pollard, D., and Thompson, S. L. (1992). Effects of boreal forest vegetation on global climate. *Nature* 359, 716–718. doi: 10.1038/359716a0

Brovkin, V., Claussen, M., Driesschaert, E., Fichefet, T., Kicklighter, D., Loutre, M. F., et al. (2006). Biogeophysical effects of historical land cover changes simulated by six earth system models of intermediate complexity. *Climate Dynamics* 26, 587–600. . doi: 10.1007/s00382-005-0092-6

Cao, Q., Wu, J., Yu, D., Wang, W. J. A., and Meteorology, F. (2019). The biophysical effects of the vegetation restoration program on regional climate metrics in the Loess Plateau, China. *Agric. For. Meteorology* 268, 169–180. doi: 10.1016/j.agrformet.2019.01.022

Chen, C., Ge, J., Guo, W., Cao, Y., Liu, Y., Luo, X., et al. (2022). The biophysical impacts of idealized afforestation on surface temperature in china: Local and nonlocal effects. *J. Climate* 35 (23), 7833–7852. doi: 10.1175/JCLI-D-22-0144.1

Chen, W., Wang, Y., Zhao, Z., Cui, F., Gu, J., and Zheng, X. (2013). The effect of planting density on carbon dioxide, methane and nitrous oxide emissions from a cold paddy field in the sanjiang plain, northeast china. *Agriculture Ecosyst. Environ.* 178, 64–70. doi: 10.1016/j.agee.2013.05.008

Chen, X., and Jeong, S.-J. (2018). Irrigation enhances local warming with greater nocturnal warming effects than daytime cooling effects. *Environ. Res. Lett.* 13 (2), 024005. doi: 10.1088/1748-9326/aa9dea

Christy, J. R., Norris, W. B., Redmond, K., and Gallo, K. P. (2006). Methodology and results of calculating central California surface temperature trends: evidence of human-induced climate change? *J. Climate* 19 (4), 548–563. doi: 10.1175/JCLI3627.1

Cierniewski, J., and Ceglarek, J. (2018). Annual dynamics of shortwave radiation of bare arable lands on a global scale incorporating their roughness. *Environ. Earth Sci.* 77 (23), 1–17. doi: 10.1007/s12665-018-7956-7

Delzeit, R., Zabel, F., Meyer, C., and Václavík, T. (2017). Addressing future trade-offs between biodiversity and cropland expansion to improve food security. *Regional Environ. Change* 17 (5), 1429–1441. doi: 10.1007/s10113-016-0927-1

Dong, Z., Wang, Z., Liu, D., Song, K., Li, L., Jia, M., et al. (2014). Mapping wetland areas using landsat-derived NDVI and LSWI: A case study of west songnen plain, northeast china. *J. Indian Soc. Remote Sens.* 42, 569–576. doi: 10.1007/s12524-013-0357-1

Dong, J., Xiao, X., Zhang, G., Menarguez, M. A., Choi, C. Y., Qin, Y., et al. (2016). Northward expansion of paddy rice in northeastern asia during 2000 -2014. *Geophysical Res. Lett.* 43 (8), 3754–3761. doi: 10.1002/2016GL068191

Du, H., He, H. S., Wu, Z., Wang, L., Zong, S., and Liu, J. (2017). Human influences on regional temperature change -comparing adjacent plains of china and russia. *Int. J. Climatology* 37 (6), 2913–2922. doi: 10.1002/joc.4888

FAO. (2018). *Food and agriculture organization of the United Nations*. Available at: http://faostat.

Feddema, J. J., Oleson, K. W., Bonan, G. B., Mearns, L. O., Buja, L. E., Meehl, G. A., et al. (2005). The importance of land-cover change in simulating future climates. *Science* 310 (5754), 1674–1678. doi: 10.1126/science.1118160

Gaupp, F., Hall, J., Hochrainer-Stigler, S., and Dadson, S. (2020). Changing risks of simultaneous global breadbasket failure. *Nat. Climate Change* 10 (1), 54–57. doi: 10.1038/s41558-019-0600-z

Gorguner, M., and Kavvas, M. L. (2020). Modeling impacts of future climate change on reservoir storages and irrigation water demands in a Mediterranean basin. *Sci. Total Environ.* 748, 141246. doi: 10.1016/j.scitotenv.2020.141246

He, Y., Lee, E., and Mankin, J. S. (2020). Seasonal tropospheric cooling in Northeast China associated with cropland expansion. *Environ. Res. Lett.* 15 (3), 034032. doi: 10.1088/1748-9326/ab6616

Huang, Y., Yu, Y., Zhang, W., Sun, W., Liu, S., Jiang, J., et al. (2009). Agro-C: A biogeophysical model for simulating the carbon budget of agroecosystems. *Agric. For. Meteorology* 149 (1), 106–129. doi: 10.1016/j.agrformet.2008.07.013

Jiang, F., Xie, X., Liang, S., Wang, Y., Zhu, B., Zhang, X., et al. (2021). Loess plateau evapotranspiration intensified by land surface radiative forcing associated with ecological restoration. *Agric. For. Meteorology* 311, 108669. doi: 10.1016/j.agrformet.2021.108669

Jin, C., Xiao, X., Dong, J., Qin, Y., and Wang, Z. (2016). Mapping paddy rice distribution using multi-temporal Landsat imagery in the Sanjiang Plain, northeast China. *Front. Earth Sci.* 10 (1), 49–62. doi: 10.1007/s11707-015-0518-3

Li, Z.-L., Tang, B. H., Wu, H., Ren, H., Yan, G., Wan, Z., et al. (2013). Satellite-derived land surface temperature: Current status and perspectives. *Remote Sens. Environ.* 131, 14–37. doi: 10.1016/j.rse.2012.12.008

Li, Y., Zhao, M., Motesharrei, S., Mu, Q., Kalnay, E., and Li, S. (2015). Local cooling and warming effects of forests based on satellite observations. *Nat. Commun.* 6 (1), 6603. doi: 10.1038/ncomms7603

Li, Y., Zhao, M., Mildrexler, D. J., Motesharrei, S., Mu, Q., Kalnay, E., et al. (2016). Potential and actual impacts of deforestation and afforestation on land surface temperature. *J. Geophysical Research: Atmospheres* 121 (24), 14–372. doi: 10.1002/2016JD024969

Li, X., Zhang, X., and Zhang, L. (2017). Observed effects of vegetation growth on temperature in the early summer over the northeast China plain. *Atmosphere* 8 (6), 97. doi: 10.3390/atmos8060097

Lian, X., Jeong, S., Park, C. E., Xu, H., Li, L. Z., Wang, T., et al. (2022). Biophysical impacts of northern vegetation changes on seasonal warming patterns. *Nat. Commun.* 13 (1), 3925. doi: 10.1038/s41467-022-31671-z

Liang, S., Li, Y., Zhang, X., Sun, Z., Sun, N., Duan, Y., et al. (2018). Response of crop yield and nitrogen use efficiency for wheat-maize cropping system to future climate change in northern china. *Agric. For. Meteorology* 262, 310–321. doi: 10.1016/j.agrformet.2018.07.019

Liu, W., Dong, J., Du, G., Zhang, G., Hao, Z., You, N., et al. (2022). Biophysical effects of paddy rice expansion on land surface temperature in northeastern asia. *Agric. For. Meteorology* 315, 108820. doi: 10.1016/j.agrformet.2022.108820

Liu, T., Yu, L., Bu, K., Yan, F., and Zhang, S. (2018). Seasonal local temperature responses to paddy field expansion from rain-fed farmland in the cold and humid Sanjiang Plain of China. *Remote Sens.* 10 (12), 2009. doi: 10.3390/rs10122009

Liu, T., Yu, L., and Zhang, S. J. (2019a). Impacts of wetland reclamation and paddy field expansion on observed local temperature trends in the Sanjiang Plain of China. *J. Geophysical Research: Earth Surface* 124 (2), 414–426. doi: 10.1029/2018JF004846

Liu, T., Yu, L., and Zhang, S. J. S. R. (2019b). Land surface temperature response to irrigated paddy field expansion: a case study of semi-arid western Jilin Province, China. *Sci. Rep.* 9 (1), 1–8. doi: 10.1038/s41598-019-41745-6

Lobell, D., Bala, G., Mirin, A., Phillips, T., Maxwell, R., and Rotman, D. (2009). Regional differences in the influence of irrigation on climate. *J. Climate* 22 (8), 2248–2255. doi: 10.1175/2008JCLI2703.1

Ma, Y., Zhou, J., Liu, S., Zhang, W., Zhang, Y., Xu, Z., et al. (2022). Estimation of evapotranspiration using all-weather land surface temperature and variational trends with warming temperatures for the river source region in southwest china. *J. Hydrology* 613, 128346. doi: 10.1016/j.jhydrol.2022.128346

Malyshev, S., Shevliakova, E., Stouffer, R. J., and Pacala, S. W. (2015). Contrasting local versus regional effects of land-use-change-induced heterogeneity on historical climate: analysis with the GFDL earth system model. *J. Climate* 28 (13), 5448–5469. doi: 10.1175/JCLI-D-14-00586.1

Moon, M., Li, D., Liao, W., Rigden, A. J., and Friedl, M. A. (2020). Modification of surface energy balance during springtime: The relative importance of biophysical and meteorological changes. *Agric. For. Meteorology* 284, 107905. doi: 10.1016/j.agrformet.2020.107905

Mu, Q., Zhao, M., and Running, S. W. (2011). Improvements to a MODIS global terrestrial evapotranspiration algorithm. *Remote Sens. Environ.* 115 (8), 1781–1800. doi: 10.1016/j.rse.2011.02.019

Pan, T., Zhang, C., Kuang, W., Luo, G., Du, G., and Yin, Z.. (2020). Large-scale rain-fed to paddy farmland conversion modified land-surface thermal properties in Cold China. *Sci. Total Environ.* 722, 137917. doi: 10.1016/j.scitotenv.2020.137917

Peng, S. S., Piao, S., Zeng, Z., Ciais, P., Zhou, L., Li, L. Z., et al. (2014). Afforestation in china cools local land surface temperature. *Proc. Natl. Acad. Sci.* 111 (8), 2915–2919. doi: 10.1073/pnas.1315126111

Pongratz, J., Reick, C., Raddatz, T., and Claussen, M. (2010). Biogeophysical versus biogeochemical climate response to historical anthropogenic land cover change. *Geophysical Res. Lett.* 37 (8). doi: 10.1029/2010GL043010

Qiu, B., Hu, X., Chen, C., Tang, Z., Yang, P., Zhu, X., et al. (2022). Maps of cropping patterns in china during 2015 -2021. *Sci. Data* 9 (1), 479. doi: 10.1038/s41597-022-01589-8

Rojas, F., Rubio, C., Rizzo, M., Bernabeu, M., Akil, N., and Martín, F. (2020). Land use and land cover in irrigated drylands: a long-term analysis of changes in the mendoza and tunuyán river basins, argentin-2018). *Appl. Spatial Anal. Policy* 13, 875–899. doi: 10.1007/s12061-020-09335-6

Sacks, W. J., Cook, B. I., Buenning, N., Levis, S., and Helkowski, J. H. (2009). Effects of global irrigation on the near-surface climate. *Climate Dynamics* 33 (2), 159–175. doi: 10.1007/s00382-008-0445-z

Schaaf, C. B., Gao, F., Strahler, A. H., Lucht, W., Li, X., Tsang, T., et al. (2002). Albedo nadir reflectance products from MODIS. *Remote Sens. Environ.* 83 (1-2), 135–148. doi: 10.1016/S0034-4257(02)00091-3

Schultz, N. M., Lawrence, P. J., and Lee, X. J. (2017). Global satellite data highlights the diurnal asymmetry of the surface temperature response to deforestation. *J. Geophysical Research: Biogeosciences* 122 (4), 903–917. doi: 10.1002/2016JG003653

Schultz, N. M., Lee, X., Lawrence, P. J., Lawrence, D. M., and Zhao, L. J. (2016). Assessing the use of subgrid land model output to study impacts of land cover change. *J. Geophysical Research: Atmospheres* 121 (11), 6133–6147. doi: 10.1002/2016JD025094

Shen, W., Li, M., Huang, C., He, T., Tao, X., and Wei, A. (2019). Local land surface temperature change induced by afforestation based on satellite observations in guangdong plantation forests in china. *Agric. For. Meteorology* 276, 107641. doi: 10.1016/j.agrformet.2019.107641

Shen, X., Liu, Y., Liu, B., Zhang, J., Wang, L., Lu, X., et al. (2022). Effect of shrub encroachment on land surface temperature in semi-arid areas of temperate regions of the Northern Hemisphere 320, 108943. doi: 10.1016/j.agrformet.2022.108943

Sun, M., Zhang, Y., Ma, J., Yuan, W., Li, X., and Cheng, X.. (2017). Satellite data based estimation of methane emissions from rice paddies in the Sanjiang Plain in northeast China. *PloS One* 12 (6). doi: 10.1371/journal.pone.0176765

Umair, M., Kim, D., Ray, R. L., Choi, M. J. A., and Meteorology, F. (2020). Evaluation of atmospheric and terrestrial effects in the carbon cycle for forest and grassland ecosystems using a remote sensing and modeling approach. *Agric. For. Meteorology* 295, 108187. doi: 10.1016/j.agrformet.2020.108187

van Dijk, M., Morley, T., Rau, M. L., and Saghai, Y. (2021). A meta-analysis of projected global food demand and population at risk of hunger for the period 2010–2050. *Nat. Food* 2 (7), 494–501. doi: 10.1038/s43016-021-00322-9

Wan, Z., Hook, S., and Hulley, G. (2015). MOD11A2 MODIS/Terra land surface temperature/emissivity 8-day L3 global 1km SIN grid V006. *Nasa Eosdis Land Processes Daac* 10, 10.5067. doi: 10.5067/MODIS/MOD11A2.006

Wei, Y., Tang, D., Ding, Y., and Agoramoorthy, G. (2016). Incorporating water consumption into crop water footprint: A case study of China's South–North Water Diversion Project. *Sci. Total Environ.* 545, 601–608. doi: 10.1016/j.scitotenv.2015.12.062

Winckler, J., Reick, C. H., and Pongratz, J. J. (2017). Robust identification of local biogeophysical effects of land-cover change in a global climate model. *J. Climate* 30 (3), 1159–1176. doi: 10.1175/JCLI-D-16-0067.1

Windisch, M. G., Davin, E. L., and Seneviratne, S. I. (2021). Prioritizing forestation based on biogeochemical and local biogeophysical impacts. *Nat. Climate Change* 11 (10), 867–871. doi: 10.1038/s41558-021-01161-z

Xin, F., Xiao, X., Dong, J., Zhang, G., Zhang, Y., Wu, X., et al. (2020). Large increases of paddy rice area, gross primary production, and grain production in northeast china during 2000–2017. *Sci. Total Environ.* 711, 135183. doi: 10.1016/j.scitotenv.2019.135183

Yang, Q., Huang, X., and Tang, Q. (2020). Irrigation cooling effect on land surface temperature across China based on satellite observations. *Sci. Total Environ.* 705, 135984. doi: 10.1016/j.scitotenv.2019.135984

Yu, L., and Liu, T. J. R. S. (2019). The impact of artificial wetland expansion on local temperature in the growing season—The case study of the Sanjiang Plain, China. *Remote Sens.* 11 (24), 2915. doi: 10.3390/rs11242915

Yuan, G., Tang, W., Zuo, T., Li, E., Zhang, L., and Liu, Y. (2022). Impacts of afforestation on land surface temperature in different regions of china. *Agric. For. Meteorology* 318, 108901. doi: 10.1016/j.agrformet.2022.108901

Zhang, W., Jansson, C., Miller, P. A., Smith, B., and Samuelsson, P. J. B. (2014a). Biogeophysical feedbacks enhance the Arctic terrestrial carbon sink in regional Earth system dynamics. *Biogeosciences* 11 (19), 5503–5519. doi: 10.5194/bg-11-5503-2014

Zhang, X., Liang, S., Zhou, G., Wu, H., and Zhao, X. (2014b). Generating Global LAnd Surface Satellite incident shortwave radiation and photosynthetically active radiation products from multiple satellite data. *Remote Sens. Environ.* 152, 318–332. doi: 10.1016/j.rse.2014.07.003

Zhang, Z., Lin, A., Zhao, L., and Zhao, B. (2022). Attribution of local land surface temperature variations response to irrigation over the North China Plain. *Sci. Total Environ.* 826, 154104. doi: 10.1016/j.scitotenv.2022.154104

Zhao, Y., Fang, Y., and Cui, C. (2012). Effects of irrigation on precipitation in the arid regions of Xinjiang, China. *J. Arid Land* 4 (2), 132–139. doi: 10.3724/SP.J.1227.2012.00132

Zhu, X., Liang, S., and Pan, Y. (2012). Observational evidence of the cooling effect of agricultural irrigation in Jilin, China. *Climatic Change* 114 (3), 799–811. doi: 10.1007/s10584-012-0435-3

Zhu, X., Liang, S., Pan, Y., Zhang, X., and Sensing, R. (2011). Agricultural irrigation impacts on land surface characteristics detected from satellite data products in Jilin Province, China. *IEEE J. Selected Topics Appl. Earth Observations Remote Sens.* 4 (3), 721–729. doi: 10.1109/JSTARS.2011.2106152

Zhu, L., Meng, J., and Zhu, L. (2020). Applying Geodetector to disentangle the contributions of natural and anthropogenic factors to NDVI variations in the middle reaches of the Heihe River Basin. *Ecol. Indic.* 117, 106545. doi: 10.1016/j.ecolind.2020.106545

Frontiers in
Environmental Science

Explores the anthropogenic impact on our natural world

An innovative journal that advances knowledge of the natural world and its intersections with human society. It supports the formulation of policies that lead to a more inhabitable and sustainable world.

Discover the latest Research Topics

See more →

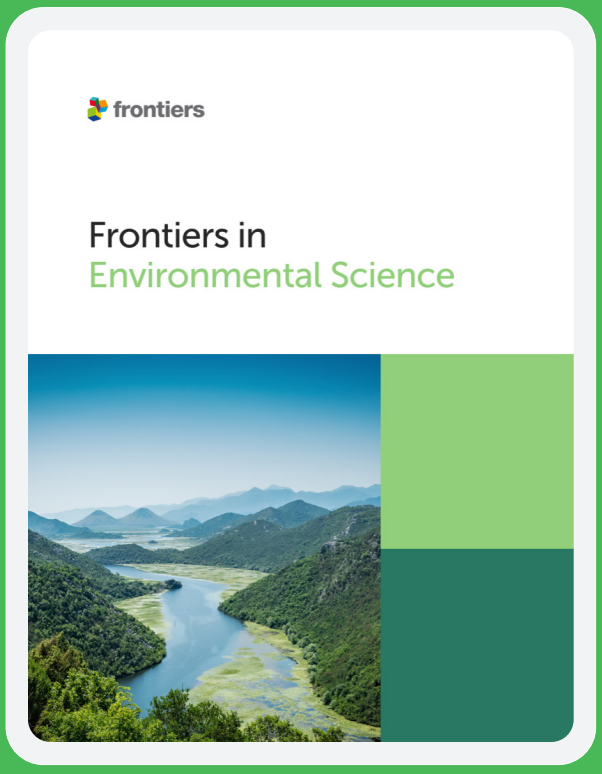

Frontiers

Avenue du Tribunal-Fédéral 34
1005 Lausanne, Switzerland
frontiersin.org

Contact us

+41 (0)21 510 17 00
frontiersin.org/about/contact